

Synthesis of molecularly-derived transition metal pnictides for efficient water-splitting

vorgelegt von

B. Sc.

Rodrigo Beltrán Suito

ORCID: 0000-0002-1997-509X

an der Fakultät II – Mathematik und Naturwissenschaften

der Technischen Universität Berlin

zur Erlangung des akademischen Grades

Doktor der Naturwissenschaften

- Dr. rer. nat. -

genehmigte Dissertation

Promotionsausschuss:

Vorsitzender: Prof. Dr. Reinhard Schomäcker

Erster Gutachter: Prof. Dr. Matthias Drieß

Zweiter Gutachter: Prof. Dr. Anna Fischer

Tag der wissenschaftlichen Aussprache: 30. Juli 2021

Berlin 2021

Die vorliegende Arbeit entstand in der Zeit von Oktober 2016 bis Dezember 2020 unter der Betreuung von Prof. Dr. Matthias Dri   am Institut f  r Chemie im Fachbereich Metallorganische Chemie und Anorganische Materialien der Technischen Universit  t Berlin.

Acknowledgments

Firstly, I would like to thank my supervisor Prof. Dr. Matthias Driess for his guidance, scientific suggestions and discussions, and scientific freedom he gave during the years I spent in the PhD. I would also like to thank Prof. Dr. Anna Fischer for reading this thesis and accepting to participate in the defense as a jury member. I also acknowledge Prof. Dr. Reinhard Schomäcker as Chairman of the doctoral commission.

Secondly, I would like to thank especially to Dr. Prashanth Menezes for his supervision in the laboratory work and scientific guidance, suggestions and help during this time. Without him, the completion and final realization of the experiments, this thesis and the publications related to it would not be possible. Dr. Vitaly Gutkin for the XPS analysis, Diplom Phys. Christoph Fahrenson from the ZELMI in TU Berlin for all the acknowledge associated to the SEM. A lot of thanks to the other colleagues former and current members of the Driess group: Dr. Carsten Walter and Jan Niklas Hausmann for reading the first drafts of this thesis and Dr. André Hermannsdorfer, Dr. Biswarup Chakraborty, Dr. Chakadola Panda, Dr Ernesto Ballesterio, Alexander Durchert, Frank Czerny, Dr. Xiaohui Deng, Christopher Eberle, Viktoria Forstner, Min Ha Kim, Dr. Terrance Handlington, Shweta Kalra, Dr. Arseni Kostenko, Dr. Marcel-Philip Lücke, Dr. Jan Paulmann, Changkai Shan, Dr. Bochao Su, Noah Subat, Dr. Yuwen Wang, Dr. Yun Xiong, and Dr. Shenglai Yao. I would also like to mention other present and former members from the TU Berlin Institut für Chemie and other research groups: Dr. Michael Schwarze, Dr. Arindam Indra, Amitava Acharya, Andreal Rahmel, Stefan Schutte, Dr. Stephan Kohl, Dr. Julia Kohl, Mandy Prilwitz, Óscar Aguilar, Dr. Weiqang Wei, Dr. Victoria Rondón, Andreas Widkamp, and Konstatin Laun. Finally, members from scientific institutions in Berlin and abroad, which helped as collaborators for this research: Prof. Dr. Holger Dau, Dr. Stefan Mebs, Dr. Michael Haumann, and Dr. Ivelina Zaharieva.

I want to acknowledge the people related to the BIG-NSE program. Without them it will be impossible to finish this work, especially to Dr. Jean Philippe Lonjaret and Tatjana Kliwer for their welcome and help during the start of the doctoral program. The funding of for this work was provided by the Deutsche Forschungsgemeinschaft (DFG, German Research Foundation) under Germany's Excellence Strategy – EXC 2008/1 – 390540038 – UniSysCat.

Finally, I would like to acknowledge my parents, sister, and extended family, for all their support for doing this work. Also, to my former advisor Prof. Dr. María del Rosario Sun Kou which whom I started my scientific career at the Pontificia Universidad Católica del Perú. Finally, special thanks to my friends in Berlin and abroad that bring me happiness and joy to everyday life: Fotis, Enrique, Jordi, Carla, Carolina, Rodrigo, Clarissa, Alberto, Javier, Javi, Dani, Lesly, Sandra, Anabella, Chiara, Julisa, Ken, Leo, Óscar, Sebastián C., Sebastián B., Carlos, José Carlos, Fiorella, Felipe, Alexandros, Katerina, Eirini, Jakob, Giulia, Ana Carolina, David, Antonella, Fabiola, and Ángela.

Rodrigo Beltrán Suito

Publications

The work presented in this thesis was carried out at the Laboratory of Metalorganics and Inorganic Materials of the Institut für Chemie, Technische Universität Berlin, under the supervision of Prof. Dr. Matthias Driess, from January 2017 to June 2020. Some of the results of this thesis are contained partially or completely in the following scientific publications:

- R. Beltrán-Suito, P. W. Menezes, M. Driess. Amorphous outperforms crystalline nanomaterials: surface modifications of molecularly derived CoP electro(pre)catalysts for efficient water-splitting, *J. Mater. Chem. A*, **2019**, 7, 15749-15756 DOI: 10.1039/c9ta04583j
- R. Beltrán-Suito, V. Forstner, J. N. Hausmann, S. Mebs, J. Schmidt, I. Zaharieva, K. Laun, I. Zebger, H. Dau, P. W. Menezes, M. Driess. A Soft Molecular 2Fe-2As Precursor Approach to Nanostructured FeAs For Efficient Electrocatalytic Water Oxidation, *Chem. Sci.* **2020**, DOI: 10.1039/D0SC04384B

Collaborative articles:

- P.W. Menezes, C. Walter, J. Niklas Hausmann, R. Beltrán-Suito, C. Schlesiger, S. Praetz, V. Y. Verchenko, A. V. Shevelkov, M. Driess. Boosting Water Oxidation through In Situ Electroconversion of Manganese Gallide: An Intermetallic Precursor Approach, *Angew. Chem.* **2019**, 131, 16722–16727; *Angew. Chem. Int. Ed.* **2019**, 58, 16569-16574 DOI: 10.1002/anie.201909904
- J. N. Hausmann, E. M. Heppke, R. Beltrán-Suito, J. Schmidt, M. Mühlbauer, M. Lerch, P. W. Menezes, M. Driess. Stannites – A New Promising Class of Durable Electrocatalysts for Efficient Water Oxidation, *ChemCatChem* **2020**, 12, 1161 – 116 DOI: 10.1002/cctc.201901705
- B. Chakraborty, S. Kalra, R. Beltrán-Suito, C. Das, T. Hellmann, P. W. Menezes, M. Driess. A Low-Temperature Molecular Precursor Approach to Copper-Based Nano-Sized Digenite Mineral for Efficient Electrocatalytic Oxygen Evolution Reaction, *Chem Asian J.* **2020**, 15, 852-859 DOI: 10.1002/asia.20200000
- B. Chakraborty, R. Beltrán-Suito, V. Hlukhyy, J. Schmidt, P. W. Menezes, M. Driess. Crystalline Copper Selenide as a Reliable Non-Noble Electro(pre)catalyst for Overall Water-Splitting, *ChemSusChem* **2020**, 13, 322-3229 DOI: 10.1002/cssc.202000445R1
- B. Chakraborty,⁺ R. Beltrán-Suito,⁺ J. N. Hausmann, S. Garai, M. Driess, P. W. Menezes. Enabling Iron-Based Highly Effective Electrochemical Water-Splitting and Selective Oxygenation of Organic Substrates through In Situ Surface Modification of Intermetallic Iron Stannide Precatalyst, *Adv. Energy Mat.* **2020**, 10, 2001377 DOI: 10.1002/aenm.202001377

- P. W. Menezes,⁺ S. Yao,⁺ R. Beltrán-Suito,⁺ J. N. Hausmann, P. V. Menezes, M. Driess. Facile Access to an Active γ -NiOOH Electrocatalyst for Durable Water Oxidation Derived From an Intermetallic Nickel Germanide Precursor, *Angew. Chem.* **2021**, *133*, 4690 – 4697; *Angew. Chem. Int. Ed.* **2021**, *60*, 4640–4647 DOI: 10.1002/anie.202014331
- A. Indra,⁺ R. Beltrán-Suito,⁺ M. Müller, R. P. Sivasankaran, M. Schwarze, A. Acharjya, B. Pradhan, J. Hofkens, A. Brückner, A. Thomas, P. W. Menezes, M. Driess. Promoting Photocatalytic Hydrogen Evolution Activity of Graphitic Carbon Nitride with Hole Transfer Agents, *ChemSusChem.* **2021**, *14*, 306-312 DOI: 10.1002/cssc.202002500
- J. Niklas Hausmann, R. Beltrán-Suito, S. Mebs, V. Hlukhyy, T.F. Fässler, H. Dau, M. Driess., P.W. Menezes, Evolving Highly Active Oxidic Iron(III) Phase from Corrosion of Intermetallic Iron Silicide to Master Efficient Electrocatalytic Water Oxidation and Selective Oxygenation of 5-Hydroxymethylfurfural *Adv. Mat.* **2021**, *33*, 2008823 DOI: 10.1002/adma.202008823R2

Conferences, events and courses attended:

- Catalysis and Energy: from Synthesis to Application Summer School. Max Planck Institute for Chemical Energy Conversion. Gelsenkirchen, Germany (02.09.2018-07.09.2018).
- English Academic Writing. TU Berlin. Berlin, Germany (11.03-12.03.2019).
- International Bunsen-Discussion-Meeting Fundamentals and Applications of (Photo)Electrolysis for Efficient Energy Storage. Deutsche Bunsen-Gesellschaft für physikalische Chemie e.V. (DBG). Taormina, Italy (01.04-05.04.2019). *Amorphous Outperforms Crystalline Nanomaterial: Molecularly Derived CoP Electrocatalysts for Efficient Water-splitting* (Poster).
- Tag der Chemie 2019. TU Berlin. Berlin, Germany (11.07.2019). *Amorphous Outperforms Crystalline Nanomaterial: Molecularly Derived CoP Electrocatalysts for Efficient Water-splitting* (Poster prize).

Zusammenfassung

Die Erzeugung von erneuerbarem und nachhaltigem Strom kann mittels Brennstoffzellen durch die Reaktion von Wasserstoff (H_2) mit Sauerstoff (O_2) erreicht werden. Um den aktuellen Energiebedarf mit Brennstoffzellen abzudecken, werden große Mengen H_2 benötigt. Die alkalische Wasserelektrolyse ist die einzige ausgereifte Energieumwandlungstechnologie für die nachhaltige Erzeugung von H_2 durch die Wasserstoffentwicklungsreaktion (HER). Die Effizienz der Wasserspaltung wird durch die andere dazugehörige Halbreaktion, die Sauerstoffentwicklungsreaktion (OER), aufgrund der damit verbundenen mehrfachen Protonen gekoppelten Elektronentransferschritte (PCET) begrenzt. Derzeit sind Katalysatoren auf Ruthenium- und Iridiumbasis sowie Platin immer noch die *Benchmark*-Katalysatoren für praktische Anwendungen von OER und HER. Ihre hohen Kosten und ihre geringe Verfügbarkeit schränken jedoch ihre Verwendung im benötigten industriellen Maßstab ein. Pniktide von Übergangsmetallen (TM) sind aufgrund ihrer geringen Wasserstoffadsorptionsenergien, der schnelleren Reaktionskinetik und der elektrischen Leitfähigkeit zu einer attraktiven Wahl als OER- und HER-Elektrokatalysatoren geworden.

Gängige Synthesen für Übergangsmetallpniktide basieren auf Festkörpermethoden, die zu Materialien mit unkontrollierter Aggregation, heterogener Morphologie und zufälliger Zusammensetzung führen. Das Design von nanostrukturierten Elektrokatalysatoren mit spezifischer Größe, Stöchiometrie und Morphologie kann durch die molekulare Zersetzung von *Single-Source*-Vorläufern (SSP) erreicht werden. Die Abstimmung der experimentellen Bedingungen (z. B. Zersetzungsverfahren, Reaktionszeit, Temperatur, Lösungsmittel) führt zu Nanostrukturen mit unterschiedlichen Eigenschaften. In dieser Arbeit wurde ein molekularer Syntheseansatz verwendet, um auf Übergangsmetallphosphide (TM-Ps) und Arsenide (TM-As) zuzugreifen. Es wurden umfangreiche Untersuchungen durchgeführt, um die Kinetik und die elektronischen Prozesse während der Katalyse zu verstehen und diese mit den chemischen und elektronischen Umwandlungen der Materialien in Zusammenhang zu bringen.

Amorphe Materialien sind bekannt für ihre große elektrochemisch aktive Oberfläche (ECSA), die im Vergleich zu ihren kristallinen Gegenstücken normalerweise höhere elektrokatalytische Aktivitäten ermöglicht. Vor diesem Hintergrund wurden amorphes und kristallines Kobaltphosphid (CoP) durch Thermolyse (*Hot-Injection* und Pyrolyse) eines SSP synthetisiert. Amorphes CoP zeigte bei allen getesteten, elektrokatalytischen Reaktionen im Vergleich zum kristallinen CoP eine deutlich höhere Aktivität. Während der OER führten die elektrochemische Korrosion und Oxidation von Phosphor zur Bildung einer Co^{III} -(oxy)hydroxidhülle auf beiden Materialien. Das Vorhandensein von aktiven Co^{IV} OER-Zentren an der Oberfläche in Kombination mit Co^{III} führte zu verzerrten CoO_6 -Oktaedern (Jahn-Teller-Effekt), die die Absorption von Sauerstoffzwischenprodukten erleichterten. Während der HER führten ein vollständiger Verlust an Oberflächenphosphor und eine Oxidation der Oberfläche zur Bildung einer Co-angereicherten-(oxy)hydroxidphase, gefolgt von einer *in situ*-Reduktion zur

Erzeugung von Co^0 -aktiven Zentren für die HER. Der Unterschied in der Aktivität hing mit den einzigartigen elektronischen Eigenschaften und der hohen ECSA von amorphen Materialien zusammen, die eine größere Anzahl aktiver Zentren und eine größere Flexibilität bei der Katalyse bietet.

TM-As haben aufgrund der hohen Toxizität von As bei Wasserspaltungsanwendungen wenig Beachtung gefunden. Ihre hohe elektrische Leitfähigkeit macht diese Materialien jedoch für die OER-Elektrokatalyse aktiv. Kristalline FeAs-Nanopartikeln wurden durch *Hot-Injection* eines SSP hergestellt. Die elektrochemischen Untersuchungen zeigten eine hohe katalytische OER-Aktivität und Stabilität im Vergleich zu den anderen in der Literatur angegebenen Referenzelektroden auf Fe-Basis. Während der OER korrodierte das Material, was zur vollständigen Oxidation und Auflösung von As in der Elektrolytlösung führte. *Ex-situ*-Charakterisierungen sowie *quasi in situ*-XAS zeigten die vollständige Elektrokonversion des FeAs in eine hochporöse, nanokristalline Eisen(oxy)hydroxidphase, das 2-Linien-Ferrihydrit. Die Halbleiternatur dieser Phase ermöglichte einen schnelleren Elektronentransport. Darüber hinaus enthielt die erzeugte Phase Jahn-Teller-verzerrte Fe^{III} -Atome als aktive Zentren für die OER. Wichtig ist, dass das gelöste Arsen erfolgreich an der Kathode zurückgewonnen wurde, wodurch der gesamte Prozess nachhaltig und energieeffizient ist.

Der Einfluss des Nichtmetalls (Pniktogen) auf die Aktivität wurde untersucht, indem TM pniktide mit gleichem Metallgehalt, Morphologie und Zusammensetzung hergestellt wurden. Eine Salzmetathese bei Raumtemperatur wurde verwendet, um auf amorphes NiAs und NiP zuzugreifen. Elektrochemische Experimente zeigten eine höhere OER-Aktivität von NiP im Vergleich zu NiAs und anderen in der Literatur angegebenen Materialien auf Ni-Basis. Die *post-operando*-Analyse ergab eine Oxidation und Auflösung des Pniktogens während der OER und die Erzeugung einer $\gamma\text{-Ni}^{\text{III}}\text{OOH}$ -Phase. Diese Phase enthielt Schichten von kantenverknüpften NiO_6 -Oktaedern, die durch einen großen Zwischenschichtabstand (7 Å) voneinander getrennt waren, was die Interkalation von Wasser und Anionen ermöglichte, die somit Zugang zu den aktiven Ni^{III} -Zentren hatten. Der Aktivitätsunterschied wurde auf den höheren Pniktogenverlust in NiP (86%) im Vergleich zu NiAs (45%) zurückgeführt, was zu einer größeren strukturellen Umwandlung des NiP in eine $\gamma\text{-Ni}^{\text{III}}\text{OOH}$ -Phase führte.

Diese Arbeit beleuchtet, dass einfache Herstellungswege zu nanoskaligen TM-As und TM-Ps unterschiedlicher Morphologie und Zusammensetzung führen können, die die für OER, HER und die gesamte Wasserspaltung erforderlichen physikalischen und elektronischen Eigenschaften besitzen. Die untersuchten Materialien zeigten unter alkalischen Bedingungen elektrokatalytische Aktivitäten, die mit denen von Katalysatoren auf Edelmetallbasis vergleichbar sind. Darüber hinaus sind die entwickelten Methoden flexibel und zeigen je nach Herstellungsweg eine breite Palette erreichbarer Produkte. Daher eröffnet diese Arbeit auch den Weg zur einfachen Herstellung von Übergangsmetallpniktiden und ihrer weiteren Anwendung in anderen Bereichen.

Abstract

The generation of renewable and sustainable electricity can be achieved through fuel cells by the reaction hydrogen (H_2) with oxygen (O_2). In order to meet the current energy demand with fuel cells, a large feedstock of H_2 is necessary. Alkaline water electrolysis is the only mature energy conversion technology for the renewable production of H_2 through the hydrogen evolution reaction (HER). The efficiency of water-splitting is limited by its other half reaction, the oxygen evolution reaction (OER), due to the multiple proton-coupled electron-transfer (PCET) steps involved in it. Currently, ruthenium- and iridium-based catalysts and elemental platinum still represent the benchmark catalysts for practical applications of OER and HER, respectively. Nonetheless, their high cost and scarce availability limit their use in large-scale applications. Transition metal pnictides have become an attractive choice as OER and HER electrocatalysts due to their low hydrogen adsorption energies, faster reactions kinetics, and electroconductivity.

Common synthesis of transition metal pnictides are based in solid-state methods, which lead to materials with uncontrolled aggregation, heterogeneous morphology, and random composition. The design of nanostructured electrocatalysts of specific size, stoichiometry, and morphology can be achieved by the molecular decomposition of single-source precursors (SSP). The tuning of the experimental conditions (i.e., decomposition method, reaction time, temperature, solvent) leads to nanostructures of different characteristics. In this work, a molecular synthetic approach has been used to access transition metal phosphides (TM-Ps) and arsenides (TM-As). Deeper investigations have been carried out to understand the kinetics and electronic processes during catalysis and relate them to the chemical and electronic transformations of the materials.

Amorphous materials are known for their large electrochemically active surface (ECSA), which usually allows higher electrocatalytic activities in comparison to their crystalline counterparts. Keeping this in mind, amorphous and crystalline cobalt phosphide (CoP) have been synthesized by the thermolysis (hot-injection and pyrolysis) of a SSP. Amorphous CoP notably displayed higher activity for all tested electrocatalytic reactions in comparison to the crystalline CoP. During OER, the electrochemical corrosion and oxidation of phosphorus led to the formation on both materials of a Co^{III} (oxy)hydroxide shell. The presence of Co^{IV} OER active sites in the surface, in combination with Co^{III} led to distorted CoO_6 octahedra (Jahn-Teller distortion) that facilitated the absorption of oxygen intermediates. During HER, a complete loss of surface phosphorus and oxidation of the surface led to the formation of a Co-enriched (oxy)hydroxide phase, followed by an *in situ* reduction to generate Co^0 active sites for HER. The difference in activity was related to unique electronic properties and surface characteristics of the high ECSA of amorphous materials, that offers a larger number of active centers and larger flexibility upon catalysis.

TM-As have received little attention in water-splitting applications due to the high toxicity of As. However, their high electrical conductivity render these materials active for OER electrocatalysis. Crystalline FeAs nanoparticles were accessed through the hot-injection of a SSP. The electrochemical exploration showed high OER catalytic activity and stability in comparison to the other Fe-based reference electrodes and Fe-based electrocatalysts reported in the literature. During OER, the material underwent corrosion, which caused the complete oxidation and dissolution of As into the electrolyte. *Ex-situ* characterizations, as well as quasi *in situ* XAS, revealed the total electroconversion of the FeAs to a highly porous nanocrystalline iron (oxy)hydroxide phase, the 2-line ferrihydrite. The semiconductor nature of this phase enabled faster electron transport. Moreover, the generated phase contained Jahn-Teller distorted Fe^{III} atoms that behaved as active centers for OER. Importantly, the dissolved As was successfully recaptured at the cathode making the complete process sustainable and energy-efficient.

The influence of the non-metal (pnictogen) in the activity was studied by preparing transition metal pnictides with equal metal content, morphology, and composition. A room temperature salt-metathesis was used to access amorphous NiAs and NiP. Electrochemical experiments revealed a higher OER activity of NiP in comparison to NiAs and other Ni-based materials reported in the literature. The *post-operando* analysis revealed oxidation and dissolution of the pnictogen during OER and generation of a γ -Ni^{III}OOH phase. This phase contained sheets of edge-sharing NiO₆ octahedra separated by a large interlayer distance (7 Å), which provided the space for the intercalation of water and anions which were exposed to the Ni^{III} active centers. The difference in activity was attributed to the higher loss of the pnictogen element in NiP (86 %) in comparison to the NiAs (45 %), which resulted in a larger structural transformation of the NiP to a γ -Ni^{III}OOH phase.

This work illuminates that easy preparation routes towards nanoscaled TM-As and TM-Ps of different morphology and composition which could ensure the physical and electronic properties necessary for OER, HER and OWS. The studied materials showed electrocatalytic activities under alkaline conditions and comparable to the ones of precious-metal-based catalysts. Moreover, the developed methods are flexible and shows a wide range of attainable products depending on the preparation route. Therefore, it opens the route to the facile preparation of transition metal pnictides and their further application in other areas.

Table of Contents

1. Introduction	1
1.1. Energy, human activity and climate change.....	1
1.2. An alternative energy for a green future: hydrogen and water-splitting	2
1.3. Electrochemical water-splitting technologies	5
1.4. Principles of electrochemical water-splitting	7
1.4.1. Fundamentals of the HER	7
1.4.2. Fundamentals of the OER	8
1.4.3. Key parameters for electrocatalytic activity evaluation	10
1.5. Electrocatalyst research and discovery	12
1.5.1. Electrocatalysts for OER and HER	15
1.5.2. Active materials for OER: electronic structure	16
1.5.3. TM phosphides.....	21
1.5.4. TM arsenides.....	25
1.5.5. The single-source precursor (SSP) approach: molecules to materials	27
2. Motivation and Objectives	31
3. Synthesis, characterization, and electrochemical behavior of cobalt phosphide (CoP)	33
3.1. Introduction.....	33
3.1.1. Cobalt phosphide	35
3.1.2. Synthesis of cobalt phosphide	36
3.2. Results and Discussion.....	37
3.2.1. Synthesis and characterization of amorphous and crystalline CoP.....	37
3.2.2. Electrochemical behavior of amorphous vs. crystalline CoP for OER and HER.....	43
3.2.3. <i>Post-operando</i> OER characterization of amorphous and crystalline CoP	52
3.2.4. <i>Post-operando</i> HER characterization of amorphous and crystalline CoP	61
3.2.5. OWS with amorphous and crystalline CoP	68
3.3. Conclusion	69
4. Synthesis, characterization, and electrochemical behavior of iron arsenide (FeAs)	72
4.1. Introduction.....	72
4.1.1. Iron arsenide	73
4.1.2. Synthesis of FeAs	75
4.2. Results and Discussion.....	75
4.2.1. Synthesis and characterization of crystalline FeAs	75
4.2.2. Electrochemical behavior of crystalline FeAs for OER	80
4.2.3. <i>Post-operando</i> OER characterization of crystalline FeAs.....	86
4.3. Conclusion	95
5. Synthesis, characterization, and electrochemical behavior of the amorphous nickel phosphide (NiP) and nickel arsenide (NiAs)	97
5.1. Introduction.....	97
5.1.1. Nickel phosphide and Nickel arsenide	98
5.1.2. Synthesis of nickel phosphide and nickel arsenide	100
5.2. Results and discussion	102
5.2.1. Synthesis and characterization of amorphous NiP and NiAs	102
5.2.2. Electrochemical behavior of amorphous NiP and NiAs for OER.....	106
5.2.3. <i>Post-operando</i> OER characterization of amorphous NiP and NiAs.....	111

5.3.	Conclusion	120
6.	Summary	122
7.	Experimental Section.....	127
7.1.	Preparative methods.....	127
7.1.1.	Chemicals and materials	127
7.1.2.	Synthesis and characterization of the molecular precursors.....	127
7.1.2.1.	Synthesis of $L^{Dipp}CoP_4CoL^{Dipp}$ (3).....	127
7.1.2.2.	Synthesis of $L^BFeAs_2FeL^B$ (6)	129
7.1.2.3.	Synthesis of NaOCE (E = P, As)	132
7.1.3.	Preparation of reference materials	133
7.1.4.	Preparation of films by EPD.....	134
7.2.	Analytical Methods	135
7.2.1.	Nuclear Magnetic Resonance (NMR)	135
7.2.2.	Infrared Spectroscopy (IR).....	135
7.2.3.	Cyclic voltammetry (CV) for molecular precursors.....	136
7.2.4.	X-ray diffraction (XRD).....	136
7.2.5.	Single-Crystal X-ray Structure Determination	137
7.2.6.	Atomic emission spectroscopy (ICP-AES)	137
7.2.7.	Scanning electron microscopy (SEM).....	138
7.2.8.	Transmission electron microscopy (TEM).....	138
7.2.9.	Selected Area Electron Diffraction (SAED).....	138
7.2.10.	X-ray photoelectron spectroscopy (XPS).....	138
7.2.11.	X-ray absorption spectroscopy (XAS)	139
7.2.12.	Resonance Raman spectroscopy.....	141
7.2.13.	BET Surface area determination N_2 adsorption	141
7.2.14.	Elemental analysis (CHN analysis)	141
7.2.15.	Resistivity measurements (four-point method).....	142
7.3.	Electrochemical methods.....	142
7.3.1.	Redox chemistry of water electrolysis.....	142
7.3.2.	General considerations.....	145
7.3.3.	Cyclic voltammetry (CV)	145
7.3.4.	Linear-sweep voltammetry (LSV).....	146
7.3.5.	Tafel slope.....	146
7.3.6.	Chronopotentiometry (CP) and Chronoamperometry (CA).....	148
7.3.7.	Electrochemical impedance spectroscopy (EIS)	149
7.3.8.	Determination of the electrochemically active surface area (ECSA).....	151
7.3.9.	Overall water-splitting (OWS)	152
7.3.10.	Determination of the Faradaic efficiency (FE).....	152
7.4.	Experimental Data	154
7.4.1.	Electrochemistry of complex 3	154
7.4.2.	Crystal data and structure refinements.....	156
7.4.3.	Amorphous CoP.....	165
7.4.4.	Crystalline CoP.....	166
7.4.5.	Crystalline FeAs.....	168
7.4.6.	Amorphous NiAs.....	170
7.4.7.	Amorphous NiP.....	170
8.	Appendix.....	172
A.1.	Appendix of Chapter 3: Amorphous CoP vs. crystalline CoP	172
A.2.	Appendix of Chapter 4: Crystalline FeAs.....	189
A.3.	Appendix of Chapter 5: Amorphous NiP and NiAs.....	217
9.	References	243

Abbreviations

ATR-IR	attenuated total reflection infrared spectroscopy
bcc	body-centered cubic
BET	Brunauer–Emmett–Teller
CA	chronoamperometry
CC	carbon cloth
CD	carbon dot
CE	counter electrode
CCD	charge-coupled device
C_{dl}	double-layer capacitance
CNT	carbon nanotube
Co-Pi	amorphous cobalt (oxide) phosphate
CP	chronopotentiometry
CPE	constant phase element
CV	cyclic voltammetry
CVD	chemical vapor deposition
DFT	density functional theory
Dipp	diisopropyl 2,6- ⁱ Pr ₂ C ₆ H ₃
DSSC	dye-sensitized solar cell
ECSA	electrochemically active surface area
ED	electrodeposition
EDX	energy-dispersive X-ray spectroscopy
EEC	electrical equivalent circuit
EIS	electrochemical impedance spectroscopy
EPD	electrophoretic deposition
EPR	electron paramagnetic resonance
EXAFS	extended X-ray absorption fine structure
FE	Faradaic efficiency
FFT	Fast Fourier transform
FT-IR	Fourier transform infrared spectroscopy
FTO	fluorine-doped tin oxide glass
GC	gas chromatography
GO	graphene oxide
HDA	hexadecylamine
HER	hydrogen evolution reaction
HR	high resolution
ICP-AES	inductively coupled plasma atomic emission spectrometry
IR	infrared
IRE	internal reflection element
ITO	indium tin oxide
j	current density (mA cm ⁻²)
JCPDS	Joint Committee on Powder Diffraction Standards
LDH	layered double hydroxide
LED	light-emitting diode
LSV	linear sweep voltammetry
NCNT	N-doped carbon nanotube
NCNHP	N-doped carbon nanotube hollow polyhedron
NF	nickel foam
NG	graphene nanosheets

NHE	normal hydrogen electrode
Ni-Bi	amorphous Ni borate
NMR	nuclear magnetic resonance
NP	nanoparticle
OER	oxygen evolution reaction
OWS	overall water-splitting
PCET	proton-coupled electron-transfer
PCP	porous carbon polyhedrons
PEM	polymer electrolyte membrane
PSD	position-sensitive detector
rGO	reduced graphene oxide
ppm	parts per million
PS II	photosystem II
PXRD	powder X-ray diffraction
QD	quantum dot
R_{ct}	resistance to charge transfer (Ω)
RDS	rate determining step
RE	reference electrode
RHE	reversible hydrogen electrode
R_p	polarization resistance
R_s	Ohmic solution resistance (Ω)
R_u	uncompensated resistance (Ω)
SAED	selected area electron diffraction
SBET	Brunauer–Emmett–Teller surface area
SEM	scanning electron microscopy
SHE	standard hydrogen electrode
SOE	solid oxide electrolyser
SSP	single-source precursor
STP	standard temperature and pressure (273.15 K, 1 bar = 10^5 Pa)
T	temperature
T_c	critic temperature
TEM	transmission electron microscopy
THF	tetrahydrofuran
TM	transition metal
TM-As	TM arsenide
TM-N	TM nitride
TM-P	TM phosphide
T_N	Neél temperature
TOP	trioctylphosphine
TOPO	trioctylphosphine oxide
TPA	triphenylarsine
WE	working electrode
WEC	water electrolyser
XANES	X-ray absorption near-edge structure spectroscopy
XAS	X-ray absorption spectroscopy
XRD	X-ray diffraction
XPS	X-ray photoelectron spectroscopy
Z_w	Warburg impedance
η	overpotential

1. Introduction

The present work is focused on water-splitting with electrocatalyst materials based on TMs (TMs, Co, Fe, Ni) phosphides and arsenides, which are examined for their electrocatalytic properties. The general aim is to make efficient and cost-effective overall splitting to obtain hydrogen (H₂) for chemical energy storage. H₂ is a “green” energy source and has the potential to play a major role in future energy supply. To accomplish this, “alternative energy” sources must replace current energetic paradigms and the social attitudes towards energy use must be rethought.

1.1. Energy, human activity and climate change

The global average atmospheric carbon dioxide (CO₂) concentration in 2019 was 409.8 parts per million (ppm). CO₂ levels today are higher than at any point in at least the past 800 000 years. The data suggests that the last time the atmospheric CO₂ was this high was more than 3 million years ago. At this time, the temperature was 2-3 °C higher than during the pre-Industrial Revolution era (mid 18th century), and the sea level was 15-25 m higher than today.^[1] Since the Industrial Revolution in the 19th century, CO₂ concentrations have been on the rise due to the burning of fossil fuels for energy. The combustion of fossil fuels for energy purposes continues to be among the main causes of CO₂ emissions. 80 % is due to this alone and the trend will continue almost unchanged with the current policy.^[2] The escalation of the world energy consumption especially during the end of the past century and first decades of the 21st century is related to the fast and global growth of the human population and the changes in living standards, which demand a steady and reliable supply of energy to support our mobility, prosperity and daily comfort (see Figure 1.1).^[3,4] The rising economic growth places nowadays an additional demand of products and services.^[5] Consequently, the average global power demand is predicted to be approximately 30 TW in 2050 and 46 TW in 2100.^[3]

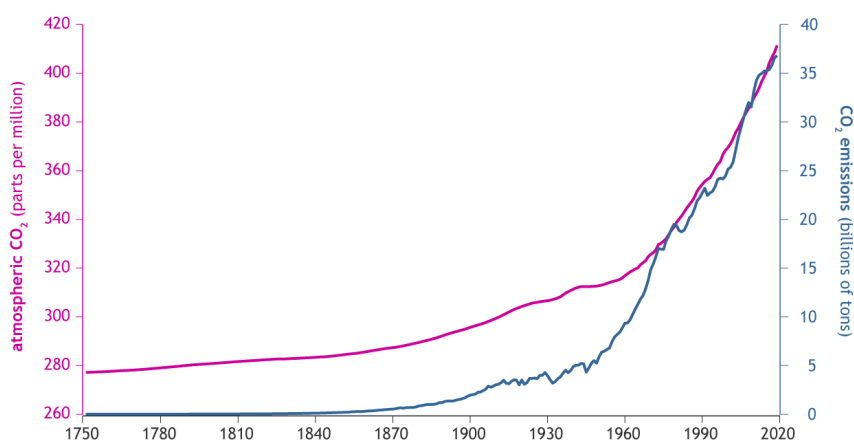


Figure 1.1. Atmospheric CO₂ has increased along with human emissions of since the start of the Industrial revolution in 1750. Obtained from NOAA Climate.gov.^[6] © 2020 NOAA

The consequences of this continuous increase in energy demand and CO₂ emissions are drastic. Climate change is a consequence of the sudden increase of atmospheric CO₂ linked to fossil fuel utilization. Recent changes in regional climate patterns have been already observed.^[7] For example, El Niño events, which cause heavy rains in equatorial regions of Western South America, usually differ substantially in their spatial pattern and intensity.^[8] However, there is evidence that suggests that these events are becoming more common and intense in the past 30 years.^[9] On the other hand, global warming, due to the greenhouse effect of CO₂ and other gases (methane CH₄ and nitrous oxide N₂O) is observed. The global annual mean temperature has increased at a rate of 0.2 K per decade at the surface and 0.4 K per decade at the troposphere since the start of the 20th century.^[10] In the 21st century, the Earth's average temperature is expected to increase from 2 to 4.5 °C. In addition, global warming caused by CO₂ leads to a rise in the sea level and triggers ocean acidification.^[11] Consequently, sea life is threatened by the alteration of the biogeochemical cycles in the seawater. The negative impact of climate change is not only restricted to marine life. It is estimated that 47 % of terrestrial non-flying threatened mammals and 23.4 % of threatened birds may have already been negatively impacted by climate change.^[12] Moreover, agriculture is also considered one of the most endangered activities due to climate change and global warming.^[13]

1.2. An alternative energy for a green future: hydrogen and water-splitting

The path we follow towards the future will depend on how efficiently and effectively we use existing and new sources of energy. In 2020, 84 % of the energy supply was related to fossil fuel sources like coal, oil, or natural gas.^[4,14] If current energy policies are maintained, this value will only decrease by 3 % in 2040.^[4] The reduction of greenhouse gases emissions that cause global warming needs a full commitment by governments and societies in the world. In 2015, the Paris Agreement of the United Nations Framework Convention on Climate Change set a limit in the rise in global temperatures to “well below” 2 °C.^[15] Although climate change efforts need to be excessively increased to achieve this objective, the years since its entry have seen more countries, regions, cities and companies establish carbon neutrality targets. Zero-carbon solutions are possible, especially in the power and transport sector. However, a complete reduction of the CO₂ emissions would require minimalizing the use of fossil fuels as much as possible. At the same time, a change in the paradigm is required to migrate to efficient, clean, affordable and sustainable energy sources.^[4,16,17]

The goals of the Paris Agreement are ambitious and global effort is required to prevent drastic consequences by 2030. However, growing population, increasing energy demand and depletion of fossil fuels sources make this strategy sensible.^[18] An adjustment of the energy supply must rely on a combination of environmentally friendly technologies in order to conserve natural resources and the ecosystem. Among them, hydropower, wind energy, solar energy, and the use of biofuels are promising renewable alternatives.^[17] This means, they produce useful energy that can be naturally replenished in a short timescale for human beings. Nonetheless, these renewable energy sources are all inherently

intermittent and generally dispersed relative to the isolated large scale facilities that currently supply the vast majority of electrical energy.^[3] The best use is therefore done by coupling the alternative energy supply with good energy-storage systems. The “energy turnaround”, i.e., the production and consumption of energy, must be also sustainable in order to remain economically viable in the long term. Batteries are a popular alternative to store energy, especially to supply energy in transportation systems. However, they suffer from age deterioration and their components are toxic.^[19] Some of the composing materials, such as lithium, have a low availability, which limits their ubiquitous use in energy storage systems. An interesting alternative is the efficient conversion and storage of solar energy in chemical bonds. For example, H₂ can be produced with solar energy and made available as fuel or converted to electricity which can then be stored.^[20]

Solar energy is the most obvious alternative energy source, providing a large excess of energy with practically zero cost.^[4] Artificial photosynthesis is a way of harnessing solar energy and use atmospheric CO₂ to produce fuels, or organic molecules, while tackling the problem of CO₂ contamination derived from fossil fuels. The simplest way is to mimic natural photosynthesis and use water as an electron or hydrogen donor. In this way, water-splitting can be used as an energy converter for H₂ as a chemical energy storage.^[21,22] H₂ has the highest chemical energy per mass (143 MJ kg⁻¹) among chemical fuels, which is three times higher than that of diesel or gasoline (47 MJ kg⁻¹).^[23] H₂ is a clean synthetic fuel that can supply energy in form of electricity to households and the economy, and an important raw material for the chemical industry (Figure 1.2).^[24,25] Highly efficient non-biological conversion of H₂ to electricity can be achieved with fuel cells, that convert H₂ and oxygen (O₂) to electricity and water.^[4] The combustion of H₂ in fuel cells is attractive because of the high reaction recyclability, the generation of carbon-free by-products (H₂O), and the possibility of use H₂ produced from renewable sources.^[3,25–28] H₂ fuel cells possess conversion efficiencies up to 60 %, but their commercial development and efficiency are limited by the cost and gas diffusion.^[4]

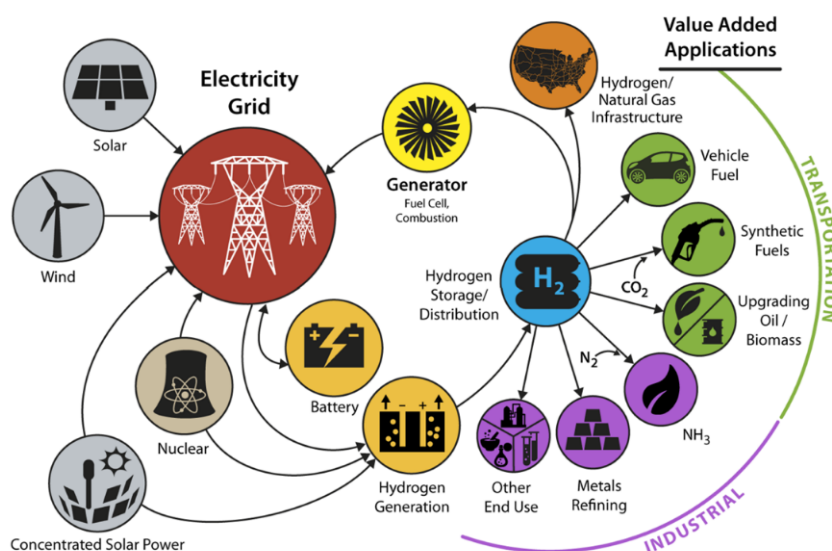
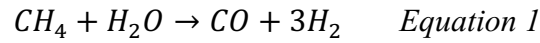
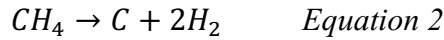


Figure 1.2. The H₂ role at the large-scale energy system. Taken from: Klahr and co-workers.^[29] © 2017 IOP Publishing.

Currently H₂ production for industrial applications is mainly based on the steam reforming of methane (CH₄) through the reaction of the hydrocarbon with water vapor at 1200 K using a Ni catalyst, based on the following reaction:^[30]



The main disadvantages of this process are the large requirement of CH₄, either from natural gas or the cracking of crude petroleum, and the CO₂ emitted during the process.^[25] H₂ can also be formed by the thermal decomposition of CH₄ using a TM catalyst:^[31]



Therefore, the use of fossil fuels, such as CH₄, to obtain H₂ should be replaced by an abundant and environment-friendly source. Water meets these characteristics and represents an almost infinite resource to provide H₂.

The total amount of water on Earth is ca. 1.388 trillion liters (1 388 000 000 000 L) of which 96.54 % is in oceans, seas and bays (see Table 1.1).^[32] Splitting directly seawater would also protect valuable freshwater which only makes a very small part of the water on the planet.^[25,27] There are three ways of producing H₂ from water: chemical, electrochemical and photochemical water-splitting.^[33] Of these three methods, photochemical water-splitting is the only one that uses solar energy alone and can then store it in the form of H₂.^[33] The Grätzel cell,^[34] also called dye-sensitized solar cell (DSSC), is one of the most well-known and frequently used photocatalytic cells.^[35] However, they have not yet made a strong contribution to the energy supply due to their low conversion efficiencies and relatively high cost.^[4,17] The use of solar energy is highly dependent on the region, as not all regions receive an equivalent radiation during the year. Additionally, yearly fluctuation due to seasons and weather restrict the ubiquitous use solar energy to generate H₂.^[4,36]

Table 1.1. Estimate of global water distribution.^[32]

Water source	Water volume (L)	Percent of freshwater	Percent of total water
Oceans, seas, and bays	1 388 000 000 000	--	96.54
Ice caps, glaciers, and permanent snow	24 064 000 000	68.7	1.74
Fresh groundwater	10 530 000 000	30.1	0.76
Saline groundwater	12 870 000 000	--	0.93
Soil moisture	16 000 500 000	0.05	0.001
Ground ice and permafrost	300 000 000	0.86	0.022
Fresh lakes	91 000 000	0.26	0.007
Saline lakes	85 400 000	--	0.006
Atmosphere	12 900 000	0.04	0.001
Swamp water	11 470 000	0.03	0.0008
Rivers	2 120 000	0.006	0.0002
Biological water	1 120 000	0.003	0.0001

Despite the large amount of energy that can be supplied by renewable sources, ca. 20 % of it remains unused, or the feed-in into the power grid is shut down when consumption drops (e.g., at night).^[37,38] The fluctuations in energy could be used to suppress the additional costs related to shutting down and restarting the power supply. The “excess” electricity could be used for electrochemical water-splitting, stored in chemical form, and consumed.^[3] A sustainable and environmentally friendly “energy turnaround” can be achieved if the water-splitting for conversion and storage is implemented with electrical energy from renewable resources. Electrocatalytic water-splitting is already commercially available and could be successful in the stable supply of energy beyond the use of batteries. In the long term, the use of H₂ as energy storage and fuel is more economical and ecological.^[25] The eventual evolution towards a hydrogen economy will depend, however, on the technical feasibility for the storage of H₂.^[4] Recent innovative approaches, such as the use of high surface area nanostructures and metal hydrides to store H₂ have appeared and are beneficial for the complete energetic transition.^[25] The use of suitable technologies to store H₂ can achieve the long-term and long-lasting electrical energy which is not possible with current battery technologies.^[25] Thus, the use of H₂-derived electricity for transportation could be possible. The use of fuel cells to provide a continuous supply of H₂-derived electricity could render transportation easier. However, for such systems to prosper, electrocatalysts for water-splitting must be efficient, stable, and cheap. Only at this point a large part of the existing power supply technology, such as oil refineries and lignite power stations, could be replaced.^[36,39,40]

1.3. Electrochemical water-splitting technologies

The electrochemical conversion of water into H₂ and O₂ is economically and technically favorable in comparison to chemical and photochemical water-splitting technologies.^[3] Electrochemical water-splitting is also an indirect storage of electrical energy with minimal energy loss.^[41] However, H₂ production via electrolysis using renewable energy sources accounts only 4 % of the current H₂ production.^[33]

H₂ production using water electrolysis technologies depends on the pH of the electrolyte. Under acidic conditions, H₂ is generated in the cathode by the reduction of hydronium ions (H₃O⁺) in proton exchange through polymer electrolyte membrane (PEM) electrolyzers. On the other hand, alkaline electrolyzers (AECs) are used to produce H₂ from water under alkaline conditions (usually 20-30 % potassium hydroxide, KOH), which is the most applied commercial technology.^[3,33,37] H₂ can also be obtained from water-splitting using solid oxide electrolyzers (SOEs).^[3] In general, all these systems are referred to as water electrolyser cells (WEC).^[42] The schematic representation and operation principles of the three main types of WECs is shown in Figure 1.3. A common water electrolysis cell consists of anode, cathode, power source and the electrolyte. The applied current causes the electrons to migrate from the anode to the cathode, where they are absorbed by the H₃O⁺ ions and form H₂ (or water in a AEC).^[43] The charge neutrality is maintained when hydroxide anions (OH⁻) migrate to the anode through the diaphragm and are oxidized, releasing the electrons (which migrate back to the cathode through the

external circuit) and producing O₂.^[3,44] In PEM, the migration of H⁺ is done through a proton exchange membrane, usually a perfluorosulfonic acid polymer (Nafion™). In SOEs, migration of O²⁻ to the anode occurs through a dense solid conductive ceramic oxide (yttria-stabilized zirconia, doped LaGaO₃, ceria-based or Bi₂O₃).^[20,25,45]

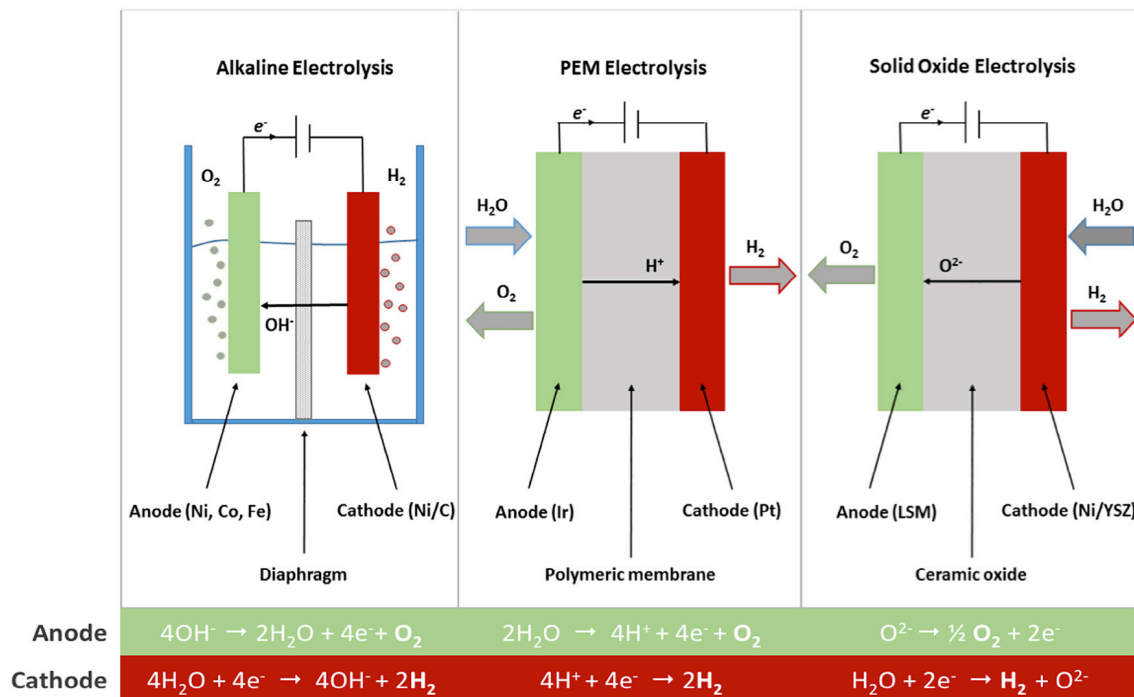


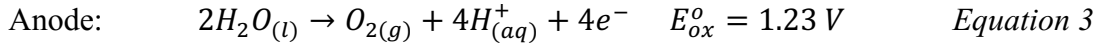
Figure 1.3. Schematic representation showing the operational principles of the three types of water electrolysis technologies. OER occurs at the anode and HER at the cathode. Taken from Sapoutnzi and co-workers.^[33] © 2017 Elsevier.

The gas generation reactions take place on the electrode surface (anode or cathode) which is in contact with the electrolyte. In solution-based WECs, these reactions occur through the inner and outer Helmholtz layers.^[46] The performance of these reactions can be measured separately using electrochemical techniques that can be used to determine the exact values of the applied potentials.^[46] In this way, it is possible to determine how efficiently an electrode material (catalyst) catalyzes the respective reaction on the surface of the anode or cathode.

Several kinetic parameters are used to evaluate the efficiency and the activity of an electrocatalyst. Among them, the overpotential (η), the current density (j) and the Tafel slope (b) provide important information about the kinetics, mechanisms and transition states of the reaction taking place (see Section 1.4.2 and 1.4.3).^[46,47] Therefore, research done on water-splitting has mainly been devoted to the development of efficient, durable and inexpensive catalysts based on the mentioned parameters. A detailed description of the electrochemical measurement techniques and parameters can be found in the following sections and are summarized in the Experimental Section (see page 127).

1.4. Principles of electrochemical water-splitting

The water-splitting reaction is divided into two half-reactions, water reduction at the cathode by the hydrogen evolution reaction (HER) and water oxidation for oxygen production at the anode (OER = oxygen evolution reaction). The splitting of water into H₂ and O₂ at standard temperature and pressure (STP, 273.15 K, 1 bar = 10⁵ Pa) is not thermodynamically spontaneous.^[37] The potential to complete the process at STP is 1.23 V relative to the reversible hydrogen electrode (RHE), as expressed by the following reactions occurring at the electrodes (under acidic conditions):



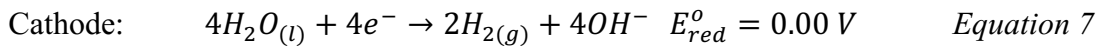
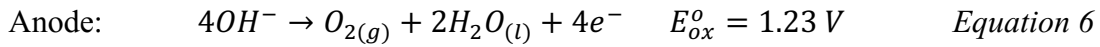
The generated electrons travel through the external circuit while the protons are reduced to H₂ in the cathode, completing the electrochemical circuit: The standard electrode potential for this reaction is, according to the convention, 0.00 V (at pH 0) against the RHE and serves as a reference point for the electrochemical series.



The overall electrochemical water-splitting reaction is the following:



Under basic conditions, the OER and HER proceed according to the following equations:^[41]

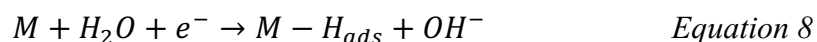


In the total process, four electrons (e⁻) and four protons (H⁺) are transferred per mole of produced dioxygen. A total charge of the 192.928 C (= 2 F) is transferred through the electrolyte per one mole of water. The OER is a complicated process involving several adsorbed species on the solid surface of the electrocatalysts and high-energy intermediates. The mechanistic complexity involved in the HER and OER will be described in the following sections.

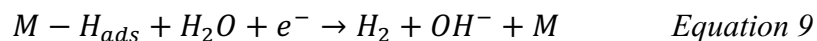
1.4.1. Fundamentals of the HER

The HER is the cathodic half reaction. It is thermodynamically more favorable than the OER, and proceeds by a two reaction mechanism with the formation of a single intermediate.^[48] The mechanism under basic conditions^[49] is the following:

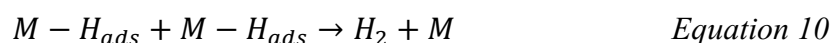
- (1) Water is reduced on active site *M* to generate one H adsorbed atom (*M* – *H_{ads}*), and liberating a hydroxide anion (OH⁻) (Volmer reaction). This step is ubiquitous to all electrocatalysts.



- (2) The second reaction involves a second electron transfer to form H₂. $M - H_{ads}$ combines with a water molecule and an electron to produce a H₂ and a hydroxide anion (Heyrovsky reaction):



- (3) The second step can also proceed through the Tafel reaction in which two adsorbed H atoms couple and produce H₂:



The occurrence of a specific mechanism and the rate-determining step can be derived from the Tafel plots (see Experimental Section, 7.3.5 Tafel slope).^[27] The Tafel slope (b) provides important information about the kinetics, mechanisms and transition states of the reaction taking place.^[46,47] The Tafel slope describes how much the potential must be increase in order to increase the resulting current density (j) by one order of magnitude (x10 or per decade, dec^{-1}).^[50] This means, how efficient and dynamically an electrode reacts to an applied potential and generates catalytic current.^[50] Tafel slopes of 118 mV dec^{-1} , 38 mV dec^{-1} , or 29 mV dec^{-1} have been ascribed to the discharge reaction (Volmer reaction), electrochemical desorption reaction (Heyrovsky reaction), or recombination reaction (Tafel reaction) as the rate determining, respectively.^[51] The occurrence of a specific mechanism is related to the coverage of the active sites by $M - H_{ads}$. If the coverage of the surface is low and the electrode surface has sufficiently available active sites (M) near $M - H_{ads}$, the adsorbed atoms will react with one water molecule and reduce to generate molecular H₂ (Heyrovsky reaction). On the contrary, in surfaces with high $M - H_{ads}$ coverage, two adjacent $M - H_{ads}$ will react and evolve a molecule of H₂ (Tafel reaction).^[52]

1.4.2. Fundamentals of the OER

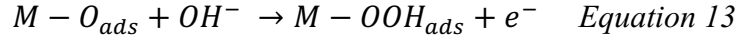
The mechanism of the OER is more demanding than the HER with complex kinetics that vary depending on the pH of the electrolyte and the catalyst material.^[52] The OER is often considered as the bottleneck of the water-splitting, as it involves four proton-coupled electron-transfer (PCET) processes with at least three highly energetic intermediates (see below). There are several reports in the literature for different mechanisms according to the nature of the catalyst and the pH of the electrolyte.^[53–57] For OER under alkaline condition, the electrochemical oxide pathway with two active sites, as well as single-site catalysis, have been established.^[41,58] The single-site mechanism is first described and explained. The description of the mechanism via two active sites can be found in the experimental section (see Section 7.3.5). First, free hydroxide ions (OH^-) are adsorbed ($M - OH_{ads}$) on an active site (M), liberating one electron:^[27]



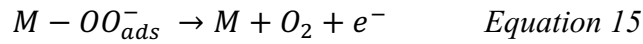
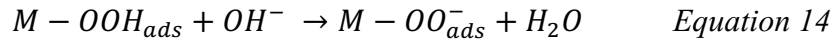
The second step involves the deprotonation-like process of the adsorbed hydroxide ion that reacts with another hydroxide ion, leaving an adsorbed oxygen atom ($M - O_{ads}$), producing water, and liberating one electron:



The third step involves the formation of an oxo-hydroxo intermediate ($M - OOH_{ads}$) by the reaction of the adsorbed oxygen atom ($M - O_{ads}$) with a free hydroxide ion from the solution:



The last step of the OER is composed of two reactions: the combination of the surface-adsorbed oxo-hydroxo intermediate with another free hydroxide ion to finally produce molecular oxygen:



Under ideal conditions with an ideal catalyst, 1.23 eV are required for the binding of the intermediates. Therefore, a total of 4.92 eV is required for all the four PCET steps.^[27] In the ideal case, there are no limitations derived from kinetic hindrance originated from the four sequential PCET steps shown before.^[49] However, in real conditions, the formation of all the intermediates ($M - O_{ads}$, $M - OH_{ads}$, $M - OOH_{ads}$, $M - OO_{ads}^-$) influence the kinetics of the reaction and have a limiting effect on the reaction rate. If the formation, adsorption or desorption of these species has unfavourable kinetics, a higher potential will be required to achieve the OER.^[58] The formation of the $M - OOH_{ads}$ intermediate is the rate determining reaction.

The proposed OER mechanisms on a single-site or on two active centers differ only slightly from one another and include the same intermediates as ($M - O_{ads}$, $M - OH_{ads}$,) (see Section 7.3.1).^[47,58] The main difference is the way the oxygen atoms react in the surface to form O_2 .^[47] The reaction via two active centers takes place by the direct combination of two $M - O_{ads}$ intermediates to form 2M and one O_2 molecule (green route, Figure 1.4). The single-site route also includes the $M - OOH_{ads}$ intermediate, which then forms an O_2 molecule (black route, Figure 1.4).^[47] The formation of the $M - OO_{ads}^-$ intermediate is rarely found in the literature, but is partly used for investigations into the kinetic barriers of OER.^[58] Despite the differences in the mechanisms, there is a general agreement that in heterogeneous electrocatalysis of OER, the binding energies of $M - O$ within the intermediates ($M - O_{ads}$, $M - OH_{ads}$, $M - OOH_{ads}$, $M - OO_{ads}^-$) determine the rate of the reaction.^[59]

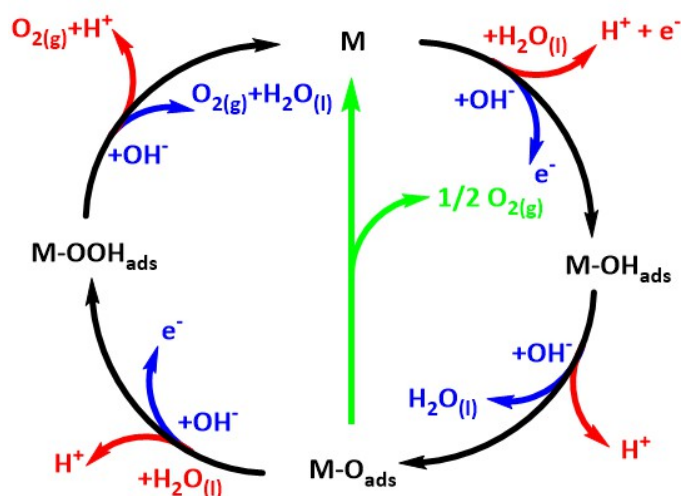


Figure 1.4. The OER mechanism under acidic (red line) and alkaline (blue line) conditions. The black line indicates that the oxygen evolution involves the formation of a peroxide ($M - OOH_{ads}$) intermediate (black line) while another route for direct reaction of two adjacent oxo ($M - O_{ads}$) intermediates (green) to produce O_2 is possible as well.^[47]

The formation of the $M - H_{ads}$ and $M - OOH_{ads}$ intermediates during HER and OER, respectively, require the largest amount of energy. Consequently, they are the kinetic barriers and are considered as rate determining steps (RDSs).^[49] The experimental consequence is the measurement of higher electrochemical potentials that deviate from the HER and OER thermodynamically required values 0 V and 1.23 V, respectively.^[60] This results in the demand of extra energy beyond the required thermodynamic potential to achieve appreciable current density, causing low-energy conversion efficiency. The difference between the thermodynamic requirement and the applied potential is known as the overpotential (η).^[49] The value of the OER overpotential can be larger or smaller and can also be changed.^[49] In particular, it requires significantly more energy than the HER due to the larger number of intermediates involved and has a high overpotential.^[49] This is the reason why materials with specific characteristics are required to enable the OER.^[61] The following section addresses the key parameters used to evaluate the feasibility of electrocatalysts for constructing WECs.

1.4.3. Key parameters for electrocatalytic activity evaluation

The OER and HER catalytic performance is usually evaluated by measuring the current density per geometric area (j , mA cm^{-2}) or the amount of gas generated. Although the reactions proceed in different electrodes, the same key experimental parameters are used to evaluate their overall electrocatalytic activity (see Figure 1.5).

Normalization on the current density is done to have a fair comparison between electrocatalysts.^[59,62,63] The geometrical surface area is the widely accepted parameter of normalization.^[41] Despite its large use, the geometric surface area does not reflect the intrinsic activity of the catalysts and does not consider the catalyst loading. Most importantly, the geometric surface area of the substrate electrode is not equal to the real

surface area of the catalyst participating in catalysis. Therefore, normalization through the electrochemically active surface area (ECSA) has been preferred.^[41,64] This parameter can reflect the intrinsic activity and is loading sensitive, but it is difficult to determine. Additionally, large experimental discrepancies have been observed between the values of ECSAs determined by different methods. The Brunauer-Emmett-Teller (BET) surface area (S_{BET}) as also been utilized for the normalization.^[41] Its ease in determination has prompted its use, although it must be used with care. S_{BET} does not reflect the intrinsic catalytic properties because gas adsorption sites are not always electrochemically active and might not show the real activity of a catalyst. Finally, the normalization by catalyst loading (mg cm^{-2}) is suitable to compare similar materials with different loadings.^[47] However, it is not useful for the activity comparison of catalysts with varying particle size, morphology, and porosity.^[41,64]

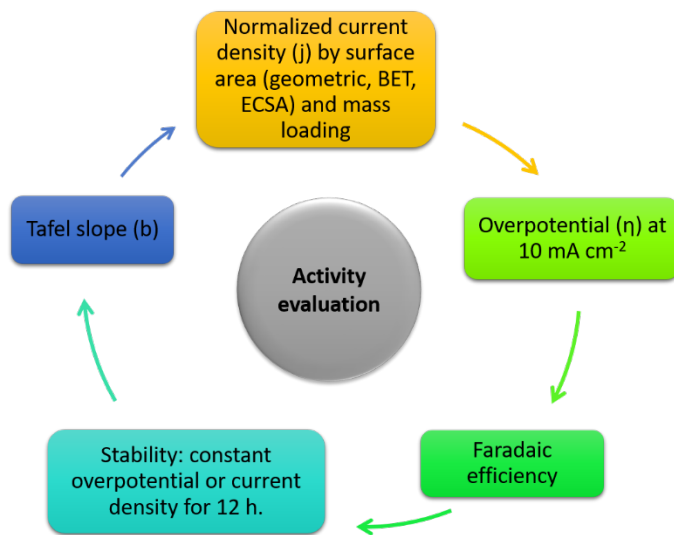


Figure 1.5. Key parameters for the evaluation of the electrocatalytic activity.

The overpotential at a certain current density is the most important indicator to evaluate the electrocatalytic performance. The overpotential is caused by kinetic hindrances of each of the reaction's steps on the electrodes (see Section 1.4.2).^[65] The overpotential intrinsically depends on the properties of the electrode surface or the electrode material. It also encloses contributions from external factors such as voltage losses from resistances originating in the measurement (Ohmic overpotential),^[49] and mass transport limitations.^[66] The uncompensated resistance (R_u) contributions can be eliminated by Ohmic drop compensation (iR-compensation). The external limitations can be easily minimized by stirring the electrolyte or using a highly concentrated electrolyte. The overpotential is usually measured at a determined current density, which is related to a specific rate of reaction.^[49] The necessary overpotential to achieve a magnitude current density per geometric area of $|j| = 10 \text{ mA cm}^{-2}$ is specifically used for comparison between electrocatalysts.^[67] This value is the approximate current density expected for an integrated solar water-splitting device under 1 sun illumination operating at 12.3 % solar-to-hydrogen efficiency if assuming there is no loss of energy.^[68]

The selectivity of an electrocatalyst towards HER and OER is evaluated by the Faradaic efficiency (FE). The FE measures the efficiency of an electrocatalyst to transfer electrons provided by an external circuit across the interface to the electroactive species to affect the electrode reactions.^[49] The FE is experimentally determined by the comparison of the quantity of evolved gas (O₂ or H₂) and the calculated amount of gas produced based on the Faraday's laws of electrolysis.^[41] If both values agree, the catalyst shows 100 % FE for a specific gas evolution reaction. This means that the catalyst is highly selective for the electrochemical reaction and there is no contribution of a side reaction to the current density (see Section 7.3.10).^[52]

The stability is another essential parameter used to evaluate the materials suitability for practical applications. It is usually estimated by chronopotentiometric (application of a constant current) or chronoamperometric (application of a constant potential) experiments (see Section 7.3.6). The degradation of the materials is evaluated by analyzing the stability of the output potential or current. It has been widely adopted that a stable current density for more than 12 h or insignificant increase in the overpotential at a selected current density (e.g., 10 mA cm⁻²) is enough to identify highly efficient electrocatalysts.^[49]

The Tafel slope (b) provides important information about the kinetics, mechanisms and transition states of the reaction taking place.^[46,47] Experimental determination of the Tafel slope can be done by various methods (see Section 1.4.2) and it can be used to determine or compare the catalytic activity. Electrocatalysts with good charge transfer ability are expected to show a small Tafel slope. It is important to note that the Tafel slope is only a quantitative characterization to reveal different kinetics and predict the mechanism of the electrocatalytic reaction under study (see Section 1.4.1 and 1.4.2).

1.5. Electrocatalyst research and discovery

In order to change the energetic paradigm towards a WEC-technology based industry, materials are required to efficiently catalyze the HER and OER for a long time and with low overpotential. Currently, WECs show an efficiency of ca. 70 % of conversion of electricity to H₂. When this step is coupled with the opposite conversion of H₂ to electricity through fuel cells (see Section 1.2), the efficiency drops to 40 %. In comparison, batteries that can store and deliver electricity with 85 % efficiency are more advanced.^[42]

The increase in efficiency is achieved by using electrocatalysts with low overpotential for water-splitting, i.e., that require low energy to catalyze the HER and, especially, the OER (see Section 1.4.2). The OER is kinetically more demanding, and the reduction of the catalytic inhibitions associated with this reaction will reduce the overpotential for the overall water-splitting (OWS). Additionally, electrochemical stability (not being corroded at high overpotential and producing constant current for a long time) and high activity (achieve high current density with a low potential) are characteristics required for a good electrocatalyst.^[49,50]

Benchmark electrocatalysts are based on noble metals, such as IrO₂ and RuO₂ for OER and Pt for HER.^[69,70] However, their high cost and scarce availability (Ru = 0.02 ppm; Ir = 0.001 ppm by mass of the Earth's crust) limit their use in the large-scale application in industrial alkaline electrolysis.^[71] Commercial use only makes sense if economic feasibility factors such as material costs and availability are also considered. The preparation of electrocatalysts with specific morphological parameters can also help to reduce the overpotential.^[72] Among them, the surface area is a key parameter influencing the activity of an electrocatalyst (see Section 1.4.3). For example, an increase in the surface area by synthesizing porous structures or nanoparticles or the preparation of thin layers on inexpensive substrates can also help to increase the activity and reduce the costs by a larger exposure of the ECSA to the electrolyte with a lower amount of electrocatalyst.^[73–75] Nonetheless, the use of smaller quantities of noble metal-based electrocatalysts is not sustainable if the objective is the broad commercial application of WECs.^[76] It is necessary to develop accessible and inexpensive electrocatalysts with low overpotentials and high stability based on low-cost and environmentally benign components.^[77,78]

A sustainable way to achieve this is to replace noble metals with Earth-abundant 3d transition metals (TM) such as Mn, Fe, Co, Ni, which have been extensively researched in the past years.^[79–81] Trasatti proposed in 1980 that the OER activity was intrinsically related to the enthalpy of transition from a lower to a higher oxidation state for binary oxides of TM.^[82] The plot in Figure 1.6 shows the relation of the overpotential to the metal-oxygen binding energy revealing a “volcano”-like behavior. This relation was the first experimental manifestation of the Sabatier principle for the OER:^[83] oxides which are oxidized with difficulty are poor catalysts due to their weak affinity for oxygen (left of the volcano), and conversely, oxides which are easily oxidized are also poor catalysts because their affinity for oxygen is too strong (right of the volcano).

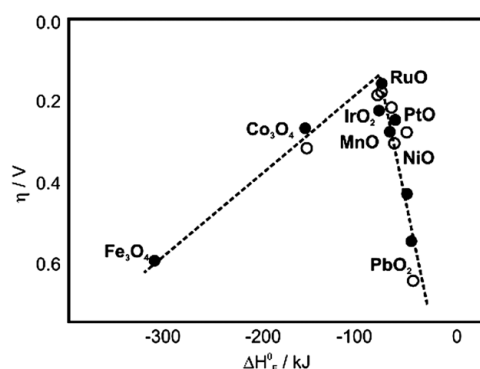


Figure 1.6. Experimental OER-derived plot of metal oxides relating the overpotential of binary oxides reported by Trasatti as function of the enthalpy of transition from a lower to a higher oxidation state (ΔH_F^0). Measurements in alkaline media are shown as open symbols and measurements in acidic conditions as filled symbols. Taken from Shao-Horn and co-workers.^[76] © 2014 The Royal Society of Chemistry.

It is important to note is that these correlations were developed without any knowledge of the OER mechanism, and only serve to identify properties that could function as predictors of the OER activity. Bockris and Otagawa^[84,85] performed systematic

investigations of perovskite oxides to elucidate the mechanism and rationalize the properties affecting the OER activity. They found an inverse linear dependence of the current density at constant overpotential on the enthalpy of $M(OH)_3$ hydroxide formation. They concluded that a common rate-determining step must be shared among the oxides, and is the desorption of OH^- . Later, density functional theory (DFT) was used to confirm potentially suitable electrocatalysts by the relation of the overpotential to the adsorption energy of the adsorbed intermediates on the catalyst surface for OER.^[86] In 2007, Nørskov and co-workers confirmed the “volcano” relation between the overpotential and the binding energy of the intermediate oxygen species (O_{ads} , OOH_{ads} , OH_{ads}) adsorbed on the catalysts for OER.^[87]

Similarly, the electrocatalytic HER activity was related to the binding energy of hydrogen ($M - H_{ads}$) to the electrocatalyst surface.^[36] The plot of the activity, measured in terms of the overpotential or the current density at a certain potential, versus the free energy of formation of the $M - H_{ads}$ intermediate (ΔG_{H^*}) revealed a “volcano” like pattern (Figure 1.7),^[49,50] analogous to the overpotential-energy relation of OER electrocatalysts.

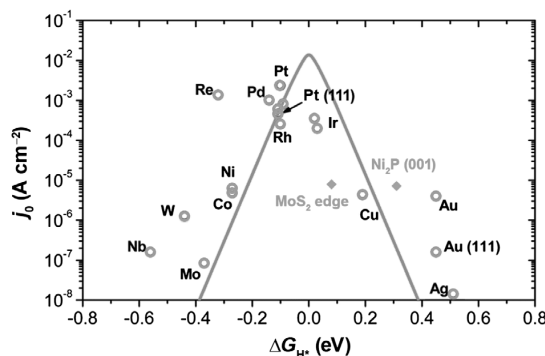


Figure 1.7. Schematic representation of the relation between the HER current density of electrocatalysts and the binding energy of hydrogen to the surface (ΔG_{H^*}) revealing a “volcano” plot. Taken from Morales-Guio and co-workers.^[88] © 2014 The Royal Society of Chemistry.

The behavior of HER electrocatalysts follows also the Sabatier principle of balanced intermediate adsorption.^[86] The catalytic efficiency relies on the binding energy of the reaction intermediate at the electrode surface.^[83] A good HER catalyst should form a sufficiently strong bond with adsorbed hydrogen ($M - H_{ads}$), but it should be also weak enough to assure the bond breaking and the release of the gaseous H_2 product.^[70] When the H-surface interaction is too weak, the reaction is inhibited by the formation of the $M - H_{ads}$ intermediate. If the adsorption is too strong, the reaction is inhibited by the desorption of hydrogen (see Section 1.4.1).^[49] Both extreme cases result in an increase in potential in order to effectively enable the reaction. Nørskov and co-workers^[89] verified the adsorption energy relationship to an electrocatalyst activity through DFT calculations. The free energy of formation of the $M - H_{ads}$ intermediate (ΔG_{H^*}) on several metallic surfaces was computed and related to the overpotential, and a similar “volcano” plot was obtained.^[89]

Empirical and theoretical studies opened the door to a vast selection of electrocatalysts based on cheap and abundant TM with great electrocatalytic activities. With a few exceptions, DFT provided good predictions about the OER and HER activity of the materials.^[90] However, the calculation of the “volcano plots” possess a limitation: they are pH-dependent, mainly for acidic electrolytes and often do not consider transformations on the surface of the electrocatalysts during OER and/or HER. Moreover, the calculated data for OER under alkaline conditions is still insufficient and sometimes deviates from the experimental results.^[76] Further experimental research and detailed theoretical studies of water-splitting under alkaline conditions are therefore necessary in order to achieve the widespread application of alkaline water electrolyzers.

1.5.1. Electrocatalysts for OER and HER

Under acidic conditions, IrO₂ and RuO₂ are considered the most stable OER electrocatalysts due to their high stability and high electrical conductivity. In the case of HER, the most notorious representative is Pt. Acidic electrolytes are efficient for electrocatalytic water-splitting because they provide a high concentration of hydronium ions (H₃O⁺) or H⁺ as reactants.^[91] However, acidic electrolytes also corrode electrodes. For example, TMs such as Fe, Co, and Ni and their oxides dissolve very quickly or show only low activity under these conditions. Thus, the stability of the electrocatalysts under certain pH conditions determines their application.

The re-discovery of the amorphous cobalt (oxide) phosphate (Co-Pi) by Nocera and co-workers^[92] set a milestone on the development of OER electrocatalysis at neutral conditions. The Co-Pi formed *in situ* over indium tin oxide (ITO) electrodes by electrodeposition (ED) in phosphate-buffered solution (pH 7) containing Co^{II} ions. The high catalytic activity of Co-Pi was pH-dependent and limited to near neutral conditions. More importantly, the Co-Pi was characterized by a “self-repair” ability, in which Co^{II} from the solution redeposited at E > 1.3 V vs. RHE, leading to long-term stability. The Co-Pi catalyst also showed a broad application in water-splitting using fresh, river, and seawater, which could reduce the overall cost of industrial-scale H₂ production significantly.^[91] Additionally, its similarity to photosystem II (PS II), the complex protein assembly where the transformation of the photon energy to chemical energy takes place, made the construction of an artificial leaf possible.^[93,94] Later, Artero and co-workers discovered the bifunctional properties of the Co-Pi catalyst:^[95] the electrodeposited catalyst showed high OER and HER activity and represents a benchmark material for OWS.

Industrial production of H₂ is done with alkaline electrolyzers containing a 20-30 % KOH alkaline solution (see Section 1.3). Therefore, stable electrocatalysts in strong alkaline electrolytes are required. Even though the activity of IrO₂ and RuO₂ was high under alkaline conditions, their stability was greatly reduced.^[96] Accelerated electrocatalyst corrosion at high potentials or mechanical degradation due to vigorous O₂ evolution also prompted the deterioration of these materials.^[97] HER kinetics are also drastically affected under alkaline conditions because of the lower concentration of H⁺ ions. The

Tafel slope measured for Pt electrodes in alkaline solutions is around 120 mV dec^{-1} , which indicates that the Volmer or the Heyrovsky step is the RDS.^[90] HER kinetics of Pt under alkaline conditions require a water dissociation step to generate OH^- (see Section 1.4.1), which is not present in acidic electrolytes. The cleavage of the water O-H bond and the transport of OH^- from the catalyst surface to the bulk of the electrolyte limited the HER kinetics under alkaline conditions.^[90]

These limitations opened the door to novel alternative materials with excellent performance solely composed of Earth-abundant materials.^[90,98] The low cost materials based on TMs showed comparable if not even better performance than noble metals and revealed higher corrosion resistance and mechanical stability. This prompted their widespread used as electrocatalysts in alkaline water electrolysis (see Figure 1.9). TM-based materials such as oxides,^[99,100] (oxy)hydroxides, and layered double hydroxides (LDH)s,^[27,101,102] phosphates,^[61,92] borophosphates,^[80] phosphites,^[79] alloys,^[103,104] intermetallics,^[81,105] chalcogenides,^[106,107] and pnictides^[5,52,62,71,108–112] have been used. Especially, materials based on Ni, Co, Fe, and Mn have established themselves as promising candidates mainly because of their variable oxidation states, 3d electrons, and morphological properties.^[48]

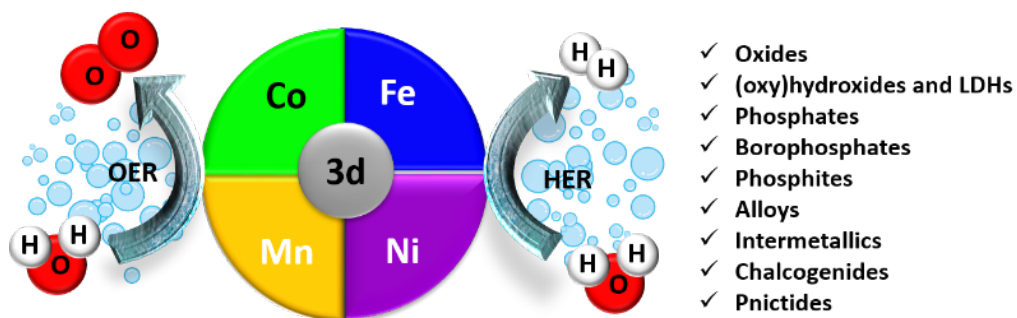


Figure 1.8. TM based materials used for OER and HER electrocatalysis under alkaline conditions.

1.5.2. Active materials for OER: electronic structure

First-row TM oxides, especially Fe, Co, and Ni, have been the most widely reported catalysts for alkaline OER. Among them, Co is the most studied because of its high stability in alkaline electrolytes. Co oxides have been used for electrochemical water-splitting for more than 65 years and are often characterized by a very low overpotential during OER catalysis.^[86] CoO , spinel-type Co_3O_4 and CoO_x are considered promising alternatives for Ir and Ru in the OER.^[71,99] Numerous studies have been focused on the synthesis of active Co oxide structures and the investigation of their mechanism for the OER.

Gerken and co-workers^[113] used X-ray absorption spectroscopy (XAS) to reveal post-catalytic transformation of CoO_x to amorphous cobalt (oxy)hydroxide $\text{CoO}_x(\text{OH})_y$, which exhibited one of the highest activities for a monometallic metal oxide or (oxy)hydroxide.

Recently, Hu and co-workers^[114] used operando XAS and Raman spectroscopy to propose a new mechanism of OER on amorphous $\text{CoO}_x(\text{OH})_y$ based on the presence of Co^{IV} species formed during catalysis. The presence of a high oxidation state active species was consistent with reports of Co_3O_4 ,^[115] CoO_x ,^[113] Co-Pi ,^[116] CoOOH nanosheets^[117] and DFT calculations.^[118] The proposed OER mechanism^[114] under alkaline conditions involved two Co^{III} active centers, (Figure 1.9). The oxidation of the first Co^{III} ion is accompanied by two PCET (A to B, B to C). A further PCET at the OH gives the Co^{IV} -O-species (C to D1), which is fundamental for the following O-O bond formation. DFT calculation and Raman spectroscopy results proved that this species is in equilibrium with a bridging superoxide species D2.^[114] Then, the release of O_2 from D2 with a concomitant H_2O binding (D2 to E) occurs, which is the RDS. Binding of another H_2O molecule and a further one electron oxidation regenerates the starting state of the catalyst.^[113,119]

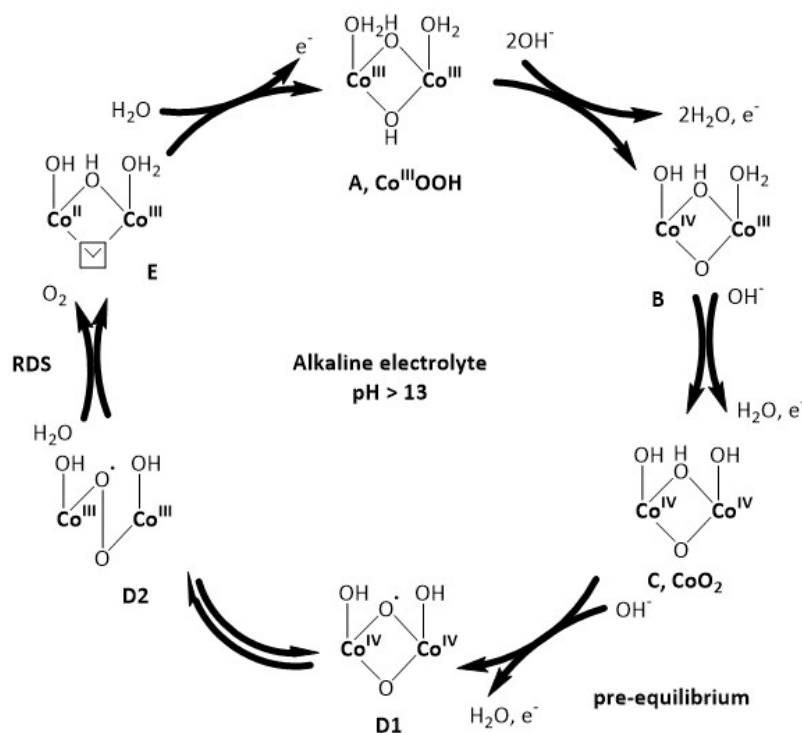


Figure 1.9. The mechanistic proposal for OER with various intermediate steps.^[114]

The anodic oxidation and transformation to amorphous phases has been also observed on Co-based oxides. For example, Co_3O_4 transformed to a less ordered $\beta\text{-CoOOH}$ phase on the surface during OER, which is the OER active phase as determined by DFT calculations.^[120] Co oxides are characterized by their low conductivity, which is a limiting factor for their electrocatalytic activity. However, it can be overcome by the preparation of composites with conducting carbon materials such as graphene, graphene oxide (GO) and carbon nanotubes (CNT)^[121] or gold particles.^[122]

Recently, Ni-based materials have shown promising OER electrocatalytic activities, and the OER activity order of the TM compounds has been classified as $\text{Fe} < \text{Co} < \text{Ni}$.^[123] Similarly to Co oxides, Ni oxides form highly active amorphous $\text{Ni}^{\text{II}}(\text{OH})_2/\text{Ni}^{\text{III}}\text{OOH}$

during OER.^[59] The origin of the activity was related to the presence of highly oxidized species (Ni^{III}), increased surface roughness, and high occurrence of oxygen vacancies in the structure.^[124,125] Differences in activity of Ni-based materials have been also related to morphological characteristics. For example, Bode and co-workers^[126] determined that poorly crystalline $\alpha\text{-Ni}(\text{OH})_2$ is electrochemically oxidized to $\gamma\text{-NiOOH}$ during OER. On the contrary, the crystalline $\beta\text{-Ni}(\text{OH})_2$ phase is oxidized to $\beta\text{-NiOOH}$, which showed the best OER electrocatalytic activity.

Binary oxides of Ni and Fe are more frequently used for OER catalysis.^[27,33,127] Nocera and co-workers showed that the systematic doping of Fe in Ni oxide modified the electronic structure of the Ni catalyst in favor of a better OER activity.^[128] Pure Fe oxides have only rarely been described for OER, as they often only showed low activity experimentally and in theoretical calculations^[82,129] due to their lower conductivity.^[101,130,131] Under anodic potentials, Fe_3O_4 gradually converts into $\alpha\text{-FeOOH}$, $\gamma\text{-FeOOH}$ and $\gamma\text{-Fe}_2\text{O}_3$ on the surface and reach an $\eta = 1240$ mV (at 10 mA cm^{-2}). Fe incorporation in Ni/Co (oxy)hydroxides is a topic of great interest due to the significant increase of OER activity when Fe ions were brought into the structure. $\text{Ni}_{1-x}\text{Fe}_x\text{OOH}$ LDHs are considered the most promising Earth-abundant electrocatalysts for OER under alkaline conditions.^[132] Fe has multiple roles in increasing the OER activity of NiOOH: (1) Fe enhances the electrical conductivity. (2) Fe affects the NiOOH electronic structure by inducing a partial-charge transfer from the NiOOH to the more-electronegative Fe, which modifies the electronic properties of the Ni^{III} centers.^[132,133] (3) Fe increases the amount of surface oxygen vacancies, which enhances the OER activity.

The high activity of TM-based materials is also related to the high degree of flexibility with regard to their oxidation states with redox potentials that match the energy of the OER. The relevance of certain oxidation states in connection to electron configuration of the metal atoms has been described for the oxygen evolution complex (OEC, $\text{CaMn}_4\text{O}_5(\text{H}_2\text{O})_4$) in PS II.^[25] Inspired by the exceptional activity of the CaMn_4O_5 , biologically mimic Mn_2O_3 showed superior catalytic OER performance in comparison to MnO_2 due to the presence of Mn^{III} . The high-spin asymmetric occupation of the antibonding orbitals of Mn^{III} ($d^4, t_{2g}^3 e_g^1$) resulted in a Jahn-Teller distortion with long Mn-O bonds (see Figure 1.10). The generated disordered structures had enhanced bond flexibility and improved the water oxidation activity.^[134]

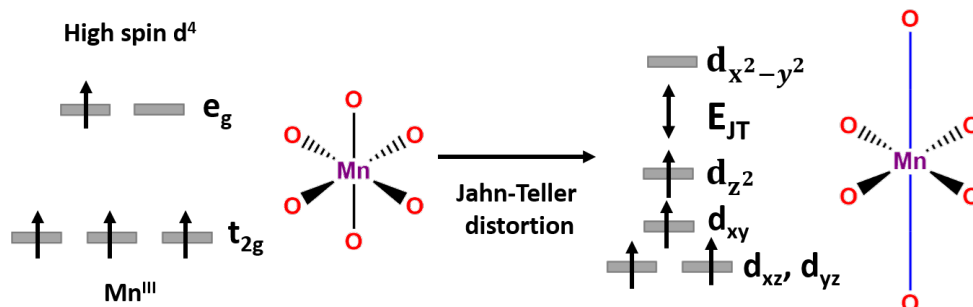


Figure 1.10. Electron configuration of high-spin Mn^{III} ($d^4, t_{2g}^3 e_g^1$) and Jahn-Teller distortion of Mn^{III} .^[135]

The degenerate high-spin electron configuration has been also observed on active OER perovskites where the effect of the electronic structure on the OER electrocatalytic activity has been established.^[33,59] Perovskites are mixed TM oxides of general formula ABO_3 in which A is a lanthanide, alkaline or alkaline earth element cation and B is a TM surrounded by 6 O atoms forming a BO_6 octahedron (Figure 1.11a). The perovskite electronic properties arise solely from the BO_6 octahedron. The orbitals of B are hybridized. The five d orbitals of the TM split into two groups whose energies depend on their orientations and hybridization with the O 2p orbitals (Figure 1.11b). The d_{z^2} and $d_{x^2-y^2}$ orbitals of the metal have a strong overlap with the O 2p orbitals. Consequently, the energy of an electron in these orbitals will be higher and corresponding to σ -bonding and σ^* -antibonding states (e_g). In contrast, the d_{xy} , d_{yz} , and d_{xz} orbitals have weaker spatial overlap with the O 2p orbitals. The energy of an electron in these orbitals is lower and constitute the π -bonding and π^* -antibonding states (t_{2g}) (Figure 1.11b).

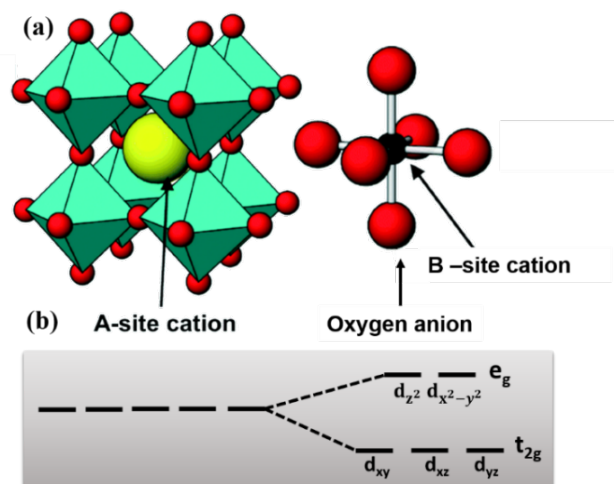


Figure 1.11. Sketch of basic ABO_3 perovskite oxide structure and electronic configuration. Adaptation from Fabbri and co-workers.^[59] © 2015 The Royal Society of Chemistry.

Matsumoto and co-workers^[136] first reported the correlation between number of electrons (oxidation state) and spin state (orbital filling) of the B atom is important to rationalize the differences in catalytic activity. The OER activity follows a volcano relationship with the occupancy of the e_g electronic state. The number of electrons in the σ^* state (e_g) determines the metal–oxygen bond strength, which resulted in the modulation of the OER overpotential in accordance with the Sabatier principle (see Section 1.5). Perovskites and oxides that have low e_g occupancy ($e_g < 1$) bind to oxygen too strongly, while oxides that have high e_g occupancy ($e_g > 1$) bind oxygen weaker. This model assumes that the σ -interaction of oxygen with the e_g states dominates over the weaker π -interaction of the t_{2g} states. The presence of unpaired electrons on the σ^* -orbital (e_g) enhances the electron transfer between OH^- and the electrode surface, promoting the water oxidation. In addition, Shao-Horn and co-workers demonstrated that 3d TM-based electrocatalysts exhibit a higher electrocatalytic activity when the e_g orbital occupancy of surface TM cations is close to unity due to the increased covalence of TM–oxygen bonds.^[137]

The observations of the relation of OER activity and oxidation state and spin state (orbital filling) can also be applied to other TM oxides, independent of their crystalline structure. TM sites (Co, Ni and Fe) with high valence states (III, IV) can accelerate the reaction kinetics to offer highly intrinsic activity.^[138] These species have been shown fundamental to the mechanism of the OER (see Figure 1.9) due to the presence of unpaired electrons in the σ^* -orbital (e_g) which enhance the electron transfer and promote the water oxidation. Grimaud and co-workers^[139] established a correlation between the oxidation state and coordination sphere at the metal atom to the OER electrocatalytic activity in pure and mixed Co oxides. The high OER activity of $\text{Sr}_4\text{Mn}_2\text{CoO}_9$, $\text{Sr}_6\text{Co}_5\text{O}_{15}$, and LaCoO_3 was related to the intermediate spin Co^{III} (d^6) state, which has an unpaired electron in the degenerate e_g orbitals (see Figure 1.12).^[139] Perovskites (LiCo_2O_4 , LaCoO_3)^[140] containing Co^{III} (d^6 , $t_{2g}^3 e_g^1$) have been investigated by Raman spectroscopy and a facile oxidation of Co^{III} to Co^{IV} was observed, where the single electron in the Jahn-Teller distorted e_g^1 orbital was easily available for catalysis.

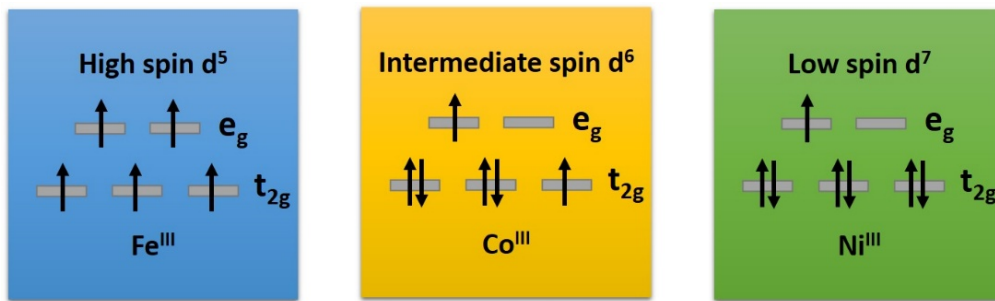


Figure 1.12. Potential TM 3d (e_g and t_{2g}) electron configuration of highly oxidized Fe^{III} , Co^{III} and Ni^{III} .^[76]

The Co^{III} can be easily oxidized to a high spin or low spin- Co^{IV} during the OER. In comparison, the combination of high spin Co^{II} in tetrahedral configuration (t_2^3) and low spin Co^{III} in octahedral configuration (0 electron in the e_g orbitals) in Co_3O_4 resulted in the lowest OER activity of the Co oxides measured in this study.^[139] Similarly, the single occupied e_g orbital of low-spin Ni^{III} (d^7 , $t_{2g}^6 e_g^1$) is the optimal electronic configuration for OER.^[141] The unpaired electron can enhance the electron transfer and promote water oxidation.^[142,143] The lower activity of Fe-based materials (see discussion above) can also be rationalized in terms of the orbital filling. The e_g orbitals in the high spin electronic configuration of Fe^{III} (d^5 , $t_{2g}^3 e_g^2$) are completely occupied, which limits the binding of the oxygen intermediate species and, consequently, the water oxidation.^[144] However, other Fe electronic configurations are beneficial for the OER. For example, low spin Fe^{III} in the octahedral configuration (d^5 , $t_{2g}^5 e_g$) has empty e_g orbitals. A Jahn Teller distortion occurs in this species, which stabilizes the t_{2g} orbitals and show a single occupied d_{z^2} orbital, which is available for oxygen binding. Similarly, Fe^{III} in the tetrahedral (d^5 , $e^4 t_2^1$) configuration also shows the t_2 orbital occupied by a single electron.

1.5.3. TM phosphides

In water-splitting electrocatalysis, electrical conductivity is often ascribed to play an important role for good activity.^[38] In this context, TM pnictides, in particular nitrides (TM-Ns) and phosphides (TM-Ps) and in a less extent arsenides (TM-As), have shown very good electrical properties. Moreover, their high surface area, porosity, resistance to harsh electrolyte environments are attractive characteristics towards OER and HER electrocatalysis.^[27,47,145,146]

The variety of compositions of TM-Ps is the origin of the diverse crystal structures and bonding in these materials, which affect their properties, such as electrical conductivity.^[69] TM-Ps can be metallic, ionic or covalent. Metallic bonding is observed in metal-rich (M_xP_y , $x > y$) or stoichiometric (M_xP_y , $x = y$) TM-Ps. The high strength of M-P bonds and high metallic content are responsible for the high thermal stability and hardness, resistance to oxidation and chemical attack.^[69] On the contrary, phosphorus-rich TM-Ps (M_xP_y , $y > x$) have significant P-P bonding and, consequently, their characteristics are completely different from the metal-rich or stoichiometric phases: they show lower thermal stability, higher reactivity and “softer” materials properties.^[69] There is a direct connection between the electrical conductivity and the phosphorus content. For example, an increasing phosphorus content in $Ni_{12}P_5$ (29 %) < Ni_2P (33 %) < Ni_5P_4 (44 %), resulted in the increase of the metallic character and conductivity, and consequently, in the OER and HER activities.^[147]

TM-Ps were initially used as high performance catalysts for hydrodesulfurization (HDS), a catalytic process used to remove sulfur impurities from hydrocarbon fuels.^[71] The similarity of the HER and HDS mechanisms by a reversible and dissociative binding of H_2 molecules on the surface of the catalyst is the reason behind the good activity of catalysts for both reactions. Electronegative phosphorus atoms can trap H^+ to promote H_2 liberation and also act as a base to withdraw electron density from the metals, which can behave as a hydride acceptor and promote HER.^[148]

The HER electrocatalytic activity and transformation of Ni and Co phosphides has been studied under alkaline^[69] and acidic conditions.^[149] For example, Ni_2P nanoparticles were an effective HER catalyst in acidic media (120 mV, 10 mA cm^{-2}) due to the exposed high density of $Ni_2P(001)$ surface, which had been theoretically predicted as active for the HER.^[150] Ni_5P_4 showed high activity and stability for HER under alkaline conditions and post-catalytic characterization studies demonstrated the formation of a protective layer of $Ni^{II}(PO_4)_x$ that prevented its dissolution and deactivation.^[151] The metallic character of the remaining TM-Ps core accelerated the charge transfer from the active catalyst surface to the electrode substrate to accomplish efficient electrocatalysis. Co_2P has also been identified as an active HER electrocatalyst,^[152] because of the advantageous Co-P bonding, which favors the exposure of abundant active sites during HER.^[153]

In 1989, Kupka and Budniok reported for the first time the use of amorphous and crystalline Ni-Co-P for OER electrocatalysis.^[154] Almost 20 years later, in 2015 Yoo and

co-workers^[155] and Yang and co-workers^[156] independently investigated the electrocatalytic performance of CoP for OER in alkaline electrolyte. Soon after, mono-metallic TM-Ps of Co, Fe, Ni, Mo, W and Cu showed promising OER activities.^[157–160] Detailed post-catalytic studies determined the changes occurring during OER electrocatalysis under alkaline conditions.^[161,162] Yoo and co-workers^[26] used X-ray photoelectron spectroscopy (XPS) and X-ray absorption near-edge structure spectroscopy (XANES) to perform post-catalytic characterization of CoP catalyst. They observed the leaching of P on the surface and formation of a layer with a porous, amorphous, and nanoweb-like dispersed morphology, which was ascribed to amorphous $\text{CoO}_x(\text{OH})_y$, as a result of the dissolution of P in the electrolyte. The oxidation of TM-P started at the particle surface, where a thick over layer is formed, but could go beyond the particle surface depending on the size and morphology of the nanostructures.^[163] The synergistic interaction between the (oxy)hydroxide shell and the remaining TM-P core explains the unique activity of these materials in comparison to the purely oxidic phases. The resulting core-shell is beneficial for the electrocatalytic activity. The shell contains high valent metal species that are the OER active sites.^[26,155] The TM-P core, due to its metallic character, is an effective electron pathway that facilitates charge transfer.^[164]

Similar transformations during alkaline OER and HER have been observed with Ni phosphides. Hu and co-workers^[161] used Ni_2P nanoparticles (NPs) for OER under alkaline conditions, during which the amorphous NiO_x was the active catalyst. A core shell structure appeared during catalysis as demonstrated by transmission electron microscopy (TEM) and energy-dispersive X-ray spectroscopy (EDX) (see Figure 1.13).

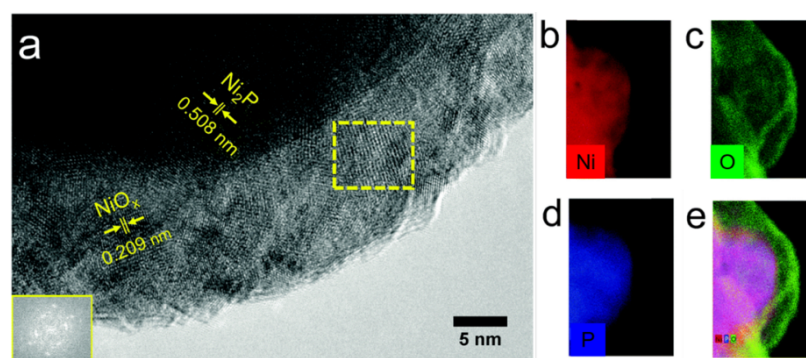


Figure 1.13. (a) TEM showing the formation during OER of a core-shell structure of Ni_2P surrounded by NiO_x , as confirmed by the EDX mapping of (b) Ni, (c) O and (s) P. Combined elemental mapping is shown on (e). Adapted from Hu and co-workers.^[161] © 2015 The Royal Society of Chemistry.

Ni phosphide phases of different stoichiometry have also shown impressive activities for the OER and HER. Menezes and co-workers^[26] compared the activity of Ni_2P and Ni_{12}P_5 for OER and HER under alkaline conditions. Both materials underwent surface passivation forming $\text{Ni}^{\text{II}}(\text{PO}_4)_x$ and $\text{Ni}^{\text{III}}\text{O}_x(\text{OH})_y$ phases because of contact with alkaline solution. During OER, the phosphorus leached out of the structure and formed the OER active phase, an amorphous $\text{Ni}^{\text{III}}\text{O}_x(\text{OH})_y$ shell that is formed around the Ni phosphide metallic core. During HER, a larger concentration of phosphide/phosphate species was found in the shell, which increased the created negative charge to trap H^+ .^[26] Similar

conclusions with other Ni phosphide phases have been observed Kucernak and co-workers, while studying the HER activity of Ni₂P₅ and Ni₂P.^[165]

The activities of Fe phosphide materials are less if compared to the Ni and Co analogues, but FeP^[111,147] and Fe₂P^[166] phases have also shown very good OER activity. Pure crystalline FeP has shown OER activity (350 mV at 10 mA cm⁻²) and very good long-term stability under OER conditions (48 h).^[157] Most importantly, Fe phosphides have also attracted attention as HER electrocatalysts because of their structural similarities with the active metal centers in hydrogenases. FeP, Fe₂P and FeP₂ are active for HER under diverse pH conditions, but their efficiencies are lower if compared to TM-Ps.^[69] Tian and co-workers^[167] uncovered the HER high activity of FeP (154 mV, 10 mA cm⁻²) and related it to the reduced surface-charge-transfer resistance in the HER process and increase in surface area. Other phases of Fe phosphide, like Fe₂P₃ have also received great attention for electrocatalytic applications. Menezes and co-workers^[111] recently used molecularly-derived Fe₂P₃ for OER ($\eta = 227$ mV, 10 mA cm⁻²) and HER (166 mV, 10 mA cm⁻²) under alkaline conditions. The high OER activity was related to the significant P leaching that created defect-structures with anionic vacancies on a Fe-rich Fe^{II}(OH)₂/Fe^{III}OOH shell over the structure. During HER, the electronegative P atoms withdraw electron density from the Fe acting as a based to trap H⁺, and Fe acted as a hydride acceptor. Moreover, the remaining FeP core enhanced the charge transfer and executed efficient electrocatalysis.

The anodic transformation of TM-Ps during OER electrocatalysis can be explained through the Pourbaix diagrams,^[51] which are plots of equilibrium potential vs. pH (*E*-pH) that determine at which condition corrosion and passivation under aqueous environments occur, but without considering the reaction kinetics (Experimental Section, see Figure 7.14). Corrosion occurs when the dissolution of TM species is favored, and passivation when a layer of M(OH)_x or MO_x(OH)_y forms over the metal, protecting it from dissolution. The behavior of the metals depends on the pH. Under acidic conditions, soluble metal ions Fe^{III}, Co^{II/III}, and Ni^{II} are favorably formed beyond the OER potential. At this pH, corrosion of the TM-Ps occurs. In neutral or alkaline conditions, MO_x(OH)_y are preferably formed beyond the OER potential. Phosphorus is favorably transformed to soluble species under potentials higher than that of the OER over a wide pH range. Therefore, the leaching of phosphorus and the oxidation of TM to form MO_x(OH)_y when a high potential is applied, is the driving force for the phase transformation during OER.

Continuous efforts have been done to increase the electrocatalytic performance of TM-Ps for OER and HER by several optimization strategies (see Figure 1.14). Morphology and crystallinity have a key role in the electrocatalytic activity.^[69] For example, a comparison between nanoparticles and rods or wire-like structures of TM-Ps, have shown the former to have superior charge transfer abilities.^[168] Moreover, amorphous Ni-P shown superior HER activity under alkaline conditions with minimal dissolution of Ni and P, in comparison to its crystalline counterpart Ni₂P.^[169] Carencio and co-workers^[170] prepared amorphous Fe_xP and crystalline FeP and Fe₂P, and demonstrated the superior

activity of the amorphous phase (230 mV , 10 mA cm^{-2}) in comparison to the crystalline phases (FeP, 330 mV ; Fe_2P , 380 mV , both at 10 mA cm^{-2}). Differences in porosity and surface area are also important to consider, as porous materials have wider exposed area, which benefits the mass/charge transport and the electrocatalytic activity. For example, various porous Co phosphide materials with 3D structures (polyhedra, nanoflowers) have been created for this aim.^[171–173] Porous urchin-like Ni_2P superstructures were reported as efficient electrocatalysts for HER under alkaline conditions due to the hierarchically microporous superstructure which provided a high ECSA.^[174]

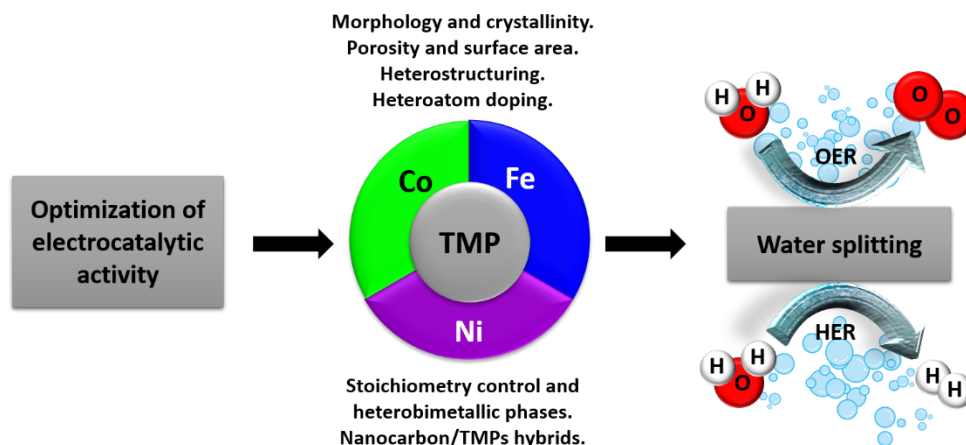


Figure 1.14. Optimization strategies to increase the electrocatalytic performance of TM-Ps.

The heterobimetallic structures tailor the electronics structures of TM-Ps to achieve highly active OER and HER catalytic performance.^[163] The introduction of secondary metal atoms with similar electronic configuration into the crystal lattice can substantially improve the electrocatalytic activity of TM-Ps.^[163] For example, heterobimetallic phosphides (FeNiP , NiCoP , FeCoP) had improved HER activity and stability compared to the monometallic phases.^[175] Yu and co-workers obtained a series of $\text{Ni}_{1-x}\text{Co}_x\text{P}$ catalysts with different Ni/Co ratios, and related the high OER activity to the increasing Co content.^[176] CoMnP has shown superior OER activity under alkaline conditions in comparison to pure Co_2P and MnP .^[177] Heteroatom doping also modifies the electronic structure of TM-Ps. Dinh and co-workers^[178] recently reported the doping of vanadium into Ni_2P nanospheres ($\text{V-Ni}_2\text{P}$), which showed an improvement in the OER activity due to the reduction of the charge transfer resistance (R_{ct}), which promoted the electroconductivity and enhancement of the ECSA. DFT calculations suggested that the Ni-V electron deficient centers conduct the Ni sites to be more active for OH^- adsorption. Fe doping has also found to enhance the electrical conductivity and, in consequence, the catalytic activity. Fe-doped Co_2P ($\text{Co}_{(2-x)}\text{Fe}_x\text{P}$) was observed to be more efficient than Co_2P , Fe_2P , the corresponding ternary oxides.^[179] A similar OER activity enhancement was observed in Fe-doped Ni_2P .^[180] Experimental and DFT calculations have also proved that Fe doping is beneficial for HER. For example, Fe-doping also benefited the HER activity of Ni_2P nanosheets, due to an increase in the ECSA and decrease in the charge transfer resistance compared with the undoped phase.^[181] DFT calculations of the

hydrogen adsorption free energy (ΔG_H) predicted that $\text{Fe}_{0.5}\text{Co}_{0.5}\text{P}$ is the best electrocatalyst for HER and is superior to the one of the monometallic phosphides.^[182]

The formation of heterostructures of TM-Ps with secondary TM-Ps and/or TMX phases (X = S, Se, C, N, etc.) boosts the OER and HER catalytic performance, due to modification of the electronic structure and increase in the electrical conductivity.^[163] For example, the hybrid structure composed of porous Ni_2P skeletons covered with vertically aligned $\text{Ni}_5\text{P}_4\text{-NiP}_2$ nanosheets transformed into a Ni-P/NiO(Ni(OH)_x) heterojunction which enhanced the OER performance due to the synergistic effect of the interfaces.^[175] DFT calculations on $\text{Ni}_2\text{P-Ni}_3\text{S}_2$ heterostructures showed that the strong coupling interaction between the components resulted in lower H_2O adsorption energy and low overpotential (210 mV, 10 mA cm^{-2}) compared to the value for the pure separated components.^[183] Similarly, $\text{Ni}_2\text{P-Ni}_5\text{P}_{14}$ hybrid nanosheets^[175] had improved HER activity and stability compared to the monometallic phases. Mixed sulfur-doped Mo phosphide and Co phosphide have been found to produce excellent HER performance, due to the small particle size, improved charge transfer, and enhanced intrinsic activity.^[184,185] Hybrid structures of amorphous nickel phosphide (Ni-P) with amorphous nickel cobalt phosphate (NiCo-Pi) afforded a very low overpotential (73 mV, 10 mA cm^{-2}). The Ni-P phases provided an active surface area, and the P atoms modulated the electronic structure of NiCo-Pi, which increased the HER activity.^[186]

The preparation of TM-P/carbon composites can improve the electrical conductivity and provide enhanced surface area.^[164] Han and co-workers,^[187] obtained FeP@C and MoP@C hybrid OER electrocatalysts. Zhang and co-workers^[188] prepared homogeneously distributed CoP on N-doped carbon. The direct incorporation of TM-Ps into carbon nanostructures such as reduced graphene oxide (rGO) or CNTs also proved to be beneficial for the OER and HER activity. The FeP-rGO@Au composite reached an $\eta = 260 \text{ mV}$ (10 mA cm^{-2}) which was lower compared to the pristine sample FeP@Au ($\eta = 320 \text{ mV}$, 10 mA cm^{-2}).^[189] Active site exposure and dispersion, and charge transfer increased by the deposition CoP from Co_3O_4 nanocrystals on CNT,^[190] ultrafine CoP nanoparticles supported on CNTs,^[191] CoP_2 nanoparticles on rGO sheets,^[192] $\text{Ni}_2\text{P/CoN}$ hybridized with N-doped porous carbon polyhedrons (PCP).^[193]

1.5.4. TM arsenides

TM arsenides (TM-As) are an important class of materials which exhibit unique electronic, semiconducting, optical, and magnetic properties.^[194-198] Binary TM-As are formed by a TM atom in M^{III} oxidation state combined with As atom in $\text{As}^{\text{-III}}$ oxidation state. A special feature in binary TM-As is the presence of polyanionic As-As bonds and polycationic M-M bonds in their structures (see Figure 1.15).^[199]

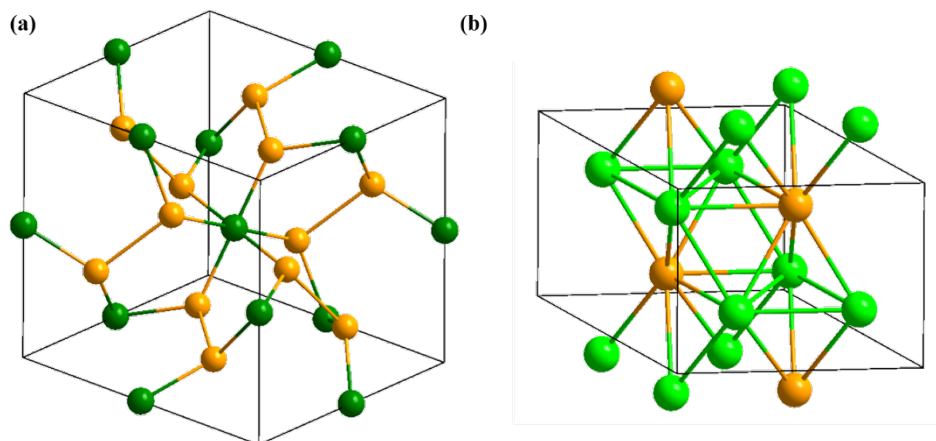


Figure 1.15. (a) CoAs_3 ($Im\bar{3}$), (b) Ni_3As ($P6_3/mmc$), showing polyanionic As-As bonds and polycationic M-M bonds are observed in the structures.

The most recent investigations have focused on main group metal arsenides like GaAs and InAs because of their potential replacement to Si in electronic, optoelectronic, and photovoltaic applications.^[200] However, recent attention has been placed in other materials such as FeAs and CoAs, due to their applications as semiconductors, anode materials for Li-ion batteries and magnets.^[201] Ferromagnetic TM-As like CrAs and MnAs are also important in the field of the spintronics, as they convert magnetic energy into electrical energy when used as components of circuits.^[201]

Despite the diverse uses of TM-As, seldom applications in electrocatalytic alkaline water-splitting have been done due to the toxic nature of As.^[202] The investigations by Schumann and co-workers on NiAs^[203] and CoAs^[204] remains as the sole examples of TM-As for alkaline OER electrocatalysis. NiAs and CoAs were synthesized by a high temperature solid state approach and then used for alkaline OER. Post-catalytic examinations showed an analogous process to observe with TM-Ps during alkaline OER electrocatalysis. As was oxidized and consequently dissolved into the electrolyte as arsenate $[\text{AsO}_4]^{3-}$ ions. The loss of As produced a shell composed of $\text{M}^{\text{III}}\text{O}_x(\text{OH})_y$ surrounding the metallic-character conductive TM-As core. Selective dissolution of As led to the creation of pores and increased accessibility of the active sites with respect to the host metal.^[202] The presence of only two examples TM-As for OER makes imperative their further investigation in electrocatalysis. Nevertheless, the high toxicity of As towards humans, animals, and the environment limit their use in large-scale alkaline water electrolysis.^[205]

TM-As have been less explored for HER in comparison to TM-Ps. Recently, Jaramillo and co-workers^[206] investigated CoAs, MoAs and Cu_3As for HER electrocatalysis under acidic conditions. The HER activity was related to the computationally calculated binding free energy of hydrogen (ΔG_{H}). CoAs bonded hydrogen too strongly, while MoAs had a moderate binding energy, which is optimized for the HER activity (see Figure 1.16).

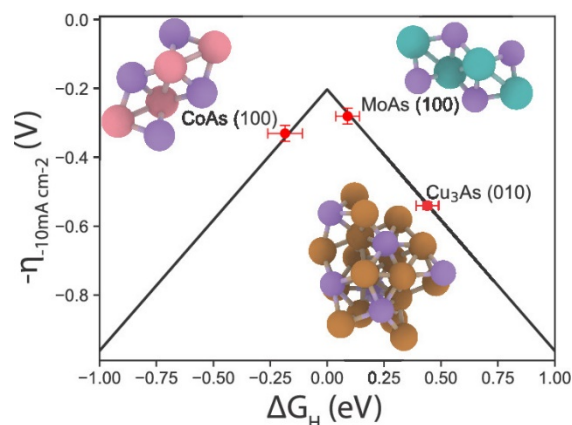


Figure 1.16. (a) HER volcano plot for TM-As explored by Jaramillo and co-workers^[206] which plots the overpotential for HER (at -10 mA cm^{-2}) as a function of the calculated binding energy of hydrogen on the catalyst surface (ΔG_H). Taken from Jaramillo and co-workers^[206] © American Chemical Society 2019

The HER also benefited from the conductive MoAs core. Therefore, MoAs showed the lowest overpotential among the materials ($\eta = 303 \text{ mV}$, 10 mA cm^{-2}). Cu_3As exhibited a larger overpotential due to the weak hydrogen binding energy. Nonetheless, post-catalysis characterization was not reported, and this investigation remains as the sole example of TM-As for HER in the literature.

1.5.5. The single-source precursor (SSP) approach: molecules to materials

The commonly applied synthetic routes to prepare TM electrocatalysts based on conventional solid-state syntheses often require highly reactive and pyrophoric reagents or high-temperatures leading to a random distribution of aggregates, an infinite number of nanostructures, small surface area, and unspecific morphology.^[69,106] Solvothermal methods are an effective pathway to synthesize nanostructured materials. The formation of nanostructured electrocatalysts in turn allows access to surface atoms on the catalyst, which is so crucial for heterogeneous catalysis.

The controlled decomposition of organometallic single-source precursors (SSPs) at the low-temperature ($< 300 \text{ }^\circ\text{C}$) affords high surface area amorphous and crystalline nanostructures.^[106,111,207,208] These precursors already contain all the required elements of the target material in a preorganized form by the ligands of the molecule.^[207] The conceptual novelty of this method relies on the decrease of the activation barrier for the nucleation of the solid phase through the metal-metal (M-M) or metal-ligand bonds in the molecular precursor, thus significantly lowering the operation temperature (see Figure 1.17).^[207,209] Therefore, the molecular structure of the precursor is defined according to the desirable structural and bonding features of the final material. The selected ligands stabilize the metallic center and contain the non-metal element (N, P, As, O, S, Se, Te) and can be quickly eliminated upon heating.^[62,207]

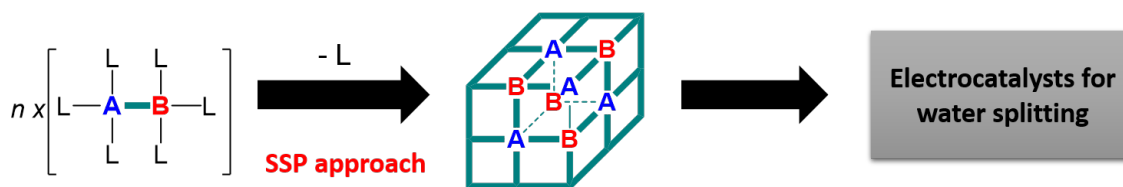


Figure 1.17 Schematic representation of the SSP approach using a molecular precursor containing the elements of interest (A and B) and the generation of the electrocatalyst by the removal of the ligand (L).

Additionally, the SSP approach allows the access to metastable or unusual phases that would not be accessible by conventional means.^[207] Solid state syntheses of inorganic materials typically proceed under thermodynamic control, i.e. the most thermodynamically stable phase under the growth conditions is formed. The use of SSP can be used to achieve metastable phases by kinetic trapping or to access phases only available at low temperatures and not obtained by the typical solid-state approaches.

The origin of the SSP approach was found during the preparation of materials through chemical vapor deposition (CVD) of liquid precursors.^[210] Manasevit and Simponto^[211,212] were the first to successfully employ the CVD to prepare semiconductors (GaAs) from molecular precursors containing the pre-existent strong σ bond between Ga and As (R_2GaAsR_2')_n (n = 1, 2, 3, etc.) or Ga(AsR₂)₃.^[213] The volatilization at intermediate temperature (< 200 °C), followed by decomposition at high temperature produced thin films of the desired materials.^[214] The SSP approach afforded better stoichiometric control and uniform size distribution in comparison to the traditional two-component synthetic methods.^[213,215] Later, TM nitrides were also prepared from volatile complexes with amido (NR₂), imido (NR) and amine (NR₃) ligands, in which the metal-nitrogen interactions remained intact during the precursor decomposition.^[216] CVD of oxido and N-containing ligand complexes (amino, amido, and imido) was then used to prepare oxide ceramics with applications in the field of superconductors, dielectrics and electron-optics.^[210] CVD was also employed to access TM chalcogenides such as FeSe^[217], Bi₂Se₃^[218] and SnS^[219] and MgTi₂O₅ thin films.^[220]

The thermal decomposition of SSP at elevated temperatures produces the loss or decomposition of any organic components to form the desired material and allows the retention of the elemental composition. The release of gaseous organic products during thermolysis influences the particle size and porosity of the produced material. A higher organic content in precursors allows a greater porosity and smaller particle sizes in their decomposition products, attributed to a greater gas escape during thermolysis.^[214] However, high organic content can also lead to undesired carbon impurities (5-10 %) or even the reduction of metals.

Calcination has been used extensively for the preparation of TM oxides from SSPs heated under air or O₂,^[214,221] such as TM oxides as Co- and Mn-doped ZnO.^[222] The pyrolysis or heating under inert atmosphere of molecular compounds^[221] has achieved diverse materials such as mixed phase Ni₂P/Ni₁₂P₅ NPs,^[223] Co-P crystalline phases,^[224] SnS and

SnSe,^[219] and Fe₃C.^[225] TM chalcogenides, CoS and CoSe, have been also prepared by the thermal decomposition of molecular precursors.^[226]

Hydrothermal synthesis has also been employed to access highly crystalline single-phase nanomaterials from SSPs.^[62,207] The hydrothermal process uses water in sealed steel pressure vessels with Teflon liners which are then heated (> 100 °C) in order to reach the pressure of vapor saturation and to develop autogenous pressure in the closed system. The hydrothermal route has been utilized to synthesize TM pnictides,^[181,227,228] TM oxides,^[229,230] TM phosphates,^[231] and TM chalcogenides.^[232,233]

CVD and thermolysis processes are comparatively limited with regard to the mobility of the crystallization nuclei that precede the phases that are formed. However, this does not occur in liquid phases. Therefore, the SSPs approach has also been successfully implemented in solvothermal processes. Solvothermal routes have been used to prepare colloidal nanomaterials like nanoclusters, nanocrystals or quantum dots (QD) from SSP. The “hot-injection” of organometallic compounds in coordinating solvents at elevated temperature (200-300 °C) is very effective in synthesizing high-quality nanocrystals with good crystallinity and narrow size distributions (see Figure 1.18). The rapid injection of SSPs into hot organic solvent can trigger a short burst of nucleation, and subsequent growth by aging can achieve this goal.

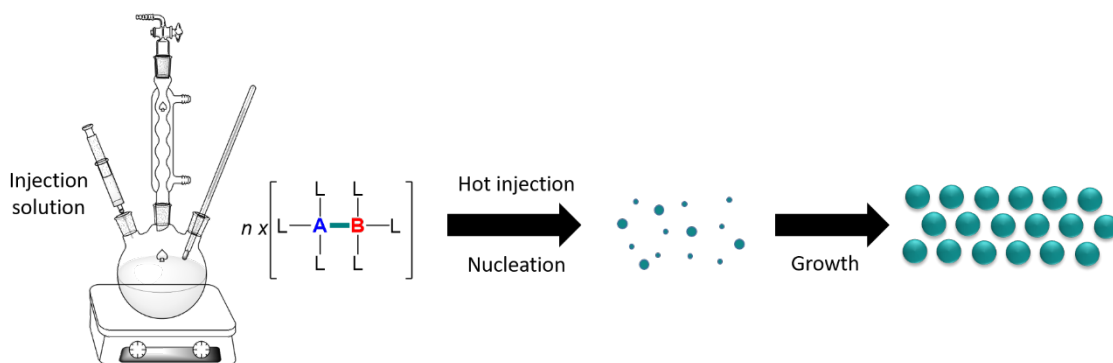


Figure 1.18. Schematic representation of the hot-injection of a molecular precursor containing the elements of interest (A and B) and the generation of the material in the hot coordinating solvent by nucleation and subsequent growth.

The hot-injection was first used in 1993 by Bawendi and co-workers^[234] to prepare high-quality nanometer sized QDs of CdS, CdSe and CdTe by controlled solution phase nucleation and growth, starting from Me₂Cd and (TMS)₂E (TMS = Me₃Si, E = S, Se, Te) reaction in TOP or TOPO at 290-320 °C. The solvent properties and reaction parameters (i.e. ratios of starting reagents, reaction temperature, reaction time, aging period) control the reactivity, shape, size, morphology, dispersity and crystallinity of the final material.^[214] Therefore, the morphology of the hot-injection-derived nanostructures is very diverse, including nanoparticles, nanospheres, nanorods and nanoplates. The colloidal synthesis using SSP was later developed to access other materials such as monometallic and heterobimetallic TM oxides.^[214,235,236] For example, the hot-injection of heterobimetallic Co_{4-x}Zn_xO₄ (x =1-3) achieved a unique cobalt-substituted crystalline

zinc oxide (Co:ZnO) that was used as stable electrocatalyst for water oxidation.^[237] SSP-derived materials have been utilized in different energy-related applications as photocatalysts, co-catalysts and electrocatalysts for OER, HER, and OWS (see Figure 1.19).^[238–240]

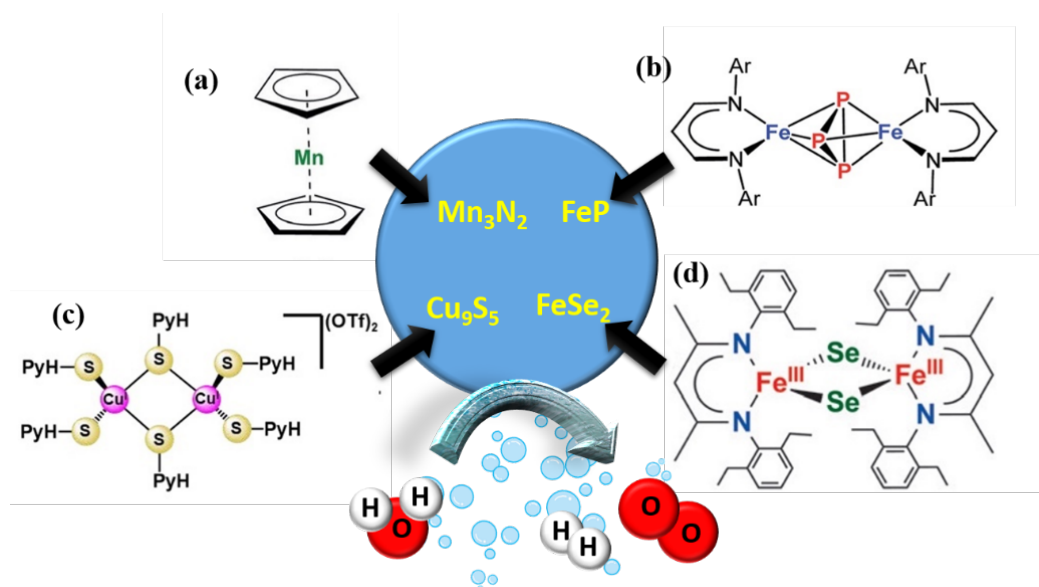


Figure 1.19. Molecular precursors employed to prepare (a) Mn_3N_2 , (b) FeP , (c) Cu_9S_5 and (d) FeSe_2 .

TM pnictides have been prepared by the SSP-approach.^[241,242] Recently, crystalline Mn_3N_2 was prepared by the annealing of manganocene ($(\text{C}_6\text{H}_5)_2\text{Mn}$, Figure 1.19a) under a constant NH_3 flow.^[208] The crystalline phase showed active and durable electrocatalytic activity for the OER under alkaline conditions.^[208] Active OER and HER FeP nanoparticles were prepared by the hot-injection of a molecular complex bearing β -Diketiminato ligand ($\text{L} = \text{CH}(\text{CRNAr})_2$ with $\text{R} = \text{alkyl}$ and $\text{Ar} = \text{aryl}$) with a $[\text{2Fe-3P}]$ core (Figure 1.19b).^[111] Molecularly-derived TM chalcogenides are also known as efficient electrocatalysts for water-splitting.^[106] For example, the hot-injection of a $[\{(\text{PyHS})_2\text{Cu}^{\text{I}}(\text{PyHS})\}_2](\text{OTf})_2$ molecular precursor (Figure 1.19c) resulted in crystalline Cu_9S_5 phase. It was used as an efficient OER electrocatalyst and showed better activities than the previously reported Cu_2S and CuS phases.^[243] FeSe_2 electrocatalysts was also accessed from a molecular precursor bearing β -Diketiminato ligands ($\text{L} = \text{CH}(\text{CRNC}_6\text{H}_4\text{Et}_2)_2$ with $\text{R} = \text{alkyl}$) which stabilized the $[\text{2Fe-2Se}]$ cluster (Figure 1.19d).^[106] The prepared material was favorable in OER and HER electrocatalysis, showing remarkable activity. TM carbides,^[225] intermetallics,^[209] perovskites,^[244] have been also prepared by the hot-injection.

2. Motivation and Objectives

The development of efficient electrocatalysts for OER and HER requires a profound understanding of the catalytic processes at atomic level. The design of materials with specific conductivity, morphology, and composition constitutes the base to improve the catalytic activity and stability of electrocatalysts. For example, TM-Ps and TM-As have a high active surface area and high electrical conductivity, which are fundamental to provide a large quantity of active sites and promote the fast electron transfer, respectively (see Section 1.5.3 and 1.5.4).

A targeted design of structures and morphology based on the rational decomposition of SSPs enables an efficient catalytic reaction and the reduction of the kinetic barriers in favor of higher catalyst activity and stability. Therefore, the SSP approach will be used to access these phases and study how their specific characteristics influence their OER, HER, and OWS electrocatalytic activity. Phosphides and arsenides of Co, Fe, and Ni will be studied, because of the high degree of flexibility of these elements with regard to their oxidation states and with redox potentials that match the energy of the OER and HER. Their oxidized species (Fe^{III} , Co^{III} , Ni^{III}) have been determined to adopt an energetically favored configuration, which enhance the electron transfer and facilitates the formation of O-O bonds. The necessary work is represented schematically on Figure 2.1.

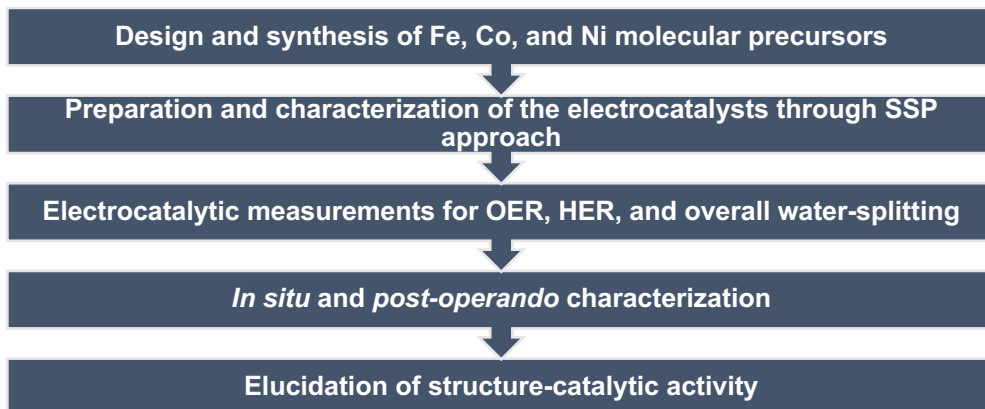


Figure 2.1. Step-by-step achieved during this investigation.

The first objective of this thesis is to establish the effect of the morphology in the electrocatalytic activity. Amorphous materials have shown larger activity in comparison to their crystalline counterparts. Therefore, the SSP methodology will be used to access amorphous and crystalline CoP by the hot-injection and pyrolysis of a β -Diketiminato [2Co-4P] molecular precursor. The synthesized materials will be explored for electrocatalytic OER and HER. The transformation of the prepared TM-Ps after catalysis will be studied to determine the nature of the active species and derive a possible mechanism for the catalytic reactions. In addition, the influence of the physical and structural properties in the activity, the identity of the phases and the active species generated during OER and HER will be investigated. Finally, the suitability of the phases

for long-term overall water-splitting will be carried out by the construction of a two-electrode alkaline electrolyser.

The second objective is the preparation of iron arsenide (FeAs) and its study for OER electrocatalysis. FeAs has attracted recent attention due to their unconventional superconductivity.^[194–198] The unique properties of this material could be beneficial for the catalytic processes, but the investigation of TM-As as OER electro(pre)catalysts remains scarce. Nanostructured FeAs will be accessed from the hot-injection of new molecular β -Diketiminato-stabilized [2Fe-2As] cluster. The OER catalysis will be studied, and the activity compared to benchmark Fe-containing reference materials (FeOOH, Fe(OH)₃ and Fe₂O₃). Of special interest is the active structure generated during the OER transformation of FeAs by the leaching of the As that will be clarified by *ex-situ* characterizations, as well as quasi *in situ* spectroscopy. Most importantly, the possible recovery of the dissolved As will be studied to determine the feasibility of FeAs in large industrial application. Finally, the new opportunities for the molecularly-derived nanostructured FeAs will be discussed.

The third objective will be the examination of the effect of the pnictogen element on the catalytic activity of TM-As and generation of the morphology and activity of the derived (oxy)hydroxide phase. Salts of 2-arsaethynolate and 2-phosphaethynolate anions (ECO)⁻ (E = As, P) will be utilized as robust sources of monoanionic phosphorus (P⁻) and arsenic (As⁻). Based on this, amorphous NiP and NiAs with similar morphology and equal stoichiometry will be prepared by the salt-metathesis reaction of NaAsCO and NaPCO with accessible NiBr₂(thf)_{1.5} complex via CO release. The prepared materials will be explored for OER electrocatalysis under alkaline conditions and compared with state-of-the-art electrocatalysts. *Post-operando* investigations by *ex-situ* characterizations, as well as quasi *in situ* spectroscopy will reveal the structural and electronic properties of the materials and the effect of the pnictogen element. Finally, a possible OER mechanism will be determined based on the identity of the generated phases and active species.

3. Synthesis, characterization, and electrochemical behavior of cobalt phosphide (CoP)

DFT calculations and electrochemical measurements have demonstrated that highly conductive materials show exceptional electrocatalytic activities, due to the rapid electron transfer.^[245,246] Amorphous materials have generally shown better electrocatalytic activity in comparison to the crystalline counterparts, due the larger ECSA.^[247] This chapter describes a systematic comparison of the transformation of SSP-derived amorphous and crystalline cobalt phosphide (CoP) during OER and HER. Of special importance is the relation of the activity to the initial crystallinity and the extension of the transformation, partially or completely, into amorphous phases during catalysis.

3.1. Introduction

The structural difference between amorphous and crystalline materials influencing the net catalytic activity has been ascribed to several reasons.^[100] Amorphous materials often show a larger flexibility, which allows self-regulation according to the electrocatalytic conditions.^[248,249] A structural reorganization occurs in amorphous materials when catalytically highly active crystallographic phases are generated *in situ*.^[247,248] Amorphous materials have abundant defect structures that result in a larger ECSA and unusual enhanced electrocatalytic activity.^[247,250] This difference is also related to their porous nature, which increases the diffusion of the electrolyte into the inner parts of the material, providing larger electrolyte-electrocatalyst interface (see Figure 3.1).

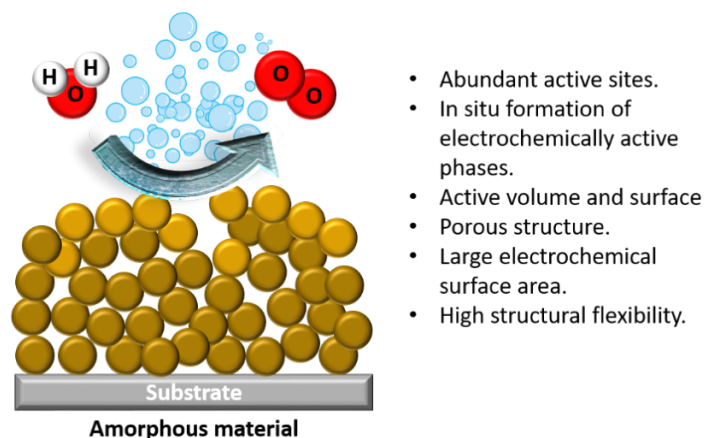


Figure 3.1. Schematic representation of OER electrocatalysis in an amorphous material and advantages for catalysis.

Amorphous materials have been used as OER and HER electrocatalysts since the late 1980s and early 1990s. The first studies by Kreysa and Hakansson^[247] demonstrated that amorphous TM alloys were better electrocatalysts for HER and OER in alkaline medium if compared to the crystalline phases of the constituent elements.^[251,252] Later, Alemu and Juttner^[251] followed by Kessler and co-workers^[251] extended the same study and observed the lower resistance to charge transfer (R_{ct}) of the amorphous phases in comparison to the crystalline ones.

Amorphous and crystalline monometallic phosphides of Ni, Fe, and Co are promising representatives of active OER and HER electrocatalysts due to their high surface area, porosity, and resistance to harsh electrolyte environments.^[27,47,145,146] Initially, Co phosphide materials were noted as attractive materials for the HER due to the similarity of the mechanism of this reaction to the HDS.^[253] In 2014 Shaak and co-workers^[149] reported multifaceted crystalline CoP NPs for HER electrocatalysis in highly acidic medium, which was the first report on Co phosphides as HER electrocatalysts. This investigation was followed by other Co phosphides with different P contents like Co₂P, CoP₂ and CoP₃.^[253] DFT calculations have proven that phosphorus atoms play an important role in the HER under acid conditions: negatively charged P^{δ-} atoms can trap H⁺ and promote H₂ liberation.^[148] In consequence, Co phosphide phases with higher P content have shown higher HER activity. The low HER activity of low-P content CoP has been compensated by the creation of 3D structures of determined morphology. For example, solvothermally-derived crystalline CoP nanoparticles deposited on Ti nanoplates (85 mV, at 20 mA cm⁻² in 0.5 M H₂SO₄)^[149] and CoP nanowire arrays over Ti mesh ($\eta = 72$ mV at 10 mA cm⁻²)^[254] showed long-term stability and high HER activity. The incorporation of CoP on carbon nanostructures has been also used to increase the HER activity. For example, high activity was obtained with CNTs decorated with CoP nanocrystals ($\eta = 40$ mV at -10 mA cm⁻² in 0.5 M H₂SO₄),^[190] self-supported nanoporous CoP nanowire arrays on carbon cloth (CC, $\eta = 67$ at 10 mA cm⁻² in 0.5 M H₂SO₄),^[255] and CoP nanoparticle films on CC ($\eta = 48$ mV at 10 mA cm⁻² in 0.5 M H₂SO₄).^[256]

In addition to HER, efforts have been done to develop Co phosphide materials as OER electrocatalysts.^[95,253] In 1989, Budniok and Kupka^[257] reported for the first time an amorphous Ni-Co-P film for OER under alkaline conditions. During OER, the material transformed to a defect rich and high surface area (oxy)hydroxide phase. The transformation can occur completely or either at the surface of the electrocatalyst forming a core-shell structure.^[258] The Co-P core acts as a conductive support providing an effective electron pathway to the active Co (oxy)hydroxide shell (see Figure 3.2).^[160] Positively charged Co^{δ+} sites in the surface can act as a hydroxyl acceptor, simultaneously facilitated by the negatively charged P^{δ-} centers that favor O₂ evolution by discharging and desorption.^[259]

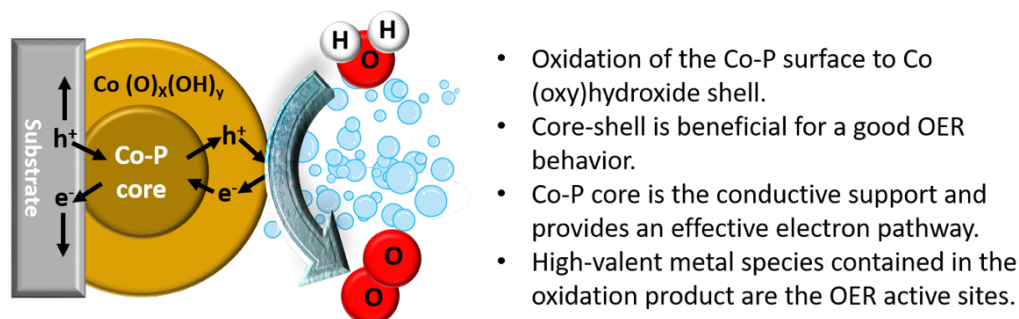


Figure 3.2. Schematic representation of the transformation of CoP during electrocatalytic OER under alkaline conditions.

The synergism of the Co-P phases with their derived oxidized products has been used to design materials of high OER activity. Highly porous amorphous Co-P/phosphate films showed high OER activity ($\eta = 330$ mV at 30 mA cm^{-2}) due to high surface area and efficient mass transport in the oxidized phosphate shell in combination with the high conductivity of the core.^[156] Similarly, the synergistic effect of *in situ* formed oxidized species was observed over Co-P nanorod bundles ($\eta = 340$ mV at 10 mA cm^{-2}),^[238] CoP nanorods ($\eta = 320$ at 10 mA cm^{-2}),^[162] and core-oxidized amorphous Co phosphide nanostructures ($\text{Co}_x\text{P}_y@\text{Co}_3\text{O}_4$) (287 mV at 10 mA cm^{-2}).^[239]

The incorporation of TMs into Co-P phases has been beneficial for the OER activity. Co_2P grown on Co-foil exhibited high OER performances ($\eta = 319$ mV at 10 mA cm^{-2}) due to increased stability and high conductivity given by the Co-foil.^[260] Fe-doped CoP porous polyhedrons showed less overpotential ($\eta = 289$ mV at 10 mA cm^{-2}) in comparison to CoP, FeP and state-of-the-start materials.^[173] Fe-incorporation in Co (oxy)hydroxide structures has been documented by Boetcher and co-workers (see Section 1.5.3).^[261] Fe incorporation allowed the intercalation of OH^- anions in the generated Co (oxy)hydroxide, and increased the interlayer distance, and the defects or edge sites in the structure. Most importantly, the Fe incorporation modified the Co electronic structure and, consequently, the OER intermediate energetics and the OER activity.^[173,261]

The conductivity can be improved by coupling catalysts with carbon materials. For example, CoP/carbon dots (CDs) composites achieved significant activity ($\eta = 400$ mV at 10 mA cm^{-2}) in comparison to bare CoP due to the rapid electron transfer property of CDs, which improved the charge transfer rate of the composite and provided a large specific surface area.^[262] The use of other conductive substrate electrodes can significantly ease the electron transfer of CoP materials.^[254] High activities have been achieved when conductive nickel foam (NF) or Cu foil were used as substrates for Co/ Co_2P nanoparticles^[263] and CoP mesoporous nanorods.^[264]

Co-P materials are also promising OWS electrocatalysts due to their high OER and HER electrocatalytic activities.^[253] CoP nanoneedle arrays have shown a low cell voltage of 1.61 V ($\eta = 480$ mV at 10 mA cm^{-2}) when used as anode and cathode, which worked continuously for over 70 h.^[265] Liu and co-workers used CoP hollow prisms for OWS on alkaline media, and reported a cell voltage of 1.52 V ($\eta = 290$ mV at 10 mA cm^{-2}).^[266] Nanostructured CoP with morphologies such as nanoframes and nanocubes^[267] have also shown great bifunctional activity ($E = 1.65$ V, $\eta = 420$ mV at 10 mA cm^{-2}) due to their hollow structure which allowed electrolyte permeation and gas emission.^[267]

3.1.1. Cobalt phosphide

In 1896, A. Granger^[268] was the first to describe attempts to combine phosphorus with Fe, Ni, and Co. Granger was able to produce the black powder of Co_2P , by the reaction of CoCl_2 and phosphorus under a heated stream of CO_2 . In the same investigation, another synthesis was reported using PCl_3 and metallic Co.^[268] This pioneering report opened the door for the preparation of other Co-P phases.

Co phosphide systems are known to have different stoichiometric ratios of Co to P and are divided into individual intermediate phases. A total of four stable intermediate phases of the Co system are distinguished:^[269] the orthorhombic phase Co_2P , the orthorhombic intermediate compound CoP , the monoclinic CoP_2 , and the cubic intermediate phase CoP_3 (see Figure 3.3).

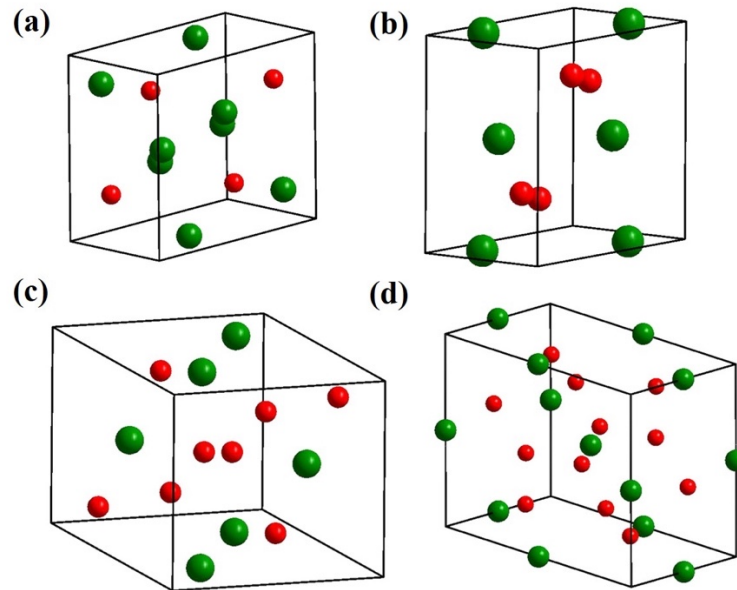


Figure 3.3. Unit cells of (a) Co_2P , (b) CoP , (c) CoP_2 , and (d) CoP_3 . The green and red atoms represent the Co and P positions on the lattice.

The high metallic character and paramagnetic orthorhombic Co_2P phase ($Pnma$, space group 62) is stable until its melting temperature ($1386\text{ }^\circ\text{C}$).^[270] The paramagnetic behavior of stable Co_2P phase has been observed in various nanostructures such as nanowires, nanorods, hollow spheres, and nanoneedles.^[271] The monoclinic CoP_2 phase ($P2_1/c$, space group 14), is a diamagnetic semiconductor and is formed at high pressure (65 kbar) and temperature ($800\text{-}1200\text{ }^\circ\text{C}$).^[272] The orthorhombic CoP ($Pnma$, space group 62) is stable at temperatures higher than $1000\text{ }^\circ\text{C}$ and shows a Curie-Weiss behavior due to its paramagnetism.^[273] Finally, the body-centered cubic (bcc) intermediate phase CoP_3 ($Im\bar{3}$, space group 204) has a skutterudite crystal structure and can be prepared by heating a mixture of Co and P under vacuum^[274] and Cl_2 atmosphere as a transporting agent.^[275] This material behaves as a diamagnetic p-type semiconductor with a substantial optical bandgap ($0.45\text{-}1.4\text{ eV}$).^[276]

3.1.2. Synthesis of cobalt phosphide

CoP systems are predominantly obtained by solid synthesis.^[69] Bulk Co phosphides can be prepared by direct combination of the metal and red phosphorus under inert atmosphere or under vacuum, but high temperatures ($> 900\text{ }^\circ\text{C}$) as well as long reaction times ($> 24\text{ h}$) are needed.^[151] Other commonly applied synthetic routes are based on conventional high-temperature phosphorization of metals or metal salts with toxic

phosphines (e.g., PH_3) or phosphorus pentachloride (PCl_5). A less toxic approach using $\text{P}(\text{SiMe}_3)_3$ and metal carbonyl complexes has been also reported.^[271]

Co-based salts can be converted into the desired phosphide species by phosphorization with NaH_2PO_2 through diverse synthetic routes.^[262] For example, Ai and co-workers^[153,160] synthesized CoP nanorod bundles from the hydrothermal treatment (120 °C) of a $\text{Co}(\text{NO}_3)_2 \cdot \text{H}_2\text{O}$ and NaH_2PO_2 solution for 9 h followed by annealing at 300 °C. Sun and co-workers prepared CoP nanowire arrays by the phosphorization of Co_3O_4 using NaH_2PO_2 .^[254] Similarly, the phosphorization of Co_3O_4 with NaH_2PO_2 has been shown as a route to access amorphous CoP,^[277] and crystalline CoP nanorods.^[162,238] Phosphorization with NaH_2PO_2 of phases derived from the decomposition of MOFs has been also reported in literature. For example, You and co-workers^[278] reported CoP/Co/NC nanopolyhedrons prepared by the direct carbonization of Co-based imidazole framework (ZIF-67) and phosphorization at 300 °C.

An alternative way to synthesize high-surface-area TM-Ps is through solvothermal conditions which allow to use alternative P sources.^[111] For example, the reaction of $\text{Co}_2(\text{CO})_8$ with $\text{P}(\text{SiMe}_3)_3$ in coordinating trioctyl phosphine (TOP) at 320 °C and 48 h was used to prepare CoP nanoparticles.^[279] Nanocrystalline CoP and Co_2P were prepared by the reaction of Na_3P and CoCl_2 in benzene at 150 °C.^[216] A similar approach was used to prepare nanocrystalline Co_2P by the reduction CoCl_2 by yellow phosphorus at 80-140 °C for 12 h in ethylenediamine.^[280]

The solvothermal decomposition of SSPs has been used to achieve Co-P crystalline phases. The close proximity of Co and P atoms in the precursor molecules makes them suitable to access various Co-P phases (see Section 1.5.5). For example, Buchwalter and co-workers^[224] used low oxidation-state organometallic clusters as precursors, $[\text{Co}_4(\text{CO})_{10}(\mu\text{-dppa})]$, $[\text{Co}_4(\text{CO})_{10}(\mu\text{-dppa})_2]$, $[\text{Co}_4(\text{CO})_8(\mu\text{-dppa})_2]$ (diphenylphosphoryl azide, $\text{dppa} = \text{Ph}_2\text{PNHPPH}_2$), to generate Co_2P and CoP. Maneeprakorn and co-workers^[226] used the molecular complex dialkyldiselenophosphinatocobalt(II) $[\text{Co}(\text{Se}_2\text{PR}_2)_2]$ (R = isopropyl ⁱPr, phenyl Ph, and tert-butyl ^tBu) to prepare crystalline orthorhombic CoP or Co_2P nanoparticles by their decomposition in TOP/trioctylphosphine oxide (TOPO) or TOP/hexadecylamine (HDA) at 300 °C. The composition was controlled by the reaction time: Co_2P was obtained after 60 min and CoP after 150 min.

3.2. Results and Discussion

3.2.1. Synthesis and characterization of amorphous and crystalline CoP

The morphology of a pure phase CoP depends on the choice of the synthesis route (see Section 1.5.5 and 3.1.2). Therefore, the SSP approach was used to obtain the phase-pure amorphous and crystalline Co-P by the variation of the decomposition method of the molecular precursor. β -Diketiminato complexes have been used as SSP to access active TM-P electrocatalysts.^[106,111] Therefore, the selected molecular precursor for this scope

is the organometallic β -Diketiminato cyclo-P₄ di-Co^I complex, whose synthesis and characterization have been reported previously by our group (see Experimental Section 7.1.2.1).^[243,281] The β -Diketiminato ligand acts as a stabilizer of the [2Co-4P] core, and easily detaches during solvolysis. The remaining [2Co-4P] core served as an ideal building block for Co-P materials. The molecular precursor was prepared according to the reported literature procedure and characterized (see Experimental Section 7.1.2.1).^[281]

The thermal decomposition of the molecular precursor under inert atmosphere to generate a crystalline Co phosphide was achieved through pyrolysis, which has been successful in the preparation of CoP and Co₂P crystalline phases.^[224] Pyrolysis experiments at different temperatures were done to determine the optimal temperature of decomposition. Pyrolysis at 300 °C and 450 °C for 2 h afforded amorphous materials as determined by powder-ray diffractometry (PXRD), with no clear reflections corresponding to a crystalline phase (see Figure A.1.1). Elemental analysis results (CHN determination) showed a partial degradation of the β -Diketiminato ligand at these temperatures, as supported by the large amount of organic content (Experimental Section, see Table 7.10). Thus, a higher temperature was applied to completely decompose the organic ligand and form the crystalline phase.

Pyrolysis at 600 °C achieved the complete decomposition of the molecular precursor, evidenced by the low organic content (7.79 %). The obtained phase after the 600 °C pyrolysis could be clearly pure by the PXRD, which showed broad and low-intensity diffraction peaks at 2θ of 31.6, 36.3, 46.2, 48.1, 48.4 and 56.8°, which represent the (011), (111), (112), (211), (202) and (301) planes of the crystalline CoP phase, as compared to the reference diffraction pattern JCPDS 029-497 (see Figure 3.5a and Experimental Section, Table 7.11 and Figure 7.21). The crystalline CoP corresponds to an orthorhombic phase (space group: *Pnma*, number 62, $a = 5.077$, $c = 5.587$).^[274] The broad reflections on the diffractogram can be attributed to the small particle size of CoP nanostructures. In the structure, each metal atom has six near phosphorus neighbors situated in a distorted octahedral configuration (see Figure 3.4a). The phosphorus atoms are surrounded by six Co atoms at the corners of a highly distorted triangular prism (see Figure 3.4b).^[274]

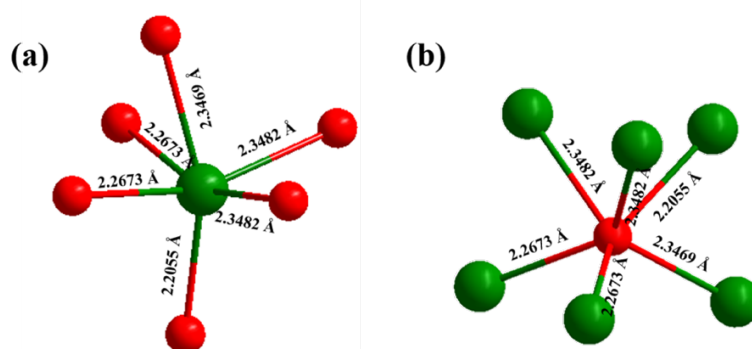


Figure 3.4. The crystalline CoP species (space group: *Pnma*, space group 62). Each metal atom has six near phosphorus neighbors situated in a distorted octahedral configuration (a). The phosphorus atoms are surrounded by six metal atoms at the corners of a highly distorted triangular prism (b). Co and P atoms are represented by green and red spheres, respectively.

The hot-injection is very effective in the preparation of nanosized materials of diverse morphology with good crystallinity and narrow size distributions (see Section 1.5.5). The hot-injection of the molecular complex in oleic acid was carried out at 300 °C, following the experimental conditions reported in the literature to prepare FeP and FeSe₂.^[106,111] The PXRD of the as-prepared product showed no sharp reflection peaks, that indicated the formation of an amorphous phase (see Figure 3.5b).

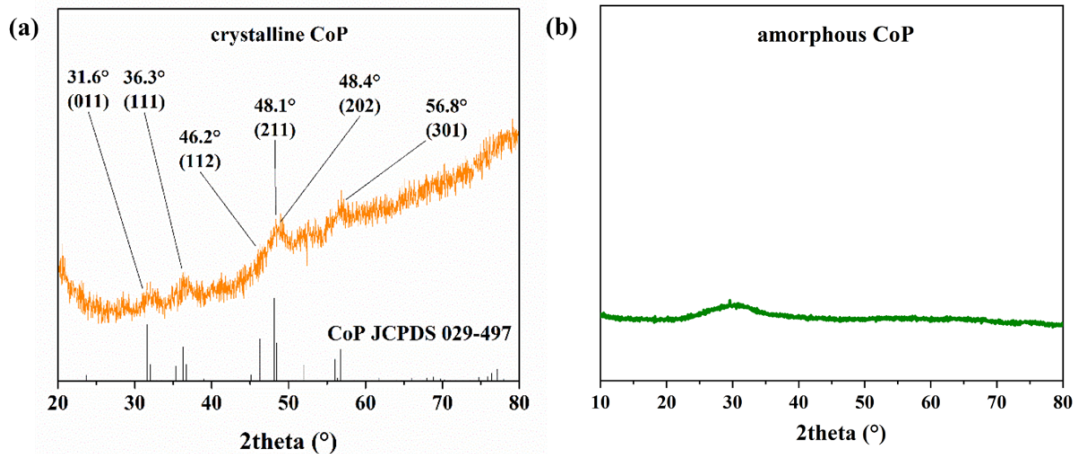


Figure 3.5. (a) PXRD pattern of crystalline CoP. The observed main diffraction peaks and their corresponding Miller indices are in accordance with the literature reported CoP (JCPDS 29-0497).^[274] (b) PXRD pattern of amorphous CoP. The obtained spectra did not reveal any sharp reflection, displaying the amorphous nature of the produced material.

The morphology of the materials was analyzed using scanning electron microscopy (SEM). SEM revealed that both materials consisted of agglomerates in the range of 400-800 nm (see Figure 3.6a, b). TEM revealed that the agglomerated materials observed by the SEM of the amorphous product was rather composed of particles with an average size of less than 10 nm (see Figure 3.7a). High-resolution TEM (HR-TEM, see Figure 3.7b) did not reveal any lattice fringes, confirming the amorphous nature of the material, that was further supported by the lack of diffraction rings in the selected area electron diffraction (SAED, see Figure 3.7c). Additionally, the material showed a low amount of organic content (Experimental Section, see Table 7.12).

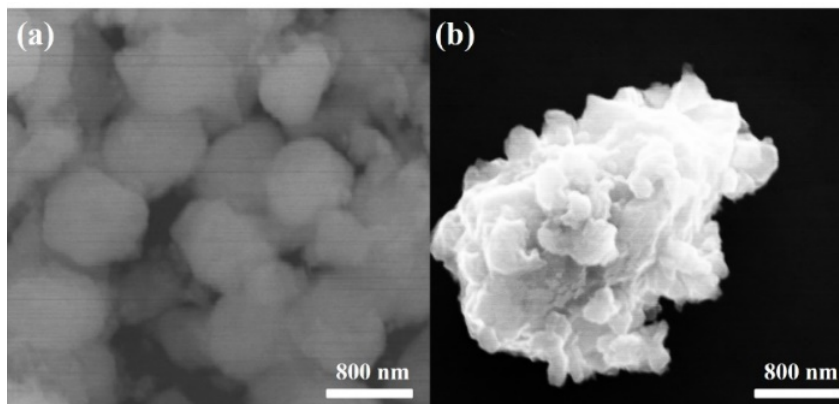


Figure 3.6. SEM images showing (a) amorphous CoP and (b) crystalline CoP.

The TEM of the product of the pyrolysis revealed agglomerates of particles (see Figure 3.7d). A closer examination via HR-TEM showed individual particles with clear crystalline fringes associated to the lattice spacing of $d(hkl) = 0.19$ nm, which corresponded to the (211) plane of the orthorhombic CoP phase (see Figure 3.7e, inset). The displayed sharp diffraction rings in the SAED were representative of the crystalline CoP phase, and unequivocally confirmed the formation of this phase already assigned by PXRD (JCPDS 29-0497, see Figure 3.7f).^[274]

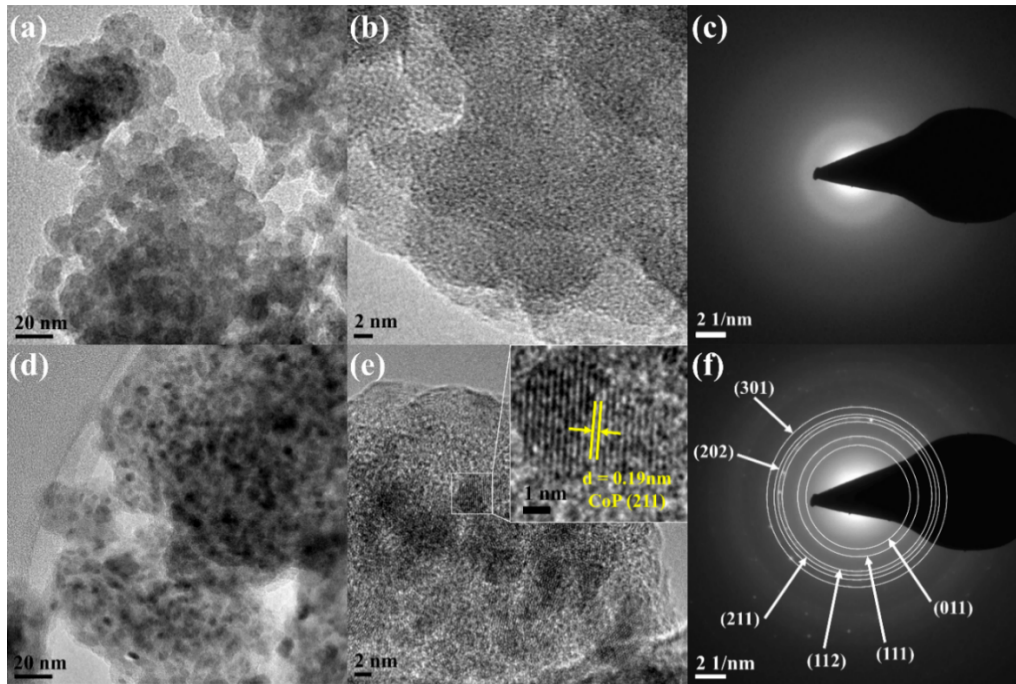


Figure 3.7. TEM, HR-TEM and SAED of the as-prepared amorphous CoP (a, b, c) and crystalline CoP (d, e, f).

The phase composition was confirmed by inductively coupled plasma atomic emission spectroscopy (ICP-AES) (see Table A.1.1) which demonstrated a ratio of 1:14 and 1:1.05 for crystalline and amorphous CoP. The elemental composition in the materials was carried out by EDX (see Figure A.1.2 and Figure A.1.3), in which a Co:P ratio of ca. 1:1 was obtained for the amorphous and crystalline materials. The investigation for homogeneity in the elemental distribution in the materials was carried out by EDX mapping. The EDX images showed an even distribution of Co (green) and P (red) within the structure of both the amorphous and the crystalline phases (see Figure 3.8 and Figure A.1.4). The EDX also revealed the presence of surface O, as a consequence of surface passivation due to exposure of the samples to air, since handling and transport were not carried out under inert conditions.

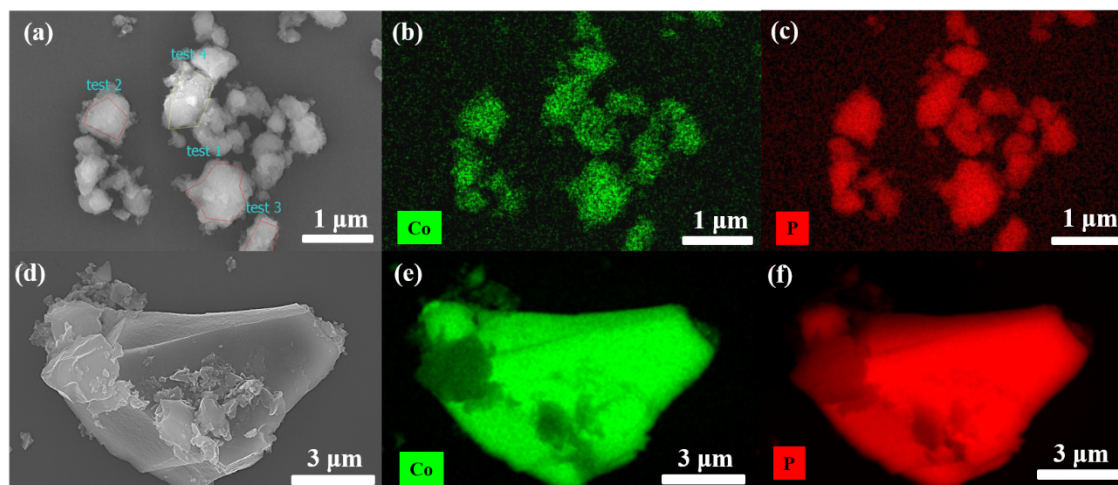


Figure 3.8. (a) SEM and elemental mapping of (b) Co (green), (c) P (red) on amorphous CoP prepared by hot-injection. The used substrate was silicon wafer. Homogenous distribution of Co and P was observed in the material particles. Similar results are observed on (d) crystalline CoP elemental mapping of (e) Co (green) and (f) P (red). O mapping for both materials is observed in Figure A.1.4.

Surface-bonded oxygen, due to air exposure was verified by Fourier-transform infrared spectroscopy (FT-IR). The FT-IR spectrum of amorphous and crystalline CoP showed bands from species generated during the surface oxidation (Experimental Section, see Figure 7.20 and Figure 7.22). The small bands appearing between $\bar{\nu} = 1250\text{-}500\text{ cm}^{-1}$ correspond to the stretching and bending vibrations of the phosphate group,^[160,282] and the small peak around 600 cm^{-1} is characteristic for the Co-O bond.^[282]

Elemental analysis revealed the presence of a small amount of carbon (Experimental Section, see Table 7.10), derived from the decomposition of the β -Diketiminato ligand into unidentified organic species. Although carbon nanomaterials have been used to improve the charge transfer efficiency and conductivity of TM-Ps (see Section 1.5.3),^[283] the amount of organic content was low (7.23 % C). Therefore, its influence in the electrocatalytic performance of the materials is negligible because the carbonaceous species are not included as a support. Similar phenomena have also been observed for MOF-derived TM-P electrocatalysts where the catalytic performance has been ascribed to the nature of metal cations and anions rather than any organic components.^[283-286]

A comprehensive investigation of the surface composition and electronic states of the synthesized amorphous and crystalline CoP was carried out by XPS (see Figure 3.9). The photoemission lines of the Co 2p spectrum resulted in a spectrum with multiple peaks due to the spin orbit splitting typical of the Co 2p spectrum to Co 2p_{3/2} and Co 2p_{1/2}, and the presence of satellite peaks.^[287] The deconvoluted high-resolution Co 2p spectrum (see Figure 3.9a) of amorphous CoP depicted peaks at 778.7 eV (2p_{3/2}) and 793.9 eV (2p_{1/2}), with a distance of 15.2 eV, which were assigned to the positively charged Co^{δ+} in CoP.^[288] The Co 2p spectrum of amorphous CoP also indicated the presence of Co in a higher oxidation state. The peaks at 782.2 eV (2p_{3/2}) and 797.8 eV (2p_{1/2}), as well as their two satellites (at 787.5 eV and 801.8 eV), were assigned to oxidized Co^{II}.^[289] The high-resolution Co 2p spectrum of crystalline CoP (see Figure 3.9b) showed only peaks at

binding energies related to Co^{II} (780.0 eV, $2p_{3/2}$ and 796.0 eV $2p_{1/2}$) due to surface oxidation,^[289] as well as satellite peaks (783.1 eV and 800.9 eV).

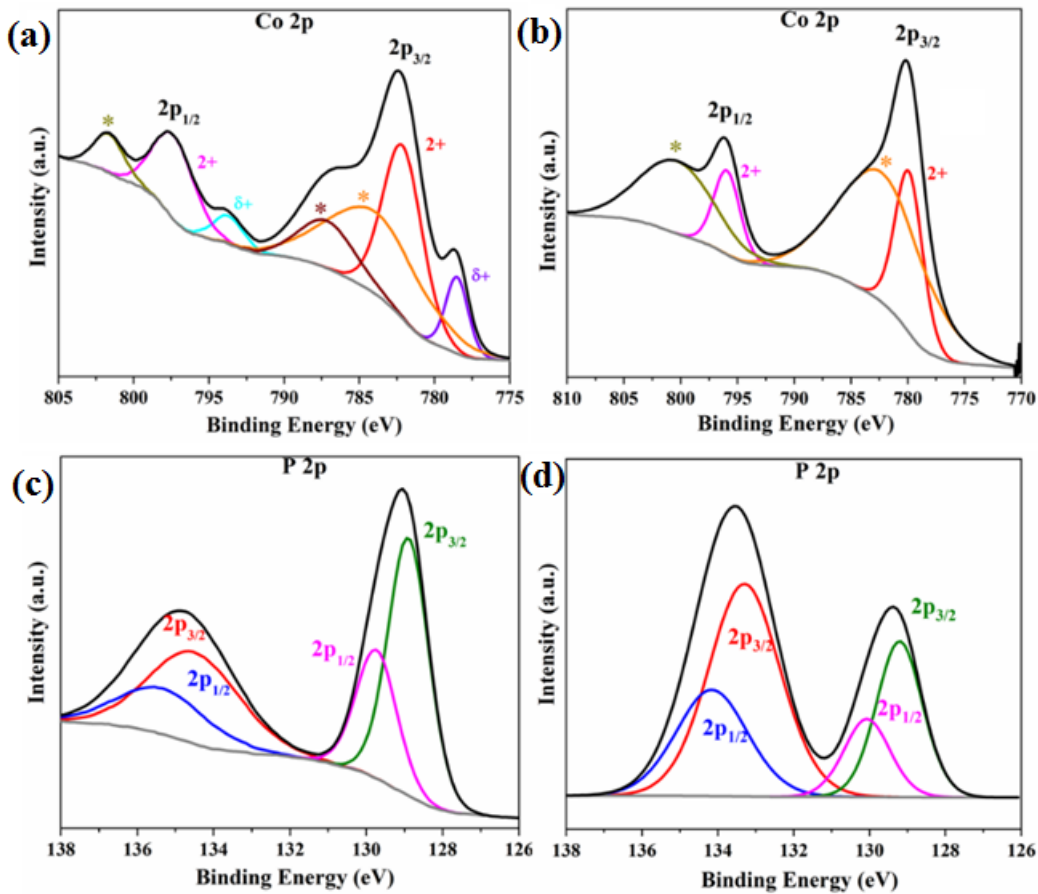


Figure 3.9. High-resolution XPS spectra for Co 2p (a,b), P 2p (c,d) for the as-prepared amorphous (left) and crystalline (right) CoP.

The P 2p spectrum of the amorphous CoP (see Figure 3.9c) showed a peak at 129.4 eV (deconvoluted into 128.9 eV $2p_{3/2}$ and 129.8 eV $2p_{1/2}$), which corresponded to the binding energy of phosphorus bound to metal, i.e. negatively charged $\text{P}^{\delta-}$ in TM-Ps.^[160] The less intense peak at 134.9 eV (deconvoluted into 134.6 eV $2p_{3/2}$ and 135.6 eV $2p_{1/2}$) was attributed to the binding energy of phosphate (PO_4^{3-}) species.^[160,162] Similarly, the crystalline CoP p 2p spectrum (see Figure 3.9d) showed a low-binding energy $\text{P}^{\delta-}$ peak at 129.4 eV (deconvoluted into 129.2 eV $2p_{3/2}$ and 130.1 eV $2p_{1/2}$) and the PO_4^{3-} species-related peak at 133.5 eV (deconvoluted into 133.3 eV $2p_{3/2}$ and 134.2 eV $2p_{1/2}$).

The presence of surface oxidized species has been reported in the literature of TM-Ps.^[255] The contact of Co phosphides with air generates a passivation layer which contains of $\text{Co}^{\text{II/III}}$ atoms and phosphate anions.^[162,290] The characterization results by EDX and FT-IR demonstrated the passivation of the surface due to contact with air. These results were supported by the O 1s spectra (see Figure A.1.5). The high-resolution O 1s spectrum of amorphous CoP showed one peak at 530.8 eV that was also deconvoluted into two peaks at binding energies of 530.5 eV (O1) and 531.9 eV (O2). The former peak was assigned

to the O species in Co-O-P and the latter to P=O.^[160,291] The high-resolution O 1s of crystalline CoP showed a major peak (531.9 eV) which was similarly deconvoluted into two peaks at 531.7 eV (O in Co-O-P) (O1) and 532.7 eV (P=O) (O2).^[160,291]

The characterization results showed the crystalline and amorphous CoP were successfully achieved starting from the pyrolysis and hot-injection, respectively, of the β -Diketiminato cyclo-P₄ di-Co^I complex. The method of decomposition of the precursor strongly influenced the morphology and crystallinity of the materials, but their elemental composition (Co:P 1:1) and carbon content (< 8 %) were similar. Therefore, it was important to determine the substantial effect of the different structures, surface characteristics, and electronic states with respect to electrocatalytic activity.

3.2.2. Electrochemical behavior of amorphous vs. crystalline CoP for OER and HER

The electrochemical investigations were carried out with a three-electrode configuration, which consisted of a Pt wire as the counter electrode (CE), a Hg/HgO reference electrode (RE) and working electrode (WE) (see Experimental Section 7.3.2). The WE consisted of films of the electrocatalysts directly deposited on fluorine-doped tin oxide (FTO) or NF. The films were produced by electrophoretic deposition (EPD). 1 mg of catalyst material was applied to a 1 × 1 cm² area of the NF substrate. The mass loading on the films prepared on FTO was around 0.4 mg (see Experimental Section 7.1.4).

The OER activity of amorphous and crystalline Co phosphide was initially determined by doing a linear sweep voltammetry (LSV) experiment (see Experimental Section 7.3.4). This experiment consists of the linear variation over time of the potential applied to the WE at a defined scan rate (mV s⁻¹) from an initial potential (E_i) to an end potential (E_f). The LSV was done with a scan rate of 10 mV s⁻¹ in 1 M KOH solution. The activities were compared to the state-of-the-art catalyst such as IrO₂ and the bare substrate (NF or FTO).

The recorded LSV of the prepared catalysts on NF substrate in 1 M KOH showed good activities for the OER (see Figure 3.10a). The attained electrocatalytic activity of the amorphous CoP for OER was very high, requiring an overpotential of $\eta = 284$ mV to achieve a current density of 10 mA cm⁻², which was a lower overpotential in comparison to the overpotentials of crystalline CoP ($\eta = 305$ mV at 10 mA cm⁻²) and commercial state-of-the-art IrO₂ ($\eta = 287$ mV at 10 mA cm⁻²) at the same current density. At 100 mA cm⁻², a similar trend in overpotentials is observed: amorphous and crystalline CoP required 314 mV and 392 mV, respectively. In comparison with other Co-based systems, the OER activity achieved on NF substrate was already one of the best OER catalysts reported to date in the literature (see Table A.1.2).

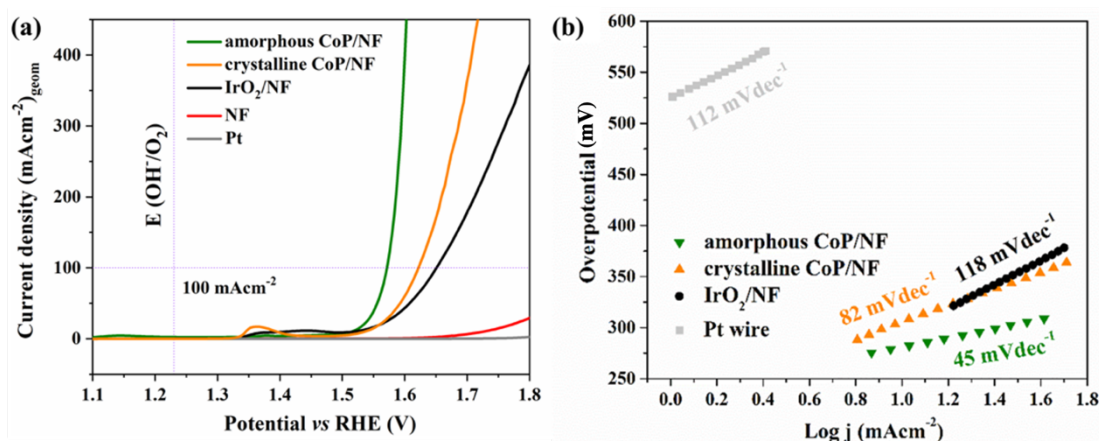
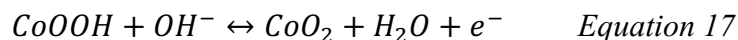
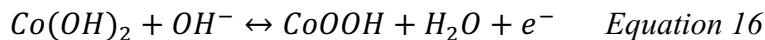


Figure 3.10. (a) Polarization curves of OER and of different CoP materials and commercial noble metal-based catalysts deposited on NF with a scan rate of 10 mV s⁻¹ in 1 M KOH (iR compensation: 85 %). (b) Tafel slopes of amorphous and crystalline CoP compared to IrO₂ deposited on NF and Pt wire. The Tafel slopes were obtained from the OER LSVs at 10 mV s⁻¹.

The electrocatalytic activity of the materials was classified according to the Tafel slopes (see Experimental Section 7.3.5). The Tafel slope (mV dec⁻¹) was obtained by the linear regression of the replot of the polarization curve as overpotential (η) vs. the logarithm of current density ($\log j$, mA cm⁻²).^[41] The Tafel slope indicates how much the potential must be increased in order to increase the resulting current density j by an order of magnitude (dec⁻¹). This means, how efficiently and dynamically an electrode reacts to an applied potential and generates catalytic current.^[50] Most importantly, Tafel slope values can also reveal information about the reaction kinetics and allow to determine which of the four processes of the PCET reactions was the RDS during OER (see Section 7.3.5).^[41,50] A low Tafel slope of 45 mV dec⁻¹ was observed for amorphous CoP, which was significantly smaller than the crystalline CoP (82 mV dec⁻¹) and IrO₂ (118 mV dec⁻¹) (see Figure 3.10b). The Tafel slope of amorphous CoP indicated that the rate-determining step is the second PCET, which involves the deprotonation-like process of the adsorbed hydroxide ion that reacts with a hydroxide ion from the electrolyte, to produce the $M - O_{ads}$ intermediate (see Section 1.4.2). In the case of the crystalline CoP, the much higher Tafel slope indicated that the OER is determined by the adsorption of the OH⁻ on the catalyst surface and the resulting formation of the adsorbed $M - OH_{ads}$ intermediate.^[41,292] The amorphous CoP catalyst reacted more dynamically and efficiently to changes in potential, which led to higher current densities with smaller increases in potential, thereby enabling better catalytic performance as shown by the calculation of the Tafel slope.^[292]

While performing the OER electrocatalysis in alkaline media, a small reversible redox couple was detected prior to the catalytic water oxidation in the range of 1.25-1.45 V vs. RHE (see Figure 3.10) on both amorphous and crystalline CoP. The redox couple became apparent when cyclic voltammetry (CV) experiments were performed (see Experimental Section 7.3.3 and Figure A.1.6). The redox peaks in both cases could be ascribed to the

oxidation of $\text{Co}^{\text{II}}/\text{Co}^{\text{III}}$ to higher oxidation species through the following electrochemical reactions:^[293]



These peaks have also been observed for other first-row 3d TM-based materials, which exhibit the formation of a $\text{M}(\text{OH})_2/\text{MOOH}$ phase at potentials between ca. 1.1 V and 1.4 V (vs. RHE) under alkaline conditions.^[293]

To evaluate the long-term stability of the catalysts, chronopotentiometric (CP) experiments were carried out maintaining a current density of 10 mA cm^{-2} . The overpotentials of amorphous and crystalline CoP were very stable for the period of 24 h (see Figure 3.11). During the CP experiments, amorphous CoP needed an overpotential of 280 mV to achieve a current density of 10 mA cm^{-2} for 24 h. A small increase in the overpotential during the experiment was due to capacitive charging of the catalyst material and the simultaneous rearrangement of the surface.^[294] A similar performance was observed for the crystalline phase, with a required overpotential of 300 mV at 10 mA cm^{-2} . This loss of activity has been observed before in Co-P-based systems and is documented in the literature.^[254,295]

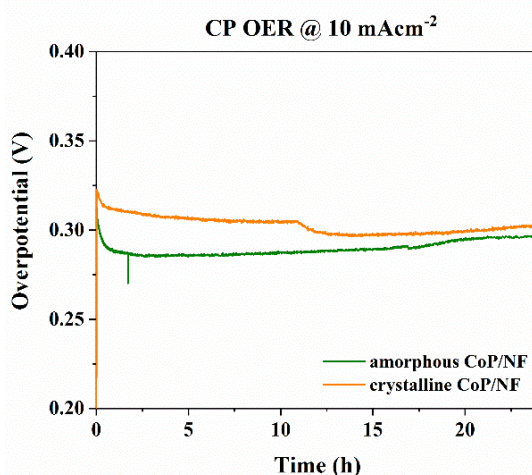


Figure 3.11. Chronopotentiometry (CP) experiment of amorphous and crystalline CoP on NF measured in OER conditions at a constant current of 10 mA cm^{-2} in 1 M KOH.

The very good results of the catalytic OER activity of the amorphous and crystalline CoP on the NF substrates was compared to further measurements of the catalytic activity on FTO, to rule out the contribution of NF in catalysis. NF is a uniform three-dimensional network of macroporous structures with a very large specific surface area and is characterized by its high electrical conductivity.^[296] In contrast, FTO is a conductive and flat substrate electrode which shows relatively less surface area but does not contribute to the catalytic activity.^[208,297] Therefore, due to the improved physical and electronic properties caused by the NF, an activity comparison of the materials deposited on FTO

should be done. The electrochemical tests for FTO were done on a three-electrode system in which Pt wire was used as the CE, and an Hg/HgO electrode was used as RE (see Experimental Section 7.3.2). The materials were electrophoretically deposited directly onto FTO and used as WEs (see Experimental Section 7.1.4).

The LSVs of the amorphous and crystalline CoP deposited on FTO showed an increase in the OER overpotential in comparison to the values obtained with the films deposited on NF (see Figure 3.12). The achieved current density was also lower due to the difference in the physical characteristics and properties of the substrates, but resulted in a similar trend of activity. Amorphous CoP achieved an overpotential of 360 mV (at 10 mA cm⁻²) which was lower than the one observed for crystalline CoP (414 mV at 10 mA cm⁻²), and even with noble metal electrodes like IrO₂ (409 mV at 10 mA cm⁻²). At 100 mA cm⁻², the difference between the overpotentials was even larger, which confirmed the higher OER electrocatalytic of amorphous CoP in comparison to its crystalline counterpart (414 vs. 592 mV). A comparison of the obtained overpotentials with reference values reported in the literature made it clear that the measurement results of this work were among the lowest published overpotentials for pure Co-P systems. Measured against other TM-based systems, the activity of amorphous CoP is one of the highest and ranked among the best catalysts for OER (see Table A.1.2).

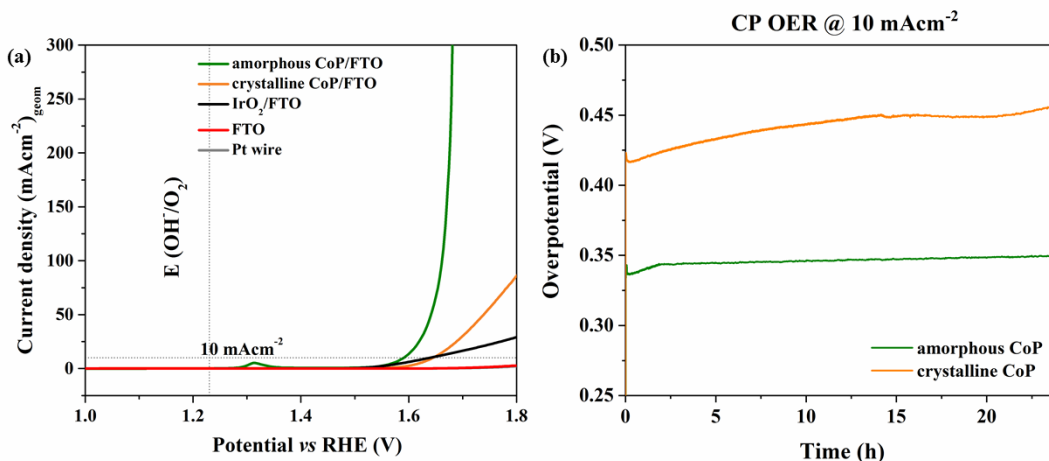


Figure 3.12. (a) OER polarization experiments in 1 M KOH. The activity of the materials follows the same trend found in NF (see Figure 3.10). Scan rate: 10 mV s⁻¹, iR compensation: 85 %. The stability was also investigated through CP (b) by applying a current of 10 mA cm⁻² for 24 h.

The long-term stability in particular delivered remarkable results, in which the difference in activity between the two phases was clearly demonstrated. The amorphous CoP reached a stable value of overpotential of 340 mV after approximately 2 h of continuous application of 10 mA cm⁻² of current density. In contrast, the crystalline CoP showed a continuous increase in the overpotential since the start of the experiment, from ca. 420 mV up to 450 mV after 15 h of continuous application of 10 mA cm⁻² of current density. After ca. 5 h of constant overpotential, it started to increase and reached 460 mV at the 24 h. This behavior could be related to the transformation observed in crystalline materials to amorphous phases during OER electrocatalysis.^[247]

The Tafel slopes of the FTO-based films were determined from the LSVs. A Tafel slope of 72 mV dec^{-1} was obtained for the amorphous CoP, which was lower in comparison to the one obtained for the crystalline CoP, 117 mV dec^{-1} (see Figure 3.13). Similarly, the Tafel slopes of the materials also outperformed the state-of-art IrO_2 . The calculated slopes in both samples suggested that the first and second PCET reactions of OER were the RDSs of the crystalline CoP and amorphous CoP, respectively (see Experimental Section 7.3.5).

Strong redox peaks were also visible during the LSVs for the OER of amorphous and crystalline CoP on FTO. In the LSV measurements in the range between 1.12-1.55 V vs. RHE, the pair consisting of the anodic and cathodic peaks could be seen again after the initial cycle (see Figure A.1.6). In this area, redox peaks can also be seen on the pure NF substrate.^[296] Since the redox peaks were also observed on FTO, the contribution of Ni species to the redox peaks was ruled out. The redox peaks occurred in the same range as determined before for the materials deposited on NF. Therefore, redox peaks could be attributed to the oxidation of $\text{Co}^{\text{II}}/\text{Co}^{\text{III}}$ to higher oxidized species.^[293]

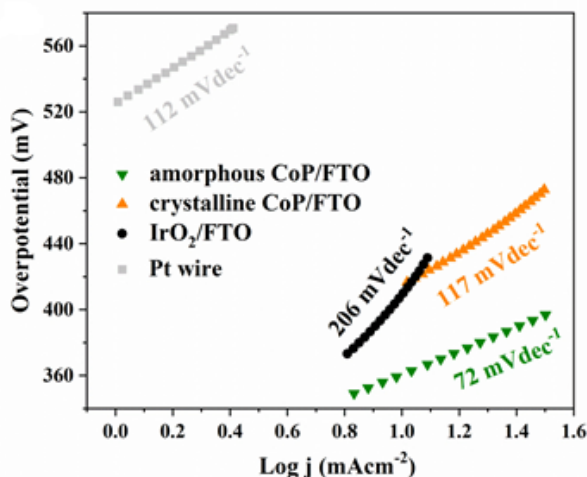


Figure 3.13. Tafel plot for OER for the as-prepared CoP materials deposited on FTO, IrO_2/FTO and Pt in aqueous 1 M KOH solution in OER. Scan rate: 1 mV s^{-1} . The amorphous CoP shows the lowest Tafel slope (72 mV dec^{-1}), which surpasses the crystalline CoP (117 mV dec^{-1}) and the state-of-the-art IrO_2/FTO (206 mV dec^{-1}) and the Pt wire (112 mV dec^{-1}).

Electrochemical investigations were similarly carried out to study the catalytic activity of amorphous and crystalline CoP towards HER. Similarly as in the OER experiments, the HER experiments were carried out with a three-electrode configuration, which consisted of a Pt wire at CE, an $\text{Hg}/\text{Hg}_2\text{SO}_4$ as RE and the films deposited on FTO and NF as WE (see Experimental Section 7.1.4 and 7.3.2). The recorded LSVs of the prepared catalysts on NF substrate in 1 M KOH showed good activities for the HER (see Figure 3.14a and zoom in Figure A.1.7). The attained electrocatalytic activity of the amorphous CoP for HER was very high, requiring an overpotential of $\eta = 143 \text{ mV}$ to achieve a current density of -10 mA cm^{-2} , which was a lower overpotential in comparison to the overpotentials of

crystalline CoP ($\eta = 261$ mV at -10 mA cm⁻²) and commercial state-of-the-art IrO₂ ($\eta = 209$ mV at -10 mA cm⁻²) at the same current density. However, the overpotential achieved by Pt, which is the best electrocatalyst for HER, was lower ($\eta = 39$ mV at -10 mA cm⁻²). The high current densities achieved by the electrocatalysts proved their electrocatalytic activity. At -100 mA cm⁻², a similar trend in overpotentials is observed: amorphous and crystalline CoP required 195 mV and 334 mV, respectively. A comparison to Co and other TM-Ps systems reported in the literature revealed that the amorphous CoP has a comparable electrocatalytic activity for HER under alkaline conditions (see Table A.1.3).

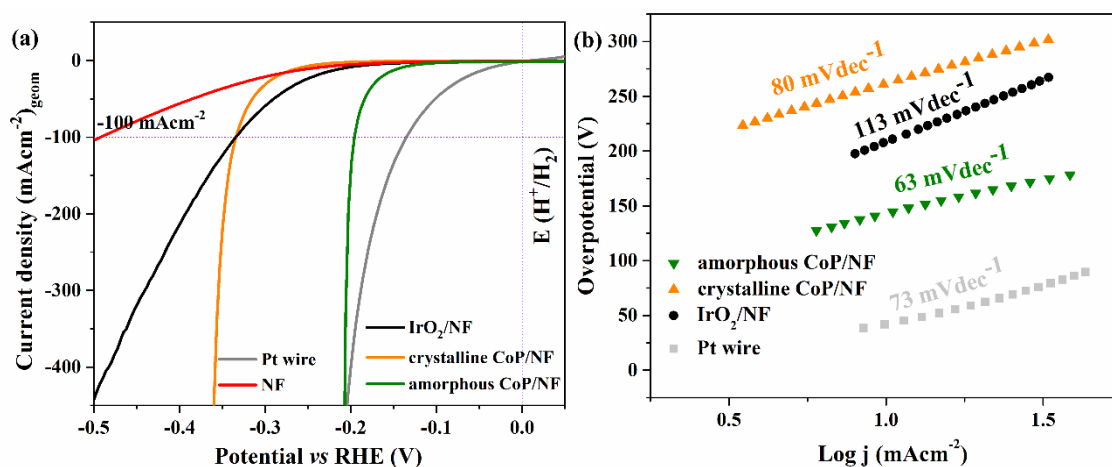


Figure 3.14. (a) Polarization curves of HER of different CoP materials and commercial noble metal-based catalysts deposited on NF with a scan rate of 10 mV s⁻¹ in 1 M KOH (iR compensation: 85 %). (b) Tafel slopes obtained for HER.

Tafel slopes were determined from the LSV curves (see Figure 3.14b). A Tafel slope of 63 mV dec⁻¹ was obtained for the amorphous CoP which was lower than that of crystalline CoP (80 mV dec⁻¹) and even state-of-the-art Pt wire (73 mV dec⁻¹) and IrO₂ (113 mV dec⁻¹). The attained values of Tafel slopes fall in the range of 40 - 120 mV dec⁻¹ which indicate that in both cases HER reaction proceeds via the Volmer-Heyrovsky mechanism on the surface.^[51] The Volmer step which occurs via a proton-coupled electron-transfer (PCET), is followed by the Heyrovsky reaction: the coupling of the $M - H_{ads}$ with H₂O accompanied by a second electron transfer to form H₂ (see Section 1.4.1).^[298] The occurrence of the Heyrovsky reaction is related to the low coverage by $M - H_{ads}$ of the electrode surface and sufficient available active sites near the $M - H_{ads}$ sites, which promote the reaction with one water molecule and reduce $M - H_{ads}$ to generate molecular H₂.^[52]

The long-term stability chronopotentiometric experiments (24 h) also demonstrated the difference in activity between the two phases. The amorphous CoP reached a stable overpotential (170 mV) after approximately 5 h of continuous application of -10 mA cm⁻² of current density. In contrast, the crystalline CoP showed a slow increase in the overpotential from ca. 300 mV up to 310 mV after 24 h of continuous application of -10 mA cm⁻² of current density.

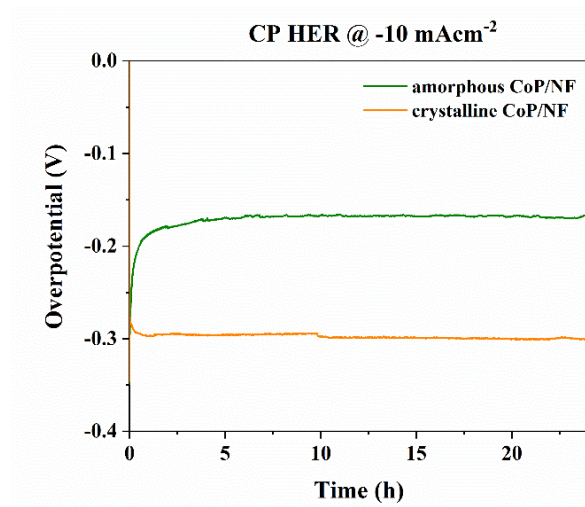


Figure 3.15. Chronopotentiometric experiments for HER (1 M KOH on NF) for amorphous and crystalline CoP on NF were investigated by applying a current of 10 mA cm^{-2} for 24 h. Both samples exhibited stable activities over 24 h.

Similarly as in the OER investigations, the activity of the materials for HER was explored on films deposited on FTO electrodes, since this substrate does not contribute to the catalytic activity due to its flat nature and conductivity.^[208,297] The electrochemical tests for FTO were done on a three-electrode system in which Pt wire was used as the CE, and a Hg/Hg₂SO₄ electrode was used as RE (see Experimental Section 7.3.2). The WE catalysts were electrophoretically deposited directly onto FTO (see Experimental Section 7.1.4).

When FTO was used instead of NF, a similar trend was observed in activity but with much lower overpotentials for the synthesized electrocatalysts (228 mV and 377 mV at -10 mA cm^{-2} for the amorphous and crystalline CoP, respectively) and IrO₂ (430 mV at -10 mA cm^{-2}) and Pt electrode (39 mV at -10 mA cm^{-2}) (see Figure 3.16a). A detailed comparison of the HER electrocatalytic activity of the prepared materials to other non-noble TM-based catalysts, TM-Ps and Co-P-based catalysts is listed in Table A.1.3.

The difference in electrocatalytic activity was even more evident during the long-term chronopotentiometric experiments, in which a constant current density of -10 mA cm^{-2} was applied to the system for 24 h (see Figure 3.16b). The amorphous CoP achieved a continuous response ($\eta = 180 \text{ mV}$) after 5 h of experiment. A much lower overpotential and stability was observed with the crystalline CoP. Initially, the activation was observed during the first hour, in which the overpotential continuously decreased until it reached 410 mV. After this, it was constant for the next 4 h, and then it increased until it was $\eta = 470 \text{ mV}$ at the final 24 h.

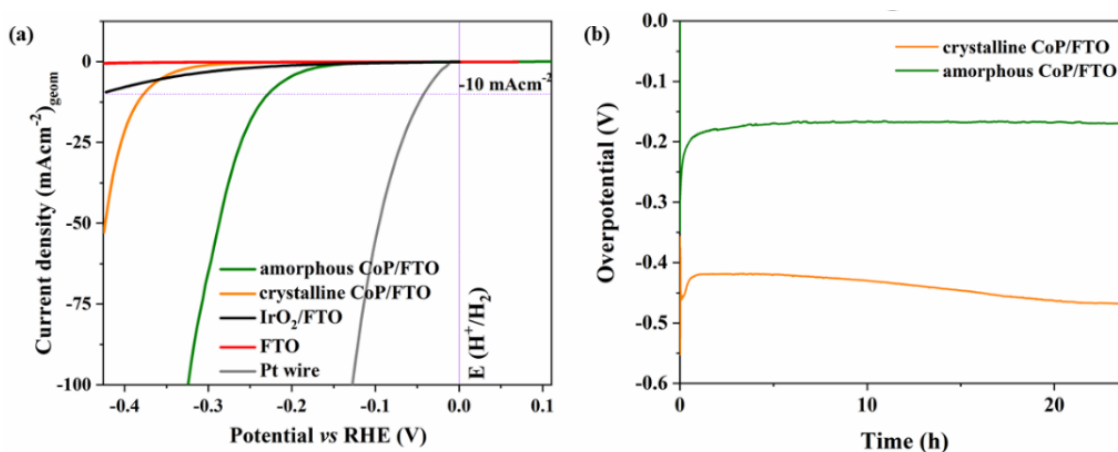


Figure 3.16. (a) HER polarization curves on 1 M KOH of amorphous and crystalline CoP, IrO₂ deposited on FTO along with, Pt wire and bare FTO. Both materials show similar activity, with lower overpotentials than IrO₂ and the bare substrate, but higher than Pt. Scan rate: 10 mV s⁻¹ (iR compensation at 85 %). (b) Chronopotentiometric experiments for HER (1 M KOH on FTO) of amorphous and crystalline CoP were carried out by applying a constant current of 10 mA cm⁻² for 24 h. The crystalline CoP showed a continuous decrease in overpotential during the 24 h experiment in comparison to the amorphous CoP, which was stable throughout the experiment.

The Tafel slopes of the FTO-based films were determined from the HER LSVs. A Tafel slope of 81 mV dec⁻¹ was obtained for the amorphous CoP, which was lower in similar to the one obtained for the crystalline CoP, 73 mV dec⁻¹ (see Figure 3.17) and outperformed the one of IrO₂ (260 mV dec⁻¹). The values of amorphous and crystalline CoP were similar to the Tafel slope value of Pt (73 mV dec⁻¹), which indicated a common mechanism on the surface. The calculated slopes suggests that for amorphous and crystalline CoP, the HER reaction proceeds via the Volmer-Heyrovsky mechanism on the surface, which confirmed the conclusions derived from the Tafel slopes on NF.^[51]

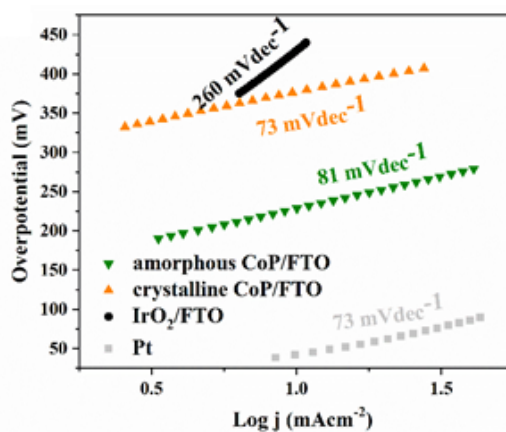


Figure 3.17. Tafel plot for HER for the as-prepared CoP materials deposited on FTO, IrO₂/FTO and Pt in aqueous 1 M KOH solution in HER. Scan rate: 1 mV s⁻¹. The crystalline CoP shows a Tafel slope which is comparable to the state-of-the-art Pt catalyst (73 mV dec⁻¹). The amorphous CoP showed a slightly lower Tafel slope (81 mV dec⁻¹) compared to the crystalline CoP (73 mV dec⁻¹), but lower overpotential. Both prepared materials significantly showed lower Tafel slopes compared to the IrO₂/FTO (260 mV dec⁻¹).

Throughout the electrochemical OER and HER measurements, the amorphous CoP activity was found to be superior to that of the crystalline phase. The activity difference arises from the surface and electronic characteristics of the materials. The electrocatalytic activity is highly influenced by the “real surface area” of the materials.^[78] The conventional geometric area of the electrodes (1 cm^2) is only useful for smooth and planar surfaces. The “real surface area” refers to the actual surface area that is available for catalysis in the nanostructured catalysts.^[41,247] The S_{BET} of the materials was initially determined by BET nitrogen (N_2) adsorption-desorption isotherms. The obtained S_{BET} of the materials were similar (ca. $28 \text{ m}^2 \text{ g}^{-1}$, see Table A.1.6), which indicated that both amorphous and crystalline CoP had a comparable number of active sites at which N_2 molecules were adsorbed and desorbed. This observation was contradictory with the higher activity of the amorphous CoP and demonstrated that not all active sites were electrochemically active. Therefore, the electrochemically active surface (ECSA) of the materials was determined. This important parameter reflects the “real surface area” of the material that is truly exposed to the electrolyte. The ECSA provides a measure of the inherent catalytic properties as it is related to the electrochemically active sites under the experimental conditions.^[299] The ECSA was determined *in situ* for each electrocatalyst and was calculated from the double-layer capacitance (C_{dl}). For this purpose, the systems were examined by CV in an area in which no Faradaic processes took place (see Section 7.3.8). The measured current in this non-Faradaic potential region is assumed to be due to double-layer charging. The C_{dl} is equal to the slope of the plot of double-layer charging current vs. scan rate, from which the ECSA could then be calculated by normalizing with the specific capacitance (C_s) which is dependent on the used substrate (see Section 7.3.8). The ECSA calculated from the C_{dl} resulted in 0.51 mF cm^{-2} for amorphous CoP which is about ~ 2.7 times larger than that of crystalline CoP, and 0.18 mF cm^{-2} (see Figure 3.18a). Both values are in the typical range for catalyst systems applied to NF and are comparable with literature values.^[67]

Amorphous catalysts have shown better HER and OER electrocatalytic activity in comparison to their crystalline counterparts (see Section 3.1).^[247] Several factors are interlinked and related to the observed activity enhancement while employing amorphous electrocatalysts.^[247] The amorphous CoP showed a higher value for the ECSA in comparison to crystalline CoP, due to the density of surface defects and coordinative unsaturated surface metal sites.^[148,300] The higher ECSA of amorphous phases is also related to the higher structural flexibility, which allows self-regulation, adaptation and reconstruction of active sites during the electrochemical conditions;^[301] and the adoption of highly active nanocrystalline phases within the amorphous matrix to enhance the activity.^[247,248]

ECSA measurements were also done after OER and HER to determine changes in the surface of the materials. The ECSA increased ~ 1.5 times in amorphous CoP ($\sim 0.49 \text{ cm}^2$) and ~ 2.1 times in crystalline CoP ($\sim 0.24 \text{ cm}^2$) owing to its increased surface transformation.^[302] Experimental data are shown on the Appendix (see Tables A.1.4, A.1.5, and Figure A.1.8, A.1.9). During catalysis, the TM-Ps surface is expected to

undergo a transformation into a highly active amorphous layer on both materials (see Sections 3.2.3 and 3.2.4), which explains the higher increase in ECSA observed for the amorphous CoP. The ECSA normalized LSV curves also confirmed the higher electrocatalytic activity of amorphous CoP for OER and HER (see Figure A.1.11).

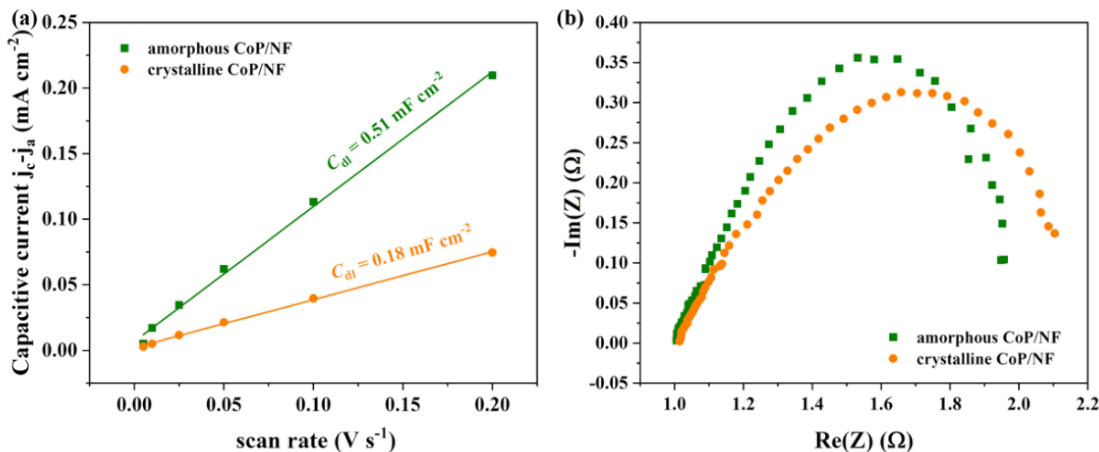


Figure 3.18. (a) Determination of the double layer capacitance from the half-of-the-slope from the plot of the capacitive current ($j_c - j_a$) vs. scan rate plot. (b) Nyquist plot of a non-Faradaic region measured between 100 mHz and 100 kHz of the amorphous CoP/NF crystalline CoP/NF. The applied potential was 0.7 V vs. Hg/HgO. From the fitting of data to semi-circle plots, it is possible to calculate the resistance of the solution (R_s) and the charge transfer resistance (R_{ct}) (see Table A.1.5).

In addition, the electrical resistance of both materials was evaluated by means of electrochemical impedance spectroscopy (EIS). The EIS measurements probe the charge transfer properties of the materials, which is determining the activity. For this purpose, the radius of the Nyquist plot was determined, which gave the resistance of the charge exchange between the catalyst surface and the electrolyte R_{ct} (see Experimental Section 7.3.7). A lower charge transfer resistance (R_{ct}) was found in the amorphous CoP/NF (0.8721 Ω) relative to crystalline CoP/NF (1.0357 Ω) (see Figure 3.18b). The R_{ct} decreased on both materials after OER and HER, indicating a higher electron mobility with faster charge transport through the bulk phase during catalysis (see Table A.1.5).

3.2.3. Post-operando OER characterization of amorphous and crystalline CoP

For a better understanding of the OER activity and the identification of active sites, the amorphous CoP and crystalline CoP were examined for structural transformations and morphological changes as well as changes in the composition and electronic properties after the electrochemical experiments. The SEM images of the amorphous and crystalline CoP films after OER are shown in Figure 3.19a and 3.19d, respectively. They reveal the exposure of the FTO conductive substrate, due to corrosion by the electrochemical oxidation or loss of the material into the electrolyte solution.

In order to investigate the properties of the films after the electrochemical OER, the composition of the surface was first analyzed by EDX. The elemental mapping after

catalysis shows the uniform distribution of Co (green) and O (blue) on the surface of the films (see Figure 3.19b, c, e, f). Compared to the freshly synthesized samples, the homogenous oxygen distribution in amorphous and crystalline CoP indicated the formation of Co oxidized species on the surface. The EDX also revealed the presence of slight amounts of phosphorus (see Figure A.1.12). The P was not only on the surface film, but also over the substrate (FTO) due to its loss from the structure, which was not observed in the as-prepared samples (see Section 3.2.1).

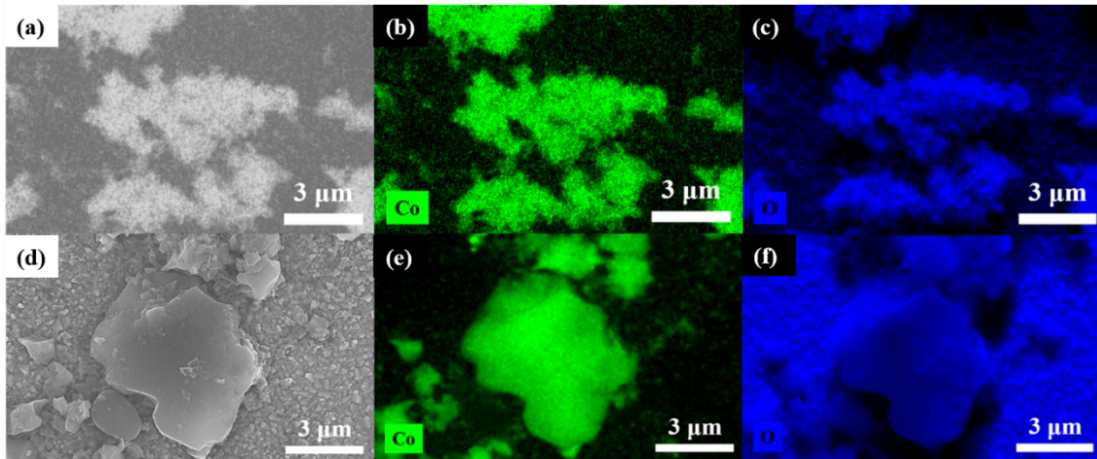


Figure 3.19. (a) SEM of amorphous CoP after OER and elemental mapping of (b) Co (green) and (c) O (blue). (d) SEM of crystalline CoP after OER and elemental mapping of (e) Co (green) and (f) O (blue). Mapping of phosphorus is shown in Figure A.1.12.

The TEM of the amorphous CoP after OER did not reveal any drastic change in the structure of the material, as the amorphous nature was maintained after catalysis (see Figure 3.20a). The SAED showed a lack of diffraction rings, which confirmed that there was no formation of a crystalline phase (see Figure 3.20b). In the case of the crystalline CoP, it was clearly visible that the particles were covered by an amorphous layer, which had no lattice planes (see Figure 3.20c). Interestingly, the corrosion was limited to the surface, and the core of the particles remained crystalline, which could be clearly demonstrated by SAED (see Figure 3.20d). The indexed reflections for the plane distance could be assigned to the (111), (211), and (301) planes of the crystalline CoP phase (JCPDS 29-0497)^[274] as found in the as-prepared sample (see Figure 3.7).

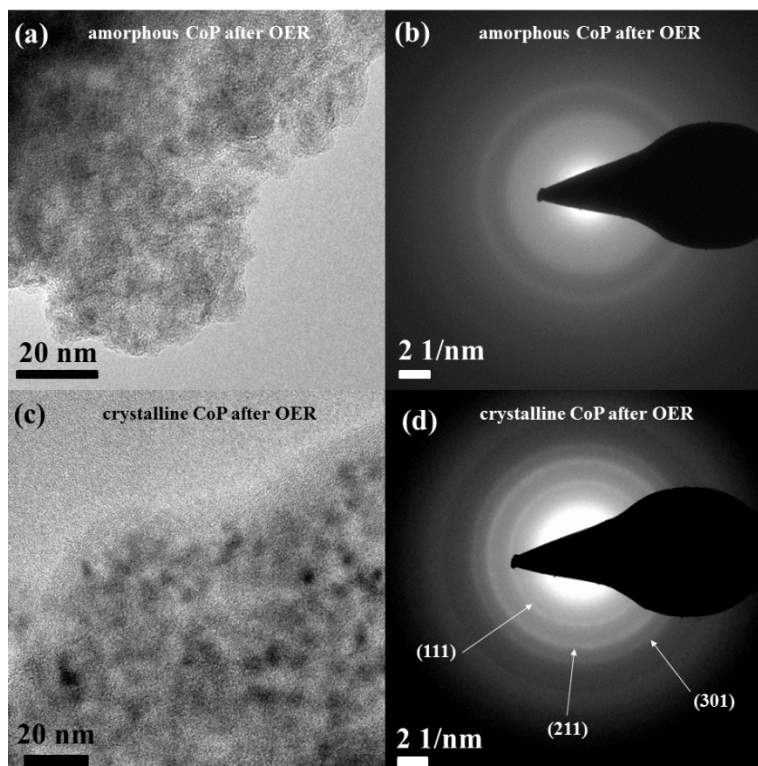


Figure 3.20. (a) TEM and (b) SAED after OER of amorphous CoP, (c) TEM and (d) SAED after OER of crystalline CoP. No diffraction rings appear in the SAED on the amorphous material. In the case of the crystalline CoP, an amorphous layer is covering the agglomerated particles. However, crystalline particles were also apparent, as confirmed by SAED pattern that is in accordance with CoP phase (JCPDS 29-0497).

ICP-AES results complemented the morphological post-catalytic analysis and revealed the leaching of phosphorus into the solution on both amorphous and crystalline CoP (see Table A.1.7). The leaching of phosphorus to the electrolyte solution occurred during the OER because of the high solubility of polyphosphate species generated under alkaline conditions.^[100,303] A higher concentration of P in the electrolyte solution was found when the amorphous CoP was used (85 %), in comparison to the crystalline CoP (11 %). The P loss, in addition to the SEM and TEM results, indicated the oxidation and the formation of an amorphous P-poor layer of Co (oxy)hydroxide, $\text{CoO}_x(\text{OH})_y$ over the conductive CoP core on both materials.^[26,101] This phenomenon agrees with the Pourbaix diagrams, which predicted the presence of highly oxidized species of cobalt and phosphorus (as PO_4^{3-}) in solutions under oxidative and alkaline conditions (Experimental Section, see Figure 7.14).

The surface oxidation and non-metal leaching is typical of TM-Ps and has been documented for Ni_2P ,^[26,161] Ni_{12}P_5 ,^[26] FeP ,^[111,147] and Fe_2P .^[166] Numerous crystalline Co phosphides phases, especially Co_2P and CoP, have been also reported to leach phosphorus and partially or completely transform to highly oxidized amorphous structures during OER under alkaline conditions.^[26,111,112,250,297,304] The surface transformation was also in agreement with the increase in the ECSA values after catalysis for both amorphous and crystalline CoP (see Section 3.2.1). The observed increase in ECSA was related to a larger number of active sites generated during OER. Previous investigations on Co phosphide

systems have demonstrated that the amorphous $\text{CoO}_x(\text{OH})_y$ shell contained highly oxidized $\text{Co}^{\text{II}}/\text{Co}^{\text{III}}$ species which are the active sites for OER.^[26,155,161,162] Amorphous CoP contained a larger number of active sites, as revealed by the higher phosphorus leaching and higher ECSA. In both cases, the remaining conductive core enabled a better charge transfer between the active centers on the surface and the substrate.^[164] The observations made on amorphous and crystalline CoP determined that similar processes took place during OER. However, the extension of the transformation was higher for the amorphous CoP and allowed a better activity in comparison to the crystalline phase.

The changes of chemical environment and oxidation state of the near-surface atoms of amorphous and crystalline CoP after OER were determined by the XPS analysis and then compared to the as-prepared samples. Figure 3.21 and 3.22 show the comparison of Co 2p, P 2p and O 1s XPS spectra of the amorphous CoP and crystalline CoP before and after OER. In the case of the amorphous material, XPS after short-term LSV and long-term CP experiments was measured to determine the effect of time on the extent of the transformation during OER. Deconvoluted spectra gave more insight into the changes occurring during catalysis.

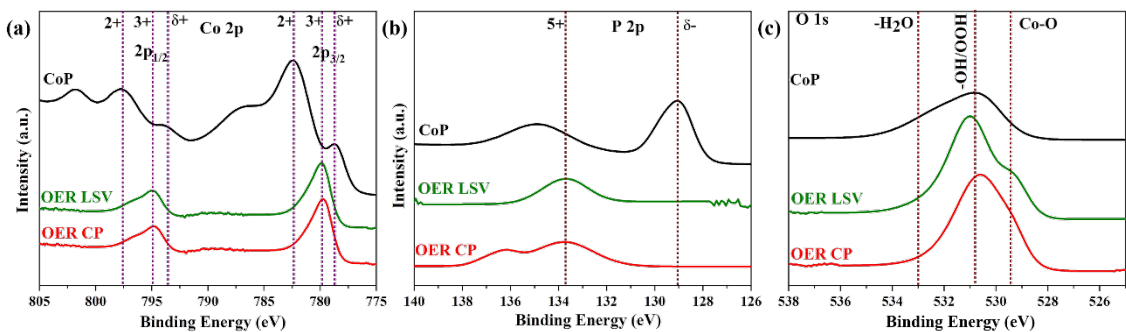


Figure 3.21. XPS spectra of amorphous CoP: (a) Co 2p, (b) P 2p and (c) O 1s. Deconvoluted spectra and details on assignments are shown in the Appendix (see Figure A.1.13).

The Co 2p XPS spectra of amorphous CoP after LSV and CP OER showed the peaks corresponding to $\text{Co}^{\delta+}$ completely disappeared after OER (see Figure 3.21a, b, c). In comparison to the freshly synthesized amorphous CoP sample, the signals were shifted to higher binding energies after OER catalysis, which indicated the oxidation of Co to higher oxidation states.^[26,156,160,162,238] The deconvoluted spectra showed strong peaks associated to Co^{II} (780.9 eV $2p_{3/2}$, 796.5 eV $2p_{1/2}$ on both LSV and CP spectra) and Co^{III} (779.7 eV $2p_{3/2}$, 794.8 eV $2p_{1/2}$ in LSV and 779.8 eV $2p_{3/2}$, 794.9 eV $2p_{1/2}$ on CP) after both the OER-LSV and the OER-CP samples (see Figure 3.21a and Figure A.1.13a). The deconvoluted spectrum of Co 2p displayed the enhancement of Co^{III} peak area after CP compared to the Co^{II} peak area suggesting a higher amount of Co^{III} after continuous OER.^[266,303]

The P 2p spectra displayed the diminishing of the $\text{P}^{\delta-}$ signal at 129.0 eV and the emergence of the signal related to oxidized phosphorus P^{V} (133.7 eV), which indicated the formation of phosphate after LSV and CP experiments (see Figure 3.21b and Figure

A.1.13b).^[160,162] Moreover, an additional peak was found in the after CP OER, corresponding to P_2O_5 (~136.2 eV).^[305] The shift towards higher binding energies was in accordance to the oxidation of phosphorus and formation of phosphate during OER under alkaline conditions. The intensity of the P signals also decreased after LSV and CP OER, which indicated less amount of P in the surface.^[26,156,160,162,238] This observation agreed with the ICP results that demonstrated the oxidation and loss of phosphorus into the electrolyte solution.

The O 1s spectra of amorphous CoP after LSV and CP OER showed peaks centered at 531.2 eV and 530.7 eV, respectively (see Figure 3.21c). The high intensity of this peak, in comparison to the as-prepared amorphous CoP O 1s spectrum, was in accordance with the oxidation of the surface generated during OER under alkaline conditions. Detailed information can be obtained from the deconvoluted spectra, which resulted into three peaks (O1, O2 and O3) (see Figure A.1.13c). Each peak can be correlated to oxygen species with different chemical environments. The first peak (O1) at 529.3 eV (on both LSV and CP OER) corresponded to the metal-oxygen bond in the active $CoO_x(OH)_y$ formed in the surface after OER.^[306] The other deconvoluted peaks also supported the surface oxidation and formation of the (oxy)hydroxide phase. The major peak (O2, 531.0 eV after LSV and 530.6 eV after CP) indicated the presence of –OH groups, which confirmed the surface hydroxylation.^[307] Finally, the peak at 532.2 eV after CP and 531.7 eV after LSV (O3) was related to adsorbed water molecules on the (oxy)hydroxide surface due to contact with the electrolyte aqueous solution.^[307]

The same trend was observed for crystalline CoP after OER CP (see Figure 3.22a, b, c) and detailed information was obtained from the deconvoluted spectra. After OER, the signals in the Co 2p spectrum (see Figure A.1.14a) appeared shifted to higher binding energies, which indicated the oxidation of Co in the surface to higher oxidation states.^[26,156,160,162,238] This observation was confirmed by the emergence of new signals in the spectrum, related to Co^{III} (deconvoluted: $2p_{1/2}$ 795.2 eV, $2p_{3/2}$ 780.0 eV) and Co^{II} (deconvoluted: $2p_{1/2}$ 796.3 eV, $2p_{3/2}$ 781.1 eV).^[288] Similarly to the amorphous CoP, the crystalline CoP after OER spectrum showed and increased intensity of the Co^{III} peak, suggesting a higher amount of this species after continuous OER.^[266,288] Therefore, the results supported the surface oxidation and formation of $Co^{II/III}O_x(OH)_y$.^[26,156,160,162,238]

The P 2p spectrum of crystalline CoP after the long term CP experiment showed only one peak at higher binding energy (133.5 eV) and the disappearance of the $P^{\delta-}$ from CoP (129.4 eV). The deconvolution of this peak resulted also in only one peak (see Figure A.1.14b). This suggested that the phosphorus species in the surface had been completely oxidized to P^V (phosphate) during the long-term chronopotentiometric measurement and confirmed by the observations from SEM and TEM of the electrochemically caused corrosion.^[160,162] This observation was in agreement with the ICP results and TEM which demonstrated the oxidation and loss of phosphorus into the electrolyte solution and the formation of amorphous $CoO_x(OH)_y$ over the metallic-like crystalline CoP core. This led

to a rapid transport of the electrons away from the surface and the generation of new electron holes that significantly improved the OER activity.

Finally, the O 1s spectrum after CP OER of crystalline CoP showed only one peak at 531.7 eV. This peak showed a high intensity in comparison to the as-prepared crystalline CoP O 1s spectrum, which supported to generation of highly oxidized species in the surface during the OER under alkaline conditions. Detailed information was obtained from the deconvoluted spectra, which resulted into three peaks (O1, O2 and O3) (see Figure A.1.14c). Similar assignments were done as in the post-OER O 1s spectra of amorphous CoP. The first peak (O1) was correlated to the Co-O bond (529.8 eV) from the electrochemically generated (oxy)hydroxide layer.^[306] This was supported by the presence of a second peak (O2), related to oxygen in –OH groups (531.7 eV).^[307] Finally, the peak at (534.0 eV) (O3) was assigned to absorbed water molecules on the amorphous (oxy)hydroxide surface due to contact with the electrolyte aqueous solution.^[307]

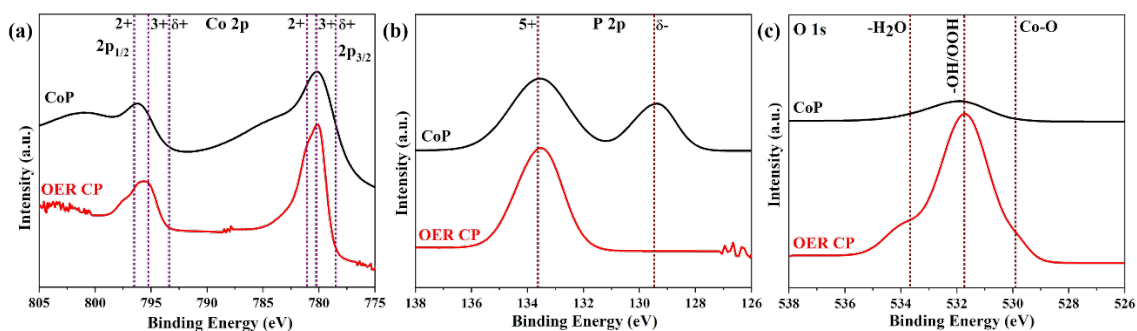


Figure 3.22. XPS spectra of crystalline CoP: (a) Co 2p, (b) P 2p and (c) O 1s before and after OER. Deconvoluted spectra and details on assignments are shown in the Appendix (see Figure A.1.14).

The FT-IR spectra of amorphous and crystalline CoP after the OER electrochemical investigations (see Figure A.1.15) showed a broad band centered at $\bar{\nu} = 3000 \text{ cm}^{-1}$, which could be assigned to the asymmetrical and symmetrical O-H stretching vibrations and confirmed the surface hydroxylation. This was caused by corrosion during the LSV and CP OER experiments of the crystalline and amorphous CoP, since these signals could not be detected on the freshly synthesized samples (see Section 3.2.1). Additionally, the bands at $\bar{\nu} = 1600 \text{ cm}^{-1}$ were assigned to the H-O-H bending vibrations. Moreover, the phosphate formation can also be concluded from the spectra. The characteristic band of phosphate between $\bar{\nu} = 1500\text{-}500 \text{ cm}^{-1}$ are attributed to P=O and P-O-P stretching vibrations.^[160,282] Finally, a peak at $\bar{\nu} = 600 \text{ cm}^{-1}$ characteristic of the stretching vibration of the Co-O bond was also present, which proved the oxidation of the phases.

The changes in the XPS signals of amorphous and crystalline CoP indicated that the valence of the Co shifted towards $\text{Co}^{\text{II}}/\text{Co}^{\text{III}}$ after OER. The electrochemical experiments also provided evidence of oxidation to higher oxidation states. A redox wave observed during the LSV OER of both materials was attributed to the oxidation of $\text{Co}^{\text{II/III}}$ (see Figure A.1.6). The formation of a mixture of $\text{Co}^{\text{II}}/\text{Co}^{\text{III}}$ species in the amorphous (oxy)hydroxide layer is generally considered essential for the OER activity.^[101] The

formation of this layer was accompanied by drastic structural changes, due to the generation of an amorphous shell, as described before by the SEM, TEM, SAED, and ICP-AES (see Figures 3.19, 3.20 and related discussion). The amorphous shell does not have any long-range order, but it is composed of disordered $\text{Co}^{\text{III}}\text{O}_x(\text{OH})_y$ sheets that are held together only by noncovalent bonds, which allows access of H_2O , OH^- , and K^+ from the electrolyte to the bulk (see Figure 3.23a).^[101,261] Dau and co-workers determined that amorphous $\text{CoO}_x(\text{OH})_y$ layers consisted of octahedrally coordinated Co^{III} ions interconnected by di- μ -oxo bridges.^[308] This disordered structure can be described as polyoxometalates with molecular dimensions of 7-16 edge-sharing CoO_6 octahedra connected by di- μ -oxido-bridges (see Figure 3.23b).

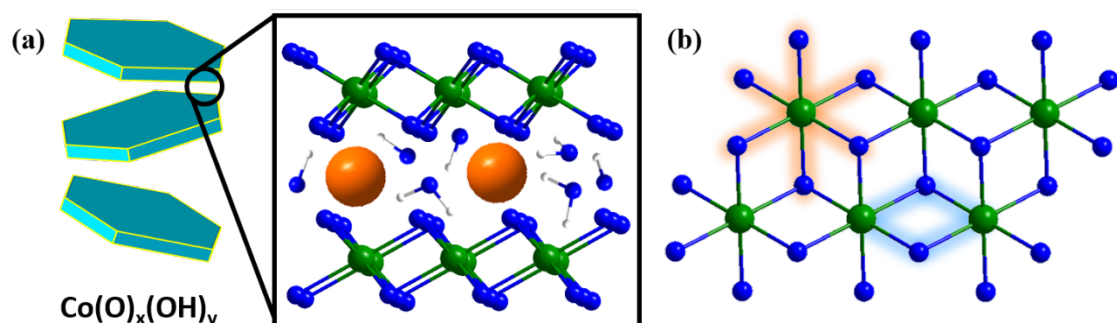


Figure 3.23. (a) Schematic representation of the structure of two exposed layers of $\text{CoO}_x(\text{OH})_y$ phase exposed to the electrolyte that contains H_2O , OH^- and K^+ . Green, blue, white, and orange spheres represent Co, O, H and K atoms. The arrangement of the interlayer species is only illustrative and strongly simplified. (b) edge-sharing CoO_6 octahedra (highlighted in orange) connected by di- μ -oxido-bridges (highlighted in blue).

The formation of three-dimensional cross-linked and layered $\text{CoO}_x(\text{OH})_y$ containing di- μ -oxido-bridged CoO_6 octahedra is favored by defects that occur frequently in disordered amorphous structures^[155,308] and is independent of the initial Co coordination and oxidation state.^[309] Dau and co-workers determined that Co_3O_4 , wurtzite-like CoO , rock-salt-like CoO and heterogenite-like $\text{CoO}_x(\text{OH})_y$ all transformed to a low-crystallinity and OER-active $\text{CoO}_x(\text{OH})_y$ phase during electrocatalysis.^[309] A similar structural motif has been also found in Ni- and Mn-based OER electrocatalysts and is described as the active structure.^[310,311] The di- μ -oxido bridging is ascribed as a key structural motif in water oxidation, because it can act as internal proton acceptor (base) during the previous steps to the O-O bond formation (see Figure 1.9).^[309,312]

The OER mechanism of the $\text{CoO}_x(\text{OH})_y$ phase containing two Co^{III} centers connected by di- μ -oxido bridging is the following. First, H_2O or OH^- is absorbed on the surface of the Co (oxy)hydroxide (see Figure 3.24, species (1)). Two consecutive PCET steps form the $\text{Co}^{\text{IV}}\text{-O}^{\text{II}}$ species (species 3) from the $\text{Co}^{\text{III}}\text{-OH}_2$ species. From this point, there are two possible pathways for the O-O bond formation.^[309,313] The first pathway involves the nucleophilic attack of hydroxide on a single $\text{Co}^{\text{IV}}\text{-O}^{\text{II}}$ species (see Figure 3.24, marked in black). In the subsequent PCET, the (oxy)hydroxide species leading to the O-O bond is formed. The $\text{Co}^{\text{II}}\text{-OOH}$ (species 3.A) is converted to $\text{Co}^{\text{III}}\text{-OO}$ (species 4) in a further

PCET and dioxygen is desorbed. Finally, a water molecule is adsorbed, which restores the original state of the catalyst. The second pathway proceeds via a PCET to generate a second $\text{Co}^{\text{IV}}\text{-O}^{\text{II}}$ species (3.B.1) from a $\text{Co}^{\text{III}}\text{-OH}$ in close proximity to the first $\text{Co}^{\text{IV}}\text{-O}^{\text{II}}$ species. In this case, the formation of the O-O bond occurs through the intramolecular O-O coupling from the $\text{Co}^{\text{IV}}\text{-O}^{\text{II}}$ species, which leads to a bridging peroxido intermediate (species 3.B.2, see Figure 3.23, marked in red). This is followed by the adsorption of a OH^- in one of the two Co centers, whereupon the Co-O bond is broken at this Co center and a $\text{Co}^{\text{III}}\text{-OO}$ species is generated (species 4). The uptake of a water molecule generates the initial $\text{Co}^{\text{III}}\text{-OH}_2$ species. Both mechanisms are plausible for the Co (oxy)hydroxide species generated in the amorphous and crystalline CoP. The occurrence of the reaction through one of the two mechanisms depends on the overpotential, as the most active and stable surface termination depends on it.^[309] High potentials will lead to highly oxidized $\text{Co}^{\text{IV}}\text{-O}^{\text{II}}$, which favors the intramolecular mechanism with two adjacent $\text{Co}^{\text{IV}}\text{-O}^{\text{II}}$ species.

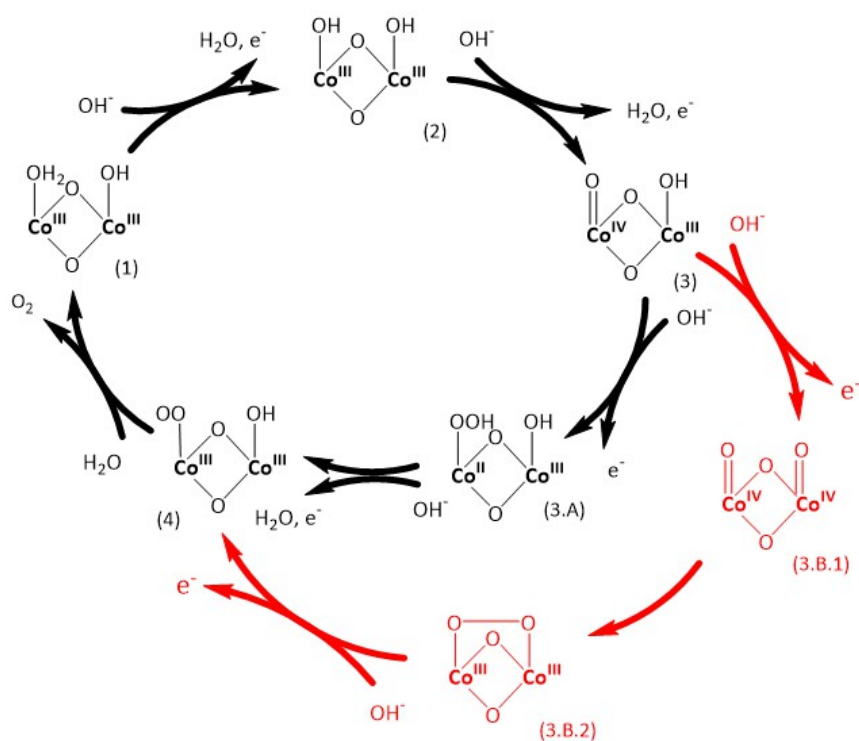


Figure 3.24. Two mechanisms for the OER on $\text{Co}^{\text{III}}\text{O}_x(\text{OH})_y$ catalysts with different O–O bond formation steps: nucleophilic attack of hydroxide (black arrows, 3.A) and intramolecular oxygen coupling (red arrows, 3.B).

The Co^{III} species identified in this work by *ex-situ* characterization could be associated to the $\text{Co}^{\text{III}}\text{-OH}^-$, $\text{Co}^{\text{III}}\text{-OOH}$, and $\text{Co}^{\text{III}}\text{-OH}_2$ species in the mechanism and it is clearly the prevalent resting state of the catalysts. The electronic configuration of Co^{III} ($d^6, t_{2g}^5 e_g^1$) has a strong influence in the structure and catalytic activity. In the octahedral coordination, the electronic configuration is degenerate (see Figure 3.25, left). A Jahn-Teller distortion occurs to remove the degeneracy and stabilize the orbitals. The d orbitals with a z component are stabilized (d_{xz} , d_{yz} , d_{z^2}), while the orbitals without a z component

are destabilized ($d_{x^2-y^2}$, d_{xy}) (see Figure 3.25, center). As a result of the distortion, the $\text{Co}^{\text{III}}\text{O}_6$ were elongated in the $\text{Co}^{\text{III}}\text{-O}$ bonds along one of the molecular 4-fold axes (see Figure 3.25, right).^[314,315] Such an elongation weakened the $\text{Co}^{\text{III}}\text{-O}$ covalent bond along this axis, facilitating the absorption of oxygen intermediates and the oxidation of the Co^{III} site.^[139,140]

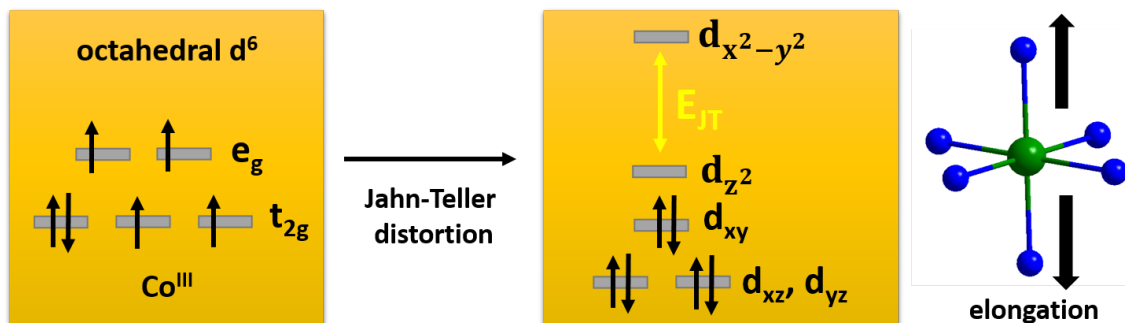


Figure 3.25. Jahn-Teller distortion on the octahedral coordination modes of intermediate spin Co^{III} (d^6) in the structure of $\text{CoO}_x(\text{OH})_y$. The stabilization can be observed by the decrease in energy of the filled orbitals. The CoO_6 octahedra suffered and elongation along the z axis. Co and O atoms are represented by green and blue spheres, respectively.

The previous mechanism postulates that Co^{III} and Co^{IV} are the electrochemically active species during the OER.^[49,309] However, highly oxidized Co^{IV} ions were not experimentally detected on amorphous and crystalline CoP because only *ex-situ* characterization has been done and the oxidation state of the catalyst material changes upon removal from the oxidative conditions in the electrolyte.^[119] Reports in the literature showed that Co^{IV} is indeed the active species for the OER in Co-based materials. Hu and co-workers^[114] found evidence that Co^{IV} is present in amorphous $\text{CoO}_x(\text{OH})_y$ during electrochemical OER and is fundamental for the O-O bond formation. The presence of Co^{IV} active species is consistent with several reports and determined in Co_3O_4 during photocatalytic OER by fast scan FT-IR,^[115] in CoO_x by electron paramagnetic resonance (EPR),^[113] and for Co-Pi films in neutral pH,^[116,118] CoOOH nanosheets,^[117] and amorphous CoOOH under alkaline conditions.^[114]

In summary, the characterization results in support of the formation of an amorphous Co (oxy)hydroxide species $\text{CoO}_x(\text{OH})_y$, through phosphorus loss into the electrolyte solution on both amorphous and crystalline CoP. The difference in the amount of leached phosphorus was related to a higher transformation of the amorphous CoP to $\text{CoO}_x(\text{OH})_y$ during OER under alkaline conditions. A larger transformation also signified a greater structural modification and formation of higher amount of surface unsaturated sites for facile reactant adsorption. In contrast, less leaching of phosphorus and oxidation was observed on the crystalline material. A crystalline metallic-character CoP core was retained during catalysis. The core-shell structure obtained in this way catalyzed the OER due to a faster charge exchange between the $\text{CoO}_x(\text{OH})_y$ layer and the conductive substrate. However, the benefit of the core-shell structure in the activity was not sufficient

to overcome the low oxidation and formation of the $\text{CoO}_x(\text{OH})_y$ layer, which was the responsible for the OER.

The (oxy)hydroxide layer ultimately contained the active centers of the OER under alkaline conditions, on both amorphous and crystalline CoP. The layer did not have any long-range crystalline structure, but the atomic structure of such electrochemically generated material is known to contain $\text{Co}^{\text{III}}\text{O}_6$ edge sharing octahedra connected by μ -oxo-bridges. The octahedral Co^{III} species exhibited a Jahn-Teller distortion, which was crucial for the generation of active sites for the water oxidation. A mechanism for OER with two possible O-O bond formation steps was postulated for the Co (oxy)hydroxide phase. The O-O bond was either formed by a nucleophilic attack of hydroxide on a metal center or by direct intramolecular coupling. Both steps require the presence of highly oxidized Co^{IV} atoms, which are capable of oxidizing water and generate O_2 . Even if the presence of Co^{IV} intermediate has not been demonstrated, *post-operando* data agreed with the mechanisms postulated in the literature. It can be concluded that the evolution of O_2 from amorphous and crystalline CoP must have taken place via a comparable mechanism due to similar *post-operando* characterization results.

3.2.4. *Post-operando* HER characterization of amorphous and crystalline CoP

Likewise, *post-operando* characterization after HER was also carried out to identify the active sites of amorphous CoP and crystalline CoP, as well as their structural transformations and changes in morphology, composition, and electronic properties after the electrochemical experiments.

The SEM images of the amorphous and crystalline CoP films (see Figure 3.26a, d) clearly show the corrosion of the materials by the electrochemical oxidation or loss of the material into the electrolyte solution, exposing the FTO substrate. The change in the composition of the phases after the electrochemical HER was investigated through EDX. The elemental mapping after catalysis revealed a homogenous distribution of Co (green), P (red) and O (blue) on the surface of the electrodes (see Figures 3.26b, c, e, f, A.1.16). In comparison to the as-prepared amorphous and crystalline CoP sample, the homogenous distribution of P and O indicated an oxidation of the surface but with retention of P, contrary to the observations during OER. P was mostly observed on the surface film, but not on the substrate (FTO) which indicated retention of P in the structure.

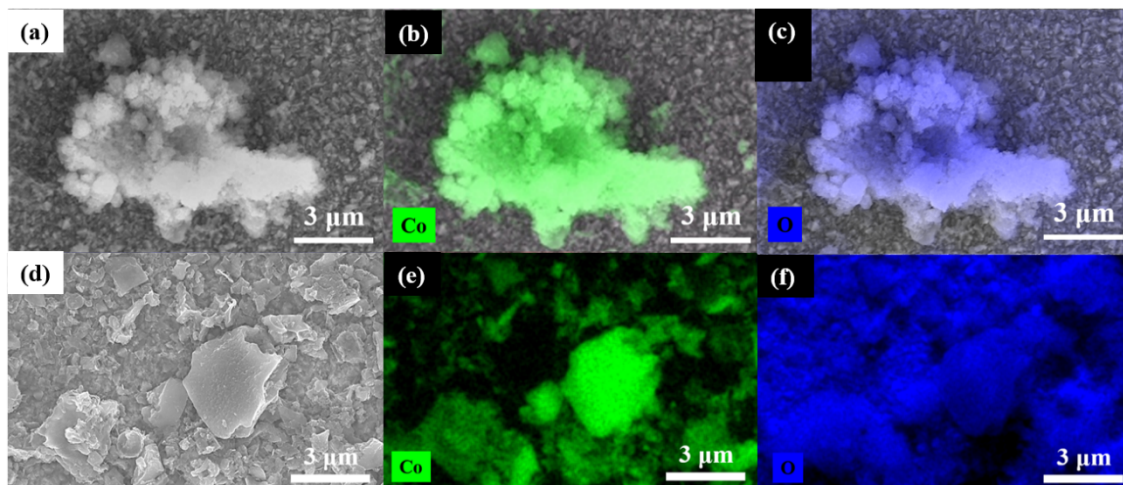


Figure 3.26. (a) SEM of amorphous CoP after HER and elemental mapping of (b) Co (green) and (c) O (blue). (d) SEM of crystalline CoP after HER and elemental mapping of (e) Co (green) and (f) O (blue). Mapping of phosphorus is shown in Figure A.1.16.

TEM analysis complemented the results from the SEM examinations. TEM and SAED of the amorphous CoP after HER did not show any apparent change in phase, as the amorphous nature was retained after catalysis. The TEM images did not reveal the appearance of crystalline fringes (see Figure 3.27a). The SAED confirmed this observation, as it did not show clear diffraction rings associated to a new formed crystalline phase (see Figure 3.27b). In the case of crystalline CoP, an amorphous layer, which had no lattice planes, was observed over the agglomerated nanoparticles (see Figure 3.27c). The SAED revealed that the amorphous layer was limited to the surface, as the crystalline core of the CoP nanoparticles was maintained after HER (see Figure 3.27d). The diffraction rings observed on the SAED corresponded the (111), (211) and (301) planes of the crystalline CoP phase (JCPDS 29-0497),^[274] as it is observed on the as-prepared samples and after the OER.

Quantitative analysis by ICP-AES complemented the post-catalytic morphological analysis and revealed the leaching of phosphorus into the electrolyte solution on both amorphous and crystalline CoP during HER. The leaching of phosphorus on both materials was lower than the amount lost during OER. The amorphous CoP showed a higher phosphorus leaching (13 %) in comparison to the crystalline phase (5 %) (see Table A.1.7). The characterization results suggest that both materials suffered low leaching of the non-metal and that an amorphous layer is formed over the crystalline CoP under strongly alkaline HER. The leaching of phosphorus to the electrolyte solution occurred during the HER because of the contact of the materials with the highly oxidative alkaline solution. This process transformed the surface of the materials to (oxy)hydroxides, as the phosphorus leached into the solution as the polyphosphate anions.^[303] It is known that during HER under alkaline conditions, the CoP surface acts as a precatalyst: the contact with the alkaline solution induced the CoP oxidation and leaching of P, which formed an amorphous (oxy)hydroxide $\text{CoO}_x(\text{OH})_y$.^[240,303] However, the application of a reductive potential limited the oxidation of both Co and P.^[303]

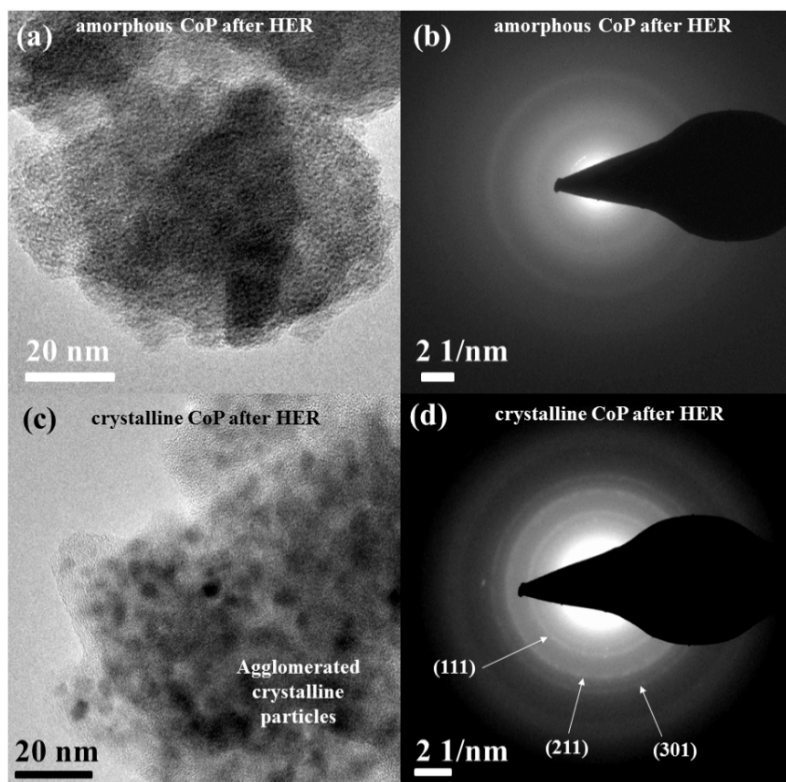


Figure 3.27. (a) TEM and (b) SAED after HER of amorphous CoP. No diffraction rings appear in the SAED after OER, indicating that the material is amorphous. (c) TEM and (d) SAED after HER of crystalline CoP. An amorphous layer was formed on the exterior of the particles. The inner part contained crystalline CoP particles, as confirmed by SAED pattern (JCPDS 29-0497).

The changes of chemical environment and effect of the application of a reduction potential on the oxidation state of the near-surface atoms of amorphous and crystalline CoP after HER were determined by the XPS analysis and then compared to the as-prepared samples. Figure 3.28 shows the comparison of Co 2p, P 2p and O 1s XPS spectra of the amorphous CoP. XPS after short-term LSV and long-term CP experiments were measured to determine the effect of time on the extent of the transformation during HER. Deconvoluted spectra gave more insight into the changes occurring during catalysis. The deconvoluted Co 2p spectrum after HER LSV revealed the total disappearance peaks associated to $\text{Co}^{\delta+}$ (see Figure A.1.17a). The signals were shifted to higher binding energies after HER catalysis, which indicated the presence of highly oxidized Co species.^[26,156,160,162,238] The peaks were associated to Co^{II} ($2p_{3/2}$ 781.7 eV and $2p_{1/2}$ 798.0 eV and satellites 784.4 eV and 789.9 eV) and Co^{III} ($2p_{3/2}$ 779.7 eV and $2p_{1/2}$ 795.1 eV and satellites 803.1 eV and 805.5 eV), which appeared due to the surface oxidation under strongly alkaline conditions.^[160,240,303] Similar results were obtained after the long-term HER CP experiment, in which peaks associated to Co^{II} ($2p_{3/2}$ 781.6 eV and $2p_{1/2}$ 797.3 eV) and Co^{III} ($2p_{3/2}$ 779.8 eV and $2p_{1/2}$ 795.8 eV) were present (see Figure A.1.17b).

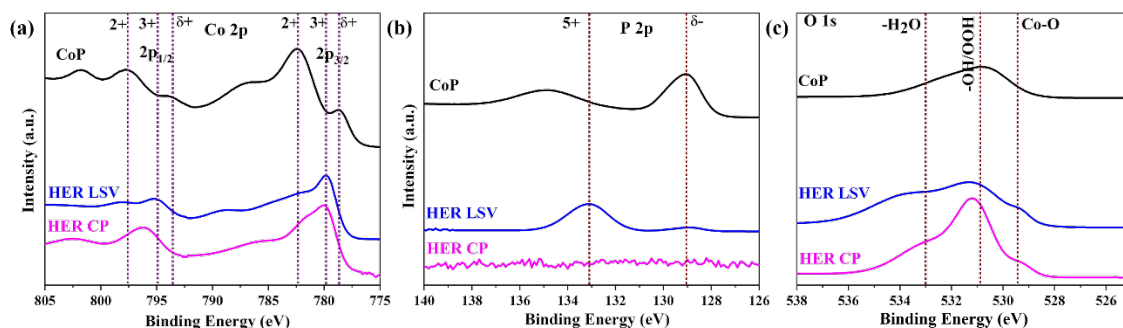


Figure 3.28. XPS spectra of amorphous CoP: (a) Co 2p, (b) P 2p and (c) O 1s before and after HER. Deconvoluted spectra and details on assignments are shown in the Appendix (see Figure A.1.17, Figure A.1.18).

The P 2p spectra revealed the oxidation of the surface phosphorus (see Figure 3.28b). Interestingly, the deconvoluted spectra showed that the phosphorus species change upon the duration of the catalysis (see Figure A.1.17c). After the short-time HER LSV experiment, the deconvoluted P 2p spectrum showed peaks related to phosphorus with two different oxidation states. The low binding energy peak at 129.0 eV corresponded to a $P^{\delta-}$ signal. The intensity of this signal was low, which indicated that less amount of $P^{\delta-}$ was left in the surface after HER LSV. Additionally, a high binding energy signal at 133.1 eV appeared, related to P^V due to the formation of phosphate. The XPS results revealed that the oxidation occurred and reduced phosphorus ($P^{\delta-}$), from pristine amorphous CoP was present.^[160,162] In the case of the long-term CP HER P 2p spectrum, the signals of phosphorus completely disappeared, further demonstrating the complete loss of this element from the surface of amorphous CoP under alkaline HER conditions (see Figure A.1.17d). The results were in accordance with the ICP-AES loss of phosphorus into the electrolyte solution (see Table A.1.7).

Finally, the O 1s spectra for LSV and CP HER were obtained (see Figure 3.28c), where one peak centered at 531.2 eV was observed. The deconvolution of both spectra resulted in three distinct peaks (O1, O2, and O3) (see Figure A.1.17e,f) which could give detailed information of the surface transformation. Each peak was assigned to oxygen species with different chemical environments. The first peak (O1) at 529.3 eV (on both LSV and CP OER) corresponded to the metal-oxygen (Co-O) bond in the oxidized surface.^[306] The second signal (O2), and most intense, was assigned to oxygen in $-OH$ groups (O2, 530.9 eV on CV and 530.6 eV on CP).^[307] The high intensity indicated that most of the O in the surface was hydroxylated,^[307] specially after the long-term CP HER experiment where the ratio of this peak is higher in comparison to the others. Finally, the peak with the largest binding energy was associated to adsorbed water molecules on the oxidized surface (O3, 532.2 eV on CV and 531.7 eV and CV).^[307]

A similar trend and assignment was observed for crystalline CoP after HER CP (see Figure 3.29d, e, f). After HER, the signals in the deconvoluted Co 2p spectrum (see Figure A.1.18a) appeared shifted to higher binding energies, which indicated the oxidation of Co in the surface. This observation was derived from the appearance of the signals related to

Co^{II} (2p_{1/2} 795.2 eV and 2p_{3/2} 780.0 eV) and Co^{III} (2p_{1/2} 796.3 eV and 2p_{3/2} 781.1 eV), as well as satellite peaks (781.7 eV, 797.0 eV).^[288] The presence of highly oxidized Co suggested the oxidation of the surface to an amorphous active CoO_x(OH)_y.^[266,288]

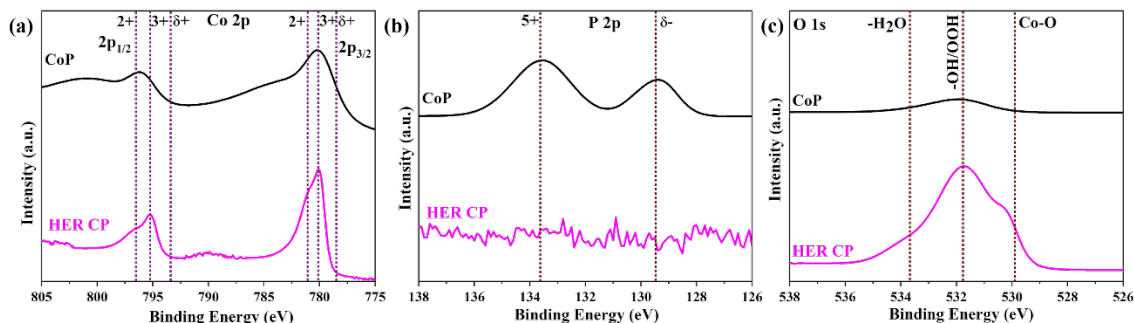


Figure 3.29. XPS spectra of crystalline CoP: (a) Co 2p, (b) P 2p and (c) O 1s before and after HER. Deconvoluted spectra and details on assignments are shown in the Appendix (see Figure A.1.17, Figure A.1.18).

The deconvoluted P 2p spectrum after HER CP (see Figure A.1.18b) did not reveal any phosphorus signal, similarly to the spectrum after the long-term chronopotentiometric experiment with the amorphous CoP. This was consistent with TEM and ICP results showing the loss of surface P into the electrolyte solution and the complete oxidation of the surface to form a (oxy)hydroxide layer over a metallic-like CoP crystalline core. This led to a rapid transport of the electrons between the surface and the conductive substrate. Similar observations have been made with other TM-Ps during HER, like Mo₃P and MoP,^[316] Ni_xP_y,^[317] Ni₁₂P₅ and Ni₂P.^[26]

Finally, the O 1s spectrum after CP HER of crystalline CoP showed only one peak at 531.7 eV (Figure 3.29c). This peak showed higher intensity in comparison to the as-prepared crystalline CoP O 1s spectrum, which supported the generation of highly oxidized species in the surface during HER under alkaline conditions. The deconvoluted spectrum provided better understanding of the changes in the surface. Three distinct peaks were obtained (O1, O2, and O3) (see Figure A.1.18c). The first peak (O1) at 530.2 eV was related to the Co-O bond, generated in the CoO_x(OH)_y layer during electrochemical HER.^[266,288,306] Additionally, the most intense second peak (O2), was related to –OH groups (531.2 eV), which confirmed the presence of this layer.^[307] The peak with the highest binding energy (O3, 533.9 eV) was assigned to absorbed water molecules on the amorphous (oxy)hydroxide surface due to contact with the electrolyte aqueous solution.^[307]

The FT-IR spectra of amorphous and crystalline CoP after the HER electrochemical investigations (see Figure A.1.19) are consistent with the transformations observed by XPS. The low intensity broad band centered at ca. $\bar{\nu} = 3000 \text{ cm}^{-1}$ was assigned to the asymmetrical and symmetrical O-H stretching vibrations and confirmed the surface hydroxylation. The complete loss of phosphorus from the surface into the electrolyte

solution was also confirmed from the FT-IR spectra. For both amorphous and crystalline CoP, the lack of peaks in the range between $\bar{\nu} = 1500\text{-}500\text{ cm}^{-1}$ discarded the presence of phosphate.^[160,282]

Furthermore, the changes in the XPS, in combination with the results from SEM, TEM, SAED, FT-IR and ICP-AES, indicated the transformation of amorphous and crystalline CoP during electrochemical HER. Initially, the surfaces of the electrocatalysts are oxidized to form a $\text{CoO}_x(\text{OH})_y$ layer due to the contact with the alkaline solution.^[26] This was supported by the appearance of Co in high oxidation state $\text{Co}^{\text{II}}/\text{Co}^{\text{III}}$ on the surface. The formation of this layer was a result of the phosphorus dissolution into the electrolyte, as concluded from the lack of phosphorus signals in the XPS after the long-term chronopotentiometric HER. This observation was complemented by the FT-IR measurements, in which no phosphate could be detected. Thus, both materials transformed to a core-shell structure, in which the remaining CoP core accelerated the charge transfer from the active catalyst surface to the electrode substrate to accomplish efficient electrocatalysis.

The transformation of CoP during HER seemed analogous to the one observed during OER. However, the ICP results demonstrated that the loss of phosphorus during HER is lower in comparison to the loss during OER. This difference is a consequence of the reduction of the oxidized species that occurred during HER. Wang and co-workers^[303] observed that the oxidized species on CoP nanoparticles surface can be reduced under the HER conditions and can be maintained during electrocatalysis. The authors observed that under HER conditions in alkaline electrolyte, the catalyst surface changed from being P-rich to Co-rich due to the electrochemical reduction of the oxidized species in CoP and dissolution of the oxidized P species (phosphate). These two phenomena rendered together a Co-rich phosphide surface. Similar conclusions can be driven from the *post-operando* characterization of amorphous and crystalline CoP. Initially, the XPS showed the presence of reduced phosphorus $\text{P}^{\delta-}$ in the surface after LSV HER (see Figure A.1.17a). However, after the CP HER 24 h experiment, the surface is transformed from P-rich to Co-rich because of the polyphosphate dissolution (see Figure A.1.17b,d).

The surface composition change had an effect on the HER mechanism. Initially, when the surface is P-rich, electronegative phosphorus species ($\text{P}^{\delta-}$) could create a negative charge to trap H^+ and influenced the desorption of H_2 .^[148] However, the long-term chronopotentiometric experiments revealed that phosphorus was lost into the electrolyte solution. Consequently, the HER mechanism should be different under these conditions. Li and co-workers^[318] demonstrated that electrocatalysts with atoms with high electronegativity favored the formation of H_2 , provided their crystalline metallic properties were retained. The superior activity of amorphous and crystalline CoP in the long-term HER could be attributed to the formation of *in situ* reduced metallic species with smaller positive charge ($\text{Co}^0/\text{Co}^{\delta+}$).^[319] The formation of reduced species in the amorphous and crystalline CoP can be demonstrated by a closer inspection of the HER LSV polarization curves. The initial polarization curve revealed a reduction peak that

occurred before the HER (at -0.10 V vs. RHE), because of the application of the negative potential (see Figure 3.30). This reduction was irreversible since it did not appear on further polarization curves. This peak was related to the *in situ* reduction of $\text{Co}^{\text{II}}/\text{Co}^{\text{III}}$ to the thermodynamically favorable Co^0 species during HER. The reduced species are higher on the amorphous CoP in comparison to the crystalline CoP, as can be seen from the difference in the areas of the reduction peaks. This phenomenon contributed to the higher HER electrocatalytic activity and lower overpotential obtained with this phase.

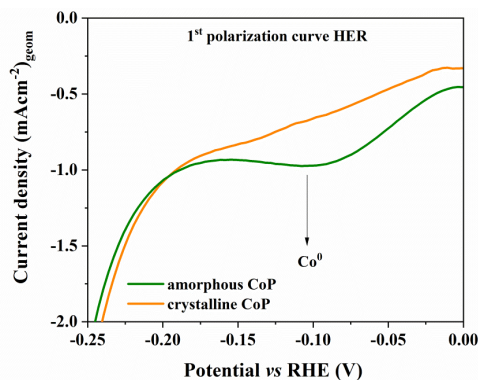


Figure 3.30. Initial polarization curve of amorphous and crystalline CoP measured in 1 M KOH on NF with a sweep rate 10 mV s^{-1} featuring a cathodic peak corresponding to the reduction of higher valent Co species to metallic cobalt (Co^0).

Similar transformations and *in situ* formation of surface Co^0 under reductive conditions are reported in the literature.^[239,302] For example, post-catalytic studies on CoP NPs supported on CNT revealed a core-shell structure with a Co-rich and reduced surface after HER under alkaline conditions.^[303] XPS studies revealed that surface oxidized species Co^{II} , Co^{III} and P^{V} (in phosphate) were electrochemically reduced to form Co^0 and $\text{P}^{\delta-}$, which served as active sites for the HER.^[303] A reductive wave was also observed during HER with electrochemically prepared $\text{H}_2\text{-CoCat}$. The redox event was associated to the *in situ* reduction of $\text{Co}^{\text{II/III}}$ to Co^0 .^[95]

An analogous behavior has been found in other TM pnictides, chalcogenides and other materials. Panda and co-workers^[112] also observed the presence of an irreversible reduction peak on the HER polarization curve while using nanostructured core-shell $\text{Cu}_3\text{N-CuO}$ for HER in 1 M KOH. The peak was related to the reduction of $\text{Cu}^{\text{I}}/\text{Cu}^{\text{II}}$ to Cu^0 species, which is the catalytically active species in the HER. Molecularly-derived FeSe_2 deposited on NF showed a strong reduction peak in the lower current density region of the HER polarization curve, which indicated the reduction of $\text{Fe}^{\text{II}}/\text{Fe}^{\text{III}}$ to Fe^0 .^[106] Extended X-ray absorption fine structure (EXAFS) experiments on helical cobalt borophosphates (LiCoBPO) showed the decrease in the oxidation state of Co towards less positive values after long term HER.^[80]

3.2.5. OWS with amorphous and crystalline CoP

Co-P materials like CoP nanoneedle arrays,^[265] CoP hollow prisms,^[266] CoP nanoframes and nanocubes,^[267] Co₂P,^[260,320] and CoP/Co₂P hybrids^[321] have been applied as bifunctional electrocatalysts in alkaline conditions (see Section 3.2.2). This fact and the outstanding OER and HER activities of crystalline CoP and especially amorphous CoP served as inspiration for the construction of an OWS device to test the bifunctional activity of the electrocatalysts. A two-electrode configuration was used, with amorphous or crystalline CoP used as both the anode and cathode (amorphous CoP/NF || amorphous CoP/NF and crystalline CoP/NF || crystalline CoP/NF) (see Figure A.1.20). A cell constructed with bare NF electrodes served as comparison to determine the activity (NF || NF). The experiments were carried in a closed system in 1 M KOH electrolyte (see Section 7.3.9). The OWS activity was measured through continuous CV starting at a potential before the thermodynamic water-splitting potential (1.23 V, see Section 1.4) and well beyond it, to determine the cell voltage at 10 mA cm⁻², and consequently, the overpotential. A long-term CP experiment (for 5 days) was also performed to determine the relative stability of the constructed system. This was accomplished by the application of constant 10 mA cm⁻² in the two-electrode cell.

The LSVs shown in Figure 3.31a demonstrated that a cell voltage of 1.65 V ($\eta = 420$ mV) is needed to reach a current density of 10 mA cm⁻² for amorphous CoP. The cell voltage obtained with the crystalline CoP cell was relatively higher, 1.79 V ($\eta = 560$ mV). However, both electrocatalysts were superior in comparison to the cell constructed with bare NF. The lower OWS overpotential of amorphous CoP was expected to be superior to the one of crystalline CoP, since this electrocatalysts showed lower overpotentials for the independent OER and HER (see Section 3.2.2). The OWS voltage of amorphous CoP was also comparable to reported values obtained with pure and mixed phase Co-P-based systems (see Table A.1.8).

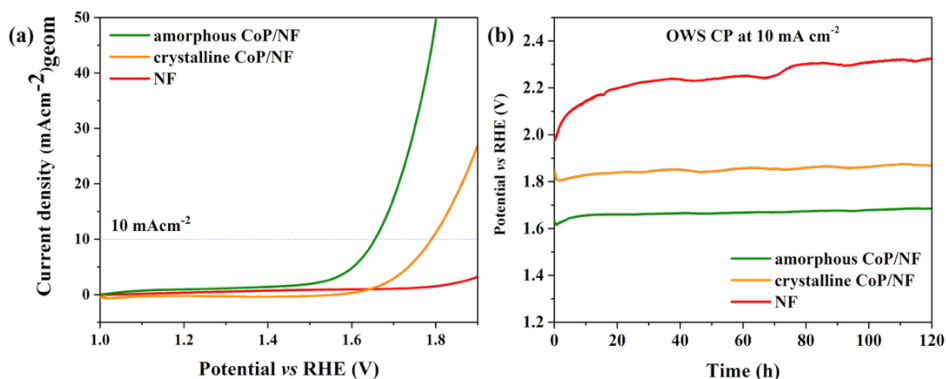


Figure 3.31. (a) LSV curves of amorphous and crystalline CoP (CoP/NF || CoP/NF) along with bare NF (NF || NF) for alkaline OWS and (b) OWS durability tests (CP at 10 mA cm⁻²) over 5 days.

The chronopotentiometric experiments demonstrated the stability over 5 days (120 h) of the constructed cells for the OWS for both amorphous and crystalline CoP (see Figure 3.31b). The cell constructed with amorphous CoP delivered an almost constant voltage

of 1.66 V ($\eta = 430$ mV) throughout the experiment. In contrast, a much higher potential was achieved by the crystalline CoP (1.83 V, $\eta = 600$ mV). The bare NF substrate showed continuous deactivation, demonstrated by the potential increase from 1.90 V ($\eta = 670$ mV) to 2.33 V ($\eta = 1.10$ V) during the 5 days of measurement. Therefore, the catalytic activity and stability of the system was inherent to the deposited films of amorphous and crystalline CoP.

Moreover, the Faradaic efficiency (FE) of amorphous CoP during OWS was determined. The FE measures the efficiency of an electrocatalyst to transfer electrons provided by an external circuit across the interface to the electroactive species to affect the electrode reactions (see Section 7.3.10).^[52] FE experiments were done with the two-electrode systems prepared with amorphous and crystalline CoP (amorphous CoP || amorphous CoP, and crystalline CoP || crystalline CoP). The FE towards OER and HER in 1 M KOH was measured in a two-electrode system. An inverted closed electrochemical cell (graduated) was used in which H₂ and O₂ could be collected separately at atmospheric pressure (see Figure A.1.21). A constant current was applied in the system (10 mA cm⁻²) in the system and an increase in the volume of gas was observed on both closed compartments containing the electrodes. The increase in the volume was noted through time and the ratio of the volumes of produced H₂ and O₂ remained almost 2:1 over one hour of electrolysis, showing an efficient selectivity and reactivity of the electrocatalysts for each half-cell reaction (see Figure A.1.22). A quantitative analysis of the evolved gases was also done to determine the FE. A similar two electrode system in a closed one-compartment cell was used. The electrolyte and cell were first degassed with argon (Ar) for one hour under constant stirring. Then, a constant current of 10 mA cm⁻² was applied on electrodes of 1 x 1 cm² area for 400 s. At the end of electrolysis, the gaseous samples were drawn from the headspace by a gas-tight syringe and analyzed by gas chromatography (GC) to determine the amount of H₂ and O₂ produced by the water electrolysis. FE of 96 % and 92 % for HER and OER, respectively, for amorphous CoP (see Section 7.3.10 for calculation details). In both materials transfer electrons and facilitated the electrochemical OER and HER. It should also be noted that in practice the FE of 100 % cannot be achieved due to thermodynamic and kinetic barriers during the reaction.^[52]

3.3. Conclusion

The search for a new preparation method to access amorphous and crystalline CoP from a defined molecular precursor was established. The decomposition by pyrolysis or hot-injection of a SSP β -Diketiminato cyclo-P₄ di-Co^I complex bearing a [2Co-4P] center led to crystalline and amorphous CoP, respectively. The obtained CoP phases were electrodeposited on conductive substrates (NF, FTO) and the resulting films were successfully used for OER, HER and OWS in alkaline media (1 M KOH). The amorphous CoP showed a high OER activity and long-term stability during catalysis. To achieve a current density of 10 mA cm⁻², the amorphous CoP only required an overpotential of 360 mV on the FTO substrate and 268 mV on NF (see Figure 3.32a). The crystalline CoP

required higher overpotential of 414 mV and 305 mV when deposited on FTO and NF, respectively. The materials activities were comparable to benchmark IrO₂ and achieved activities and overpotentials similar or better to other Co-P-based and non-noble TM-Ps systems (see Table A.1.2). Both materials show long-term stability for 24 h, in which constant overpotentials of 280 mV and 300 mV were achieved at 10 mA cm⁻² by amorphous and crystalline CoP deposited on NF, respectively. Similarly, the amorphous CoP showed a high HER activity and long-term stability, and required 228 mV on the FTO and 143 mV on NF to reach -10 mA cm⁻². This material surpassed the crystalline phase ($\eta = 377$ mV and 261 mV on FTO and NF, respectively) and the state-of-the-art IrO₂, as well as other Co-P-based and non-noble TM-Ps systems reported in the literature (see Table A.1.3). A long-term stability (24 h) was also observed for the HER, in which constant overpotentials of 170 mV and 310 mV were achieved at -10 mA cm⁻² by amorphous and crystalline CoP deposited on NF, respectively (see Figure 3.32b). The bifunctional catalytic activity of both materials was also tested using a two-electrode cell. The amorphous CoP exhibited a low voltage (1.66 V, $\eta = 430$ mV) and over 100 h stability for OWS, in comparison to a much larger cell voltage obtained with the crystalline CoP (1.83 V, $\eta = 600$ mV).

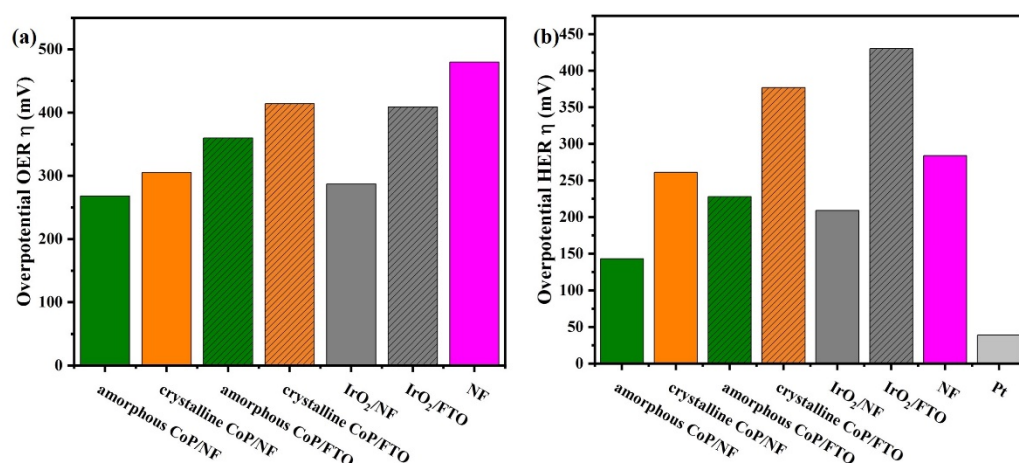


Figure 3.32. Comparison of the overpotentials required for the (a) OER, and (b) HER electrocatalysis to achieve a current density of 10 mA cm⁻² in a 1 M KOH.

Post-operando analysis revealed that under the strongly alkaline and oxidative conditions, electrochemical corrosion promoted the oxidation of phosphorus to polyphosphates and their dissolution into the electrolyte on both materials. As a result, they transformed into a highly oxidized amorphous Co (oxy)hydroxide, which provided a high-surface-area "enriched" with defects. This layer was composed of disordered CoO_x(OH)_y sheets with a common structural motif generated by corrosion: Co^{III}O₆ edge sharing octahedra connected by μ -oxo-bridges. The octahedral Co^{III} species ($d^6, t_{2g}^5 e_g^1$ configuration) exhibited Jahn-Teller distortion, which was crucial for the generation of active sites for the water oxidation. The elongation weakened the Co^{III}-O covalent bond along this axis and facilitated the absorption of oxygen intermediates and the oxidation to Co^{IV}, which is an important intermediate in the OER catalytic cycle. A mechanism for

OER with two possible O-O bond formation steps was postulated. The O-O bond was either formed by a nucleophilic attack of hydroxide on a metal center or the direct intramolecular coupling. Both steps required the presence of highly oxidized Co^{IV} atoms, which are capable of oxidizing water and generate O_2 . The similarity of the *post-operando* characterization results concluded that the evolution of O_2 in amorphous and crystalline CoP must have taken place via a comparable mechanism.

Similarly, *post-operando* characterization revealed that two simultaneous processes occurred during HER. First, a transformation similar to the one occurring during OER took place. The contact of the materials with the strongly alkaline solution led to the oxidation of the surface of the amorphous and crystalline CoP. The corrosion caused the oxidation of phosphorus to polyphosphate species, which are highly soluble in the alkaline electrolyte. Continuous contact with the solution caused the outer surface to transform into a Co-enriched $\text{CoO}_x(\text{OH})_y$. Second, under the reductive HER conditions, the continuous application of a negative potential prompted the *in situ* reduction of $\text{Co}^{\text{II/III}}$ species to less positively charged Co^0 , which was detected electrochemically and assigned as the active species for HER.

The higher dissolution rate of phosphorus into the alkaline solution of the amorphous CoP during OER and HER suggested a larger structural transformation towards Co (oxy)hydroxide of the amorphous CoP. The larger amount of $\text{CoO}_x(\text{OH})_y$ was responsible for the higher electrocatalytic activity of amorphous CoP. This was also confirmed by the higher ECSA of amorphous CoP, compared to crystalline CoP (0.30 vs. 0.11 cm^2), which indicated that the amorphous phase had more surface defects which increased the exposure of active sites to the electrolyte solution. A core-shell structure was formed after OER and HER catalysis. The oxidized layer surrounded the retained metallic-character CoP core. The metallic-character of the remaining CoP core contributed to catalysis by improving the charge transfer between the active $\text{CoO}_x(\text{OH})_y$ layer and the electrode substrate. However, in the case of the crystalline CoP, the benefit in the activity of the core-shell structure was not sufficient to overcome the low oxidation and extension of the $\text{CoO}_x(\text{OH})_y$ layer, which contained the active sites responsible for the OER. The larger oxidation that occurred in the amorphous CoP contributed to an improved activity and stability for OER, HER, and OWS.

4. Synthesis, characterization, and electrochemical behavior of iron arsenide (FeAs)

TM-As, the heavier congeners of TM-Ps, are an important class of materials which exhibit unique electronic, semiconducting, optical, and magnetic properties,^[194–198] but remain unexplored for electrocatalytic applications. Their high electrical conductivity could be an indicative of their possible high OER electrocatalytic activity.^[246] The following chapter describes the use of a SSP approach towards crystalline FeAs nanoparticles and their use for OER electrocatalysis. Extensive *in situ* and *ex-situ* analyses were performed to determine the characteristics of the generated phase during OER, and identity of the active species.

4.1. Introduction

Since the discovery in 2006 of the high-temperature superconductivity of Fe-based pnictide LaFePO (critic temperature, $T_c = 26$ K),^[322] several efforts have been made for the identification of superconductivity in a series of rare-earth doped Fe oxypnictide-based materials LnFeEO (rare-earth Ln = La, Ce, Sm, Gd, Nd, Pr; E = P, As).^[323] Since then, new O-free Fe arsenides materials as AFe_2As_2 (A = Ca, Ba, Sr, alkaline-earth) and $AFeAs$ (A = Li, Na, alkaline) have emerged.^[198,324] The common structural motif in these materials are [FeAs] layers intercalated with cations of alkaline or alkaline-earth elements (see Figure 4.1).^[198,325] The layered [FeAs] structure is crucial to reach a high T_c .^[326] Therefore, binary TM-As (1:1 TM:As ratio), like FeAs, can be considered as “proxy” structures of potential arsenide-based superconductors.^[326]

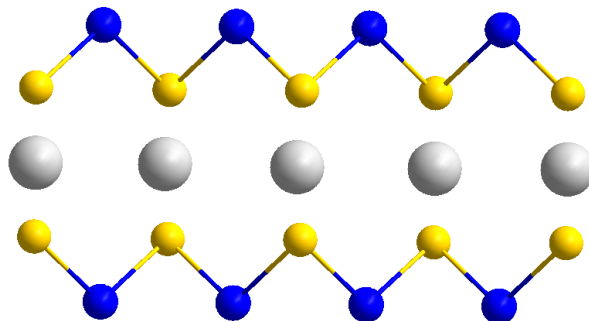


Figure 4.1. Crystal structures of $CaFe_2As_2$. Blue, yellow, and grey sphere represent atoms of Fe, As and Ca, respectively.^[198,325]

Binary arsenides have also attracted special attention due to their structural and compositional diversity that results in a wide range of desirable electronic and magnetic properties.^[327] Consequently, they have been used as thin films and components of electronic devices.^[194–198] The most recent investigations have been based on main group metal arsenides semiconductors like GaAs and InAs because of their potential replacement to Si in electronic, optoelectronic, solar cells, light-emitting diodes (LEDs), thermoelectric devices, and biosensing.^[200,328,329]

Recent attention has been devoted to arsenides of first row TMs (CoAs, CrAs, MnAs, FeAs), due to their applications as semiconductors, anode materials for Li-ion batteries, and magnets.^[201] Bulk metallic CoAs has shown no long-range magnetic order, but CoAs nanostructures have magnetic properties. Nath and co-workers^[330] prepared CoAs nanoparticles (10-15 nm) by hot-injection of triphenylarsine in a solution of $\text{Co}_2(\text{CO})_8$ in HDA. The nanostructures were ferromagnetic at low temperatures and superparamagnetic at high temperatures, which made them suitable for spintronics. Other ferromagnetic TM-As like CrAs and MnAs are also important in the field of the spintronics, since they convert magnetic energy into electrical energy when used as components of circuits.^[201] CrAs adopts an orthorhombic structure that suffers of phase transition from NiAs-type to MnP-type at 800 K, and further cooling below this temperature the CrAs became a double helix, which exhibits antiferromagnetism.^[331] Similarly, MnAs adopts a MnP-type structure and is regarded as a ferromagnetic material with high Curie temperature (600 K). MnAs has attractive physical properties for practical use in ferromagnetism. However, the unique properties of binary arsenides and its possible influence on catalytic processes has not yet been researched due to concerns about toxicity and possible As-related contamination.^[194–198,332]

4.1.1. Iron arsenide

Iron arsenides were discovered in mixtures of minerals. They were first described in 1873 by Weisbach^[333] as a minor component of domeykite (Cu_3As) obtained from the San Antonio mine in Chile. Later, Sandberger^[334] reported the composition of the Co loads from the abandoned locality of Bieber (Hesse), which contained a mixture of several minerals, including smaltine (cobalt iron nickel arsenide (Co,Fe,NiAs)), cloanthine (NiAs), and leucopyrite (FeAs_2). In 1897 Smith and co-workers^[335] found Fe arsenide phase while studying the composition and the thermal and electric conductivity properties of pyrite (FeS_2). The presence of arsenopyrite (FeAs) or pure iron arsenide (FeAs_2) in FeS_2 influenced the melting point of the final phase, but not the heat capacity or electrical conductivity.

In 1912, Dieckmann and Hilpert^[336] reported for the first time the synthesis of a pure iron arsenide phase (FeAs_2) by heating fine powder of Fe with an excess of As for 6-8 h at 700 °C. This pioneering report opened the door the synthesis of other arsenide phases. Brukl^[337] reported in 1923 the general synthesis of TM arsenides by bubbling arsenide (AsH_3) on solutions of metallic salts. In 1925 Vigoroux^[338] reported Fe arsenides systems with different stoichiometric ratios of Fe and As and divided them into individual intermediate phases. A total of four stable intermediate phases of the Fe-As system were reported: the orthorhombic phases FeAs and FeAs_2 , the tetragonal Fe_2As and the rhombohedral $\text{Fe}_{12}\text{As}_5$ (see Figure 4.2).^[339]

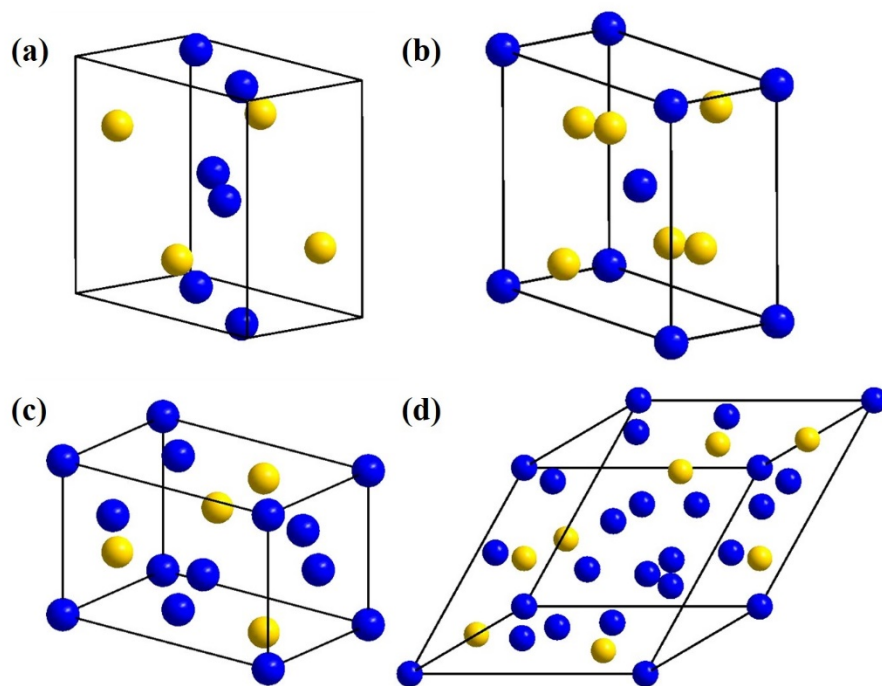


Figure 4.2. Crystal structures of (a) FeAs, (b) FeAs₂, (c) Fe₂As, and (d) Fe₁₂As₅.^[339]

The FeAs₂ phase shows a FeS₂-type orthorhombic structure (*Pnmm*, space group 58).^[340,341] In the nature, it can be found as the mineral löllingite, and is often associated with arsenopyrite (FeAs). FeAs₂ is a diamagnetic semiconductor with a band gap of 0.22 V.^[342] Tetragonal Fe₂As (*P4/nmm*, space group 129) is isomorphous with Cu₂Sb and it contains [FeAs] layers intercalated by Fe ions. It also showed an antiferromagnetic transition with a Neél temperature (magnetic ordering temperature) of $T_N = 353$ K. It could be possible for Fe₂As to become a superconductor if the antiferromagnetic order is suppressed. However, the application of high pressure, even up to 100 GPa did not produce any modification in the conductivity above 2 K.^[343] The rhombohedral Fe₁₂As₅ (*R32*, space group 155) exists only at high pressure and its magnetic and electronic properties remain unexplored.^[344]

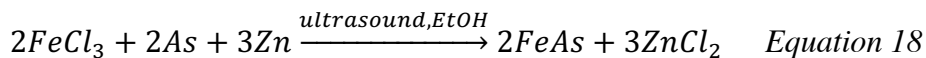
Binary FeAs is an antiferromagnetic ($T_N = 70$ K) semiconductor material that crystallizes in the orthorhombic MnP structure type (*Pnma*, space group 62) and exhibits helimagnetism: the spins of neighboring magnetic moments arrange themselves in a spiral or helical pattern, due to the characteristic arrangement of the Fe^{III} spin along the *c*-axis.^[200] Within the Fe-As phases, it has attracted much attention and has been studied extensively for its unconventional superconductivity and magnetic properties, which made it an important electrical component of semiconductors, secondary high temperature batteries, magnetic storage media, and catalysts.^[194–198,332] Similarly, it has recently been utilized as a promising anode for Li-ion battery.^[345] Its potential applications in electrocatalytic water-splitting are currently unexplored and pros for its electrocatalytic investigation have recently been noted in the literature (see Section 1.5.4).^[202]

4.1.2. Synthesis of FeAs

Much of the synthesis of FeAs has been done by the traditional solid-state methods, that typically require high temperature (800 °C), and sometimes requires arc melting to produce the final crystalline phase. The toxic nature of the As precursors, like AsCl₃, AsH₃ and metallic As, employed in solid-state methods, limits their extensive use.^[336,346] Various alternative approaches have been used to access TM-As, among them CVD,^[213] the molten fluxes approach,^[347] ED,^[348] hydrothermal synthesis,^[227,349] and solid state metathesis.^[350,351]

Nanocrystalline FeAs was prepared for the first time by Qian and co-workers^[352] by a solvothermal reductive process using Zn as reductant of FeCl₃ and AsCl₃. The precursors were placed in an autoclave filled with ethanol and the reaction held at 150 °C for 12 h. The purity of the FeAs material was demonstrated by PXRD and TEM, which revealed spherical particles of 20 nm of diameter. The reaction route was a reductive recombination pathway in which the components were reduced to the elements (Fe, As).

The former work served as an inspiration to the room temperature sonochemical route developed by Du and co-workers.^[327] Elemental As powder, which is the less toxic As feedstock, reacted with FeCl₃ under high-intensity ultrasonic irradiation for 4 h in ethanol with Zn as reductant to obtain Fe⁰ under the ultrasonic irradiation. Ultrasonic waves, which are intense enough to produce cavitation, provided sufficient energy for the reaction of As with the generated Fe⁰ to form nanocrystalline FeAs:



The ultrasonic irradiation played a crucial role in the crystalline character of the particles as it affected the interparticle collision and generated shockwaves in the solution. When less intensity ultrasonic waves were used, XRD measurements demonstrated that no stable phase could be obtained, even with longer reaction times.

A soft-chemical synthetic route was recently developed by Nath and co-workers to access crystalline superparamagnetic FeAs.^[324] The hot-injection of a solution of Fe(CO)₅ in a mixture of triphenylarsine (TPA, As source) and HDA (solvent and surfactant) under inert atmosphere at 300 °C generated FeAs nanoparticles (13 nm diameter). The authors discussed a possible reaction mechanism by the ligand exchange between the Fe complex and TPA, which formed a probable intermediate that acted as SSP, thereby facilitating the low-temperature reaction in the absence of any catalyst.

4.2. Results and Discussion

4.2.1. Synthesis and characterization of crystalline FeAs

The hot-injection has proven to be very effective in the preparation materials of diverse morphology by the controlled thermal decomposition of organometallic compounds. For example, materials as amorphous CoP (see Section 3.2.1)^[250] or crystalline nanosized

materials like FeP and FeSe₂ (see Section 1.5.5).^[106,111] These active electrocatalyst materials have been prepared by the thermal decomposition in hot coordinating solvent of complexes bearing a metal-pnictogen/chalcogenide core stabilized by β -Diketiminato ligands.^[106,111] Similarly, a molecular precursor bearing Fe-As center stabilized by β -Diketiminato ligands was suitable for the preparation of FeAs by the SSP approach.

Stable and robust As-carrying molecules could be employed as suitable As sources. The facile synthesis and isolation of stable and robust arsaethynolate anion (AsCO⁻) was reported by Goicoechea and co-workers,^[353] and later by our group.^[354] This anion has been shown to react towards electrophiles and to form highly reactive arsinidenes through spontaneous or photocatalytic CO release. Thus, it serves as a building block towards new heterocyclic compounds, diarsenes, and terminal pnictides.^[353,355,356] The reactivity of this anion towards β -Diketiminato and mesityl stabilized Ni complexes^[356,357] and Zn complexes^[355] has been explored in the past. However, the reactivity towards Fe-complexes is yet to be explored. Consequently, a two-step procedure towards a novel dinuclear arsenido Fe complex with a [2Fe-2As] containing complex was developed. The treatment of a β -Diketiminato (L^B) ligated Fe complex with NaOCAs·(dioxane)_{2.1} achieved the L^BFeAs₂FeL^B complex, as determined by extensive characterization results (see Experimental Sections 7.1.2.2 and 7.1.2.3).

The new molecular β -Diketiminato stabilized [2Fe-2As] cluster complex then served as a SSP for the synthesis of nanostructured FeAs. The β -Diketiminato ligand acted as a stabilizer of the [2Fe-2As] core, which detached easily during solvolysis. The remaining [2Fe-2As] core served as an ideal building block for Fe arsenide materials. The hot-injection of the molecular complex in oleylamine was carried out at 250 °C, following experimental conditions for the preparation of amorphous CoP (see Section 3.2.1)^[250] and Fe-based electrocatalysts^[106,111] from molecular precursors.

The hot-injection afforded a crystalline material as determined by PXRD, which showed broad diffraction peaks at 2θ of 30.3, 33.9, 34.6, 43.5, 45.4, 48.2, 53.0, 54.4, 59.8, 64.1, 65.7, 73.0°, which represent the (011), (120), (111), (121), (211), (130), (031), (002), (311), (140), (122) and (222) planes of the crystalline FeAs phase, as compared to the reference (JCPDS 76-458) (see Figure 4.3 and Experimental Section, Table 7.13 and Figure 7.23). The broad reflections on the diffractogram can be attributed to the small particle size of FeAs nanostructures. The solid-state crystal structure of FeAs belongs to the MnP structure type (orthorhombic, *Pnma*, space group number 62, with the lattice parameters $a = 5.442 \text{ \AA}$ and $c = 3.3727 \text{ \AA}$) (see Section 4.1.1).^[358-360] The unit cell of FeAs comprises of four Fe and four As atoms (see Figure 4.2a). In the structure, each Fe atom is octahedrally coordinated to six near As atoms and each As atom is surrounded by six near Fe atoms in a trigonal prismatic configuration (see Figure A.2.1). Both coordination polyhedra are far from their regular shapes, leading to a distorted structure.^[359] Elemental analysis results (CHN determination) showed an almost complete elimination of the β -Diketiminato, as supported by the low amount of organic content (Experimental Section, see Table 7.14).

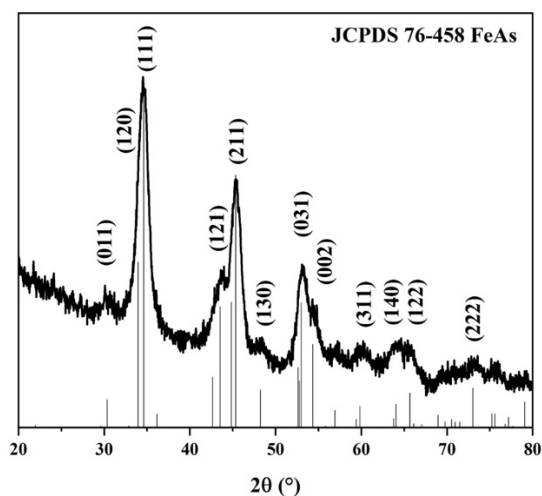


Figure 4.3. Powder X-ray diffraction (XRD) pattern of FeAs-prepared by hot-injection. The obtained diffractogram reveals reflections matching the FeAs phase (JCPDS 76-458). The solid state crystal structure of FeAs (JCPDS 76-458) belongs to the MnP structure type (orthorhombic, *Pnma* (62) space group, with lattice parameters $a = 5.442 \text{ \AA}$ and $c = 3.3727 \text{ \AA}$).^[358–360]

The morphology of the materials was analyzed using SEM. The latter revealed that the solid was composed of agglomerated particles (see Figure A.2.2). TEM revealed that the agglomerates observed by the SEM were rather composed of round-shaped crystalline nanoparticles of $\sim 10 \text{ nm}$ in size (see Figure 4.4 and Figure A.2.3). A closer inspection of the nanoparticles via HR-TEM unveiled the clear crystalline fringes that arise on the individual nanoparticles. The crystalline fringes were associated to a lattice spacing of $d(hkl) = 0.258 \text{ nm}$ which was associated to the (111) plane of the orthorhombic FeAs phase (see Figure 4.4b), which was the plane that achieved the highest intensity on the diffractogram (see Figure 4.3). Moreover, a Fourier transformation (FT) was applied to the HR-TEM images to ensure the determination of the crystalline plane associated to the measured interplanar distances. This mathematical operation produced a pattern that confirmed the assignment of the measured lattice spacing to specific planes of the crystalline FeAs phase (see Figure A.2.4). The FT revealed two rings corresponding to the lattice distances 0.255 nm and 0.199 nm , which were consistent with the (111) and (211) crystallographic planes of orthorhombic FeAs (JCPDS 76-458). In addition, the SAED pattern confirmed the identity of the crystal lattice and excluded the formation of an amorphous phase. The displayed diffraction rings are representative of the (111), (211), (031), (311), (122), (341) planes of the nanocrystalline FeAs phase and agreed with the phase assigned by PXRD (JCPDS 76-458, see Figure 4.4c).^[358–360]

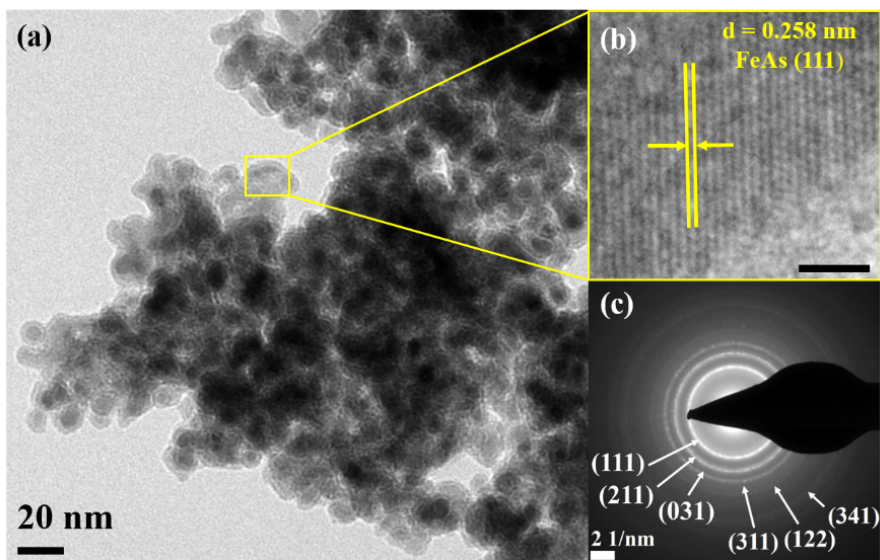


Figure 4.4. a) TEM image of agglomerated FeAs nanoparticles of ~ 10 nm diameter, (b) HR-TEM image displaying crystalline fringes with an interlayer distance of 0.258 nm corresponding to the FeAs (111) crystalline plane showing the highest intensity on the PXRD pattern, (c) SAED pattern with diffraction rings matching the (111), (211), (031), (311), (122) and (341) planes of FeAs phase (JCPDS 76-458) (see Figure 4.3).

The phase and elemental composition was confirmed by ICP-AES (see Table A.2.1) and EDX (see Figures A.2.5, A.2.6) which demonstrated a Fe:As ratio of $\sim 1:1$ through all the measurements (see Table A.2.1). EDX mapping was done to investigate the elemental dispersion in the material. The EDX images showed a homogenous distribution of Fe (blue) and As (yellow) within the structure (see Figure 4.5). The EDX spectra also revealed the presence of surface O, because of surface passivation due to exposure of the samples to air, since handling and transport were not carried out under inert conditions.

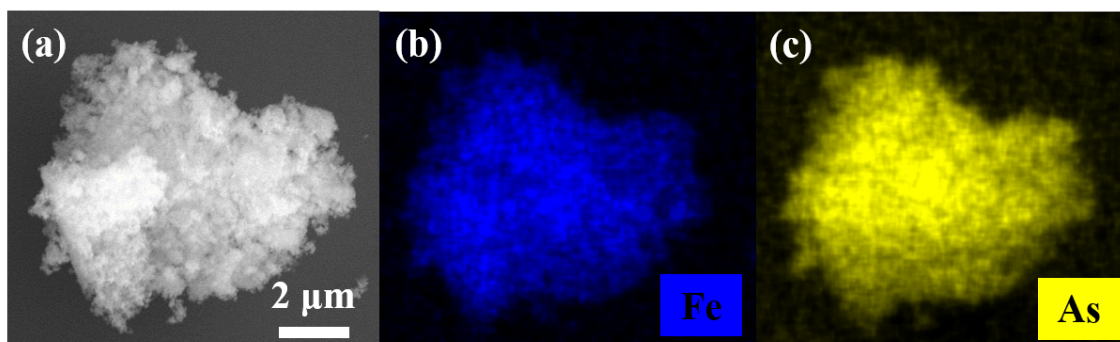


Figure 4.5. SEM image showing agglomerated particles of FeAs and EDX mapping of homogeneously distributed (e) Fe and (f) As.

An efficient way to identify the symmetry and frequency of phonon excitations in superconducting oxypnictide materials is (resonance) Raman spectroscopy (see Section 4.1.1).^[361] Therefore, the Raman active bands of the as-prepared FeAs crystalline phase were coincident with the reported bands for both bulk and FeAs nanoparticles.^[324] The obtained phonon bands could be assigned to the: low-frequency A_{1g} of As (168 cm^{-1}),

B_{1g} of Fe (208 cm^{-1}) and high-frequency E_g of Fe (274 cm^{-1}) (see Figure A.2.7).^[361,362] Small deviations from reported values ($\pm 2\text{ cm}^{-1}$) can be caused by thermal effects or laser power.^[363]

XPS was performed to gain information on chemical composition and electronic states of the as-prepared FeAs (see Figure 4.6). The photoemission lines of the Fe 2p resulted in a complex spectrum due to the spin orbit splitting typical of the Fe 2p spectrum to Fe $2p_{3/2}$ and Fe $2p_{1/2}$ and the presence of satellite peaks.^[364] The high resolution Fe 2p deconvoluted spectrum (see Figure 4.6a) shows the two low binding energy peaks at 705.9 eV ($2p_{3/2}$) and 719.0 eV ($2p_{1/2}$), with a distance of 13.1 eV, that were assigned to positively charged $\text{Fe}^{\delta+}$ in FeAs.^[365,366] The remaining higher binding energy peaks were associated with Fe atoms in high oxidation state, due to surface passivation. The peaks at 709.8 eV ($2p_{3/2}$) and 723.1 eV ($2p_{1/2}$), as well as their two satellites 714.5 eV ($2p_{3/2}$) and 718.2 eV ($2p_{1/2}$), were assigned to Fe^{II} .^[366] Further oxidation was also observed due to the presence of Fe^{III} peaks at 711.5 eV ($2p_{3/2}$) and 725.3 eV ($2p_{1/2}$), and two pairs of satellites at 728.5 eV ($2p_{3/2}$) and 732.7 eV ($2p_{1/2}$). The As 3d spectrum of FeAs (see Figure 4.6b) showed two peaks. The low binding energy peak at 40.4 eV (deconvoluted into 40.3 eV $3d_{5/2}$ and 41.0 eV $3d_{3/2}$), which corresponded to the binding energy of As bound to metal, was related to $\text{As}^{\delta-}$.^[367,368] A slightly intense peak appeared at higher binding energy 43.2 eV, which was attributed to As oxidized species. This binding energy has been associated to arsenite species (AsO_3^{3-}) and to As^{III} cations in As_2O_3 .^[367,368] The presence of As in high oxidation state was caused by the surface passivation. The deconvolution of the As^{III} peak revealed that it was composed of two peaks due to spin-orbital coupling, giving rise to 42.3 eV ($3d_{5/2}$) and 43.4 eV ($3d_{3/2}$).

The presence of oxidized species in the surface of TM pnictides and other electrocatalysts has been reported in the literature.^[162,290] The characterization results by EDX have shown that the passivation due to contact with air generates an oxidized layer, which explained the presence of Fe^{II} , Fe^{III} , and As^{III} . These results were supported by the O 1s spectra (see Figure A.2.8). The high-resolution O 1s spectrum of FeAs showed one peak at 529.6 eV which was also deconvoluted into three peaks: 529.4 eV (O1) and 530.6 eV (O2), which were associated to O bounded to the two elements of FeAs: Fe-O^[366] and As-O,^[367,368] respectively. The third peak (O3, 531.8 eV) was associated with hydroxylation on the surface.^[366] The peak at higher binding energy (O4, 534.7 eV) was associated to adsorbed water on the surface, from the exposure of the material to air.^[366]

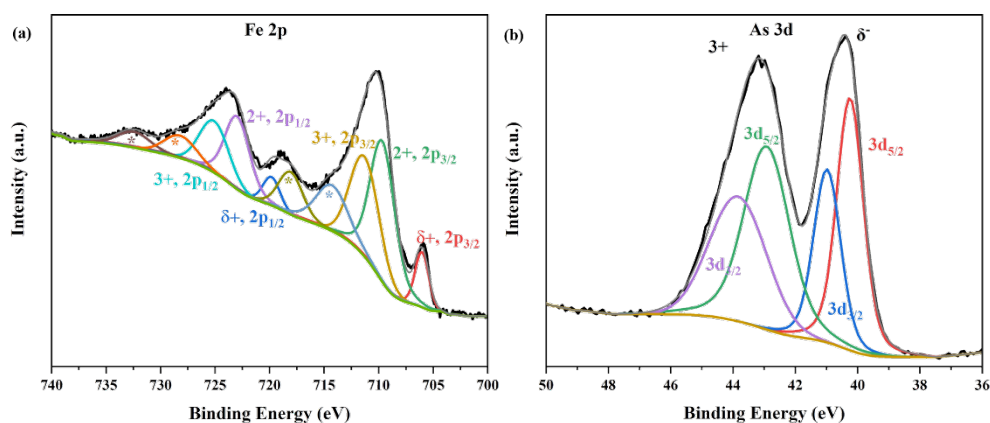


Figure 4.6. Deconvoluted XPS of FeAs: (a) Fe 2p and (b) As 3d.

4.2.2. Electrochemical behavior of crystalline FeAs for OER

The as-prepared FeAs nanoparticles were electrophoretically deposited on NF to investigate their catalytic activity (see Experimental Section 7.1.4). The prepared films (FeAs/NF) were characterized before their use. The SEM images revealed FeAs nanoparticles deposited uniformly over the NF substrate without change in their morphology (see Figure A.2.9). A ratio of Fe:As of $\sim 1:1$ determined by EDX proved that the composition of the materials was maintained during the EPD (see Figure A.2.10). This was also confirmed by the elemental mapping, which revealed a homogeneous distribution of Fe and As over the NF (see Figure A.2.11).

The investigations to study the electrochemical behavior of the FeAs for OER were carried out in a three-electrode system in 1 M KOH (see Experimental Section 7.3.4). The films deposited on NF were used directly as WEs. In order to have a better understanding of the OER electrochemical activity of FeAs, iron oxide (Fe_2O_3), hydroxide ($\text{Fe}(\text{OH})_3$), and (oxy)hydroxide (FeOOH) were used as reference materials. This highly oxidized Fe-based materials have been observed as the transformation products of various TM pnictides during OER under alkaline conditions (see Section 1.5.3 and 1.5.4).^[304,369] Therefore, $\text{Fe}(\text{OH})_3$, FeOOH , and Fe_2O_3 materials were prepared and characterized to determine their composition and crystallinity (see Experimental Section 7.1.3). The PXRD measurements revealed that $\text{Fe}(\text{OH})_3$ was amorphous and FeOOH and Fe_2O_3 crystalline materials (Experimental Section, see Figure 7.9 to Figure 7.11). These materials were then deposited on NF and their activity to compare to FeAs.

Initially, CV experiments were carried out to activate the films. Activation experiments have been done previously to reach stable states and are reported in the literature.^[370,371] Continuous CVs were done for a specific time until no changes were observed on the electrochemical behavior, i.e. when the shape of the CV curve showed no more variation and the overpotential was constant. These experiments demonstrated that 25 continuous cycles are needed to activate the materials (see Figure A.2.12). After the activation, the

OER electrocatalytic activity was determined by LSV experiments at a defined rate of 5 mV s^{-1} (see Experimental Section 7.3.4). The measured current density was related to the geometric area (cm^2), and plotted against the applied potential (E vs. RHE) (see Figure 4.7).

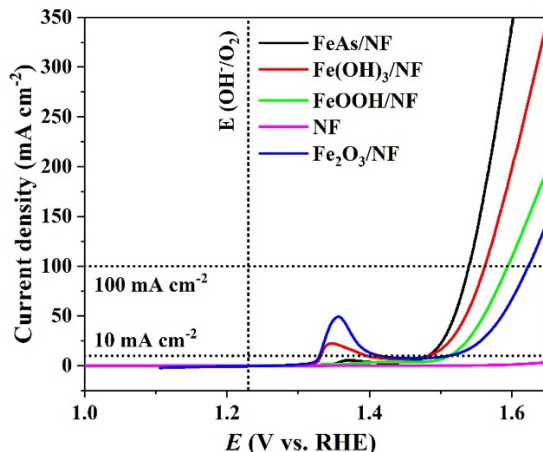


Figure 4.7. (a) LSV (1 mV s^{-1}) of FeAs and Fe reference materials loaded on NF (1 mg cm^{-2}), (b) Tafel slopes obtained from LSV of materials deposited on NF (1 mV s^{-1}).

The FeAs/NF showed an excellent catalytic OER activity and reached a catalytic current density of 10 mA cm^{-2} at an overpotential of 252 mV and 100 mA cm^{-2} at = 309 mV. In contrast, the Fe-based reference materials were less active materials and required higher overpotentials to achieve a current density of 10 mA cm^{-2} : Fe(OH)₃/NF (275 mV), FeOOH/NF (283 mV), and Fe₂O₃/NF (312 mV). At 100 mA cm^{-2} , a similar trend is observed and even much higher overpotentials are needed to reach this current density: Fe(OH)₃/NF (333 mV), FeOOH/NF (364 mV), and Fe₂O₃/NF (397 mV). The electrocatalytic OER activity of pure NF (violet line) was included as a control in order to be able to rule out a significant influence of the Ni species. The contribution of NF to the activity was proved insignificant as the bare NF achieved a high overpotential of 480 mV at 10 mA cm^{-2} (see Figure 4.7). Additionally, a continuous deactivation and minimum current density ($< 12 \text{ mA cm}^{-2}$) was observed during 10 h chronoamperometry (CA) (see Figure A.2.13). The contribution of remaining carbon from remaining ligand or solvent used during the synthesis has been demonstrated as minimal in previous investigations of MOF-derived TM-Ps electrocatalysts (see Section 3.1.2).^[283–286] The possible contribution of the decomposed β -Diketiminato ligand was tested by the preparation of carbon films derived from it. The films were prepared by ED of a solution that contained the ligand. A potential of -10 V was applied to decompose it, and the products of decomposition were deposited on FTO and NF substrates. No further characterization was done on these films. The derived films showed a very low activity for the OER, which ruled out the contribution of carbon to the electrochemical activity (see Figure A.2.14). Finally, a direct comparison of the OER overpotential of FeAs/NF with other Fe-based electrocatalysts described in the literature also showed that FeAs/NF had a considerable activity (see Table A.2.2).

Electrocatalytic kinetics were studied by constructing Tafel plots (see Figure 4.8) derived from LSVs with a scan rate of 1 mV s^{-1} . FeAs attained the lowest Tafel slope of $32 \pm 1 \text{ mV dec}^{-1}$ compared to $\text{Fe}(\text{OH})_3$ ($51 \pm 1 \text{ mV dec}^{-1}$), FeOOH ($53 \pm 1 \text{ mV dec}^{-1}$) and Fe_2O_3 ($56 \pm 2 \text{ mV dec}^{-1}$). These results indicated a more favorable OER rate for the FeAs/NF electrode (see Section 7.3.5).^[292] It can be deduced that the FeAs/NF reacted very dynamically and efficiently to an increase in potential, whereby higher catalytic currents could be achieved faster in comparison with the Fe-based reference materials. This led to a significantly better OER catalytic performance of FeAs/NF. The value of the slope also allows to determine which of the four processes of the PCET reactions was the RDS during OER (see Section 7.3.5).^[41] The values of the Tafel slopes for FeAs/NF suggested that the OER rate was determined by the second PCET, which involves the deprotonation-like process of the adsorbed hydroxide ion which reacts with other hydroxide ion, to produce $(M - O_{ads})$ intermediate (see Section 1.4.2). The Fe-based reference material showed a Tafel slope closer to 60 mV dec^{-1} , which revealed that the reaction rate was determined by the adsorption of the OH^- on the catalyst surface and the resulting formation of the adsorbed $M - \text{OH}_{ads}$ intermediate (see Section 7.3.5).^[41]

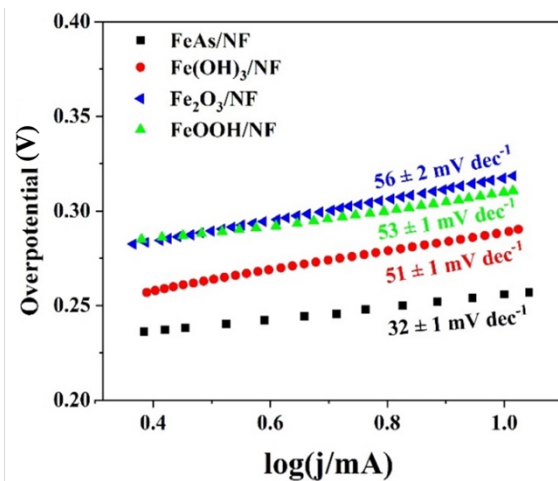


Figure 4.8. Tafel slopes obtained from LSV of materials deposited on NF (1 mV s^{-1}).

EIS experiments were performed to evaluate the electron transfer efficiency of the films under OER conditions and relate it to the activities of the prepared materials (see Section 7.3.7).^[372] A potential of 1.51 V vs. RHE was selected to provide considerable catalytic activity ($> 10 \text{ mA cm}^{-2}$) for all the materials.^[373] The EIS results in Figure 4.9 showed that the smallest charge transfer resistance (R_{ct}) across the electrolyte/electrode interface was accomplished with FeAs ($R_{ct} = 1.2 \pm 0.4 \Omega$) compared to the Fe-based reference materials. A detailed discussion of the calculation and selection of the equivalent circuit is described in the Appendix (see Figure A.2.15 and Table A.2.3). Therefore, FeAs showed a significantly faster charge transfer kinetics between the electrolyte and the catalyst or the electrode substrate during the OER process. This also explains the better catalytic behavior of FeAs/NF. Furthermore, the EIS measurements could exclude an excessive influence of NF and thus the Ni species on the catalytic behavior. NF achieved

a $R_{ct} = 48.0 \pm 1.2$, which was 40 times greater than that of FeAs/NF and also higher in comparison to the ones achieved with the Fe-based reference materials.

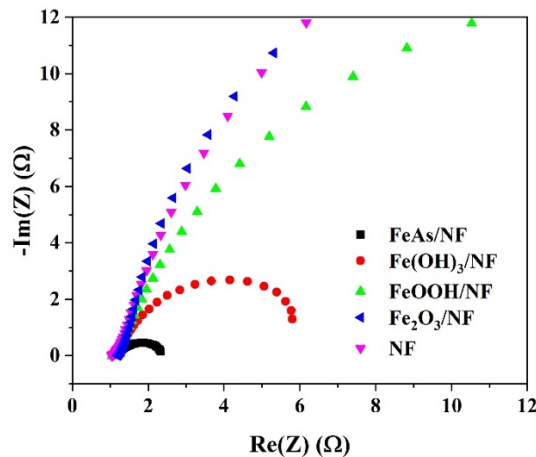


Figure 4.9. Nyquist plot constructed from EIS experiment at 1.51 V vs. RHE. The curves were fitted to a Randles equivalent circuit (details of fitting on Appendix, see Figure A.2.15).^[374]

Long-term CP measurements of FeAs/NF and the Fe-based reference materials were conducted by the application of a constant current density of at 10 mA cm^{-2} for continuous 24 h to investigate the electrochemical stability (see Figure 4.10). During the CP, a stable constant overpotential of 265 mV, which is lower than that of the Fe-based reference materials. In the case of these materials, a variation in the overpotential was observed during the same period, and reached final values of 296, 300, and 320 mV for Fe(OH)₃, FeOOH, and Fe₂O₃. Due to the very good results for long-term stability, the CP at higher current density (100 mA cm^{-2}) was performed. This experiment also revealed a stable overpotential of 330 mV for 24 h (see Figure A.2.16).

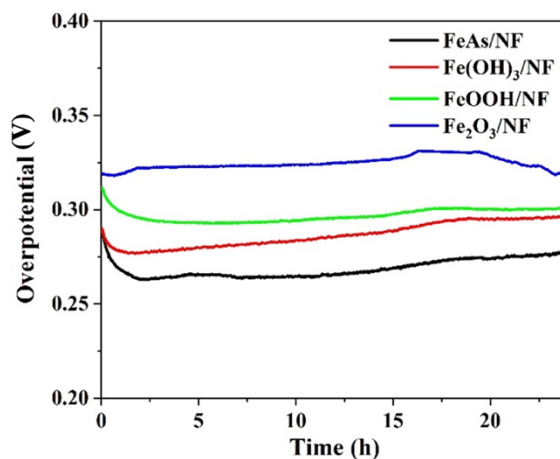


Figure 4.10. 24 h CP measurement of FeAs and Fe-based reference materials deposited on NF.

The FE of FeAs/NF was calculated to determine the efficiency of the electrocatalyst to transfer electrons provided by an external circuit across the interface to the electroactive species to realize the electrode reactions (see Experimental Section 7.3.10).^[52] The FE

OER was measured in 1 M KOH in a two-electrode configuration where FeAs/NF was used as anode and Pt as cathode in a closed one-compartment electrochemical cell (FeAs/NF || Pt). Constant currents (50 and 100 mA cm⁻²) were applied on electrodes of 1 x 1 cm² area for 360 s and the amount of O₂ and H₂ were determined by GC (see Figure A.2.17). The quantified amount of released gas was compared with the charge that corresponded to the current consumed during the water-splitting. The experimentally measured amount of O₂ agreed very well with the theoretically possible values and an efficiency of > 95 % could be determined, which indicated a very high efficiency of the catalyst at both 50 and 100 mA cm⁻² (see Table A.2.4). It should also be noted that in practice the Faraday efficiency of 100 % cannot be achieved due to thermodynamic and kinetic barriers during the reaction.^[52]

The C_{dl} values were determined by performing continuous CV experiments with different scan rates in a potential range where no apparent faradaic process occurred (see Experimental Section 7.3.8).^[68] The difference in cathodic and anodic current was plotted *versus* the scan rate, from which the value of C_{dl} was obtained (see Figure 4.11). A higher value of C_{dl} was related to a higher concentration of active sites of the surface, which resulted in higher ECSA. The C_{dl} was 0.218 mF cm⁻² before the electrocatalytic testing and increased ~3 times up to 0.629 mF cm⁻² after the long-term CP experiment. The increase in the C_{dl} , and therefore ECSA was related to a formation of a catalytically active structure. This surface possibly contained more Fe sites, which were exposed to the electrolyte, which originated the increase in ECSA. The new active surface most possibly formed through the loss of the pnictogen (As) into the electrolyte. Such phenomenon has already been well demonstrated for other TM-Ps materials during OER under alkaline conditions (see Section 1.5.3 and 1.5.4).^[302,304]

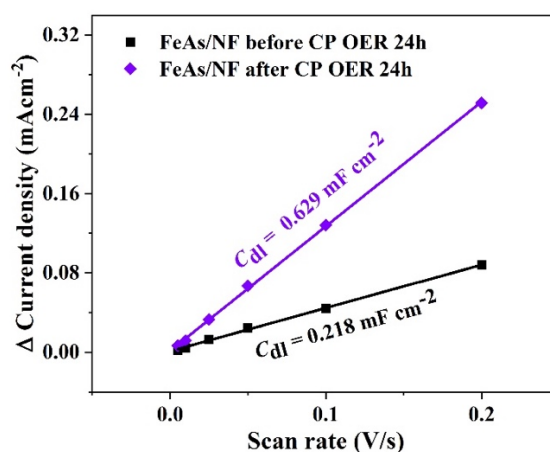


Figure 4.11. Difference in anodic and cathodic current density at the center of the potential range of the CVs measured at different scan rates (see Figure A.2.18). The value of C_{dl} is obtained from half of the slope of the graphs. After OER, there is an increase in ca. 3 times of the C_{dl} , suggesting the possibility of formation of surface defects as noted for non-oxidic materials during OER.^[203,250,297]

The trends in activity of the FeAs and the Fe-based reference materials were determined in films deposited on FTO, to confirm the results obtained on NF. The deposited FeAs

films on FTO were also characterized, in which the chemical character and morphology of FeAs remained, as proved by various characterization and spectroscopic techniques. The details of the characterization of these films are included in the Appendix (see Figure A.2.19 to Figure A.2.25). The OER electrocatalytic activity was compared to films of Fe(OH)₃, FeOOH, and Fe₂O₃ deposited on FTO with the same mass loading. The electrochemical tests for FTO were done on a three-electrode system in which Pt wire was used as the CE, and an Hg/HgO electrode was used as RE (see Experimental Section 7.3.2). The materials were activated by performing 25 continuous CV before the LSV measurement (see Figure A.2.26). The electrocatalytic activity measured by LSV revealed that the overpotential of the FeAs/FTO was only $\eta = 395$ mV (10 mA cm⁻²), which is substantially lower than that of Fe(OH)₃/FTO (577 mV), FeOOH/FTO (609 mV) and Fe₂O₃/FTO (639 mV) at the same current density (see Figure A.2.27). Long-term chronopotentiometric experiments at 10 mA cm⁻² of FeAs/FTO displayed a good stability for 10 h with a $\eta = 380$ mV, in contrast to the Fe-based reference materials which showed deactivation during the OER electrocatalysis and reached the following overpotentials: Fe(OH)₃ ($\eta = 580$ mV), FeOOH ($\eta = 610$ mV), Fe₂O₃ ($\eta = 650$ mV) (see Figure A.2.28). The observed trend in activity is the same as in the NF deposited films, which confirmed the superior performance of FeAs. However, there is a sustained decrease in activity in all the explored materials due to the less amount of material deposited on FTO (see Experimental Section 7.1.4) and the higher conductivity and larger surface area of the NF.^[296]

It has been shown that the catalytic activity is also highly dependent on the mass loading of the materials over the conductive substrate.^[375] The loading achieved by a certain EPD time might not be equal for all the materials under study. EPD time variation experiments (from 4s to 480 s) were done for FeAs/FTO. Subsequently, the EPD experiments provided different loading of the materials (see Table A.2.5). OER LSVs experiments were measured under identical conditions and the polarization curves revealed different overpotentials at 10 mA cm⁻² (see Figures A.2.29, A.2.30). Similar experiments were conducted with Fe(OH)₃, which was the most active catalyst among the Fe-based reference materials (see Table A.2.6, Figures A.2.31, A.2.32) The polarization curves showed that the best OER activity was achieved with a loading of 0.4 mg cm⁻² and 2.4 mg cm⁻² for FeAs/FTO and Fe(OH)₃/FTO, respectively.

In addition, other electrochemical experiments were also carried-out to verify the OER electrocatalytic activity of FeAs/FTO. The Tafel slopes of the FTO-based films were determined from the LSVs. A Tafel slope of 108 ± 1 mV dec⁻¹ was obtained for the FeAs/FTO, which was lower in comparison the one obtained for the other Fe-based reference materials (see Figure A.2.33). The calculated slopes suggested that the OER was determined by the adsorption of the water on the catalyst surface and the resulting formation of the adsorbed $M - OH_{ads}$ intermediate (see Experimental Section 7.3.5).

EIS experiments performed at 1.58 V vs. RHE on the films deposited on FTO revealed a similar trend as the ones obtained with the films deposited over NF. The smallest R_{ct} was

accomplished with FeAs ($R_{ct} = 260.3 \pm 0.3 \Omega$) compared to the Fe-based reference materials and the bare substrate (see Figure A.2.34). The Nyquist plots were fitted to a similar equivalent circuit to the one used when exploring the films deposited over NF (see Figure 4.9). The values of the parameters R_{ct} , R_s and Q and a_2 obtained from the fitting are shown in the Appendix (see Table A.2.7). FeAs showed a significantly faster charge transfer kinetics between the electrolyte and the catalyst or the electrode substrate during the OER process. This also explains the better catalytic behavior of FeAs, independent of the used substrate. In addition, *ex-situ* four-point probe resistivity measurements (see Experimental Section 7.2.15) were done to determine the surface resistivity of FeAs and to demonstrate increased charge mobility of this material. The as-deposited FeAs/FTO with $1.86 \times 10^2 \Omega \text{ cm}$ had more than 10^2 - 10^3 times lower surface resistance in comparison to Fe(OH)₃/FTO (5.60×10^4), FeOOH/FTO (2.30×10^5), and Fe₂O₃/FTO (2.45×10^5). Therefore, the FeAs/FTO had a higher electron mobility with faster charge transport through the bulk phase than the oxidic species and thus facilitated catalytic processes (see Table A.2.8). The higher resistivity of Fe-oxidized phases has been reported in literature, as they are known to be poor electrical conductors.^[129,131,261] It should be noted, however, that the *ex-situ* conductivity measurements are not necessarily able to predict the electron transport abilities of materials under OER conditions.^[376]

A reversible redox couple appeared between 1.20 and 1.45 V vs. RHE in the LSVs of the materials deposited on NF (see Figure 4.7), but not when films were prepared over FTO (see Figure A.2.27). This redox peak could be possibly related to the formation of Ni-FeOOH, a benchmark material for the OER. Literature reports have shown that the incorporation of Fe impurities in NiOOH significantly affected the electrocatalytic activity of this phase.^[132] Therefore, it was necessary to rule out the formation of mixed Ni-FeOOH during the OER experiments with FeAs/NF. A comparison of the evolution of the redox peak through the CV at the same scan rate (5 mV s^{-1}) of FeAs/NF and bare NF (see Figure A.2.35, A.2.36) showed that there is almost no difference in the position of the anodic (1.36 V) and cathodic (1.28 V) peaks and in the achieved current (ca. 6 mA cm^{-2}). Several investigations have reported that Fe incorporation in Ni-FeOOH generates an anodic shift to higher potentials and a decrease in the current achieved by the peak.^[132,377,378] The contribution of Ni-FeOOH in the electrocatalytic activity can be ruled out, because of the similar current densities and positions of the peaks. Therefore, the observed redox peak could only be associated with redox processes occurring on the NF surface (Ni^{II}/Ni^{III}). A similar behavior has been observed before for other materials deposited and/or derived from NF.^[379,380]

4.2.3. *Post-operando* OER characterization of crystalline FeAs

FeAs films on FTO and NF changed during catalysis. An inspection of the films determined a change of color from black (FeAs) to orange (see Figure A.2.37) after OER. In order to gain a detailed understanding of the structural transformations occurring during catalysis and the origin of the electrocatalytic activity, the FeAs was characterized after the OER. The long term CP OER experiment on FeAs/NF showed that this material

achieved a stable overpotential (380 mV at 10 mA cm⁻²) after ca. 2 h (see Figure A.2.28). SEM-EDX analysis performed at this point revealed an almost complete loss of the As, which resulted in a 1:0.06 ratio of Fe:As (see Figure A.2.38 and Figure A.2.39). A severe increase in the O signal was also observed in the EDX, which demonstrated the formation of an Fe-containing oxidized phase. At this point it was clear that the FeAs suffered an almost complete transformation after the 2 h of constant application of a potential. The transformation of the material could also occur in a short time.^[381] Therefore, similar characterization experiments were carried out after the first CV cycle and showed an initial loss of As, which was expressed by the change in the Fe:As ratio to 1:0.91 (see Figure A.2.40, A.2.41). These results confirmed that the complete transformation of the FeAs does not occur with the first CV scan, and longer time is needed. Further characterization was done after 24 h CP OER (hereafter “after OER”) to ensure the determination of the product that resulted from the full transformation of the material.

The PXRD of the film deposited on FTO after OER was done to determine if a new crystalline phase was formed during catalysis. The PXRD pattern of the film after catalysis showed reflexes at $2\theta = 26.5, 33.9, 27.9, 51.8, 54.8, 61.9, 65.9,$ and 78.7° related to the (110), (101), (200), (211), (220), (310), (301), (321) crystalline planes of FTO (cassiterite, SnO₂, JCPDS 41-1445) (see Figure A.2.42a).^[382] A close inspection on the after catalysis PXRD revealed that the signals related to the orthorhombic FeAs (JCPDS 6-458) did not appear (see Figure A.2.42a).^[358–360] Consequently, this was an indication that the FeAs was completely transformed during catalysis. Diffraction peaks related to oxidic Fe or As phases were not found in the PXRD, which are the expected products of transformation during OER (see Section 1.5.4). The obtained PXRD pattern of the sample after OER was complemented with other characterizations with spectroscopic techniques.

SEM after 24 h OER CP showed that the film was composed of agglomerated particles (see Figure A.2.43a), with a possible loss of film material into the electrolyte due to the exposure of the FTO substrate (see Figure A.2.43b).^[383] Elemental mapping and EDX results revealed a homogenous distribution of Fe and O on the remaining film. An almost complete depletion of As, which resulted in a 1:0.05 ratio of Fe:As (see Figure A.2.44 and Figure A.2.45), indicated that 96 % of As was liberated into solution, similar to the value found after 2 h of electrocatalysis (see discussion above). The post-catalytic characterization by SEM-EDX on a FeAs/NF after analogous electrochemical OER experiments revealed a similar loss of the As into the solution (see Figure A.2.46), which left only Fe and O on the film (see Figure A.2.47, A.2.48).

The loss of the non-metal in solution is a common phenomenon and has been observed before for TM chalcogenides and TM-Ps (see Section 1.5.3),^[258,304] and during the investigation of amorphous and crystalline CoP for the OER (see Section 3.2.3). Therefore, the As loss was expected during OER with FeAs. Moreover, the oxidation of As in oxidizing and alkaline conditions to generate soluble species (AsO₄³⁻) contributed to its dissolution into the electrolyte (see Pourbaix diagram of As in Figure 7.14).^[384] Since a high concentration of As is undesirable due to negative effects on humans and

animals,^[205] and the environment,^[385] the loss of As was quantitatively determined by ICP-AES on the electrolyte solution (see Table A.2.9). Surprisingly, the electrolyte showed only a 6.3 % of content of the initial As amount deposited on the film on FTO. This observation seemed contradictory with the EDX results that determined that a complete loss of As from FeAs was achieved in 24 h of OER. A close examination of the used Pt CE after OER catalysis exhibited the deposition of the dark film in the surface that was in contact with the solution (see Figure A.2.49).

The effect of strong As adsorption on Pt electrodes under alkaline electrochemical conditions is known in the literature.^[386] SEM and EDX mapping investigations were performed on the dark film which confirmed the presence of As adsorbed at the surface of the Pt CE (see Figure A.2.50). Consequently, by the replacement of the Pt CE with higher surface area CEs (NF, graphite rod), it was possible to recover ~100 % of dissolved As from the electrolyte in its elemental form. Besides, the discovery of As deposition at the CE during OER was interesting and unique, as the loss of the non-metal during OER is restricted to its dissolution in the electrolyte solution.^[304,387] The observed deposition phenomenon might be interesting for other areas, such as water treatment, in which ED is a promising and convenient method to remove the As from aqueous solutions.^[388,389] The replacement of the Pt CE by cathodes with large surface area could suppress the HER activity limitations, if any, generated by the deposition of As at the Pt CE.^[386] Therefore, the replacement of the Pt CE by a graphitic carbon rod as CE produced no change in the overpotential (see Figure A.2.51) because the interactions of As with Pt and with carbon electrodes are mechanistically similar under alkaline anodic conditions.^[390,391]

More structural insights on the product of the transformation of the FeAs electrode were gathered by TEM. HR-TEM revealed the formation of crystalline nanodomains with an interlayer distance of 0.25 nm (see Figure 4.12a), which were not observed on the as-prepared FeAs. The presence of these crystalline nanodomains explained the lack of diffraction peaks on the *post-operando* PXRD pattern. Fast Fourier transforms (FFT) on the nanostructures (see Figure 4.12b) confirmed a lattice spacing of 0.25 nm (110) which agreed with the initial interlayer distance determined by TEM. The SAED pattern (see Figure 4.12c) did not show any diffraction rings related to the initial FeAs, instead, two broad diffraction rings at a distance of 0.15 nm and 0.25 nm were found. These two diffraction rings corresponded to the (115) and (110) planes of 2-line ferrihydrite.^[392–394] The TEM-EDX confirmed the oxidation of the FeAs during catalysis. The ratios of Fe:As and Fe:O were 1:0.019 and 1:1.67, respectively (see Figure A.2.52). These results indicated that 1.73 % of As is left after OER, related to an almost complete transformation of the FeAs to an oxidized phase, as determined by the results from SEM-EDX and ICP-AES.

The ferrihydrite phase is a natural (and artificial) iron (oxy)hydroxide (FeOOH) mineral that occurs on pristine soils and sediments,^[394] however it has not been reported during the transformation of Fe-based materials during OER electrocatalysis.^[129,395] It is characterized by its extremely high surface area and reactivity and has been vastly used

in decontamination applications by adsorption and precipitation.^[396–398] Ferrihydrite nanoparticles tend to have poor crystallinity as their PXRD patterns usually result in two- or six-broad lined patterns, giving origin to “2-line” and “6-line” designation.^[399]

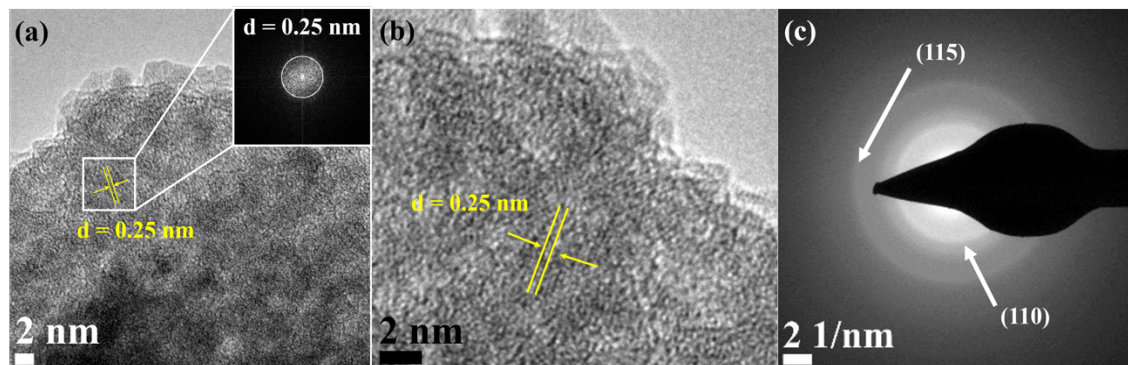


Figure 4.12. (a) High resolution (HR)-TEM and Fast Fourier Transform (FFT) (inset) of the selected area of FeAs/FTO after OER. The FFT reveals a lattice distance of ~ 0.25 nm, which corresponds to the (110) plane in 2-line ferrihydrite.^[392–394] (b) HR-TEM of FeAs electro(pre)catalyst after OER forming nanostructure with a lattice spacing of ~ 0.25 nm (110). (c) The SAED displayed two broad diffraction rings indicative of 2-line ferrihydrite.

Several nanocrystalline phases of Fe-based oxides and hydroxides, apart from the 2-line ferrihydrite, could be formed at the same time during OER. In order to ascertain the identity of the product after OER, FT-IR and (resonance) Raman spectroscopy were performed. Both spectroscopic methods are capable to distinguish several iron (oxy)hydroxide phases (α -FeOOH, γ -FeOOH, δ -FeOOH) and 2-line ferrihydrite by the specific absorption and phonon bands, as reported in the literature.^[397,400,401] The results from the FT-IR and Raman measurements supported the conclusions from the previous results and confirmed the surface transformation to 2-line ferrihydrite and ruled out the formation of other Fe (oxy)hydroxide species.^[397,400,401] The FT-IR spectrum after OER (see Figure A.2.53) showed a broad absorption band at 3168 cm^{-1} , which was attributed to the bending vibration of water or stretching vibrations of OH, which are present in the 2-line ferrihydrite structure.^[397] The bands at 1531 cm^{-1} , 1345 cm^{-1} and 885 cm^{-1} were assigned to Fe-O stretching and Fe-OH bending vibrations, respectively.^[397,399,402] In the (resonance) Raman spectrum taken after OER showed broad bands at the frequency of phonon excitations at 700 cm^{-1} , 510 cm^{-1} and 360 cm^{-1} (see Figure A.2.54). These could be assigned to the ν_3 , ν_2 , and ν_3 Raman active FeO modes of vibration in the FeO₆ octahedra of 2-line ferrihydrite were.^[396,401,403,404]

Further information about the processes on the surface of the materials was provided by more detailed X-ray spectroscopic (XPS and XAS) investigations (see Experimental Sections 7.2.10 and 7.2.11). They showed that the transformation of the FeAs into a 2-line ferrihydrite after the OER was also accompanied by a significant change in the electronic structure. Both the results from the XPS and XAS measurements showed drastic changes in the oxidation states of Fe and As after the electrochemical OER. A comparison of the Fe 2p, As 3d and O 1s XPS spectra of the FeAs and the film after OER is shown in Figure 4.13. The biggest change in the Fe 2p spectrum was the disappearance

of the low binding energy peaks associated to $\text{Fe}^{\delta+}$ in the FeAs ($2p_{3/2}$ 705.9 eV and $2p_{1/2}$ 719.0 eV). Consequently, high binding energy peaks associated with the presence of Fe oxidized species were present. The deconvoluted Fe 2p spectrum revealed the oxidized species that were present after OER: Fe^{II} ($2p_{3/2}$ 709.1 eV and $2p_{1/2}$ 722.3 eV) and Fe^{III} ($2p_{3/2}$ 710.9 eV and $2p_{1/2}$ 724.5 eV) (see Figure A.2.55a).^[366] The presence of the oxidized species was further confirmed by the assignment of characteristic satellite peaks of Fe^{II} ($2p_{3/2}$ 714.3 eV and $2p_{1/2}$ 727.5 eV) and Fe^{III} ($2p_{3/2}$ 718.4 eV and $2p_{1/2}$ 731.6 eV).^[106] Moreover, a peak related to Sn ($3p_{3/2}$) appeared at 714.5 eV, due to the exposure of the FTO-glass substrate after catalysis (see SEM after OER, Figure A.2.43).^[405]

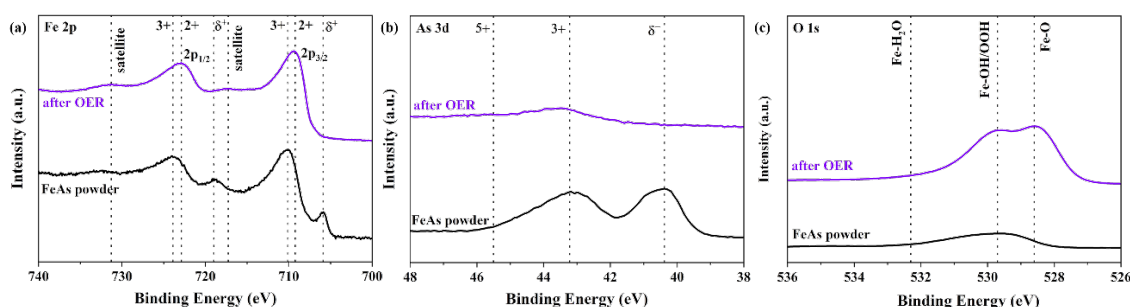


Figure 4.13. The XPS spectra of the FeAs (black line) compared to FeAs after OER (purple line) for (a) Fe 2p, (b) As 3d and (c) O 1s.

The differences in the As 3d spectrum before and after the OER were clear (see Figure 4.13b). The deconvoluted As 3d spectrum (see Figure A.2.55b) showed the loss of peak associated to reduced $\text{As}^{\delta+}$, which indicated that the As was completely oxidized during OER. A low-intensity peak appeared at higher binding energy, which was ascribed to As^{V} (at 43.5 eV, deconvoluted into 43.5 eV $3d_{5/2}$ and 44.2 eV $3d_{3/2}$). Previous results by ICP-AES and EDX have determined the complete loss of As into the electrolyte solution and the transformation to a 2-line ferrihydrite phase under the OER conditions. Therefore, the presence of As in the surface could be assigned to adsorbed $[\text{AsO}_4]^{3-}$ species from the electrolyte solution.^[367]

Finally, the O 1s core-level spectrum showed a peak with two maxima, related to the presence of oxygen atoms with at least two chemically distinct oxygen environments (see Figure 4.13c). The deconvolution of the O 1s spectrum revealed peaks that could be assigned to the species generated during the oxidation of the FeAs (see Figure A.2.55c). The peaks at 528.5 eV (O1) and 529.8 eV (O2) were associated to the binding energies of O atoms present in the 2-line ferrihydrite structure: Fe-O-Fe and Fe-O-H, respectively.^[365,366,406] Additionally, a low-intensity peak at 530.9 eV (O3) was associated the binding energy of O-As in the oxidized AsO_4^{3-} species.^[367]

Quasi *in situ* XAS was carried out to gather further information on the structure and the electronic state of Fe and As during the OER. XANES provided information about the formal valence and the coordination chemistry of the selected elements. *Post-operando* investigations revealed significant structural and electronic changes suggesting the oxidation and conversion of FeAs to a $\text{Fe}^{\text{III}}\text{O}_x\text{H}_y$ phase, which was coincident with the

electronic and atomic structure of 2-line ferrihydrite. The measured Fe X-ray absorption near-edge (XANES) spectra was examined with two standards: metallic Fe and α -FeOOH, which served as basis for comparison of the oxidation state of Fe (see Figure 4.14a). The spectrum disclosed a change in edge shape and position after OER in comparison to the as-prepared FeAs powder XANES spectrum. The initial half-edge-position for the FeAs powder was close to the one of Fe metal foil ($\text{Fe}^0/\text{Fe}^{\delta+}$), which confirmed the metallic character of the prepared material. After the OER, the edge position and shape came closer to the one observed for reference material α -FeOOH. This change revealed the complete oxidation of the Fe atoms in the FeAs to Fe^{III} . This observation agreed with the proposed transformation of the FeAs to the 2-line ferrihydrite during alkaline oxidative conditions determined by the ICP-AES, XPS, TEM, and SAED. Moreover, the edge-energy position of the As-XANES shifted to higher energy during OER (see Figure 4.14b). This shift suggested increase in the oxidation state of As, as evidenced by XPS (see Figure A.2.55b). Besides, the very low raw intensities of the As spectrum confirmed that most of the As left the structure during OER (see Figure A.2.56), which agreed with the ICP-AES, EDX and XPS results. XANES measurements were carried out in the volume phase as the X-rays pass through the sample. Therefore, they confirmed that the transformation of the FeAs to the 2-line ferrihydrite phase during OER was not limited to the surface but complete.

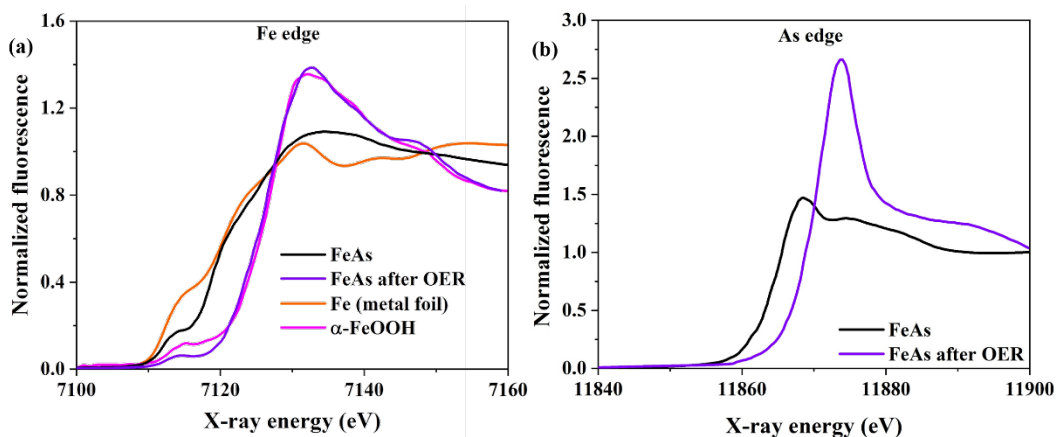


Figure 4.14. (a) Fe K-edge XANES spectra of metallic Fe and α -Fe^{III}OOH reference compounds as well as FeAs powder and FeAs after OER, (b) As K-edge XANES spectra of FeAs powder and FeAs after OER.

EXAFS revealed the near neighbor atomic distances and the coordination around atomic species in the structure of the FeAs. The FT of the EXAFS spectra showed separated peaks of high intensity, each related to a specific coordination shell around the selected atom. The distances of the FT-EXAFS spectrum are generally shifted due to phase-shift, in which a shift of -0.5 \AA is usual.^[407] All distances mentioned from this point have been corrected by the phase shift. The FT of the Fe-EXAFS spectra of the as-synthesized FeAs showed a low populated Fe-O shell at 2.05 \AA , which indicated a minor passivation of the FeAs due to contact with air (see Figure 4.15, for k^3 -weighted χ spectra of Fe see Figure A.2.57). Moreover, the most intense peak at 2.45 \AA corresponded to the average Fe-As distance of the distorted FeAs₆ octahedron of the orthorhombic FeAs structure (see Figure

A.2.1). The lower intensity peaks of longer distance (3.38, 3.99, 4.12, 4.33 and 4.52 Å) matched to the other Fe-As and Fe-Fe distances of two edge-sharing or corner-sharing FeAs₆ octahedra (see Figure A.2.58).^[358–360]

A similar conclusion was drawn from the As-EXAFS spectra (k^3 -weighted χ spectra of As shown in Figure A.2.57b) for the As-As (2.90, 3.47, 3.81, and 4.89 Å) and As-Fe (2.40, 2.51, 4.10, 4.74, and 5.17 Å) distances in the AsFe₆ distorted trigonal prismatic structure of the orthorhombic FeAs.^[358–360] A small contribution of As-O at (1.76 Å) was also observed, which could be derived from surface passivation. A detailed analysis of all shells revealed that the EXAFS distances agreed with the crystallographic data of FeAs for the Fe-As, Fe-Fe and As-As bond distances (for R_{EXAFS} vs. R_{XRD} values see Table A.2.10 and Table A.2.11, and Figure A.2.58).

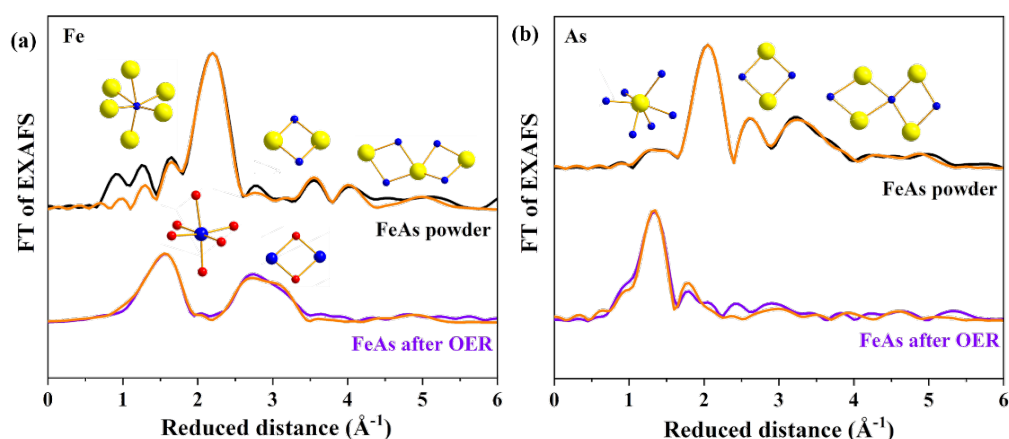


Figure 4.15. (a) Fe- and (b) As-EXAFS spectra of FeAs powder and FeAs after OER (Fe- and As-EXAFS spectra in k -space are shown in the Figure A.2.57). Structural motifs of FeAs and 2-line ferrihydrite are included. Blue, yellow and red spheres represent Fe, As and O atoms, respectively. On the top of (a) and (b), FeAs₆ octahedron and the trigonal prismatic AsFe₆ polyhedron are shown next to the most intense peaks. Detailed bond distances and assigns are described in Figure A.2.58 and Figure 4.16, and Table A.2.10 to Table A.2.12.

Quasi in situ OER EXAFS was done to determine the identity of the active species. Freeze quenching of a FeAs/FTO sample after the constant application of a current density of 10 mA cm⁻² for 6 h was done (see Experimental Section 7.2.11). After this time, the material completely transformed as determined before by the ICP-AES and SEM-EDX composition results. Atomic distances derived from the EXAFS spectra could be fitted the nanocrystalline structure of 2-line ferrihydrite.^[408] The crystalline nanostructure of 2-line ferrihydrite could be structurally described by a single-phase model with the hexagonal space group $P6_3mc$ (space group 183).^[393] The ideal structure is composed of a central FeO₄ tetrahedron coordinated by μ_4 -oxo bridges to 12 octahedrally coordinated Fe atoms arranged in edge-sharing groups of three, each one forming a FeO₆ octahedron. The structure ideally consists of 20 % FeO₄ tetrahedra and 80 % FeO₆ octahedra, but the presence of tetrahedrally coordinated Fe varies, as most of the Fe^{III} ions in the surface are tetrahedrally coordinated.^[392,393]

The Fe-EXAFS spectrum could be fitted with the expected 2-line ferrihydrite phase. There was an almost perfect agreement in the interatomic distances compared to the crystallographic data (see Table A.2.12, R_{EXAFS} vs. R_{XRD} values). No peaks related to Fe-Fe or Fe-O bond distances from FeAs before catalysis could be observed on the *quasi in situ* FT-Fe-EXAFS, in accordance with the complete transformation of the FeAs during OER (see Figure 4.15a). The *in situ* FT Fe-EXAFS was dominated by two broad intense peaks. The first one was composed of two peaks (1.90 and 2.02 Å) which corresponded to the bond of Fe to the nearest oxygen neighbors (O, OH or OH₂) (see Figure 4.16a)^[409] The second peak centered at 3.25 Å was broad and a result of two Fe-Fe coordination shells. The first shell with a radius of 3.02 Å could be ascribed to the Fe-Fe distance of edge-sharing FeO₆ octahedra (see Figure 4.16b). The second shell of this peak with a radius of 3.45 Å was related to the distance between two bent corner-sharing FeO₆ octahedra in the structure of 2-line ferrihydrite (see Figure 4.16b,c).^[393,409–411] This last distance could also be related to tetrahedral FeO₄ units present in the structure of ferrihydrites. In such case, a more pronounced pre-edge feature at 7113.5 eV would be present.^[409] The experimental results revealed that in the after OER film, the pre-edge feature was even less pronounced than in crystalline α -FeOOH, which contains no tetrahedral units (see Figure 4.14). Therefore, the ubiquitous structural motif of the FeAs OER film was FeO₆ octahedra with edge and corner-sharing as connective elements. This structural motif corresponded to the one of 2-line ferrihydrite.^[409] Moreover, the As-EXAFS spectrum (see Figure 4.15b) showed the absence of the Fe-As bonds. Only a peak assigned to the As-O bond (1.70 Å) was present, which indicated that the minor amount of remaining As was present as AsO_x as a separate phase without Fe bonding.

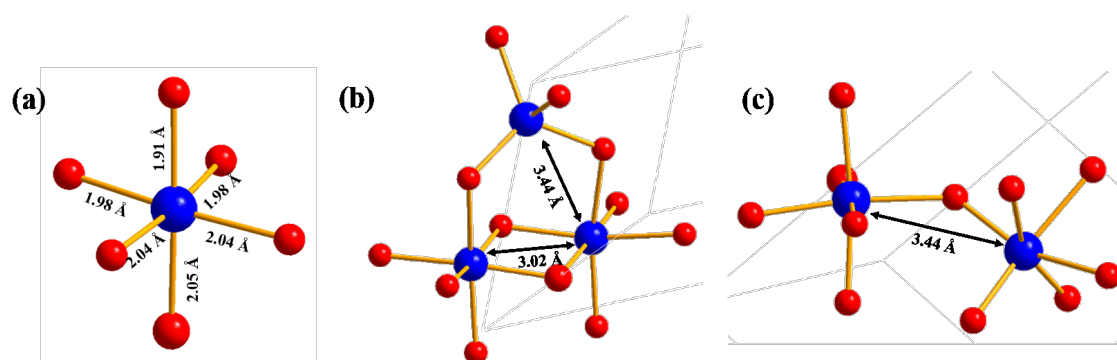


Figure 4.16. Structural motifs of the 2-line ferrihydrite structure.^[393] The expected distances between Fe atoms (blue) and O atoms (red) are shown. Three different coordination environments for Fe in the 2-line ferrihydrite are shown: (a) FeO₆ octahedron, (b) two edge-sharing FeO₆ octahedra and one-corner sharing between the two FeO₆ octahedra and one FeO₄ tetrahedron (c) bent one-corner sharing between two FeO₆ octahedra.

Therefore, the post-catalysis characterization results could satisfactorily explain the differences in activity between the formed 2-line ferrihydrite and the Fe-based reference materials. First, the semiconductor nature of the two-line ferrihydrite^[412–414] could contribute to the high OER electrocatalytic activity, in contrast to poor conductivity of the Fe-based oxidic phases.^[129,131,261,415] Specific resistivity measurements have shown that the after CP OER FeAs sample was 10 to 100 times more conductive in comparison

to the oxidized Fe-based reference materials (see Table A.2.8). The lower resistivity of the phase could arise from O-vacancies generated during OER, which could significantly improve the conductivity and facilitate adsorption of H₂O.^[416–418]

Second, it is also possible that the *in situ* formation of the new phase induced some defected edges/sites which could behave as active centers during catalysis, which would explain its higher OER activity.^[310,419–421] The new phase has no long-range order in its lattice structure, but the experimental results obtained from EXAFS have revealed that the 2-line ferrihydrite contained Fe^{III} atoms in octahedral and tetrahedral coordination that can serve as active sites for OER.^[386,393] Tetrahedrally coordinated Fe^{III} are specially important because of the larger amount of this species in the surface of 2-line ferrihydrite.^[392,393] The electronic configuration of Fe^{III} has a strong influence in the structure and catalytic activity. A Jahn-Teller distortion can occur both in FeO₆ octahedra (d⁵, t_{2g}⁵e_g) and FeO₄ tetrahedra (d⁵, e⁴t₂¹) in the low spin coordination (see Figure 4.17).

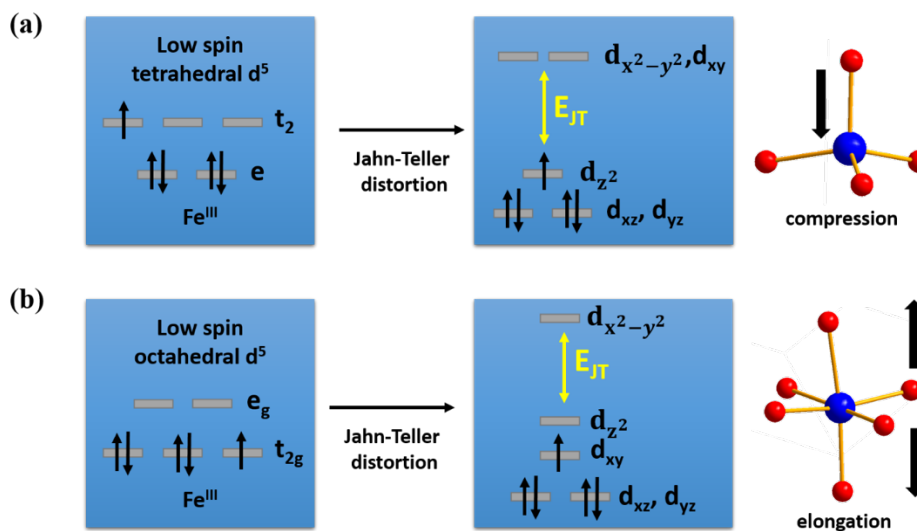


Figure 4.17. Jahn-Teller distortion on the (a) tetrahedral and (b) octahedral coordination modes of low spin Fe^{III} (d⁵) in the structure of 2-line ferrihydrite. The stabilization can be observed by the decrease in energy of the filled orbitals. The FeO₄ tetrahedra suffer a Jahn-Teller distortion and the Fe-O bond is compressed along the z axis. The FeO₆ octahedra suffer and elongation along the z axis.

In the tetrahedral coordination, the incompletely occupied t₂¹ of the e⁴t₂¹ configuration in the Fe^{III} species is split to stabilize the partially filled d_{z²} orbital. As a result there is compression of the Fe^{III}-O bond on the z axis, which has a shorter distance (1.96 Å) in comparison to the Fe^{III}-O trigonal bonds (2.02 Å) (see Figure 4.16). In the case of the octahedral configuration, the incompletely occupied t_{2g}⁵ of the t_{2g}⁵e_g configuration in the Fe^{III} species is split to stabilize the partially filled d_{xy} orbital. The Jahn-Teller distortion in the Fe^{III}O₆ octahedra is observed by the elongation of the Fe^{III}-bonds along one of the molecular 4-fold axes (see Figure 4.16). This elongation weakens the Fe^{III}-O covalent bond along this axis, facilitating the absorption of oxygen intermediates and the oxidation of the Fe^{III}. The Jahn-Teller distortion also generated changes in the electronic configuration of Fe in the tetrahedral and octahedral coordination modes. In both cases,

the final electronic configuration possesses an unpaired electron, which can enhance the electron transfer between OH^- and the electrode surface and promote water oxidation. Moreover, the formation of the defect structure gave the 2-line ferrihydrite additional flexibility and thus a higher OER activity. Finally, the high activity of the 2-line ferrihydrite was also related to its extremely high surface area,^[412–414] as revealed by the increment in the C_{dl} during OER.

4.3. Conclusion

A new molecular β -Diketiminato-stabilized 2Fe-2As cluster complex has been synthesized and structurally characterized and utilized as an SSP to access a monodisperse and nanocrystalline FeAs phase which is indeed unachievable by common solid-state approaches. This synthesis represents the first molecular preparation approach to obtain crystalline FeAs.

The FeAs was electrophoretically deposited on FTO and NF to prepare films and examine them for OER electrocatalysis in strongly oxidizing alkaline media (1 M KOH) in comparison to $\text{Fe}(\text{OH})_3$, FeOOH , and Fe_2O_3 . The prepared FeAs showed outstanding catalytic activity in comparison to the Fe-reference materials. FeAs/NF required an overpotential of only 252 mV to achieve a catalytic current density of 10 mA cm^{-2} , which was less in comparison to the Fe-based materials (see Figure 4.18). Further experimental comparisons with reports in the literature showed that FeAs was one of the most active Fe-based electrocatalysts (Table A.2.2). Additionally, a small Tafel slope and low charge transfer resistance also contributed to the high OER activity. A FE of $> 95 \%$ for the OER also proved the high water oxidation performance of FeAs. The long-term CP measurement of FeAs/NF achieved high overpotential stability over 24 h, in comparison to the Fe-based reference materials that required higher overpotentials and showed deactivation during the duration of the experiment. The influence of the Ni species (from the NF) and generation of Ni-FeOOH on the OER activity could be ruled out because of the similar current densities and positions of the anodic and cathodic peaks achieved during CVs. Additionally, further measurements on inert substrates such as FTO proved that the achieved activity trend was independent of the substrate.

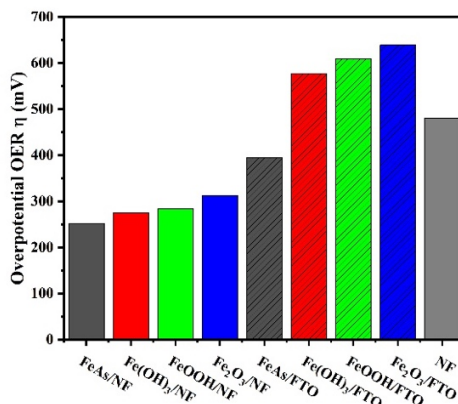


Figure 4.18. Comparison of the overpotentials required for the (a) OER electrocatalysis to achieve a current density of 10 mA cm^{-2} in a 1 M KOH.

The advanced *ex-situ* analytical methods as well as *in situ* XAS results demonstrated that the As leached almost completely after 2 h of electrocatalysis and was transformed to a 2-line ferrihydrite phase. The structurally disordered 2-line ferrihydrite also showed enhanced ECSA (see Figure 4.11), which provided a higher density of active centers for catalysis. This transformation demonstrated to be a crucial factor in accelerating the OER reaction, as well as its semiconducting nature demonstrated by the 10-100 times lower resistivity in comparison to the Fe-based reference materials, which enabled faster electron transport. The presence Fe^{III} (d⁵) in tetrahedral (e⁴t₂¹) and octahedral (t_{2g}⁵e_g) coordination atoms suffered a Jahn-Teller distortion by the stabilization of the partially filled orbitals. The compression and elongation of Fe^{III}-O bonds in the tetrahedral and octahedral coordination, respectively, were experimentally observed by EXAFS. The elongation weakened the Fe^{III}-O covalent bond along this axis, facilitating the absorption of oxygen intermediates and promoted the OER electrocatalytic activity. Ultimately, the high surface area 2-line ferrihydrite could be the “true” active center for the OER.

The presented study shows that molecularly-derived TM-As materials can be efficiently used as water oxidation catalysis. Most notably, the dissolved As could be successfully recovered at the cathode/CE making the whole process sustainable and energy-efficient. However, this will depend on the surface area of the cathode. Besides, this work presents a facile design and development of unexplored classes of TM-non-metal materials towards several applications beyond OER, such as magnetism, superconductivity, supercapacitors, light-driven photocatalytic HER, fuel cells, and metal-air batteries.

5. Synthesis, characterization, and electrochemical behavior of the amorphous nickel phosphide (NiP) and nickel arsenide (NiAs)

This chapter explores the influence of the pnictogen element in the TM:pnictogen stoichiometry and nature of the leaving anions as agents in the formation of a specific (oxy)hydroxide phase during the OER.^[422] The salt-metathesis synthesis of amorphous NiAs and NiP is described first, followed by OER electrochemical investigations and the determination of the pnictogen role in the OER electrocatalytic activity and transformation.

5.1. Introduction

Ni-based materials are the most widely investigated TM-based electrocatalysts.^[423] Ni phosphides were initially investigated for the HER due to the mechanism similarities of this reaction and HDS.^[150] Later studies demonstrated that Ni phosphides phases can also efficiently catalyze OER.^[26] Ni₂P is by far the most reported Ni-P-based OER electrocatalyst in the literature. Hu and co-workers^[161] showed for the first time the use of Ni₂P nanoparticles for OER under alkaline conditions, which delivered a low overpotential (290 mV at 10 mA cm⁻²). The high activity was ascribed to the formation of an amorphous Ni^{III}O_x(OH)_y layer over the crystalline Ni₂P core, the former contained high valent metallic species which act as active sites for OER (see Figure 5.1),^[203,304] as observed in other TM-Ps (see Section 1.5.3). Nanostructured Ni₂P of different morphologies such as nanowires and nanoparticles,^[424] and urchin-like porous Ni₂P structures have shown high OER activity ($\eta = 200$ mV at 10 mA cm⁻²).^[174]

Other Ni-P phases have been reported for the OER. Liu and co-workers prepared a NiP which achieved high catalytic current density (191 mA cm⁻² at 350 mV) and excellent long-term stability without degradation (10 mA cm⁻² at 1.45 V vs. RHE for 26 h).^[175] Menezes and co-workers^[26] investigated the activity of Ni₁₂P₅ for the OER, which showed an enhanced performance (295 mV, 10 mA cm⁻²) due to the formation of an amorphous Ni^{III}O_x(OH)_y shell on a modified multiphase with a disordered phosphide/phosphite core. Antonietti and co-workers^[151] showed the solid-state derived Ni₅P₄ which accomplished a low OER overpotential (290 mV at 10 mA cm⁻²) due to the presence of highly oxidized species in the surface.^[151]

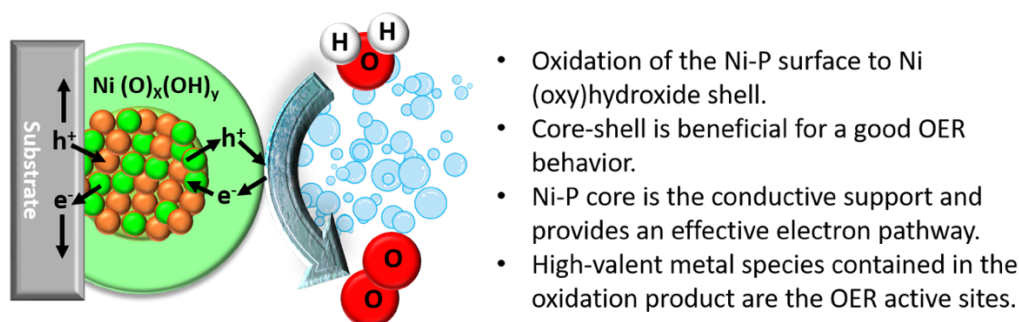


Figure 5.1. Schematic representation of the transformation of Ni phosphide during electrocatalytic OER under alkaline conditions.

The electrocatalytic activity of Ni phosphides towards OER and HER has been increased by common strategies (see Section 1.5.3). The doping of the Ni phosphides with Fe,^[181] Cu,^[425] and Au^[426] has resulted in great activity in comparison to non-doped phases. A similar effect has been noted during the preparation of bimetallic phosphides or the combination with other phases to form favorable heterostructures. For example, hierarchical MoP/Ni₂P/NF structures showed a superior OER performance (309 mV at 20 mA cm⁻²) attributed to unique heterostructure, the synergistic effect of the presence of two metals, and the 3D porous structure which enabled fast mass transfer.^[298] The combination with oxide phases provides highly oxidized metal centers for OER electrocatalysis. For example, the active core-shell structures of Ni_xP-Fe₃O₄^[159] and Ni_yP@NiO_x^[427] have shown greater activities in comparison to the independent components. Finally, combination with highly conductive carbon nanostructures has shown a beneficial effect in the OER. This has been observed in Ni_xP_y NPs composite with rGO,^[428] Ni₂P@graphitized carbon fibers,^[429] and NiP_x on carbon fibers.^[430]

In contrast to crystalline Ni phosphide phases, studies of amorphous phases as OER electrocatalysts remain limited. Shervedani and co-workers^[431] explored for the first time the transformation of amorphous Ni-P during OER electrocatalysis. Phosphorus leaching resulted in the formation of a Ni (oxy)hydroxide porous structure with high ECSA and electrocatalytic activity.^[431] Sun and co-workers^[169] reported the generation of Ni oxides and (oxy)hydroxides during OER using amorphous Ni-P electrocatalysts derived from EPD. The OER activity of amorphous Ni phosphide phases has benefited from the incorporation of other TM. For example, Xiong and co-workers developed an amorphous NiFeP with high conductivity due to the synergy of Ni and Fe, which enabled fast charge transfer that resulted in a very low overpotential (219 mV at 10 mA cm⁻²).^[432]

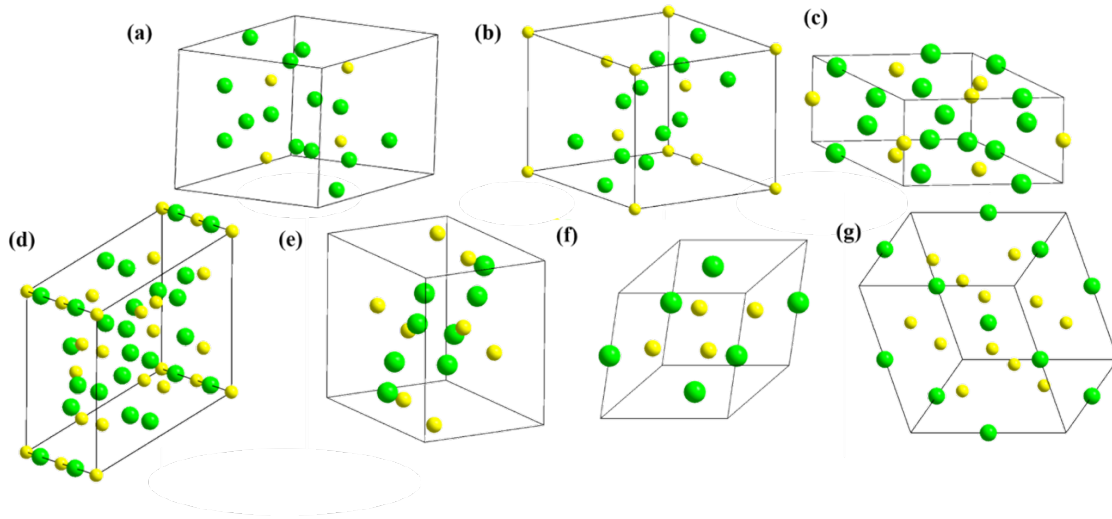
Ni arsenides are unknown for their application in electrocatalysis applications (see Sections 1.5.4 and 4.2.2).^[204,433] Recently, Schumann and co-workers^[203] reported the solid-state synthesis of crystalline NiAs and its use in electrocatalytic OER under alkaline conditions, which showed moderate performance ($\eta = 360$ mV at 10 mA cm⁻²). Post-catalytic examinations on NiAs showed the selective dissolution of As and formation of a porous layer of Ni^{III}O_x(OH)_y with high ECSA.^[202–204]

5.1.1. Nickel phosphide and Nickel arsenide

Nickel phosphide was initially reported in 1895 during the study of the composition of meteorites.^[434] Nickel phosphides and their synthesis were first mentioned in 1896 by Granger,^[268] which described the preparation of crystalline Ni₂P by the reaction of NiCl₂ and P under a heated stream of CO₂. In 1900, Maronneau^[435] reported the synthesis of NiP by the heating of metallic Ni with copper nitride. Two more phases of the Ni-P system, NiP₂ and NiP₃, were noted in 1910 by Jolibois through the reaction of 5 % Ni:Sn alloy with P at 700 °C. In this synthesis, the ratio of P to Ni determined the formation of a specific phase.^[436] A total of seven stable intermediate phases of the Ni-P are distinguished and its properties summarized below (see Table 5.1 and Figure 5.2).^[437]

Table 5.1. Crystal structure data of Ni-P phases.^[437]

Formula	Crystal system	Space group symbol	Space group
Ni ₃ P	tetragonal	$I\bar{4}$	82
Ni ₁₂ P ₅	tetragonal	$I4/m$	87
Ni ₂ P	hexagonal	$P\bar{6}2m$	189
Ni ₅ P ₄	hexagonal	$P6_3mc$	186
NiP	orthorhombic	$Pbca$	61
NiP ₂	monoclinic	$C2/c$	15
NiP ₃	cubic	$Im\bar{3}$	204

**Figure 5.2.** Crystal structures of (a) Ni₃P, (b) Ni₁₂P₅, (c) Ni₂P, (d) Ni₅P₄, (e) NiP, (f) NiP₂, (g) NiP₃.^[437]

Various phases of the Ni-As system are also known. The first Ni-As phase was reported by Sandberger in 1874.^[334] NiAs (niccolite) was found mixed with other As-containing minerals such as smaltine (cobalt iron nickel arsenide (Co,Fe,Ni)As), and leucopyrite (FeAs₂). Later, more phases of the Ni-As were discovered in natural hydrothermal deposits, such as maucherite (Ni₁₁As₈) and rammelsbergite (NiAs₂).^[438] In 1909, Vigoroux reported the first synthesis of Ni arsenides.^[439] The formation of NiAs and Ni₃As₂ phases occurred when vapor of AsCl₃ reacted with Ni at high temperature. A total of five stable intermediate phases of the Ni-As system are distinguished and its properties summarized below (see Table 5.2 and Figure 5.3).^[440]

Table 5.2. Crystal structure data of Ni-As phases.^[440]

Formula	Crystal system	Space group symbol	Space group
Ni ₅ As ₂	hexagonal	Pb_3cm	185
Ni ₁₁ As ₈	tetragonal	$P4_12_12$	92
NiAs	hexagonal	$P6_3/mmc$	194
α -NiAs ₂	orthorhombic	$Pbca$	61
β -NiAs ₂	orthorhombic	$Pnmm$	58

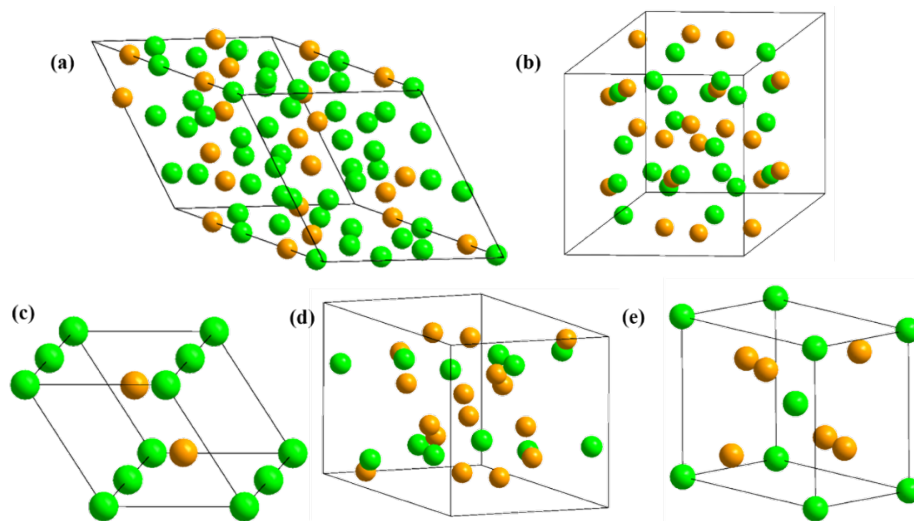


Figure 5.3. Crystal structures of (a) Ni_5As_2 , (b) $\text{Ni}_{11}\text{As}_8$, (c) NiAs , (d) $\alpha\text{-NiAs}_2$, (e) $\beta\text{-NiAs}_2$.

5.1.2. Synthesis of nickel phosphide and nickel arsenide

The solid-state reaction is the preferred approach to access phases of NiAs and NiP . For example, crystalline NiAs and NiP have been prepared by the direct combination of the powders of the elements and heating at $900\text{ }^\circ\text{C}$ and $1100\text{ }^\circ\text{C}$ for more than 15 h.^[203,206,441] The hydrothermal synthesis is an alternative to high-temperature solid-state approach to access Ni arsenide and phosphide phases. Crystalline nanosheets of $\text{Ni}_{11}\text{As}_8$ were obtained by the reaction of elemental Ni with an excess of As_2O_3 in aqueous ammonia at $190\text{ }^\circ\text{C}$ for 12-24 h in autoclave.^[227,349] Similarly, amorphous Ni_xP_y was prepared through a hydrothermal route with NaH_2PO_2 as phosphorus source and NF as a backbone for the synthesis.^[442,443] The hydrothermal route has also been successful to prepare crystalline Ni phosphide phases. Menezes and co-workers^[26] investigated the hydrothermal reaction of red P and $\text{Ni}(\text{CH}_3\text{COO})_2 \cdot 4\text{H}_2\text{O}$. Two distinct phases formed depending on the temperature: Ni_{12}P_5 at $200\text{ }^\circ\text{C}$ and Ni_2P at $140\text{ }^\circ\text{C}$. Additionally, room-temperature electrodeposition has proven a successful method to access TM-Ps. For example, solutions of $\text{H}_3\text{PO}_3/\text{NiCO}_3$,^[431] $\text{NiSO}_4 \cdot 7\text{H}_2\text{O}$ and NaH_2PO_2 ,^[444] and NiCl_2 and NaH_2PO_2 ^[169] have been used to access amorphous Ni phosphide films by electrodeposition.

Another efficient method is the chemical reduction. Usually, TM-Ps for catalytic applications are obtained by the reduction with H_2 of a TM salt together with $(\text{NH}_4)_3\text{PO}_4$ at high temperature ($400\text{-}1000\text{ }^\circ\text{C}$) for few hours.^[445] Other salts containing phosphorus can be also used. For example, the direct reduction with H_2 of $\text{NH}_4\text{NiPO}_4 \cdot \text{H}_2\text{O}$ at $820\text{ }^\circ\text{C}$ achieved crystalline Ni_2P .^[199,446] An analogous synthesis of TM-As has been accomplished by the reduction of $\text{NH}_4\text{NiAsO}_4$ at $400\text{ }^\circ\text{C}$ to access NiAs .^[199,446] An As-rich nickel arsenide $\text{Ni}_3\text{As}_{2+x}$ phase was prepared by the reduction of $\text{Ni}_3(\text{AsO})_2$ with H_2 at $420\text{ }^\circ\text{C}$, and then used as catalyst for hydrogenation of olefins.^[447]

Crystalline TM-Ps and TM-As have been also prepared by the salt-metathesis of a TM halide with sodium pnictides (Na_3E , $\text{E} = \text{As}, \text{P}$).^[448] This method consists in the combination of the solid precursors at high temperature to favor the formation of crystalline phases.^[203,206,441,449] Metathesis procedures in organic solvents at lower temperatures can accomplish particles of smaller size. For example, crystalline Ni_3P and NiAs were prepared by reacting NiBr_2 and NiCl_2 with Na_3P and Na_3As , respectively, under reflux in toluene for 48 h.^[351] Liquid ammonia mediated metathesis has been used to access M_3E ($\text{E} = \text{As}, \text{P}$) from metal halides and sodium pnictides (Na_3E).^[448]

The reaction between a Ni salt and an excess of a P-containing compound (TOP, TOPO, phosphine) in a high-boiling point solvent is ideal to access nanoscaled Ni phosphide materials.^[445] Amorphous Ni_2P was prepared by the direct thermolysis at 230 °C for 1 h of $\text{Ni}(\text{acac})_2$ and TOP in oleylamine.^[159] Grobert and co-workers^[450] prepared amorphous Ni phosphide nanoparticles by the solvothermal decomposition of $\text{Ni}(\text{acac})_2$ and triphenylphosphane in oleylamine under inert atmosphere at 220 °C. Ni phosphides have been also prepared through the decomposition of SSPs. The thermolysis of hexamethylenetetramine precursors under inert atmosphere at 600, 700, or 800 °C was fundamental for the specific formation of nanoparticles of Ni_2P , Ni_{12}P_5 , or Ni_3P phases with high surface areas.^[451] Additionally, the solvothermal decomposition of SSP has been used by Vela and co-workers^[209] to access NiAs by thermolysis of $[\text{ClNi}(\text{o-Ph}_2\text{P-C}_6\text{H}_4)_3\text{As}]\text{Cl}$ at 600 °C under inert atmosphere.

The following table lists the advantages and disadvantages of the synthetic methods applied to Ni phosphides and arsenides.

Table 5.3. Common methods to access amorphous and crystalline Ni phosphides and arsenides.

Method	Advantages	Disadvantages
Solid-state synthesis	<ul style="list-style-type: none"> – access to various crystalline phases – facile laboratory work 	<ul style="list-style-type: none"> – bulk phases – elevated T and reaction time – use of elemental P and As
Hydrothermal synthesis	<ul style="list-style-type: none"> – access to various crystalline phases – mild temperature reaction – alternative As and P sources 	<ul style="list-style-type: none"> – long reaction time
ED	<ul style="list-style-type: none"> – access to amorphous phases – direct film preparation – room or mild T reaction 	<ul style="list-style-type: none"> – no access to nanostructures
Chemical reduction	<ul style="list-style-type: none"> – access to various crystalline phases 	<ul style="list-style-type: none"> – elevated T – H_2 is required
Salt-metathesis	<ul style="list-style-type: none"> – solid-state or in solution – crystalline or amorphous phases are accessible 	<ul style="list-style-type: none"> – elevated T – use of elemental P and As or compounds of them
Solvothermal synthesis	<ul style="list-style-type: none"> – numerous nanoscaled crystalline phases – mild T reaction – short reaction time – possibility to use SSPs 	<ul style="list-style-type: none"> – long work-up required to remove solvent – use of elemental P and As or compounds of them

5.2. Results and discussion

5.2.1. Synthesis and characterization of amorphous NiP and NiAs

The solid-state metathesis has been used several times to prepare TM-As, and usually requires high temperature to increase the reactivity of the precursors and the formation of crystalline phases.^[203,206,441,449] Alternative salt-metathesis procedures at lower temperatures have been accomplished in organic solvents (toluene, benzene) or liquid ammonia, which served as media for the precursor dissolution.^[351,448] Despite its general use, the salt-metathesis approach requires an inert atmosphere and mild temperatures to accomplish the formation of the materials.

Stable and robust pnictogen-carrying molecules could be employed as a replacement of commonly toxic and difficult to handle As and P sources. For example, salts of the stable and robust (AsCO⁻)^[353,354] and (PCO⁻)^[356,452,453] have been reacted with electrophiles through spontaneous or photocatalytic CO release. Thus, it serves as a building block towards new heterocyclic compounds, diarsenes, and terminal pnictides.^[353,355,356] Therefore, the robust NaECO (E = As, P) salts could be used as As and P source to access other TM pnictogen. These salts were used for the salt-metathesis with NiBr₂(thf)_{1.5} complex at room temperature to form Ni arsenide and phosphide phases in a 1:1 stoichiometry with spontaneous CO release (see Experimental Section 7.4.6 and 7.4.7).

The reaction afforded black powders whose crystallinity was determined by PXRD. The PXRD showed a lack of diffraction peaks in the 2θ range between 10° to 80° (see Figure 5.4a,b). In both cases, a broad low intensity peak was observed, centered at 28 and 34° for the Ni arsenide and Ni phosphide materials, respectively. These results indicated that the materials were apparently amorphous. However, broad reflections have been observed on the diffractograms of nanocrystalline materials, especially when the size of a nanostructures is small.^[111] To confirm this, the morphology of the materials was analyzed using SEM.

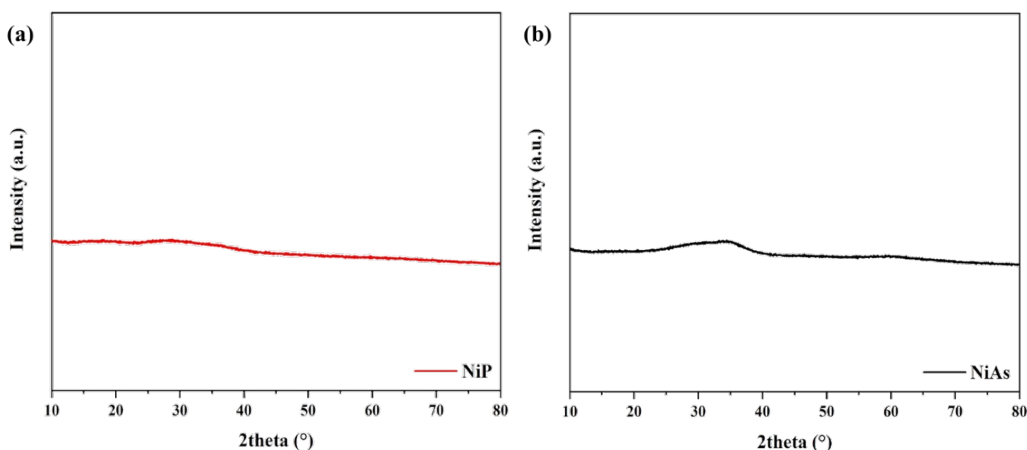


Figure 5.4. PXRD pattern of (a) amorphous NiP and (b) amorphous NiAs. The obtained spectra do not show any diffraction peak associated to a crystalline structure, revealing the amorphous nature of the materials.

SEM revealed that materials were composed of agglomerated spherical particles of ca. 200 nm (see Figures A.3.1, A.3.2). TEM revealed similar results as the SEM, in which large nanoparticles of size > 100 nm were observed (see Figure 5.5). Additionally, no apparent crystalline fringes were observed on the TEM images. A HR-TEM was done in order to rule out nanocrystallinity of the materials, which revealed a lack of crystalline fringes (see Figures A.3.3, A.3.4). In addition, the SAED patterns did not show any crystalline rings, which confirmed the amorphous nature of both materials (see Figure 5.5, insets).

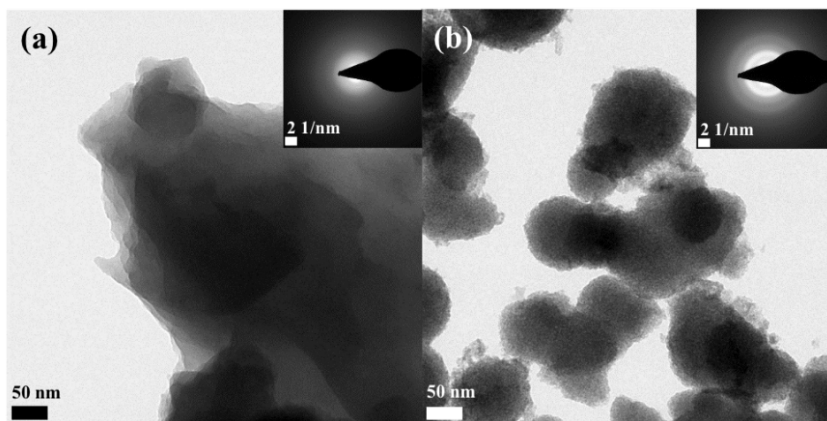


Figure 5.5. TEM images of (a) amorphous NiP and (b) amorphous NiAs. No diffraction rings appear on the SAEDs (inset in a, b), confirming the amorphous nature of the material.

The phase and elemental composition was confirmed by ICP-AES (see Table A.3.1) and SEM-EDX (see Figure A.3.5, Figure A.3.6) and TEM-EDX (see Figure A.3.7, Figure A.3.8). The results showed Ni:As and Ni:P ratios of ~1:1 through all the measurements, which confirmed that the initial stoichiometry used during the synthesis was maintained. EDX mapping was done to investigate the elemental distribution in the materials. The EDX images showed a homogenous distribution of Ni (green) and As (yellow) or phosphorus (yellow) within the structure of the amorphous NiAs and NiP (see Figure 5.6). The EDX spectra also revealed the presence of surface oxygen (< 1 %) and carbon (< 5 %). The first element originated from the surface passivation due to exposure of the samples to air, since handling and transport were not carried out under inert conditions. The carbon content was verified by elemental analysis (see Figure A.3.9), which demonstrated a small amount of organic content (< 5 %). In this case, the presence of carbon could be attributed to remaining solvent or from unreacted NaECO. The catalytic performance of electrocatalysts has been ascribed to the nature of metal cations and anions rather than any organic components,^[283–286] as it has been described for the CoP and FeAs materials described in the previous chapters (see Sections 4.2 and 3.2). Therefore, the influence of remaining carbon from the solvent in the electrocatalytic performance of the materials is negligible.

The reported Raman spectra of Ni arsenides^[448] and Ni phosphides^[454–456] materials in the literature do not show Raman active phonon bands. Examples on the literature only showed phonon bands related to graphitic species present in the material at 1367 and

1550 cm^{-1} . Therefore, the (resonance) Raman spectra of the synthesized amorphous NiAs and NiP phases (see Figure A.3.9) did not show any active band, which discarded the presence of graphitic carbon.

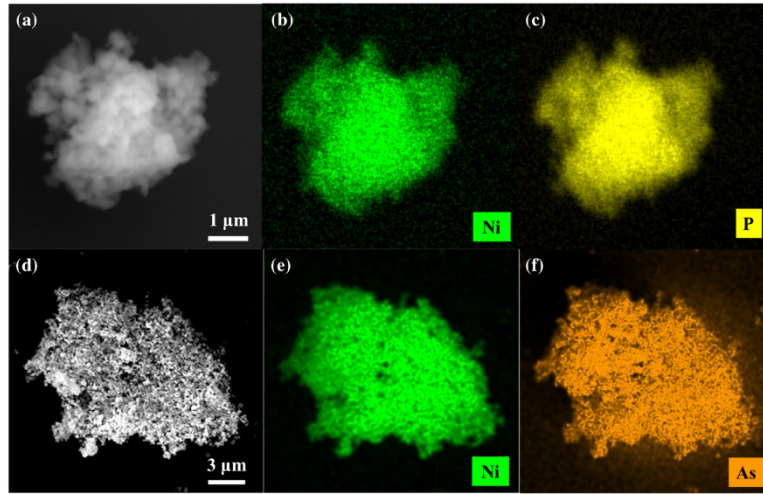


Figure 5.6. (a) SEM of agglomerated NiP and elemental mapping of (b) Ni (green) and (c) P (yellow); (d) SEM of agglomerated NiAs and elemental mapping of (e) Ni (green) and (f) As (orange). The homogenous distribution of Ni and the pnictogen is observed on both materials.

FT-IR provided information of the surface passivation, as the most representative signals on the spectra were related to oxidized groups. In the case of NiAs, a broad peak at 3300 cm^{-1} corresponding to the stretching vibration of O-H was observed (see Figure A.3.10). The peak at 1600 cm^{-1} could be attributed to vibrational modes of adsorbed water.^[457] In the case of the NiP, similar signals related to oxidation were observed: the stretching vibration mode of the O-H bond (ca. 3300 cm^{-1}) and the peak at 1635 cm^{-1} , attributed to vibrational modes of adsorbed water (see Figure A.3.10).^[457] However, low-frequency FT-IR ($< 600 \text{ cm}^{-1}$) revealed vibrations associated to Ni-As and Ni-P bonds.^[458,459] The low-frequency NiAs spectrum showed representative signals at $354, 410, 529 \text{ cm}^{-1}$, which could be assigned to ν_1, ν_2, ν_4 stretching vibrations of Ni-As bonds (see Figure A.3.11a).^[460,461] The low-frequency NiP spectrum showed representative signals at $352, 403, 461, \text{ and } 525 \text{ cm}^{-1}$, which were assigned to $\nu_1, \nu_2, \nu_3, \nu_4$ stretching vibrations of Ni-P bonds (see Figure A.3.11b).^[462]

XPS was performed to gain information on the chemical composition and electronic states of the prepared materials (see Figure 5.7). The photoemission lines of the Ni 2p resulted in a complex spectrum due to the spin-orbit splitting typical of the Ni 2p signals into Ni $2p_{3/2}$ and Ni $2p_{1/2}$ and the presence of satellite peaks (see Figure 5.7a).^[364] In the case of NiAs, the deconvoluted Ni 2p spectrum showed two low binding energy peaks ($2p_{3/2}$ 853.1 eV and $2p_{1/2}$ 871.7 eV , with a distance of 18.6 eV) associated to reduced $\text{Ni}^{\delta+}$.^[26,147,424,463,464] This peak was associated to $\text{Ni}^{\delta+}$ and has been observed in other Ni-based pnictides and chalcogenides.^[203,328,465] The remaining higher binding energy peaks were associated with Ni at higher oxidation state, due to surface passivation. The presence of Ni^{II} was verified by the deconvolution of the spectrum, which showed peaks at

854.5 eV $2p_{3/2}$ and 872.5 eV $2p_{1/2}$, as well as various satellite peaks (856.2 eV, 860.7 eV, 865.5 eV, 878.4 eV). The deconvoluted As 3d spectrum of NiAs (see Figure 5.7b) showed two peaks. The low binding energy peak centered at 41.7 eV related to $As^{\delta-}$ in NiAs (deconvoluted into 41.3 eV $3d_{5/2}$ and 42.0 eV $3d_{3/2}$), which corresponded to the binding energy of As bound to metal, therefore related to $As^{\delta-}$.^[328,465] The peak of higher intensity that appeared at 44.6 eV was attributed to oxidized As species. This peak has been associated to arsenite species (AsO_3^{3-}) and to As^{III} cations in As_2O_3 .^[367,368] The presence of As in high oxidation state was caused by the surface passivation, as observed for the other synthesized materials (see Sections 3.2.1 and 4.2.1) and other electrocatalysts reported in the literature.^[162,290] The deconvolution of the As^{III} peak revealed that it was composed of two peaks due to spin-orbital coupling, giving rise to 44.4 eV ($3d_{5/2}$) and 45.1 eV ($3d_{3/2}$). The surface oxidation of the materials was supported by the O 1s spectra (see Figure 5.7c). The high-resolution O 1s spectrum of NiAs showed one peak at 530.4 eV, which was deconvoluted into two peaks: 530.3 eV (O1) and 531.7 eV (O2). These two peaks were associated to oxygen-bounded to Ni-O^[366] and As-O species,^[367,368] respectively.

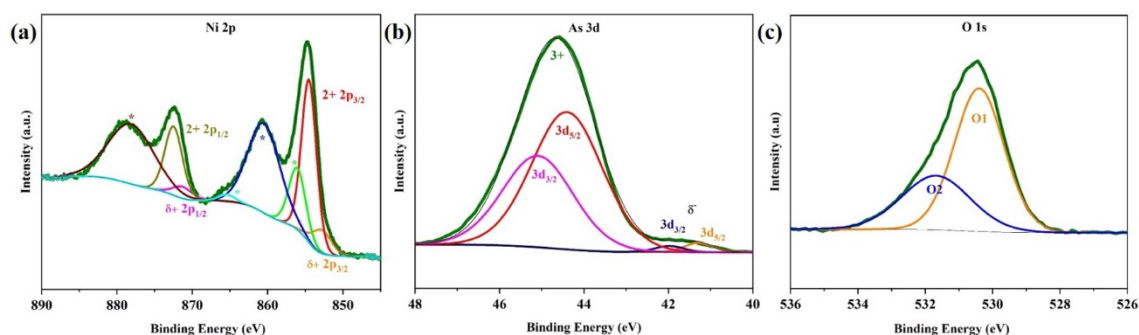


Figure 5.7. Deconvoluted XPS of as-prepared NiAs: (a) Ni 2p, (b) As 3d and (c) O 1s.

Analogous chemical composition and electronic states were found for NiP by its deconvoluted XPS spectra. The deconvoluted Ni 2p spectrum (see Figure 5.8a) showed binding energy peaks related to $Ni^{\delta+}$ in NiP (deconvoluted into $2p_{3/2}$ 851.9 eV and $2p_{1/2}$ 871.3 eV, distance of 19.4 eV).^[26,147,424,463,464] These two peaks have been observed at similar binding energies in the Ni 2p XPS spectrum of crystalline NiP.^[26,203] The deconvolution also resulted in high binding energy peaks, which were associated to Ni in higher oxidation state. These peaks were related to Ni^{II} (deconvoluted into $2p_{3/2}$ 854.5 eV and $2p_{1/2}$ 872.4 eV), caused by the contact of the material with air. Various satellite peaks were also present (856.0 eV, 860.6 eV, 865.6 eV, 874.2 eV and 878.8 eV). The P 2p spectrum showed only one peak at 131.6 eV, which was deconvoluted into two peaks at $2p_{3/2}$ 131.4 eV and $2p_{1/2}$ 132.2 eV (see Figure 5.8b). A comparison with reported values of binding energy of phosphorus demonstrated that this peak corresponded to a phosphite species (P^{III}), formed during the surface passivation due to contact with air.^[162] The presence of phosphorus in high oxidation state has also been demonstrated on the surface of other TM-Ps materials, such as the prepared amorphous and crystalline CoP (see Section 3.2.1). Interestingly, the spectrum did not show any peak related to $P^{\delta-}$ at lower

binding energies, indicating that the surface was completely oxidized. The presence of oxidized species was further confirmed by the assignments of the deconvoluted O 1s XPS spectrum (see Figure 5.8c). This spectrum showed one peak at 530.6 eV. The deconvolution showed only two peaks related to products derived from air exposure of the material: Ni-O=P (O1, 530.4 eV) and Ni-O or P=O (O2, 531.7 eV).^[160]

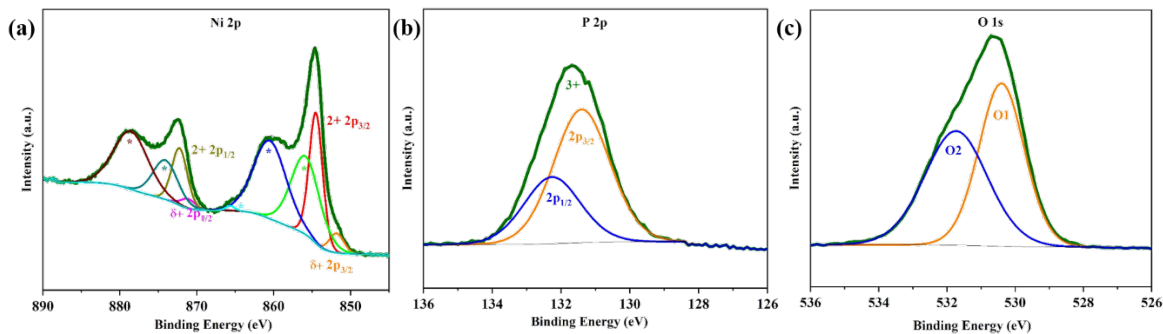


Figure 5.8. Deconvoluted XPS of as-prepared NiP: (d) Ni 2p, (e) As 3d and (f) O 1s.

5.2.2. Electrochemical behavior of amorphous NiP and NiAs for OER

The as-prepared NiAs and NiP were electrophoretically deposited on FTO to investigate their catalytic activity (see Experimental Section 7.1.4). The prepared films (NiAs/FTO and NiP/FTO) were characterized before their use. The PXRD revealed only crystalline planes related to FTO (cassiterite, SnO₂, JCPDS 41-1445) (see Figure A.3.12a).^[382] The crystallinity of the materials did not change during the EPD, as demonstrated by the lack of new diffraction peaks in the PXRD of the as-prepared samples. SEM revealed uniform films with complete coverage of the FTO substrate. The films were composed of agglomerated particles of similar morphology of the as-prepared materials (see Figure A.3.13, A.3.14). The EDX and elemental mapping demonstrated their uniform composition, in which the ratios of Ni:As and Ni:P were ~1:1, as well as the presence of O due to the contact of the films with air (see Figure A.3.15 to A.3.18).

Further characterization by Raman spectroscopy demonstrated that there were no active phonon bands in the investigated range of frequencies, which was coincident with the spectra of the as-prepared materials (see Figure A.3.9, A.3.10). However, there is an increase in the intensity due to the contribution of the bare substrate (FTO) during the measurement (see spectrum of bare FTO in the Appendix, Figure A.2.24). The FT-IR spectra were similar to the spectra of the as-prepared materials. They revealed the bands at 3300 cm⁻¹ and 1600 cm⁻¹ that were associated to the stretching vibration of O-H, associated to adsorbed water (see Figure A.3.10).^[457] Finally, the XPS measurements confirmed that there was no electronic and chemical transformation of the materials during their preparation. A detailed analysis is provided in the Appendix (see Figure A.3.19-A.3.20).

Therefore, the characterization of the NiAs/FTO and NiP/FTO films has demonstrated the chemical and composition integrity of the materials after the EPD. Consequently,

electrochemical investigations were carried out to study the electrochemical behavior of the materials for OER. A three-electrode system in 1 M KOH (see Experimental Section 7.3.4) was used, in which the films deposited on FTO were used directly as WEs. The electrocatalytic activity measured by LSV revealed that the overpotential of the NiP/FTO was only $\eta = 335$ mV (10 mA cm^{-2}), which was lower than that of NiAs/FTO (372 mV) at the same current density (see Figure 5.9a).

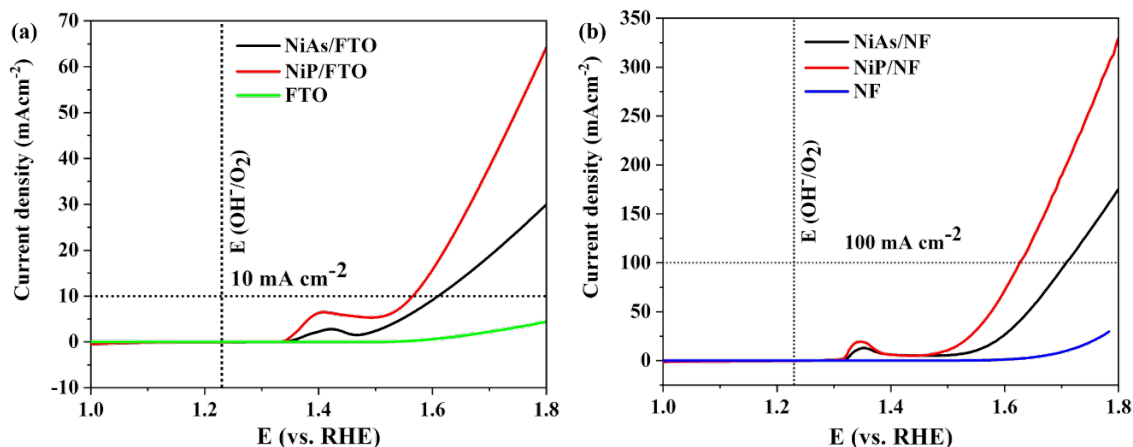


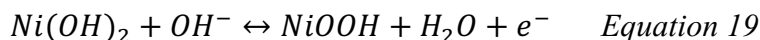
Figure 5.9. (a) LSV (1 mV s^{-1}) of NiAs and NiP loaded on FTO (0.4 mg cm^{-2}), (b) LSV (1 mV s^{-1}) of the prepared materials loaded on NF (1.3 mg cm^{-2}).

Investigations with CoP and FeAs (see Sections 3.2.2 and 4.2.2) revealed that a better electrocatalytic activity was obtained when depositing the materials over NF, due to the larger surface area and higher electrical conductivity of this substrate.^[296] In comparison, FTO showed less surface area and its flat area does not contribute to catalysis.^[208,297] Thus, films were prepared by the EPD of amorphous NiAs and NiP over NF (see Experimental Section 7.1.4). The prepared films on NF were analogously characterized as those on FTO. The SEM images revealed the uniform deposition of amorphous NiAs nanoparticles over the NF substrate without change in their morphology (see Figure A.3.21). In the case of NiP, the film was composed of agglomerations in which individual particles could not be seen (see Figure A.3.22). However, the EDX results demonstrated that the chemical composition of the films remained intact due to the determined $\sim 1:1$ ratio of Ni:As and Ni:P (see Figures A.3.23, A.3.24). The elemental mapping of the films also demonstrated a homogenous distribution of constituent elements over the NF (see Figures A.3.25, A.3.26). Additionally, a homogenous distribution of O was also observed, which originated from the oxidation of the surface due to air exposure of the films. Therefore, the characterization results demonstrated the chemical and composition stability of the films over NF during their preparation by EPD.

The electrocatalytic activity of the samples over NF was then measured. The observed OER overpotentials were lower in comparison to the ones with FTO films, due to the increase in the amount deposited, larger surface area, and larger conductivity of the substrate. NiP/NF reached an overpotential of 267 mV at 10 mA cm^{-2} , which was lower in comparison to the one of NiAs/NF (315 mV) (see Figure 5.9b). The obtained

overpotentials are comparable to the activities of other Ni phosphides and pnictides (see Table A.3.3).

During the evaluation of the OER electrocatalytic performance in alkaline medium, a redox feature was observed before the water oxidation in the range of 1.3-1.45 V vs. RHE on both NiAs and NiP (see Figure 5.9a). The redox couple became apparent when CV experiments were performed (see Experimental Section 7.3.3 and Figure A.3.27). To rule out the contribution of the NF substrate to this phenomenon, CVs were performed on the materials deposited on FTO in which a redox peak was also observed on the same potential range (see Figures 5.9b, A.3.28). This observation confirmed that the observed redox feature could be ascribed to a redox process that occurred on both materials. This peak was related to the oxidation of Ni^{II} to Ni^{III}, that has been regarded as the catalytically active OER species (see Section 1.5.2):^[293]



Similar redox phenomena have been reported in the literature related to Ni-based electrocatalysts and other the first-row TM-based materials, which exhibited M(OH)₂/MO_x(OH)_y phase formation at potentials between ca. 1.1-1.4 V vs. RHE.^[203,293,466] This redox feature occurred on the amorphous and crystalline CoP (see 3.2.2) and FeAs (see Section 4.2.2) discussed before in this investigation.

Electrocatalytic kinetics were studied by constructing Tafel plots (see Figure 5.10) derived from the steady-state method (see Experimental Section 7.3.5). NiP/NF attained a lower Tafel slope ($68 \pm 1 \text{ mV dec}^{-1}$) in comparison to NiAs/NF ($84 \pm 2 \text{ mV dec}^{-1}$). These results indicated a more favorable OER rate for the NiP/NF.^[292] Consequently, a much faster reaction kinetics were observed on the NiP/NF, which led to a better OER catalytic performance.

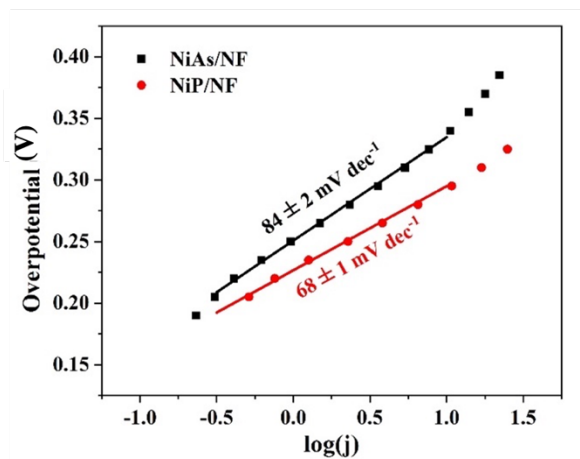


Figure 5.10. Tafel slopes obtained of materials deposited on NF obtained by the steady-state method (see Experimental Section 7.3.5).

The value of the slopes also allowed to determine which of the four processes of the PCET reactions were the RDS during OER (see Experimental Section 7.3.5).^[41] The values of

the Tafel slopes for NiP/NF and NiAs/NF suggested that the OER rate was determined by the adsorption of the OH^- on the catalyst surface and the resulting formation of the adsorbed $M - \text{OH}_{ads}$ intermediate.^[41] Tafel slopes were derived from LSV experiments (at 1 mV s^{-1}) with films deposited on FTO (see Experimental Section 7.3.5). The trend was maintained with the change of conductive substrate. The NiP/FTO showed a lower Tafel slope ($151 \pm 5 \text{ mV dec}^{-1}$) in comparison to the NiAs/FTO ($218 \pm 10 \text{ mV dec}^{-1}$) (see Figure A.3.29), which confirmed the OER limitations by the same PCET step.

EIS experiments were performed to evaluate the electrode transfer efficiency under OER conditions and relate it to the electrocatalytic activity (see Section 7.3.7).^[372] The EIS results after the application of a 1.50 V vs. RHE potential determined that the smallest R_{ct} across the electrolyte/electrode interface was accomplished with NiP ($R_{ct} = 10.37 \pm 1.76 \Omega$) in comparison to the NiAs ($19.96 \pm 0.22 \Omega$) (see Figure A.3.30). The values of R_{ct} were obtained from the fitting of the curves to a Randles equivalent circuit, where R_1 and R_2 and Q are equivalent to the Ohmic resistance of the solution and electrode (R_s), the charge transfer resistance (R_{ct}) and a constant phase element (CPE).^[374] A detailed discussion of the calculation and selection of the equivalent circuit is described in the Experimental Section 7.3.7 (see Figure 7.16). The values of the parameters derived from the fitting and a comparison of the experimental data to the fitting are also shown in the Appendix (see Table A.3.4).

Therefore, NiP showed a significantly faster charge transfer kinetics between the electrolyte and the catalyst or the electrode substrate during the OER process, which explains the better catalytic activity in comparison to NiAs. Furthermore, the influence of the NF (and the Ni species) in the EIS measurements was excluded to the high $R_{ct} = 47.97 \pm 1.19 \Omega$ achieved with bare NF, which was greater than that of the investigated materials. EIS experiments performed of 1.65 V vs. RHE on the films deposited on FTO revealed a similar trend as the ones obtained with the films deposited over NF (see Figure A.3.31). The Nyquist plots were fitted to a similar equivalent circuit to the one used when exploring the films deposited over NF and the values of the derived parameters are shown in the Appendix (see Table A.3.4). An R_{ct} of only $4.78 \pm 1.22 \Omega$ was obtained for NiP/FTO, which was lower in comparison to the one obtained with the NiAs/FTO ($13.17 \pm 1.03 \Omega$) and the bare FTO substrate ($3809 \pm 2 \Omega$).

Long-term CP measurements at constant 10 mA cm^{-2} were done for 24 h to investigate the electrochemical stability of the materials deposited on NF (see Figure 5.11) and FTO (see Figure A.3.32). During the CP, stable overpotentials 275 and 305 mV were obtained for NiP/NF and NiAs/NF, respectively. The films deposited on FTO delivered decreasing overpotentials during the first hours of experiments, reaching stable overpotentials of 350 mV and 390 mV after ca. 2 h and 5 h of measurement for NiP/FTO and NiAs/FTO, respectively.

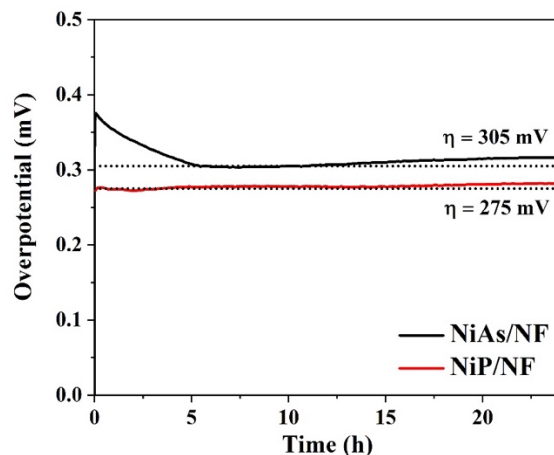


Figure 5.11. 24 h CP measurement of NiAs/NF and NiP/NF at 10 mA cm^{-2} .

The FE of the amorphous materials deposited on NF was obtained to determine their efficiency to transfer electrons for the OER provided by an external circuit (see Experimental Section 7.3.10).^[52] The FE of the OER in 1 M KOH was measured in a two-electrode configuration where NiAs/NF and NiP/NF was used as anode and Pt as cathode in a closed one-compartment electrochemical cell (NiAs/NF || Pt and NiP/NF || Pt), respectively. A constant current of 50 mA cm^{-2} was applied on electrodes of $1 \times 1 \text{ cm}^2$ area for 600 s and the amount of O_2 and H_2 were determined by GC and compared with the theoretical value of produced gas. The experimental values agreed well with the theoretical values and an efficiency of 96 % (NiAs) and 98 % (NiP) could be determined for both materials, which indicated a very high efficiency (see Table A.3.5). It should also be noted that in practice a FE of 100 % cannot be achieved due to thermodynamic and kinetic barriers during the reaction.^[52]

Throughout the electrochemical OER measurements, the amorphous NiP showed superior activity in comparison to the crystalline phase. Activity differences arise from the surface and electronic characteristics of the materials. The ECSA is an important comparison parameter because it reflects the surface area available for catalysis.^[67] The ECSA is directly proportional to the C_{dl} . The C_{dl} was determined by performing continuous CV experiments at different scan rates in a potential range in which no Faradaic processes took place (see Experimental Section 7.3.8).^[68,467] From this, the difference in cathodic and anodic current was plotted versus the scan rate, from which the value of C_{dl} was obtained (see Figure A.3.33). The C_{dl} of bare NF was $0.453 \pm 0.002 \text{ mF cm}^{-2}$. After deposition, the C_{dl} increased to $0.625 \pm 0.001 \text{ mF cm}^{-2}$ and $1.285 \pm 0.002 \text{ mF cm}^{-2}$ for NiAs and NiP, respectively (see Table A.3.6). The results agreed with the observed order of activity. The higher value for the C_{dl} of NiP compared to NiAs led to the conclusion that the surface of this material had a higher density of surface defects and coordinative unsaturated surface metal sites available for reaction.^[250] A similar trend was found when the C_{dl} was calculated on the films deposited on FTO and their comparison to the bare substrate. Experimental data are shown on the Appendix (see Table A.3.7 and Figure A.3.34).

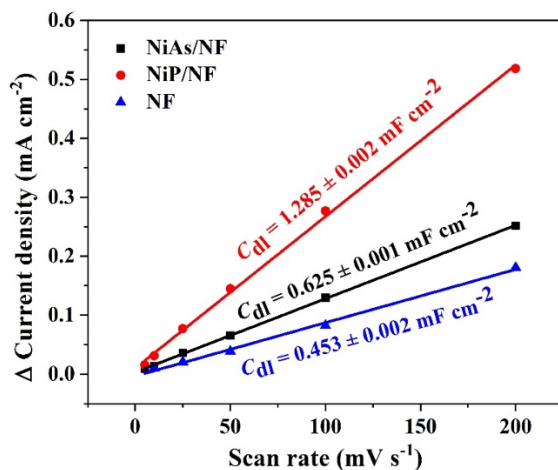


Figure 5.12. Linear fit derived CV measurements (see Figure A.3.33) to obtain C_{dl} of the materials deposited on NF.

The enhanced activity of amorphous materials in comparison to their crystalline counterparts has been previously discussed while studying the differences between amorphous and crystalline CoP (see Section 3.2.2). Amorphous materials, such as the prepared NiAs and NiP, have also a higher structural flexibility, which allows self-regulation, adaptation and reconstruction of active sites during the electrochemical conditions.^[301] The ECSA normalized LSV curves also confirmed the higher electrocatalytic activity of NiP (see Figure A.3.35). Since both materials showed an amorphous morphology, the differences in activity should be related to characteristics of the generated phases during the OER. Reports in the literature and in this investigation (see Sections 3.2.3 and 4.2.3), have shown that during OER under alkaline conditions, TM-Ps and TM-As suffer the loss of the pnictogen element into the solution.^[26,163] Therefore, it is important to understand, through *post-operando* characterization, if the leaving pnictogen element has a directing effect in the materials transformation that could contribute to the observed higher activity of NiP in comparison to NiAs.

5.2.3. *Post-operando* OER characterization of amorphous NiP and NiAs

Post-operando OER PXRD of the film deposited on FTO after OER was done to determine the emergence of any new crystalline phase during catalysis. The PXRD pattern of the film after catalysis showed reflexes at 26.5, 33.9, 27.9, 51.8, 54.8, 61.9, 65.9, and 78.7° that were related to the (110), (101), (200), (211), (220), (310), (301), (321) crystalline planes of FTO (cassiterite, SnO₂, JCPDS 41-1445), in a similar way as in the as-prepared materials (see Figure A.3.36).^[382] Consequently, this was an indication that no crystalline phase was formed after catalysis. The obtained PXRD pattern of the sample after OER was complemented with other characterization and spectroscopic techniques.

To gain more insight into the transformation of the material, SEM was done. SEM images after 24 h OER CP showed that the films were composed of agglomerated particles. On some areas, the conductive substrate was exposed. This could be related to the possible

loss of film material into the electrolyte due to the exposure of the FTO substrate (see Figure A.3.37a, A.3.38a).^[383] This was also observed before during the OER electrocatalysis with FeAs (see Section 4.2.3). The high magnification SEM images showed that both NiAs and NiP particles had a similar morphology as before catalysis. Elemental mapping revealed a homogenous distribution of Ni and O on the remaining films, and a small presence of the pnictogen element (see Figures 5.13, A.3.39). The examination of the composition by EDX determined that the P and As were lost into the solution. A complete dissolution of P and As resulted in Ni:P and Ni:As ratios of 1:0.009 and 1:0.024, respectively (see Figures A.3.40, A.3.41). The post catalytic characterization by SEM-EDX on the samples deposited on NF after analogous electrochemical OER experiments revealed a similar transformation of the materials (see Figures A.3.42, A.3.43), uniform distribution of Ni and O in the films (see Figures A.3.44, A.3.45) and loss of the pnictogen element into the solution as evidenced by the ratios of Ni:P (1:0.001) and Ni:As (1:0.018) determined by EDX (see Figures A.3.46, A.3.47).

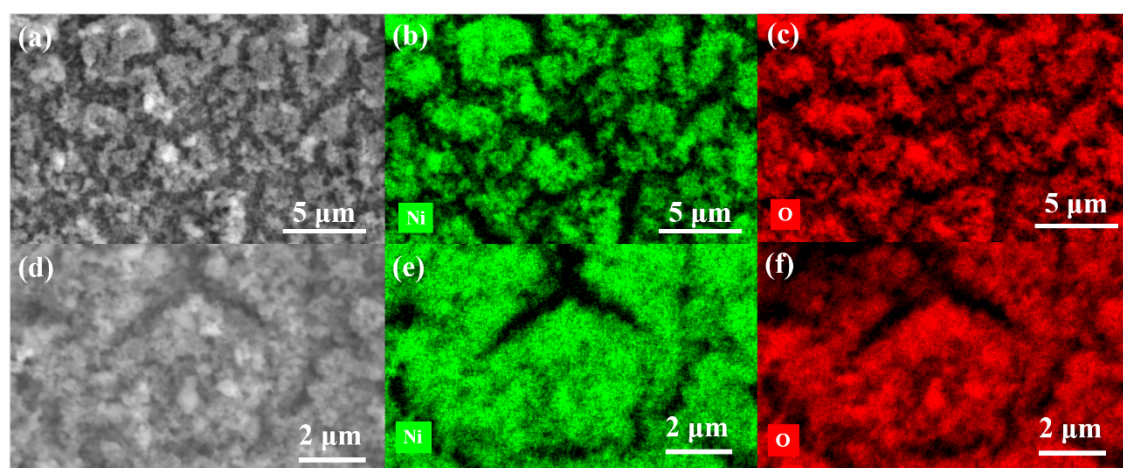


Figure 5.13. (a) SEM of NiP/FTO after OER and elemental mapping of (b) Ni (green), (c) O (red). (d) SEM of NiAs/FTO after OER and elemental mapping of (e) Ni (green), (f) O (red). The mapping shows the homogeneous distribution of the elements on the surface of the material. Elemental mapping of P and As is shown in Figure A.3.39.

The preferential and gradual loss of the pnictogens and formation of oxidized species is a common phenomenon and is essential to preserve the electrochemical performance of the materials.^[202,304,427] The loss of the non-metal in solution is a common phenomenon and has been observed previously for TM chalcogenides, phosphides and arsenides (see Section 1.5.3),^[258,304] and in this investigation (see Section 3.2.3 and 4.2.3). Therefore, the loss of As and P from NiAs and NiP was expected during OER. The loss of pnictogen was quantitatively determined by measuring the concentration of these elements in the electrolyte by ICP-AES after the long-term experiment (see Table A.3.8). The results determined a loss of the pnictogen, which was in accordance with the composition change obtained by EDX. The results showed a loss of the pnictogen of 45 % and 86 % for NiAs and NiP, respectively, due to the oxidation of the materials. Previous observations have demonstrated that P and As were oxidized to $[\text{PO}_4]^{3-}$ and $[\text{AsO}_4]^{3-}$. These anions are

highly soluble on the alkaline electrolyte. Therefore, they dissolved and favored the formation of a Ni (oxy)hydroxide layer.^[202,304,384]

Insights of the post-catalytic OER structural transformation were also obtained by TEM. The films after the long-term 24 h CP OER experiments were scratched and tested by TEM. The HR-TEM of NiAs after OER revealed the presence of crystalline nanodomains of different interlayer distance (see Figure 5.14a). The presence of these crystalline nanodomains explained the lack of diffraction peaks on the *post-operando* PXRD pattern. HR-TEM of the post-OER NiAs catalyst showed crystalline fringes with interlayer distances of 0.209 nm and 0.237 nm, which correspond to the (105) and (102) planes of γ -NiOOH (JCPDS 6-75).^[468] The SAED pattern (see Figure 5.14a, inset) showed several broad diffraction rings which correspond to the (003), (102), (105), (110), and (205) planes of the same phase determined by TEM.^[468] The TEM-EDX confirmed the oxidation of the NiAs during catalysis. The ratios of Ni:As and Ni:O were 1:0.018 and 1:1.37, respectively (see Figure A.3.48). These results confirmed an almost complete transformation of the NiAs to an oxidized phase, as determined by the results from SEM-EDX and ICP-AES.

Similarly, HR-TEM of the post-OER NiP was done to determine the outcome of the transformation. The HR-TEM of NiP after OER revealed the presence of crystalline nanodomains as observed on the post-OER NiAs sample. The crystalline nanodomains showed an interlayer distance of 0.209 nm, which corresponded to the (105) plane of γ -NiOOH (JCPDS 6-75) (see Figure 5.14b).^[468] To gain more insight into the crystallinity, the post-OER NiP SAED was obtained (see Figure 5.14b, inset). Two broad diffraction rings appeared and could be further assigned to the crystalline phase determined by the interlayer distances. The two rings were assigned to the (105) and (102) planes of γ -NiOOH (JCPDS 6-75).^[468] The TEM-EDX results confirmed the oxidation of NiP and the loss of phosphorus into solution (see Figure A.3.49), with ratios of Ni:P and Ni:O of 1:0.014 and 1:1.31, respectively.

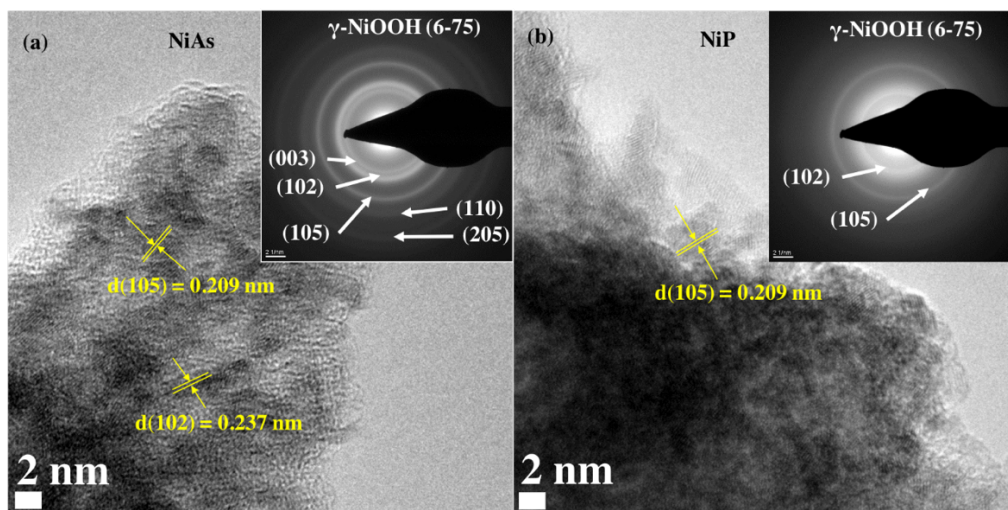


Figure 5.14. HR-TEM images of (a) NiAs/FTO after OER (SAED, inset) and (b) NiP/FTO after OER (SAED, inset). The diffraction rings correspond to the γ -NiOOH phase (JCPDS 6-75).

Vibrational spectroscopies, such as IR and Raman, were employed in order to get further information about the local structure. The FT-IR spectrum after OER (see Figure A.3.50) showed a broad absorption band centered at 3230 cm^{-1} that was assigned to stretching vibrations of water molecules that are adsorbed or in the interlayers.^[469,470] The bands at 1642 and 1458 cm^{-1} for NiAs/FTO after OER and 1646 and 1461 cm^{-1} for NiP/FTO after OER were related to bending vibration of H_2O and structural OH groups.^[469,470] The band at 1361 cm^{-1} could be attributed to C-O stretching vibrations of $[\text{CO}_3]^{2-}$ anions, which apparently appeared because of the KOH electrolyte that consumes of CO_2 from ambient air in the form of dissolved carbonate.^[469,470] Such intercalation is possible due to the layered structure of $\gamma\text{-NiOOH}$ (see following discussion, Figure 5.19).^[471]

Raman spectroscopy was done to uncover the structure of the active electrocatalysts. *Quasi in situ* and *ex-situ* experiments were performed, as Ni hydroxides and (oxy)hydroxides are very sensitive towards vibrational spectroscopy.^[472] The as-prepared powders and films on FTO did not show any distinguishable feature (see Figure A.3.9). *Quasi in situ* (resonance) Raman spectra were obtained after the freeze quenching of samples held at constant potential for 24 h (see Experimental Section 7.2.12). The obtained spectra revealed the presence of two peaks at 480 and 560 cm^{-1} on NiAs after OER and 484 and 558 cm^{-1} on NiP after OER (see Figure 5.15). The first band was clearly assigned to the depolarized E_g mode (bending, $\delta(\text{Ni}^{\text{III}}\text{-O})$), while the second band was assigned to the polarized A_{1g} mode (stretching, $\nu(\text{Ni}^{\text{III}}\text{-O})$) of $\gamma\text{-NiOOH}$.^[473,474] Similar features were observed in the *ex-situ* spectra (see Figure 5.15). These results confirmed that $\gamma\text{-NiOOH}$ is the active structure for OER, as determined by TEM and SAED. In addition, a broad band between 850 and 1200 cm^{-1} also appeared on the spectra obtained through the *quasi in situ* measurements of both NiAs and NiP that has been previously attributed to the $\nu(\text{O-O})$ stretching vibration of an active oxygen species ($\text{Ni}^{\text{III}}\text{-OO}^-$) in the (oxy)hydroxide structure (see Figure 5.15).^[473,475-477]

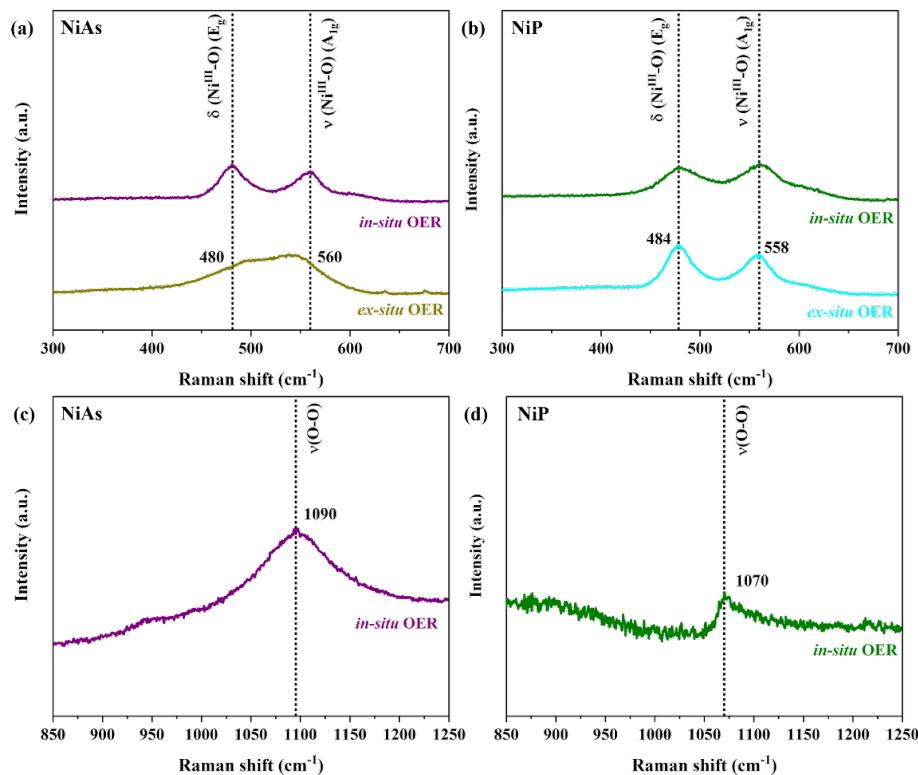


Figure 5.15. *Quasi in situ* and *ex-situ* (resonance) Raman spectroscopy of (a) NiAs and (b) NiP on FTO collected after OER CP, 24 h, 10 mA cm⁻² in alkaline electrolyte. The stretching A_{1g} and bending E_g vibrational modes of γ -NiOOH are observed.^[473,474] The high wavenumber region (800-1300 cm⁻¹) of (c) NiAs and (d) NiP showed a signal suggesting Ni sites evolve O₂ through an active oxygen species (Ni-O-O⁻).^[473,475-477]

Further information about the transformation was carried out by XPS investigations (see Experimental Section 7.2.10). The XPS results showed that the transformation of the NiAs and NiP into a γ -NiOOH phase after the OER produced a significant change in the electronic structure. Figure 5.16 shows the Ni 2p, As 3d and O 1s XPS spectra of the materials after OER, in comparison to the XPS spectra of powders and as deposited samples. The Ni 2p deconvoluted spectrum showed peaks at high binding energy that were associated to Ni in higher oxidation state (see Figure A.3.51a). Two major broad peaks (2p_{3/2}, 854.3 eV and 2p_{1/2} 872.0 eV) were associated to Ni^{II}, as well as various satellite peaks, which could be associated to oxidized Ni species in Ni^{II}(OH)₂ (855.8 eV) and Ni^{III}OOH (860.5 eV).^[26,478,479] However, a low binding energy peak associated to Ni^{δ+} was present (2p_{3/2} 852.8 eV and 2p_{1/2} 871.3 eV), which indicated that some NiAs remained after catalysis.^[26] The As 3d spectrum showed the complete oxidation of the surface As due to the loss of the peak associated to reduced As^δ. The high binding energy peak at 44.7 eV (deconvoluted in 3d_{5/2}, 44.5 eV and 3d_{3/2} 45.2 eV) corresponded to As^{III} (see Figure A.3.51b). The ICP-AES, EDX and TEM have determined the complete loss of surface As into the electrolyte solution and the transformation to γ -NiOOH phase under the OER conditions. Therefore, the presence of As in the surface could be assigned to adsorbed [AsO₄]³⁻ species from the electrolyte solution.^[367] Similar results have been also observed during the post-OER XPS characterization of FeAs (see Section 4.2.3). Finally, the O 1s core-level spectrum shows that the main peak (530.5 eV) which was

deconvoluted into two peaks at 530.4 eV (O1) and 531.1 eV (O2). The low binding energy peak was associated to Ni-O on the highly Ni oxidized species generated during the OER ($\text{Ni}^{\text{II}}(\text{OH})_2/\text{Ni}^{\text{III}}\text{OOH}$) and adsorbed water ($\text{Ni}-\text{OH}_2$).^[161,479] A minor contribution of the $\text{As}^{\text{IV}}-\text{O}$ from the AsO_4^{3-} species could also be possible (530.3 eV).^[367]

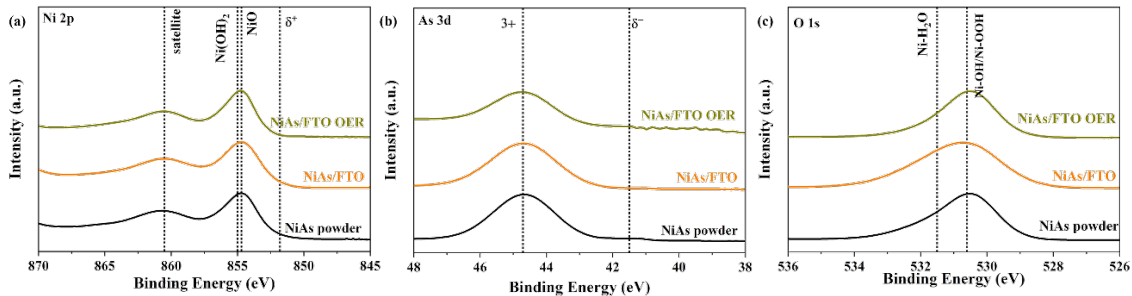


Figure 5.16. XPS spectra of the films after OER compared to the *as-prepared* powders and films by EPD on FTO, and films after OER for NiAs: (a) Ni 2p, (b) As 3d and (c) O 1s.

The electronic transformations on the surface of NiP were also investigated after OER by XPS (Figure 5.17). The Ni 2p deconvoluted spectrum showed the small intensity peaks associated to $\text{Ni}^{\delta+}$ from NiP at low binding energy ($2p_{3/2}$ 853.7 eV and $2p_{1/2}$ 871.9 eV). Similarly to the NiAs and reported Ni-P-based materials,^[26] the after OER spectrum revealed the appearance of large and broad peaks at higher binding energies, which were associated to Ni^{II} ($2p_{3/2}$ 854.6 eV and $2p_{1/2}$ 872.2 eV), $\text{Ni}^{\text{II}}(\text{OH})_2$ (855.9 eV) and $\text{Ni}^{\text{III}}\text{OOH}$ (860.7 eV) and satellite peaks (865.6 eV, 873.6 eV and 879.0 eV) (see Figure A.3.51d). The deconvoluted P 2p spectrum showed the complete oxidation of the surface phosphorus to higher oxidation states (see Figure A.3.51e). The spectrum showed a low binding energy peak at 132.0 eV (deconvoluted into $2p_{3/2}$ 131.7 eV and $2p_{1/2}$ 132.7 eV) which was associated to phosphite (P^{III}).^[162] The high binding energy peak (137.0 eV, deconvoluted into $2p_{3/2}$ 136.8 eV and $2p_{1/2}$ 137.9 eV) showed the highest intensity and was related to oxidized P^{V} from $[\text{PO}_4]^{3-}$.^[480] This observations agreed with the SEM, TEM, and ICP results, which demonstrated the oxidation and loss of phosphorus into the electrolyte solution and the formation of the γ -NiOOH phase. Finally, the O 1s spectrum after CP OER of NiP showed only one peak at 530.7 eV with a shoulder at higher binding energy (531.8 eV). Detailed information was obtained from the deconvoluted spectra, which resulted into three peaks (O1 and O2) (see Figure A.3.51f). Similar assignments were done as in the post-OER NiAs O 1s spectrum. The first peak (O1) was correlated to the $\text{Ni}^{\text{II/III}}-\text{O}$ bond (530.4 eV), from the electrochemically generated (oxy)hydroxide layer that contains $\text{Ni}^{\text{II}}(\text{OH})_2$ and $\text{Ni}^{\text{III}}\text{OOH}$.^[306] The second peak (O2) at 531.5 eV could be related to $\text{Ni}-\text{OH}_2$ bond.^[161,479]

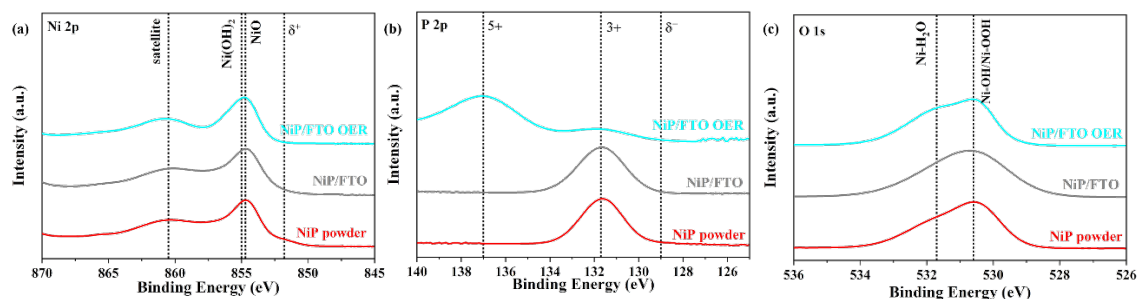


Figure 5.17. XPS spectra of the films after OER compared to the *as-prepared* powders and films by EPD on FTO, and films after OER for NiP: (a) Ni 2p, (b) P 2p and (c) O 1s.

The changes in the XPS signals of NiAs and NiP indicated that the valence of the Ni shifted towards Ni^{II}/Ni^{III} after OER, as reported in the literature for Ni-based materials under similar conditions.^[59] The electrochemical experiments supported the oxidation of Ni to higher oxidation states. The redox wave observed during the LSV OER of both materials is attributed to the oxidation to Ni^{II/III} (see Figure A.3.27 and Figure A.3.28). The oxidation of the metal was accompanied by the loss of the pnictogen element into the solution and a drastic structural change, due to the generation of a highly oxidized γ -NiOOH, as described before by Raman spectroscopy, FT-IR and ICP-AES characterization of the materials after catalysis.

Ni-based electrocatalysts generally transform into highly OER active Ni^{II}(OH)₂/Ni^{III}OOH phase during catalysis.^[59] It is important to consider that the γ -NiOOH phase could have been generated by electrochemical redox process on other Ni hydroxides and (oxy)hydroxides phases generated during the oxidation of NiAs and NiP. It is known from the literature that Ni hydroxides and (oxy)hydroxides, can be produced from similar phases. In 1966, Bode described that α -Ni(OH)₂, β -Ni(OH)₂, β -NiOOH, and γ -NiOOH can be transformed into each other by charge and discharge processes or aging (see Figure 5.18a).^[126,481] The reversible oxidation of β -Ni^{II}(OH)₂ can produce the β -Ni^{III}OOH phase. The γ -Ni^{III}OOH can be generated by the overcharge of the β -Ni^{III}OOH or by the oxidation of α -Ni^{II}(OH)₂. The α -Ni^{II}(OH)₂ is also unstable in strongly alkaline electrolyte (6 M KOH), and if a potential is applied, it can form crystalline β -Ni^{II}(OH)₂ under prolonged aging times.^[482]

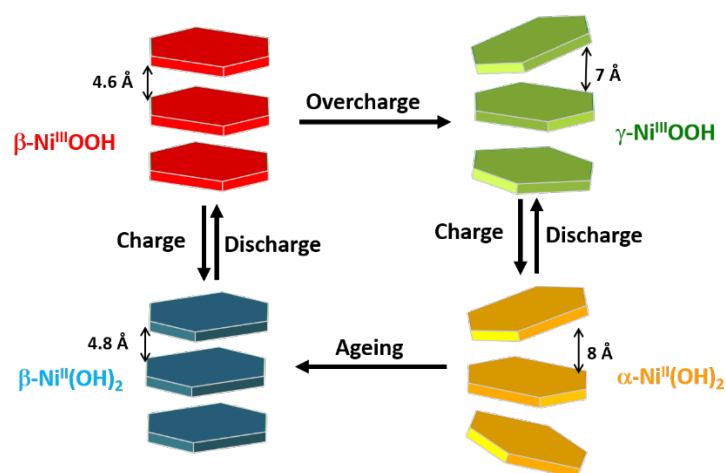


Figure 5.18. Diagram of the transformation between the Ni hydroxides and (oxy)hydroxide phases.^[126,481]

The γ -NiOOH structure is composed of unordered two-dimensional layers of NiO₆ octahedra that interact via weak non-covalent bonds to form layered three-dimensional structures.^[483,484] The two-dimensional layers lack a long-range order, giving rise to an amorphous nature. The structural properties of this phase have been described in the literature during the study of Ni-based materials for OER electrocatalysis. Nocera and co-workers studied the transformation of Ni-Bi (borate) films during OER and determined the structure of the generated γ -NiOOH phase.^[485] The γ -NiOOH phase is composed of bis-oxo/hydroxo-bridged Ni centers organized into sheets of edge-sharing NiO₆ octahedra.^[485–487] The structure is analogous to the amorphous CoO_x(OH)_y obtained during the OER under alkaline conditions of amorphous and crystalline CoP (see Section 3.2.3). The γ -NiOOH possess a 7 Å interlayer distance.^[483,484] This distance is specially suitable for intercalation of water or foreign ions dissolved in the electrolyte (K⁺, OH⁻ or CO₃²⁻) (see Figure 5.19).^[488] The large interlayer distance especially favors the presence of OH⁻ anions, which are in contact with the Ni^{II/III} active sites for OER.^[488–491] This is also consistent with the previous study on the role of interlayer anions in NiFe- or Ni-based LDHs where the highest catalytic OER activity can be achieved when hydroxide/carbonates species are present in the interlayers of LDH.^[489,491]

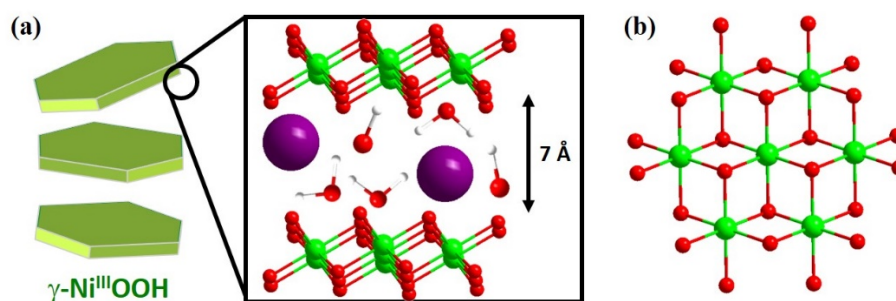


Figure 5.19. (a) Schematic representation of the structure of two exposed layers of NiO_x(OH)_y phase exposed to the electrolyte that contains H₂O, OH⁻ and K⁺. Green, red, white, and purple spheres represent Co, O, H and K atoms. The arrangement of the interlayer species is only illustrative and strongly simplified. (b) Fragment of the general structure composed of NiO₆ octahedra.^[492]

The OER mechanism of Ni-based electrocatalysts was recently studied by Nocera and co-workers and proposed the formation of a catalytically active species via an oxidative deprotonation of a Ni (oxy)hydroxide structure in which Ni^{III} ions were the active centers.^[142] This mechanism is not particular for Ni and has been reported for Co, Fe- and Mn-based catalysts (see Section 1.4.2).^[115,493,494] The mechanism for the OER was comparable to that of the CoO_x(OH)_y generated during OER on the amorphous and crystalline CoP (see Section 3.2.3).

The electronic structure of Ni^{III} in γ -NiOOH has been studied and is characterized by a Jahn-Teller distortion.^[485] The distortion on the low-spin d⁷ Ni^{III} centers gives rise to an elongation on the z axis and an equatorial contraction in the NiO₆ octahedra.^[485] The distortion gives rise to a stabilization of the orbitals in the octahedral configuration. The orbitals containing a z component (d_{z^2} , d_{xz} , d_{yz}) are stabilized due to the Jahn-Teller distortion (see Figure 5.20), while the orbitals without a z component are destabilized ($d_{x^2-y^2}$, d_{xy}). The Jahn-Teller distortion also generated changes in the electronic configuration of Ni. The final electronic configuration possess an unpaired electron, which can enhance the electron transfer between OH⁻ and the electrode surface and promote water oxidation. The elongation on the z-axis also weakens the Ni^{III}-O covalent bond along this axis, facilitating the absorption of oxygen intermediates and the oxidation of the Ni^{III}. Therefore, the γ -NiOOH phase is the actual OER electrocatalyst due to presence of high valent metallic species (Ni^{II}, Ni^{III}) which act as active sites for OER.^[203,304]

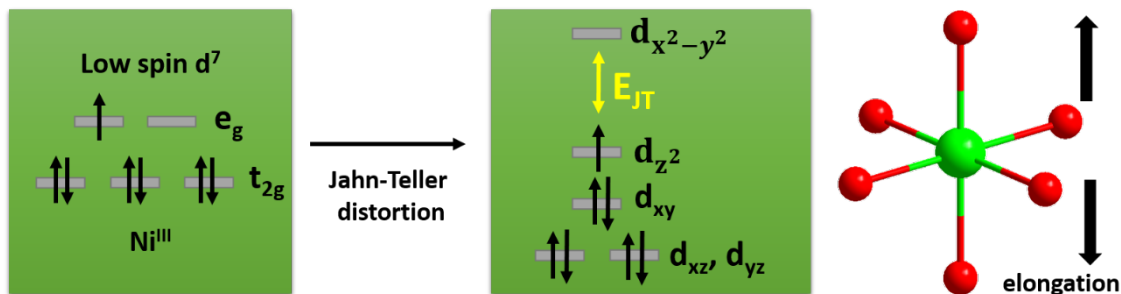


Figure 5.20. Jahn-Teller distortion on the (b) octahedral coordination modes of low spin Ni^{III} (d⁷) in the structure of γ -NiOOH. The stabilization can be observed by the decrease in energy of the filled orbitals. The NiO₆ octahedra suffer and elongation along the z-axis.

The activity of an electrocatalyst has been also related to morphological characteristics (see Section 1.5.2).^[124,125] Amorphous NiAs and NiP transformed in to similar γ -NiOOH phases, therefore their activities should be the same if the substrate and mass loading were equal. However, the electrocatalytic properties of the evolved phases were not equal, as demonstrated by the difference in the OER overpotentials (267 vs. 315 mV at 10 mA cm⁻² when deposited on NF). This divergence could be related to the surface characteristics of the electrochemically generated species. Therefore, C_{dl} measurements were conducted to determine the increase of active sites (ECSA) on films deposited on NF and FTO and compared to the bare substrate and the films before catalysis (see

Figures A.3.52, A.3.53). An increase in the C_{dl} in comparison to the as-prepared materials was observed, due to the transformation to γ -NiOOH phase during the water oxidation. The generated phase had a high interlayer distance (7 Å) which favored the exposure to the electrolyte and resulted in a larger number of exposed active sites, and consequently higher C_{dl} .^[250,488–491] The increase in the C_{dl} after catalysis and its relation to the enhancement of the electrocatalytic activity has been observed previously during the study of the differences between amorphous and crystalline CoP (see Section 3.2.2) and the transformation of FeAs to 2-line ferrihydrite (see Section 4.2.2) in the present investigation. Additionally, it has been reported previously in the literature for Ni-based materials for OER under alkaline conditions. For example, a core-shell NiOOH@Ni₂P structure formation during electrochemical OER led to an increase in the C_{dl} and ECSA after catalysis in comparison to the pristine Ni₂P catalyst.^[111,250,495]

The pnictogen had a directing effect on the extension of the oxidized phase since the extension of the transformation is related to the leaching ability (solubility) of the formed anions in the alkaline solution and the applied potential.^[202,304] The preferential and gradual loss of the pnictogen and formation of oxidized species has been observed before in TM pnictides and is essential to preserve the electrochemical performance of the materials. The dissolution process of the pnictogen started at the surface of the catalyst and continued inside, which led to a depletion of the pnictogen and an enrichment of Ni to form the γ -NiOOH phase. As mentioned above, the selective dissolution of the anions led to a surface area enhancement (and higher C_{dl}) by the creation of a porous structure on the film, which is fundamental to enhance the electrochemical performance.^[26,202,250,427] The formation of γ -NiOOH was reflected in the increase in C_{dl} , which depended on the identity of the material. The C_{dl} increase (+71 %) of NiP/NF after long-term OER was higher in comparison to NiAs/NF (+22 %) (see Table A.3.9). An analogous increase in the C_{dl} was observed when the films over FTO after OER were studied (see Table A.3.9). Additionally, these results agreed with the activity trend and C_{dl} of the pristine materials (see Figure 5.12). The transformation of the materials was directly related to the loss of the pnictogen in the electrolyte solution. A higher concentration of phosphorus (as [PO₄]³⁻, 86 %) in comparison to arsenic (as [AsO₄]³⁻, 45 %) was related to the major reconstruction to γ -NiOOH during catalysis in the case of NiP. The C_{dl} increase of NiP after OER (71 % on NF, 116 % on FTO) was superior to the one from NiAs (22 % on NF, 65 % on FTO), which proved that NiP underwent a larger transformation towards γ -NiOOH, which explained its higher electrocatalytic activity.^[202,496]

5.3. Conclusion

A salt-metathesis reaction of robust NaECO (E = As, P) with the NiBr₂(thf)_{1.5} complex at room temperature was used to access amorphous NiAs and NiP in a 1:1 stoichiometry. The prepared materials were electrophoretically deposited on FTO and NF to prepare films and examined for OER electrocatalysis in strongly oxidizing alkaline media (1 M KOH). The prepared amorphous NiP showed outstanding catalytic activity in

comparison to the amorphous NiAs. The NiP/NF required an overpotential of 267 mV to achieve a catalytic current density of 10 mA cm^{-2} , which was less in comparison to the NiAs/NF (315 mV, see Figure 5.21). Further experimental comparison with reports in the literature found a comparable activity to reported Ni-based materials and TM-Ps and TM-As (see Table A.3.3). Additionally, a small Tafel slope (68 mV dec^{-1}) and low R_{ct} (10.37Ω) also contributed to the high OER activity. A FE of $> 96 \%$ for the OER also proved that both materials were very efficient water oxidation electrocatalyst. The long-term CP measurement of NiAs and NiP achieved high overpotential (305 mV and 275 mV) stability over 24 h. Further measurements on inert substrates such as FTO proved that the achieved activity trend was independent of the substrate.

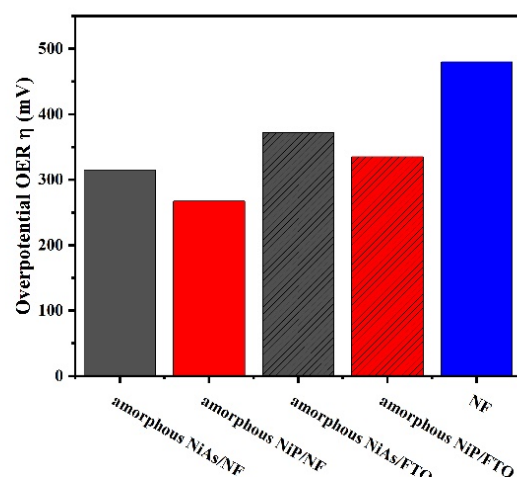


Figure 5.21. Comparison of the overpotentials required for the (a) OER electrocatalysis to achieve a current density of 10 mA cm^{-2} in a 1 M KOH.

The *post-operando* characterization results demonstrated that the pnictogen element initially contained in the structure leached after 24 h of electrocatalysis and was responsible for the generation of γ -NiOOH phase, which was the actual OER electrocatalyst, as observed in other Ni- and TM-based pnictides.^[202,496] The higher activity and stability of NiP was assigned to the easier loss of the pnictogen in NiP (86 %) in comparison to NiAs (45 %) after the long-term experiments (24 h). A higher structural transformation to the γ -NiOOH phase was also found in NiP, reflected in the higher increase of ECSA. The identity of this phase could be demonstrated *ex-situ* characterizations, as well as quasi *in situ* Raman spectroscopy. The γ -NiOOH phase was composed of bis-oxo/ hydroxo-bridged Ni centers organized into sheets of edge-sharing NiO₆ octahedra and interlayer distance of 7 Å.^[483–487] The large interlayer distance demonstrated to be a crucial factor in the OER catalytic activity, as it favored the contact between the OH⁻ anions, and the Ni^{III} active sites for OER.^[488–491] The Ni^{III} (d^7 , the $t_{2g}^6 e_g^1$) suffered a Jahn-Teller distortion that gave rise an elongation on the z axis and equatorial contraction in the NiO₆ octahedra.^[485] The elongation weakened the Ni^{III}–O covalent bond along this axis, facilitating the absorption of oxygen intermediates and the oxidation of the Ni^{III}. The similarity of the *post-operando* characterization results of NiAs and NiP concluded that the evolution must have taken place via comparable mechanisms.

6. Summary

The general aim of this Ph. D. thesis was to develop a molecular route to TM pnictides for efficient OER, HER, and OWS electrocatalysis and to study the influence of the morphology, conductivity, and composition. A common molecular synthetic pathway towards the target nanoscaled TM-Ps and TM-As materials was achieved, based on the decomposition of SSP under a scalable, green and low-temperature scheme. Overall, the SSP approach permitted preparation of amorphous and crystalline materials with high active surface area, high electrical conductivity, and defined stoichiometry.

Section 3 describes the synthesis of amorphous and crystalline CoP by the decomposition through the hot-injection and pyrolysis, respectively, of a [2Co-4P] β -Diketiminato molecular precursor (see Figure 6.1). The materials were utilized as electro(pre)catalysts for the reaction of OER, HER and OWS in alkaline media.

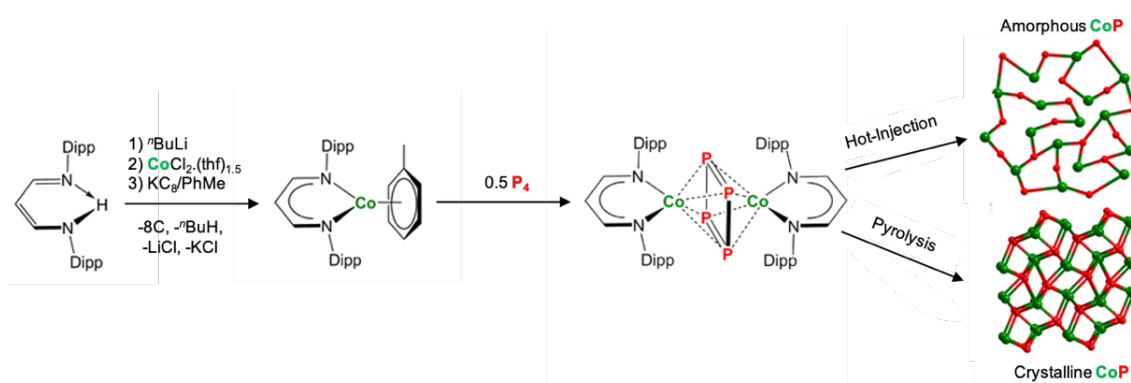


Figure 6.1. Preparation of a [2Co-4P] β -Diketiminato molecular complex and then used as amorphous and crystalline CoP as effective OER and HER electrocatalysts.

The amorphous CoP showed higher OER, HER and bifunctional activity and stability in comparison with the crystalline CoP, when deposited on FTO and NF (see Table 6.1). The measurements carried out here showed that the amorphous CoP activity was comparable to benchmark IrO_2 and other Co-P-based and other TM-Ps systems.

Table 6.1. Overpotentials for OER, HER, and OWS of amorphous and crystalline CoP deposited on NF and FTO.

Material	$\eta_{\text{OER}} @$ 10 mA cm ⁻² (mV)	$\eta_{\text{OER}} @$ 10 mA cm ⁻² 24 h (mV)	$\eta_{\text{HER}} @$ -10 mA cm ⁻² (mV)	$\eta_{\text{HER}} @$ -10 mA cm ⁻² 24 h (mV)	$\eta_{\text{OWS}} @$ 10 mA cm ⁻²
amorphous CoP/NF	284	280	143	170	430
crystalline CoP/NF	305	300	261	300	--
amorphous CoP/FTO	360	340	228	180	600
crystalline CoP/FTO	414	420	377	410	--

Electrochemical corrosion during OER led to the oxidation and dissolution of phosphorus and oxidation of the materials to amorphous $\text{Co}^{\text{III}}\text{O}_x(\text{OH})_y$. This phase showed a high ECSA and contained active Co^{IV} , which are capable of oxidizing water and generating O_2 . The combination of this atoms with Co^{III} in Jahn-Teller distorted CoO_6 octahedra were fundamental for the OER. The elongation and weakening of the $\text{Co}^{\text{III}}\text{-O}$ covalent bond facilitated the absorption of oxygen intermediates and promoted the OER. The similarity of the *post-operando* characterization results in both materials concluded a common mechanism for OER based on a nucleophilic attack of hydroxide on a metal center or direct intramolecular coupling for the formation of the O-O bond. On the other hand, during HER, the initial contact with the strongly alkaline solution led to the oxidation of the surface and transformation to Co-enriched $\text{CoO}_x(\text{OH})_y$. The continuous application of a negative potential prompted the *in situ* reduction of $\text{Co}^{\text{II/III}}$ species to less positively charged Co^0 , which was the active species for HER.

The higher electrocatalytic activity and stability of amorphous CoP in comparison to crystalline CoP was attributed to the higher dissolution rate of phosphorus and larger transformation towards $\text{CoO}_x(\text{OH})_y$ with higher ECSA (0.30 vs. 0.11 cm^2). This difference indicated that the post-OER amorphous phase had a surface with increased active sites and larger porosity. The remaining non-oxidized core with metallic properties provided higher electroconductivity and acted as a highly electrically conductive “bridge” between the active $\text{CoO}_x(\text{OH})_y$ layer on the surface of the catalyst and the electrode substrate. In the crystalline CoP, the benefit in the activity of the core-shell structure was not sufficient to overcome the low oxidation and extension of the $\text{CoO}_x(\text{OH})_y$ layer. The investigations carried out showed that the combination of an initial amorphous structure, the high phosphorus loss and surface oxidation, and the remaining conductive core rendered a highly active catalyst species with high activity and stability.

Section 4 explored FeAs as efficient OER electrocatalyst due to its unique superconductivity properties and their influence on catalytic processes. Nanostructured FeAs was prepared through the hot-injection of a novel β -Diketiminato [2Fe-2As] complex (see Figure 6.2). This synthesis represented the first ever molecular preparation approach to obtain nanocrystalline FeAs.

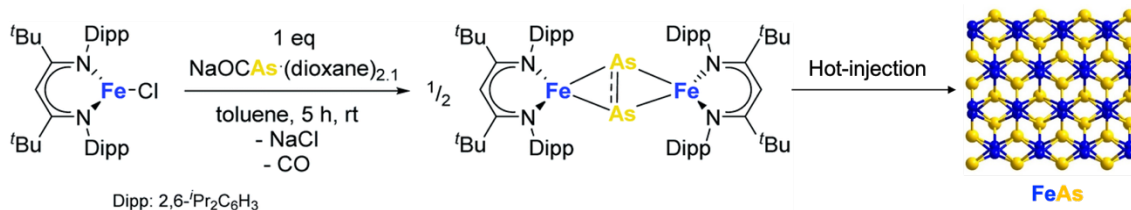


Figure 6.2. Molecularly-derived nanoscaled crystalline FeAs transformed was prepared through the hot-injection of a β -Diketiminato [2Fe-2As] complex.

The FeAs nanoparticles were utilized as electro(pre)catalysts for the OER under alkaline media. The superior activity and stability of FeAs was obtained in comparison to $\text{Fe}(\text{OH})_3$, FeOOH , Fe_2O_3 , and Fe-based electrocatalysts reported in the literature (see

Table 6.2). Additionally, a small Tafel slope (32 mV dec⁻¹) and low charge transfer resistance contributed to the high OER activity. A FE of > 95 % for the OER also proved that FeAs is not only active, but also a very efficient water oxidation electrocatalyst.

Table 6.2. Overpotentials for OER of FeAs, Fe(OH)₃, FeOOH, and Fe₂O₃ deposited on NF and FTO.

Material	η_{OER} @ 10 mA cm ⁻² (mV)	η_{OER} @ 10 mA cm ⁻² 10 h (mV)
FeAs/NF	252	265
Fe(OH) ₃ /NF	275	296
FeOOH/NF	283	300
Fe ₂ O ₃ /NF	312	320
FeAs/FTO	400	380
Fe(OH) ₃ /FTO	578	580
FeOOH/FTO	610	610
Fe ₂ O ₃ /FTO	640	650

The analysis of the composition, morphology, electronic and chemical structure of FeAs by *ex-situ* characterizations and quasi *in situ* XAS, revealed the total electroconversion of the FeAs to a nanocrystalline Fe (oxy)hydroxide phase, the 2-line ferrihydrite, due to the complete oxidation and dissolution of As after 2 h of electrocatalysis. However, the dissolved As from the FeAs electrode could be successfully recovered at the cathode making the whole process sustainable and energy-efficient.

The OER activity was related to the enhanced ECSA of the highly porous 2-line ferrihydrite phase. Surface octahedral and tetrahedral coordinated Fe^{III} atoms suffered a Jahn-Teller distortion, experimentally observed by EXAFS, which weakened the Fe^{III}-O bonds, facilitated the absorption of oxygen intermediates, and promoted the OER electrocatalytic activity. Moreover, the semiconductor nature of this phase enabled faster electron transport away from the catalyst surface to provide new active sites and contributed to the low charge transfer resistance. The resulting conductivity also increased the OER activity in comparison to the 10-100 times higher resistivity of Fe-based materials.

Section 5 in this thesis is devoted to the study of the influence of the pnictogen element in the transformation of TM pnictides to a TM (oxy)hydroxide phase of specific morphology and activity during OER. For this purpose, a room-temperature salt-metathesis of NaECO (E = As, P) and NiBr₂(thf)_{1.5} was used to access amorphous NiP and NiAs in a 1:1 stoichiometry (see Figure 6.3).



Figure 6.3. Preparation of amorphous NiAs and NiP prepared through room temperature salt-metathesis.

The electrochemical investigations of both materials showed a high OER electrocatalytic activity under alkaline media (Table 6.3). The achieved high activity was comparable to other Ni-based materials and TM-Ps and TM-As known from the literature. Amorphous NiP showed higher activity and stability in comparison to NiAs when deposited on both substrates. A FE of > 96 % for the OER also proved that both materials were very efficient water oxidation electrocatalysts.

Table 6.3. Overpotentials for OER of amorphous NiP and NiAs deposited on NF and FTO.

Material	η_{OER} @	η_{OER} @
	10 mA cm ⁻² (mV)	10 mA cm ⁻² 24 h (mV)
NiP/NF	274	275
NiAs/NF	339	305
NiP/FTO	342	350
NiAs/FTO	384	390

The post-catalytic analysis revealed the oxidation and dissolution into the electrolyte after 24 h of the pnictogen atoms and generation of the γ -Ni^{III}OOH shell. The shell was composed of bis-oxo/ hydroxo-bridged Ni centers organized into sheets of edge-sharing NiO₆ octahedra with an interlayer distance of 7 Å, which permitted the intercalation of water and anions (OH⁻, CO₃²⁻) and their exposure to catalytically active Ni^{III} centers. The latter were present in a Jahn-Teller distorted octahedral configuration that facilitated the absorption of oxygen intermediates. The extent of the transformation was determined by the identity of the pnictogen. A higher loss of P (86 %) was observed in NiP in comparison to loss of As in NiAs (45 %). This resulted in a larger structural transformation of the NiP to a γ -Ni^{III}OOH phase, which showed enhanced the ECSA and OER catalytic activity. Additionally, the faster kinetics (lower Tafel slope) and low charge transfer resistance of NiP contributed to the increase in the OER activity.

Overall, the research scope of this work emerges from the electrocatalytic investigation of molecularly derived TM-Ps and TM-As for OER (see Figure 6.4), as well as for HER and OWS. It was found that the limitations on the water-splitting electrocatalysis can be overcome by modulating the properties of the electrocatalysts. A high active surface area provides high accessibility to active sites, generally observed with amorphous materials.

Additionally, materials with high conductivity promote a fast electron transfer, which results in faster reaction kinetics. Finally, the selection of the pnictogen in a determined stoichiometry favors the formation during OER of a specific TM (oxy)hydroxide phase. This phase ultimately contains highly oxidized metal atoms (Fe^{III}, Co^{III}, Ni^{III}) which adopted an energetically favored configuration for the OER.

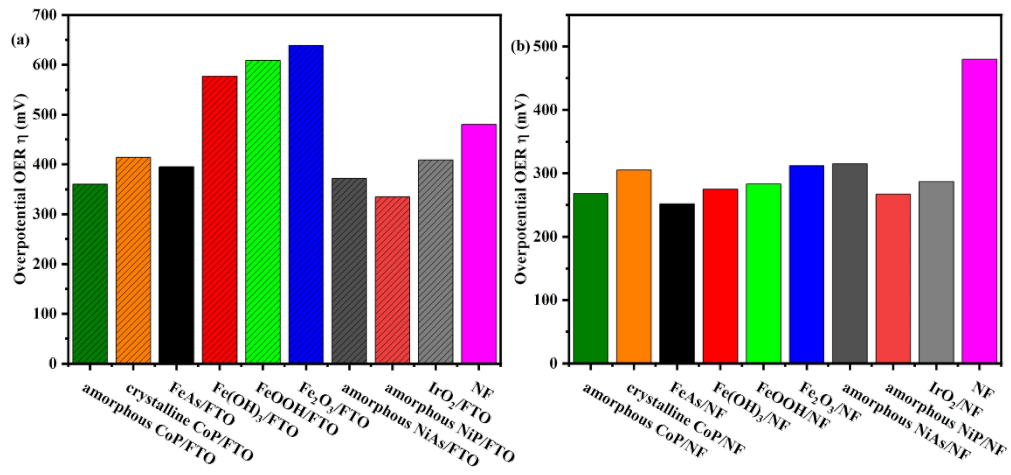


Figure 6.4. Comparison of the OER activities of the amorphous CoP, crystalline CoP, FeAs, amorphous NiAs, and amorphous NiP to the reference materials for OER deposited on (a) FTO and (b) NF.

7. Experimental Section

7.1. Preparative methods

All preparation procedures were carried out with state-of-the-art laboratory equipment from different manufacturers. Molecular synthetic procedures were done under inert atmosphere (N_2) to avoid contamination with atmospheric O_2 and moisture using standard Schlenk techniques or a M. Braun dry box containing an atmosphere of inert purified nitrogen. Solvents (hexane, THF, diethyl ether, toluene, ethanol, acetone, oleic acid, oleylamine) were dried and deoxygenated in a solvent purification system (MBraun), degassed (three freeze-pump cycles), and stored under molecular sieves (3-4 Å) prior use.^[497] For low temperature reaction, an isopropanol/dry ice or ice bath was used as cooling system and specified in the synthetic procedure. A Universal 320 Hettich centrifuge was used for the separation of solids and liquids.

7.1.1. Chemicals and materials

Chemicals and solvents used in the synthesis of precursors and catalysts were used as purchased, no additional procedures were done to purify them. Used chemicals: n -BuLi (2.5 M in hexanes, Sigma-Aldrich), Fe_2O_3 (Sigma-Aldrich), IrO_2 (Alfa Aesar, 99 %), I_2 (Merck, double sublimated), white phosphorus P_4 (Sigma-Aldrich, 99 %), tetrabutylammonium hexafluorophosphate (Sigma-Aldrich, 99 %). The presence of Fe on the electrolyte solution (1 M KOH, Sigma-Aldrich) was ruled out by purifying it before its use following literature procedure.^[132] NF and FTO (resistivity 8–12 Ω sq^{-1}) were obtained from Racemat BV and Sigma Aldrich, respectively.

7.1.2. Synthesis and characterization of the molecular precursors

7.1.2.1. Synthesis of $L^{Dipp}CoP_4CoL^{Dipp}$ (3)

Synthesis of 1. The Nacnac ligand (1,3-Diketimine, β -Diketimine) was prepared according to a published procedure.^[498]

Synthesis of $CoCl_2(thf)_{1.5}$. The $CoCl_2(thf)_{1.5}$ was prepared according to a published procedure.^[498]

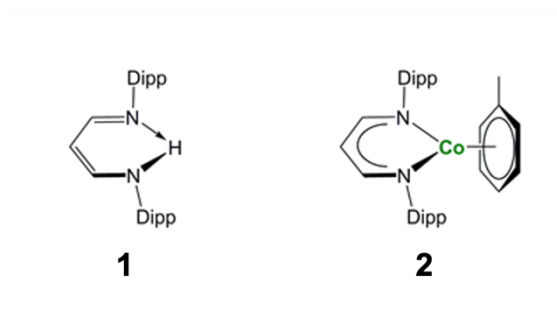


Figure 7.1. Molecular structures of 1,3-Diketimine ligand (L^{Dipp} , Dipp = 2,6- i -Pr $_2$ C $_6$ H $_3$) and Nacnac (1,3-Diketimine, β -Diketimine) cobalt (I) toluene complex ($L^{Dipp}Co^I(tol)$).

Synthesis of 2. To a cooled (-30 °C) solution of **1** (4.05 g, 10.35 mmol) in THF (40 ml) was added ⁿBuLi (5.5 mL, 2.5 M in hexane, 13.75 mmol) with stirring. The reaction mixture was allowed to warm to room temperature and stirred further for 3 h. CoCl₂·(thf)_{1.5} (2.44 g, 10.25 mmol) was added and the mixture was refluxed overnight. After cooled to room temperature, 10 mL toluene and 1.92 g KC₈ (14.20 mmol) were added. The reaction mixture was further stirred for 17 h and the color of the resulted mixture turned to dark red. Volatiles were removed *in vacuo*, and the residue was extracted with diethyl ether (3 x 25 mL). After filtration and concentration, the saturated solution was cooled to -20 °C for 24 h, **2** crystallized from the solution as dark red crystals (3.66 g, 6.77 mmol, 66 %).

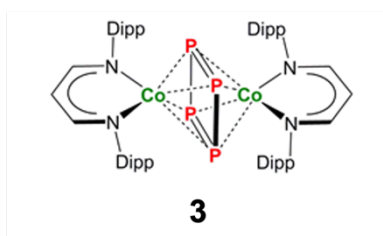


Figure 7.2. Molecular precursor L^{Dipp}CoP₄CoL^{Dipp}. The complex bears a cyclo P₄ structure.

Synthesis of 3. The precursor **3** was prepared according to literature procedure.^[281] To a solution of **2** (1.10 g, 2.04 mmol) in toluene (20 mL), white phosphorus (P₄) (0.126 g, 1.01 mmol) was added at room temperature. After stirring for 3 h, the color of the solution changed from dark red to dark pink and a dark brown red precipitate of **3** formed. After filtration, the precipitate was collected and dried under reduced pressure to give the first crop of the title complex as a dark brown solid. Concentration of the filtrate and cooled to -20 °C for 2 days afforded the second crop as dark brown crystals. The combined isolated yield amounted 0.74 g (0.74 mmol, 72 %). Elemental analysis (%): calculated for C₅₄H₇₄N₄Co₂P₄: C, 63.53; H, 7.31; N, 5.49. Found: C, 62.77; H, 8.73; N, 7.52.

¹H NMR (paramagnetic, 200 MHz, C₆D₆, 300K) δ (ppm): s 16.42 (3.68, 4H), d 9.72 (8.00, 8 H, ¹J_{H-H} = 7.52 Hz), t 5.43 (4.34, 4 H, ¹J_{H-H} = 7.38 Hz), s 3.98 (7.58, 8 H) s 1.34 (25.97, 24 H), s 1.06 (25.72, 24 H), s -24.14 (1.51, 1 H).

FT-IR $\bar{\nu}$ (cm⁻¹) = 556 (w), 606 (w), 668 (w), 738 (m), 755(m), 774 (w), 798 (w), 1058 (w), 1091 (w), 1106 (w), 1197 (w), 1242 (w), 1255 (w), 1290 (s), 1319 (w), 1360 (w), 1380 (w), 1433 (s), 1461 (m), 1502 (m), 1565 (m), 2862 (w), 2923 (w), 2956 (s), 3067 (w).

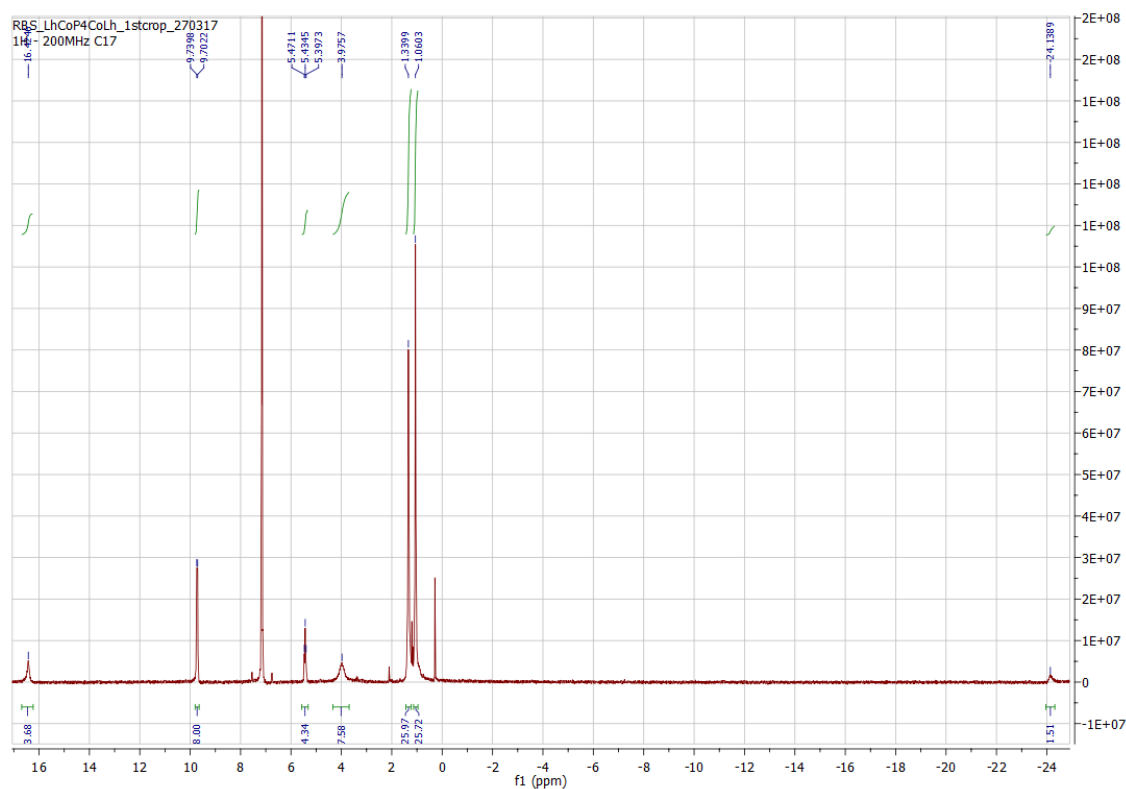


Figure 7.3. $^1\text{H-NMR}$ of the molecular precursor in THF-d_8 .

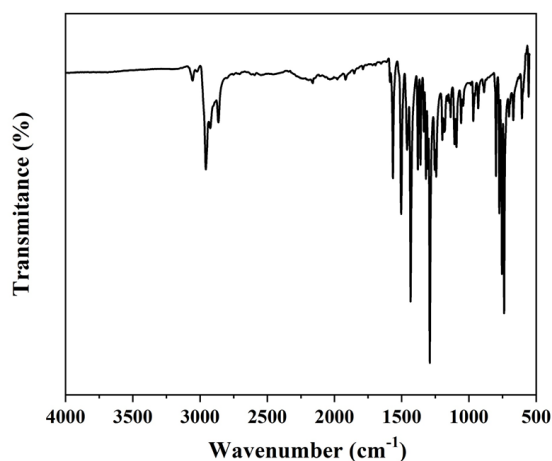


Figure 7.4. FT-IR of **3** under N_2 . All observed bands are consistent with the reported complex.^[281]

7.1.2.2. Synthesis of $\text{L}^{\text{B}}\text{FeAs}_2\text{FeL}^{\text{B}}$ (**6**)

Synthesis of 4. $\text{L}^{\text{B}}\text{FeCl}$ ($\text{L}^{\text{B}} = \text{CH}(\text{C}^t\text{BuNDipp})_2$, $\text{Dipp} = 2,6\text{-}i\text{-Pr}_2\text{C}_6\text{H}_3$) was prepared according to literature procedure.^[354,499–501]

Synthesis of 5. $\text{NaOCAs} \cdot (\text{dioxane})_{2.1}$ was prepared according to literature procedures.^[354,499–501]

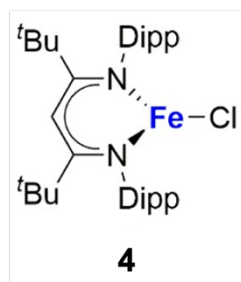
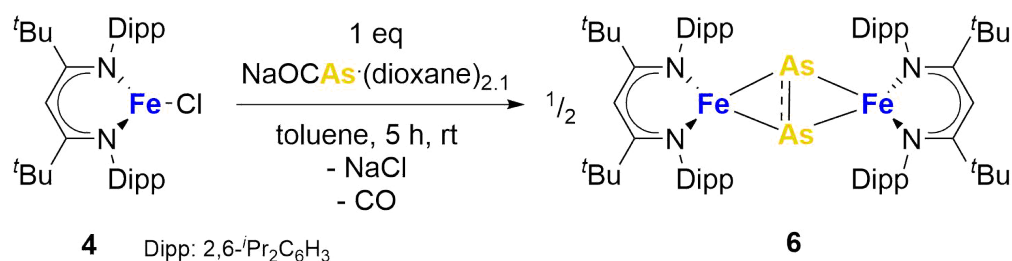


Figure 7.5. Molecular structure of L^BFeCl .

The $AsCO^-$ anion has been shown to react towards electrophiles and to form highly reactive arsinidenes through spontaneous or photocatalytic CO release. Thus, it serves as a building block towards new heterocyclic compounds, diarsenes, and terminal pnictides.^[353,355,356] The reactivity of this anion towards β -Diketiminato stabilized Fe-complexes was explored.

Synthesis of 6 (see Scheme 1). L^BFeCl (447 mg; 0.75 mmol; 1.0 eq.) and $NaOCAs \cdot (dioxane)_{2.1}$ (258 mg; 0.83 mmol; 1.1 eq.) were stirred in 50 mL toluene for 5 h at room temperature, during which the initially dark red solution turned dark brown. The reaction mixture was filtered, and the residue washed again with 10 mL toluene. The filtrate was then carefully concentrated to one-sixth of its volume so that a dark red crystalline solid could be isolated after one day at 5 °C. The dinuclear iron arsenide cluster complex $L^BFeAs_2FeL^B$ was obtained in 40 % yield (220 mg, 0.15 mmol) relative to the iron precursor. Two molecules of toluene co-crystallized with the compound. Elemental analysis: (%) calculated: C: 69.60, H: 8.50, N: 3.87; found: C: 66.89, H: 8.14, N: 3.69. The slight difference in carbon content can be explained by the high sensitivity of the molecule. Compound **6** was isolated and characterized by elemental analysis, 1H NMR and IR spectroscopy, and a single-crystal X-ray diffraction (XRD) analysis (see below). Due to severe fragmentation, no indication of the synthesized complex could be observed in mass spectrometry.



Scheme 1. Synthesis of molecular of precursor **6**.^[433]

The complex **6** crystallizes in the monoclinic space group $P2_1/n$ (see Figure 7.6) as a $FeAs$ dimer with two co-crystallized toluene molecules in the unit cell. The $[2Fe-2As]$ core is symmetrical, with $Fe-As$ distances (2.4023(4) Å and 2.4087(4) Å) in the common range of $Fe-As$ single bonds.^[502–504] Strikingly, unlike other $2M-2E$ complexes ($M = metal, E = P, As$), the iron arsenide cluster core in **6** has not a butterfly-like structure.^[356,505–507] The

coordination geometry around the iron atoms is tetrahedral instead, generating a planar 2Fe-2As unit. Such a cluster core structure is unprecedented in TM-pnictido chemistry. With 2.3447(5) Å, the As-As bond in **6** was significantly longer than expected for an As-As double bond (2.23 Å) in butterfly-like M₂As₂ complexes.^[357,508,509] Contrary to other butterfly-like 2M-2E systems (E = P, As), complex **6** was paramagnetic in solutions as shown by ¹H NMR spectroscopy (see Figure 7.7). The experimental shifts were very similar to those from the chlorido iron(II) precursor **4**, but the FT-IR spectrum of **6** (see Figure 7.8) shows an irrefutable change in the absorption pattern.

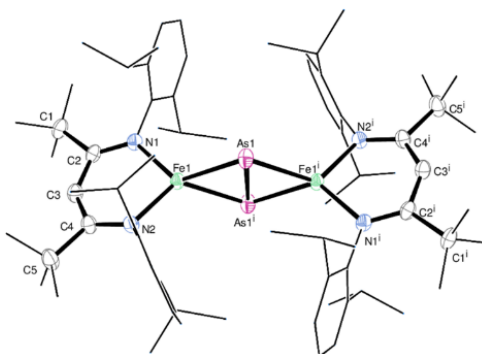


Figure 7.6. Molecular structure of **6**. Ellipsoids are set at 50 % probability; hydrogen atoms and co-crystallized toluene have been omitted for clarity. One of the ⁱPr groups in the ligand is disordered over two positions, hence only one configuration is shown. Selected bond lengths [Å] and angles [°]: As1-As1ⁱ 2.3447(5), Fe1-As1 2.4023(4), Fe1-As1ⁱ 2.4087(4), Fe1-N1 2.0085(18), Fe1-N2 2.0096(18), Fe1...Fe1ⁱ 4.201, N1-Fe1-N2 95.95(7), As1-Fe1-As1ⁱ 60.969(13), Fe1-As1-Fe1ⁱ 121.664(12). Symmetry operation for (i): -x+1, -y+1, -z+1 (Crystal data and structure refinement are shown in the Appendix. CCDC 1989143 contains the supplementary crystallographic. This data is provided free of charge by The Cambridge Crystallographic Data Centre.^[433]

¹H NMR (paramagnetic, 200 MHz, C₆D₆): δ (ppm): s 104.23 (1H, γ-*H*)*; s 41.98 (18H, ^tBu-*H*)*; m 7.03 (tol); s 2.11 (tol); 1.28*; -27.58 (12H, Dipp-*CH*₃)*; -108.88 (2H, *p-H*)*; -112.01 (12H, Dipp-*CH*₃)*. Because of the paramagnetic nature of the compound and the extreme broadening observed, signals could only be tentatively assigned. Signals marked with (*) have been observed for the iron chloride precursor as well. These signals appeared both *in situ* and in solutions from sufficiently pure crystalline samples and can thus be assigned to the iron arsenide complex. It has to be noted that many three-coordinate iron complexes L^BFeR (with R = hydride, halide, alkyl, amide) exhibit very similar signal patterns and shifts.^[499,500,510–512]

FT-IR $\bar{\nu}$ (cm⁻¹) = 2957 (s), 2922 (s), 2906 (s), 2865 (s), 1999 (w), 1920 (w), 1535 (w), 1485 (s), 1460 (m), 1443 (m), 1432 (m), 1400 (w), 1379 (s), 1358 (s), 1311 (s), 1280 (m), 1251 (m), 1214 (m), 1200 (w), 1188 (s), 1177 (s), 1154 (m), 1126 (m), 1097 (m), 1054 (m), 1028 (m), 957 (w), 934 (m), 918 (w), 899 (w), 888 (w), 878 (w), 839 (w), 815 (w), 799 (m), 776 (s), 764 (m), 754 (s), 730 (s), 717 (w), 695 (m), 677 (m), 664 (w), 647 (w)

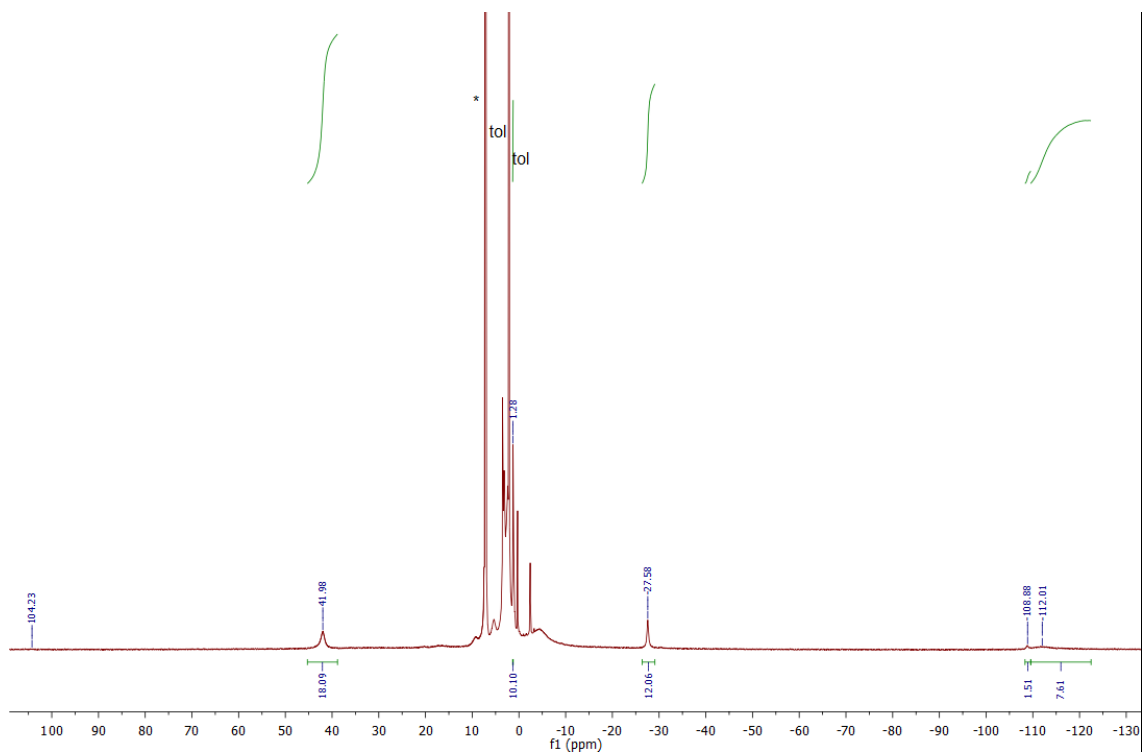


Figure 7.7. ¹H-NMR of the molecular precursor **6** in THF-d₈.

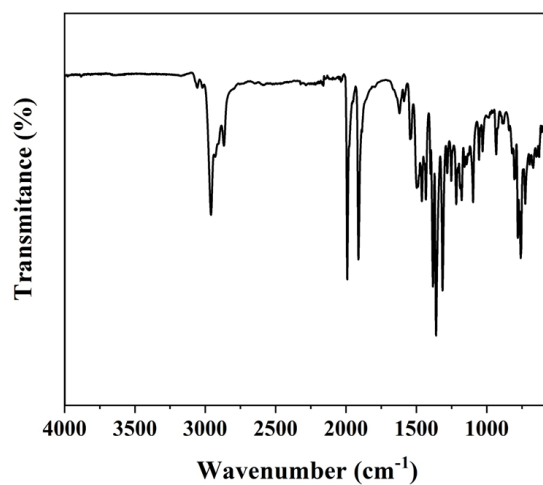


Figure 7.8. FT-IR of **6** under N₂.

7.1.2.3. Synthesis of NaOCE (E = P, As)

The NaOCP·(dioxane)_{2.1} NaOCAs·(dioxane)_{2.1} were prepared according to literature procedures.^[354,453]

7.1.3. Preparation of reference materials

Synthesis of amorphous Fe(OH)₃ and FeOOH. Amorphous Fe(OH)₃ was synthesized by precipitation of iron(III) nitrate following a reported protocol and FeOOH by precipitation of iron(II) sulphate followed by oxidation with H₂O₂.^[80,513] The purity of the Fe-based reference materials was proved by PXRD.

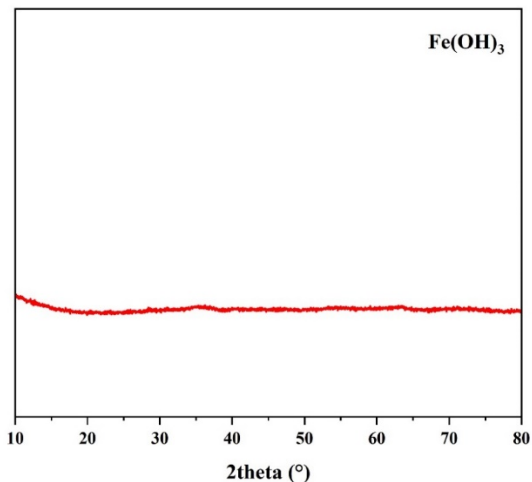


Figure 7.9. XRD patterns of the prepared Fe(OH)₃. The obtained material was amorphous.^[513]

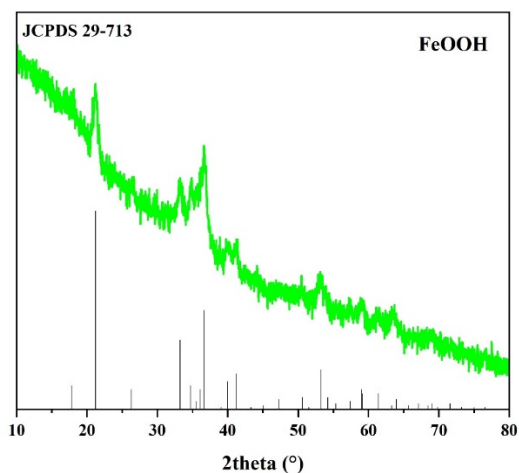


Figure 7.10. XRD patterns of the prepared FeOOH and its comparison to the diffraction peaks observed for α-FeOOH (goethite, JCPDS 29-713).

Fe₂O₃. Fe₂O₃ was obtained commercially from Sigma-Aldrich and its purity and crystallinity demonstrated by PXRD.

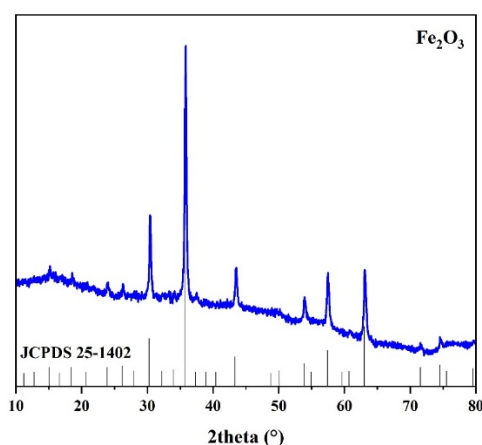


Figure 7.11. XRD patterns of the prepared Fe_2O_3 and its comparison to the diffraction peaks observed for Fe_2O_3 (maghemite, JCPDS 25-1402).

7.1.4. Preparation of films by EPD

The investigated materials were deposited electrophoretically (EPD) by a quick and inexpensive well-established method on both NF and FTO.^[79,80,104,250,514] The electrophoresis is achieved by the motion of charged particles on a suspension towards an electrode of the opposite charge under the application of an electric field (see Figure 7.12). Depending on the particle charge and the value of the applied potential, cathodic or anodic deposits can be obtained. The EPD is an advantageous method since it is independent on the shape and size of the used substrate. The charges of particles in the suspension originate from various sources, as adsorbed inorganic ions or from dispersants.^[515]

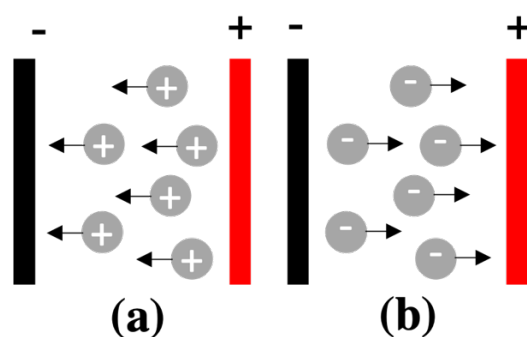


Figure 7.12. Schematic representation of EPD: (a) cathodic EPD, (b) anodic EPD.

Suspensions are prepared on organic solvents because of their lower dielectric constant, which limits the charge on the particles because of the lower dissociating power. However, the electric charge on the catalyst in acetone is insufficient for EPD, as very small amounts of free ions exist in acetone. When iodine is used as the dispersant, it can react with acetone through the keto-enol tautomerization to produce H^+ as per the following reaction:

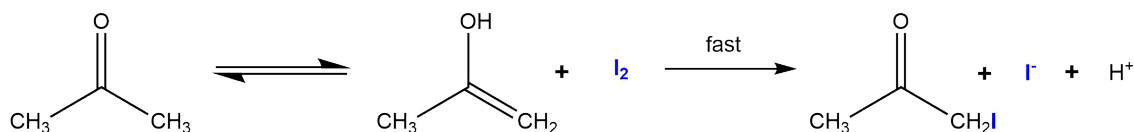


Figure 7.13. Keto-enol tautomerization during the EPD. The addition of I₂ stabilizes the enol form and produces H⁺ that are adsorbed into the materials particles.

Thus, formed H⁺ are adsorbed on the surface of the suspended particles by making them positively charged. The applied electric field induces the positively charged particles to migrate towards and deposit on the cathode. Typically, 30-40 mg of the catalyst powder and 3 mg of iodine were added to 10 mL acetone and sonicated for 1 hour. The EPD was conducted at -10.0 V for 2 min on a 1 × 1 cm² electrode area using a two-electrode system (two FTO electrodes, two NF electrodes or one FTO electrode and one NF electrode) and thin uniform films were obtained. The potential was controlled using a BioLogic Potentiostat SP-200.

7.2. Analytical Methods

7.2.1. Nuclear Magnetic Resonance (NMR)

Nuclear Magnetic Resonance (NMR) is based on the measurement of the absorption of electromagnetic radiation between 4-900 MHz by the nuclei. The analyte is subjected to a strong constant magnetic field in order to generate the energy states that can absorb the electromagnetic radiation. The system is perturbed by several weak oscillating magnetic pulses, which produce each a signal in the time domain which decays during the interval time between pulses. Each nucleus produces an electromagnetic signal that is dependent on their chemical environment. The signals are then converted by a Fourier transform into the frequency domain and a spectrum is obtained. In the spectrum each signal can be assigned to a specified nucleus.^[516]

¹H-NMR spectra were recorded on a Bruker Spectrometer AV200 at 300 K. C₆D₆ (d 7.15 ppm), and THF-d₈ (d 1.72 ppm) residual signals were used as internal standards. The signals of the ¹H-NMR were integrated relative to the number of protons, and their multiplicity is described using the following abbreviations: s = singlet; d = doublet; t = triplet; m = multiplet.

7.2.2. Infrared Spectroscopy (IR)

IR spectra result from the transitions between quantized vibrational energy states. IR can give information about functional groups and bonds that contribute to the elucidation of the structure of the materials. The excitation of the bonds to high vibrational energy states creates absorption bands resulting in the IR spectrum. The wavenumber $\bar{\nu}$ is correlated to the wavelength (λ) of the radiation by the following equation:

$$\bar{\nu} = \frac{\nu}{c} = \frac{1}{\lambda} \quad \text{Equation 20}$$

Where ν is the frequency of the light source, c is the speed of light. Light absorption occurs if the dipole moment (μ) of the bond changes from the resulting vibration. If not, the vibration is IR inactive.^[517] In the ATR-IR (attenuated total reflection infrared spectroscopy) technique the sample is placed in contact with an internal reflection element (IRE). The IR light beam is passed through the IRE and absorbed by the sample. The radiation resulting from excitations in the surface of the material is then reflected multiple times on the IRE. Extended measurement times and multiple reflections achieve a higher sensitivity.^[517] IR spectra were recorded on powder solids or on FTO-deposited films using a Thermofisher Nicolet iS5 IR spectrometer (with ATR-Diamond) under inert conditions (for molecular precursors) or aerobic conditions (for electrocatalysts). The spectra were recorded with the OMNIC Software (version 9.3.30).

7.2.3. Cyclic voltammetry (CV) for molecular precursors

Cyclic voltammetry (CV) measurements of the molecular precursor were performed in a standard three-electrode electrochemical cell having Pt-wire used as an auxiliary electrode, glassy carbon (3 mm diameter) as WE and Ag/Ag⁺ as a pseudo RE at 295 K using a Biologic SP-150 potentiostat. All cyclic voltammograms were referenced against the Cp₂Fe/Cp₂Fe⁺ redox couple (Fc/Fc⁺), which was used as an internal standard. 0.3 M tetrabutylammonium hexafluorophosphate (TBAPF₆) in THF was used as an electrolyte. The iR-drop was determined and compensated by using the impedance measurement technique implemented in the EC-Lab Software V10.37.

7.2.4. X-ray diffraction (XRD)

In powder X-ray diffraction (PXRD) the materials are identified by the diffraction pattern originated from the reflection and dispersion of the electric component of X-rays and the electrons on ordered atoms of a crystalline solid. The atoms should have a regular spacing (i.e. crystalline materials) and the distance between the atoms (d_{hkl}) should be approximately equal to the diffraction angle.^[516] Characteristic diffraction patterns are a result of the constructive and destructive interactions. Constructive interactions between incident rays and the sample occur when the following equation is satisfied (Bragg's law):

$$2d_{hkl} \sin \theta_{hkl} = n\lambda \quad \text{Equation 21}$$

Where θ_{hkl} is the incident angle and n are integers. The radiation that is reflected creates the diffraction pattern, which is unique for each material. PXRD enables the identification of the crystalline phases present in the sample, revealing the purity of the sample and the lack of undesirable impurities. The X-rays are generated by a cathode ray tube, filtered to produce a monochromatic radiation, then collimated to concentrate the radiation and direct it to the sample.

PXRD patterns were obtained on a Bruker AXS D8 advanced automatic diffractometer equipped with a position-sensitive detector (PSD) and a curved germanium (111) primary monochromator using Cu-K_{a1} radiation ($\lambda = 1.5418 \text{ \AA}$). The XRD patterns of films were

obtained on a Rigaku SmartLab 3 kW diffractometer (Rigaku Corporation, Japan) with monochromatic Cu-K_{α1}-radiation (K_{α1}-unit, Johansson's monochromator; curved Ge(111) crystal; $\lambda = 1.5418 \text{ \AA}$). The evaluation of the diffractograms was done with STOE Powder Diffraction Software Package WinX^{POW} (version 1.04).

7.2.5. Single-Crystal X-ray Structure Determination

Single-Crystal XRD follows the similar principle as in PXRD. However, in this case single crystals of molecular or materials are studied. This method provides information about the internal lattice of crystalline substances (unit cell dimension, bond-lengths, bond-angles and details about the order of the atoms). Single-crystals are placed inside the diffractometer, where a goniometer allows exploring the transmission, reflection and diffraction of the X-rays through the crystal lattice.

The crystals of new molecular species **6** was mounted on a glass capillary in per-fluorinated oil and measured in a cold N₂ flow. The data of **6** was collected on an Oxford Diffraction Supernova, Single source at offset, Atlas at 150 K (Cu- K α -radiation, $\lambda = 1.5418 \text{ \AA}$). The structure was solved by direct method and refined on F² with the SHELX-97 software package.^[518] The positions of the H atoms were calculated and considered isotropically according to a riding model. CCDC 1989143 contains the supplementary crystallographic data. These data can be obtained free of charge by contacting The Cambridge Crystallographic Data Centre, 12, Union Road, Cambridge CB2 1EZ, UK; fax: +44 1223 336033.

7.2.6. Atomic emission spectroscopy (ICP-AES)

The quantitative determination of the metal and non-metal content in the synthesized materials and the electrolyte solutions after catalysis was done by inductively coupled plasma atomic emission spectroscopy (ICP-AES). In this method, the analyte (solution) is introduced nebulized and introduced into a plasma jet. The energy of the plasma excites the valence electrons of the atoms into higher energy levels. When the excited electrons return to the fundamental state, visible and UV radiation is emitted. The energy of this radiation is specifically related to an element. Quantitative determination of the elements can be done using standard solution and considering separated emission lines for the studied elements.^[516]

The ICP-AES was conducted on a Thermo Jarrell Ash Trace Scan analyzer. Solid samples were digested in aqua regia HCl:HNO₃ 4:1 v/v (nitric acid, SUPRA-Qualität ROTIPURAN® Supra 69 % and hydrochloric acid, SUPRA-Qualität ROTIPURAN® Supra 30 %) and the average of three reproducible independent experiments is reported. The digestion volume (2.5 mL) was diluted with Milli-Q water up to 15 mL. Calibration curves were prepared for Co, P, Fe, As and Ni with concentrations between 1 mg L⁻¹ and 100 mg L⁻¹ from standard solutions (1000 mg L⁻¹ Single-Element ICP-Standard Solution ROTI STAR).

7.2.7. Scanning electron microscopy (SEM)

Scanning electron microscopy (SEM) provides information about the physical nature of the surface of solids. Especially, they can provide detailed information about the morphology such as distribution of shapes and sizes of the particles and insights into sample heterogeneity.^[69] The sample is scanned with a tightly focused electron beam. The electrons of the beam interact with the electron on the conduction band of the surface atoms, emitting backscattered electrons and secondary electrons which provide information about the morphology and X-rays which provides the elementary composition of the material, and confirm the phase assignment.^[516] SEM was performed on a GeminiSEM500 NanoVP microscope (ZEISS) integrated with an energy dispersive X-ray spectrometer detector (Bruker Quantax XFlash® 6|60). The most abundant elements were selected from the EDX spectrum. Data handling and analysis were achieved with the software package EDAX. The SEM experiments were conducted at the Zentrum für Elektronenmikroskopie (ZELMI) of the TU Berlin.

7.2.8. Transmission electron microscopy (TEM)

During transmission electron microscopy (TEM) an electron beam is transmitted through a solid. The interaction between the electron beam and the sample electrons creates an image. TEM data can corroborate bulk structural and compositional information. Lattice spacing, angles and structural motifs can be observed by high-resolution TEM (HR-TEM). Therefore, HR-TEM can confirm the assigned structure and provide information of the exposed facets.^[69] TEM was performed on an FEI Tecnai G2 20 S-TWIN transmission electron microscope (FEI Company, Eindhoven, Netherlands) equipped with a LaB₆ source at 200 kV acceleration voltage. For the investigation of the films after electrocatalysis, the films were scratched from the electrode substrate and transferred onto a carbon-coated copper grid. EDX analyses were achieved with an EDAX r-TEM SUTW detector (Si (Li) detector), and the images were recorded with a GATAN MS794 P charge-coupled device (CCD) camera. The TEM experiments were conducted at the Zentrum für Elektronenmikroskopie (ZELMI) of the TU Berlin.

7.2.9. Selected Area Electron Diffraction (SAED)

Selected area electron diffraction is performed during the TEM measurement. The high-energy electron beam is diffracted by the atoms inside a crystalline structure from the selected area of study. The electrons are scattered to form a particular diffraction pattern. Then, the pattern can be related to the crystal structure to determine the interplanar distance.

7.2.10. X-ray photoelectron spectroscopy (XPS)

X-ray photoelectron spectroscopy (XPS) provides information about the chemical environments of the surface atoms in crystalline and amorphous materials.^[69,519] XPS is based on the photoelectric effect arising when high energy photons (in the range of keV)

hit a material with the consequent emission of electron (photoexcited electrons). The photoelectron effect is described by the following equation:

$$E_k = h\nu - E_B - \Phi_S \quad \text{Equation 22}$$

The incident radiation ($h\nu$) induces changes in the kinetic energy (E_k) of the electrons emitted from the surface. E_B is the binding energy of the atomic orbital from which the electron is emitted and Φ_S is the work function of the spectrometer. Each element has a unique binding energy in its different oxidation states and affected by diverse chemical environments. In consequence, an XPS spectrum displaying all the accessible energy states can be used to obtain quantitative and qualitative information of the sample. Chemical shifts of the energy positions are related to the different oxidation states and chemical environments. Additionally, the intensity of the emitted photoelectrons is related to the concentration of the chemical species.

The XPS measurements on amorphous CoP, crystalline CoP, amorphous NiP, amorphous NiAs and derived *post-operando* samples were conducted on a Kratos Axis Ultra X-ray photoelectron spectrometer (Kratos Analytical Ltd., Manchester, U.K.) using an Al K α monochromatic radiation source (1486.7 eV) with a 90° take off angle (normal to analyzer). The vacuum pressure in the analysis chamber was kept at 2×10^{-9} Torr. The XPS spectra were collected for O 1s, Co 2p, Ni 2p, P 2p and As 3d levels with a pass energy of 20 eV and a step of 0.1 eV. The binding energies were calibrated relative to the C 1s peak energy position at 285.0 eV. Data analyses were carried out using Casa XPS (Casa Software Ltd.) and the Vision data processing program (Kratos Analytical Ltd.).

The XPS measurements on crystalline FeAs and derived *post-operando* samples were carried out using a ThermoScientific K-Alpha+ X-ray photoelectron spectrometer. All samples were analyzed using a micro-focused, monochromatic Al-K α X-ray source (1486.68 eV; 400 μ m spot size). The analyzer had pass energy of 200 eV (survey), and 50 eV (high-resolution spectra), respectively. The XPS spectra were collected for Fe 2p, P 2p and As 3d levels. Binding energies were calibrated to the C 1s peak at 284.8 eV. To prevent any localized charge build-up during analysis the K-Alpha+ charge compensation system was employed at all measurements. The samples were mounted on conductive carbon tape or measured directly from the FTO substrate. The resulting spectra were analyzed using the Avantage software from ThermoScientific.

7.2.11. X-ray absorption spectroscopy (XAS)

X-ray absorption spectroscopy (XAS) provides insights into the bulk and local structure of catalytic materials.^[69] The absorption of X-rays process is the result of an excitation of an inner level electron to a higher energy level by an incident photon. The transmission mode on foil thin single crystals or homogeneous samples prepared from powders is the most common method of XAS detection. XAS follows the Beer-Lambert law:

$$\ln \frac{I_0}{I} = \mu(E)x \quad \text{Equation 23}$$

Where I and I_0 are the transmitted and incident radiation beams, x is the thickness of the sample and $\mu(E)$ is the mass absorption coefficient, which depends on the energy (E) of the radiation. The mass absorption coefficient of materials with multiple components is the sum of the weight average of all the components. In consequence, each material has a characteristic energy level structure and therefore produce a characteristic spectrum, which depends on the energy of the incident radiation.^[520] The spectra show sharp absorption edges at specific photon energies, which are different for each element. When the I_0 is large enough, electrons from the core level are excited into higher excited states and there is a strong increase in the absorption intensity, which leads to strong energy difference between these two levels. Generated photoelectron waves are scattered and influenced by the neighbor atoms. Constructive and destructive interferences generate a characteristic absorption spectrum, which is the final XAS spectrum, which depends on the incident energy (E). In general, XAS spectra are composed of two regions: the X-ray absorption near edge structure (XANES) and the X-ray absorption fine structure (EXAFS).^[521] The XANES region gives information of the effective charge (valence state) of the absorbing atom by the location of the absorption edge, the energy bandwidth and bond angles. The EXAFS originates from an interference effect of the outgoing photoelectrons excited from the inner core levels by resonant radiation and backscattered electrons from near neighbor atoms. They modulate altogether the final state energy of the absorbing atom. The interatomic distances, near neighbor coordination numbers and lattice dynamics can be explored through EXAFS.^[520] An increase in the formal oxidation state is related to a shift of the X-ray edge position to high energies on the XANES spectrum. The shape of the spectra also differs for each compound.^[521]

The experiments were conducted at the KMC3 beamline of the BESSY synchrotron operated at the Helmholtz-Zentrum Berlin (HZB). Data collection was performed at 20 K in a liquid-helium cryostat in fluorescence detection mode using a 13 element silicon drift detector (Rayspec). Over 20 spectra were averaged for each compound in order to improve the signal-to-noise ratio. Averaged spectra were background-corrected and normalized using in-house software. Subsequently, unfiltered k^3 -weighted spectra and phase functions from FEFF8.5^[522] were used for the least-squares curve-fitting of the EXAFS with in-house software and for calculation of Fourier-transforms representing k -values between 1.6 \AA^{-1} and 14 \AA^{-1} . Data were multiplied by a fractional cosine window (10 % at low and high k -side); the amplitude reduction factor S_0^2 was 0.75 for Fe and 1.00 for As.

The samples were kept for 6 h under constant current of 10 mA cm^{-2} using FeAs/FTO as WE, Pt wire as CE and Hg/HgO electrode (CH Instruments) as RE on a three electrode system on 1 M KOH. After this time, the experiment was stopped, and the sample was immediately immersed on liquid N_2 (77 K) to freeze quench it. The sample was stored and taken to BESSY for measurement.

7.2.12. Resonance Raman spectroscopy

Resonance Raman spectroscopy is used to increase the intensity of the vibrations by using a wavelength which is in resonance with the electronic absorption wavelength of the analyte.^[516] Resonance Raman spectroscopy can be used in selective resonance to a specific absorption. The main difference to Raman spectroscopy is that no relaxation to less energy excited vibrational states is observed. Raman resonance requires the use of high intensity lasers usually lying on the UV range of radiation. To prevent sample damage by heating, the sample is cooled with liquid N₂.

Resonance Raman spectra were recorded using the 458 nm emission of an Argon ion laser (Innova 70, Coherent) for excitation and a confocal Raman spectrometer (Lab Ram HR-800 Jobin Yvon) equipped with a liquid-nitrogen cooled CCD camera for data acquisition. The typical laser power at the sample ranged between 2 mW to 3 mW. The samples were measured using a Linkam Cryostage THMS600 cryostat. The temperature of the samples was kept at 80 K throughout the measurements. The spectrometer was calibrated before each experiment using toluene as an external standard. Baseline subtraction/processing from FTO was performed for analyzing the data.

7.2.13. BET Surface area determination N₂ adsorption

Gas adsorption on solids is the most employed technique to determine the surface area of a material. The adsorption of gas molecules on a solid surface is explained by the Brunauer-Emmet-Teller (BET) theory. The BET theory takes into consideration that gas molecules physically adsorb on solid layers infinitely, gas molecules only interact with adjacent layers and that the Langmuir theory can be applied to each layer. Thermodynamical considerations are taken in this theory: the enthalpy of adsorption for the first layer is constant and greater than the second (and higher layers) and the enthalpy of adsorption of the second (and higher) layers is the same as the enthalpy of liquefaction.^[523] The adsorption-desorption of N₂ at 77 K is explored by varying the initial pressure on the system (p_0) and measuring the adsorbed N₂ (p , V). The adsorbed volume of N₂ can be related to the relative pressure (p/p_0) can be related through the following equation:

$$\frac{1}{V\left(\frac{p_0}{p}-1\right)} = \frac{C-1}{V_m C} \left(\frac{p}{p_0}\right) + \frac{1}{V_m C} \quad \text{Equation 24}$$

Where V_m is the volume of gas adsorbed on the first monolayer and C is the BET constant. Determination of the surface area was performed by Nitrogen sorption using the BET method. Measurements were performed with a Nova 4000e from Quantachrome Instruments. Degassing was performed at 120 °C for 12 h before doing the measurement.

7.2.14. Elemental analysis (CHN analysis)

Determination of carbon, hydrogen, and nitrogen in organic compounds is based on systems that utilize the quantitative detection of the combustion products by a thermal

conductivity detector placed within the flowing gas stream.^[524] The CHN analysis was used to confirm the identity of the prepared molecular precursors and to identify the organic content on the prepared materials. Elemental analysis was carried out with a Thermo Flash EA 1112 Organic Elemental Analyzer by dynamic flash combustion at 1020 °C at the Messezentrum AC/OC at Institut für Chemie at TU Berlin.

7.2.15. Resistivity measurements (four-point method)

Measurements of electrical conductivity can provide important information about the relationship between the conductivity and the catalytic activity.^[525] The four-point method is a special form of four-wire measurement and it is mainly used in semiconductor production to determine the resistance of surfaces.^[526] The measurement is accomplished by placing four measuring tips that are equally spaced on the surface to be measured. The outer tips permit the flow of a constant current into the measurement object and the two inner tips determine the voltage produced across the material.^[526] This method is advantageous since no current flows on the measuring line (inner tips), which means that resistances arising from the feed line and connection contacts are not included in the measurement and thus no voltage drop occurs. Therefore, even the smallest resistances can be measured.^[526]

A Signature Pro4 System measured the resistivity with Keithley 2400 source-measure unit (SP4-40045TBY) using a four-point probe resistivity technique. The spacing between tungsten carbide tips was 1.016 mm with a radius of 0.245 mm, and a spring pressure was 45 g. The specific resistivity was measured on the films electrophoretically deposited on FTO. The average result of five repetitions was reported.

7.3. Electrochemical methods

7.3.1. Redox chemistry of water electrolysis

A cell reaction from A to B can be expressed as:



When the electrochemical reaction takes place, $n \cdot N_A$ electrons are transferred from the reducing agent to the oxidizing agent per mole of reaction. The charge transferred between the electrodes is $n \cdot N_A \times (-e)$, which can be expressed as $-n \cdot F$. The constant F is the Faraday constant, and corresponds to the magnitude of electric charge per mole of electrons:

$$F = eN_A = 96485 \text{ C mol}^{-1} \quad \text{Equation 26}$$

The electrical work (w) done when the charge travels from the anode to the cathode is equal to the product of the charge and the potential difference E between the two electrodes (in V):

$$w = -nF \times E \quad \text{Equation 27}$$

When the work is done reversibly at constant temperature and pressure, the electrical work is equal to reaction Gibbs energy:

$$-nF \times E = \Delta_r G \quad \text{Equation 28}$$

Consequently, the work done by the cell is equal to the value of ΔG for the reaction. Therefore, by measuring the cell potential, it is possible to know a thermodynamic quantity. Conversely, if ΔG for a reaction is known, it is possible to calculate the cell potential.

The cell potential E varies with the composition:

$$\Delta_r G = \Delta_r G^\circ + RT \ln Q \quad \text{Equation 29}$$

Where, $\Delta_r G^\circ$ is the standard reaction Gibbs energy and Q is the reaction quotient for the cell reaction. Combining equations 28 and 29, the Nernst equation is obtained:

$$E = E^\circ - \frac{RT}{nF} \ln Q \quad \text{Equation 30}$$

With $Q = c_{red}/c_{ox}$. Electrochemical OER and HER are the pair of reactions occurring during water-splitting. In the OER, the reduced form water (H_2O) is oxidized to O_2 ($\text{O}_2/\text{H}_2\text{O}$). In the HER, the oxidized form H^+ is reduced to H_2 (H^+/H_2). At $T = 298.15 \text{ K}$ and when $c_{red} = c_{ox} = 1 \text{ mol L}^{-1}$, the cell potential E equals the standard cell potential (E°):

$$E = E^\circ \quad \text{Equation 31}$$

Each redox system has a characteristic E° . This parameter indicates the strength of the reducing or oxidizing effect of the system, i.e. the ability of the system to be reduced or oxidized. A cell in which all the reactants and products are in their standard states is not in general attainable, it is better to describe this value as the standard Gibbs energy of the reaction expressed as a potential. The value of the potentials of a redox couple cannot be determined experimentally, only the potential difference of two redox pairs can be obtained. However, one electrode can be assigned a value zero and the other assigned relative values on that basis. The specially selected electrode is the standard hydrogen electrode (SHE): $\text{Pt}_{(s)} \parallel \text{H}_{2(g)}/\text{H}^+_{(aq)}$. It is composed of a platinum electrode in contact with a solution of $a_{\text{H}^+} = 1$ at atmospheric pressure (101325 Pa). The normal hydrogen electrode (NHE) is often given as a reference, in which $a_{\text{H}^+} \approx c_{\text{H}^+} = 1 \text{ M}$.^[527]

The potential of a cell is also highly dependent on the pH of the electrolyte. If we consider OER equation (Section 1.4, Equation 6), the activity coefficient for this reaction is under atmospheric pressure:

$$Q = \frac{a_{H^+} \cdot \left(\frac{P_{O_2}}{P^o}\right)}{a_{H_2O}^2} = a_{H^+} \approx c_{H^+} \quad \text{Equation 32}$$

Replacing Q in the Nernst equation and $n = 4$ in equation 30:

$$E_{OER} = E_{(O_2/H_2O)}^o - \frac{RT}{4 \times F} \times \ln(c_{H^+}) \quad \text{Equation 33}$$

The relation between the potential for the OER and pH can be established:

$$E_{OER} = 1.23 - 0.059 \times pH \text{ (V vs. RHE)} \quad \text{Equation 34}$$

A similar derivation can be done for the HER, as it is also influenced by the pH of the electrolyte. Considering the HER equation, the activity coefficient for this reaction is under atmospheric pressure:

$$Q = \frac{a_{H^+}}{P_{H_2}^{1/2}} = a_{H^+} \approx c_{H^+} \quad \text{Equation 35}$$

Replacing Q in the Nernst equation and $n = 1$ in equation 30:

$$E_{HER} = E_{(H_2/H^+)}^o - \frac{RT}{1 \times F} \times \ln(c_{H^+}) \quad \text{Equation 36}$$

The relation between the potential for the HER and pH can be established:

$$E_{OER} = 0.00 - 0.059 \times pH \text{ (V vs. RHE)} \quad \text{Equation 37}$$

The Nernst equation reflects the thermodynamic equilibrium at which the electrochemical reactions occur. However, as discussed before (see Section 1.4.3), an overpotential (η) is always needed. The potential is usually larger than the one obtained by the Nernst equation and is described by the following equation:

$$E = E^o + iR + \eta \quad \text{Equation 38}$$

Where iR is the potential Ohmic drop of current flow in ionic electrolyte. This value depends on the conductivity of the electrolyte as well as the electrode position and is corrected before each measurement (see Section 7.3.2).

The presence of thermodynamically stable phases in an aqueous electrochemical system is expressed in Pourbaix diagrams.^[51] These are plots of equilibrium potential vs. pH (E -pH) and indicate the regions of stability of a particular metal (or non-metal) in several possible chemical forms containing the element and H and/or O. Therefore, given a E -pH condition, it is possible to determine the identity of the species. It is important to mention that these diagrams are constructed taking into consideration thermodynamic criteria and do not consider the kinetics of the reactions occurring under aqueous environments. The Pourbaix diagrams of Fe, Co, Ni, P and As are shown in Figure 7.14.

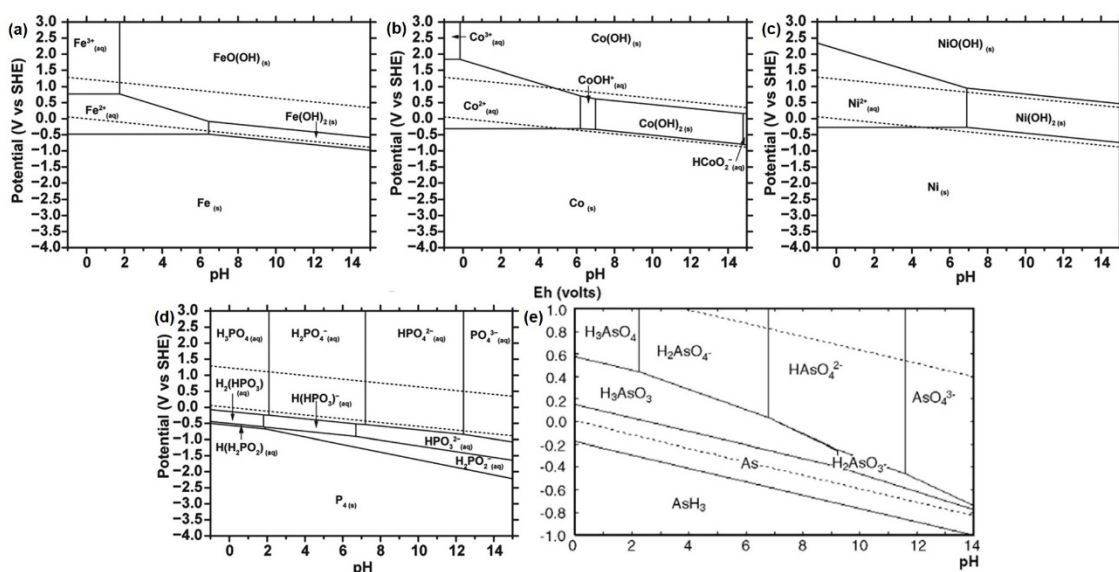


Figure 7.14. Pourbaix–pH diagrams for (a) Fe, (b) Co, (c) Ni, (d) P, and (e) As species under standard conditions (298 K, 1 atm). The concentration of soluble species except for H^+ is 0.1 M. These E–pH diagrams only represent the ideal systems with indicated species and were obtained from Liu and co-workers^[163] and Escobar and co-workers.^[528] © 2019 The Royal Society of Chemistry and © 2006 Elsevier.

7.3.2. General considerations

A typical electrocatalytic run was carried out in a standard three-electrode setup consisting of a RE, a CE and the catalyst-modified WE. The three were immersed in an aqueous electrolyte (1 M KOH, Sigma Aldrich). The presence of Fe on it was ruled out by purifying the electrolyte before its use following the literature procedure.^[132] A potentiostat (SP-200, BioLogic Science Instruments) controlled by the EC-Lab v10.20 software package was used for all the experiments. The electrodes (NF/FTO) with samples deposited served as the WE, Pt wire (0.5 mm diameter × 230 mm length; A-002234, BioLogic) as the CE and Hg/HgO (OER) or Hg/Hg₂SO₄ (HER) as the RE (CH Instruments, Inc.). EC-Lab software was used for all the measurements (version 11.10). The potential of the RE was referenced to the RHE through calibration, and in 1 M KOH the potential was calculated using the following equations:

$$E(\text{RHE, OER}) = E(\text{Hg/HgO}) + 0.098V + (0.059 \times \text{pH})V \quad \text{Equation 39}$$

$$E(\text{RHE, HER}) = E(\text{Hg/Hg}_2\text{SO}_4) + 0.650V + (0.059 \times \text{pH})V \quad \text{Equation 40}$$

7.3.3. Cyclic voltammetry (CV)

Cyclic voltammetry (CV) is a dynamic method to study the mechanism of simple redox reactions and multielectron transfer processes.^[529] A stationary WE is immersed on a stationary (non-stirred) electrolyte solution. The potential of the stationary WE is changed linearly with time (E_t) starting from a potential (E_i) where no electrode reaction occurs and moving to potentials where reduction or oxidation of the analyte of study occurs. After traversing the potential region in which the reactions take place, the direction of the

linear sweep is reversed and the E_t return to E_i .^[516,530] The scan rate (dE/dt) varies between 1-20 mV s^{-1} . If a redox reaction lies within the selected potential range, an increase in the current (i.e. Faraday current) would be observed. Consequently, a closed cyclic current-potential curve is obtained. CVs provide thermodynamic parameters of the reaction (redox potential) and also kinetic information of the electrode reactions.^[529] In the three electrode set-up that is used, the value of the WE potential is always related to the non-polarized RE Hg/HgO (OER) or Hg/Hg₂SO₄ (HER). The current is conducted between the WE and the Pt CE, while the RE remains without current. Currents that are too high can be avoided and prevent damage on the RE. Moreover, the iR drop can be kept low by positioning the RE close to the WE or compensated using the potentiostat.^[529]

CV was performed without stirring and with an applied iR compensation of 85 %, applied before each experiment. The R_u was acquired by impedance spectroscopy at 100 MHz. The potential ranges were 1.0 to 1.8 V vs. RHE for OER on NF, 1.2 to 1.9 V vs. RHE for OER on FTO. The overpotential for OER was determined from the resulting polarization curves and from thermodynamic potential values of the OER and HER in alkaline solution (see Section 7.3.2).

7.3.4. Linear-sweep voltammetry (LSV)

Linear-sweep voltammetry is similar to CV. The potential applied to the WE is varied linearly with time at a defined scan rate (mV s^{-1}). However, there is no return to the initial potential (E_i) after reaching the end potential (E_f).

7.3.5. Tafel slope

The Tafel slope can provide information about the kinetics of the electrocatalyst under study.^[41] Electrocatalysts that possess high charge transfer ability should show a small Tafel slope. The Tafel plot can be obtained by replotting the polarization (LSV or CV) curve as overpotential (η) vs. the logarithm of current density ($\log j$) or by the steady state method. In the steady-state method, CA experiments were performed for 3 min at various potentials, and the average obtained current density for each is stepped is plotted against the overpotential. For either methods, the slope is calculated according to the Tafel equation:

$$\eta = b \log j + a \quad \text{Equation 41}$$

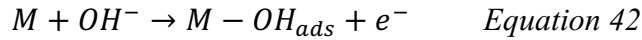
Where η is the overpotential (V), j is the current density (mA cm^{-2}), and b is the Tafel slope (mV dec^{-1}). The LSV from which the Tafel slope is derived should be done at the lowest possible scan rate to prevent the effect of high capacitance. The selected range of currents should be close to the region in which the current density of 10 mA cm^{-2} is observed.

The Tafel slope is usually used to predict how much faster the reaction occurs on an electrocatalytic interface and to compare the activities of various electrocatalysts, provided that the given experimental conditions are the same.^[41] The Tafel slope b

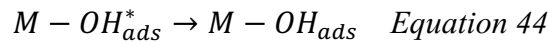
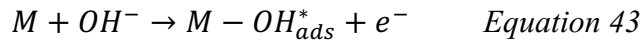
indicates much the potential must increase in order to increase the resulting current density j by an order of magnitude ($\times 10$ or per decade, dec^{-1}).^[50] This means, how efficient and dynamically an electrode reacts to an applied potential and generates catalytic current.^[50] This also takes into account any changes in the mechanism at different overpotentials.^[50] The reaction rate is also related to the geometric surface of the electrodes and described by the current density (j , mA cm^{-2}). The current density is a measurement of how strong a reaction is going forward or backward, and it depends on the electrocatalytic activity of the material.^[50]

The determination of the electrode kinetics through a Tafel analysis requires the selection of an appropriate potential range. The selected range must not be too small, because it would lead to an incorrect small Tafel slopes. Consequently, incorrect assumptions of the reaction mechanism and a misinterpretation of the rate-limiting step could be made.^[50] The optimal range for the Tafel slope determination is the one where the current density increases exponentially with the applied voltage.^[50] However, the potential at which the reaction generates current that is limited solely by mass transport should be avoided.^[50]

The Tafel slope (b) can be used to determine which of the four PCET reactions is the RDS on the OER kinetics (see Section 1.4.2). The OER is initiated by adsorption and formation of the hydroxy species ($M - OH_{ads}$) on an active site (M), on the surface:^[27]



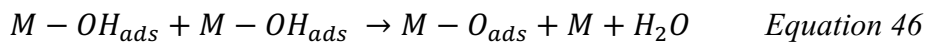
A Tafel slope of 120 mV dec^{-1} is obtained when this reaction is the RDS of the OER. The former reaction can be replaced by two sub-reactions, each one with a Tafel slope of 60 mV dec^{-1} , as it occurs on IrO₂-based electrocatalysts:^[531]



In this step, the adsorbed intermediate $M - OH_{ads}^*$ and $M - OH_{ads}$ have the same chemical structure but differ in their energy state. A Tafel slope of 60 mV dec^{-1} indicates that the OER kinetics are determined by this reaction.^[531] The following step is the electrochemical formation of a $M - O_{ads}$ intermediate with a further electron-proton transfer.



A Tafel slope of 40 mV dec^{-1} is obtained when this reaction is the RDS. The $M - O_{ads}$ intermediate can be also formed by the combination of two $M - OH_{ads}$ species:



If the kinetics of the reaction are determined by this step, a Tafel slope of 30 mV dec^{-1} is observed. Ultimately, the formation of the oxygen occurs:

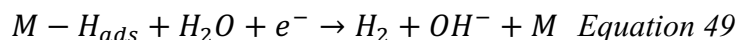


The kinetics of this reaction are determined exclusively by the formation of the O-O bond and the subsequent O₂ desorption. The Tafel slope of this mechanism is 15 mV dec⁻¹ and is the last of the OER catalytic cycle.^[531]

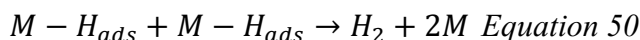
The kinetics of the HER can also be investigated by the construction of the Tafel plots. The HER is determined by three sub-steps, the Volmer, Heyrovsky and Tafel step (see Section 1.4.1). The Volmer reaction is characterized by the adsorption and discharge at the active center on the surface



It is the determining step of the HER when a Tafel slope of 120 mV dec⁻¹ is obtained.^[58] The Heyrovsky reaction takes place on surfaces where the concentration of the active centers is rather low. In this step, a second water molecule is adsorbed at the same active site, followed by discharge by electron uptake and chemical desorption of the H₂ from the surface. A Tafel slope of 40 mV dec⁻¹ is related to this step.^[58]



The Tafel reaction is often the dominant mechanism when a large number of active centers exist on the surface of the catalyst. Therefore, two adsorbed H atoms couple and produce H₂:



Additionally, the distance between the two active centers must be smaller than the *van der Waals* radius of two adsorbed H atoms. If this reaction is the limiting step, a Tafel slope of 30 mV dec⁻¹ is obtained.^[58]

7.3.6. Chronopotentiometry (CP) and Chronoamperometry (CA)

Long-term experiments were done to measure the stability of the electrocatalytic activity, for oxidation (OER) or reduction (HER) over time. CP measurements consist of the application of a constant current to the WE over a long period of time. A stable activity is considered if a stable current density of 10 mA cm⁻² (for CP) or stable overpotential at 10 mA cm⁻² (for CA) is observed for more than 12 h.^[52] In the absence of stirring, a diffusion layer builds up in the near area of the electrode. This layer grows over time and leads to a drop in the current. To prevent this phenomenon, the solution is stirred, and the mass transport limitation is kept to minimum. The potential at the WE is measured, producing a potential-time plot. The desired reaction (oxidation or reduction) will occur depending on the selected current.

The CP measurements were performed in 1 M KOH, an applied iR compensation of 85 % and at a constant current density of +10 mA cm⁻² (OER) and -10 mA cm⁻² (HER).

7.3.7. Electrochemical impedance spectroscopy (EIS)

Electrochemical impedance spectroscopy (EIS) is a powerful tool to study the mechanisms in electrochemical reactions, charge transfer processes in materials, and surface properties of electrodes. EIS provides information about the electrical conductivity of materials and allows conclusions about the ability of materials to store electrical energy and to transfer electrical charge.^[532]

We can use an electrical equivalent circuit (EEC) to represent an electrochemical reaction that takes place at the electrode/electrolyte interface:



Where O is the oxidant, n is the number of electrons transferred and R is the reduced product (reductant).^[533] The flow of current (charge transfer) through the interface due to the electrochemical reaction always contains both faradaic and non-faradaic components. The faradaic component arises from the electron transfer due to the reaction across the interface by overcoming an appropriate activation barrier, the polarization resistance (R_p) along the uncompensated solution resistance (R_s). The non-faradaic current results from the charging of the C_{dl} .^[533]

When the charge transfer takes place at the interface, the mass transport of the reactant and product determine the rate of electron transfer due to the changes of the concentration of reactant and product near the electrode surface. The mass transport provides another impedance (Warburg impedance, Z_w) which is observed as a peak on the CV plot. All the parameters mentioned until now can form an EEC, as described by Randles (see Figure 7.15a).^[533] The activation barrier at any potential is represented by R_p , and the barrier becomes the charge-transfer resistance, R_{ct} at the standard electrode potential.

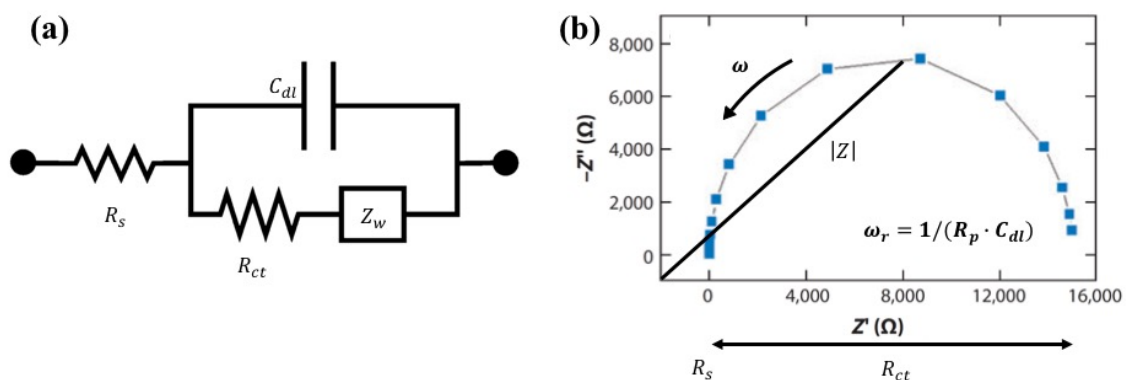


Figure 7.15. Randles equivalent circuit showing the R_p or R_{ct} , R_s , the C_{dl} and the Warburg impedance (Z_w). (b) Nyquist plot. Adapted from Chang and co-workers.^[533] © 2010 Annual Reviews, Inc.

The sample is measured in a three-electrode system. The potentiostat transmits an alternating voltage with varying frequency (ω) to the sample and generates a voltage signal proportional to the current flowing through the sample.^[532] An analyzer then

determines from the alternating current flowing through the sample and the alternating voltage generated by a generator, the impedance Z of the system.^[532] The frequency-dependent impedance Z consist of a rather complex expression that can be simplified at high frequencies ($\omega \rightarrow \infty$) as:

$$Z = Z' - jZ'' \quad \text{Equation 52}$$

Where Z' is the real impedance or $\text{Re}(Z)$ and the Z'' or $\text{Im}(Z)$ is the imaginary impedance and j is the current density. After the measurement, an equivalent circuit diagram must be determined for the system, which is done by evaluating the measurement data of certain frequency ranges or by using equivalent circuit diagrams of similar systems from the literature. In this case, the circuit shown in Figure 7.15 was used. This circuit is described by the equation:

$$Z(\omega) = R_s + \frac{R_{ct}}{1 + \omega^2 R_{ct}^2 C_{dl}^2} - j \frac{\omega R_{ct}^2 C_{dl}}{1 + \omega^2 R_{ct}^2 C_{dl}^2} = Z'(\omega) - jZ''(\omega) \quad \text{Equation 53}$$

R_p is equal to the R_{ct} , which indicates how well the charge exchange between the electrode and electrolyte can be. R_s is the R_u from the solution. The equation can be transformed to the following:

$$\left(Z' - \frac{2 \times R_s + R_{ct}}{2} \right)^2 + (Z'')^2 = \left(\frac{R_{ct}}{2} \right)^2 \quad \text{Equation 54}$$

Which is the equation of the semicircle of the Nyquist plot ($-Z''(\omega)$ vs. $-Z'(\omega)$), with center at $Z' = R_s + R_{ct}/2$ and radius $R_{ct}/2$. The resulting Nyquist plot shows the correspondence of these parameters to the observed plot.

EIS experiments were recorded at determined potential (see Table 7.1) to obtain the Nyquist plots. The amplitude of the sinusoidal wave was examined in a frequency range of 100 kHz to 1 mHz. The EIS curves obtained for amorphous and crystalline CoP were fitted to a Randles equivalent circuit, where R_s , CPE, and R_{ct} are the equivalent series resistance, CPE of the C_{dl} , and the charge transfer resistance, respectively.^[68,250,374] The EIS curves obtained for the electrodes constructed with crystalline FeAs, amorphous NiP, and amorphous NiAs were fitted to a circuit which contains two resistors R_1 and R_2 , and Q_2 a CPE (see Figure 7.16).

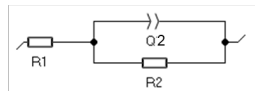


Figure 7.16. Randles equivalent circuit showing two resistors R_1 is the Ohmic resistance of the solution and electrode (R_s), R_2 is the charge transfer resistance (R_{ct}) and a CPE (Q_2).

This circuit has been previously used to fit TM-based systems during OER reaction conditions.^[534–537] The assignment of the elements is consistent in the literature and can be applied to the working systems: R_1 is the Ohmic resistance of the solution and electrode

(R_s), R_2 is the charge transfer resistance (R_{ct}) and a CPE (Q_2). This model is used because it fits better with the impedance behavior and the characteristics of the materials under study. Inhomogeneities in the surface of the electrodes result in non-ideal capacitance in the C_{dl} at the solid/electrolyte interface.^[535] Therefore, this model was preferred as it includes a CPE rather than a capacitor (C). Q_2 represents the value of a non-ideal capacitor and has units of $F \times s^{(a_2-1)}$, where a is an ideality factor which ranges from 0 to 1. When $a_2 = 1$ the interface is said to behave as an ideal capacitor ($Q_2 = C_{dl}$). Normally, a_2 is found in the range 0.8-1, and indicates non-ideal behavior due to surface roughness and irregularities in surface termination, porosity, and complexity in the double layer structure. Therefore, C_{dl} values are not possible to derive from this model and compare them to the results obtained from the voltammetric data.^[535]

Table 7.1. Applied potential for EIS experiments.

material	applied potential E vs. RHE (V)
amorphous CoP/NF	1.61
crystalline CoP/NF	1.61
crystalline FeAs/NF	1.51
crystalline FeAs/FTO	1.58
amorphous NiP/NF	1.50
amorphous NiP/FTO	1.65
amorphous NiAs/NF	1.50
amorphous NiAs/FTO	1.65

7.3.8. Determination of the electrochemically active surface area (ECSA)

The ECSA is the active area available for catalysis. The ECSA is the preferred measure of the surface area since the geometric surface area or the BET surface area, which only considers the area of the catalysts available to gas adsorption and depends on the size of the adsorbed gas molecule.^[41] In that way, it is possible to compare the activity of catalysts which are different in size, shape, morphology, topography and porous nature.^[41]

It is derived from the electrochemical double-layer capacitance of the catalytic surface.^[68] The C_{dl} was determined by measuring the non-Faradaic capacitive current associated with double-layer charging from the scan-rate dependence of CVs.^[68] From the already measured LSV for OER, a potential range in which no faradaic process (no catalysis) is occurring was selected (see Table 7.2). LSVs were done at different scan rates (5 mV s^{-1} to 200 mV s^{-1}). The WE was held at each potential vertex for 10 s before the beginning the next sweep. The charging current i (difference of anodic current, i_a and cathodic current, i_c) measured at the midpoint potential for each LSV curve were plotted as a function of the scan rate (5 mV s^{-1} to 200 mV s^{-1}). The double layer charging current is equal to the product of the scan rate, v , and the C_{dl} , as related on the following equation:

$$i = vC_{dl} \quad \text{Equation 55}$$

Thus, the slope of the of the plot of i as a function of ν corresponds to the C_{dl} .^[41,67,68] The ECSA is directly proportional to C_{dl} .^[250] The ECSA can be calculated from the following equation:

$$ECSA = \frac{C_{dl}}{C_s} \quad \text{Equation 56}$$

Where C_s is the specific capacitance of the sample or the capacitance of an atomically smooth planar surface of the material per unit area under identical electrolyte conditions. The following value was used: $C_s = 1.7 \text{ mF cm}^{-2}$ for 1 M KOH on NF and $C_s = 0.04 \text{ mF cm}^{-2}$ for similar conditions on FTO.^[538]

Table 7.2. Potential ranges and midpoint potential used for C_{dl} and ECSA determination on the investigated electrodes.

material	potential range <i>E vs. RHE (V)</i>	midpoint potential <i>E vs. RHE (V)</i>
amorphous CoP/NF	0.624-0.674	0.674
crystalline CoP/NF	0.624-0.674	0.674
crystalline FeAs/NF	0.881-0.931	0.906
amorphous NiP/NF	0.856-0.956	0.906
amorphous NiAs/NF	0.856-0.956	0.906

7.3.9. Overall water-splitting (OWS)

Overall water-splitting (OWS) experiments were done on a two electrode system in which the films of the materials deposited on NF were used as WE (anode) and CE (cathode). LSVs were performed without stirring and with an applied iR compensation of 85 %, applied before each experiment. The uncompensated resistance (R_u) was acquired by impedance spectroscopy at 100 MHz. The explored potential range was 1.0 to 2.0 vs. RHE. The CP measurements were performed in 1 M KOH at a constant current density of $+10 \text{ mA cm}^{-2}$. The overpotential was calculated from the difference of the potential to the thermodynamic potential for water-splitting, 1.23 V.^[539]

The OWS was also investigated using an inverted two-electrode cell under constant current density of 10 mA cm^{-2} in 1 M KOH for 1 h to allow the collection of H_2 and O_2 separately at atmospheric pressure. This experiment was done using an amorphous CoP || amorphous CoP electrolyser and a crystalline CoP || crystalline CoP electrolyser. The initial level of the electrolyte was noted and then the valves were closed. During electrolysis, because of evolution and collection of H_2 and O_2 at the upper part of the cell, the level of electrolyte goes down. The change in volume over time was noted and the ratio of the volumes of H_2 and O_2 was plotted over time.

7.3.10. Determination of the Faradaic efficiency (FE)

The Faradaic efficiency (FE) is the efficiency of an electrocatalyst to transfer electrons provided by an external circuit across the interface to the electroactive species to affect

the electrode reactions.^[52] The FE towards OER and HER in 1 M KOH was measured in a two-electrode configuration. Amorphous CoP/NF, crystalline CoP/NF, amorphous NiAs/NF and amorphous NiP/NF were used as cathode and anode and tested for OWS. Crystalline FeAs/NF was tested as anode for OER and Pt as cathode. Both electrodes were placed inside a closed electrochemical cell. The electrolyte and cell were first degassed with argon (Ar) for 1 hour under constant stirring. Afterward, a constant amount of current was applied on a 1 x 1 cm² for a specified period of time (see Table 7.3). At the end of electrolysis, the gaseous samples were drawn from the headspace by a gas-tight syringe and analyzed by a GC calibrated for H₂ and O₂. Each injection was repeated at least three times, and the average value is presented. The FE is calculated based on:

$$FE(H_2, \%) = \frac{V_{H_2} \times 2 \times F}{V_m \times j \times t} \times 100\% \quad \text{Equation 57}$$

$$FE(O_2, \%) = \frac{V_{O_2} \times 4 \times F}{V_m \times j \times t} \times 100\% \quad \text{Equation 58}$$

V_{H_2} and V_{O_2} are the evolved volume of H₂ and O₂, F is the Faraday constant (96485.33289 C mol⁻¹), V_m is the molar volume of the gas, j is the current density (in mA cm⁻²) and t is the time of electrolysis (in s).

The value of the FE relative to Pt can also be calculated, as Pt is known to show 100 % of FE for H₂.^[37-38] The value of FE is:

$$FE(O_{2,\%}) = \frac{V_{O_2}}{\frac{V_{H_2}}{2}} \times 100\% \quad \text{Equation 59}$$

Table 7.3. Experimental conditions of FE experiment on the tested materials.

anode	cathode	Current density (mA cm ⁻²)	time (s)
amorphous CoP/NF	amorphous CoP/NF	10	400
FeAs/NF	Pt	50	360
amorphous NiP/NF	amorphous NiP/NF	50	600
amorphous NiAs/NF	amorphous NiAs/NF	50	600
FeAs/NF*	Pt	50 and 100	360

*the experiment at 100 mA cm⁻² was done with a previously activated FeAs/NF by CV (1.2-1.7 V vs. RHE) for 2 h.

7.4. Experimental Data

7.4.1. Electrochemistry of complex 3

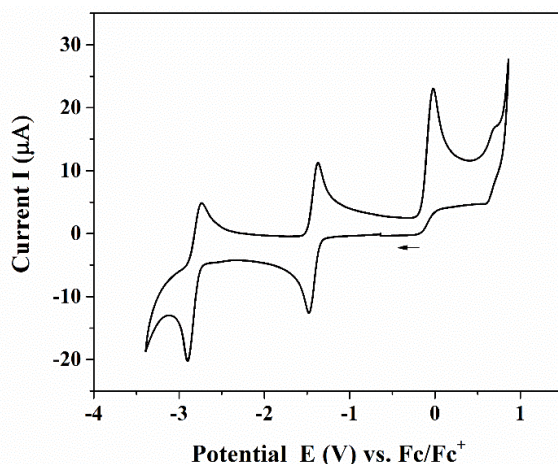


Figure 7.17. CV of molecular precursor **3** (1 mM in THF/ 0.3 M TBAPF₆). It shows two reversible redox events at $E_{1/2} = -1.42$ V (vs. Fc/Fc⁺) and $E_{1/2} = -2.81$ V (vs. Fc/Fc⁺) and one irreversible event at $E_{pa} = -0.03$ V (vs. Fc/Fc⁺) at a scan rate of $v = 100$ mV s⁻¹.

The reversibility of the redox events was confirmed by recording the CV at different scan rates from 50 to 800 mV s⁻¹ (see Figure 7.18 and Table 7.4).

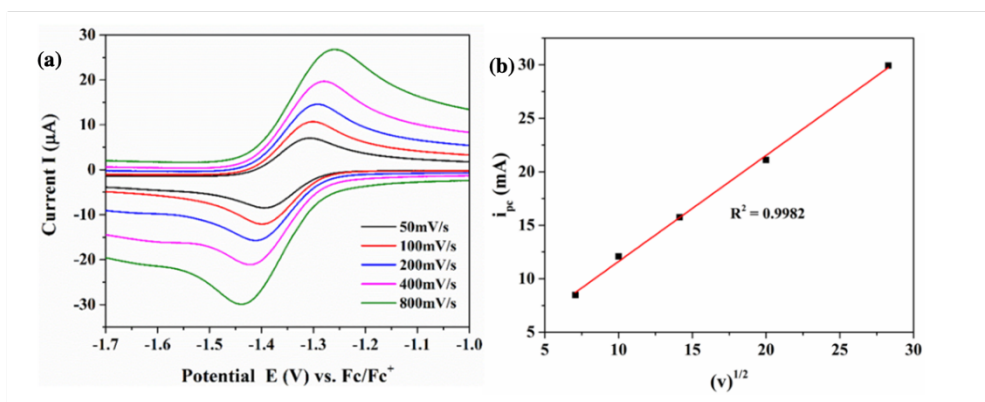


Figure 7.18. CV of precursor **3** (1 mM in THF/ 0.3 M TBAPF₆) centered at -1.42 V and recorded at different scan rates (50-800 mV s⁻¹) (a). The plot of forward peak current vs. square root of scan rates (b).

Table 7.4. Electrochemical data for the reversibility of the redox couple at $E_{1/2} = -1.42$ V (vs. Fc/Fc⁺) for complex **1**.

v (m Vs ⁻¹)	E_{pc} (V)	E_{pa} (V)	ΔE_p (V)	i_{pc} (μ A)	i_{pa} (μ A)	i_{pa}/i_{pc}	$i_{pc}/(v^{1/2})$
50	-1.393	-1.307	86	8	7	0.83	1.20
100	-1.399	-1.301	98	12	11	0.89	1.21
200	-1.411	-1.292	119	16	15	0.93	1.11
400	-1.423	-1.280	143	21	20	0.93	1.06
800	-1.439	-1.258	181	30	27	0.90	1.06

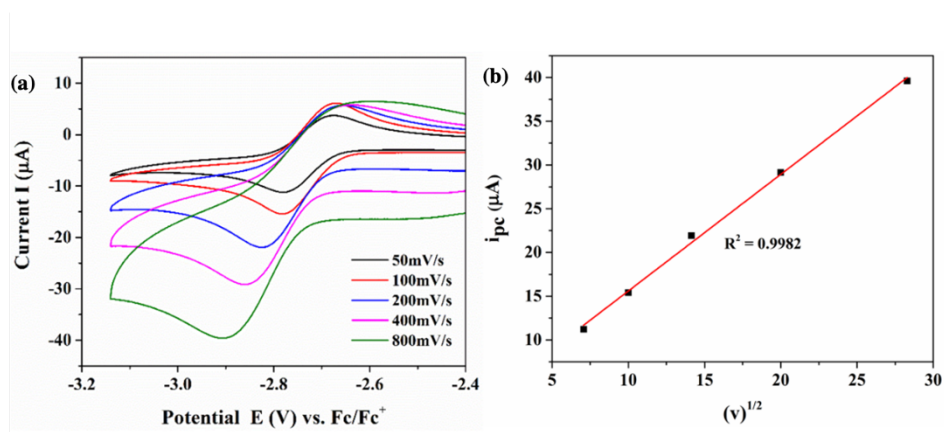


Figure 7.19. CV of precursor **3** (1 mM in THF/ 0.3 M TBAPF₆) centred at -2.81 V and recorded at different scan rates (50-800 mV s⁻¹) (a). The plot of forward peak current vs. square root of scan rates (b).

Table 7.5. Electrochemical data for the reversibility of the redox couple at $E_{1/2} = -2.81$ V (vs. Fc/Fc⁺) for complex **3**.

ν (m Vs ⁻¹)	E_{pc} (V)	E_{pa} (V)	ΔE_p (V)	i_{pc} (μA)	i_{pa} (μA)	i_{pa}/i_{pc}	$i_{pc}/(\nu^{1/2})$
50	-2.781	-2.675	106	11	4	0.33	1.59
100	-2.781	-2.672	110	15	6	0.40	1.54
200	-2.824	-2.655	169	22	6	0.26	1.55
400	-2.860	-2.637	223	29	6	0.20	1.46
800	-2.908	-2.597	311	40	6	0.16	1.40

7.4.2. Crystal data and structure refinements

Table 7.6. Crystal data and structure refinement for 6·2 tol.

Empirical formula	$C_{84}H_{122}N_4Fe_2As_2$	
Formula weight	1449.38	
Crystal system	monoclinic	
Space group	$P2_1/n$	
Unit cell dimensions	$a = 13.4664(2) \text{ \AA}$ $b = 14.7987(2) \text{ \AA}$ $c = 19.6270(3) \text{ \AA}$	$\alpha = 90^\circ$ $\beta = 91.2700(10)^\circ$ $\gamma = 90^\circ$
Cell Volume	$3910.41(10) \text{ \AA}^3$	
Z	2	
Temperature	150.(2) K	
Crystal size	0.226 x 0.208 x 0.064 mm ³	
Density	1.23 mg·m ⁻³	
$F(100)$	1544	
Absorption coefficient	4.240 mm ⁻¹	
Transmission max/min	1.00000/0.63919	
Refinement method	Full-matrix least-squares on F^2	
Absorption correction	Semi-empirical from equivalents	
Wavelength	1.54184 (Cu) \AA	
Collected/independent reflections	26275/7050 (0.0463)	
Index ranges	$-15 \leq h \leq 16$ $-17 \leq k \leq 12$ $-23 \leq l \leq 23$	
Theta range for data collection	3.741 - 67.496 °	
Completeness to theta = 67.49 °	100.00 %	
Data / restraints / parameter	7050 / 261 / 525	
$R_1/wR_2 [I > 2\sigma(I)]$	0.0364/0.0929	
R_1/wR_2 (all data)	0.0455/0.1001	
Goodness-of-fit on F^2	1.033	
Largest diff. peak and hole	0.612/-0.425 e· \AA^{-3}	

Table 7.7. Atomic coordinates ($\times 10^4$) and equivalent isotropic displacement parameters ($\text{\AA}^2 \times 10^3$) for kria. $U(\text{eq})$ is defined as one third of the trace of the orthogonalized U^{ij} tensor.

	x	y	z	U(eq)
As(1)	5070(1)	5383(1)	5522(1)	28(1)
Fe(1)	4719(1)	6233(1)	4502(1)	22(1)
N(1)	5594(1)	7164(1)	4073(1)	24(1)
N(2)	3429(1)	6857(1)	4274(1)	24(1)
C(12)	2607(2)	6577(2)	4679(1)	26(1)
C(2)	5232(2)	7798(1)	3650(1)	25(1)
C(4)	3362(2)	7540(2)	3825(1)	26(1)
C(24)	6621(2)	7119(2)	4294(1)	27(1)
C(3)	4210(2)	7890(2)	3519(1)	27(1)
C(13)	2012(2)	5841(2)	4473(1)	32(1)
C(25)	7285(2)	6558(2)	3950(1)	34(1)
C(17)	2435(2)	7033(2)	5294(1)	37(1)
C(1)	5850(2)	8507(2)	3234(1)	32(1)
C(14)	1208(2)	5613(2)	4873(1)	40(1)
C(29)	6933(2)	7616(2)	4872(1)	36(1)
C(15)	992(2)	6095(2)	5454(1)	43(1)
C(26)	8282(2)	6572(2)	4153(2)	46(1)
C(5)	2386(2)	8025(2)	3568(1)	36(1)
C(16)	1604(2)	6788(2)	5663(1)	41(1)
C(27)	8612(2)	7113(2)	4682(2)	53(1)
C(11)	2250(2)	7821(2)	2803(1)	49(1)
C(6)	5445(2)	9466(2)	3353(2)	50(1)
C(33)	6966(2)	5961(2)	3356(1)	43(1)
C(28)	7943(2)	7613(2)	5044(2)	47(1)
C(21)	2201(2)	5303(2)	3832(1)	45(1)
C(10)	2509(2)	9053(2)	3666(2)	48(1)
C(7)	5699(3)	8280(2)	2474(1)	55(1)
C(35)	7196(2)	4970(2)	3509(2)	47(1)
C(23)	2340(2)	4301(2)	3987(2)	53(1)
C(8)	6970(2)	8575(2)	3377(2)	48(1)
C(9)	1397(2)	7784(2)	3905(2)	54(1)
C(30)	6269(8)	8189(5)	5260(4)	46(2)
C(18)	3093(3)	7786(2)	5561(2)	60(1)
C(22)	1353(3)	5396(2)	3295(2)	71(1)
C(20)	3603(2)	7507(3)	6234(2)	68(1)
C(34)	7445(4)	6208(2)	2683(2)	80(1)
C(32)	6238(7)	7847(5)	5998(4)	51(2)
C(19)	2518(4)	8672(2)	5667(2)	82(1)
C(31)	6597(7)	9185(3)	5261(3)	67(2)
C(36)	687(4)	10472(4)	5733(3)	86(2)

C(37)	212(4)	10007(4)	6330(3)	52(1)
C(41)	-212(9)	9985(6)	7512(4)	68(2)
C(40)	-685(8)	9166(5)	7421(3)	66(2)
C(42)	233(9)	10407(5)	6967(4)	58(2)
C(39)	-679(5)	8748(4)	6789(3)	58(1)
C(38)	-226(4)	9167(4)	6247(3)	50(1)
C(36B)	523(10)	11454(11)	7223(9)	88(4)
C(37B)	396(11)	10219(13)	6426(11)	80(5)
C(41B)	-400(30)	9973(18)	7462(12)	74(5)
C(40B)	-640(20)	9122(18)	7259(13)	87(5)
C(42B)	150(20)	10510(14)	7055(12)	76(5)
C(39B)	-421(19)	8842(16)	6622(13)	95(6)
C(38B)	109(14)	9385(15)	6209(10)	96(5)
C(31B)	5811(11)	9019(6)	5152(5)	55(3)
C(30B)	6098(15)	8059(7)	5380(7)	35(3)
C(32B)	6400(14)	8118(9)	6138(7)	52(3)

Table 7.8. Bond lengths [Å] and angles [°] for 6·2 tol.

As(1)-As(1)#1	2.3447(5)	C(27)-C(28)	1.376(5)
As(1)-Fe(1)	2.4023(4)	C(27)-H(27)	0.95
As(1)-Fe(1)#1	2.4087(4)	C(11)-H(11A)	0.98
Fe(1)-N(2)	2.0085(18)	C(11)-H(11B)	0.98
Fe(1)-N(1)	2.0096(18)	C(11)-H(11C)	0.98
N(1)-C(2)	1.338(3)	C(6)-H(6A)	0.98
N(1)-C(24)	1.443(3)	C(6)-H(6B)	0.98
N(2)-C(4)	1.342(3)	C(6)-H(6C)	0.98
N(2)-C(12)	1.438(3)	C(33)-C(34)	1.526(4)
C(12)-C(13)	1.407(3)	C(33)-C(35)	1.529(4)
C(12)-C(17)	1.407(3)	C(33)-H(33)	1
C(2)-C(3)	1.401(3)	C(28)-H(28)	0.95
C(2)-C(1)	1.577(3)	C(21)-C(23)	1.525(4)
C(4)-C(3)	1.402(3)	C(21)-C(22)	1.543(4)
C(4)-C(5)	1.571(3)	C(21)-H(21)	1
C(24)-C(25)	1.404(3)	C(10)-H(10A)	0.98
C(24)-C(29)	1.408(3)	C(10)-H(10B)	0.98
C(3)-H(3)	0.95	C(10)-H(10C)	0.98
C(13)-C(14)	1.392(3)	C(7)-H(7A)	0.98
C(13)-C(21)	1.516(4)	C(7)-H(7B)	0.98
C(25)-C(26)	1.392(4)	C(7)-H(7C)	0.98
C(25)-C(33)	1.518(4)	C(35)-H(35A)	0.98
C(17)-C(16)	1.394(4)	C(35)-H(35B)	0.98
C(17)-C(18)	1.510(4)	C(35)-H(35C)	0.98
C(1)-C(8)	1.531(4)	C(23)-H(23A)	0.98
C(1)-C(7)	1.538(4)	C(23)-H(23B)	0.98
C(1)-C(6)	1.540(3)	C(23)-H(23C)	0.98
C(14)-C(15)	1.380(4)	C(8)-H(8A)	0.98
C(14)-H(14)	0.95	C(8)-H(8B)	0.98
C(29)-C(28)	1.393(4)	C(8)-H(8C)	0.98
C(29)-C(30)	1.458(11)	C(9)-H(9A)	0.98
C(29)-C(30B)	1.654(19)	C(9)-H(9B)	0.98
C(15)-C(16)	1.373(4)	C(9)-H(9C)	0.98
C(15)-H(15)	0.95	C(30)-C(32)	1.537(6)
C(26)-C(27)	1.376(4)	C(30)-C(31)	1.539(6)
C(26)-H(26)	0.95	C(30)-H(30)	1
C(5)-C(11)	1.540(4)	C(18)-C(20)	1.532(5)
C(5)-C(10)	1.541(4)	C(18)-C(19)	1.540(5)
C(5)-C(9)	1.542(4)	C(18)-H(18)	1
C(16)-H(16)	0.95	C(22)-H(22A)	0.98

C(22)-H(22B)	0.98	C(40B)-H(40B)	0.95
C(22)-H(22C)	0.98	C(39B)-C(38B)	1.356(13)
C(20)-H(20A)	0.98	C(39B)-H(39B)	0.95
C(20)-H(20B)	0.98	C(38B)-H(38B)	0.95
C(20)-H(20C)	0.98	C(31B)-C(30B)	1.535(8)
C(34)-H(34A)	0.98	C(31B)-H(31D)	0.98
C(34)-H(34B)	0.98	C(31B)-H(31E)	0.98
C(34)-H(34C)	0.98	C(31B)-H(31F)	0.98
C(32)-H(32A)	0.98	C(30B)-C(32B)	1.537(7)
C(32)-H(32B)	0.98	C(30B)-H(30B)	1
C(32)-H(32C)	0.98	C(32B)-H(32D)	0.98
C(19)-H(19A)	0.98	C(32B)-H(32E)	0.98
C(19)-H(19B)	0.98	C(32B)-H(32F)	0.98
C(19)-H(19C)	0.98	As(1)#1-As(1)-Fe(1)	60.969(13)
C(31)-H(31A)	0.98	As(1)#1-As(1)-Fe(1)#1	60.695(13)
C(31)-H(31B)	0.98	Fe(1)-As(1)-Fe(1)#1	121.664(12)
C(31)-H(31C)	0.98	N(2)-Fe(1)-N(1)	95.95(7)
C(36)-C(37)	1.514(7)	N(2)-Fe(1)-As(1)	125.38(5)
C(36)-H(36A)	0.98	N(1)-Fe(1)-As(1)	126.97(5)
C(36)-H(36B)	0.98	N(2)-Fe(1)-As(1)#1	123.66(5)
C(36)-H(36C)	0.98	N(1)-Fe(1)-As(1)#1	127.04(5)
C(37)-C(42)	1.382(5)	As(1)-Fe(1)-As(1)#1	58.335(12)
C(37)-C(38)	1.384(5)	C(2)-N(1)-C(24)	123.56(18)
C(41)-C(40)	1.380(6)	C(2)-N(1)-Fe(1)	122.16(15)
C(41)-C(42)	1.386(6)	C(24)-N(1)-Fe(1)	114.17(13)
C(41)-H(41)	0.95	C(4)-N(2)-C(12)	122.56(18)
C(40)-C(39)	1.387(5)	C(4)-N(2)-Fe(1)	122.50(15)
C(40)-H(40)	0.95	C(12)-N(2)-Fe(1)	114.65(13)
C(42)-H(42)	0.95	C(13)-C(12)-C(17)	121.0(2)
C(39)-C(38)	1.385(5)	C(13)-C(12)-N(2)	120.3(2)
C(39)-H(39)	0.95	C(17)-C(12)-N(2)	118.7(2)
C(38)-H(38)	0.95	N(1)-C(2)-C(3)	121.6(2)
C(36B)-C(42B)	1.520(11)	N(1)-C(2)-C(1)	126.8(2)
C(36B)-H(36D)	0.98	C(3)-C(2)-C(1)	111.59(19)
C(36B)-H(36E)	0.98	N(2)-C(4)-C(3)	121.1(2)
C(36B)-H(36F)	0.98	N(2)-C(4)-C(5)	126.8(2)
C(37B)-C(42B)	1.357(13)	C(3)-C(4)-C(5)	112.11(19)
C(37B)-C(38B)	1.358(13)	C(25)-C(24)-C(29)	121.0(2)
C(37B)-H(37B)	0.95	C(25)-C(24)-N(1)	119.9(2)
C(41B)-C(40B)	1.357(13)	C(29)-C(24)-N(1)	119.0(2)
C(41B)-C(42B)	1.361(13)	C(2)-C(3)-C(4)	133.8(2)
C(41B)-H(41B)	0.95	C(2)-C(3)-H(3)	113.1
C(40B)-C(39B)	1.357(13)	C(4)-C(3)-H(3)	113.1

C(14)-C(13)-C(12)	118.0(2)	H(11A)-C(11)-H(11B)	109.5
C(14)-C(13)-C(21)	119.3(2)	C(5)-C(11)-H(11C)	109.5
C(12)-C(13)-C(21)	122.7(2)	H(11A)-C(11)-H(11C)	109.5
C(26)-C(25)-C(24)	118.2(3)	H(11B)-C(11)-H(11C)	109.5
C(26)-C(25)-C(33)	119.0(2)	C(1)-C(6)-H(6A)	109.5
C(24)-C(25)-C(33)	122.8(2)	C(1)-C(6)-H(6B)	109.5
C(16)-C(17)-C(12)	118.0(2)	H(6A)-C(6)-H(6B)	109.5
C(16)-C(17)-C(18)	118.9(2)	C(1)-C(6)-H(6C)	109.5
C(12)-C(17)-C(18)	123.0(2)	H(6A)-C(6)-H(6C)	109.5
C(8)-C(1)-C(7)	107.5(2)	H(6B)-C(6)-H(6C)	109.5
C(8)-C(1)-C(6)	105.2(2)	C(25)-C(33)-C(34)	114.0(3)
C(7)-C(1)-C(6)	108.0(2)	C(25)-C(33)-C(35)	110.8(2)
C(8)-C(1)-C(2)	118.5(2)	C(34)-C(33)-C(35)	108.2(2)
C(7)-C(1)-C(2)	107.2(2)	C(25)-C(33)-H(33)	107.9
C(6)-C(1)-C(2)	110.0(2)	C(34)-C(33)-H(33)	107.9
C(15)-C(14)-C(13)	121.4(3)	C(35)-C(33)-H(33)	107.9
C(15)-C(14)-H(14)	119.3	C(27)-C(28)-C(29)	121.6(3)
C(13)-C(14)-H(14)	119.3	C(27)-C(28)-H(28)	119.2
C(28)-C(29)-C(24)	117.7(3)	C(29)-C(28)-H(28)	119.2
C(28)-C(29)-C(30)	118.8(4)	C(13)-C(21)-C(23)	111.5(2)
C(24)-C(29)-C(30)	123.3(4)	C(13)-C(21)-C(22)	112.6(3)
C(28)-C(29)-C(30B)	121.9(6)	C(23)-C(21)-C(22)	108.0(2)
C(24)-C(29)-C(30B)	119.9(6)	C(13)-C(21)-H(21)	108.2
C(16)-C(15)-C(14)	119.7(2)	C(23)-C(21)-H(21)	108.2
C(16)-C(15)-H(15)	120.1	C(22)-C(21)-H(21)	108.2
C(14)-C(15)-H(15)	120.1	C(5)-C(10)-H(10A)	109.5
C(27)-C(26)-C(25)	121.2(3)	C(5)-C(10)-H(10B)	109.5
C(27)-C(26)-H(26)	119.4	H(10A)-C(10)-H(10B)	109.5
C(25)-C(26)-H(26)	119.4	C(5)-C(10)-H(10C)	109.5
C(11)-C(5)-C(10)	109.0(2)	H(10A)-C(10)-H(10C)	109.5
C(11)-C(5)-C(9)	106.7(2)	H(10B)-C(10)-H(10C)	109.5
C(10)-C(5)-C(9)	105.4(2)	C(1)-C(7)-H(7A)	109.5
C(11)-C(5)-C(4)	107.7(2)	C(1)-C(7)-H(7B)	109.5
C(10)-C(5)-C(4)	109.0(2)	H(7A)-C(7)-H(7B)	109.5
C(9)-C(5)-C(4)	118.7(2)	C(1)-C(7)-H(7C)	109.5
C(15)-C(16)-C(17)	121.5(3)	H(7A)-C(7)-H(7C)	109.5
C(15)-C(16)-H(16)	119.2	H(7B)-C(7)-H(7C)	109.5
C(17)-C(16)-H(16)	119.2	C(33)-C(35)-H(35A)	109.5
C(28)-C(27)-C(26)	119.9(3)	C(33)-C(35)-H(35B)	109.5
C(28)-C(27)-H(27)	120.1	H(35A)-C(35)-H(35B)	109.5
C(26)-C(27)-H(27)	120.1	C(33)-C(35)-H(35C)	109.5
C(5)-C(11)-H(11A)	109.5	H(35A)-C(35)-H(35C)	109.5
C(5)-C(11)-H(11B)	109.5	H(35B)-C(35)-H(35C)	109.5

C(21)-C(23)-H(23A)	109.5	C(33)-C(34)-H(34B)	109.5
C(21)-C(23)-H(23B)	109.5	H(34A)-C(34)-H(34B)	109.5
H(23A)-C(23)-H(23B)	109.5	C(33)-C(34)-H(34C)	109.5
C(21)-C(23)-H(23C)	109.5	H(34A)-C(34)-H(34C)	109.5
H(23A)-C(23)-H(23C)	109.5	H(34B)-C(34)-H(34C)	109.5
H(23B)-C(23)-H(23C)	109.5	C(30)-C(32)-H(32A)	109.5
C(1)-C(8)-H(8A)	109.5	C(30)-C(32)-H(32B)	109.5
C(1)-C(8)-H(8B)	109.5	H(32A)-C(32)-H(32B)	109.5
H(8A)-C(8)-H(8B)	109.5	C(30)-C(32)-H(32C)	109.5
C(1)-C(8)-H(8C)	109.5	H(32A)-C(32)-H(32C)	109.5
H(8A)-C(8)-H(8C)	109.5	H(32B)-C(32)-H(32C)	109.5
H(8B)-C(8)-H(8C)	109.5	C(18)-C(19)-H(19A)	109.5
C(5)-C(9)-H(9A)	109.5	C(18)-C(19)-H(19B)	109.5
C(5)-C(9)-H(9B)	109.5	H(19A)-C(19)-H(19B)	109.5
H(9A)-C(9)-H(9B)	109.5	C(18)-C(19)-H(19C)	109.5
C(5)-C(9)-H(9C)	109.5	H(19A)-C(19)-H(19C)	109.5
H(9A)-C(9)-H(9C)	109.5	H(19B)-C(19)-H(19C)	109.5
H(9B)-C(9)-H(9C)	109.5	C(30)-C(31)-H(31A)	109.5
C(29)-C(30)-C(32)	109.3(6)	C(30)-C(31)-H(31B)	109.5
C(29)-C(30)-C(31)	112.3(7)	H(31A)-C(31)-H(31B)	109.5
C(32)-C(30)-C(31)	109.1(6)	C(30)-C(31)-H(31C)	109.5
C(29)-C(30)-H(30)	108.7	H(31A)-C(31)-H(31C)	109.5
C(32)-C(30)-H(30)	108.7	H(31B)-C(31)-H(31C)	109.5
C(31)-C(30)-H(30)	108.7	C(37)-C(36)-H(36A)	109.5
C(17)-C(18)-C(20)	110.4(3)	C(37)-C(36)-H(36B)	109.5
C(17)-C(18)-C(19)	112.5(3)	H(36A)-C(36)-H(36B)	109.5
C(20)-C(18)-C(19)	109.2(3)	C(37)-C(36)-H(36C)	109.5
C(17)-C(18)-H(18)	108.2	H(36A)-C(36)-H(36C)	109.5
C(20)-C(18)-H(18)	108.2	H(36B)-C(36)-H(36C)	109.5
C(19)-C(18)-H(18)	108.2	C(42)-C(37)-C(38)	119.4(3)
C(21)-C(22)-H(22A)	109.5	C(42)-C(37)-C(36)	120.3(5)
C(21)-C(22)-H(22B)	109.5	C(38)-C(37)-C(36)	120.2(5)
H(22A)-C(22)-H(22B)	109.5	C(40)-C(41)-C(42)	120.2(4)
C(21)-C(22)-H(22C)	109.5	C(40)-C(41)-H(41)	119.9
H(22A)-C(22)-H(22C)	109.5	C(42)-C(41)-H(41)	119.9
H(22B)-C(22)-H(22C)	109.5	C(41)-C(40)-C(39)	119.6(4)
C(18)-C(20)-H(20A)	109.5	C(41)-C(40)-H(40)	120.2
C(18)-C(20)-H(20B)	109.5	C(39)-C(40)-H(40)	120.2
H(20A)-C(20)-H(20B)	109.5	C(37)-C(42)-C(41)	120.3(4)
C(18)-C(20)-H(20C)	109.5	C(37)-C(42)-H(42)	119.9
H(20A)-C(20)-H(20C)	109.5	C(41)-C(42)-H(42)	119.9
H(20B)-C(20)-H(20C)	109.5	C(38)-C(39)-C(40)	120.0(4)
C(33)-C(34)-H(34A)	109.5	C(38)-C(39)-H(39)	120

C(40)-C(39)-H(39)	120	C(30B)-C(32B)-H(32F)	109.5
C(37)-C(38)-C(39)	120.3(4)	H(32D)-C(32B)-H(32F)	109.5
C(37)-C(38)-H(38)	119.8	H(32E)-C(32B)-H(32F)	109.5
C(39)-C(38)-H(38)	119.8	Symmetry transformations used to generate equivalent atoms: #1 -x+1,-y+1,-z+1	
C(42B)-C(36B)-H(36D)	109.5		
C(42B)-C(36B)-H(36E)	109.5		
H(36D)-C(36B)-H(36E)	109.5		
C(42B)-C(36B)-H(36F)	109.5		
H(36D)-C(36B)-H(36F)	109.5		
H(36E)-C(36B)-H(36F)	109.5		
C(42B)-C(37B)-C(38B)	119.9(5)		
C(42B)-C(37B)-H(37B)	120		
C(38B)-C(37B)-H(37B)	120		
C(40B)-C(41B)-C(42B)	119.9(6)		
C(40B)-C(41B)-H(41B)	120.1		
C(42B)-C(41B)-H(41B)	120.1		
C(41B)-C(40B)-C(39B)	119.9(6)		
C(41B)-C(40B)-H(40B)	120		
C(39B)-C(40B)-H(40B)	120		
C(37B)-C(42B)-C(41B)	119.9(5)		
C(37B)-C(42B)-C(36B)	113.7(17)		
C(41B)-C(42B)-C(36B)	126.4(17)		
C(38B)-C(39B)-C(40B)	119.9(5)		
C(38B)-C(39B)-H(39B)	120		
C(40B)-C(39B)-H(39B)	120		
C(39B)-C(38B)-C(37B)	120.1(5)		
C(39B)-C(38B)-H(38B)	119.9		
C(37B)-C(38B)-H(38B)	119.9		
C(30B)-C(31B)-H(31D)	109.5		
C(30B)-C(31B)-H(31E)	109.5		
H(31D)-C(31B)-H(31E)	109.5		
C(30B)-C(31B)-H(31F)	109.5		
H(31D)-C(31B)-H(31F)	109.5		
H(31E)-C(31B)-H(31F)	109.5		
C(31B)-C(30B)-C(32B)	106.8(10)		
C(31B)-C(30B)-C(29)	111.2(10)		
C(32B)-C(30B)-C(29)	115.9(13)		
C(31B)-C(30B)-H(30B)	107.5		
C(32B)-C(30B)-H(30B)	107.5		
C(29)-C(30B)-H(30B)	107.5		
C(30B)-C(32B)-H(32D)	109.5		
C(30B)-C(32B)-H(32E)	109.5		
H(32D)-C(32B)-H(32E)	109.5		

Table 7.9. Anisotropic displacement parameters ($\text{\AA}^2 \times 10^3$) for 6·2 tol. The anisotropic displacement factor exponent takes the form: $-2p^2[h^2 a^* U^{11} + \dots + 2 h k a^* b^* U^{12}]$.

	U^{11}	U^{22}	U^{33}	U^{23}	U^{13}	U^{12}
As(1)	37(1)	24(1)	24(1)	3(1)	3(1)	3(1)
Fe(1)	20(1)	21(1)	25(1)	5(1)	5(1)	1(1)
N(1)	21(1)	25(1)	26(1)	3(1)	7(1)	0(1)
N(2)	20(1)	27(1)	24(1)	3(1)	5(1)	3(1)
C(12)	18(1)	33(1)	29(1)	7(1)	6(1)	2(1)
C(2)	31(1)	21(1)	24(1)	0(1)	8(1)	-1(1)
C(4)	27(1)	26(1)	25(1)	2(1)	4(1)	5(1)
C(24)	24(1)	25(1)	32(1)	8(1)	6(1)	-3(1)
C(3)	31(1)	26(1)	25(1)	7(1)	4(1)	2(1)
C(13)	25(1)	41(1)	30(1)	7(1)	1(1)	-4(1)
C(25)	28(1)	41(1)	35(1)	14(1)	11(1)	5(1)
C(17)	37(1)	38(1)	36(1)	0(1)	13(1)	2(1)
C(1)	36(1)	26(1)	34(1)	7(1)	10(1)	-4(1)
C(14)	26(1)	56(2)	40(2)	10(1)	3(1)	-11(1)
C(29)	31(1)	27(1)	50(2)	4(1)	-2(1)	-5(1)
C(15)	25(1)	63(2)	42(2)	15(1)	12(1)	1(1)
C(26)	26(1)	57(2)	54(2)	20(1)	14(1)	10(1)
C(5)	28(1)	38(1)	42(1)	12(1)	5(1)	9(1)
C(16)	37(2)	49(2)	38(2)	3(1)	18(1)	7(1)
C(27)	22(1)	65(2)	71(2)	25(2)	-2(1)	-6(1)
C(11)	37(2)	64(2)	45(2)	12(1)	-9(1)	8(1)
C(6)	48(2)	28(1)	77(2)	10(1)	14(2)	-2(1)
C(33)	43(2)	57(2)	31(1)	2(1)	9(1)	22(1)
C(28)	33(2)	43(2)	65(2)	9(1)	-11(1)	-13(1)
C(21)	44(2)	55(2)	37(2)	-4(1)	8(1)	-22(1)
C(10)	45(2)	38(2)	62(2)	10(1)	6(1)	18(1)
C(7)	73(2)	62(2)	31(2)	6(1)	19(1)	-24(2)
C(35)	44(2)	50(2)	46(2)	0(1)	10(1)	9(1)
C(23)	45(2)	53(2)	60(2)	-12(2)	2(1)	-12(1)
C(8)	34(2)	45(2)	66(2)	28(1)	11(1)	-9(1)
C(9)	29(1)	64(2)	70(2)	30(2)	8(1)	19(1)
C(30)	38(4)	45(3)	55(3)	-17(3)	-9(4)	-6(3)
C(18)	68(2)	62(2)	50(2)	-23(2)	36(2)	-25(2)
C(22)	102(3)	68(2)	42(2)	6(2)	-23(2)	-26(2)
C(20)	41(2)	79(2)	85(3)	-48(2)	9(2)	-2(2)
C(34)	133(4)	63(2)	45(2)	13(2)	40(2)	40(2)
C(32)	50(4)	48(4)	57(4)	-21(3)	23(3)	-12(3)
C(19)	149(4)	46(2)	51(2)	-9(2)	19(2)	-3(2)
C(31)	105(6)	34(2)	62(3)	-15(2)	6(3)	6(3)
C(36)	68(4)	103(4)	87(3)	31(3)	12(3)	-22(3)

C(37)	36(3)	61(3)	59(2)	17(2)	-2(2)	3(2)
C(41)	71(6)	85(4)	47(2)	7(3)	-14(3)	12(4)
C(40)	76(4)	72(3)	52(3)	30(2)	15(3)	13(3)
C(42)	46(4)	55(3)	71(3)	8(2)	-13(3)	4(3)
C(39)	50(4)	57(3)	67(3)	18(2)	6(2)	3(2)
C(38)	34(3)	68(2)	49(2)	5(2)	3(2)	-3(2)
C(36B)	34(7)	130(10)	98(11)	19(8)	-23(7)	4(7)
C(37B)	34(8)	119(11)	87(9)	26(7)	-10(7)	42(8)
C(41B)	53(10)	100(10)	68(9)	23(7)	-24(7)	27(7)
C(40B)	56(11)	118(10)	84(11)	9(9)	-34(9)	7(9)
C(42B)	41(9)	106(10)	79(9)	27(7)	-19(7)	32(7)
C(39B)	67(13)	119(12)	99(13)	-1(9)	-22(11)	22(9)
C(38B)	53(12)	136(13)	98(10)	4(8)	-13(8)	34(10)
C(31B)	78(9)	37(4)	52(5)	-1(3)	8(5)	18(5)
C(30B)	38(7)	27(4)	39(5)	-14(4)	5(4)	6(4)
C(32B)	68(8)	45(7)	43(5)	-7(5)	-8(5)	4(6)

7.4.3. Amorphous CoP

Preparation:

To a three-necked round bottom Schlenk flask fitted with a temperature sensor and a condenser, 25 mL oleic acid (Fisher Scientific) was added. The solvent was degassed by a three-cycle freeze-pump method. The whole set up was degassed using vacuum followed by nitrogen refill three times and then the flask was heated to 300 °C. The precursor (0.47 g, 0.46 mmol) was dissolved in 5 mL of dry oleic acid at 30 °C in another flask. The solution was transferred to the three-necked flask at 300 °C by injection under inert conditions. The reaction temperature was maintained at 300 °C for one more hour and then the mixture was allowed to cool down naturally to room temperature. The whole reaction mixture was transferred into a centrifuge tube and centrifuged along with an additional 20 mL methanol at 9000 rpm to produce a black solid. Washing with methanol was repeated thrice more to remove any excess ligand and oleic acid. The precipitate was then washed with acetone and dried to store for further use.

Yield: 109.0 mg (97.8 %)

Characteristics: dark brown powder

IR (ATR-Diamond): the small bands between 1250 and 500 cm^{-1} could correspond to the stretching and bending vibrations of the phosphate group, originated from surface oxidation.^[160,282] The small peak around 600 cm^{-1} which appears on both materials is characteristic of the Co-O bond, which may be present as the sample contain O.^[282]

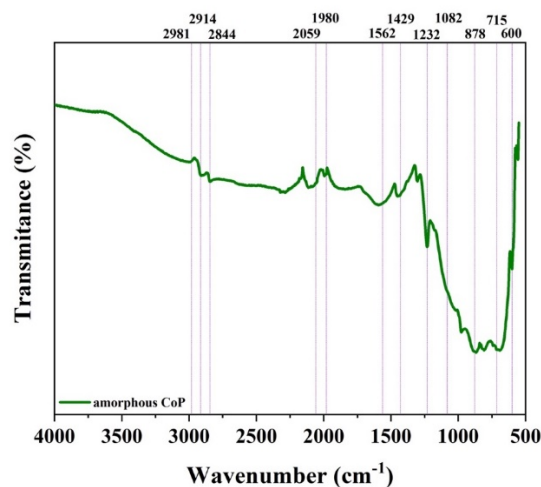


Figure 7.20. FT-IR of amorphous CoP. The small bands between 1250 and 500 cm^{-1} which could correspond to the stretching and bending vibrations of the phosphate group, originated from surface oxidation.^[160,282] The small peak around 600 cm^{-1} which appears on both materials is characteristic of the Co-O bond, which may be present as the samples contain O.^[282] The attained FT-IR spectra is in accordance with the other CoP based materials.

Table 7.10. Determination of C, H and O content by elemental analysis. The presence of C, H and N arise from the β -Diketiminato ligand of the precursor.

Material	% C	% H	% N
Amorphous CoP	6.49	0.61	0.98

7.4.4. Crystalline CoP

Preparation:

0.20 g (0.20 mmol) of the precursor were introduced in a quartz tube under an inert atmosphere and subsequently introduced on a tube furnace SR-A60-300/12 GERO (Neuhausen). The sample was then heated up at 10 $^{\circ}\text{C min}^{-1}$ from room temperature and held at 600 $^{\circ}\text{C}$ for 2 h under Ar. After cooling to room temperature, a black powder was collected and washed with acetone for several times. The use of a lower temperature (300 and 450 $^{\circ}\text{C}$) resulted in the formation of materials with a large amount of carbon due to the incomplete decomposition of molecular precursor (see Table 7.12 and Figure A.1.1).

Yield: 42.8 mg (90.2 %)

Characteristics: dark brown crystalline powder

Table 7.11. Reflex list of crystalline CoP.

Number	Position (2Theta (°))	h	k	l
1	31.62	0	1	1
2	36.32	1	1	1
3	46.20	1	1	2
4	48.15	2	1	1
5	48.44	2	0	2
6	56.84	3	0	1

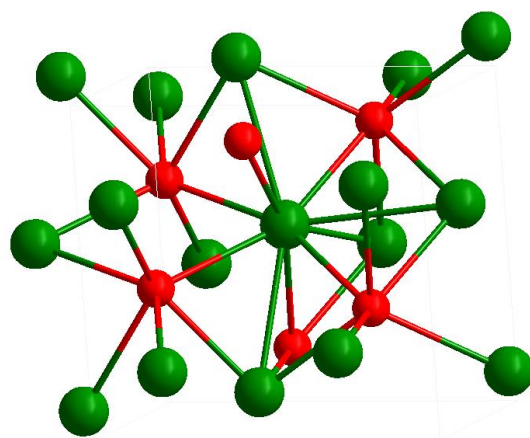


Figure 7.21. Representation of the crystal structure of CoP phase JCPDS 029-497, orthorhombic phase (*Pnma* (62) space group, $a = 5.077$, $c = 5.587$). Green and red spheres represent Co and P atoms, respectively.

Table 7.12. CHN analysis pyrolysis products from the molecular precursor obtained at 300 °C and 450 °C and 600 °C.

Pyrolysis temperature (°C)	% N	% C	% H
300	2.59	34.81	3.98
450	1.14	18.43	2.51
600	0.27	7.23	0.29

IR (ATR-Diamond): the small bands between 1250 and 500 cm^{-1} could correspond to the stretching and bending vibrations of the phosphate group, originated from surface oxidation.^[160,282] The small peak around 600 cm^{-1} which appears on both materials is characteristic of the Co-O bond, which may be present as the sample contain O.^[282]

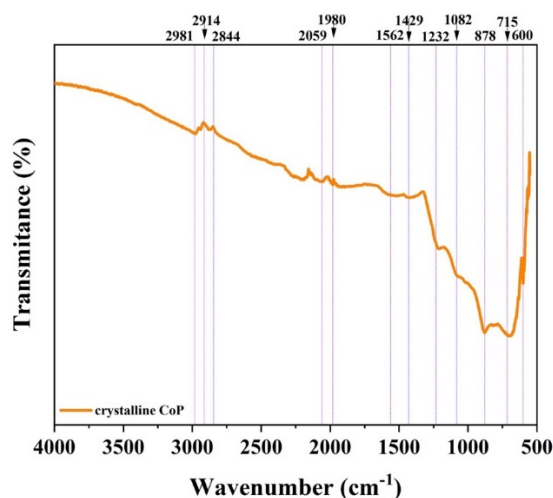


Figure 7.22. FT-IR of crystalline CoP. The small bands between 1250 and 500 cm^{-1} which could correspond to the stretching and bending vibrations of the phosphate group, originated from surface oxidation.^[160,282] The small peak around 600 cm^{-1} which appears on both materials is characteristic of the Co-O bond, which may be present as the samples contain O.^[282] The attained FT-IR spectra is in accordance with the other CoP based materials.

7.4.5. Crystalline FeAs

Preparation:

The modification of a previously developed procedure was used.^[250] To a three-necked round bottom Schlenk flask fitted with a temperature sensor and a condenser, 25 mL oleylamine (Sigma-Aldrich) was added. The solvent was previously degassed by a 3-cycle freeze-pump method and stored with molecular sieves (3 Å). The whole set up was degassed using a vacuum followed by nitrogen refill three times and then the flask was heated to 250 °C. The $\text{L}^{\text{B}}\text{FeAs}_2\text{FeL}^{\text{B}}$ precursor (1449.46 g mol^{-1} ; 150 mg; 0.103 mmol) was dissolved in 5 mL of dry oleylamine at 35 °C in another flask. The solution was transferred to the three-necked flask at 250 °C by injection under inert conditions. The reaction temperature was maintained at 250 °C for one more hour and then the mixture was allowed to cool down naturally to room temperature. The whole reaction mixture was transferred into a centrifuge tube and centrifuged along with additional 20 mL ethanol at 9000 rpm to produce a black solid. The mixture was placed 15 min in the ultrasonic bath to remove any excess ligand and oleylamine. Sonication and centrifugation cycles were repeated for four additional times. The precipitate was then washed with acetone and dried overnight at 60 °C and used for characterizations.

Yield: 24.0 mg (88.2 %)

Characteristics: black powder

Table 7.13. Reflex list of crystalline FeAs.

Number	Position (2Theta (°))	h	k	l
1	30.10	1	1	0
2	34.53	1	1	1
3	43.81	1	2	1
4	45.36	2	1	1
5	48.23	1	3	0
6	53.16	0	3	1
7	54.32	0	0	2
8	57.23	2	3	0
9	60.21	3	1	1
10	64.19	1	4	0
11	65.48	1	2	2
12	73.01	2	2	2
13	79.06	3	1	2

IR (ATR-Diamond): no strong absorption bands were observed in the measuring range.

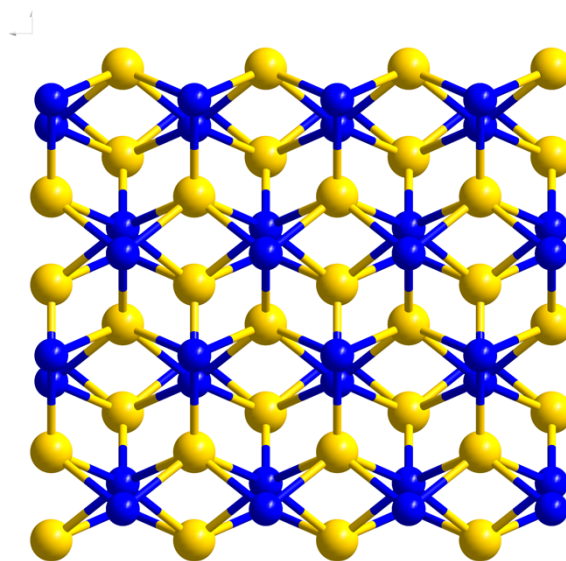


Figure 7.23. Representation of the crystal structure of FeAs (JCPDS 76-458), which belongs to the MnP structure type (orthorhombic, *Pnma* (62) space group, with lattice parameters $a = 5.442 \text{ \AA}$ and $c = 3.3727 \text{ \AA}$). Blue and yellow spheres represent Fe and As atoms, respectively.

Table 7.14. Determination of C, H and O content by elemental analysis. The presence of C, H, and N arises from the L^B ligand of the precursor.

% C	% H	% N
5.0038	0.479	0.009

7.4.6. Amorphous NiAs

Preparation:

200.3 mg (0.613 mmol) of $\text{NiBr}_2(\text{thf})_{1.5}$ and 185.5 mg (0.614 mmol) of $\text{NaOCAs} \cdot (\text{dioxane})_{2.1}$ were taken separately in 20 mL of dry THF in two Schlenk flasks at $-20\text{ }^\circ\text{C}$. Under vigorous stirring conditions, the later solution was slowly transferred (dropwise added over 30 min) to the former solution using a cannula to result in the formation of black precipitate. The mixture was allowed to stir for 4 h and then exposed to air. Then the mixture was centrifuged and washed three times with ethanol and one time with acetone ($4 \times 40\text{ mL}$) sequentially to remove any unreacted reagents. The resulting black powder was dried overnight at $60\text{ }^\circ\text{C}$ and used for characterizations.

Yield: 77.8 mg (95.0 %)

Characteristics: black powder

IR (ATR-Diamond): The most representative signals are related to surface oxidation from the NiAs due to contact with air. Signals related from metal-As vibrations could not be identified as they appear $< 500\text{ cm}^{-1}$.^[458,459] The broad peak at 3300 cm^{-1} and correspond to the stretching vibration of O-H. The peak at 1600 cm^{-1} could be attributed to vibrational modes of adsorbed water.^[457] The peaks at 800 cm^{-1} and 730 cm^{-1} could be related to surface oxidation symmetric stretch vibration $\nu(\text{As-O})$.^[540-543] The peak at 650 cm^{-1} is related to the stretching vibration of the As-OX (with $\text{X} = \text{H}^+$, cation or H_2O).^[544]

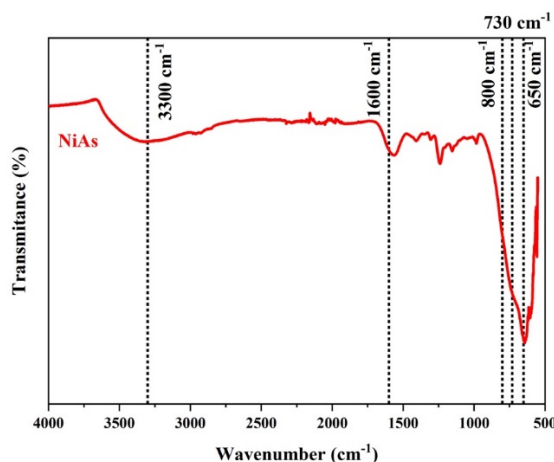


Figure 7.24. IR of amorphous NiAs.

7.4.7. Amorphous NiP

Preparation:

211.8 mg (0.648 mmol) of $\text{NiBr}_2(\text{thf})_{1.5}$ and 197 mg (0.652 mmol) of $\text{NaOCP} \cdot (\text{dioxane})_{2.5}$ were taken separately in 20 mL of dry THF in two Schlenk flasks at

-20 °C. Under vigorous stirring conditions, the later solution was slowly transferred (dropwise added over 30 min) to the former solution using a cannula to result in the formation of black precipitate. The mixture was allowed to stir for 4 h and then opened to air. Then the mixture was centrifuged and washed three times with ethanol and one time with acetone (4×40 mL) sequentially to remove any unreacted reagents. The resulting black-brown powder was dried overnight at 60 °C and used for characterizations.

Yield: 53.8 mg (92.5 %)

Characteristics: black powder

IR (ATR-Diamond): NiP shows the stretching vibration from the O-H bond is observed (ca. 3300 cm^{-1}). The peak at 1635 cm^{-1} could be attributed to vibrational modes of adsorbed water.^[457] Finally, the peaks at 1040 cm^{-1} and 920 cm^{-1} indicate the presence of $[\text{PO}_4]^{3-}$ and $[\text{HPO}_4]^{2-}$, respectively, confirming the surface oxidation.^[457]

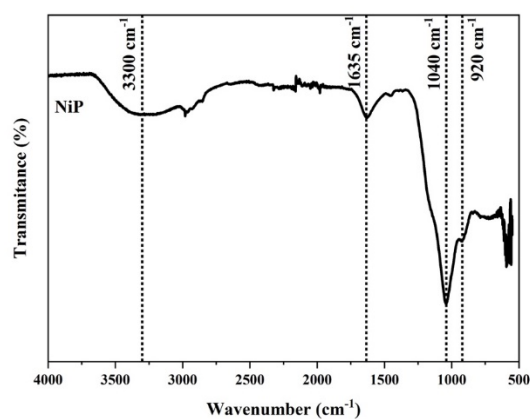


Figure 7.25. IR of amorphous NiP.

8. Appendix

A.1. Appendix of Chapter 3: Amorphous CoP vs. crystalline CoP

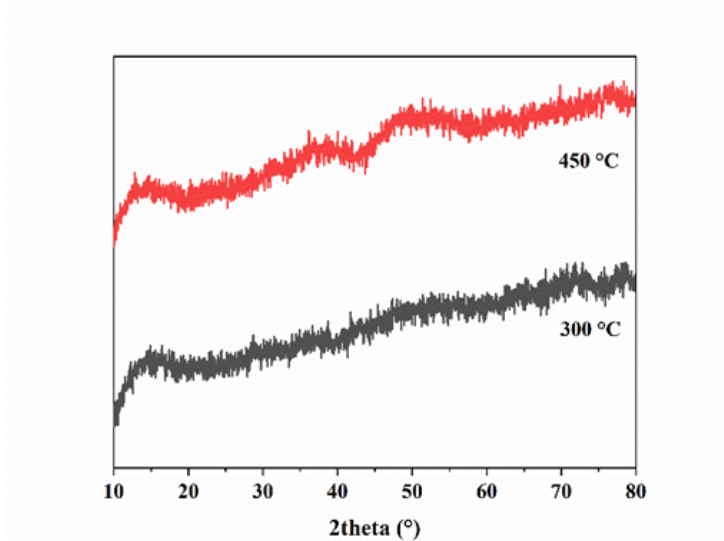


Figure A.1.1. Effect of pyrolysis temperature on the crystallinity of the resulting Co-P phase. The PXRD patterns of pyrolysis products from the molecular precursor obtained at 300 °C and 450 °C do not show any distinguishable peak, confirming that total decomposition does not occur until 600 °C.

Table A.1.1. Determination of the Co and P content in the prepared materials by ICP-AES.

Material	Co:P (ICP-AES)
Crystalline CoP	1:1.14
Amorphous CoP	1:1.05

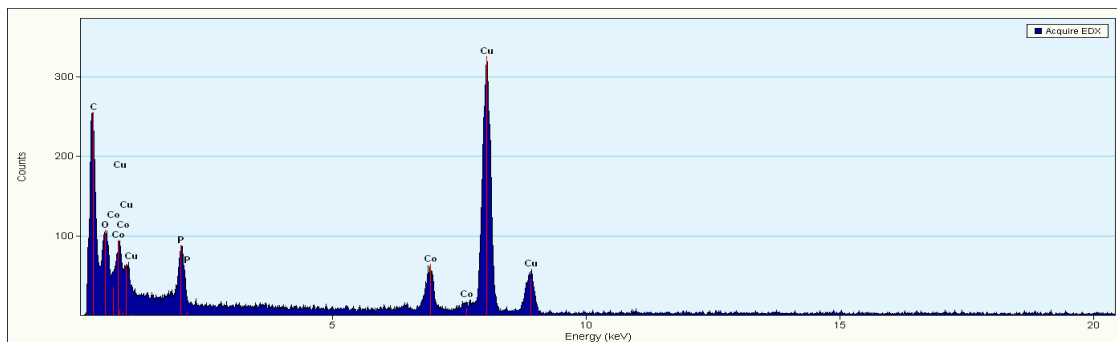


Figure A.1.2. EDX of amorphous CoP, which confirms the presence of Co and P. The presence of Cu peaks is due to the TEM grid (carbon film on 300 mesh Cu-grid). The EDX values of Co:P were ~1:1.

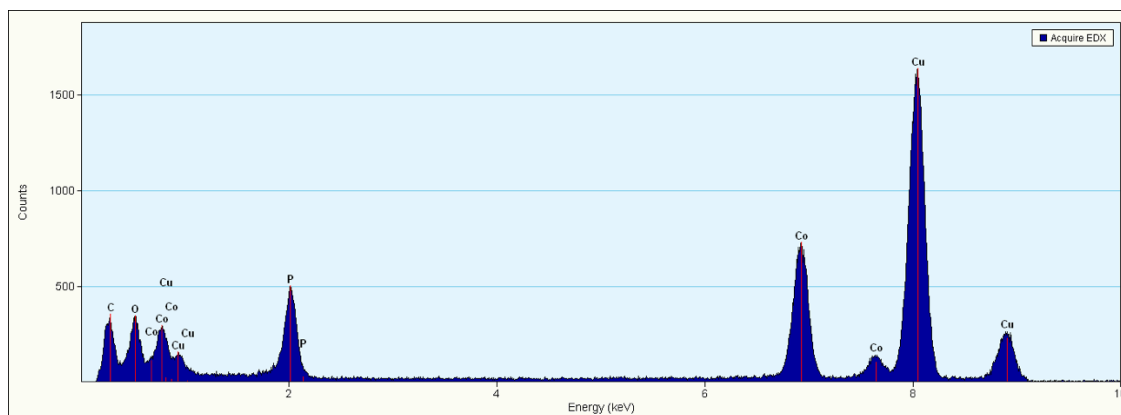


Figure A.1.3. EDX of crystalline CoP, which confirms the presence of Co and P. The presence of Cu peaks is due to the TEM grid (carbon film on 300 mesh Cu-grid). The EDX values of Co:P were \sim 1:1.

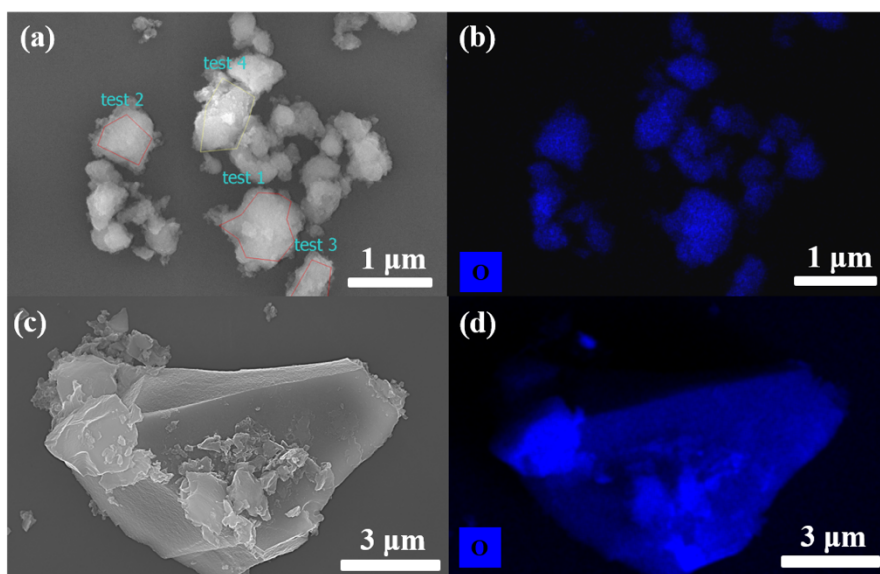


Figure A.1.4. SEM of amorphous and crystalline CoP and elemental mapping of O (blue). The used substrate was silicon wafer. The presence of O is due to the surface passivation.

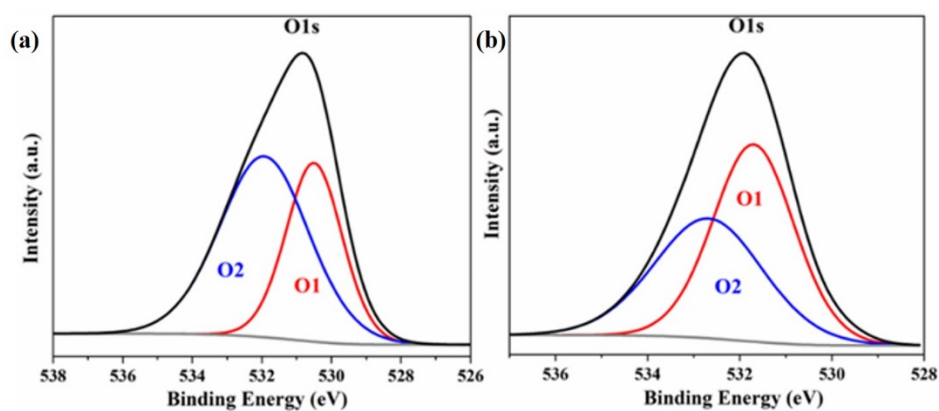


Figure A.1.5. High-resolution XPS spectra for O 1s for the as-prepared (a) amorphous CoP and (b) crystalline CoP.

Comparison of prepared materials activity for OER to other materials

Table A.1.2. Overpotentials at 10 mA cm⁻² of Co phosphide-based catalysts, non-noble TM-based catalysts, and non-noble TM-P-based catalysts at 1 M KOH for OER.

Catalyst	Current density (mA cm ⁻²)	Overpotential η (mV)	Reference
Amorphous CoP/NF	10	284	This work
	100	341	This work
Crystalline CoP/NF	10	305	This work
	100	392	This work
Amorphous CoP/FTO	10	360	This work
	100	414	This work
Crystalline CoP/FTO	10	414	This work
	100	592	This work
IrO₂/NF	10	287	This work
	100	413	This work
IrO₂/FTO	10	409	This work
	100	-	This work
Pt	10	654	This work
	100	-	This work
Ni ₁₁ (HPO ₃) ₈ (OH) ₆ /NF	10	232	[79]
Ni ₂ P/Ni/NF	10	200	[151]
Porous Co-P/phosphate thin film	10	330	[156]
Surface phosphate modified Co-P nanorod bundles	10	310	[160]
Ni ₂ P/NF	10	290	[161]
Ni ₂ P/FTO	10	400	[161]
Co Phosphide Nanorods	10	320	[162]
Ni _x P _y -325	10	320	[169]
CoP@GC	10	345	[171]
Porous Co Phosphide Polyhedrons	10	289	[173]
CoMnP	10	330	[177]
Co ₂ P/GCE	10	370	[177]
FeP/Au	10	290	[189]
Nanostructured Co-P based films	10	340	[238]
Core-Oxidized Amorphous Co-P	10	287	[239]
Amorphous Co-P films/Cu	10	345	[240]
CoP nanowire on Ti mesh	10	310	[254]
CoP hollow polyhedron	10	400	[259]
Co ₂ P/Co foil	10	319	[260]
Co phosphide/carbon dots composite	10	400	[262]
Co/Co ₂ P nanoparticles/NF	10	190	[263]
CoP mesoporous nanorods	10	290	[264]
CoP nanoneedle arrays/CC	10	281	[265]
CoP nanocubes	10	354	[267]
CoP nanoframes	10	323	[267]
Co-P/NC nano-Polyhedrons	10	319	[278]
CoP/Co ₂ P	10	317	[321]
Ni-P	10	300	[424]
FeCoNiP	10	200	[545]
CoP/NF	10	300	[546]

CoP NPs@P-doped dual carbon shells	10	280	[547]
Hollow CoP@N-doped carbon	10	320	[548]
CoP NPs@N-doped porous carbon spheres	10	350	[549]
Co _x P@ N-doped carbon porous polyhedrons	10	380	[550]
Fe-Ni-P hybrid catalyst	10	154	[551]
CoP/NCNHP	10	310	[552]
CoP@NG	10	354	[553]
CoP/rGP-400	10	340	[554]
Co-P@NC-800	10	370	[555]
Co ₃ O ₄ / NiCo ₂ O ₄ DSNCs	10	340	[556]
CoCo LDH	10	393	[557]
NiFe-LDH	10	300	[557]
NiCo-LDH	10	335	[557]
NiFe oxides	10	300	[558]
FeCoW oxy-hydroxides	10	191	[559]
Co ₃ O ₄ /Au	10	400	[560]
CoCr ₂ O ₄	10	422	[561]
CoCr ₂ O ₄ /CNT	10	326	[561]
FeNi-rGO LDH	10	195	[562]
FeNi-GO LDH	10	210	[562]
CoS	10	361	[563]
(Ni,Co)Se _{0.85} -NiCo LDH	10	216	[564]
Ni-P film	10	344	[565]

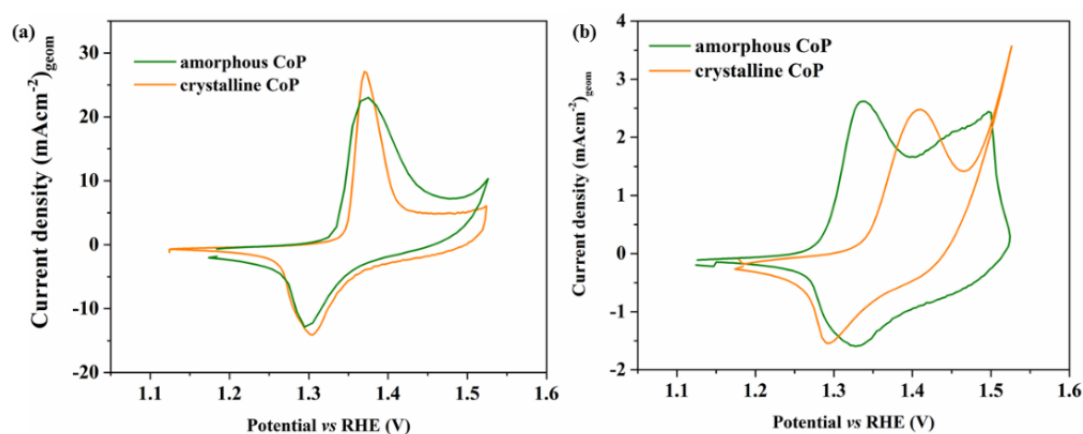


Figure A.1.6. CV (scan rate 10 mV s^{-1} , iR compensation at 85 %) of amorphous and crystalline CoP and on (a) NF and on (b) FTO measured between 1.12 V and 1.52 V (vs. RHE) in 1 M KOH. The materials on both substrates featured a pair of anodic and cathodic peaks corresponding to the reaction of oxidation of the Co hydroxide in alkaline media: $\text{Co}(\text{OH})_2 + \text{OH}^- \rightarrow \text{CoOOH} + \text{H}_2\text{O} + \text{e}^-$. Eventually, the produced CoOOH could be furtherly oxidized to the CoO₂ during anodic polarization: $\text{CoOOH} + \text{OH}^- \rightarrow \text{CoO}_2 + \text{H}_2\text{O} + \text{e}^-$.^[293] These peaks have been also often observed for most of the first-row TM-based materials, which exhibited M(OH)₂/MOOH phase formation at potentials between ca. 1.1 V and 1.4 V (vs. NHE).^[293]

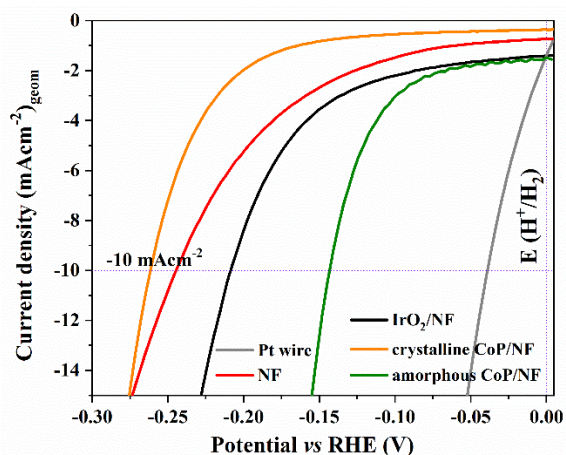


Figure A.1.7. (a) Polarization curves of HER of different CoP materials and commercial noble metal-based catalysts deposited on NF with a scan rate of 10 mV s^{-1} in 1 M KOH (iR compensation: 85 %).

Comparison of prepared materials activity for HER to other materials

Table A.1.3. Activity comparison of as-prepared CoP materials with other highly efficient non-noble TM-based, Co phosphide-based catalysts, non-noble TM-Ps-based catalysts, Co phosphide-based catalysts at 1 M KOH for HER.

Catalyst	Current density (mA cm^{-2})	Overpotential η (mV)	Reference
Amorphous CoP/NF	-10	143	This work
Crystalline CoP/NF	-10	195	This work
Amorphous CoP/FTO	-10	228	This work
Crystalline CoP/FTO	-10	377	This work
IrO₂/NF	-10	209	This work
IrO₂/FTO	-10	430	This work
Pt	-10	39	This work
Ni₂P/NF	-10	85	[26]
Ni₁₂P₅/NF	-10	170	[26]
Ni₁₁(HPO₃)₈(OH)₆/NF	-10	121	[79]
Ni_xP_y-325	-20	160	[169]
Porous Co Phosphide Polyhedrons	-10	116	[173]
Nanostructured Co-P films	-10	196	[238]
Co-phosphorus derived films/Cu	-10	94	[240]
Ni₂P/GC	-10	220	[240]
CoP nanowire on Ti mesh	-10	72	[254]
CoP/CC	-10	209	[255]
CoP hollow polyhedron	-10	159	[259]
Co₂P/Co foil	-10	157	[260]
CoP nanoneedle arrays/CC	-10	95	[265]

CoP nanoframes	-10	136	[267]
CoP/Co ₂ P	-10	103	[321]
Co-P/NC nano-Polyhedrons	-10	154	[278]
MoP/Ni ₂ P/NF	-10	75	[298]
CoP/NF	-10	100	[546]
CoP NPs@P-doped dual carbon shells	-10	153	[547]
CoP NPs@N-doped porous carbon spheres	-10	112	[549]
Co _x P@ N-doped carbon porous polyhedrons	-10	187	[550]
Fe-Ni-P hybrid catalyst	-10	14	[551]
CoP/NCNHP GCE	-10	115	[552]
CoP@NG	-10	182	[553]
CoP-rGO-400	-10	150	[554]
Ni ₅ P ₄ film	-10	180	[557]
Ni-P electrodeposited	-10	93	[565]
CoN _x	-10	170	[566]
NiCo ₂ P _x nanowires	-10	58	[567]
Ni _{1-x} Co _x Se nanosheet	-10	85	[568]
FeP nanowire arrays	-10	194	[569]
Ni ₅ P ₄ (pellet)	-10	49	[570]
MoNi ₄ /MoO ₂ cuboids	-10	15	[571]
Co ₂ P films/Co	-10	174	[572]
Urchin-like CoP microspheres film/TiO ₂	-10	60	[573]
CoP/Co ₂ P@NC-2	-10	198	[574]
Ni ₂ P	-10	87	[575]

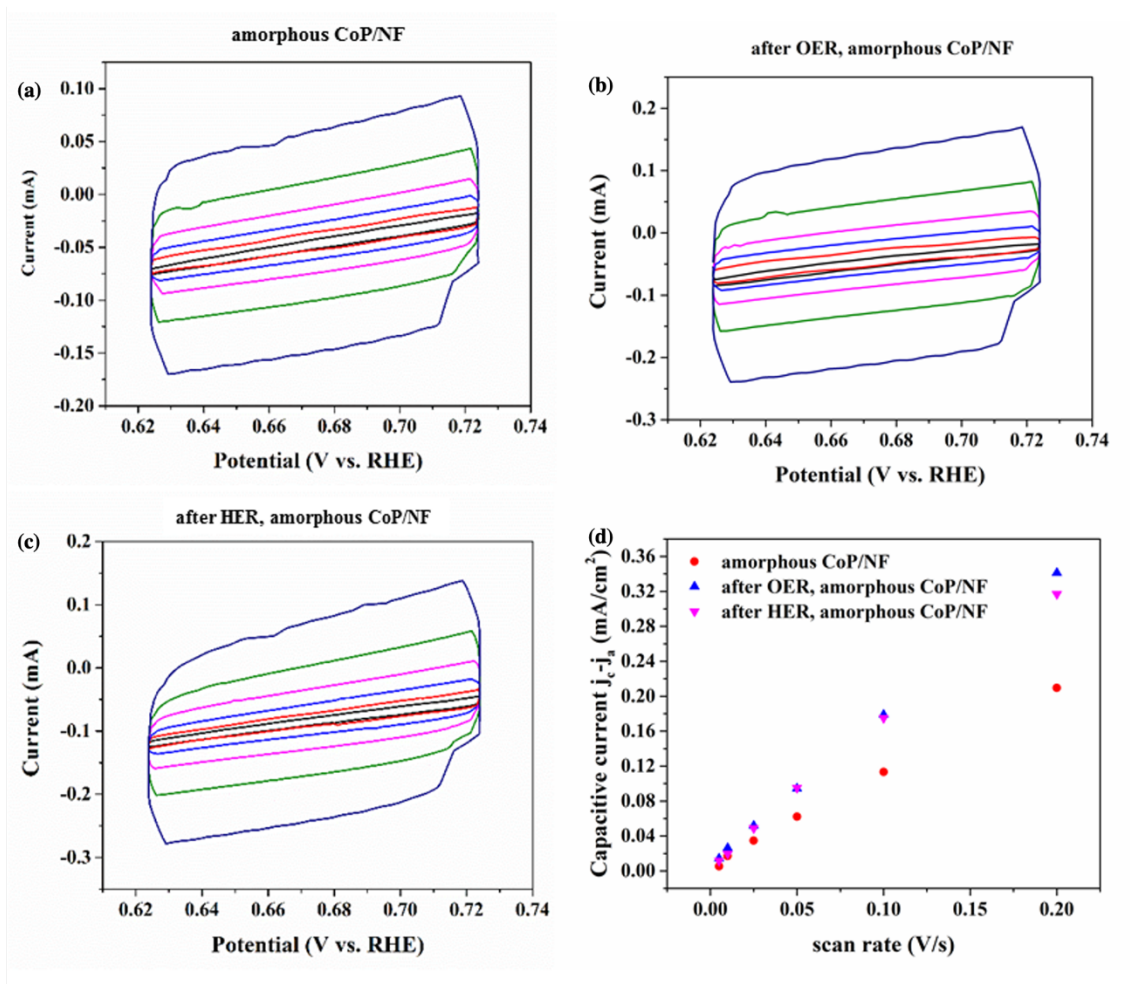


Figure A.1.8. The CV of (a) amorphous CoP/NF, (b) after OER and (c) after HER at a non-faradaic process region at different scan rates. Scan rates: 5 mV s^{-1} (black), 10 mV s^{-1} (red), 25 mV s^{-1} (blue), 50 mV s^{-1} (fuchsia), 100 mV s^{-1} (green), 200 mV s^{-1} (dark blue). The C_{dl} was determined as the half of the slope from the plot of the capacitive current *vs.* scan rate plot (d).

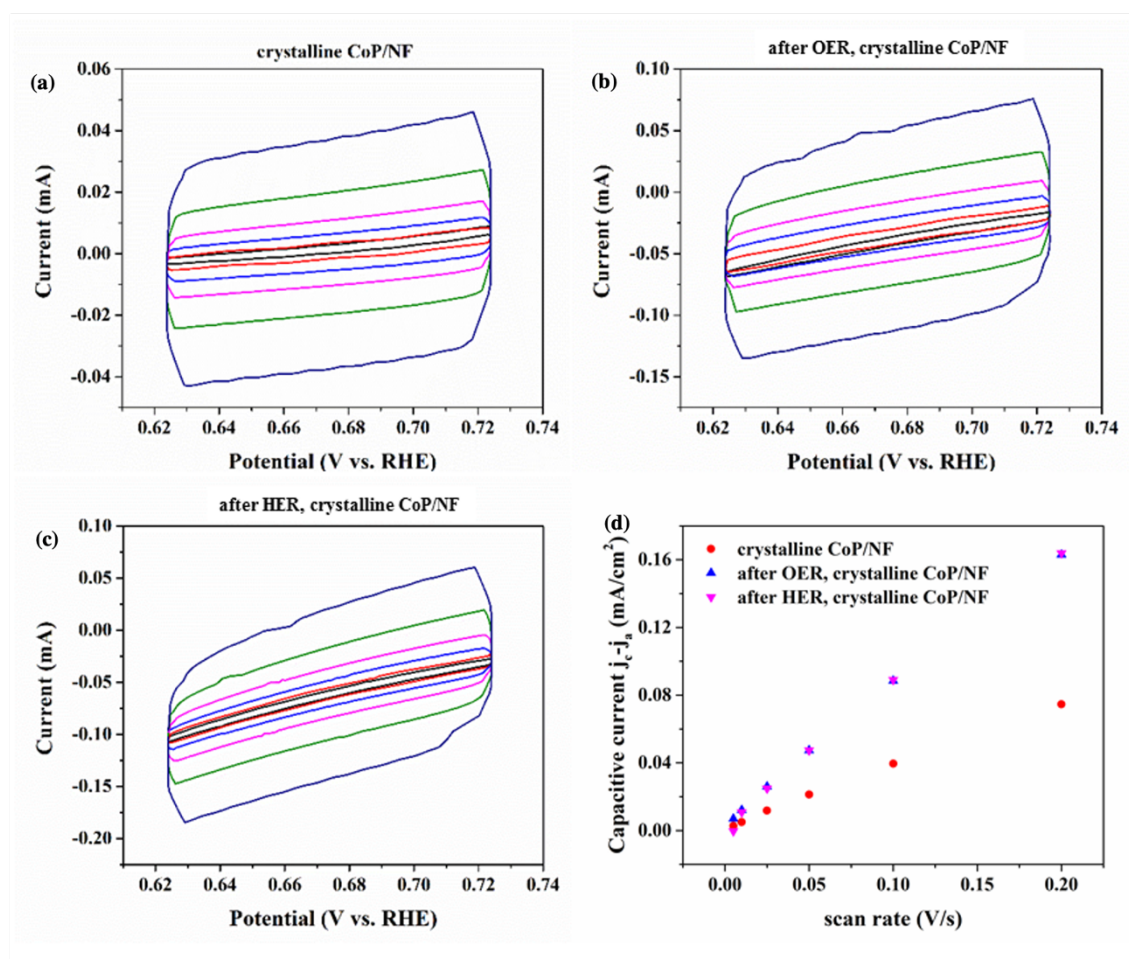


Figure A.1.9. The CV of (a) crystalline CoP/NF, (b) after OER and (c) after HER at a non-faradaic process region at different scan rates. Scan rates: 5 mV s^{-1} (black), 10 mV s^{-1} (red), 25 mV s^{-1} (blue), 50 mV s^{-1} (fuchsia), 100 mV s^{-1} (green), 200 mV s^{-1} (dark blue). The C_{dl} was determined as the half of the slope from the plot of the capacitive current vs. scan rate plot (d).

Table A.1.4. Correlation factor (R^2) of the linear plot of capacitive current vs. scan rate, C_{dl} , and calculated ECSA of the prepared materials over NF.

Material	R^2	C_{dl} (mF cm^{-2})	ECSA (cm^2)
amorphous CoP/NF	0.9985	0.5143	0.30
crystalline CoP/NF	0.9995	0.1833	0.11
OER amorphous CoP/NF	0.9998	0.8341	0.49
HER amorphous CoP/NF	0.9984	0.7842	0.46
OER crystalline CoP/NF	0.9992	0.3990	0.23
HER crystalline CoP/NF	0.9975	0.4115	0.24

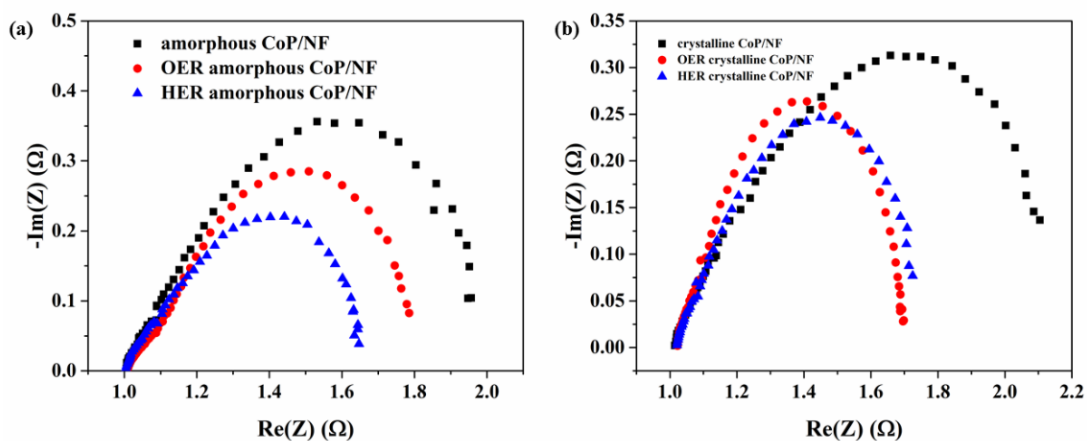


Figure A.1.10. Nyquist plot of a non-Faradaic region measured between 100 mHz and 100 kHz of (a) the amorphous CoP/NF and (b) crystalline CoP/NF compared to the materials after the OER and HER. The applied potential was 0.7 V vs. Hg/HgO. From the fitting of data to semi-circle plots, the R_s and the R_{ct} were calculated.

Table A.1.5. R_{ct} and R_s of the prepared materials over NF obtained from the Nyquist plot during the EIS experiments.

Material	R_{ct} (Ω)	R_s (Ω)
amorphous CoP/NF	0.8721	1.021
crystalline CoP/NF	1.0357	1.006
OER amorphous CoP/NF	0.6701	1.023
HER amorphous CoP/NF	0.6107	1.015
OER crystalline CoP/NF	0.6787	1.009
HER crystalline CoP/NF	0.5241	1.005

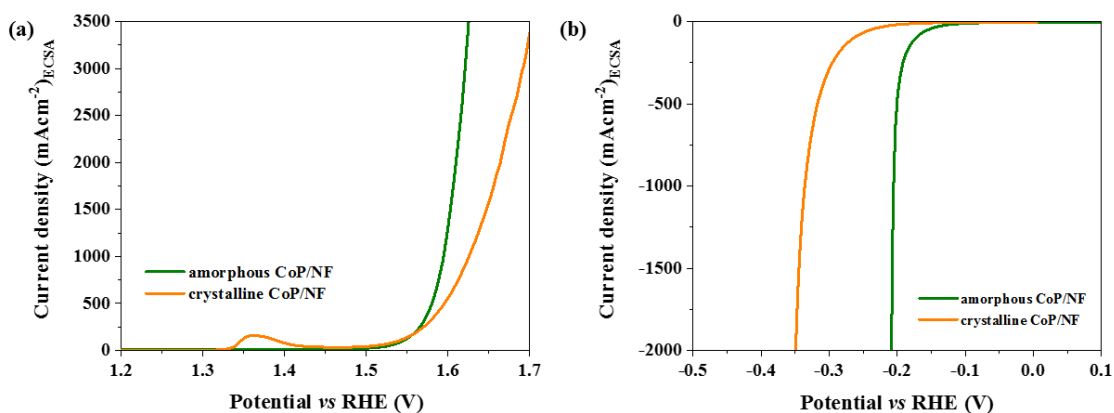


Figure A.1.11. Polarization curves of (a) OER and (b) HER of different CoP materials normalized by ECSA.

Table A.1.6. Surface area values obtained from BET experiment.

Material	Surface area ($\text{m}^2 \text{g}^{-1}$)
Crystalline CoP	27.50
Amorphous CoP	28.41

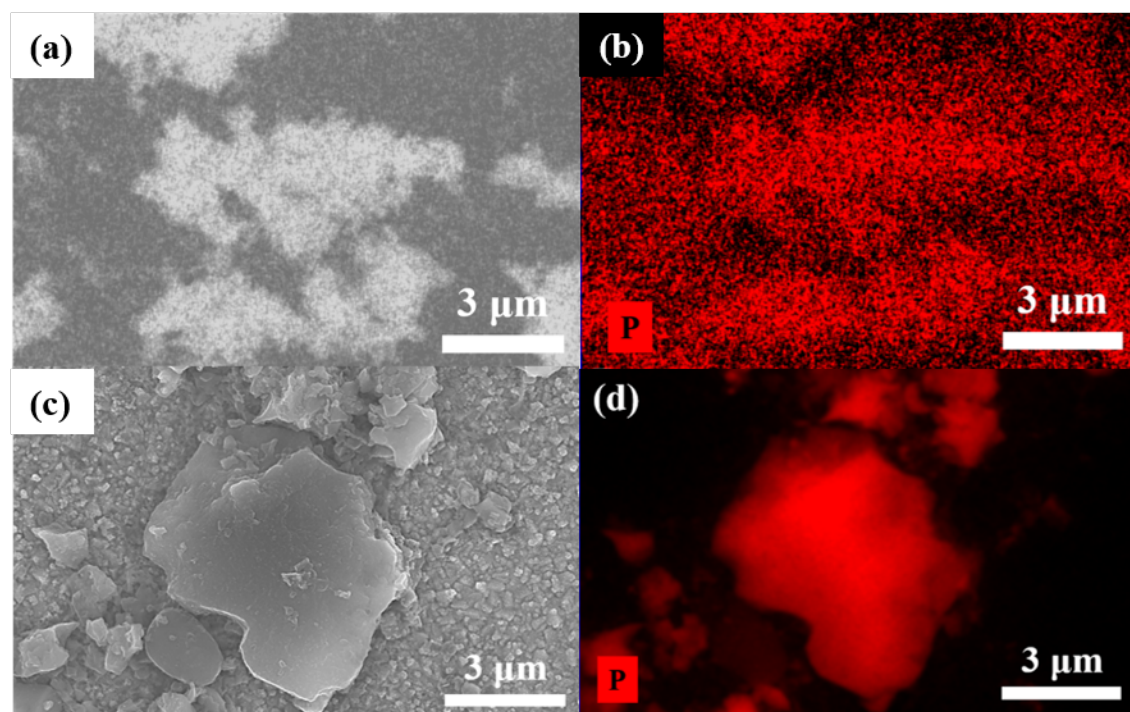


Figure A.1.12. (a) SEM of amorphous CoP after OER and elemental mapping of (b) P (red). (c) SEM of crystalline CoP after OER and elemental mapping of (d) P (red).

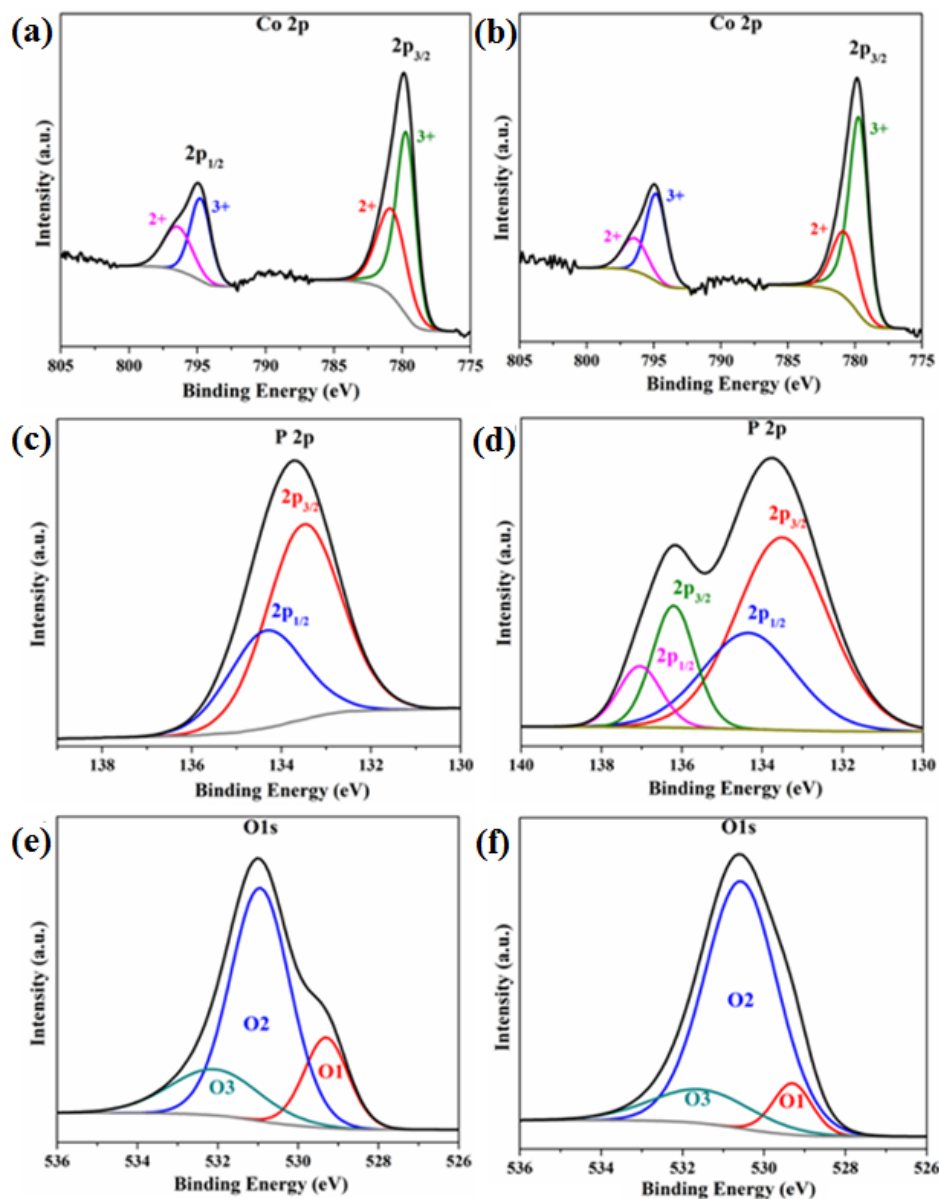


Figure A.1.13. The Co 2p, P 2p and O 1s XPS spectra of amorphous CoP after OER LSV (a, c and e) and OER CP (b, d and f). In both cases, total disappearance of the peaks associated to $\text{Co}^{\delta+}$ in CoP (778.7 eV in $2p_{3/2}$ and 793.9 eV and $2p_{1/2}$)^[288] was observed with additional strong peaks corresponding to $\text{Co}^{\text{II}}/\text{Co}^{\text{III}}$. The deconvolution spectra of Co 2p displayed the enhancement of Co^{III} peak area after CP compared to the Co^{II} peak area suggesting a greater amount of Co oxidation under continuous OER. Similarly, after both LSV and CP experiments, $\text{P}^{\delta-}$ (peak at 129.0 eV) completely disappears and the oxidized P^{V} (133.7 eV) peak appears.^[160,162] Moreover, after CP OER, the peak centered at ~ 136.2 eV corresponding to P_2O_5 was also evolved.^[305] The O 1s spectra shows three peaks (O1, O2 and O3) that can be correlated to the metal-oxygen bond in metal oxide (O1),^[306] oxygen in $-\text{OH}$ groups, indicating that the surface of the material is hydroxylated (O2),^[307] and the absorbed water molecules on the materials (O3),^[307] respectively.

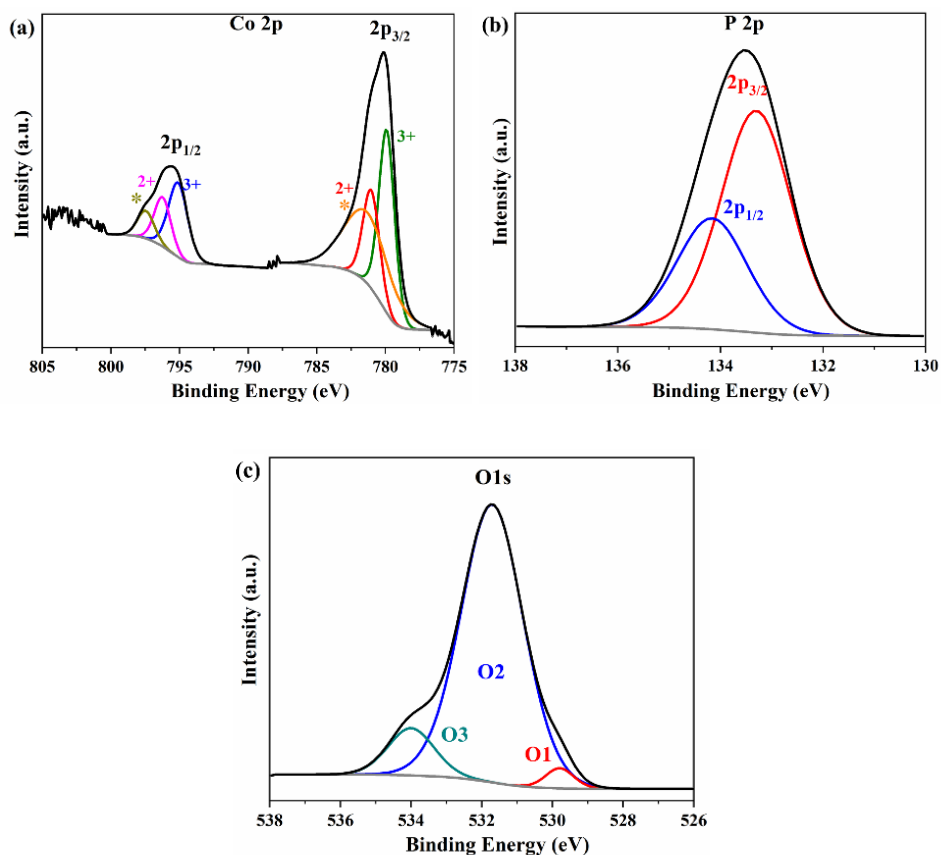


Figure A.1.14. The Co 2p, P 2p and O 1s XPS spectra of crystalline CoP after OER CP (a, b, c). After OER, the peak of Co^{III} (deconvoluted: 795.2 eV, 780.0 eV)^[288] increased its intensity in comparison to the Co^{II} peak (deconvoluted: 796.3 eV, 781.1 eV).^[288] After CP OER, only oxidized species P^V (133.5 eV)^[160,162] peak is observed. The reduced P^{δ-} peak (129.4 eV, see Figure 3.9) disappears. The O 1s spectra shows three peaks (O1, O2 and O3) that can be correlated to the metal-oxygen bond in metal oxide (O1),^[306] oxygen in –OH groups, indicating that the surface of the material is hydroxylated (O2),^[307] and the absorbed water molecules on the materials (O3),^[307] respectively.

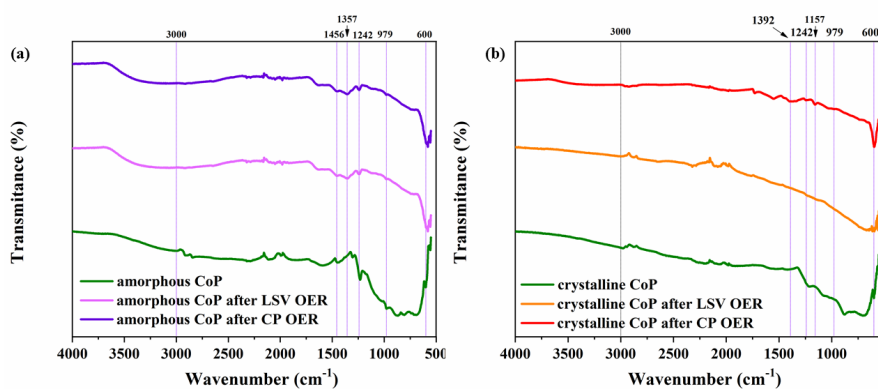


Figure A.1.15. Comparison of FT-IR spectra of the materials after LSV and CP OER catalysis of amorphous and crystalline CoP. A broad band centered at ca. 3000 cm⁻¹ appears on the spectra of the amorphous material and corresponds to adsorbed H₂O or possibly from the formed (oxy)hydroxide layer after surface oxidation. The small bands between 1500 cm⁻¹ and 500 cm⁻¹ are attributed to P=O stretching vibration and P-O-P stretching vibration on the phosphate groups.^[160,282] The peak at 600 cm⁻¹ is characteristic of Co-O bond.^[282]

Table A.1.7. The concentration of Co and P in the electrolyte solution after CP OER and CP HER experiments. The concentration was determined by ICP-AES of the solution. Phosphorus concentration in solution increases because of the high solubility of the generated polyphosphate species in the electrolyte.^[100,303] Only a small amount of Co leaches into the solution, which could be explained by the difference in solubility of the oxidized Co species in the alkaline electrolyte, which is lower in comparison to the P-containing species.^[302]

Sample	Co (mg L ⁻¹)	P (mg L ⁻¹)	% of element loss in solution	
			% Co	% P
1 M KOH	0.00	0.00	-	-
Amorphous CoP after OER CP	0.21	5.87	2	85
Amorphous CoP after HER CP	0.15	0.89	1	13
Crystalline CoP after OER CP	0.18	0.84	1	11
Crystalline CoP after HER CP	0.42	0.36	3	5

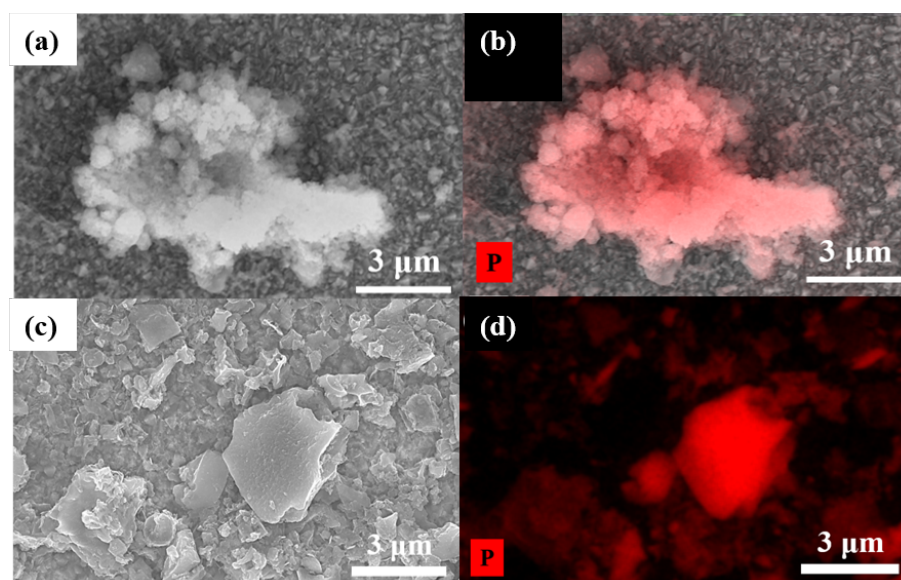


Figure A.1.16. (a) SEM of amorphous CoP after HER and elemental mapping of (b) P (red). (c) SEM of crystalline CoP after HER and elemental mapping of (d) P (red).

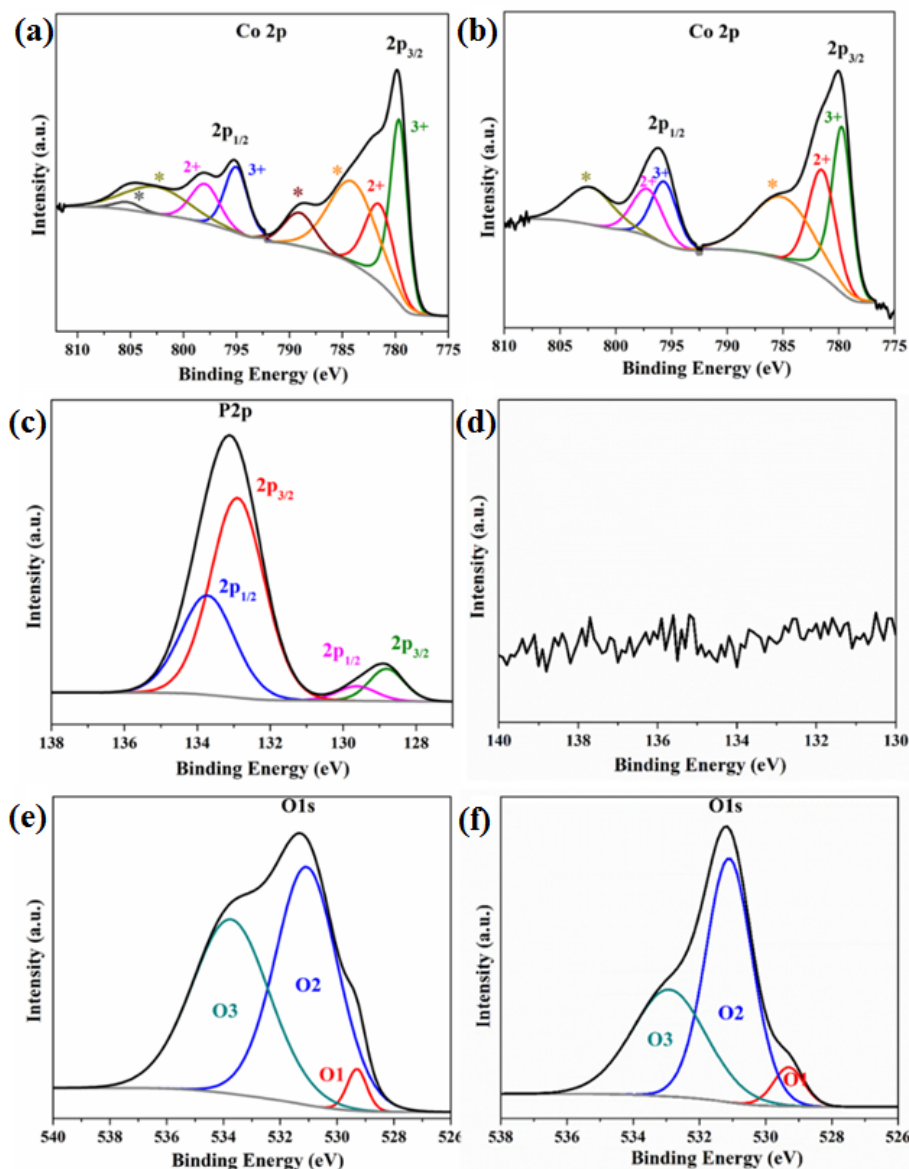


Figure A.1.17. The Co 2p, P 2p and O 1s XPS spectra of amorphous CoP after HER LSV (a, c and e) and HER CP (b, d, f) for amorphous CoP. In the Co 2p spectra, similar peaks were obtained in both cases, with a total disappearance peaks associated to of the $\text{Co}^{\delta+}$ and appearance of peaks for Co^{II} and Co^{III} which is due to the surface passivation under strongly alkaline conditions.^[160] The peak of $\text{P}^{\delta-}$ (129.0 eV) in the spectra after LSV HER has a reduced intensity if compared to the initial spectrum, with the most intense peak corresponding to P^{5+} (133.1 eV).^[160,162] In the case of the spectrum after CP, the peaks for P was completely disappeared further demonstrating the loss of P in HER conditions that match with ICP-AES results (Table A.1.1). The O 1s spectrum for LSV and CP showed three distinct peaks (O1, O2 and O3) corresponding to the metal-oxygen bond in metal oxide (O1),^[306] oxygen in $-\text{OH}$ groups, indicating that the surface of the material is hydroxylated (O2),^[307] and the absorbed water molecules on the materials (O3),^[307] respectively.

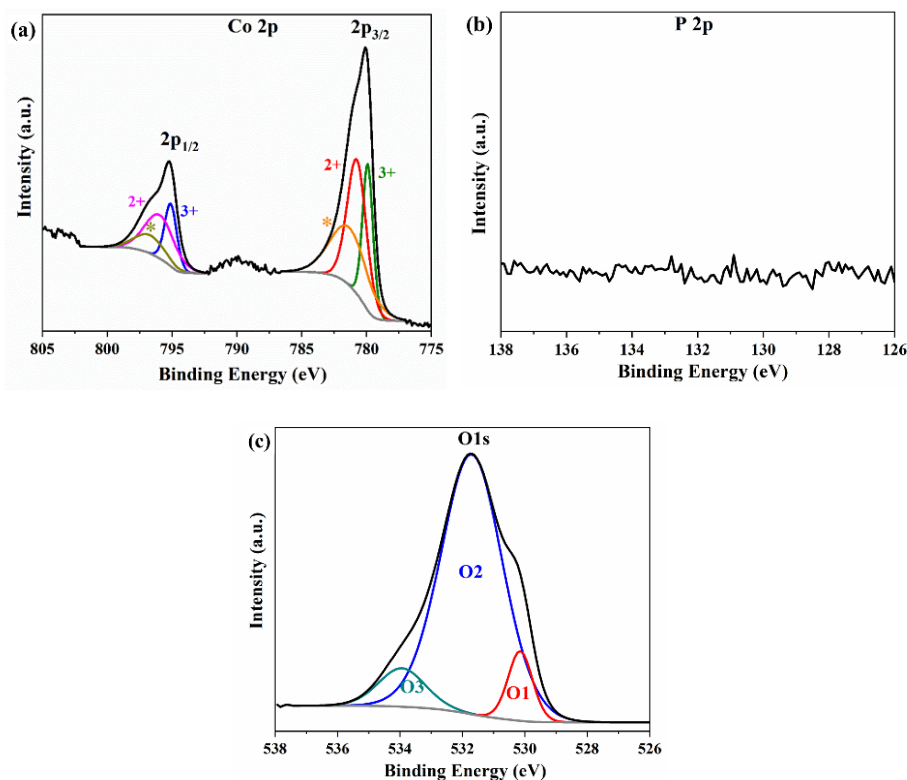


Figure A.1.18. XPS of Co, P and O after HER CP (a, b, c, respectively) for crystalline CoP. The Co 2p, P 2p and O1s spectra could be described similar to Figure A.1.17.

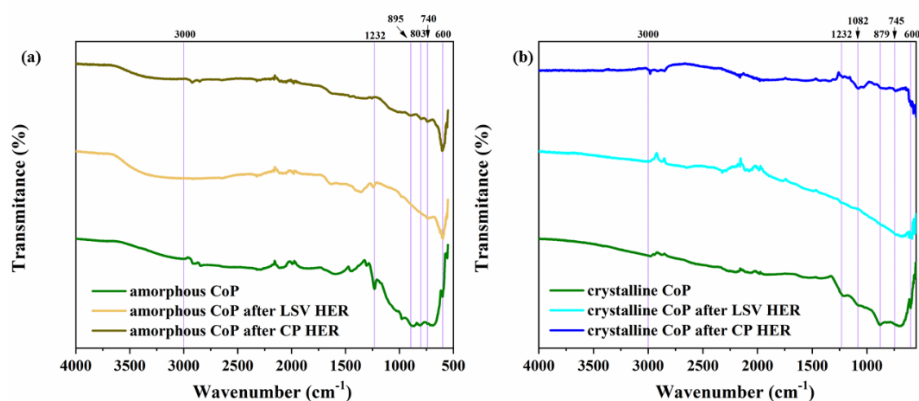


Figure A.1.19. Comparison of FT-IR of the obtained materials after LSV and CP HER catalysis of amorphous and crystalline CoP. A broad band centered at ca. 3000 cm⁻¹ appears in the spectra of the amorphous material and corresponds to adsorbed H₂O or possibly from the formed (oxy)hydroxide shell after surface oxidation. The broad lower transmittance range between 1250 cm⁻¹ and 500 cm⁻¹, where peaks associated to phosphate groups appear,^[160,282] shows no intense peaks indicating a loss of phosphate.

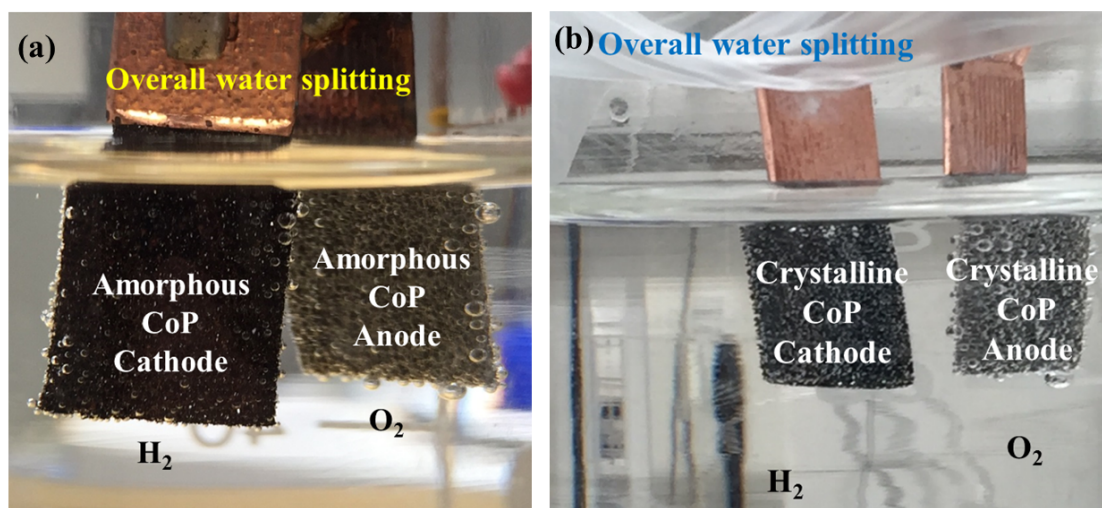


Figure A.1.20. OWS with (a) amorphous and (b) crystalline CoP on a CoP/NF || CoP/NF two-electrode system in 1 M KOH solution. Vigorous bubble formation on the cathode and anode was observed during the experiment.

Table A.1.8. Overpotentials at 10 mA cm⁻² of Co phosphide-based catalysts at 1 M KOH for OWS.

Catalyst	Cell potential (V)	Reference
CoP-films/Au	1.74	[238]
Co-P films/Cu foil	1.56	[240]
Co ₂ P/Co foil	1.71	[260]
CoP nanoneedle arrays/CC	1.61	[265]
CoP hollow prisms	1.52	[266]
CoP nanocubes	1.75	[267]
CoP nanoframes	1.65	[267]
Co ₂ P nanocrystals	1.56	[320]
CoP/Co ₂ P	1.65	[321]
CoP/NF	1.62	[546]
CoP@CC	1.68	[576]
CoP NPs@P-doped dual carbon shells	1.66	[547]
Hollow CoP@N-doped carbon	1.72	[548]
CoP NPs@N-doped porous carbon spheres	1.64	[549]
Co _x P@ N-doped carbon porous polyhedrons	1.71	[550]
Meso-Co/Co ₂ P	1.57	[577]

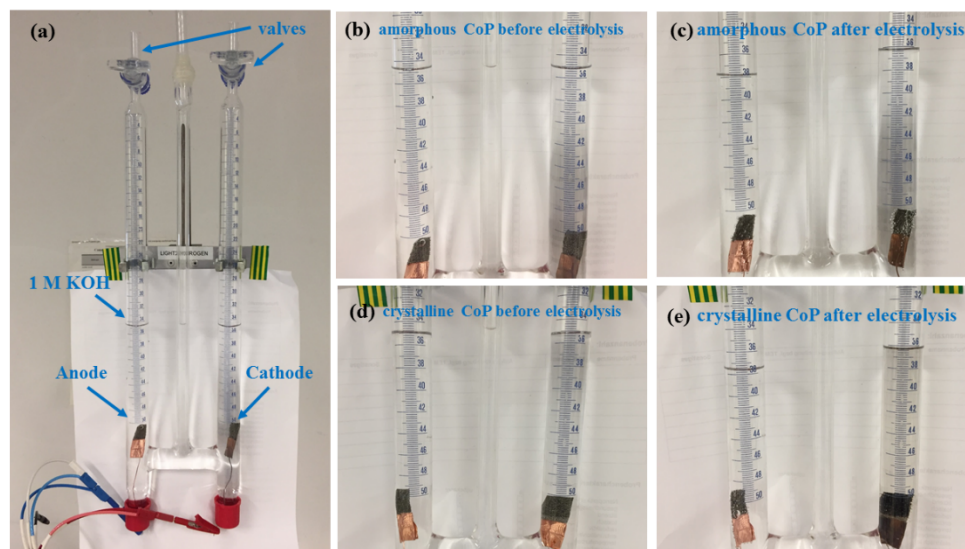


Figure A.1.21. (a) In inverted two-electrode amorphous CoP || amorphous CoP electrolyzer was used under constant current density of 10 mA cm^{-2} in 1 M KOH to allow the collection of H_2 and O_2 separately at atmospheric pressure. (b) The initial level of the electrolyte was noted and then the valves were closed. During electrolysis, because of evolution and collection of H_2 and O_2 at the upper part of the cell, the level of electrolyte goes down and the change in volume over time was noted. (c) The ratio of volumes of H_2 and O_2 remained almost 2:1 over one hour of electrolysis. A similar system was built using a two-electrode crystalline CoP || crystalline CoP electrolyser (d and e).

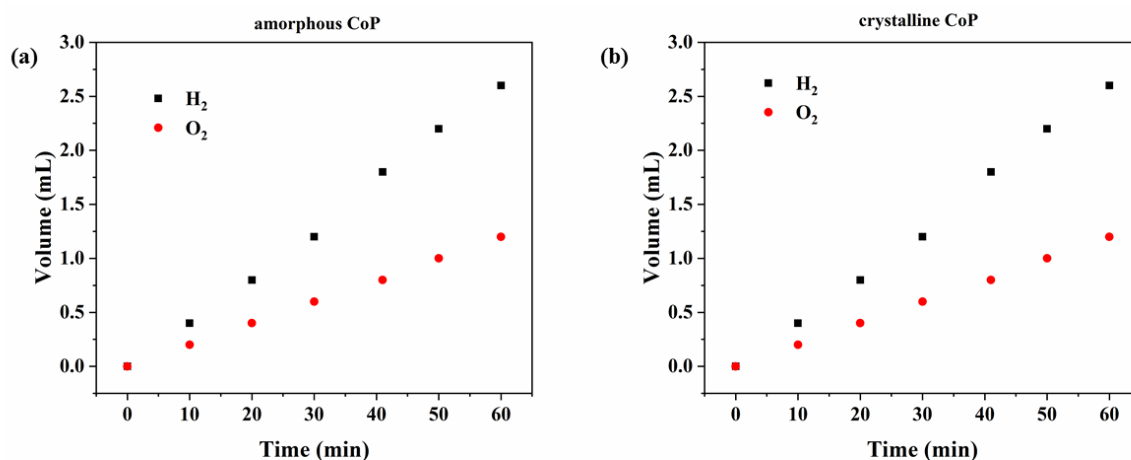


Figure A.1.22. The plot of volume change as result of H_2 and O_2 evolution in the experiments respect to time for (a) amorphous CoP and (b) crystalline CoP. The ratios of H_2 and O_2 were obtained from the electrodes of both materials deposited on NF as both cathode and anode in 1 M KOH solution at a current of 10 mA cm^{-2} for 1 h. The attained ratios directly confirmed the evolution of gases as well as the amount of H_2 was approximately twice larger than the O_2 demonstrating the efficient selectivity and reactivity of the catalysis.

Table A.1.9. Calculation of FE for amorphous CoP.

	j (mA cm^{-2})	t (s)	V_{H_2} (mL)	V_{O_2} (mL)	$V_{\text{H}_2}:V_{\text{O}_2}$	FE (H_2 , %)	FE (O_2 , %)
Amorphous CoP	10	400	0.44	0.21	2.07	96	92

A.2. Appendix of Chapter 4: Crystalline FeAs

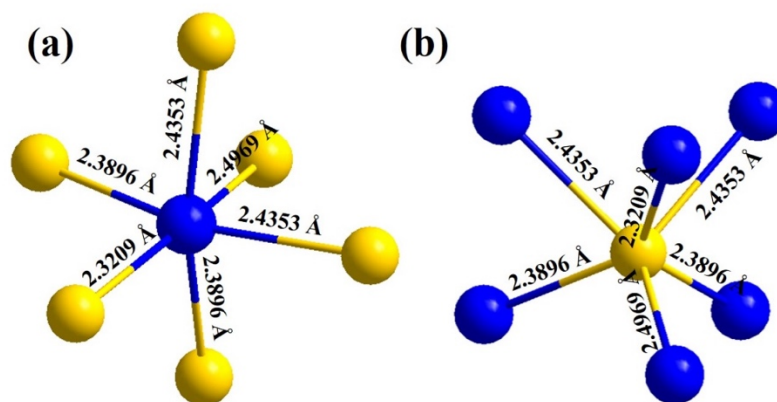


Figure A.2.1. The crystalline FeAs species (space group: *Pnma*, space group 62). Each Fe metal atom has six near As neighbors situated in a distorted octahedral configuration (a). The As atoms are surrounded by six Fe atoms at the corners of a highly distorted triangular prism (b). Fe and As atoms are represented by blue and yellow spheres, respectively.

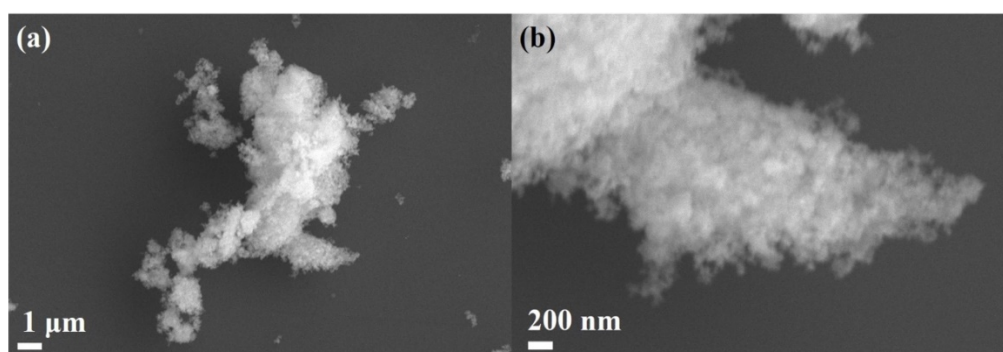


Figure A.2.2. SEM images showing agglomerations of particles of FeAs at (a) 5000x and (b) 25000x.

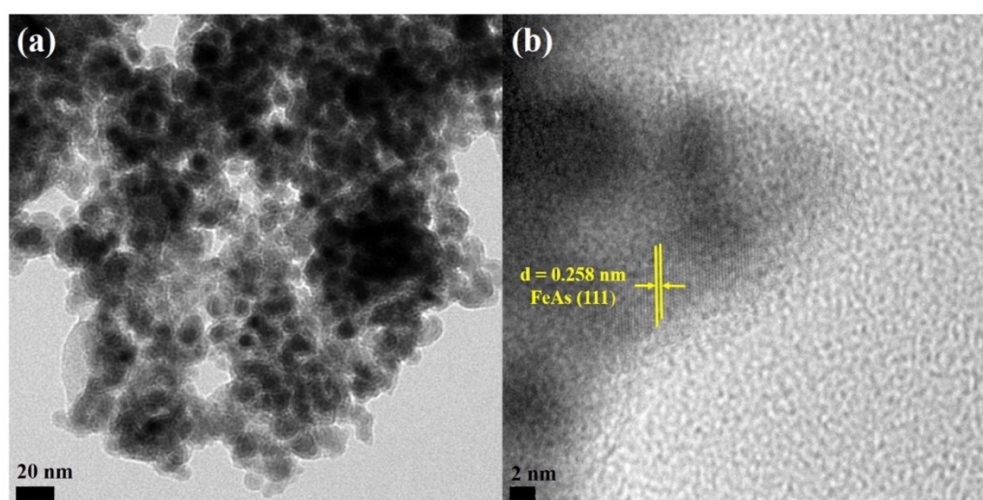


Figure A.2.3. TEM image of (a) aggregated FeAs nanoparticles (~10 nm diameter) and (b) HR-TEM image showing the crystalline fringes associated to a lattice spacing of 0.258 nm corresponding to the (111) plane of the FeAs phase.

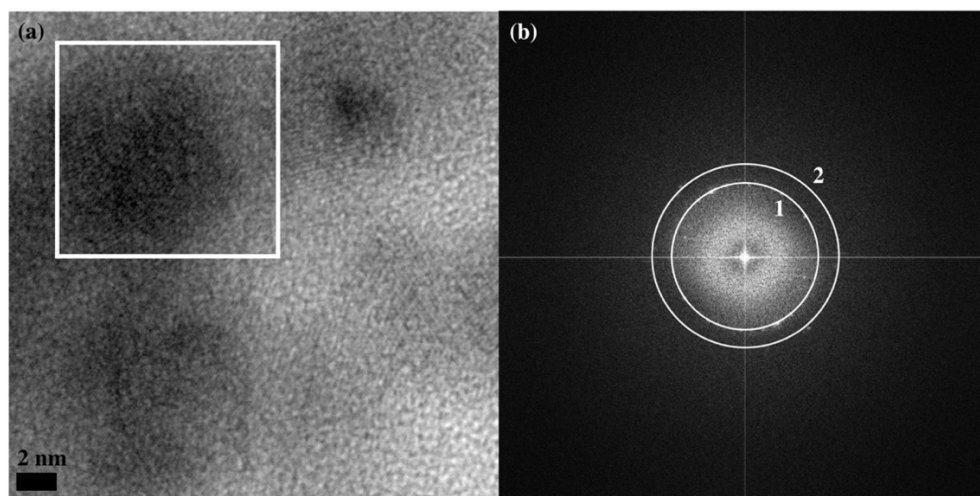


Figure A.2.4. (a) HR-TEM image of FeAs particles with white framed areas containing lattice fringes and its respective (b) Fourier transform (FT) revealing the lattice distances 0.258 nm (ring marked with 1) and 0.199 nm (ring marked with 2) indicating the FeAs crystallographic planes (111) and (211), respectively (JCPDS 76-458).

Table A.2.1. Determination of the Fe and As content in the prepared FeAs by ICP-AES, EDX-SEM, and EDX-TEM.

Fe:As (ICP-AES)	Fe:As (EDX-SEM)	Fe:As (EDX-TEM)
1:1.04	1:1.12	1:0.82

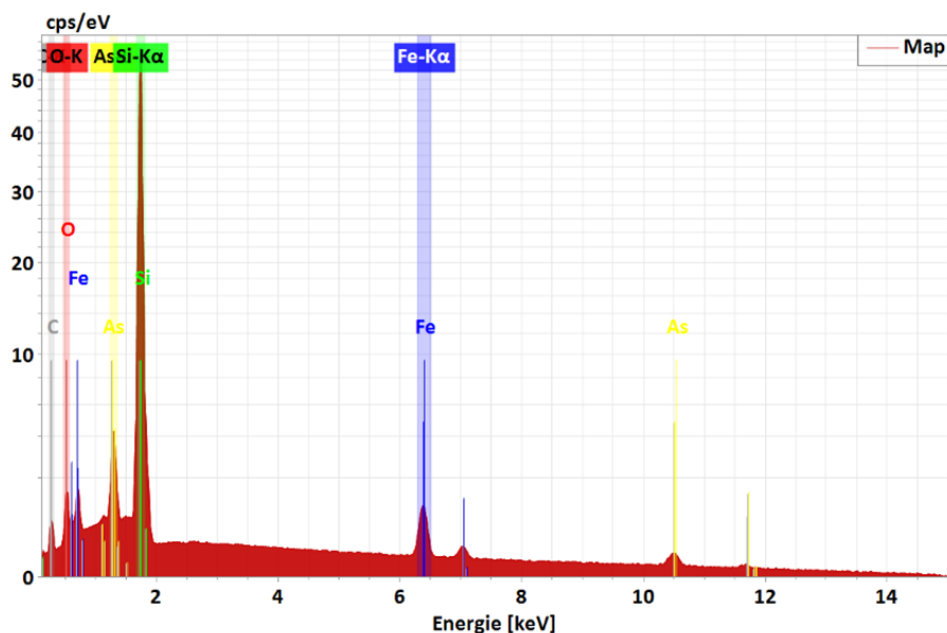


Figure A.2.5. SEM-EDX of FeAs-prepared by hot-injection which confirms the presence of Fe and As. The presence of O is inevitable due to surface passivation. The presence of Si peaks arises from the Si wafer supported used in SEM. The determined Fe:As ratio was 1:1.12.

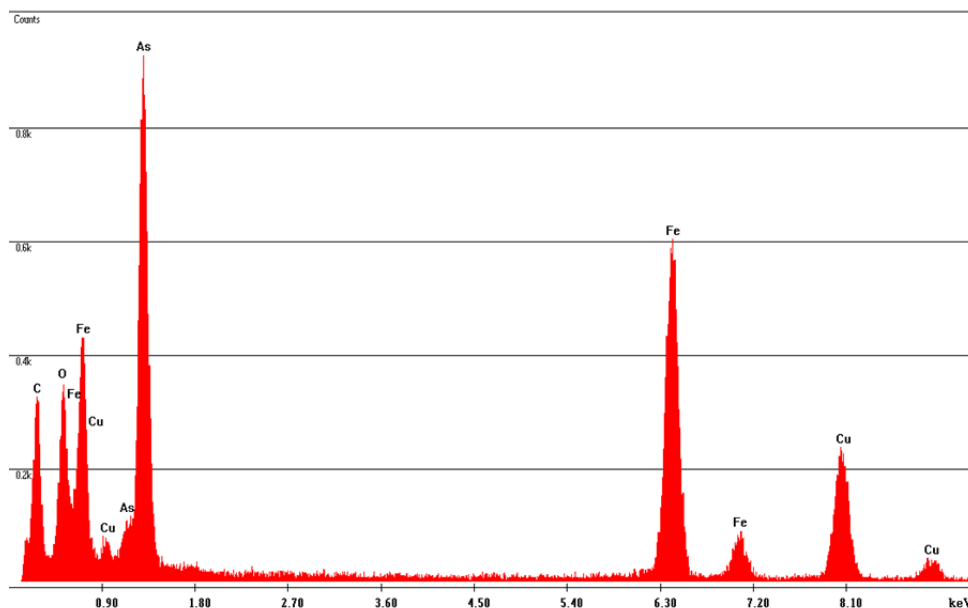


Figure A.2.6. TEM-EDX of FeAs-prepared through hot-injection, which confirms the presence of Fe and As. The presence of Cu peaks arises from the TEM grid (carbon film on 300 mesh Cu-grid). The determined Fe:As ratio was 1:0.82.

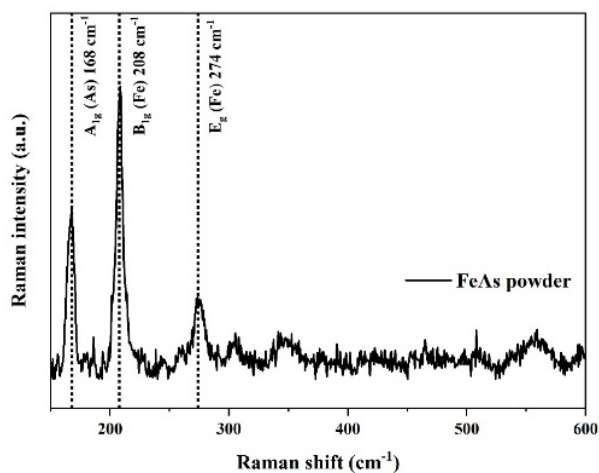


Figure A.2.7. (Resonance) Raman spectra of FeAs powder. The shown bands match with the reported bands for bulk and FeAs nanoparticles^[324] and can be assigned to the following phonon modes: low-frequency A_{1g} of As (168 cm^{-1}), B_{1g} of Fe (208 cm^{-1}) and high-frequency E_g of Fe (274 cm^{-1}).^[361,362] Small deviations from reported values can be caused by thermal effects or laser power.

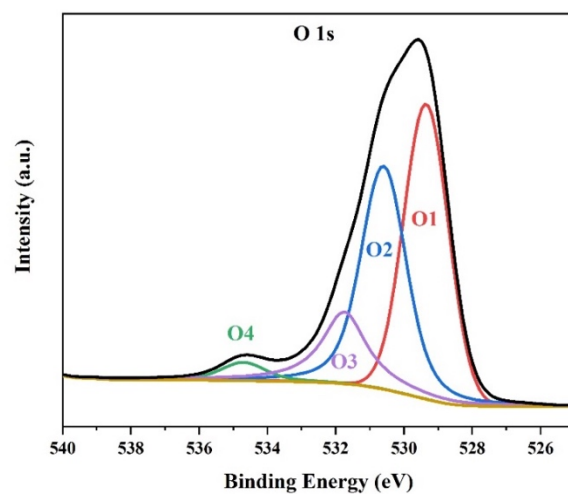


Figure A.2.8. Deconvoluted XPS O 1s of FeAs.

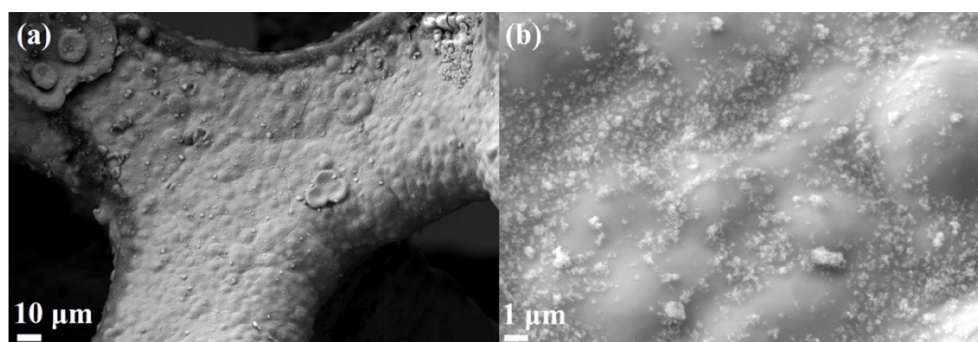


Figure A.2.9. SEM of the FeAs films deposited on NF at (a) 500x and (b) 5000x. The high magnification image shows that the morphology of the FeAs particles is maintained (compare to as-prepared FeAs SEM on Figure A.2.2).

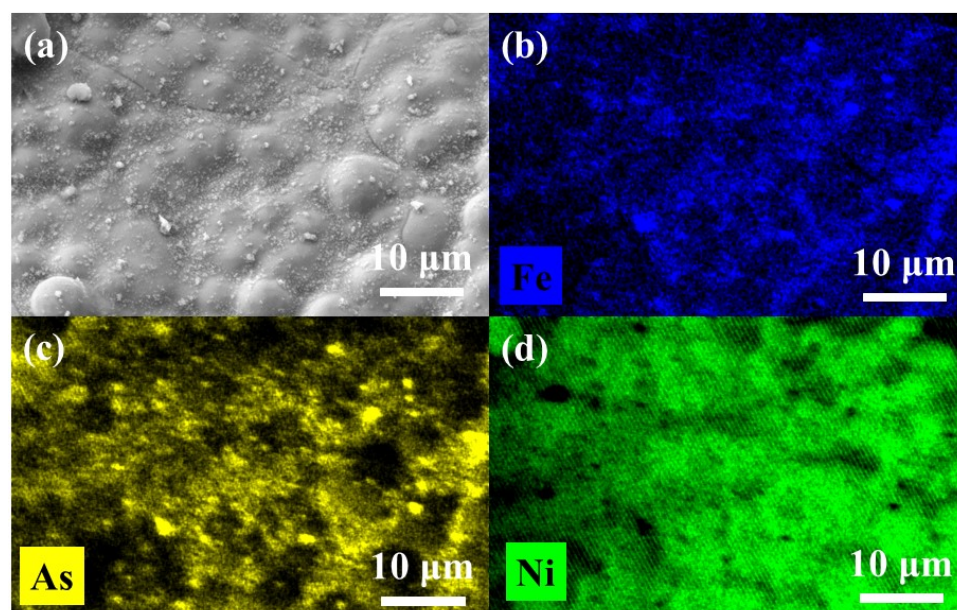


Figure A.2.10. (a) SEM of FeAs/NF and elemental mapping of (b) Fe (blue), (c) As (yellow) and (d) Ni (green). Ni arises from the NF substrate. Homogenous distribution of Fe and As was observed in the particles deposited on NF.

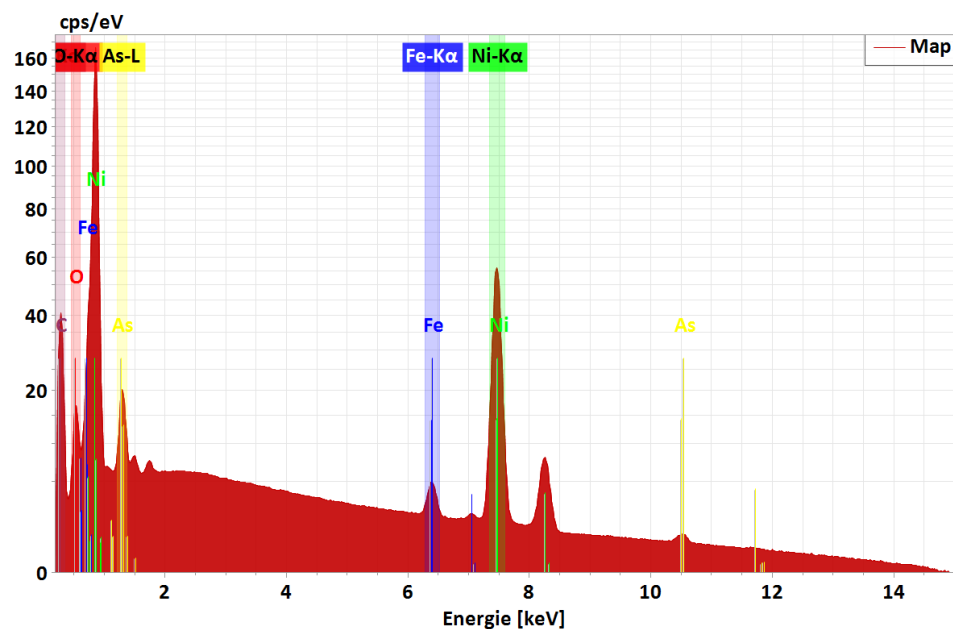


Figure A.2.11. SEM-EDX of the film of FeAs/NF that confirmed the presence of Fe and As. The presence of Ni peaks arises from the NF substrate. The peaks between 1.5-2 keV correspond to Al ($K\alpha_1$, $K\alpha_2$ at 1.487 keV, 1.486 keV and $K\beta_1$ at 1.557 keV) and Si ($K\alpha_1$, $K\alpha_2$ at 1.740 keV, 1.739 keV and $K\beta_1$ at 1.836 keV); they arise from the Al sample holder and the Si wafer used during the measurement, respectively. The Fe:As ratio was $\sim 1:1$ as determined by SEM-EDX.

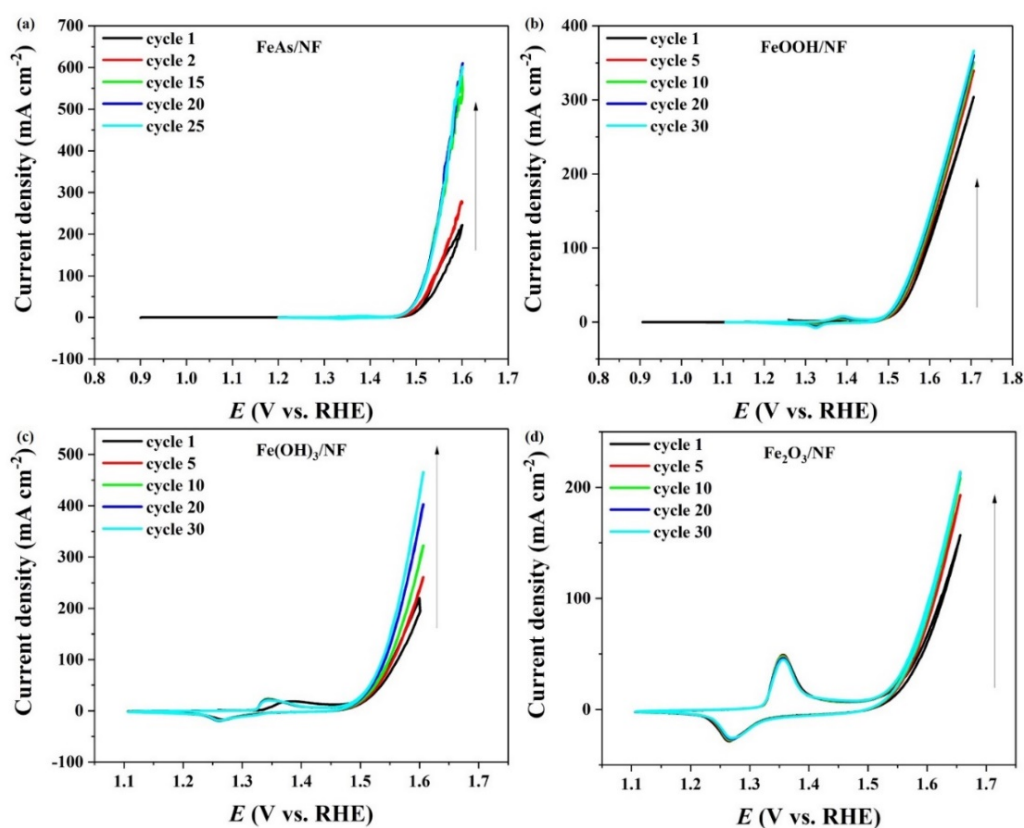


Figure A.2.12. Activation of the (a) FeAs/NF, (b) Fe(OH)₃/NF, (c) FeOOH/NF, and (d) Fe₂O₃/NF by CV in 1 M KOH.

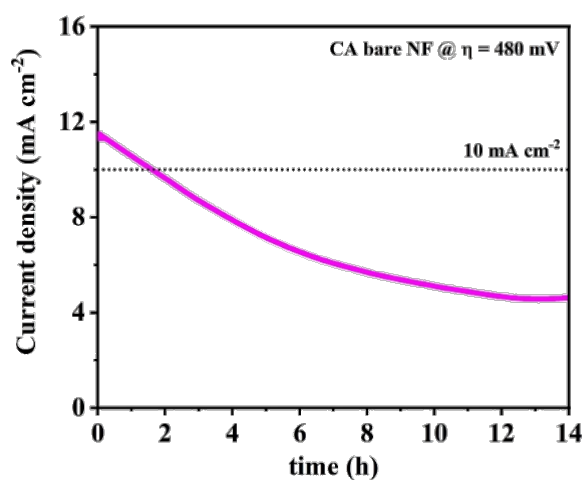


Figure A.2.13. CA at $\eta = 480$ mV (1.71 V vs. RHE, 0.81 V vs. Hg/HgO) of bare NF.

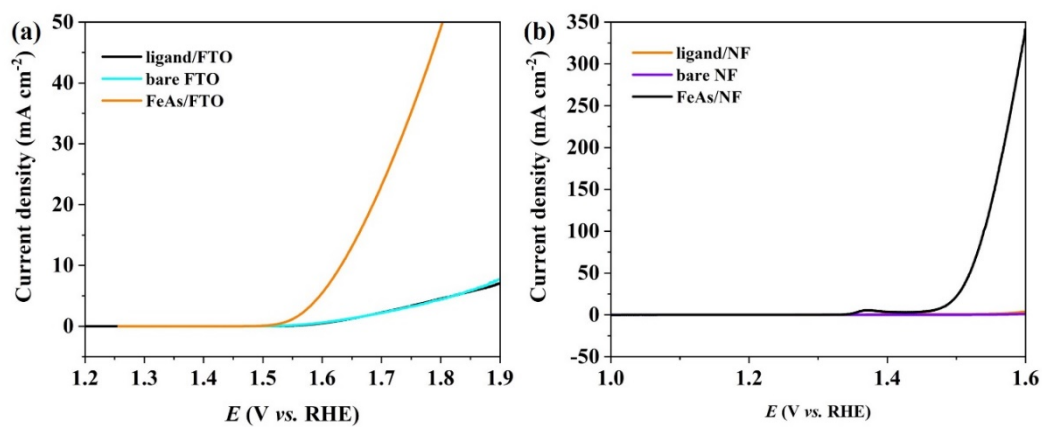


Figure A.2.14. Electrochemical activity of films prepared from the β -Diketiminato ligand deposited on (a) FTO and (b) NF compared to the FeAs and the bare substrate.

Table A.2.2. Activity comparison of the as-prepared FeAs and reference Fe-based materials with other highly efficient Fe-based pnictides in 1 M KOH for OER.

Catalyst	Current density (mA cm ⁻²)	Overpotential η (mV)	Reference
FeAs/NF	10	252	This work
	100	309	This work
FeAs/FTO	10	400	This work
Fe(OH)₃/NF	10	275	This work
	100	333	This work
Fe(OH)₃/FTO	10	578	This work
FeOOH/NF	10	283	This work
	100	364	This work
FeOOH/FTO	10	610	This work
Fe₂O₃/NF	10	312	This work
	100	397	This work
Fe₂O₃/FTO	10	640	This work
FeSe ₂ /NF	10	245	[106]
FeP/NF	10	227	[111]
FeP nanorods/CP	10	350	[157]
FeP/Au	10	290	[189]
FeP RGO/Au	10	260	[189]
FeP ultra small nanoparticles/Au @Au	10	320	[189]
NiAs/GC	10	360	[203]
FeSe ₂ nanoplates/NF	10	330	[233]
FeMnP	10	250	[578]
FeP nanotubes/CC	10	288	[579]
FeMnP	10	250	[580]
Ultrathin FeOOH nanosheets	10	428	[581]
Ultrathin Ni-FeOOH nanosheets	10	274	[581]
FeS/IF	10	238	[582]
FeB ₂	10	296	[583]
FeOOH/GC	10	530	[584]
FeOOH/NF	10	290	[585]
FeOOH nanosheet/NF	10	390	[586]
RGO/Ni-FeOOH/FTO	10	260	[587]
Fe ₂ O ₃ hollow nanorod/CNT/GC	10	383	[588]
γ -Fe ₂ O ₃ -CNT/GC	10	340	[589]
CNT@FeOOH sheet/CC	10	250	[590]
Fe@C-NG/NCNTs/GC	10	450	[591]
FeP@RGO (50:50)/CP	10	290	[592]
Fe _x N/graphene-NF	10	238	[593]
Fe ₇ S ₈ nanosheets/GC	10	270	[594]
FePO ₄ /NF	10	215	[595]
2D FePO ₄ sheets/NF	10	218	[596]
FeHP/GC	10	442	[597]

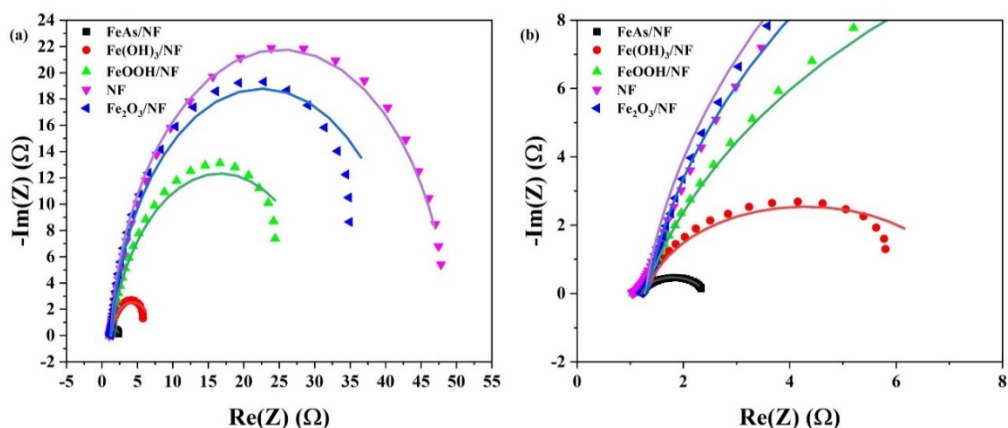


Figure A.2.15. (a) Nyquist plot constructed from the EIS experiment of materials deposited on NF. The spectra were collected with an anodic polarization potential of 1.51 V vs. RHE. (b) Zoom of the Nyquist plot. The continuous lines show the fitting to the circuit that contains two resistors R_1 and R_2 and Q a CPE (see Figure 7.16). This circuit has been previously used to fit TM-based systems during OER reaction conditions.^[534,535,537] The assignment of the elements is consistent in the literature and can be applied to the system under study: R_1 is the Ohmic resistance of the solution and electrode (R_s), R_2 is the charge transfer resistance (R_{ct}), and a CPE (Q_2). Details of assignments are discussed on the Experimental Section 7.3.7.

Table A.2.3. R_2 (Ω) (R_{ct}), R_1 (Ω), (R_s), Q ($F \times s^{(a_2-1)}$) and a_2 of FeAs, Fe(OH)₃, FeOOH, and Fe₂O₃ deposited on NF and its comparison to the bare NF substrate.

Material	R_{ct} (Ω)	R_s (Ω)	Q ($F \times s^{(a_2-1)}$)	a_2
NF	48.0 ± 1.2	1.3 ± 0.3	$1.5 \times 10^{-1} \pm 1.4 \times 10^{-2}$	$9.4 \times 10^{-1} \pm 6.6 \times 10^{-2}$
FeAs/NF	1.2 ± 0.4	1.2 ± 0.1	$1.9 \times 10^{-1} \pm 2.0 \times 10^{-2}$	$8.6 \times 10^{-1} \pm 1.0 \times 10^{-2}$
Fe(OH) ₃ /NF	6.0 ± 4.3	1.3 ± 0.7	$8.7 \times 10^{-2} \pm 1.3 \times 10^{-3}$	$8.9 \times 10^{-1} \pm 9.9 \times 10^{-2}$
FeOOH/NF	30.8 ± 3.2	1.3 ± 0.6	$6.2 \times 10^{-3} \pm 1.3 \times 10^{-3}$	$8.6 \times 10^{-1} \pm 5.6 \times 10^{-2}$
Fe ₂ O ₃ /NF	42.4 ± 3.1	1.3 ± 0.3	$5.7 \times 10^{-3} \pm 8.2 \times 10^{-4}$	$9.2 \times 10^{-1} \pm 6.2 \times 10^{-2}$

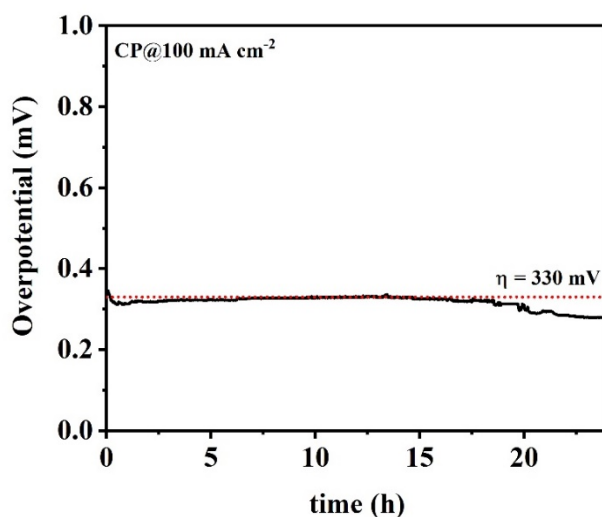


Figure A.2.16. CP of FeAs/NF (1 mg cm^{-2}) at 100 mA cm^{-2} .

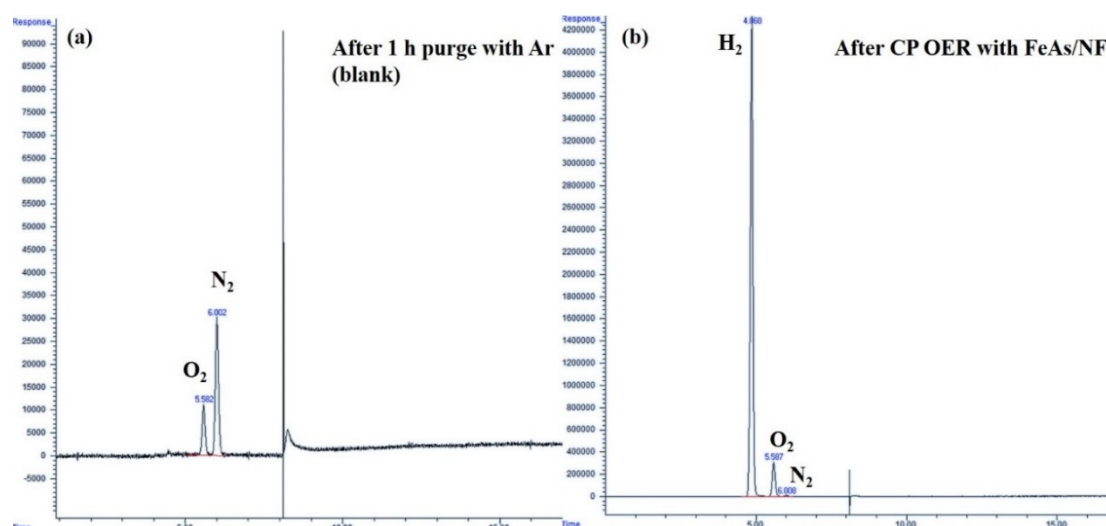


Figure A.2.17 (a) Chromatogram obtained after 1 h purge with Ar. Remnants of air (O₂ and N₂) are detected. These detected quantities are used for the calibration. (b) Chromatogram after CP OER 100 mA cm⁻² for 360 s using FeAs/NF as anode and Pt rod as the cathode in a closed single-compartment electrochemical cell. H₂ and O₂ are produced from the electrolysis of water, N₂ (trace) is also present.

Table A.2.4. Calculation of FE for FeAs/NF.

j (mA cm ⁻²)*	t (s)	V_{H_2} (mL)	V_{O_2} (mL)	$V_{H_2}:V_{O_2}$	FE (H ₂ , %)	FE (O ₂ , %)	FE O ₂ (rel. to H ₂)**
49.39	360	2.15	1.06	2.01	95	94	99%
99.28	360	4.32	2.14	2.02	97	96	99%

* j (mA cm⁻²) corresponds to the actual current density measured during the CP experiment.

**the FE of O₂ relative to H₂ was calculated assuming 100 % of FE for H₂ with Pt.

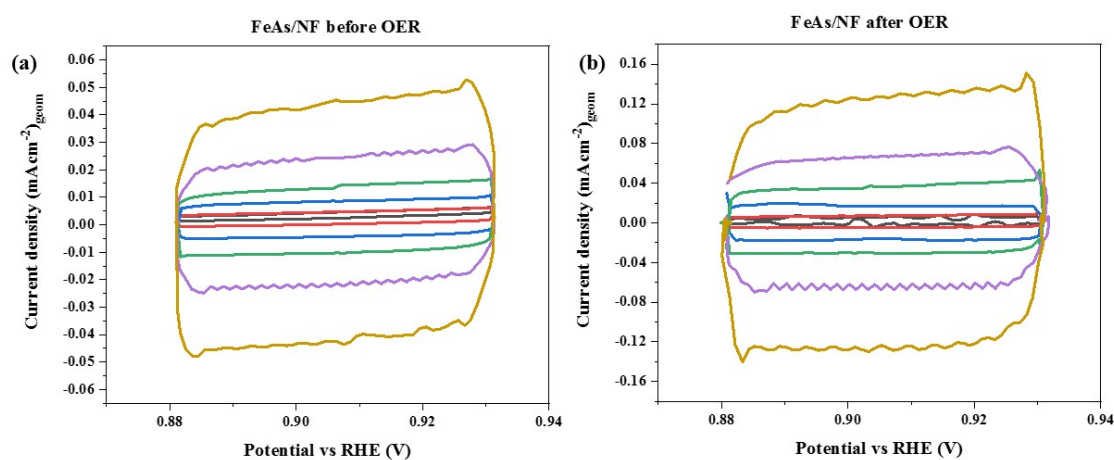


Figure A.2.18. CV measurements at a non-faradaic process region at different scan rates for (a) FeAs/NF and (b) FeAs/NF after OER. Scan rates: 5 mV s⁻¹ (black), 10 mV s⁻¹ (red), 25 mV s⁻¹ (blue), 50 mV s⁻¹ (green), 100 mV s⁻¹ (purple), 200 mV s⁻¹ (dark yellow). The C_{dl} was determined as half of the slope from the plot of the capacitive current vs. scan rate plot. The value of C_{dl} is proportional to the ECSA.

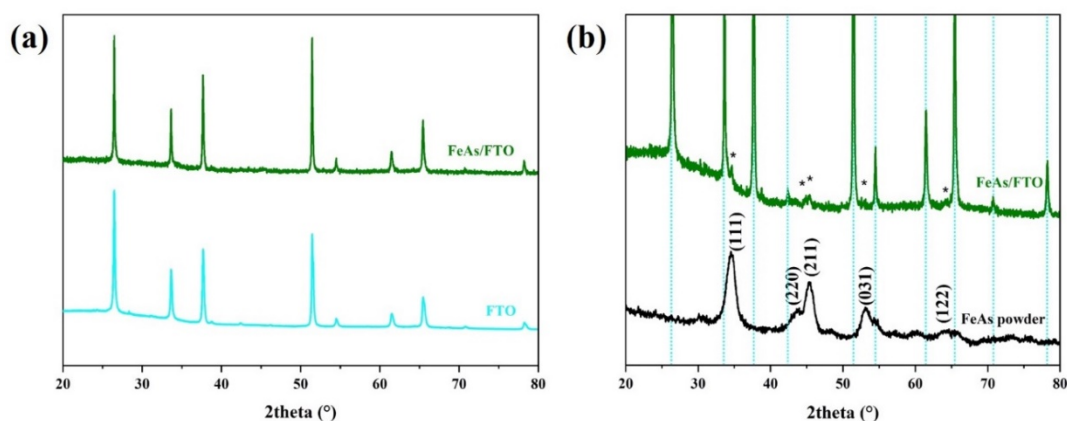


Figure A.2.19. (a) XRD patterns of FeAs/FTO compared to bare FTO, (b) zoom-in of the XRD spectra of FeAs/FTO compared to powder FeAs, showing the signals emerging on the diffraction pattern after deposition. The light blue lines represent the diffractions peaks at 2θ of 26.5, 33.9, 27.9, 51.8, 54.8, 61.9, 65.9, and 78.7 are associated to the (110), (101), (200), (211), (220), (310), (301), (321) crystalline planes of FTO (cassiterite, SnO_2 , JCPDS 41-1445).^[382] A closer inspection of the diffractogram (b) revealed low-intensity signals at which were related to the (111), (220), (211), (031) and (122) planes of orthorhombic FeAs (JCPDS 6-458),^[358–360] which proved that the deposition of the FeAs was accomplished without variation on the crystal structure.

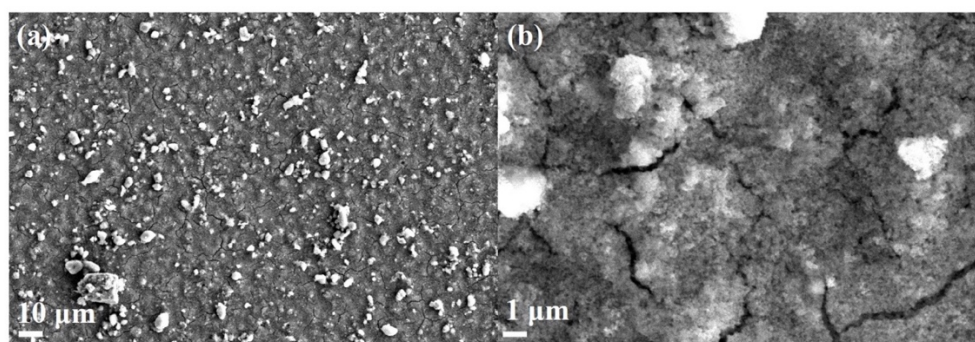


Figure A.2.20. SEM of the FeAs films deposited on FTO at (a) 500x and (b) 5000x. Agglomerated FeAs particles can be observed on the low magnification figure. The obtained films were uniform as the FTO substrate was completely covered by the material. The high magnification figure proves that the morphology of the material is the maintained after the deposition (compare to as-prepared FeAs SEM Figure A.2.2).

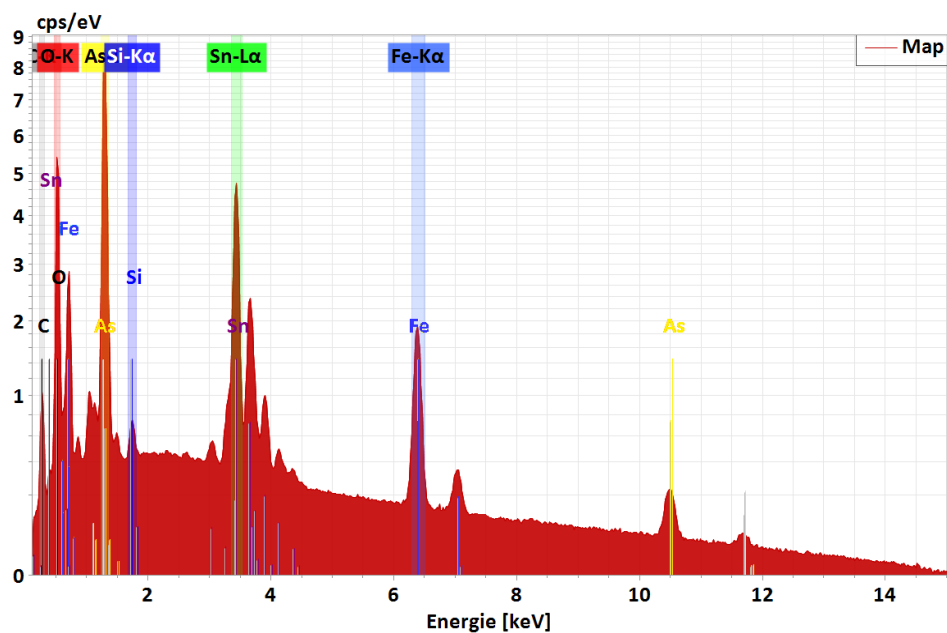


Figure A.2.21. SEM-EDX of the FeAs film deposited on FTO, which confirmed the presence of Fe and As. The presence of Si emission peaks ($K\alpha_1$, $K\alpha_2$ at 1.740 keV, 1.739 keV and $K\beta_1$ at 1.836 keV) arises from the Si wafer used in the measurement. Sn signals arise from the FTO substrate. Fe:As ratio on the film is 1:1.24 as determined by SEM-EDX. The value was equivalent to the ratio found by EDX of the FeAs powder (Appendix, see Table A.2.1).

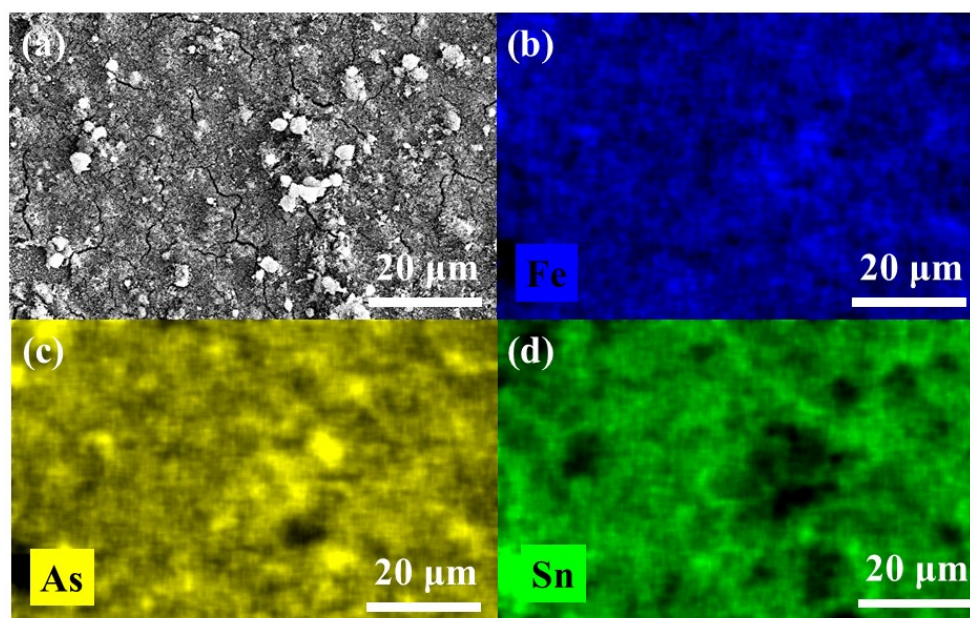


Figure A.2.22. (a) SEM of FeAs/FTO and elemental mapping of (b) Fe (blue), (c) As (yellow) and (d) Sn (green). Sn arises from the FTO glass substrate. Homogenous distribution of Fe and As was observed in the particles deposited on FTO, which indicated that the FeAs particles did not suffer any chemical transformation during the EPD.

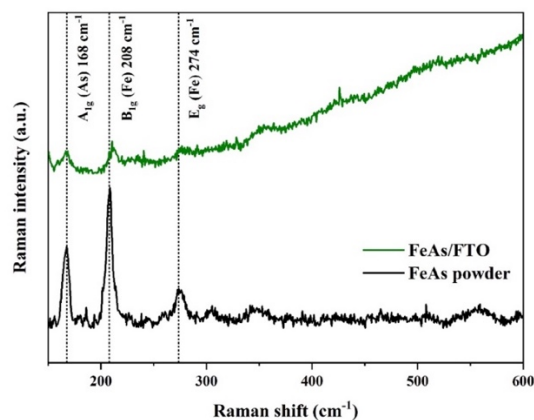


Figure A.2.23. (Resonance) Raman spectra of FeAs/FTO compared to FeAs powder. The spectrum shows three maximum intensity bands at 168, 208, and 274 cm^{-1} which corresponded to the A_{1g} (As), E_{1g} (Fe), and B_{1g} (Fe) phonon bands of FeAs nanoparticles.^[361,362] The (resonance) Raman spectrum of are FTO was used as a reference during this measurement (see Figure A.2.24).

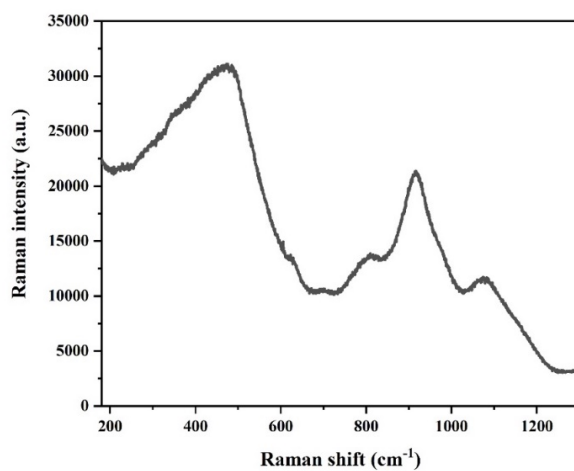


Figure A.2.24. (Resonance) Raman spectrum of bare FTO. This spectrum was used as a reference in order to assign band frequencies referring only to FeAs.

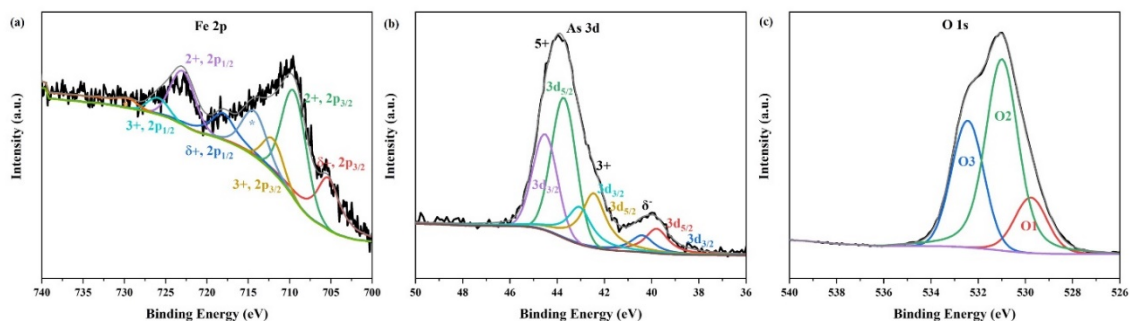


Figure A.2.25. XPS measurements confirmed that there was no electronic and chemical transformation on the surface of the FeAs/FTO films during their preparation. The deconvoluted XPS spectra of FeAs/FTO are shown on (a) Fe 2p, (b) As 3d and (c) O 1s. The Fe 2p deconvoluted spectrum shows two peaks for $\text{Fe}^{\delta+}$ at low binding energies of $2p_{3/2}$ 705.5 eV and $2p_{1/2}$ 718.2 eV,^[365] and at higher binding energy associated to oxidized species due to contact with air: Fe^{II} ($2p_{3/2}$ 709.7 eV and $2p_{1/2}$ 723.1 eV) and Fe^{III} ($2p_{3/2}$ 712.4 eV and $2p_{1/2}$ 726.1 eV), and one pair of satellite peaks from Fe^{II} ($2p_{3/2}$ 714.5 eV and $2p_{1/2}$ 729.6 eV). The As 3d deconvoluted spectrum shows two peaks related to remaining $\text{As}^{\delta-}$ present in FeAs (40.0 eV), deconvoluted into 39.8 eV ($3d_{5/2}$) and 40.4 eV ($3d_{3/2}$), and oxidized As^{III} (43.2 eV) and As^{V} (43.9 eV) due to air exposure, deconvoluted into 42.5 eV ($3d_{5/2}$) and 43.1 eV ($3d_{3/2}$), and 43.8 eV ($3d_{5/2}$) and 44.5 eV ($3d_{3/2}$), respectively.^[367] Finally, the O 1s spectrum revealed surface passivation due to contact with air. The spectrum shows one peak (531.1 eV) which is deconvoluted into three peaks derived from air exposure: Fe-O (O1, 529.8 eV)^[366] and As-O (O2, 531.0 eV).^[367,368] The peak at higher binding energy (O3, 532.5 eV) is associated to adsorbed water on the surface.^[366]

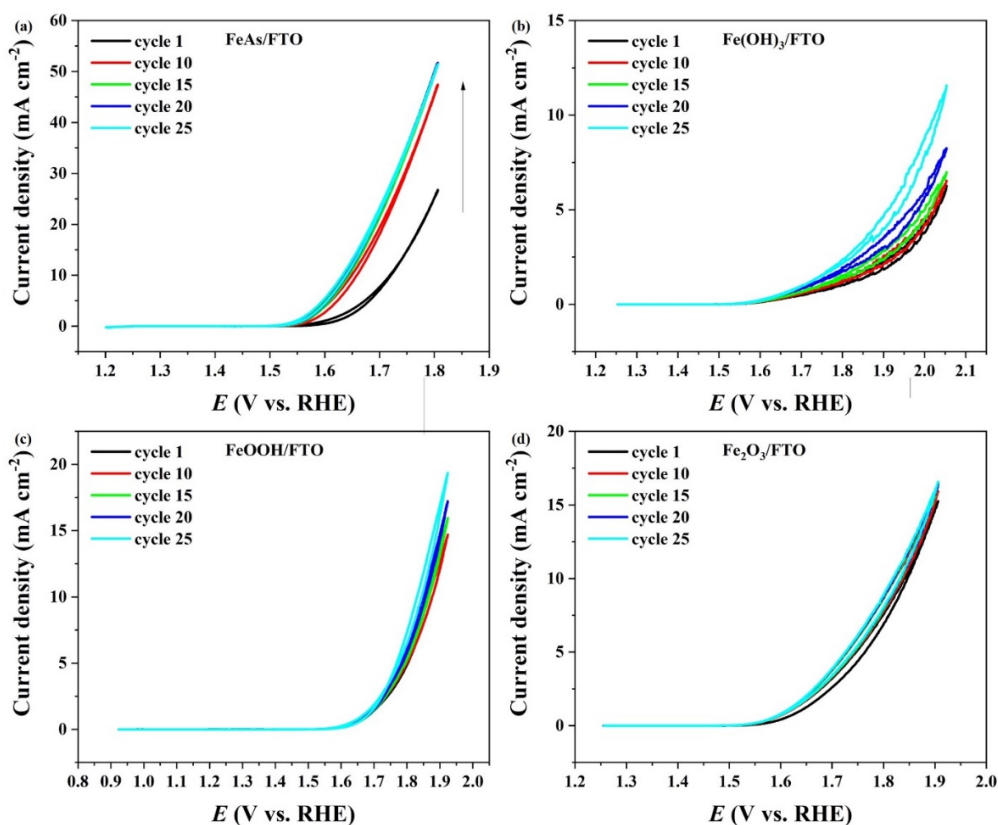


Figure A.2.26. Activation of the (a) FeAs/FTO, (b) $\text{Fe}(\text{OH})_3/\text{FTO}$, (c) FeOOH/FTO , and (d) $\text{Fe}_2\text{O}_3/\text{FTO}$ by CV in 1 M KOH, scan rate: 5 mV s^{-1} .

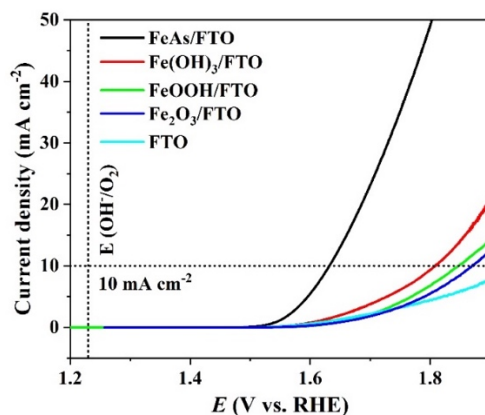


Figure A.2.27. LSV (scan rate: 5 mV s^{-1}) of FeAs and Fe reference materials loaded on FTO (0.5 mg cm^{-2}). The order found for the overpotentials was the same as in the case of NF. For FeAs/FTO, $\eta = 395 \text{ mV}$ (10 mA cm^{-2}) was obtained, which is substantially lower than Fe(OH)₃/FTO (577 mV), FeOOH/FTO (609 mV) and Fe₂O₃/FTO (639 mV).

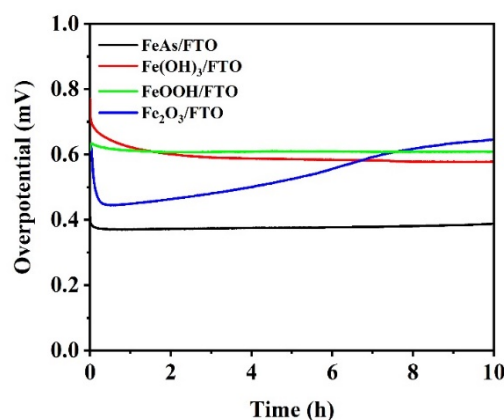


Figure A.2.28. CP at 10 mA cm^{-2} for 10 h on FTO. A slight increase of the overpotential was observed during the experiment for the FeAs/FTO ($\eta = 380 \text{ mV}$). The Fe-based reference materials show all deactivation after 10 h of continuous electrolysis: Fe(OH)₃ ($\eta = 580 \text{ mV}$), FeOOH ($\eta = 610 \text{ mV}$), Fe₂O₃ ($\eta = 650 \text{ mV}$).

Table A.2.5. Deposition time, mass loading on 1 cm^2 , and overpotential (10 mA cm^{-2}) of FeAs films over FTO.

Deposition time (s)	Mass loading (mg)	Overpotential (mV @ 10 mA cm^{-2})	Current density at $\eta = 500 \text{ mV}$
4	0.0062*	633 ± 4	4.43
7.5	0.0125*	604 ± 3	4.60
15	0.025*	533 ± 5	7.88
30	0.05*	530 ± 3	7.93
60	0.1 ± 0.1	448 ± 2	14.23
120	0.2 ± 0.1	442 ± 5	16.68
240	0.4 ± 0.1	392 ± 4	34.35
480	0.6 ± 0.1	402 ± 4	31.39

*weight determined by extrapolation of higher time deposition weights. The weight difference was not possible to measure precisely due to limitations in the used scale.

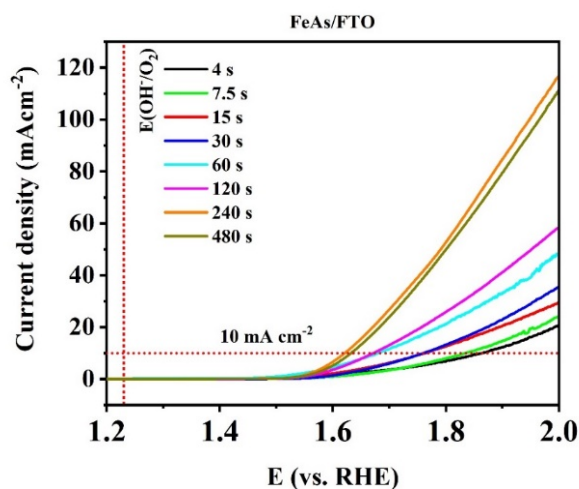


Figure A.2.29. Polarization curves recorded for films prepared with different mass loadings of FeAs on 1 cm² FTO surface in 1 M KOH solution with a sweep rate of 20 mV s⁻¹ (4 s to 480 s).

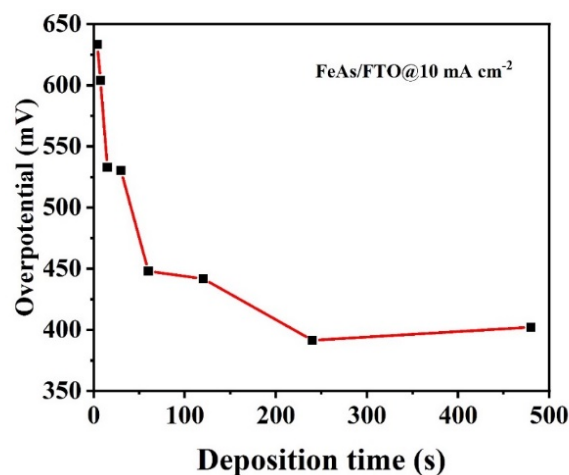


Figure A.2.30. The overpotentials of FeAs on 1 cm² FTO surface with respect to deposition time of 4 s to 480 s (varying mass loadings; see Table A.2.5).

Table A.2.6. Deposition time, mass loading on 1 cm², and overpotential (10 mA cm⁻²) of Fe(OH)₃ films over FTO.

Deposition time (s)	Mass loading (mg)	Overpotential (mV @10 mA cm ⁻²)	Current density at $\eta = 600$ mV
4	0.05*	**	0.20
7.5	0.1 ± 0.1	**	0.39
15	0.2 ± 0.1	836 ± 5	2.16
30	0.5 ± 0.1	763 ± 6	3.48
60	1.0 ± 0.1	723 ± 3	4.40
120	1.6 ± 0.1	648 ± 4	6.93
240	2.4 ± 0.1	583 ± 5	11.31
480	3.0 ± 0.1	598 ± 5	10.11

*weight determined by extrapolation of higher time deposition weights. The weight difference was not possible to measure precisely due to limitations in the used scale.**the overpotential was not determined because the current densities were below 10 mA cm⁻² (Figure A.2.31).

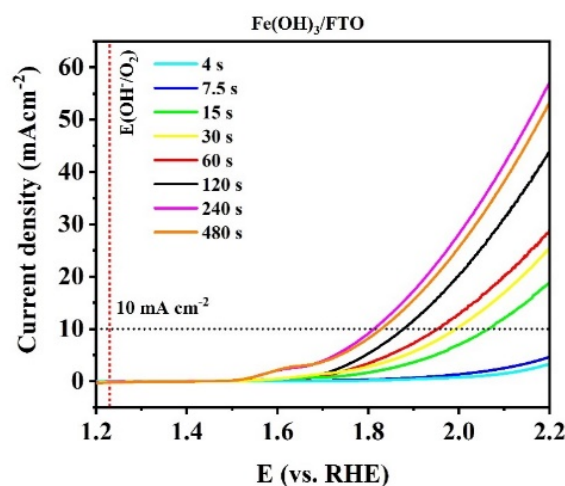


Figure A.2.31. Polarization curves recorded for films prepared with different mass loadings of $\text{Fe}(\text{OH})_3$ on 1 cm^2 FTO surface in 1 M KOH solution with a sweep rate of 20 mV s^{-1} (4 s to 480 s).

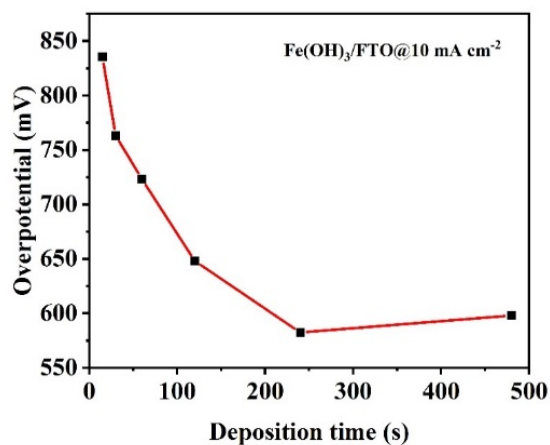


Figure A.2.32. The overpotentials of $\text{Fe}(\text{OH})_3$ on 1 cm^2 FTO surface with respect to deposition time of 4 s to 480 s (varying mass loadings; see Table A.2.6).

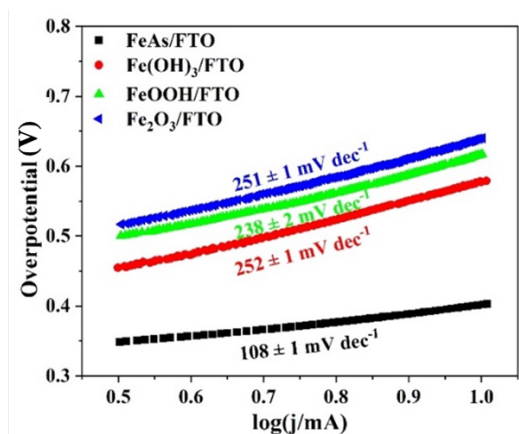


Figure A.2.33. Tafel slopes obtained from LSVs (1 mV s^{-1}) of FeAs/FTO , and Fe reference materials loaded on FTO (0.5 mg cm^{-2}). The FeAs/FTO has the lowest Tafel slope, indicating faster reaction kinetics.^[292] The Tafel slope increased in the order $\text{FeAs}/\text{FTO} < \text{Fe}(\text{OH})_3/\text{FTO} < \text{FeOOH}/\text{FTO} < \text{Fe}_2\text{O}_3/\text{FTO}$ and follows the same order as obtained for the samples deposited on NF.

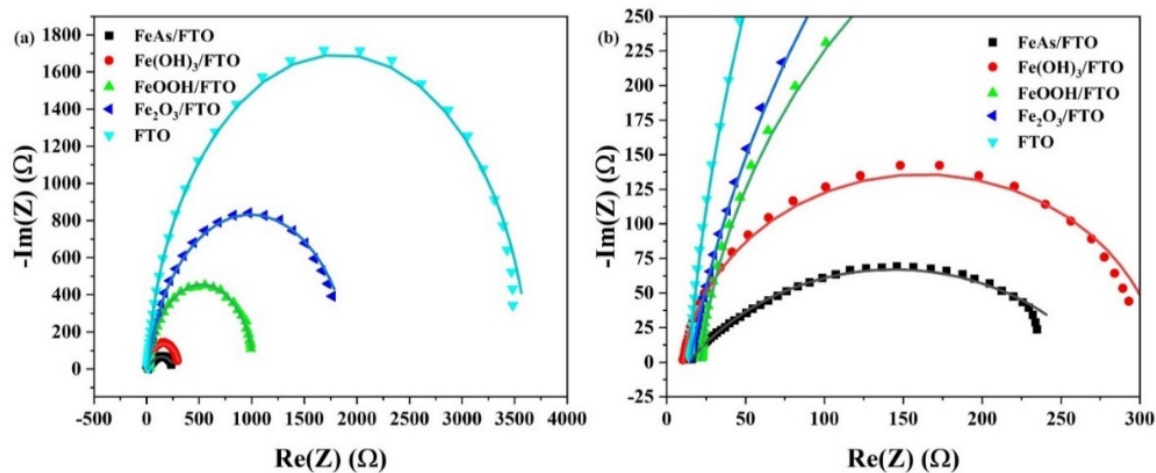


Figure A.2.34. Nyquist plot constructed from the EIS experiment of materials deposited on FTO. The spectra were collected with an anodic polarization potential of 1.58 V vs. RHE. (b) Zoom of the Nyquist plot. The continuous lines show the fitting to the circuit that contains two resistors R_1 and R_2 and Q a CPE (see Figure 4.9 and Figure 7.16). The discussion of the fitting of the parameters is shown on Figure A.2.15.

Table A.2.7. R_2 (Ω) (R_{ct}), R_1 (Ω) (R_s), Q ($F \times s^{(a_2-1)}$) and a_2 of FeAs, Fe(OH)₃, FeOOH and Fe₂O₃ deposited on FTO, compared to the bare FTO.

Material	R_{ct} (Ω)	R_s (Ω)	Q ($F \times s^{(a_2-1)}$)	a_2
FTO	3626.0 ± 0.6	14.3 ± 0.2	$9.0 \times 10^{-6} \pm 1.3 \times 10^{-8}$	$9.6 \times 10^{-1} \pm 1.0 \times 10^{-2}$
FeAs/FTO	260.3 ± 0.3	13.9 ± 0.3	$5.1 \times 10^{-4} \pm 9.7 \times 10^{-6}$	$6.1 \times 10^{-1} \pm 1.1 \times 10^{-2}$
Fe(OH) ₃ /FTO	303.3 ± 0.9	10.4 ± 0.3	$1.7 \times 10^{-5} \pm 4.8 \times 10^{-7}$	$9.3 \times 10^{-1} \pm 1.2 \times 10^{-2}$
FeOOH/FTO	1000.2 ± 0.4	21.5 ± 0.3	$1.4 \times 10^{-5} \pm 9.9 \times 10^{-8}$	$9.4 \times 10^{-1} \pm 1.1 \times 10^{-2}$
Fe ₂ O ₃ /FTO	1949.0 ± 1.8	14.8 ± 0.3	$2.8 \times 10^{-5} \pm 3.8 \times 10^{-8}$	$9.0 \times 10^{-1} \pm 1.0 \times 10^{-2}$

Table A.2.8. Specific resistivity ρ (Ω cm) of FeAs, Fe(OH)₃, FeOOH, Fe₂O₃, and FeAs after CP OER deposited on FTO.

Material	ρ (Ω cm)
FeAs/FTO	1.86×10^2
FeAs/FTO after OER	3.09×10^3
Fe(OH) ₃ /FTO	5.60×10^4
FeOOH/FTO	2.30×10^5
Fe ₂ O ₃ /FTO	2.45×10^5

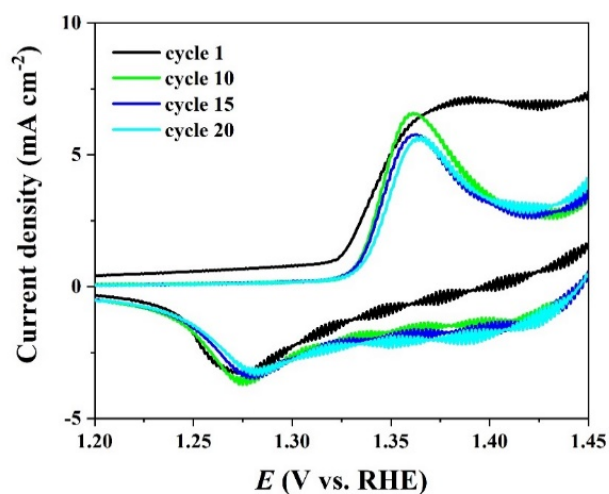


Figure A.2.35. Evolution of redox peak observed for FeAs/NF. The anodic and cathodic peaks appear at 1.36 V and 1.28 V, respectively (vs. RHE). Scan rate: 5 mV s⁻¹.

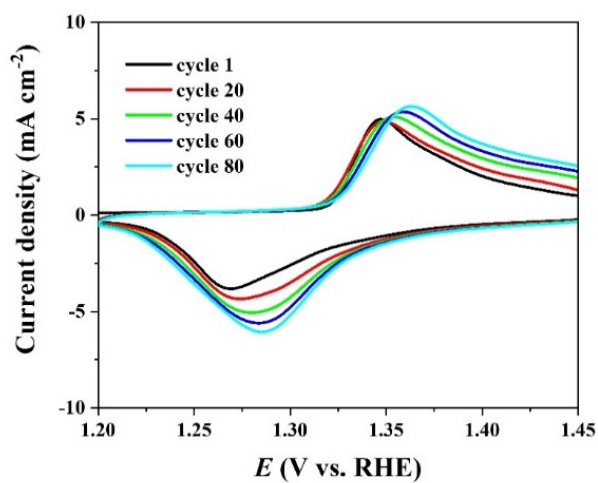


Figure A.2.36. Evolution of redox peaks observed for bare NF. The anodic and cathodic peaks appear at 1.36 V and 1.28 V, respectively (vs. RHE). Scan rate: 5 mV s⁻¹.

Post catalytic characterization

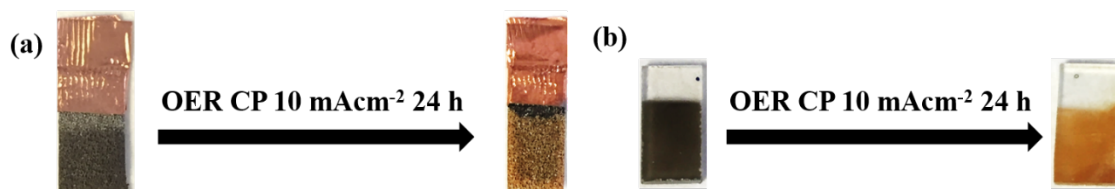


Figure A.2.37. Change of color of FeAs films deposited on (a) NF and (b) FTO during long-term OER CP 10 mA cm⁻² experiment.

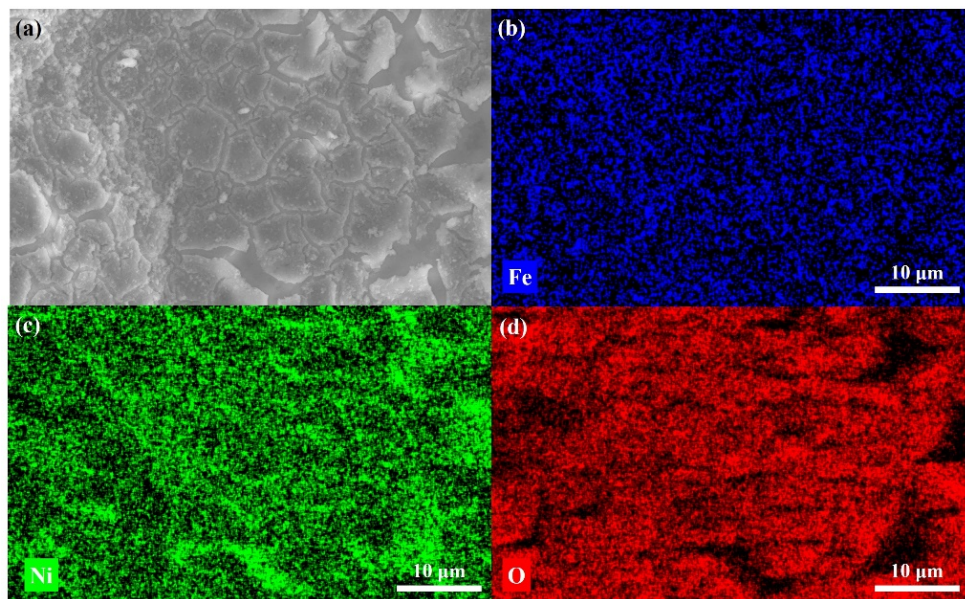


Figure A.2.38. (a) SEM of FeAs/NF after continuous CP OER for 2 h of activation and elemental mapping of (b) Fe (blue), (c) Ni (green) and (d) O (red). Sn arises from the FTO glass substrate. Homogenous distribution of Fe and O can be observed on the areas where the film is remaining. As mapping is not included since As leaches into the solution (see EDX below). Ni arises from the NF.

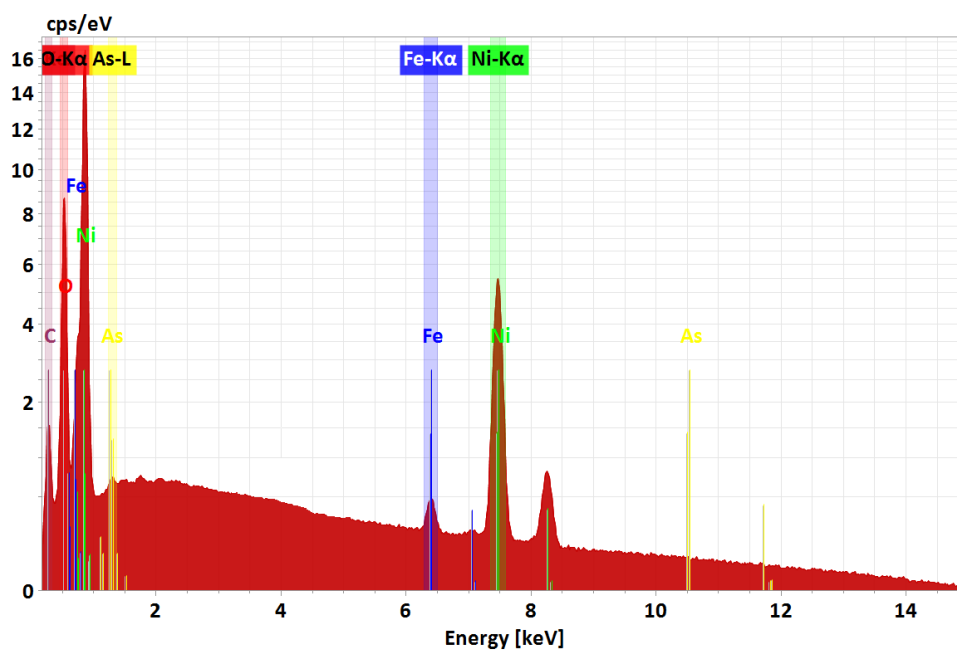


Figure A.2.39. SEM-EDX of the film of FeAs/NF after CP OER for 2 h of activation. Fe is present after OER. The peaks corresponding to the high-energy emission of As ($K\alpha_1$, $K\alpha_2$ at 10.54 keV, 10.51 keV and $K\beta_1$ at 11.73 keV) do not appear. SEM-EDX Fe:As ratio was 1:0.06.

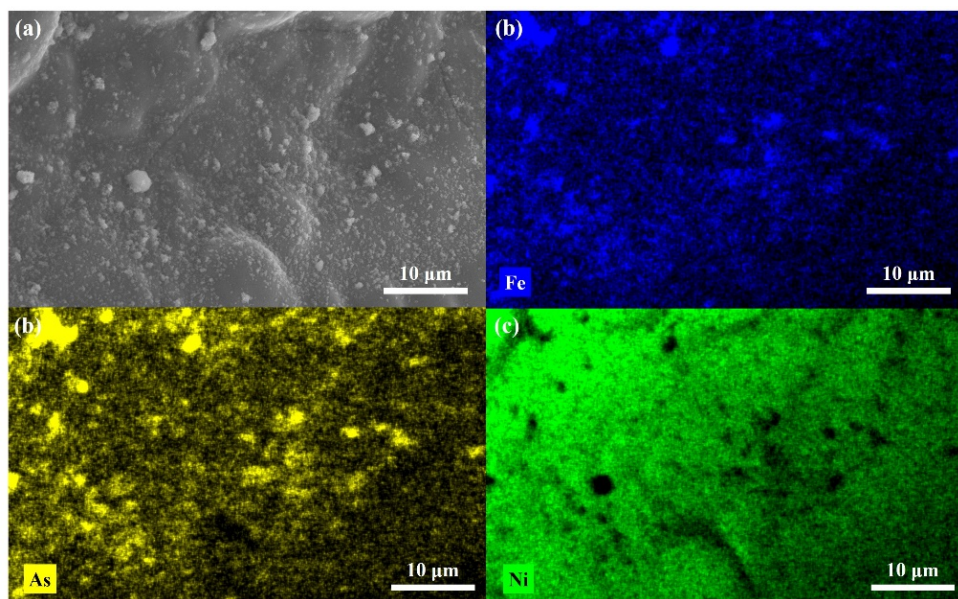


Figure A.2.40. (a) SEM of FeAs/NF after one CV and elemental mapping of (b) Fe (blue), (c) As (yellow) and (d) Ni (green). Ni arises from the NF.

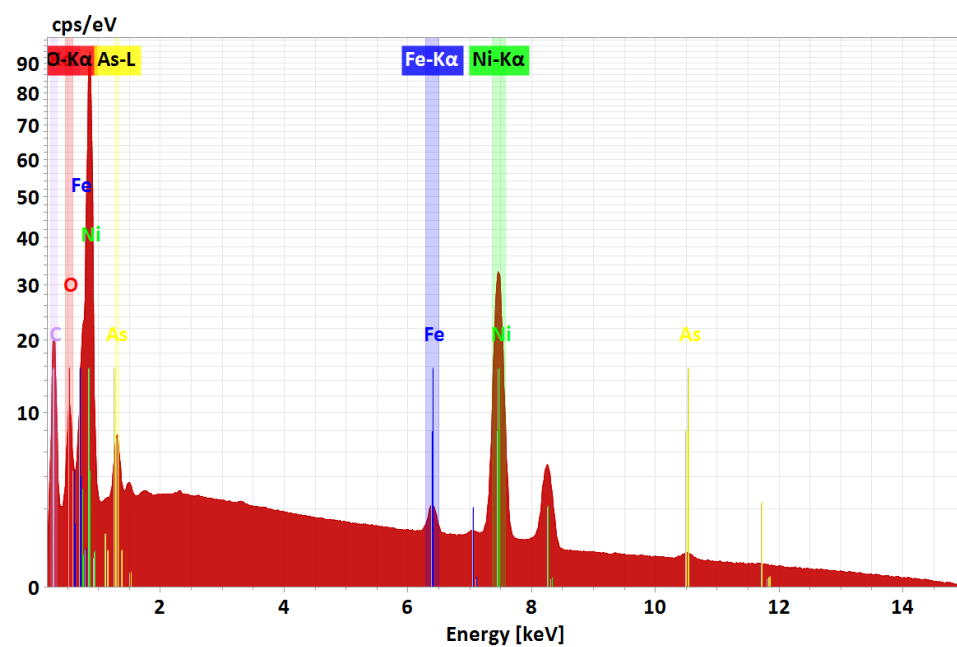


Figure A.2.41. SEM-EDX of the film of FeAs/NF after one CV. Fe is present after OER. The attained SEM-EDX Fe:As ratio was 1:0.91.

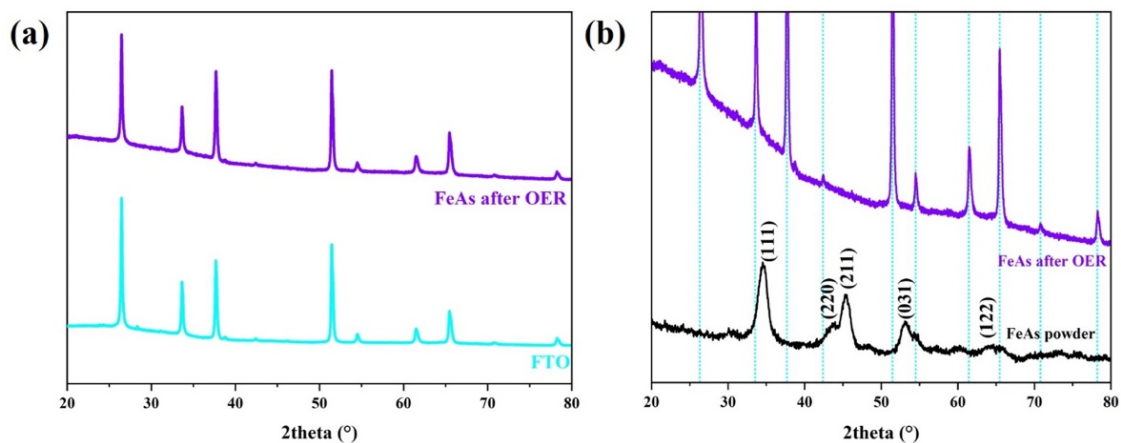


Figure A.2.42. (a) XRD patterns of FeAs/FTO after OER compared to bare FTO, (b) zoom-in of the XRD spectra of FeAs/FTO after OER compared to powder FeAs, showing no signals of FeAs are left after OER which indicates the transformation of the material (compare to as-prepared FeAs/FTO XRD pattern on Figure A.2.19). The light blue lines represent the diffractions peaks associated with FTO (cassiterite, SnO_2 , JCPDS 41-1445).

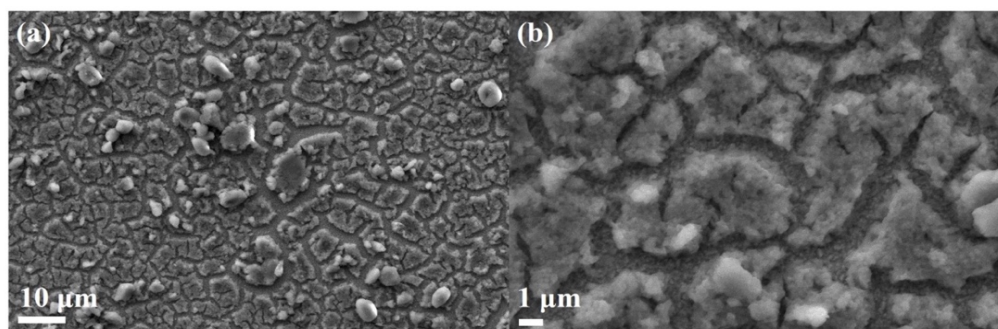


Figure A.2.43. SEM of the FeAs/FTO after OER at (a) 1000x and (b) 5000x. The image shows the cracking of the film, exposing FTO. The cracking appears during the drying process as reported before in the literature.^[383]

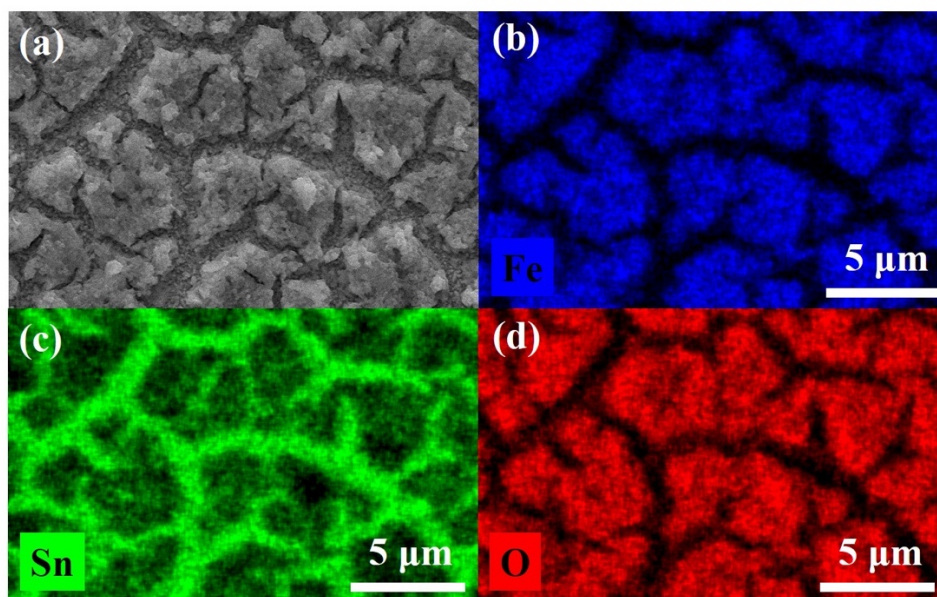


Figure A.2.44. (a) SEM of FeAs/FTO after OER and elemental mapping of (b) Fe (blue), (c) Sn (green) and (d) O (red). Homogenous distribution of Fe and O can be observed on the areas where the film is remaining. As mapping is not included since 96 % of As leaches into the solution (see Figure A.2.45). Sn arises from the FTO glass substrate.

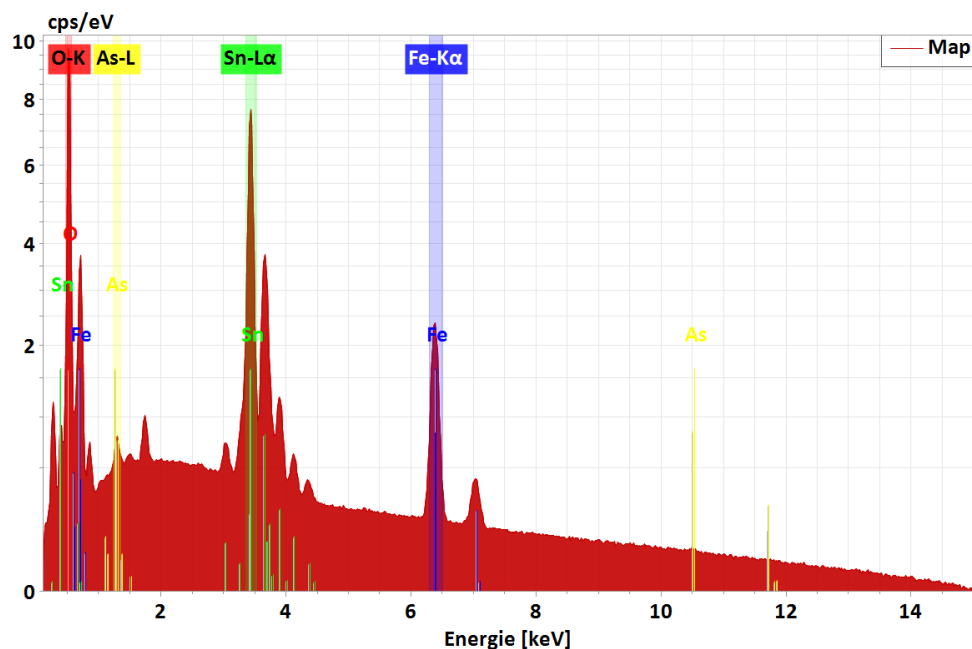


Figure A.2.45. SEM-EDX of the film of FeAs/FTO after OER. Fe is present after OER, however the peaks corresponding to the high-energy emission of As ($K\alpha_1$, $K\alpha_2$ at 10.54 keV, 10.51 keV and $K\beta_1$ at 11.73 keV) do not appear, indicating a loss of As into the solution. The attained SEM-EDX Fe:As ratio was 1:0.04. The emission peaks in the 1.5-2 keV region correspond to Al ($K\alpha_1$, $K\alpha_2$ at 1.487 keV, 1.486 keV and $K\beta_1$ at 1.557 keV) and Si ($K\alpha_1$, $K\alpha_2$ at 1.740 keV, 1.739 keV and $K\beta_1$ at 1.836 keV) arise from the Al sample holder and the Si wafer used during the measurement, respectively.

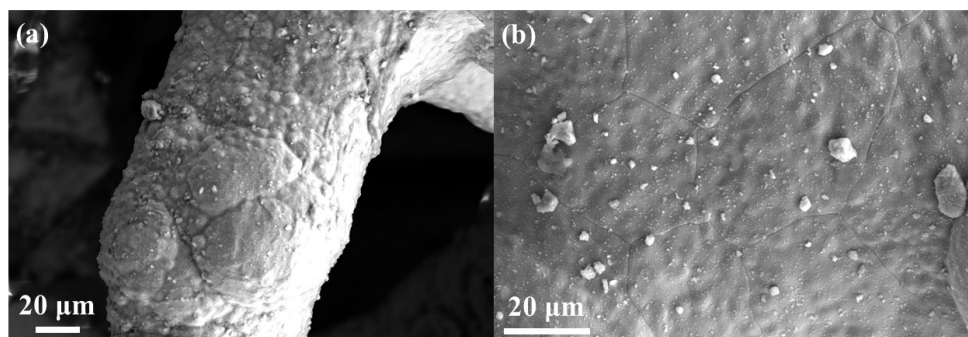


Figure A.2.46. SEM of the FeAs/NF after OER.

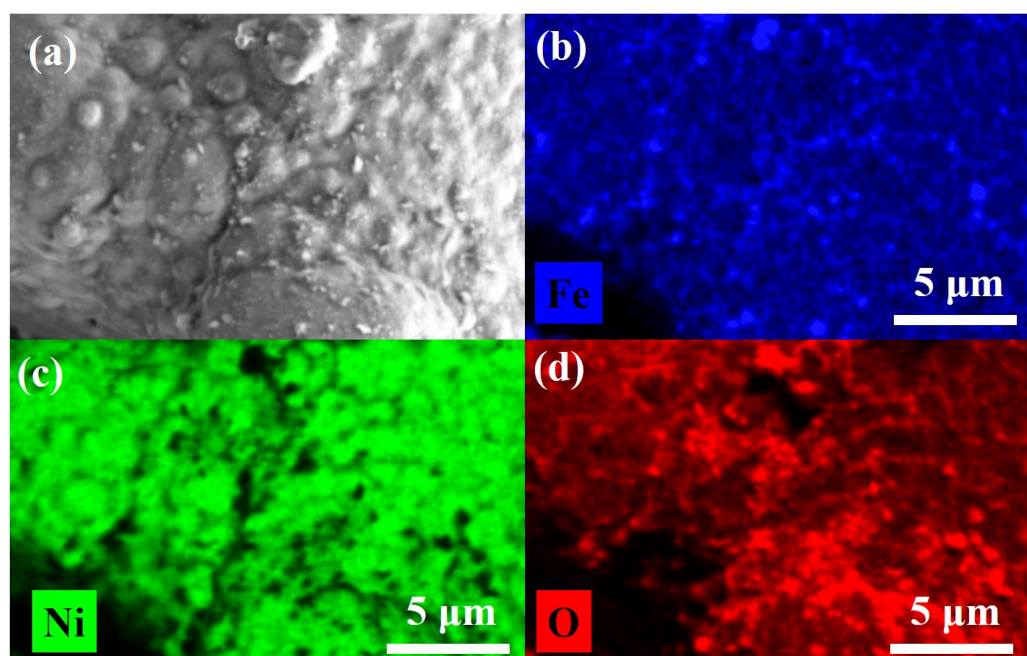


Figure A.2.47. (a) SEM of FeAs/NF after OER and elemental mapping of (b) Fe (blue), (c) As (yellow), (d) Sn (green) and (e) O (red). Homogenous distribution of Fe and O can be observed on the areas where the film is remaining. As mapping is not included since 95 % of As leaches into the solution (see Figure A.2.48). Ni arises from the NF.

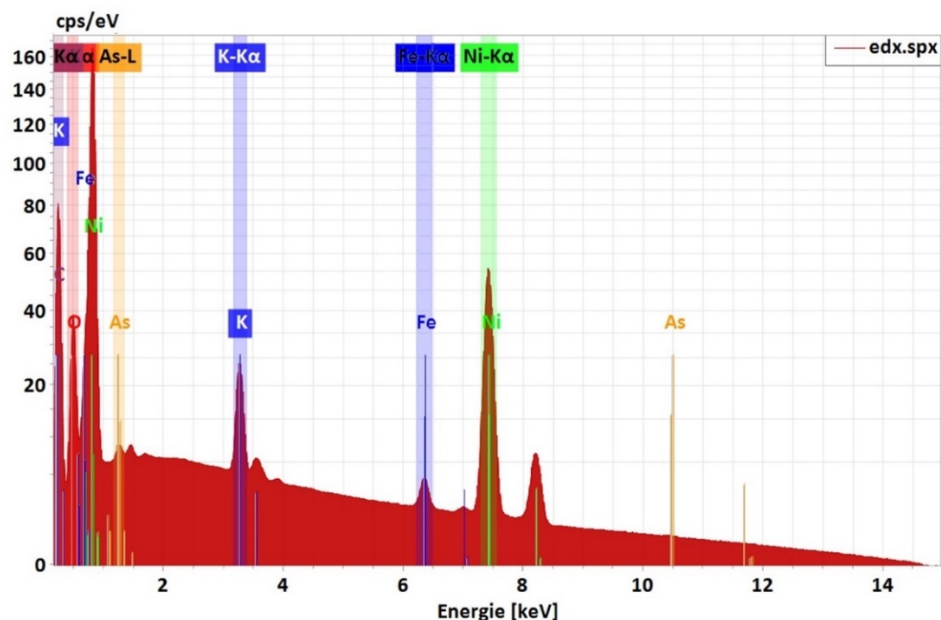


Figure A.2.48. SEM-EDX of the film of FeAs/NF after OER. Fe is present after OER, in a similar way as in the experiment on FTO (see Figure A.2.45) the peaks corresponding to the high-energy emission of As ($K\alpha_1$, $K\alpha_2$ at 10.54 keV, 10.51 keV and $K\beta_1$ at 11.73 keV) do not appear. The attained SEM-EDX Fe:As ratio was 1:0.05. The emission peaks in the 1.5-2 keV region correspond to Al ($K\alpha_1$, $K\alpha_2$ at 1.487 keV, 1.486 keV and $K\beta_1$ at 1.557 keV) and Si ($K\alpha_1$, $K\alpha_2$ at 1.740 keV, 1.739 keV and $K\beta_1$ at 1.836 keV) arise from the Al sample holder and the Si wafer used during the measurement, respectively. The presence of K is due to KOH 1M electrolyte used for the experiment.

Table A.2.9. The concentration of Fe and As in the electrolyte solution after CP OER on FTO and NF. The concentration was determined by ICP-AES of the solution. For each long-term experiment, 45 mL of 1 M KOH were used. The electrolyte solution was divided into three parts (15 mL each) and each one measured by ICP-AES. The average value of three independent measurements is shown on the table. The percentage of element loss in solution was calculated from the concentration in solution, the initial Fe:As ratio and the mass loading of the films.

Sample	Fe (mg L ⁻¹)	As (mg L ⁻¹)	Fe:As ratio	% of element loss in solution	
				% Fe	% As
1 M KOH	0.00	0.00	-	-	-
FeAs/FTO OER CP 24 h	0.13	0.33	2.00	3.4 %	6.3 %
FeAs/NF OER CP 24 h	0.29	2.33	6.02	3.1 %	18.0 %



Figure A.2.49. Pt CE used during the OER experiments with FeAs/FTO. The lower part (which was in contact with the 1 M KOH solution) turned black due to the deposition of As.

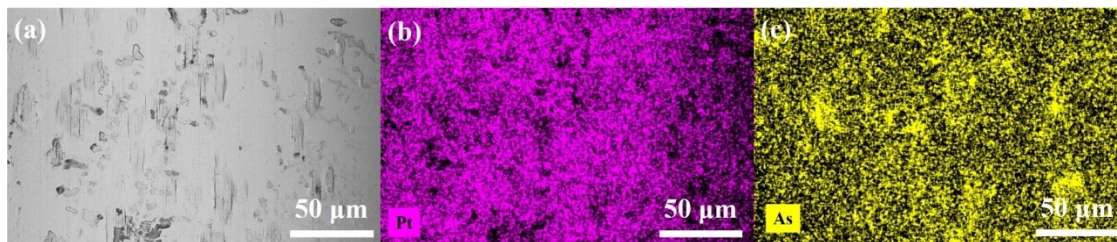


Figure A.2.50. (a) SEM of the Pt CE used during the OER experiments. Elemental mapping of (b) Pt (violet) and (c) As (yellow). The same measurements were done on the non-exposed part of the Pt CE, and no presence of As was found.

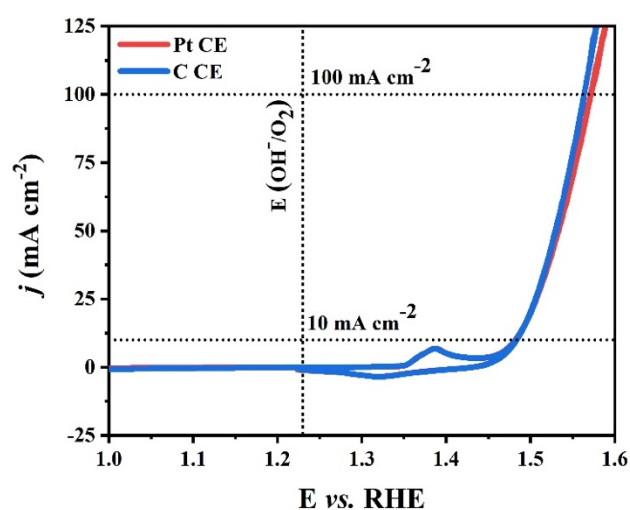


Figure A.2.51. LSV (1 mV s^{-1}) for OER under 1 M KOH of FeAs/NF using a three-electrode system. The effect of changing the CE was explored and Pt was replaced by a graphitic carbon rod. The difference in overpotential obtained by each material is minimum (1 mV).

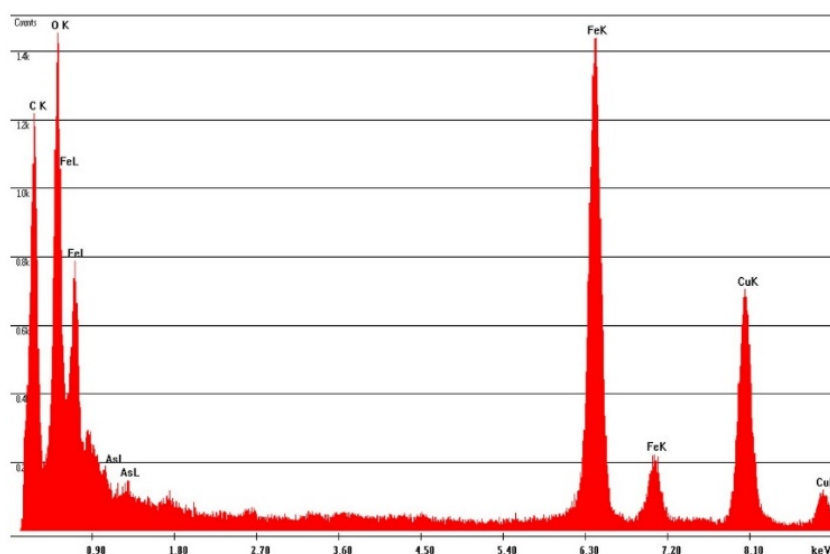


Figure A.2.52. TEM-EDX of FeAs/FTO after OER (CP OER 24 h). The presence of C and Cu arise from the carbon film substrate deposited on the 300 mesh Cu-grid used during the measurement. The Fe:As and Fe:O ratio can be derived from this experiment, resulting in 1:0.019 and 1:1.67, respectively. The EDX results indicate that only 1.73 % of As is left after catalysis.

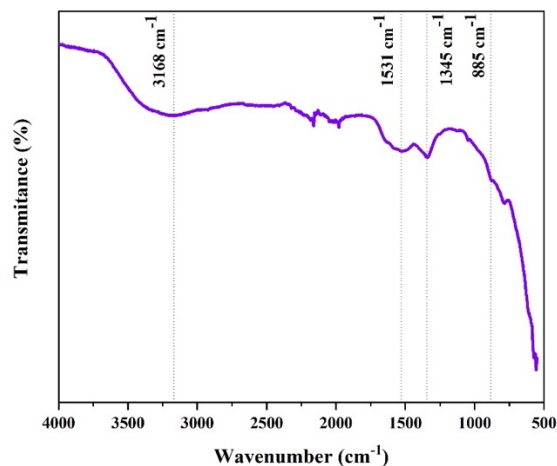


Figure A.2.53. IR spectrum of FeAs/FTO after OER. The noted absorption bands have been observed before on pure 2-line ferrihydrite: (i) the absorption band at 3168 cm^{-1} is attributed to OH stretching, (ii) the bands at 1531 cm^{-1} and 1345 cm^{-1} are related to Fe-OH bending and Fe-O stretching, respectively, and (iii) at 885 cm^{-1} band corresponding to the bending vibration of the hydroxyl groups of Fe hydroxides (Fe-OH).^[397]

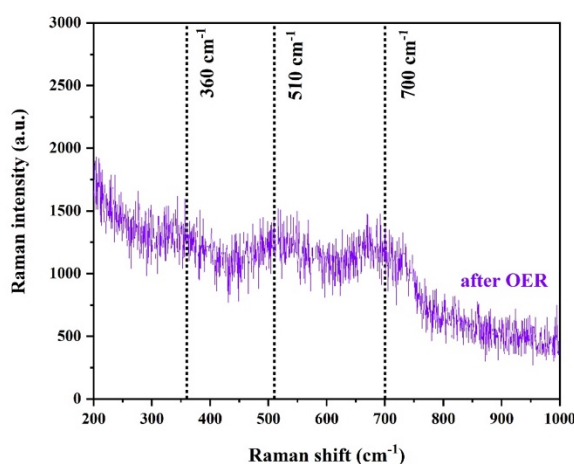


Figure A.2.54. Raman spectrum of FeAs/FTO after CP OER 24 h. It shows three broad absorption bands that have been observed before on 2-line ferrihydrite.^[396,397,401,403,404]

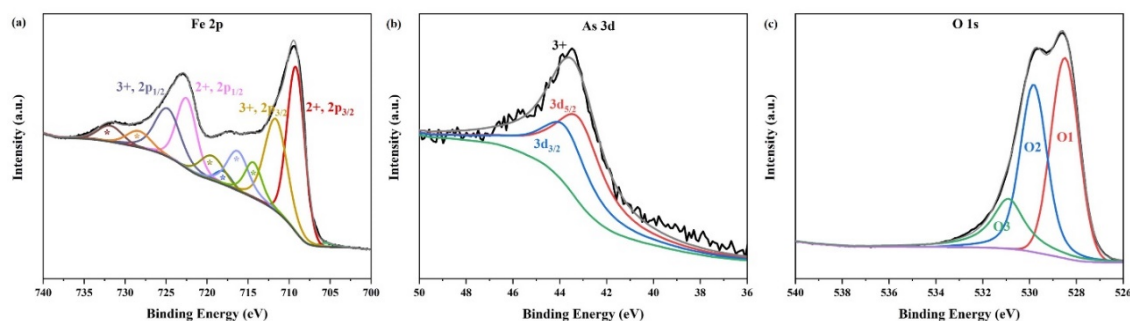


Figure A.2.55. Deconvoluted XPS of FeAs/FTO after OER: (a) Fe 2p, (b) As 3d and (c) O 1s.

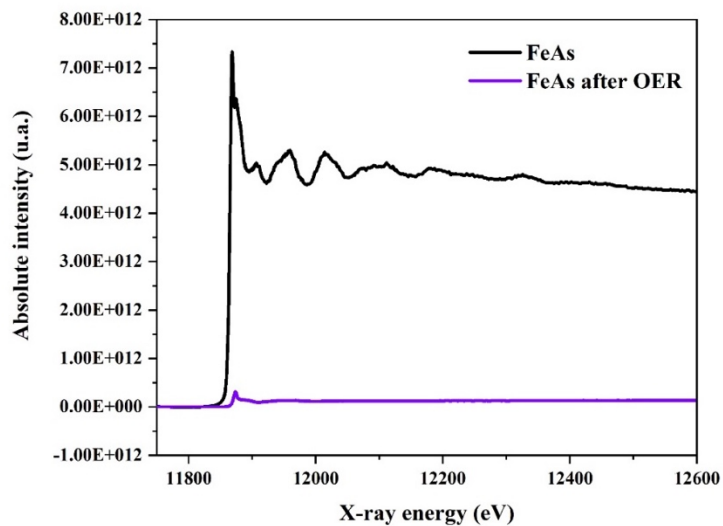


Figure A.2.56. Absolute intensity of As-XANES fluorescence absorption for FeAs powder and FeAs after OER. A case of “missing edge” is shown, in which the intensity of the signals after OER is reduced to a minimum due to the loss of As into the solution.

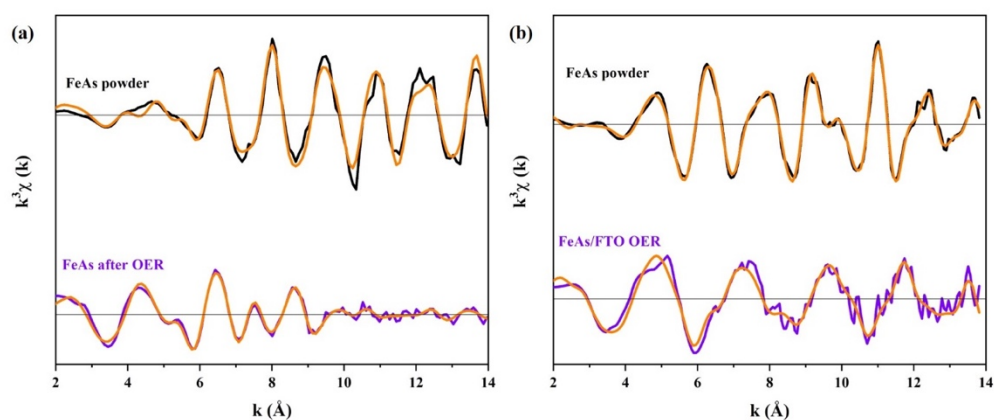


Figure A.2.57. k^3 -weighted EXAFS of (a) Fe and (b) As for FeAs powder and FeAs after OER.

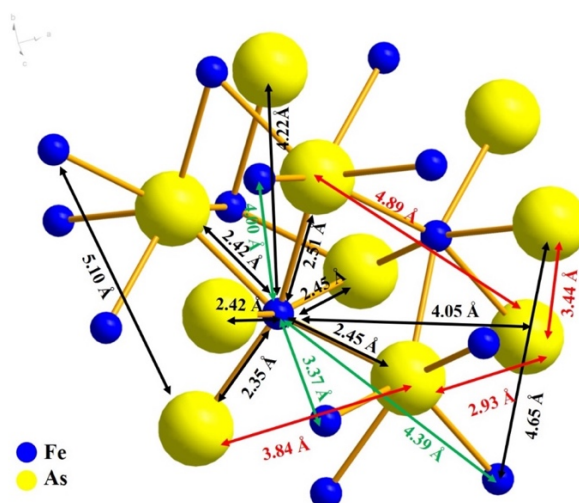


Figure A.2.58. Distance between atoms on the FeAs structure (JCPDS 76-458, orthorhombic). Fe-As distances are shown in black, Fe-Fe in green and As-As in red.

Table A.2.10. Fe-EXAFS fit parameters for the FeAs powder.

FeAs powder Fe-EXAFS (Rf = 14.0)							
type	N	err	R	R_{XRD}	err	DW	err
Fe-O	1.4	0.3	2.05		0.01	0.039	0.004
Fe-As	3.7	0.4	2.45	2.44	0.00	0.060	0.004
Fe-Fe	1.1	0.4	3.38	3.37	0.02	0.060	0.004
Fe-Fe	4.5	2.0	3.99	4.00	0.02	0.060	0.004
Fe-As	4.0	3.9	4.12	4.05	0.03	0.060	0.004
Fe-As	3.3	2.9	4.33	4.22	0.05	0.060	0.004
Fe-Fe	3.0	1.9	4.52	4.39	0.04	0.060	0.004

Table A.2.11. As-EXAFS fit parameters for the FeAs powder.

FeAs powder As-EXAFS (Rf = 5.3)							
type	N	err	R	R_{XRD}	err	DW	err
As-O	0.7	0.2	1.76		0.02	0.043	0.014
As-Fe	3.0	0.5	2.40	2.41	0.01	0.043	0.018
As-Fe	1.8	0.3	2.51	2.48	0.01	0.043	0.018
As-As	1.4	0.3	2.90	2.93	0.00	0.043	0.018
As-As	3.8	1.8	3.47	3.44	0.01	0.078	0.018
As-As	4.9	2.8	3.81	3.84	0.01	0.078	0.018
As-Fe	2.0	1.5	4.10	4.13	0.03	0.078	0.018
As-Fe	4.4	5.1	4.74	4.65	0.03	0.078	0.018
As-As	7.7	9.0	4.89	4.89	0.01	0.078	0.018
As-Fe	5.4	4.7	5.17	5.10	0.03	0.078	0.018

Table A.2.12. Fe-EXAFS fit parameters for the FeAs after OER.

FeAs OER Fe-EXAFS (Rf = 9.9)							
type	N	err	R	R_{XRD}	err	DW	err
Fe-O	2.5	0.0	1.90	1.95	0.00	0.070	0.000
Fe-O	3.4	0.0	2.02	2.10	0.00	0.070	0.000
Fe-Fe	2.7	0.0	3.02	3.02	0.00	0.087	0.000
Fe-Fe	5.5	0.0	3.45	3.44	0.00	0.087	0.000
Fe-O	8.5	0.0	3.60	3.58	0.00	0.087	0.000
Fe-O	3.1	0.0	3.92	3.89	0.00	0.087	0.000
Fe-Fe	2.0	0.0	5.09	5.30	0.00	0.087	0.000
Fe-Fe	3.7	0.0	5.22	5.40	0.00	0.087	0.000

A.3. Appendix of Chapter 5: Amorphous NiP and NiAs

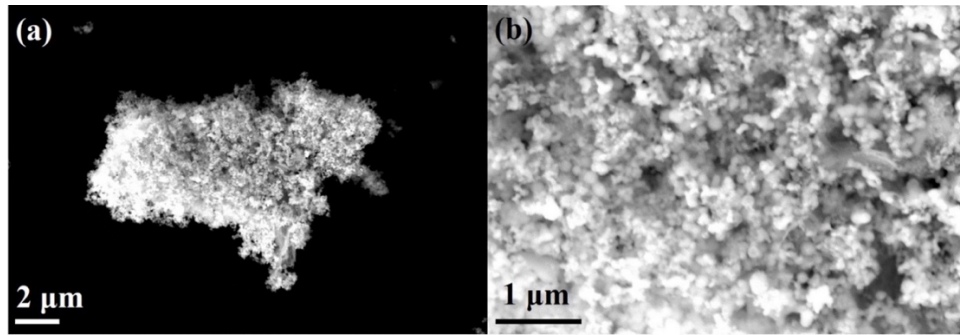


Figure A.3.1. SEM image of agglomerated particles of NiAs at (a) 5000x and (b) 20000x. Particles of ca. 200 nm are observed.

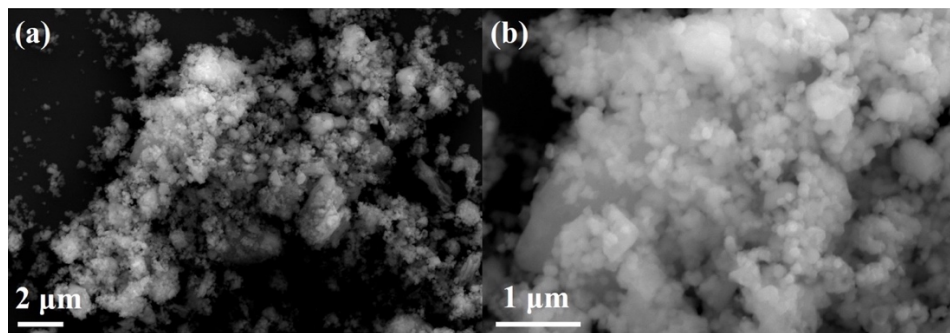


Figure A.3.2. SEM image of agglomerated particles of NiP at (a) 5000x and (b) 20000x. Particles of ca. 200 nm are observed.

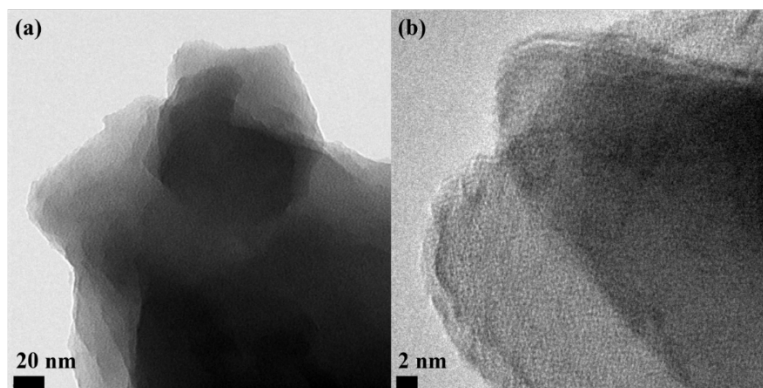


Figure A.3.3. TEM image of (a) NiP nanoparticles and (b) HR-TEM image. The HR-TEM shows the presence of amorphous solid in which no crystalline phases can be observed, confirming the amorphous nature of the material.

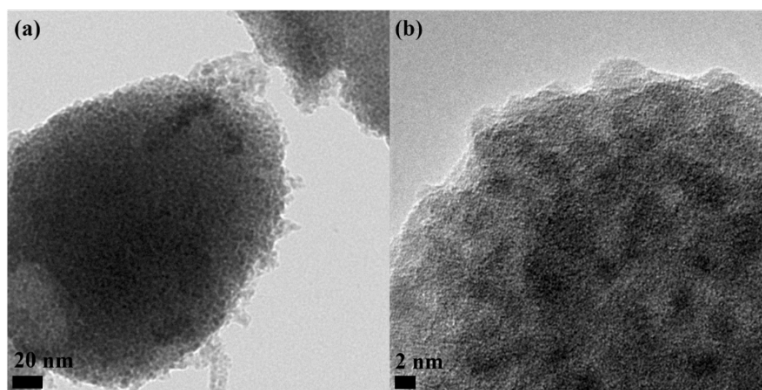


Figure A.3.4. TEM image of (a) NiAs nanoparticles and (b) HR-TEM image. The HR-TEM shows the presence of nanoparticles in which no apparent crystalline phase can be observed, confirming the amorphous nature of the material.

Table A.3.1. Ni:E ratio (E = P, As) in NiP and NiAs by ICP-AES, EDX-SEM, and EDX-TEM.

Material	Ni:E (ICP-AES)	Ni:E (EDX-SEM)	Ni:E (EDX-TEM)
NiP	1:1.05	1:1.26	1:1.02
NiAs	1:1.05	1:0.95	1:1.07

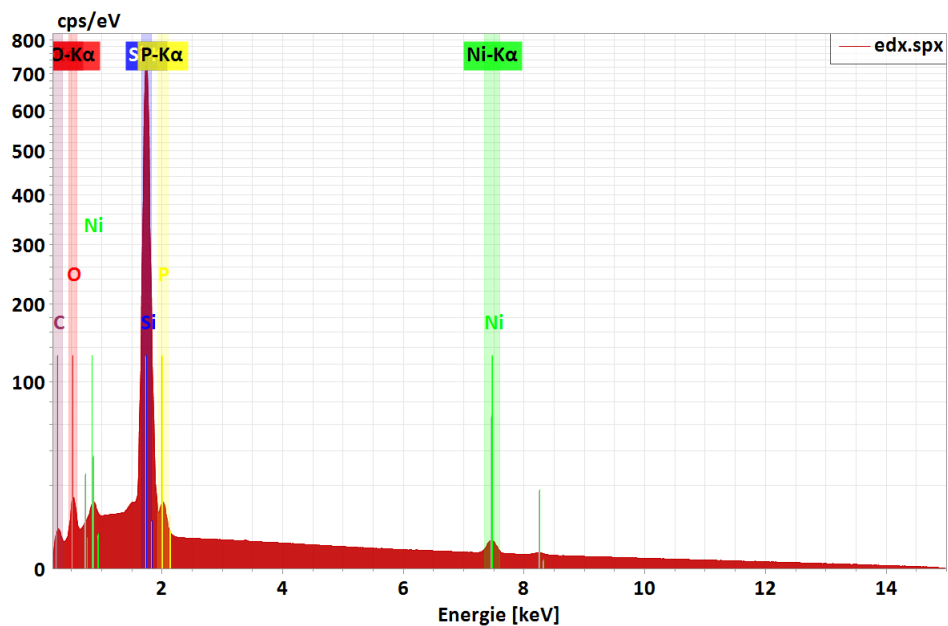


Figure A.3.5. SEM-EDX of NiP, which confirms the presence of Ni and P. The Ni:P ratio is 1:1.26. The presence of O is due to surface passivation. Si signals ($K\alpha_1$, $K\alpha_2$ at 1.740 keV, 1.739 keV and $K\beta_1$ at 1.836 keV) arise from the Si wafer used as support during the measurement.

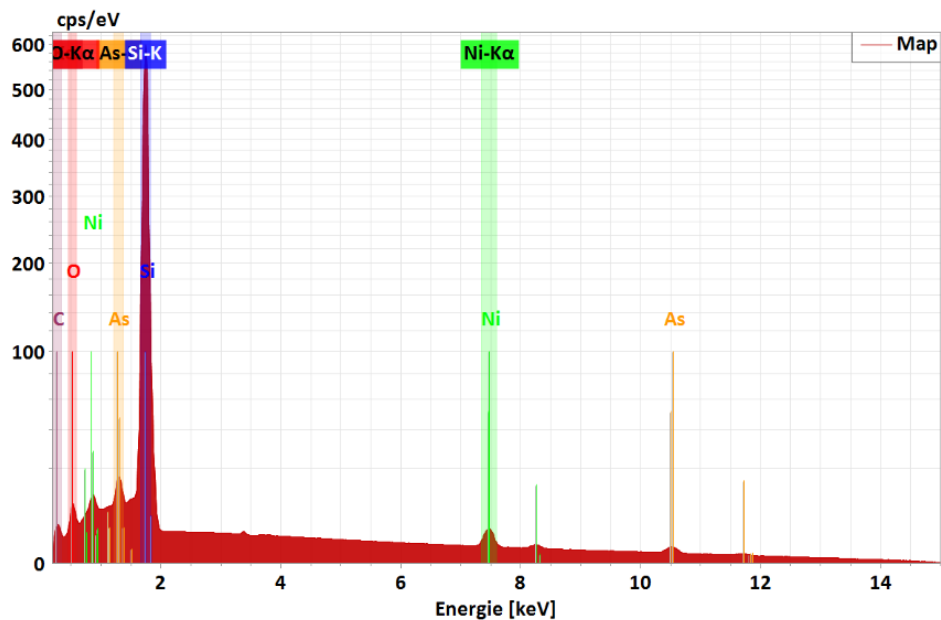


Figure A.3.6. SEM-EDX of NiAs, which confirms the presence of Ni and As. The Ni:As ratio is 1:0.95. The presence of O is due to surface passivation. Si signals ($K\alpha_1$, $K\alpha_2$ at 1.740 keV, 1.739 keV and $K\beta_1$ at 1.836 keV) arise from the Si wafer used as support during the measurement.

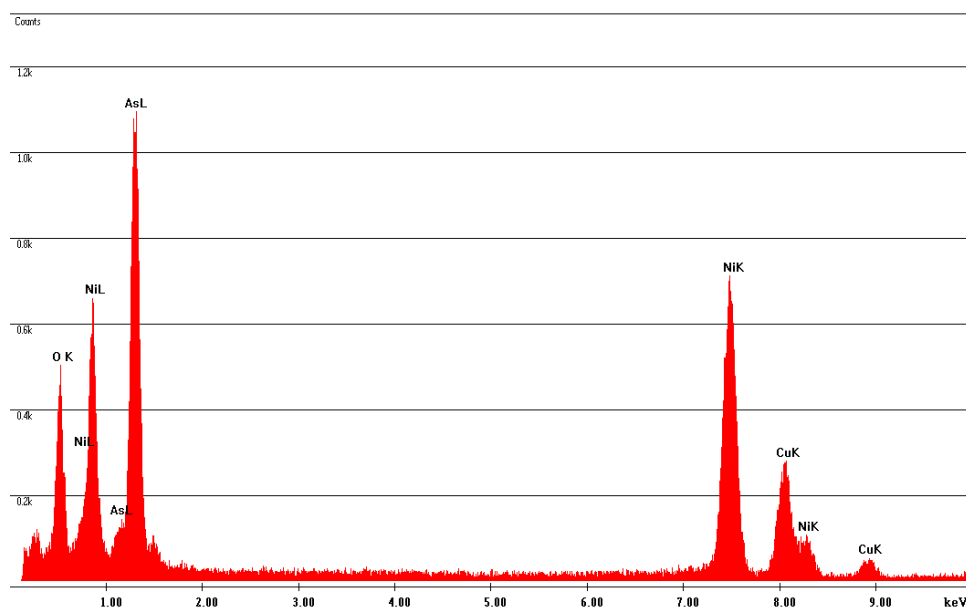


Figure A.3.7. TEM-EDX of NiAs, which confirms the presence of Ni and As. The Ni:As ratio 1:1.02. The presence of O is due to surface passivation. Cu signals arise from the TEM grid (carbon film on 300 mesh Cu-grid).

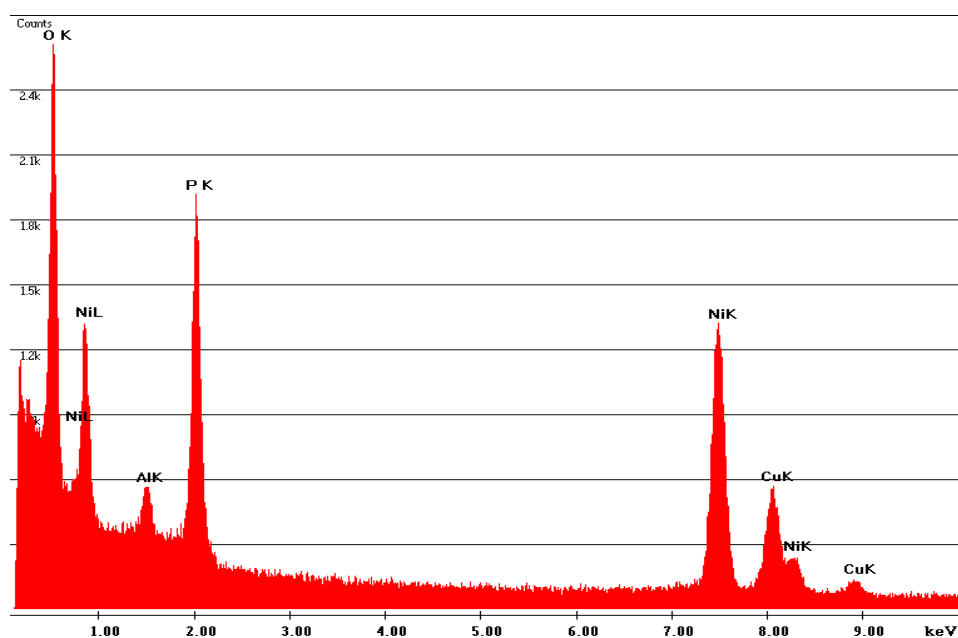


Figure A.3.8. TEM-EDX of NiP, which confirms the presence of Ni and P. The Ni:P ratio 1:1.07. The presence of O is due to surface passivation. Cu and C signals arise from the TEM grid (carbon film on 300 mesh Cu-grid). Al signals arise from the support.

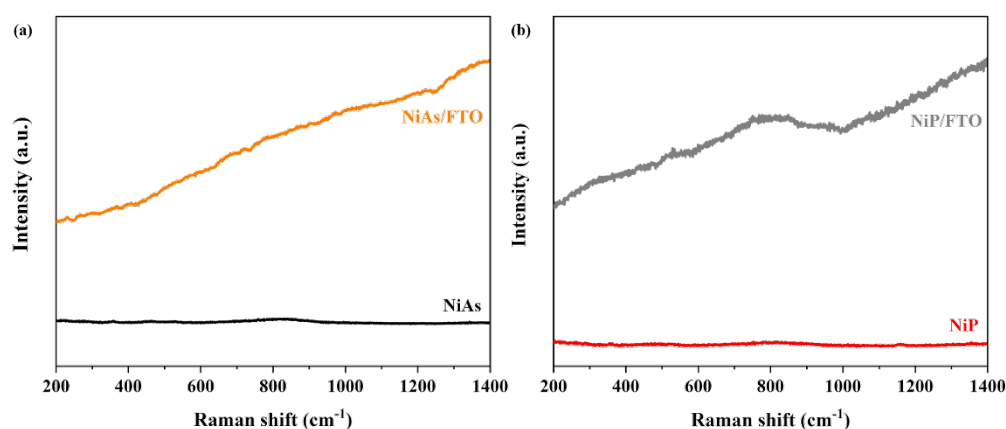


Figure A.3.9. (Resonance) Raman spectra of (a) NiAs and (b) NiP. The characterization of the as-prepared powders demonstrated that NiAs and NiP materials did not show any band active phonon band. The (resonance) Raman spectra of the films deposited on FTO agreed. There were no active phonon bands in the investigated range of frequencies, however, there is an increase in the intensity due to the contribution of the bare substrate (FTO) during the measurement (see FTO (resonance) Raman spectrum in the Appendix, Figure A.2.24).

Table A.3.2. Determination of C, H and O content by elemental analysis. The presence of remaining C and H arise from NaOCE (E = P, As) and solvents.

Material	% C	% H	% N
NiAs	1.72	0.97	0.00
NiP	4.42	3.09	0.00

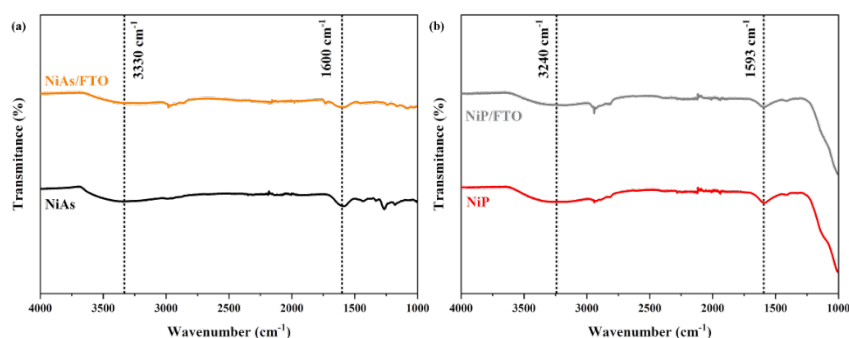


Figure A.3.10. FT-IR of (a) NiAs as-prepared compared to the material after deposition on FTO (NiAs/FTO). The most representative signals are related to surface oxidation from the NiAs due to contact with air. The broad peak at 3300 cm^{-1} and correspond to the stretching vibration of O-H. The peak at 1600 cm^{-1} could be attributed to vibrational modes of adsorbed water.^[457] The (b) NiP and NiP/FTO spectra are very similar, indicating that the material does not change after the deposition. In both cases, the stretching vibration from the O-H bond is observed (ca. 3300 cm^{-1}). The peak at 1635 cm^{-1} could be attributed to vibrational modes of adsorbed water.^[457]

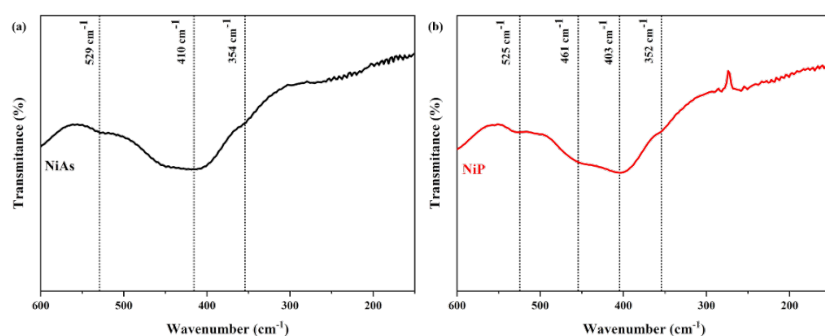


Figure A.3.11. Low-frequency FT-IR of (a) NiAs and (b) NiP.

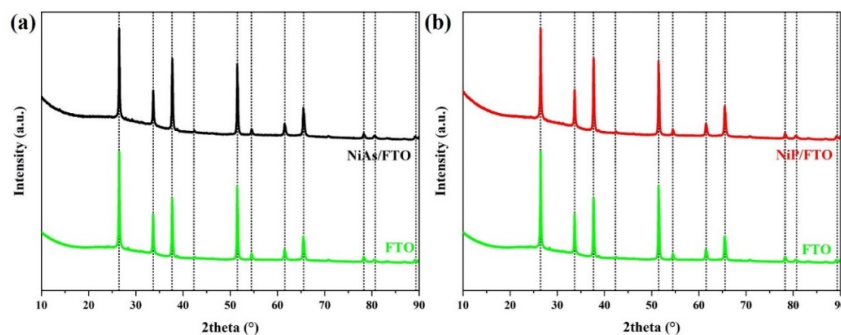


Figure A.3.12. XRD of as deposited materials (a) NiAs/FTO and (b) NiP/FTO compared to bare FTO. The diffraction peaks appearing at 26.5 , 33.9 , 27.9 , 51.8 , 54.8 , 61.9 , 65.9 , and 78.7 are related to the (110), (101), (200), (211), (220), (310), (301), (321) crystalline planes of FTO (cassiterite, SnO_2 , JCPDS 41-1445).^[382] The crystallinity of the materials did not change during the EPD, as demonstrated by the lack of new diffraction peaks in the PXRD of the as-prepared samples.

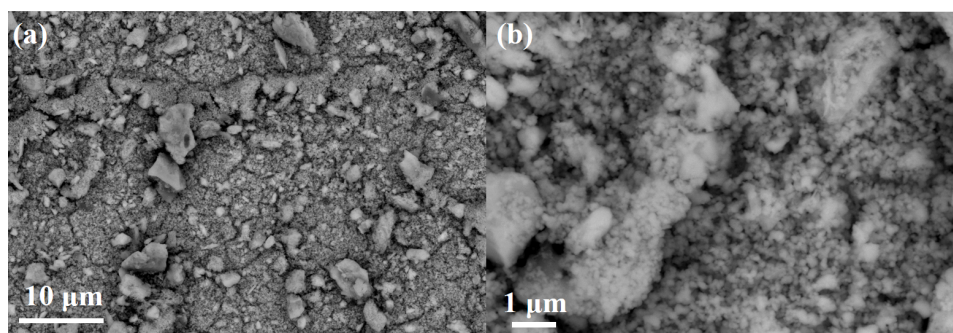


Figure A.3.13. SEM images of the NiAs films deposited on FTO at (a) 2000x and (b) 10000x. The high magnification image (b) shows that the film is composed of agglomerated particles and that the morphology was uniform and maintained during the EPD. The particles achieved complete coverage of the FTO.

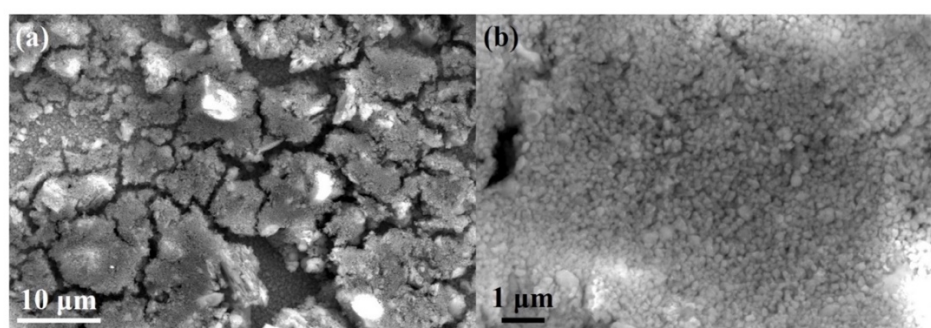


Figure A.3.14. SEM images of the NiP films deposited on FTO at (a) 2000x and (b) 10000x. The high magnification image (b) shows that the film is composed of agglomerated particles and that the morphology was uniform and maintained during the EPD. The particles achieved complete coverage of the FTO.

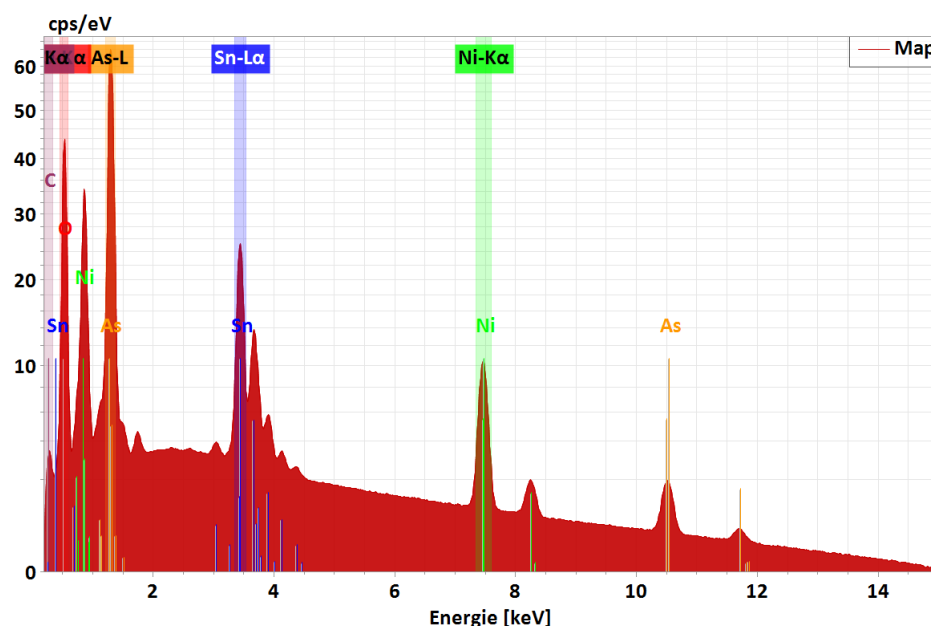


Figure A.3.15. SEM-EDX of NiAs/FTO, which confirms the presence of Ni and As. The presence of Sn peaks arise from the FTO glass substrate. The Ni:As ratio is ca. 1:1 as determined by SEM-EDX (see Figure A.3.5, Figure A.3.6). The peaks between 1.5-2 keV correspond to Al ($K\alpha_1$, $K\alpha_2$ at 1.487 keV, 1.486 keV and $K\beta_1$ at 1.557 keV) and Si ($K\alpha_1$, $K\alpha_2$ at 1.740 keV, 1.739 keV and $K\beta_1$ at 1.836 keV) arising from the Si wafer and Al support, respectively.

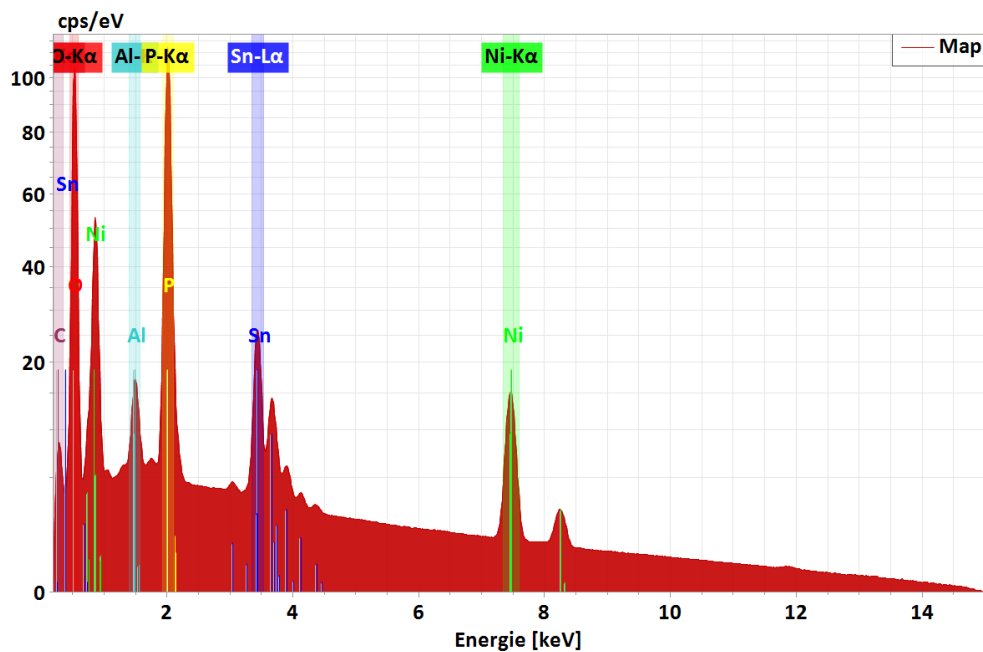


Figure A.3.16. SEM-EDX of NiP/FTO, which confirms the presence of Ni and P. The presence of Sn peaks is due to the FTO glass substrate. The Al peaks comes from the sample support. The Ni:P ratio is ca. 1:1 as determined by SEM-EDX (see Figure A.3.5). The peaks between 1.5-2 keV correspond to Al ($K\alpha_1$, $K\alpha_2$ at 1.487 keV, 1.486 keV and $K\beta_1$ at 1.557 keV) and Si ($K\alpha_1$, $K\alpha_2$ at 1.740 keV, 1.739 keV and $K\beta_1$ at 1.836 keV) arising from the Si wafer and Al support, respectively.

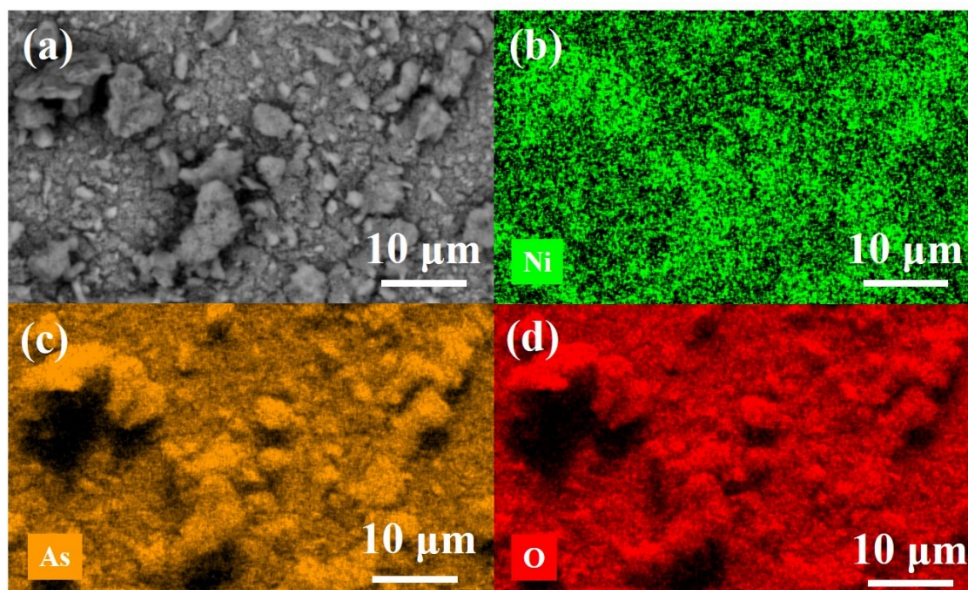


Figure A.3.17. (a) SEM of NiAs/FTO and elemental mapping of (b) Ni (green), (c) As (orange) and (d) O (red). Homogenous distribution of Ni and As is observed on the film. The presence of O due to the contact of the films with air.

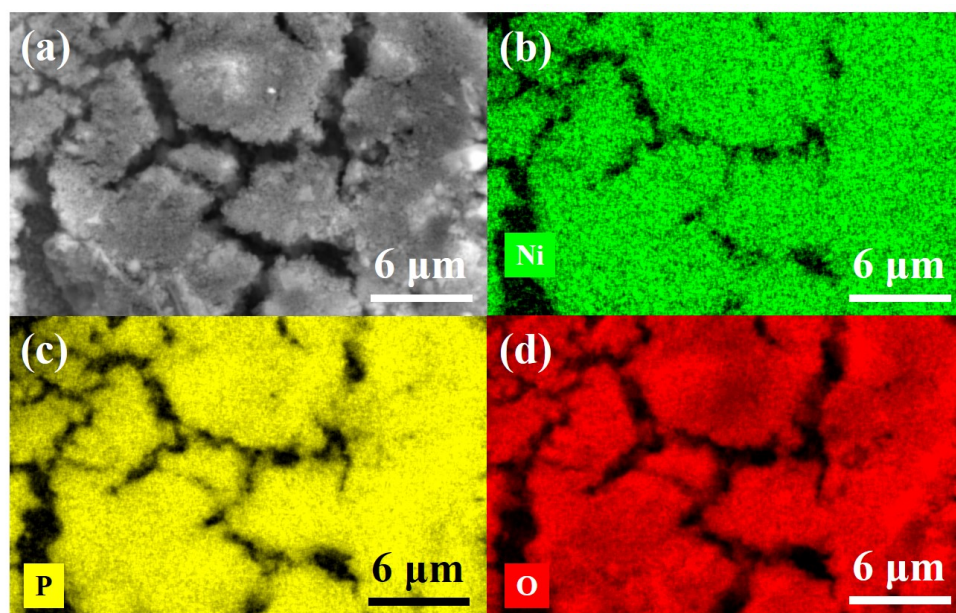


Figure A.3.18. (a) SEM of NiP/FTO and elemental mapping of (b) Ni (green), (c) P (yellow) and (d) O (red). Homogenous distribution of Ni and P is observed on the film. The presence of O due to the contact of the films with air.

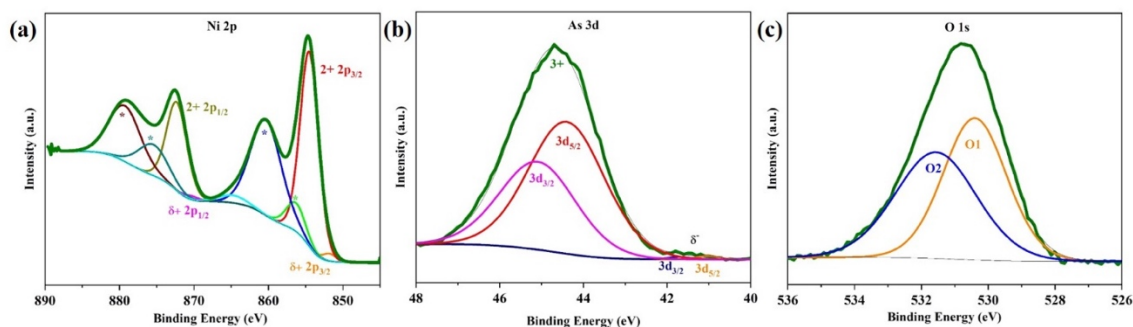


Figure A.3.19. Deconvoluted XPS of as-prepared NiAs/FTO and NiP/FTO. (a) The Ni 2p spectrum of NiAs/FTO showed low binding energy peaks related to $\text{Ni}^{\delta+}$ ($2p_{3/2}$ 852.0 eV and $2p_{1/2}$ 870.3 eV), which has been shown in the literature reports of TM pnictides.^[26,147,424,463,464] The remaining higher binding energy peaks were associated to higher oxidation Ni^{II} species, which were caused by the contact of the material with air. Due to the spin-orbital coupling, the two peaks of Ni^{II} were 854.6 eV ($2p_{3/2}$) and 872.4 eV ($2p_{1/2}$). Various satellite peaks also appeared in the spectrum (856.6 eV, 860.5 eV, 875.9 eV and 879.5 eV). (b) The As 3d spectrum showed two peaks. The first at the low binding energy peak of 41.1 eV, which was related to $\text{As}^{\delta-}$ in TM arsenides and deconvoluted into 41.0 eV ($2p_{3/2}$) and 41.7 eV ($2p_{1/2}$).^[328,465] The second larger peak (44.7 eV) was associated to As at a high oxidation state (As^{III}) as a consequence of surface oxidation by contact with air.^[367,368] This peak was further convoluted into 44.4 eV ($3d_{5/2}$) and 45.2 eV ($3d_{3/2}$). (c) The O 1s spectrum confirmed the incorporation of O in the surface due to air exposure (see Figure A.3.19c). One peak was observed at 530.7 eV, which could be deconvoluted into two peaks that were associated to from As-O (O1, 530.4 eV)^[367,368] and Ni-O (O2, 531.6 eV).^[26]

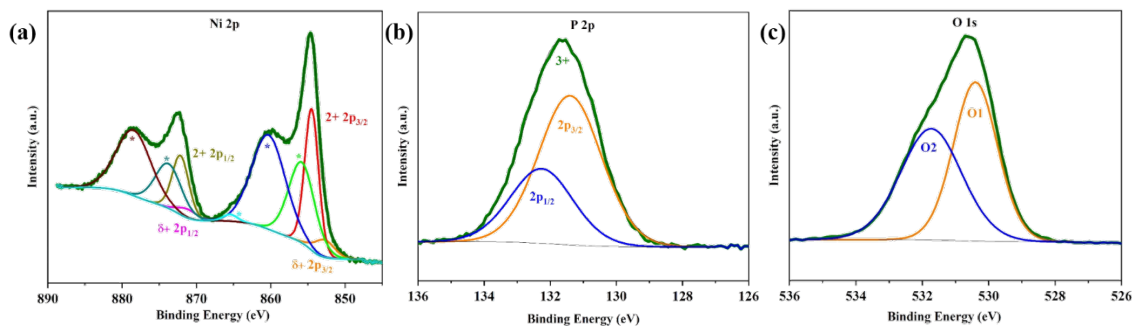


Figure A.3.20. Deconvoluted XPS of as-prepared NiAs/FTO and NiP/FTO. The deconvoluted spectra show similar results as in the as-prepared materials (see Figure 5.8). (a) The Ni 2p XPS spectrum showed low binding energy peaks related to $\text{Ni}^{\delta+}$ ($2p_{3/2}$ 853.0 eV and $2p_{1/2}$ 871.3 eV).^[26,147,424,463,464] These peaks are related to Ni atoms in low oxidation state and have been shown in reported Ni phosphides in the literature.^[26,203] The high binding energy peaks ($2p_{3/2}$ 854.6 eV and $2p_{1/2}$ 872.3 eV) were related highly oxidized species Ni^{II} , caused by the contact of the material with air. Additional satellite Ni peaks were also observed on the spectrum (856.0 eV, 860.4 eV, 865.5 eV, 874.0 eV and 878.7 eV). (b) The P 2p spectrum showed one peak at 131.6 eV, which was deconvoluted into two peaks at 131.4 eV ($2p_{3/2}$) and 132.3 eV ($2p_{1/2}$), which were related to phosphite (P^{III}) species, formed during the passivation of the surface due to contact with air.^[162] No peak related to $\text{P}^{\delta-}$ appears at lower binding energies, which that the surface is oxidized. The as-prepared NiP showed similar characteristics (see Figure 5.8e). (c) Finally, the O 1s XPS spectrum showed one peak (530.7 eV) which was further deconvoluted into two peaks. These two peaks were related to products derived from the exposure of the material to air: Ni-O=P (O1, 530.4 eV) and Ni-O or P=O (O2, 531.6 eV).^[160]

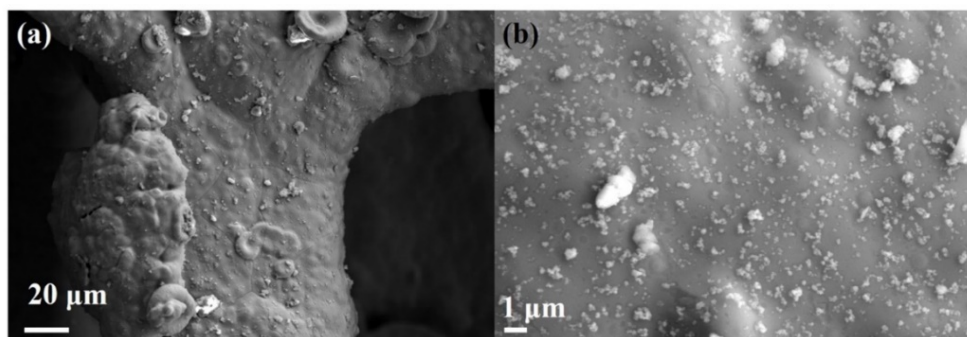


Figure A.3.21. (a) SEM images of the NiAs films deposited on NF. (b) The high magnification image shows the deposition of the NiAs particles is observed over the NF surface.

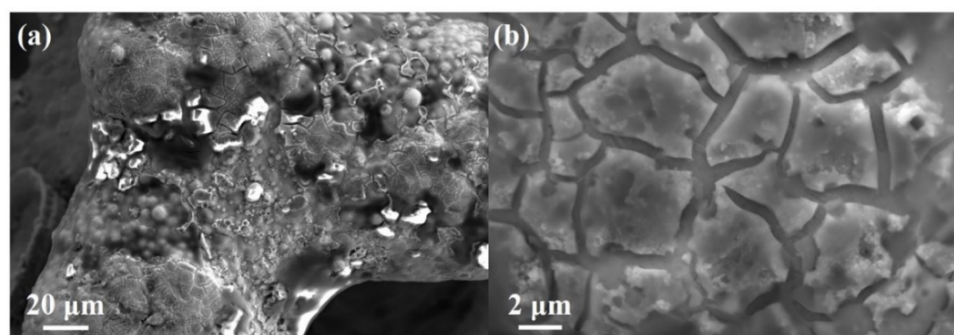


Figure A.3.22. (a) SEM image of the NiP films deposited on NF. (b) The high magnification image shows a film of NiP deposited over the NF.

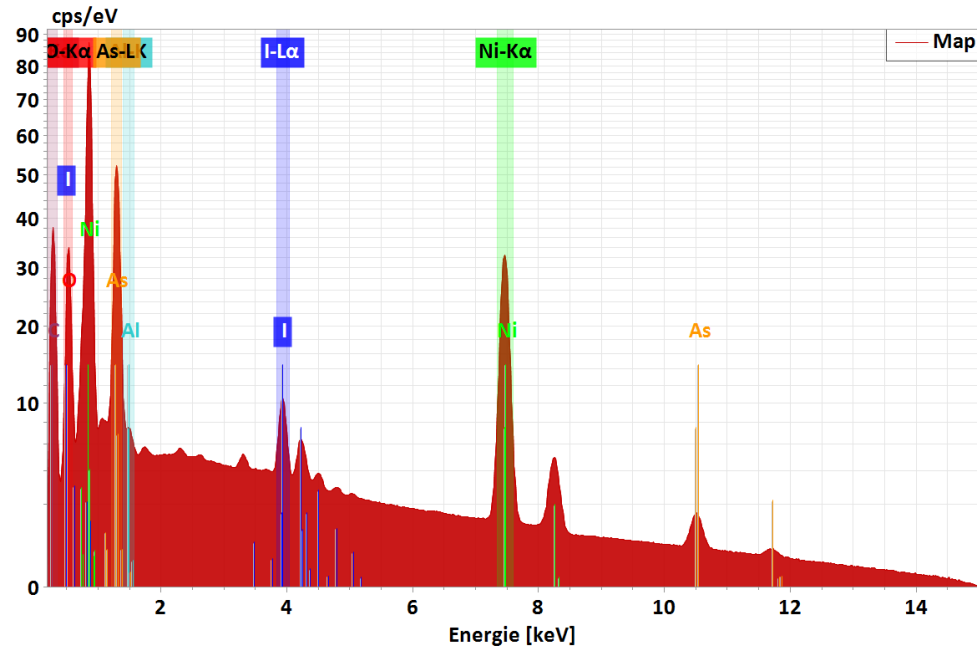


Figure A.3.23. SEM-EDX of NiAs/NF, which confirms the presence of Ni and As. The presence of iodine is due to the I₂ used in the EPD process (L α ₁, L α ₂, L β ₁, L β ₂, L γ ₁ at 3.938 keV, 3.926 keV, 4.221 keV, 4.508 keV and 4.801 keV, respectively). The peaks between 1.5-2 keV correspond to Al (K α ₁, K α ₂ at 1.487 keV, 1.486 keV and K β ₁ at 1.557 keV) and Si (K α ₁, K α ₂ at 1.740 keV, 1.739 keV and K β ₁ at 1.836 keV) arising from the Si wafer and Al support, respectively. The ratio could not be determined because of the contribution of Ni from the background (NF substrate).

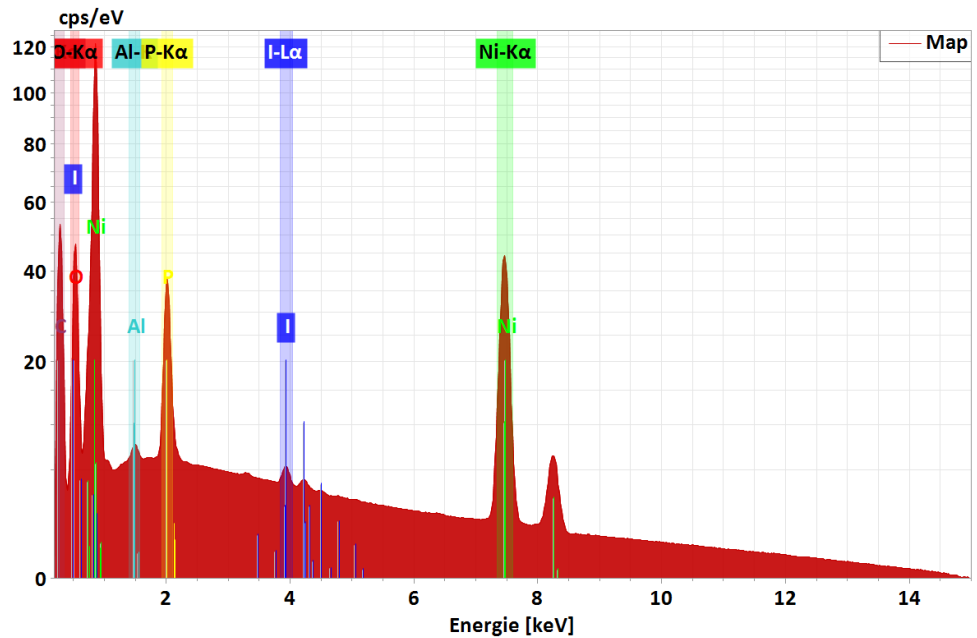


Figure A.3.24. SEM-EDX of NiP/NF, which confirms the presence of Ni and P. The presence of iodine is due to the I₂ used in the EPD process (L α ₁, L α ₂, L β ₁, L β ₂, L γ ₁ at 3.938 keV, 3.926 keV, 4.221 keV, 4.508 keV and 4.801 keV, respectively). Aluminum (K α ₁, K α ₂ at 1.487 keV, 1.486 keV and K β ₁ at 1.557 keV) comes from sample holder used for the measurement. The ratio could not be determined because of the contribution of Ni from the background (NF substrate).

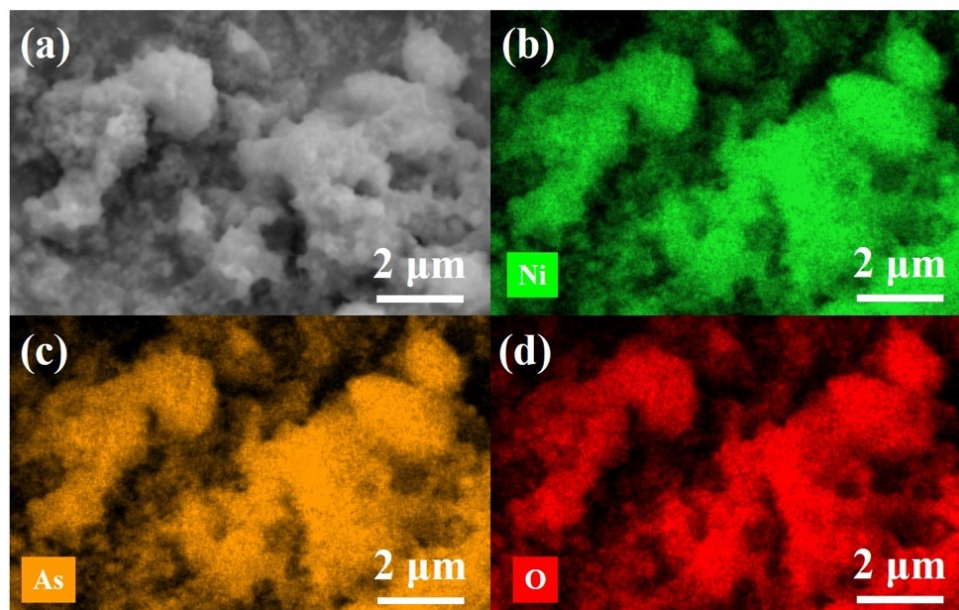


Figure A.3.25. (a) SEM of NiAs/NF and elemental mapping of (b) Ni (green), (c) As (orange) and (d) O (red). Homogenous distribution of Ni and As is observed on the film.

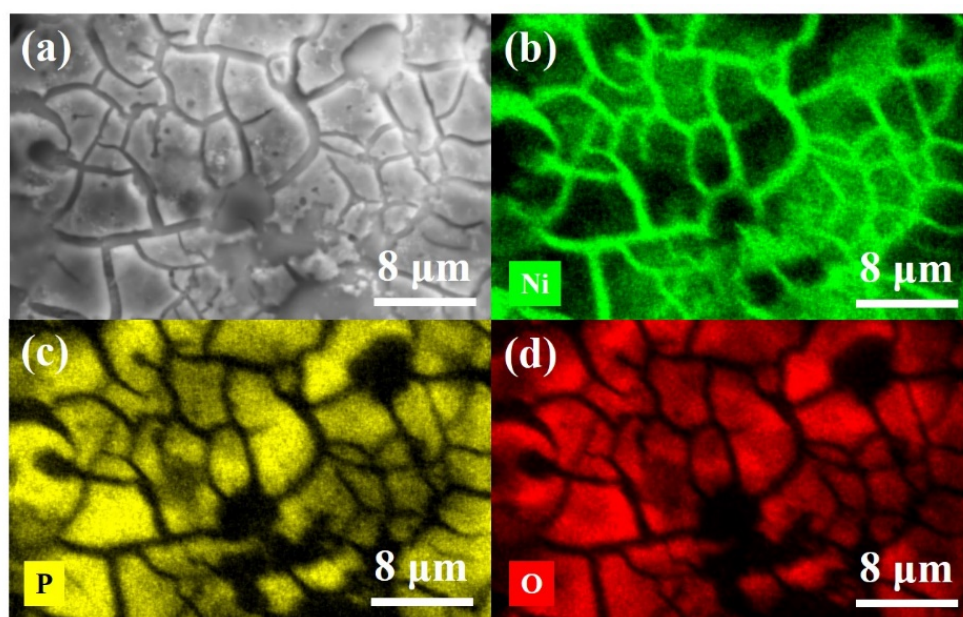


Figure A.3.26. (a) SEM of NiP/NF and elemental mapping of (b) Ni (green), (c) P (yellow) and (d) O (red). Homogenous distribution of Ni and P is observed on the film.

Table A.3.3. Activity comparison of as-prepared NiP and NiAs and reference Ni-based materials with other highly efficient pnictides at 1 M KOH for OER.

Catalyst	Current density (mA cm ⁻²)	Overpotential η (mV)	Reference
NiP/FTO	10	342	This work
NiAs/FTO	10	384	This work
NiP/NF	10	274	This work
	100	402	This work
NiAs/NF	10	339	This work
	100	507	This work
Ni ₁₂ P ₅	10	295	[26]
Ni ₂ P	10	330	[26]
FeP/NF	10	227	[111]
	100	292	[111]
Cu ₃ N–CuO/FTO	10	286	[112]
Cu ₃ N–CuO/NF	10	118	[112]
Ni ₅ P ₄ film	10	290	[151]
FeP nanorods/CP	10	350	[157]
Ni-P films	10	344	[169]
Porous Urchin-Like Ni ₂ P	10	260	[174]
FeP/Au	10	290	[189]
FeP rGO/Au	10	260	[189]
NiAs/GC	10	360	[203]
NiP/GC	10	350	[203]
Carbon fiber@NiPx	10	200	[430]
Ni-P nanoparticles/Ni foam	10	309	[444]
Amorphous CoP	10	284	[457]
Crystalline CoP	10	305	[457]
FeMnP	10	250	[578]
FeP	10	288	[579]
FeMnP	10	250	[580]
FeP@rGO (50:50)/CP	10	290	[592]
Ni ₂ P	10	290	[598]
Cu ₃ P NB/ Cu	10	380	[599]
Cu ₃ P@NF	10	320	[600]
Ni ₅₉ Cu ₁₉ P ₉ /Cu	10	307	[601]

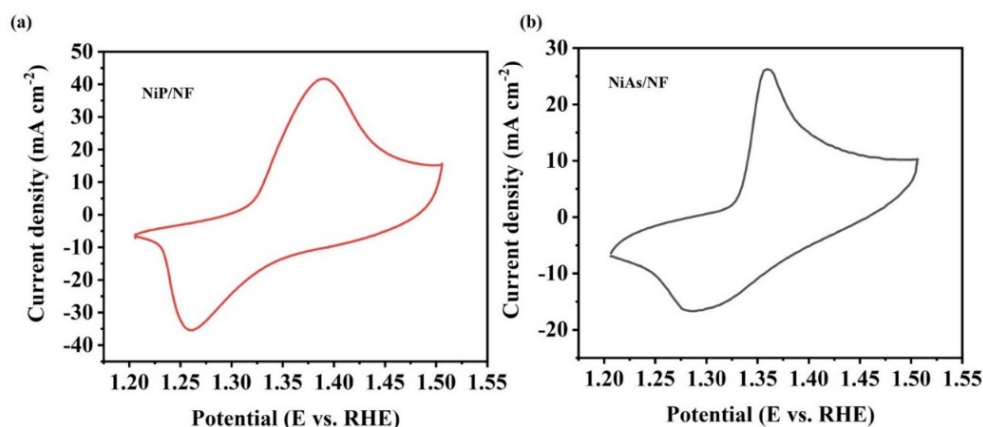


Figure A.3.27. CV (scan rate 10 mV s^{-1} , iR compensation at 85 %) of (a) NiP/NF and (b) NiAs/NF measured between 1.2 V and 1.5 V (vs. RHE) in 1 M KOH. The CVs show a pair of peaks corresponding to the reaction of oxidation of Ni in alkaline media: $\text{Ni}(\text{OH})_2 + \text{OH}^- \rightarrow \text{NiOOH} + \text{H}_2\text{O} + \text{e}^-$.^[293] These peaks have been also often observed for most of the first-row TM-based materials, which exhibit $\text{M}(\text{OH})_2/\text{MOOH}$ phase formation at potentials on a similar potential range.^[293]

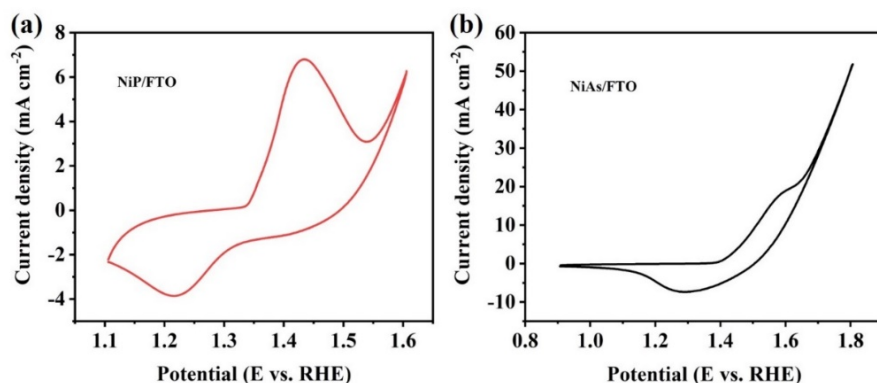


Figure A.3.28. CV (scan rate 10 mV s^{-1} , iR compensation at 85 %) of (a) NiP/FTO and (b) NiAs/FTO. The materials shows a pair of peaks corresponding to the reaction of oxidation of Ni the in alkaline media: $\text{Ni}(\text{OH})_2 + \text{OH}^- \rightarrow \text{NiOOH} + \text{H}_2\text{O} + \text{e}^-$.^[293]

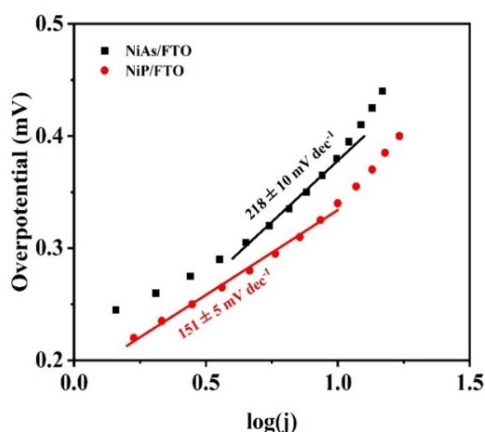


Figure A.3.29. Tafel plot of NiAs/FTO and NiP/FTO on 1 M KOH solution in OER. The Tafel slope of NiP/FTO is lower compared to NiAs/FTO, indicating faster reaction kinetics for OER.

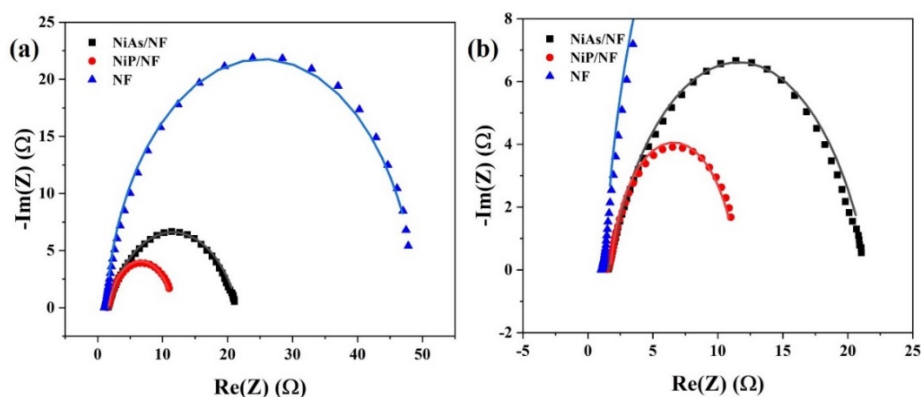


Figure A.3.30. (a) Nyquist plot constructed from the EIS experiment of NiAs/NF, NiP/NF and bare NF and (b) zoom to visualize the spectra of the electrocatalysts. The spectra were collected with an anodic polarization potential of 1.50 V vs. RHE. The curves were fitted to a Randles equivalent circuit. The continuous lines show the fitting to the circuit, which contains two resistors R_1 , and R_2 and Q a CPE (see Figure 7.16). This circuit has been previously used to fit TM-based systems during OER reaction conditions.^[534,535,537] The assignment of the elements is consistent in the literature and can be applied to the system under study: R_1 is the Ohmic resistance of the solution and electrode (R_s), R_2 is the charge transfer resistance (R_{ct}), and a CPE (Q). Details of assignments are discussed on the Experimental Section 7.3.7.

Table A.3.4. R_2 (Ω) (R_{ct}), R_1 (Ω) (R_s), Q ($F \times s^{(a_2-1)}$) of NiAs, NiP and comparison to bare substrates (NF, FTO). The values were obtained from the fitting of the plots to a Randles equivalent circuit (see Experimental Section, Figure 7.16).

Material	R_2 (Ω)	R_1 (Ω)	Q ($F \times s^{(a_2-1)}$)	a_2
NF	47.97 ± 1.19	1.28 ± 0.33	0.15 ± 0.01	0.94 ± 0.66
NiAs/NF	19.96 ± 0.22	1.59 ± 0.20	0.07 ± 0.003	0.74 ± 0.58
NiP/NF	10.37 ± 1.76	1.55 ± 0.16	0.66 ± 0.20	0.83 ± 0.70
FTO	3809 ± 2.37	14.94 ± 0.27	$11.65 \times 10^{-6} \pm 14.52 \times 10^{-9}$	0.96 ± 0.50
NiAs/FTO	13.17 ± 1.03	11.18 ± 0.15	$2.61 \times 10^{-2} \pm 5.40 \times 10^{-3}$	0.94 ± 0.98
NiP/FTO	4.78 ± 1.22	12.06 ± 4.05	$3.10 \times 10^{-1} \pm 1.21 \times 10^{-2}$	0.97 ± 1.00

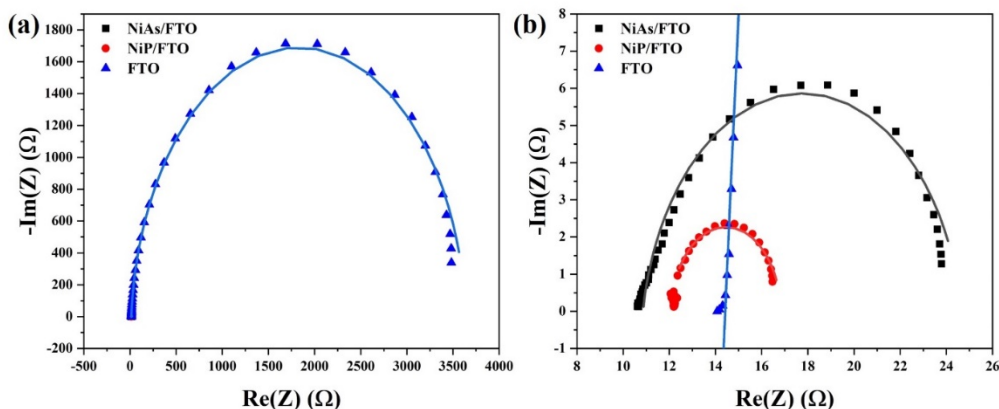


Figure A.3.31. (a) Nyquist plot constructed from the EIS experiment of NiAs/FTO, NiP/FTO and bare FTO and (b) zoom to visualize the spectra of the electrocatalysts. The spectra were collected with an anodic polarization potential of 1.65 V vs. RHE. The curves were fitted to a Randles equivalent circuit.

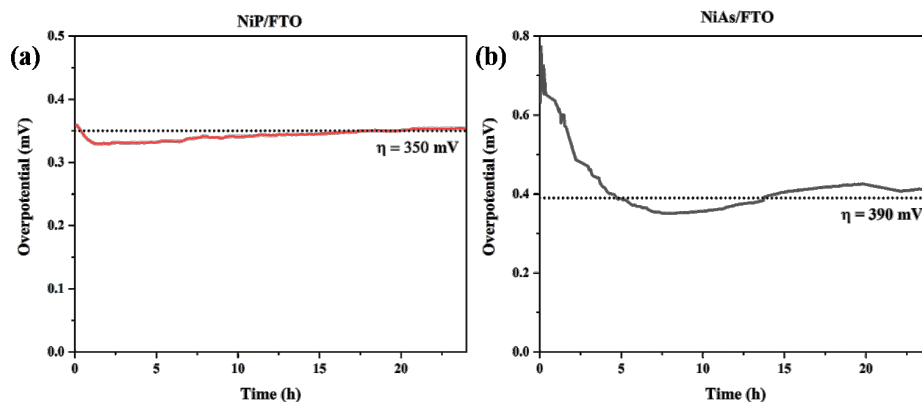


Figure A.3.32. CP for OER (10 mA cm^{-2} , 24 h, KOH 1M) for (a) NiP/FTO and (b) NiAs/FTO.

Table A.3.5. Calculation of FE of the materials.

	j (mA cm^{-2})	t (s)	V_{H_2} (mL)	V_{O_2} (mL)	$V_{\text{H}_2} : V_{\text{O}_2}$	FE (H_2 , %)	FE (O_2 , %)
NiAs/NF	49.33	600	3.56	1.82	1.96	94	96
NiP/NF	49.33	600	3.61	1.87	1.93	95	98

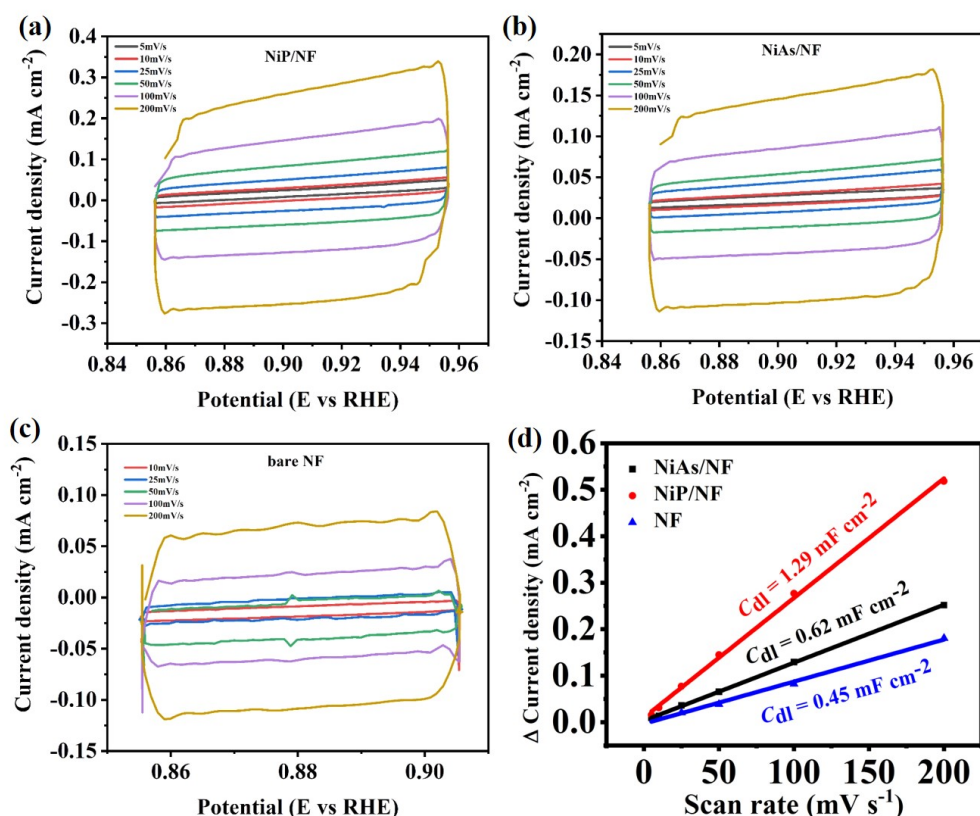


Figure A.3.33. CV measurements at a non-faradaic process region at different scan rates for (a) NiP/NF, (b) NiAs/NF and (c) bare NF. Scan rates: 5 mV s^{-1} (black), 10 mV s^{-1} (red), 25 mV s^{-1} (blue), 50 mV s^{-1} (green), 100 mV s^{-1} (purple), 200 mV s^{-1} (dark yellow). The double layer capacitance (C_{dl}) was determined as the half of the slope from the plot of the capacitive current vs. scan rate plot (d).

Table A.3.6. Correlation factor (R^2) of the linear plot of capacitive current vs. scan rate and double layer capacitance (C_{dl}) of NiAs and NiP deposited on NF.

Material	R^2	C_{dl} (mF cm^{-2})
NF	0.99	0.453 ± 0.002
NiP/NF	0.99	1.285 ± 0.002
NiAs/NF	0.99	0.625 ± 0.001

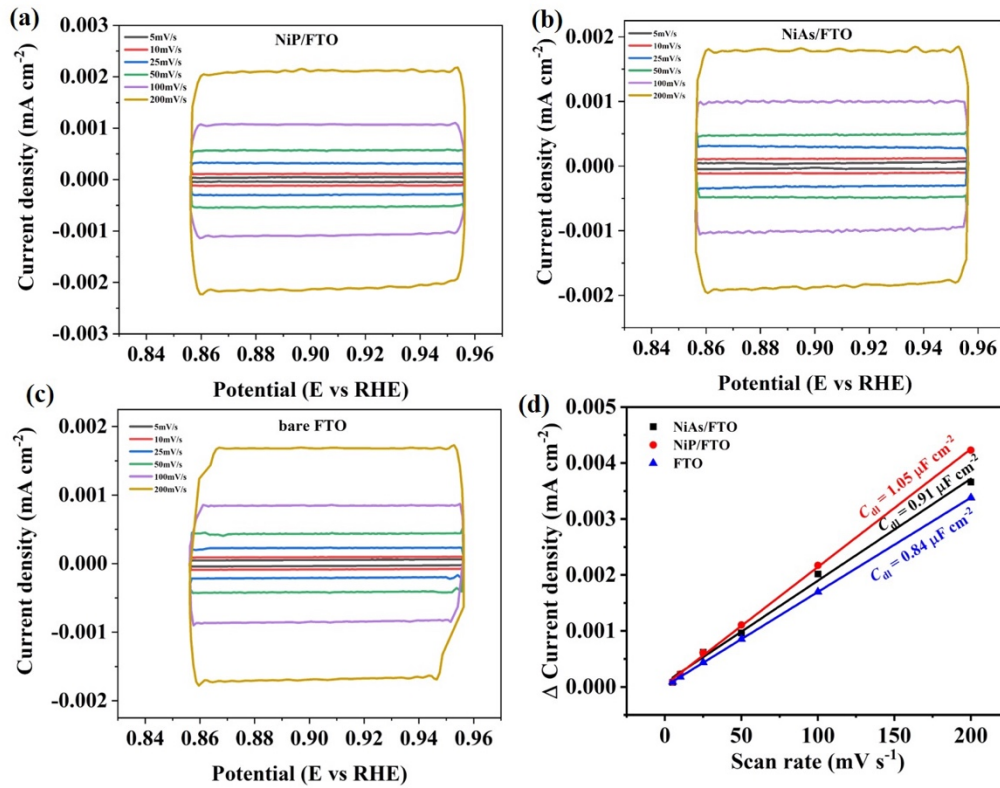


Figure A.3.34. CV measurements at a non-faradaic process region at different scan rates for (a) NiP/FTO, (b) NiAs/FTO and (c) bare FTO. Scan rates: 5 mV s^{-1} (black), 10 mV s^{-1} (red), 25 mV s^{-1} (blue), 50 mV s^{-1} (green), 100 mV s^{-1} (purple), 200 mV s^{-1} (dark yellow). The C_{dl} was determined as the half of the slope from the plot of the capacitive current vs. scan rate plot (d).

Table A.3.7. Correlation factor (R^2) of the linear plot of capacitive current vs. scan rate, double layer capacitance (C_{dl}) of NiAs and NiP deposited on FTO.

Material	R^2	C_{dl} ($\mu\text{F cm}^{-2}$)
FTO	0.9998	8.429 ± 0.015
NiP/FTO	0.9993	10.540 ± 0.122
NiAs/FTO	0.9953	9.110 ± 0.279

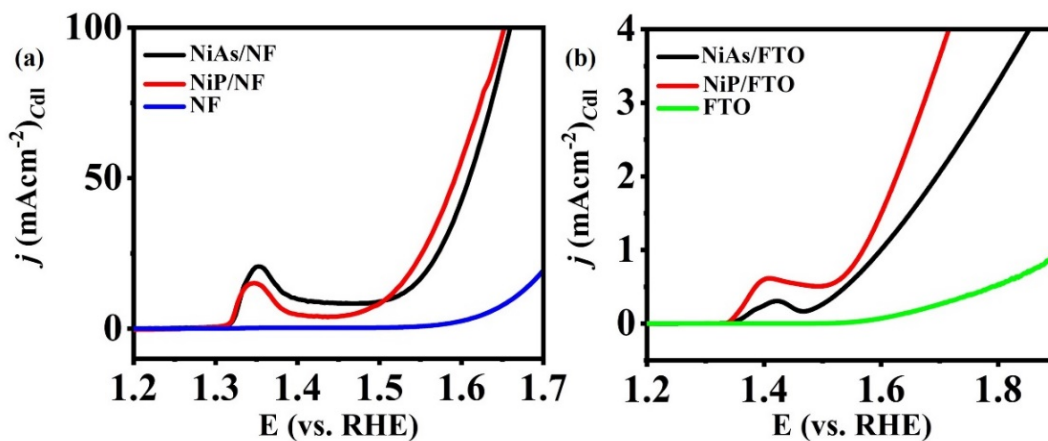


Figure A.3.35. ECSA normalized activity of NiAs and NiP deposited on (a) NF and (b) FTO.

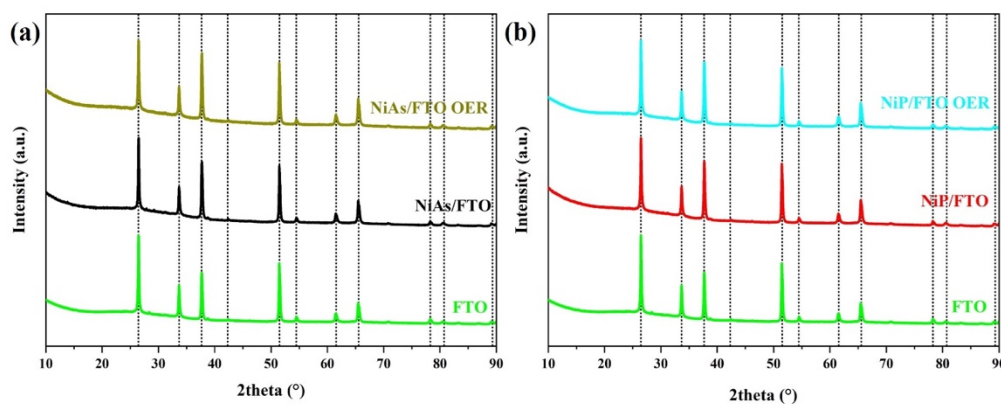


Figure A.3.36. PXRD of as deposited materials after OER for (a) NiAs/FTO and (b) NiP/FTO compared to the as-prepared films. The diffraction peaks appearing on the sample correspond to SnO₂ (cassiterite, JCPDS 41-1445).

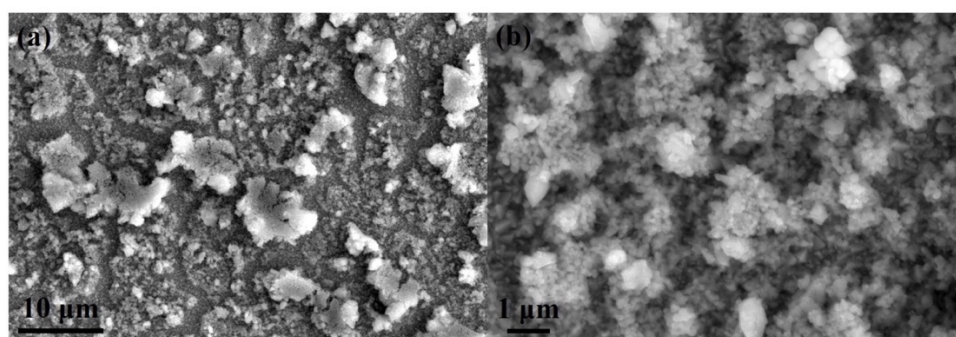


Figure A.3.37. SEM of the NiP/FTO after OER at (a) 2000x and (b) 10000x. The figures show that the film has detached from the conductive substrate on some areas, leaving the FTO exposed into solution. The high magnification image shows particles of ca. 250 nm that are similar as before catalysis (see Figure A.3.2).

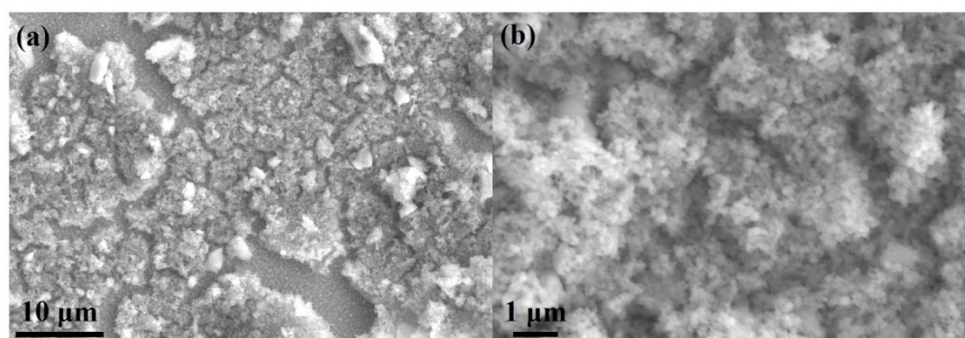


Figure A.3.38. SEM of the NiAs/FTO after OER at (a) 2000x and (b) 10000x. The images show that the film has detached from the conductive substrate on some areas, leaving the FTO exposed into solution. The high magnification figure shows particles of ca. 250 nm that are similar to the ones observed before catalysis (see Figure A.3.1).

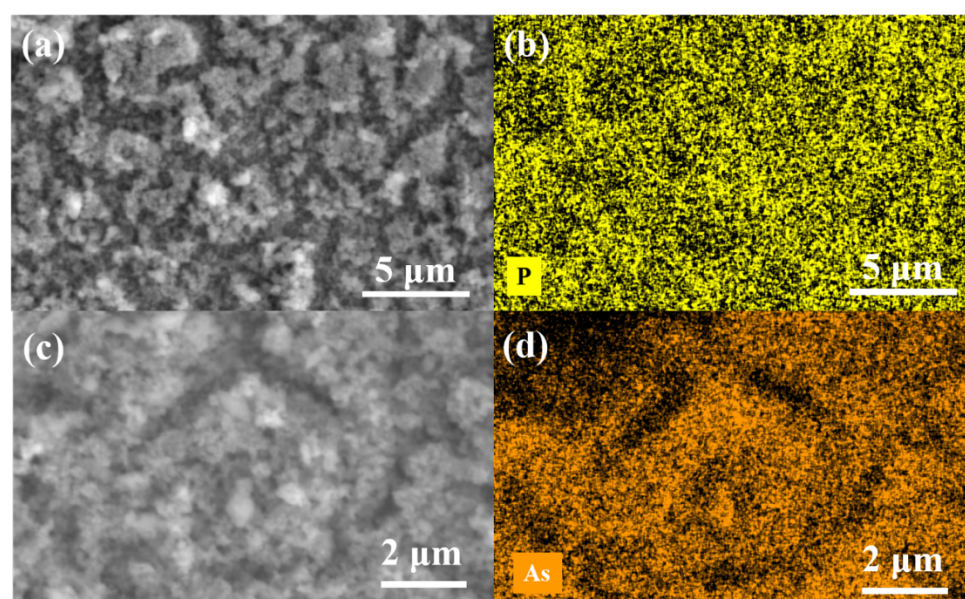


Figure A.3.39. (a) SEM of NiP/FTO after OER and elemental mapping (b) P (yellow). (c) SEM of NiAs/FTO after OER and elemental mapping (d) As (orange).

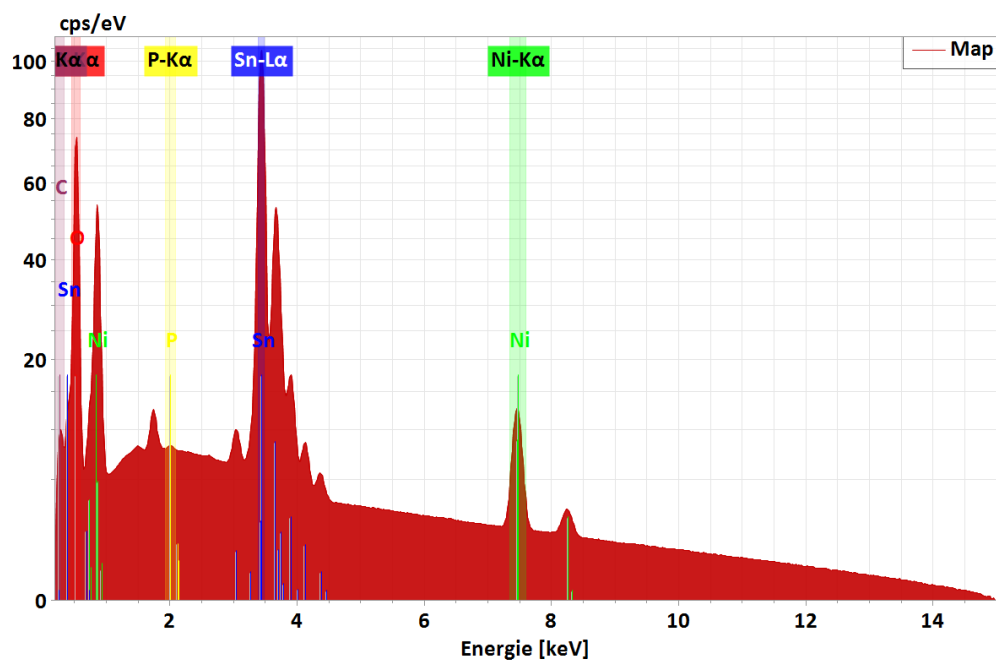


Figure A.3.40. SEM-EDX of the film of NiP/FTO after OER. The presence of Sn is due to the FTO substrate. The peaks between 1.5-2 keV correspond to Al ($K\alpha_1$, $K\alpha_2$ at 1.487 keV, 1.486 keV and $K\beta_1$ at 1.557 keV) and Si ($K\alpha_1$, $K\alpha_2$ at 1.740 keV, 1.739 keV and $K\beta_1$ at 1.836 keV) arising from the Si wafer and Al support, respectively. The Ni:P ratio is 1:0.009, related to the P loss into solution (see Table A.3.8).

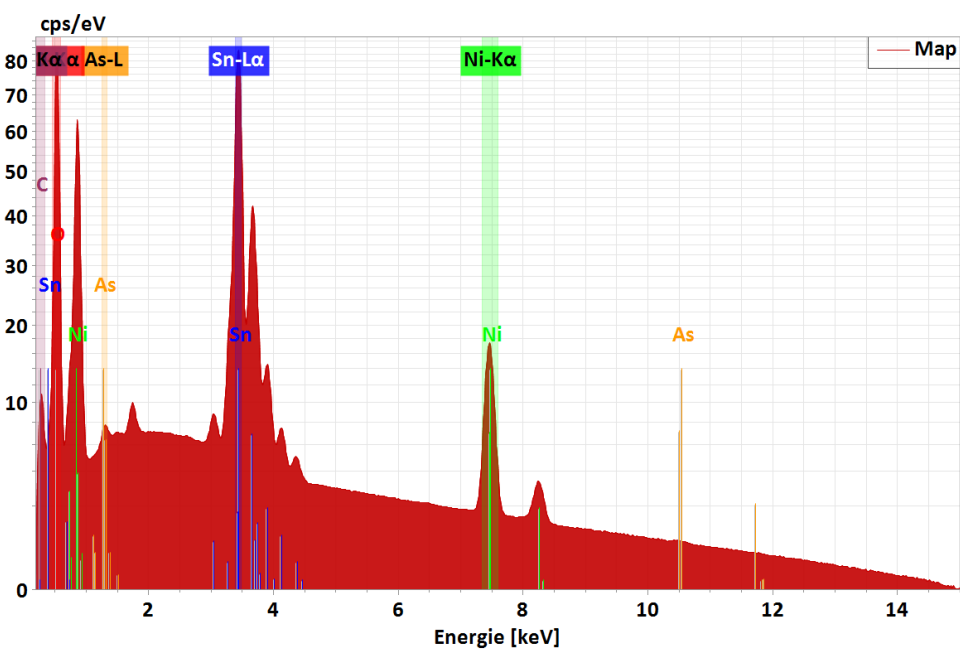


Figure A.3.41. SEM-EDX of the film of NiAs/FTO after OER. The presence of Sn is due to the FTO substrate. The Ni:As ratio is 1:0.024, related to the As loss into solution (see Table A.3.8). The peaks between 1.5-2 keV correspond to Al ($K\alpha_1$, $K\alpha_2$ at 1.487 keV, 1.486 keV and $K\beta_1$ at 1.557 keV) and Si ($K\alpha_1$, $K\alpha_2$ at 1.740 keV, 1.739 keV and $K\beta_1$ at 1.836 keV) arising from the Si wafer and Al support, respectively.

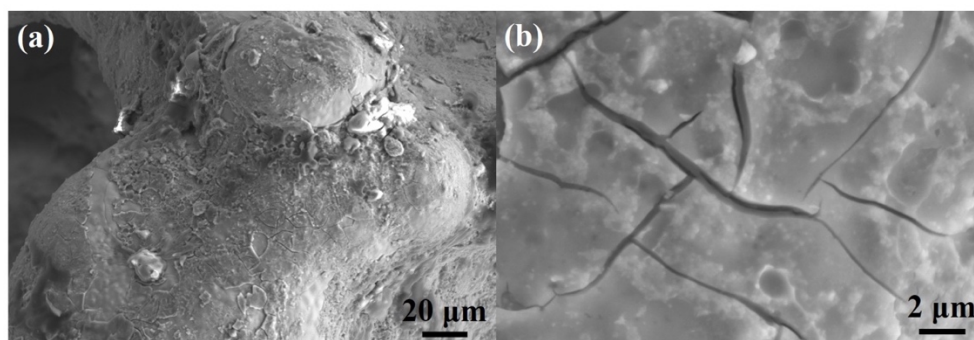


Figure A.3.42. SEM image of the NiP/NF after OER at (a) 500x and (b) 5000x. The images shows the NiP film with cracks after OER, as observed before catalysis.

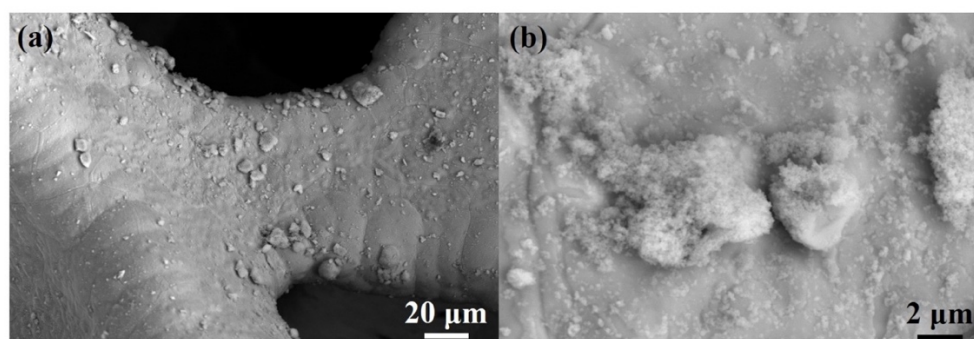


Figure A.3.43. SEM images of the NiAs/NF after OER at (a) 500x and (b) 5000x. The images show the agglomeration of NiAs particles on the surface of NF after OER. The high magnification figure shows particles of ca. 100 nm as before catalysis (see Figure A.3.1).

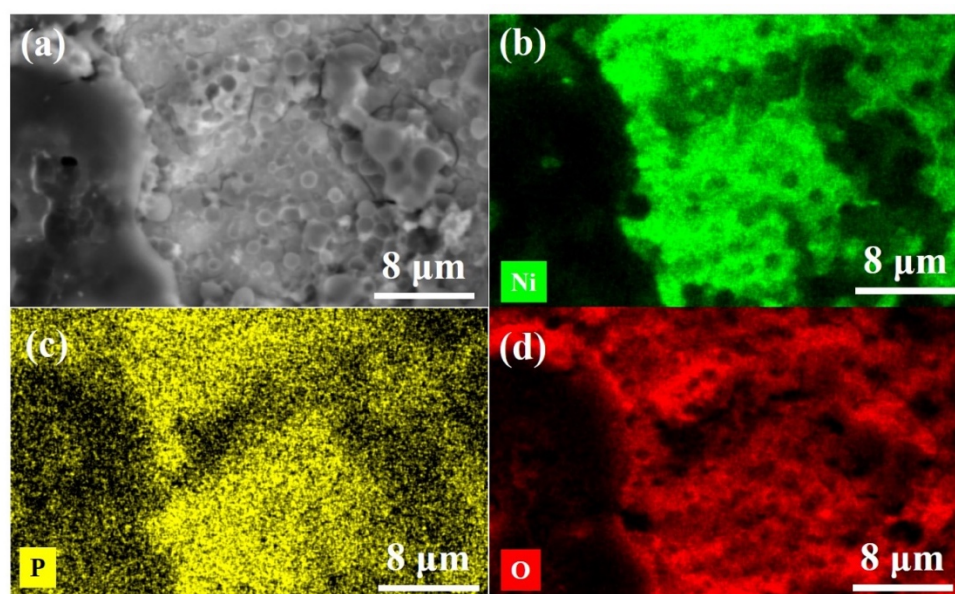


Figure A.3.44. (a) SEM and elemental mapping of (b) Ni (green), (c) P (yellow) and (d) O (red) of NiP/NF after OER. The mapping shows the homogeneous distribution of the elements on the surface of the material.

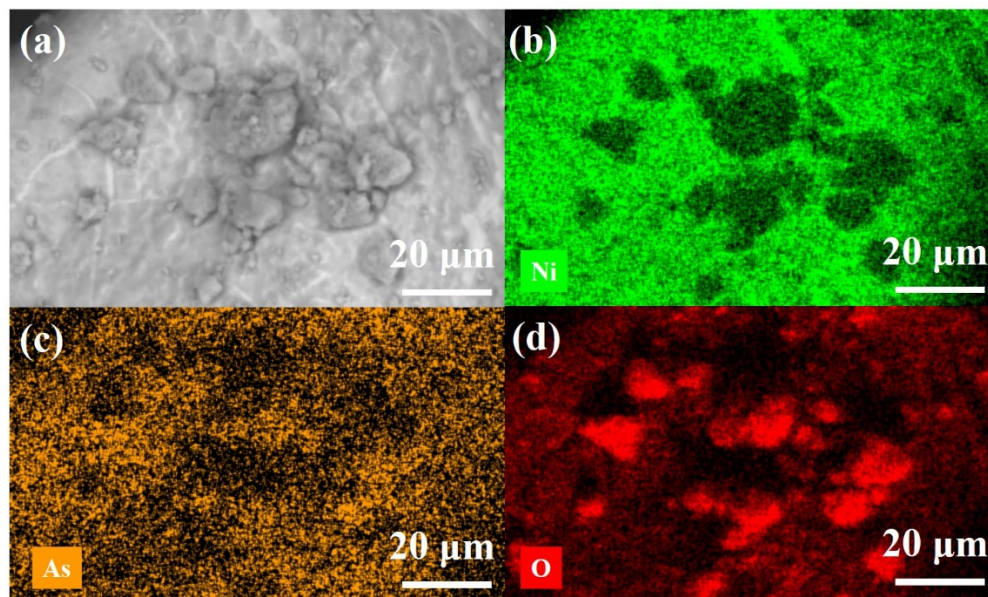


Figure A.3.45. (a) SEM and elemental mapping of (b) Ni (green), (c) As (orange) and (d) O (red) of NiAs/NF after OER. The mapping shows the homogeneous distribution of the elements on the surface of the material. The particles on the image correspond to KOH derived species of the large concentration of O and because Ni can only be seen on the NF surface.

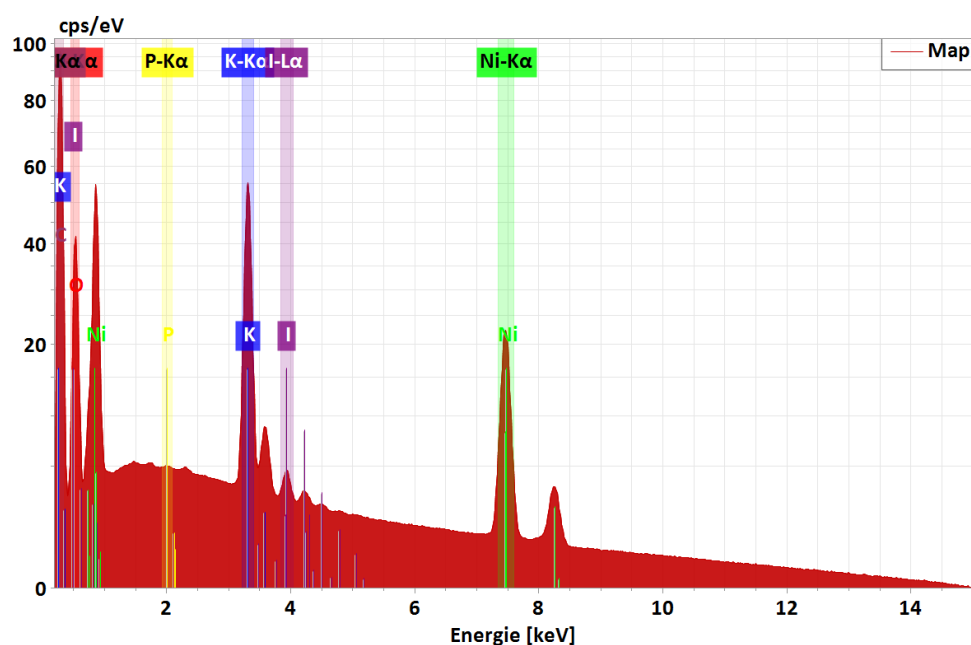


Figure A.3.46. SEM-EDX of the film of NiP/NF after OER. The presence of K and I is due to the KOH electrolyte used during catalysis and the I_2 used during the film preparation ($L\alpha_1$, $L\alpha_2$, $L\beta_1$, $L\beta_2$, $L\gamma_1$ at 3.938 keV, 3.926 keV, 4.221 keV, 4.508 keV and 4.801 keV, respectively). The peaks between 1.5-2 keV correspond to Al ($K\alpha_1$, $K\alpha_2$ at 1.487 keV, 1.486 keV and $K\beta_1$ at 1.557 keV) and Si ($K\alpha_1$, $K\alpha_2$ at 1.740 keV, 1.739 keV and $K\beta_1$ at 1.836 keV) arising from the Si wafer and Al support, respectively. The Ni:P ratio is 1:0.001, related to the P loss into solution (see Table A.3.8).

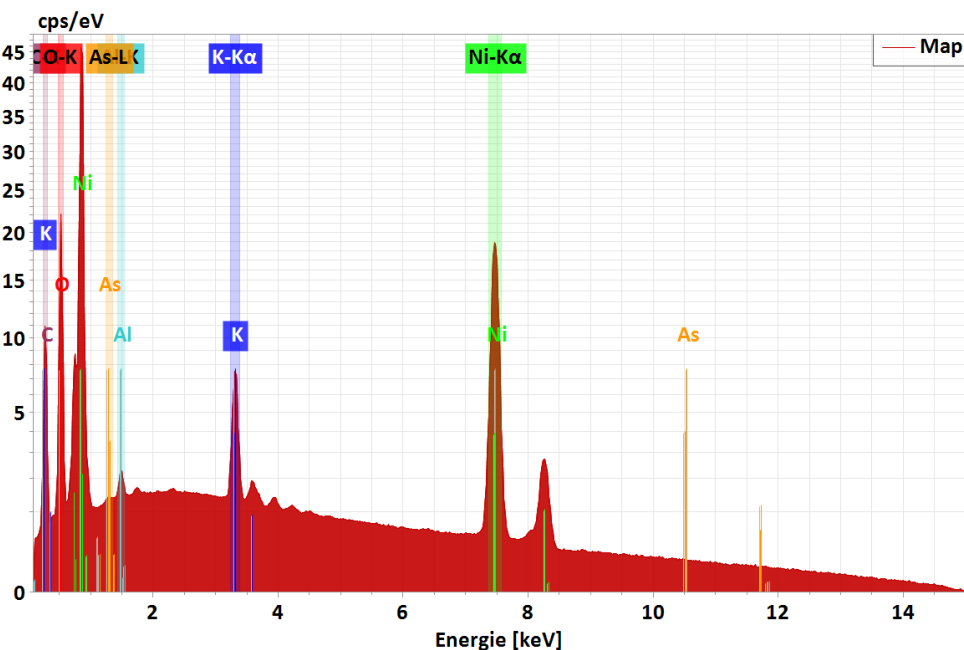


Figure A.3.47. SEM-EDX of the film of NiAs/NF after OER. The peaks between 1.5-2 keV correspond to Al ($K\alpha_1$, $K\alpha_2$ at 1.487 keV, 1.486 keV and $K\beta_1$ at 1.557 keV) and Si ($K\alpha_1$, $K\alpha_2$ at 1.740 keV, 1.739 keV and $K\beta_1$ at 1.836 keV) arising from the Si wafer and Al support, respectively. The presence of K is due to the KOH electrolyte used during the experiments. The peaks between 3.5-5 eV ($L\alpha_1$, $L\alpha_2$, $L\beta_1$, $L\beta_2$, $L\gamma_1$ at 3.938 keV, 3.926 keV, 4.221 keV, 4.508 keV and 4.801 keV, respectively) correspond to iodine used during the preparation process of the films (EPD). The Ni:As ratio is 1:0.018, related to the As loss into solution (see Table A.3.8).

Table A.3.8. The concentration of Ni and pnictogen E (E = As, P) in the electrolyte solution after CP OER on FTO and NF. The concentration was determined by ICP-AES of the solution. For each long-term experiment, 45 mL of 1 M KOH were used. The electrolyte solution was divided in three parts (15 mL) and the concentration of Ni, As, and P measured by ICP-AES. The average value of three independent measurements is shown on the table. The percentage of element loss in solution was calculated from the concentration in solution, the initial Ni:E (E = P, As) ratio and the weight of the films (0.4 mg on FTO).

Sample	Ni (mg L ⁻¹)	As (mg L ⁻¹)	P (mg L ⁻¹)	Ni:E ratio (atomic, E = As, P)	% of element loss in solution	
					% Ni	% E
NiAs/FTO OER CP 24 h	0.041	5.589	-	1:114	0.4	45
NiP/FTO OER CP 24h	0.030	-	6.638	1:493	0.2	86

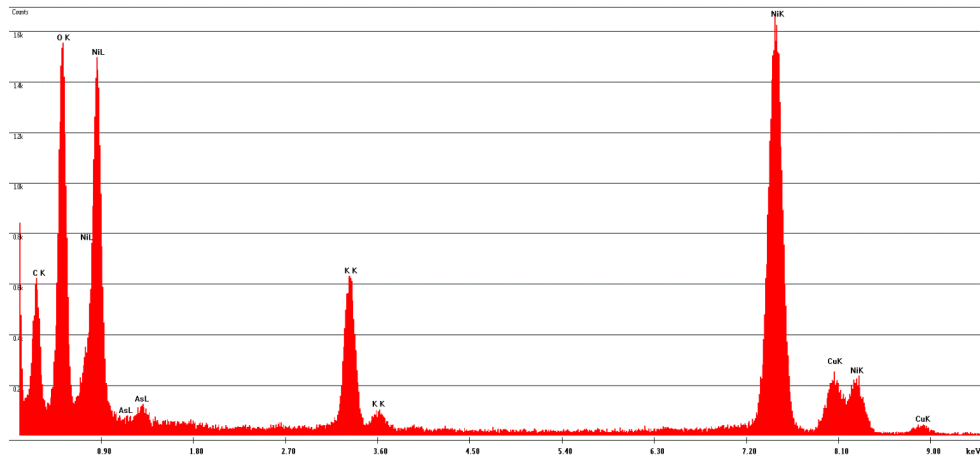


Figure A.3.48. TEM-EDX of (a) NiAs/FTO after OER. The Ni:As ratio is 1:0.018 and the Ni:O ratio is 1:1.37. The presence of O indicates the oxidation of the material. The presence of K is due to the 1 M KOH electrolyte used during the experiments. Cu and C signals arise from the TEM grid (carbon film on 300 mesh Cu-grid).

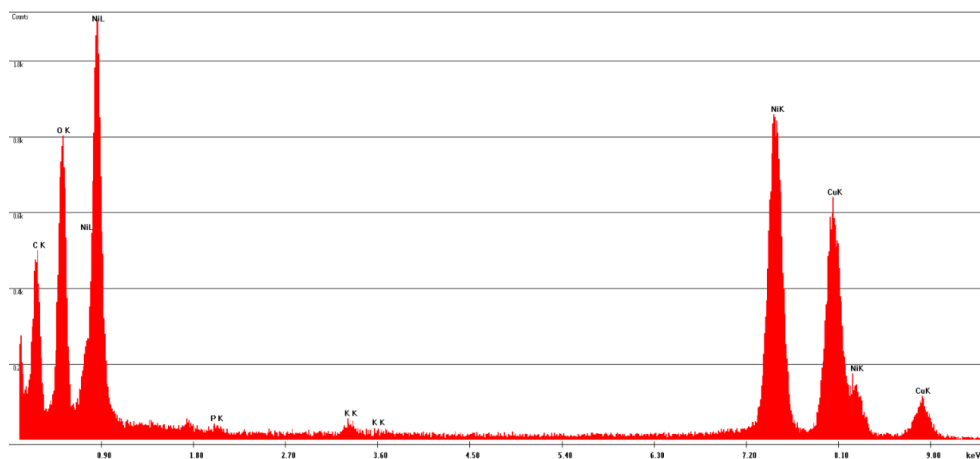


Figure A.3.49. TEM-EDX of (a) NiP/FTO after OER. The Ni:P ratio is 1:0.014 and the Ni:O ratio is 1:1.31. The presence of O indicates the oxidation of the material. The presence of K is due to the 1 M KOH electrolyte used during the experiments. Cu and C signals arise from the TEM grid (carbon film on 300 mesh Cu-grid).

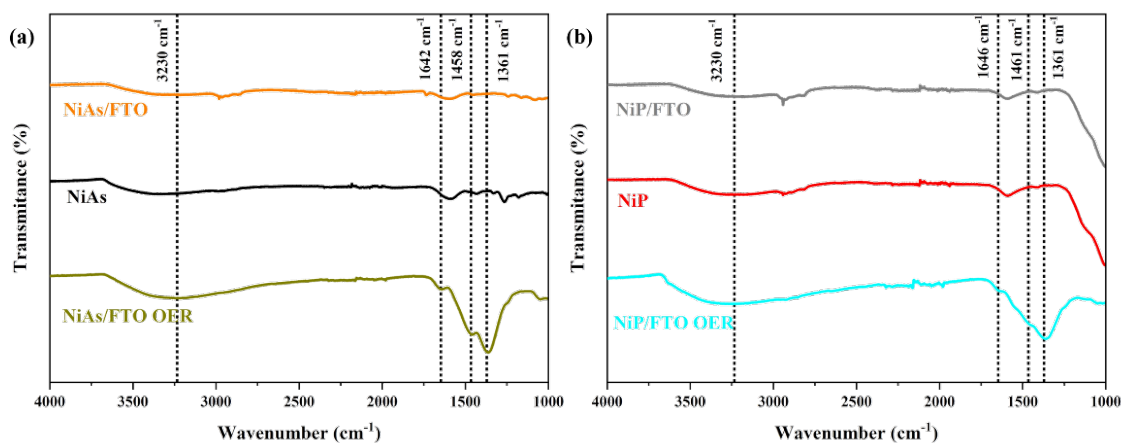


Figure A.3.50. FT-IR of (a) NiAs/FTO and (b) NiP/FTO after OER compared to the spectra of the powder and the as-deposited sample. The after OER spectra of the materials are very similar and could be related to the same phase. The broad band centered at 3230 cm^{-1} could be assigned to stretching vibrations of water molecular that are adsorbed or in the interlayers. The bands at 1642 and 1458 cm^{-1} for NiAs/FTO after OER and 1646 and 1461 cm^{-1} for NiP/FTO after OER are related to bending vibration of H_2O and structural OH groups and are present. The band at 1361 cm^{-1} can be attributed to C-O stretching vibrations of $(\text{CO}_3)^{2-}$ anions, which appeared because of the KOH electrolyte that consumes of CO_2 from ambient air in the form of dissolved carbonate. Such intercalation is possible due to the layered structure of the $\alpha\text{-Ni}(\text{OH})_2$.^[471]

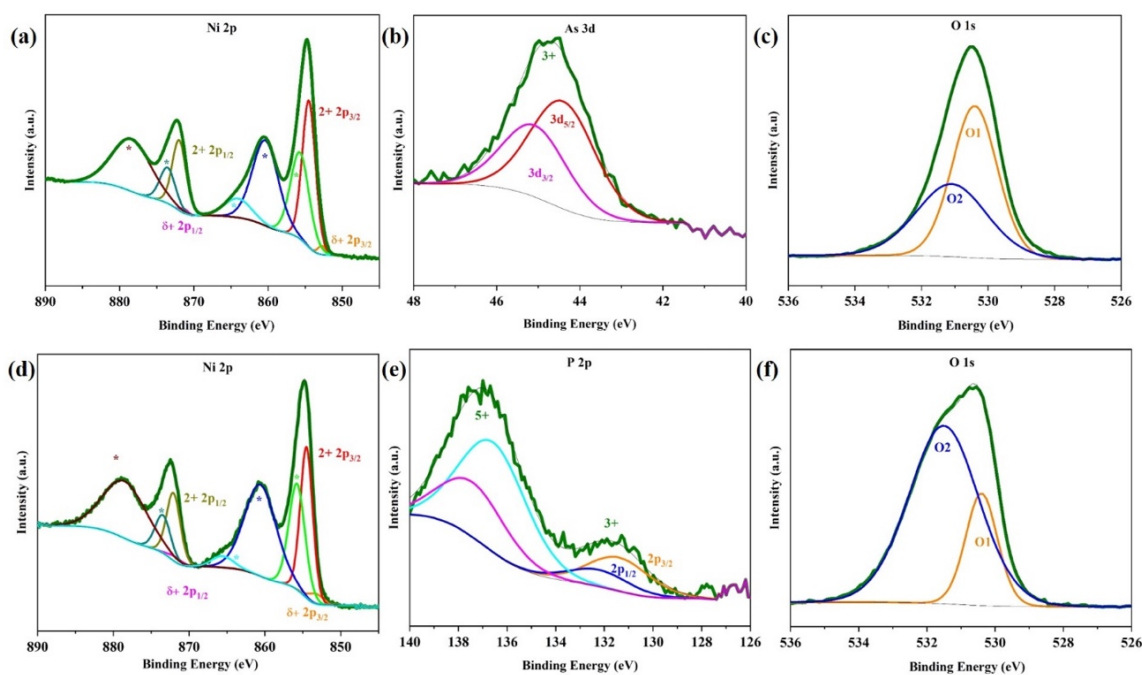


Figure A.3.51. Deconvoluted XPS after OER for NiP/FTO: (a) Ni 2p, (b) P 2p and (c) O 1s; and NiAs/FTO: (d) Ni 2p, (e) As 3d and (f) O 1s.

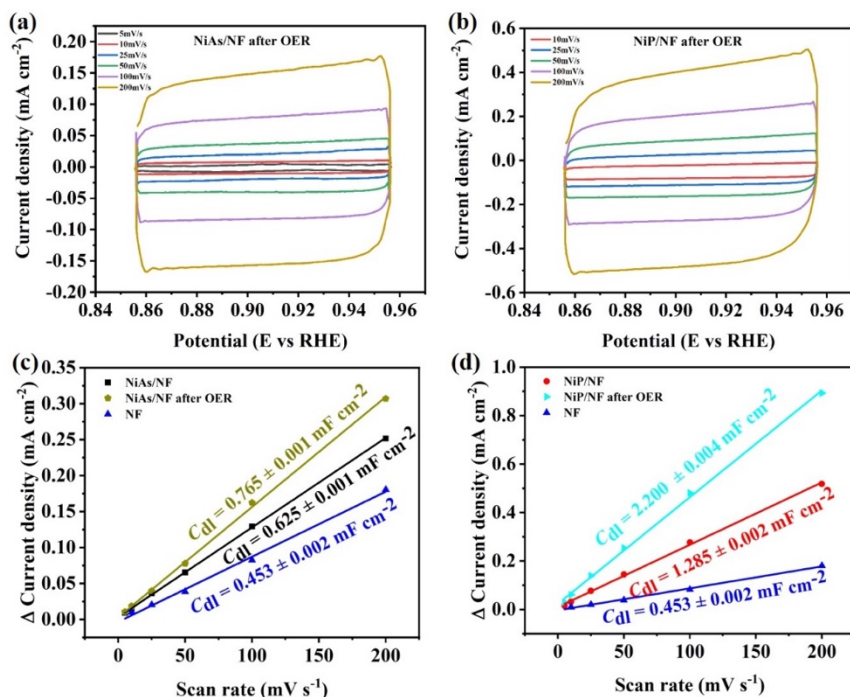


Figure A.3.52. CV measurements at a non-faradaic process region at different scan rates for (a) NiP/NF after OER, (b) NiAs/NF after OER. Scan rates: 5 mV s⁻¹ (black), 10 mV s⁻¹ (red), 25 mV s⁻¹ (blue), 50 mV s⁻¹ (green), 100 mV s⁻¹ (purple), 200 mV s⁻¹ (dark yellow). The double layer capacitance (C_{dl}) was determined as the half of the slope from the plot of the capacitive current vs. scan rate plot (d).

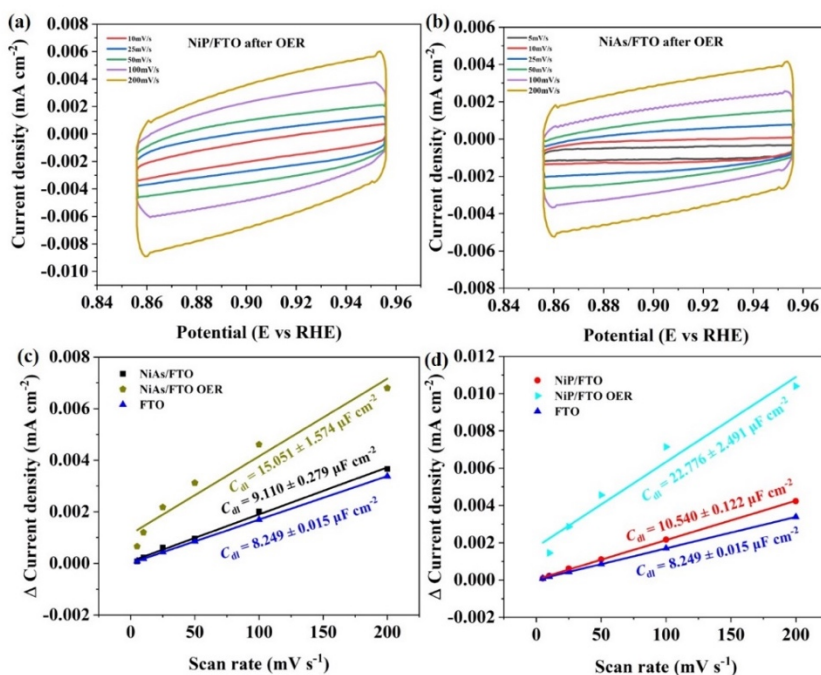


Figure A.3.53. CV measurements at a non-faradaic process region at different scan rates for (a) NiP/FTO after OER, (b) NiAs/FTO after OER. Scan rates: 5 mV s⁻¹ (black), 10 mV s⁻¹ (red), 25 mV s⁻¹ (blue), 50 mV s⁻¹ (green), 100 mV s⁻¹ (purple), 200 mV s⁻¹ (dark yellow). The double layer capacitance (C_{dl}) was determined as the half of the slope from the plot of the capacitive current vs. scan rate plot (c,d).

Table A.3.9. Correlation factor (R^2) of the linear plot of capacitive current vs. scan rate, double layer capacitance (C_{dl}) of NiAs and NiP deposited on FTO.

Material	R^2	C_{dl}
NiP/NF after OER	0.9992	$2.200 \pm 0.004 \text{ mF cm}^{-2}$
NiAs/NF after OER	0.9996	$0.765 \pm 0.001 \text{ mF cm}^{-2}$
NiP/FTO after OER	0.9890	$22.776 \pm 2.791 \text{ } \mu\text{F cm}^{-2}$
NiAs/FTO after OER	0.9788	$15.051 \pm 1.574 \text{ } \mu\text{F cm}^{-2}$

9. References

- [1] A. Ganopolski, R. Winkelmann, H. J. Schellnhuber, *Nature* **2016**, *529*, 200–203.
- [2] B. Koerner, J. Klopatek, *Environ. Pollut.* **2002**, *116*, 45–51.
- [3] C. Acar, I. Dincer, *Int. J. Hydrogen Energy* **2014**, *39*, 1–12.
- [4] M. S. Dresselhaus, I. L. Thomas, *Nature* **2001**, *414*, 332–337.
- [5] B. You, Y. Sun, *Acc. Chem. Res.* **2018**, *51*, 1571–1580.
- [6] R. Lindsey, NOAA, “Climate Change: Atmospheric Carbon Dioxide,” can be found under <https://www.climate.gov/news-features/understanding-climate/climate-change-atmospheric-carbon-dioxide>, **2020**.
- [7] D. G. Vaughan, G. J. Marshall, W. M. Connolley, C. Parkinson, R. Mulvaney, D. A. Hodgson, J. C. King, C. J. Pudsey, J. Turner, *Clim. Change* **2003**, *60*, 243–274.
- [8] L. E. Wells, *Geology* **1990**, *18*, 1134–1137.
- [9] M. B. Freund, B. J. Henley, D. J. Karoly, H. V. McGregor, N. J. Abram, D. Dommenges, *Nat. Geosci.* **2019**, *12*, 450–455.
- [10] S. C. Solomon, H. L. Liu, D. R. Marsh, J. M. McInerney, L. Qian, F. M. Vitt, *Geophys. Res. Lett.* **2018**, *45*, 1567–1576.
- [11] S. C. Doney, V. J. Fabry, R. A. Feely, J. A. Kleypas, *Ann. Rev. Mar. Sci.* **2009**, *1*, 169–192.
- [12] J. Rogelj, A. Popp, K. V. Calvin, G. Luderer, J. Emmerling, D. Gernaat, S. Fujimori, J. Strefler, T. Hasegawa, G. Marangoni, V. Krey, E. Kriegler, K. Riahi, D. P. van Vuuren, J. Doelman, L. Drouet, J. Edmonds, O. Fricko, M. Harmsen, P. Havlík, F. Humpenöder, E. Stehfest, M. Tavoni, *Nat. Clim. Chang.* **2018**, *8*, 325–332.
- [13] A. Raza, A. Razzaq, S. Mehmood, X. Zou, X. Zhang, Y. Lv, J. Xu, *Plants* **2019**, *8*, 34.
- [14] OECD, *World Energy Outlook 2019*, OECD, **2019**.
- [15] C. J. Rhodes, *Sci. Prog.* **2016**, *99*, 97–104.
- [16] M. Höök, X. Tang, *Energy Policy* **2013**, *52*, 797–809.
- [17] S. Chu, A. Majumdar, *Nature* **2012**, *488*, 294–303.
- [18] N. S. Lewis, D. G. Nocera, *Proc. Natl. Acad. Sci.* **2006**, *103*, 15729–15735.
- [19] D. Larcher, J. M. Tarascon, *Nat. Chem.* **2015**, *7*, 19–29.
- [20] T. Hua, R. Ahluwalia, L. Eudy, G. Singer, B. Jermer, N. Asselin-Miller, S. Wessel, T. Patterson, J. Marcinkoski, *J. Power Sources* **2014**, *269*, 975–993.
- [21] N. S. Lewis, *Science* **2007**, *315*, 798–801.
- [22] T. Faunce, S. Styring, M. R. Wasielewski, G. W. Brudvig, A. W. Rutherford, J. Messinger, A. F. Lee, C. L. Hill, H. Degroot, M. Fontecave, D. R. MacFarlane, B. Hankamer, D. G. Nocera, D. M. Tiede, H. Dau, W. Hillier, L. Wang, R. Amal, *Energy Environ. Sci.* **2013**, *6*, 1074–1076.
- [23] L. Schlapbach, A. Züttel, *Nature* **2001**, *414*, 353–358.
- [24] I. Staffell, D. Scamman, A. Velazquez Abad, P. Balcombe, P. E. Dodds, P. Ekins, N. Shah, K. R. Ward, *Energy Environ. Sci.* **2019**, *12*, 463–491.
- [25] G. W. Crabtree, M. S. Dresselhaus, *MRS Bull.* **2008**, *33*, 421–428.
- [26] P. W. Menezes, A. Indra, C. Das, C. Walter, C. Göbel, V. Gutkin, D. Schmeißer, M. Driess, *ACS Catal.* **2017**, *7*, 103–109.
- [27] X. Li, X. Hao, A. Abudula, G. Guan, *J. Mater. Chem. A* **2016**, *4*, 11973–12000.
- [28] B. You, X. Liu, X. Liu, Y. Sun, *ACS Catal.* **2017**, *7*, 4564–4570.
- [29] B. M. Klahr, D. R. Peterson, K. L. Randolph, E. L. Miller, *ECS Trans.* **2017**, *75*, 3–11.
- [30] P. Nikolaidis, A. Poullikkas, *Renew. Sustain. Energy Rev.* **2017**, *67*, 597–611.
- [31] A. C. Lua, H. Y. Wang, *Appl. Catal. B Environ.* **2014**, *156–157*, 84–93.
- [32] P. H. Gleick, *Water in Crisis : A Guide to the World’s Fresh Water Resources*, Oxford University Press, New York, Oxford, **1993**.
- [33] F. M. Sapountzi, J. M. Gracia, C. J. Weststrate, H. O. A. Fredriksson, J. W. Niemantsverdriet, *Prog. Energy Combust. Sci.* **2017**, *58*, 1–35.
- [34] B. O’Regan, M. Grätzel, *Nature* **1991**, *353*, 737–740.
- [35] K. J. Young, L. A. Martini, R. L. Milot, R. C. Snoeberger, V. S. Batista, C. A. Schmuttenmaer, R. H. Crabtree, G. W. Brudvig, *Coord. Chem. Rev.* **2012**, *256*, 2503–2520.
- [36] I. Roger, M. A. Shipman, M. D. Symes, *Nat. Rev. Chem.* **2017**, *1*, 0003.
- [37] J. Chi, H. Yu, *Chinese J. Catal.* **2018**, *39*, 390–394.
- [38] F. Lyu, Q. Wang, S. M. Choi, Y. Yin, *Small* **2019**, *15*, 1804201.
- [39] H. L. Ferreira, R. Garde, G. Fulli, W. Kling, J. P. Lopes, *Energy* **2013**, *53*, 288–298.
- [40] M. E. Khodayar, S. D. Manshadi, H. Wu, J. Lin, *IEEE Trans. Sustain. Energy* **2016**, *7*, 1634–1645.

- [41] S. Anantharaj, S. R. Ede, K. Karthick, S. Sam Sankar, K. Sangeetha, P. E. Karthik, S. Kundu, *Energy Environ. Sci.* **2018**, *11*, 744–771.
- [42] V. R. Stamenkovic, D. Strmcnik, P. P. Lopes, N. M. Markovic, *Nat. Mater.* **2016**, *16*, 57–69.
- [43] F. Barbir, *Sol. Energy* **2005**, *78*, 661–669.
- [44] K. Zeng, D. Zhang, *Prog. Energy Combust. Sci.* **2010**, *36*, 307–326.
- [45] M. Ni, M. K. H. Leung, D. Y. C. Leung, *Int. J. Hydrogen Energy* **2008**, *33*, 2337–2354.
- [46] J. Suntivich, E. E. Perry, H. A. Gasteiger, Y. Shao-Horn, *Electrocatalysis* **2013**, *4*, 49–55.
- [47] N.-T. T. Suen, S.-F. F. Hung, Q. Quan, N. Zhang, Y.-J. J. Xu, H. M. Chen, *Chem. Soc. Rev.* **2017**, *46*, 337–365.
- [48] A. R. Zeradjanin, J. P. Grote, G. Polymeros, K. J. J. Mayrhofer, *Electroanalysis* **2016**, *28*, 2256–2269.
- [49] H. Dau, C. Limberg, T. Reier, M. Risch, S. Roggan, P. Strasser, *ChemCatChem* **2010**, *2*, 724–761.
- [50] M. G. Walter, E. L. Warren, J. R. McKone, S. W. Boettcher, Q. Mi, E. A. Santori, N. S. Lewis, *Chem. Rev.* **2010**, *110*, 6446–6473.
- [51] M. Pourbaix, *Atlas of Electrochemical Equilibria in Aqueous Solutions*, National Association Of Corrosion, Houston, **1974**.
- [52] S. Anantharaj, S. R. Ede, K. Sakthikumar, K. Karthick, S. Mishra, S. Kundu, *ACS Catal.* **2016**, *6*, 8069–8097.
- [53] K. J. Young, L. A. Martini, R. L. Milot, R. C. Snoeberger, V. S. Batista, C. A. Schmuttenmaer, R. H. Crabtree, G. W. Brudvig, *Coord. Chem. Rev.* **2012**, *256*, 2503–2520.
- [54] M. D. Kärkäs, O. Verho, E. V. Johnston, B. Åkermark, *Chem. Rev.* **2014**, *114*, 11863–12001.
- [55] B. E. Conway, B. V. Tilak, *Adv. Catal.* **1992**, *38*, 1–147.
- [56] D. E. Hall, *J. Electrochem. Soc.* **1983**, *130*, 317–321.
- [57] J. O. M. Bockris, *J. Chem. Phys.* **1956**, *24*, 817–827.
- [58] T. Shinagawa, A. T. Garcia-Esparza, K. Takanabe, *Sci. Rep.* **2015**, *5*, 1–21.
- [59] E. Fabbri, A. Habereder, K. Waltar, R. Kötz, T. J. Schmidt, *Catal. Sci. Technol.* **2014**, *4*, 3800–3821.
- [60] Y. Cheng, S. P. Jiang, *Prog. Nat. Sci. Mater. Int.* **2015**, *25*, 545–553.
- [61] P. W. Menezes, C. Panda, C. Walter, M. Schwarze, M. Driess, *Adv. Funct. Mater.* **2019**, *29*, 1–12.
- [62] M.-R. Gao, Y.-F. Xu, J. Jiang, S.-H. Yu, *Chem. Soc. Rev.* **2013**, *42*, 2986–3017.
- [63] Y. Shi, B. Zhang, *Chem. Soc. Rev.* **2016**, *45*, 1529–1541.
- [64] T. Binninger, E. Fabbri, R. Kötz, T. J. Schmidt, *J. Electrochem. Soc.* **2013**, *161*, H121–H128.
- [65] M. Wiechen, M. M. Najafpour, S. I. Allakhverdiev, L. Spiccia, *Energy Environ. Sci.* **2014**, *7*, 2203–2212.
- [66] J. H. Kim, D. H. Youn, K. Kawashima, J. Lin, H. Lim, C. B. Mullins, *Appl. Catal. B Environ.* **2018**, *225*, 1–7.
- [67] C. C. L. McCrory, S. Jung, I. M. Ferrer, S. M. Chatman, J. C. Peters, T. F. Jaramillo, *J. Am. Chem. Soc.* **2015**, *137*, 4347–4357.
- [68] C. C. L. L. McCrory, S. Jung, J. C. Peters, T. F. Jaramillo, *J. Am. Chem. Soc.* **2013**, *135*, 16977–16987.
- [69] J. F. Callejas, C. G. Read, C. W. Roske, N. S. Lewis, R. E. Schaak, *Chem. Mater.* **2016**, *28*, 6017–6044.
- [70] Y. Zheng, Y. Jiao, M. Jaroniec, S. Z. Qiao, *Angew. Chemie Int. Ed.* **2015**, *54*, 52–65.
- [71] J. Wang, W. Cui, Q. Liu, Z. Xing, A. M. Asiri, X. Sun, *Adv. Mater.* **2016**, *28*, 215–230.
- [72] M. A. Khan, H. Zhao, W. Zou, Z. Chen, W. Cao, J. Fang, J. Xu, L. Zhang, J. Zhang, *Recent Progresses in Electrocatalysts for Water Electrolysis*, Springer Singapore, **2018**.
- [73] I. C. Man, H. Y. Su, F. Calle-Vallejo, H. A. Hansen, J. I. Martínez, N. G. Inoglu, J. Kitchin, T. F. Jaramillo, J. K. Nørskov, J. Rossmeisl, *ChemCatChem* **2011**, *3*, 1159–1165.
- [74] Y. Pi, N. Zhang, S. Guo, J. Guo, X. Huang, *Nano Lett.* **2016**, *16*, 4424–4430.
- [75] G. Li, S. Li, J. Ge, C. Liu, W. Xing, *J. Mater. Chem. A* **2017**, *5*, 17221–17229.
- [76] W. T. Hong, M. Risch, K. A. Stoerzinger, A. Grimaud, J. Suntivich, Y. Shao-Horn, *Energy Environ. Sci.* **2015**, *8*, 1404–1427.
- [77] B. You, Y. Sun, *Adv. Energy Mater.* **2016**, *6*, 1502333.
- [78] K. Kadakia, M. K. Datta, O. I. Velikokhatnyi, P. H. Jampani, P. N. Kumta, *Int. J. Hydrogen Energy* **2014**, *39*, 664–674.
- [79] P. W. Menezes, C. Panda, S. Loos, F. Bunschei-Bruns, C. Walter, M. Schwarze, X. Deng, H. Dau, M. Driess, *Energy Environ. Sci.* **2018**, *11*, 1287–1298.

- [80] P. W. Menezes, A. Indra, I. Zaharieva, C. Walter, S. Loos, S. Hoffmann, R. Schlögl, H. Dau, M. Driess, *Energy Environ. Sci.* **2019**, *12*, 988–999.
- [81] P. W. Menezes, C. Panda, S. Garai, C. Walter, A. Guillet, M. Driess, *Angew. Chemie Int. Ed.* **2018**, *57*, 15237–15242.
- [82] S. Trasatti, *J. Electroanal. Chem. Interfacial Electrochem.* **1980**, *111*, 125–131.
- [83] P. Sabatier, *Berichte der Dtsch. Chem. Gesellschaft* **1911**, *44*, 1984–2001.
- [84] J. O. M. Bockris, T. Otagawa, *J. Phys. Chem.* **1983**, *87*, 2960–2971.
- [85] T. W. Schneider, M. Z. Ertem, J. T. Muckerman, A. M. Angeles-Boza, *ACS Catal.* **2016**, *6*, 5473–5481.
- [86] B. M. Hunter, H. B. Gray, A. M. Müller, *Chem. Rev.* **2016**, *116*, 14120–14136.
- [87] J. Rossmeisl, Z. W. Qu, H. Zhu, G. J. Kroes, J. K. Nørskov, *J. Electroanal. Chem.* **2007**, *607*, 83–89.
- [88] C. G. Morales-Guio, L. A. Stern, X. Hu, *Chem. Soc. Rev.* **2014**, *43*, 6555–6569.
- [89] J. K. Nørskov, T. Bligaard, A. Logadottir, J. R. Kitchin, J. G. Chen, S. Pandalov, U. Stimming, *J. Electrochem. Soc.* **2005**, *152*, J23.
- [90] N. Dubouis, A. Grimaud, *Chem. Sci.* **2019**, *10*, 9165–9181.
- [91] Z. Zhou, Z. Pei, L. Wei, S. Zhao, X. Jian, Y. Chen, *Energy Environ. Sci.* **2020**, *13*, 3185–3206.
- [92] M. W. Kanan, D. G. Nocera, *Science* **2008**, *321*, 1072–1075.
- [93] P. Du, R. Eisenberg, *Energy Environ. Sci.* **2012**, *5*, 6012–6021.
- [94] D. G. Nocera, *Acc. Chem. Res.* **2012**, *45*, 767–776.
- [95] S. Cobo, J. Heidkamp, P.-A. Jacques, J. Fize, V. Fourmond, L. Guetaz, B. Jousset, V. Ivanova, H. Dau, S. Palacin, M. Fontecave, V. Artero, *Nat. Mater.* **2012**, *11*, 802–807.
- [96] F. Song, L. Bai, A. Moysiadou, S. Lee, C. Hu, L. Liardet, X. Hu, *J. Am. Chem. Soc.* **2018**, *140*, 7748–7759.
- [97] S. Cherevko, S. Geiger, O. Kasian, N. Kulyk, J. P. Grote, A. Savan, B. R. Shrestha, S. Merzlikin, B. Breitbach, A. Ludwig, K. J. J. Mayrhofer, *Catal. Today* **2016**, *262*, 170–180.
- [98] N. Yuan, Q. Jiang, J. Li, J. Tang, *Arab. J. Chem.* **2020**, *13*, 4294–4309.
- [99] P. W. Menezes, A. Indra, D. González-Flores, N. R. Sahraie, I. Zaharieva, M. Schwarze, P. Strasser, H. Dau, M. Driess, *ACS Catal.* **2015**, *5*, 2017–2027.
- [100] A. Indra, P. W. Menezes, N. R. Sahraie, A. Bergmann, C. Das, M. Tallarida, D. Schmeißer, P. Strasser, M. Driess, *J. Am. Chem. Soc.* **2014**, *136*, 17530–17536.
- [101] M. S. Burke, L. J. Enman, A. S. Batchellor, S. Zou, S. W. Boettcher, *Chem. Mater.* **2015**, *27*, 7549–7558.
- [102] A. Azarpira, J. Pfrommer, K. Olech, C. Höhn, M. Driess, B. Stannowski, T. Schedel-Niedrig, M. Lublow, *J. Mater. Chem. A* **2016**, *4*, 3082–3090.
- [103] L. Rößner, M. Armbrüster, *ACS Catal.* **2019**, *9*, 2018–2062.
- [104] C. Panda, P. W. Menezes, S. Yao, J. Schmidt, C. Walter, J. N. Hausmann, M. Driess, *J. Am. Chem. Soc.* **2019**, *141*, 13306–13310.
- [105] P. W. Menezes, C. Walter, J. N. Hausmann, R. Beltrán-Suito, C. Schlesiger, S. Praetz, V. Yu. Verchenko, A. V. Shevelkov, M. Driess, *Angew. Chemie Int. Ed.* **2019**, *58*, 16569–16574.
- [106] C. Panda, P. W. Menezes, C. Walter, S. Yao, M. E. Miehlich, V. Gutkin, K. Meyer, M. Driess, *Angew. Chemie Int. Ed.* **2017**, *56*, 10506–10510.
- [107] Y. Sun, C. Liu, D. C. Grauer, J. Yano, J. R. Long, P. Yang, C. J. Chang, *J. Am. Chem. Soc.* **2013**, *135*, 17699–17702.
- [108] B. You, Y. Sun, *ChemPlusChem* **2016**, *81*, 1045–1055.
- [109] X. Peng, C. Pi, X. Zhang, S. Li, K. Huo, P. K. Chu, *Sustain. Energy Fuels* **2019**, *3*, 366–381.
- [110] H. Du, R. M. Kong, X. Guo, F. Qu, J. Li, *Nanoscale* **2018**, *10*, 21617–21624.
- [111] S. Yao, V. Forstner, P. W. Menezes, C. Panda, S. Mebs, E. M. Zolnhofer, M. E. Miehlich, T. Szilvási, N. Ashok Kumar, M. Haumann, K. Meyer, H. Grützmacher, M. Driess, *Chem. Sci.* **2018**, *9*, 8590–8597.
- [112] C. Panda, P. W. Menezes, M. Zheng, S. Orthmann, M. Driess, *ACS Energy Lett.* **2019**, *4*, 747–754.
- [113] J. B. Gerken, J. G. McAlpin, J. Y. C. Chen, M. L. Rigsby, W. H. Casey, R. D. Britt, S. S. Stahl, *J. Am. Chem. Soc.* **2011**, *133*, 14431–14442.
- [114] A. Moysiadou, S. Lee, C. S. Hsu, H. M. Chen, X. Hu, *J. Am. Chem. Soc.* **2020**, *142*, 11901–11914.
- [115] M. Zhang, M. De Respinis, H. Frei, *Nat. Chem.* **2014**, *6*, 362–367.
- [116] J. G. McAlpin, Y. Surendranath, M. Dincă, T. A. Stich, S. A. Stoian, W. H. Casey, D. G. Nocera, R. D. Britt, *J. Am. Chem. Soc.* **2010**, *132*, 6882–6883.

- [117] J. Zhou, Y. Wang, X. Su, S. Gu, R. Liu, Y. Huang, S. Yan, J. Li, S. Zhang, *Energy Environ. Sci.* **2019**, *12*, 739–746.
- [118] L. P. Wang, T. Van Voorhis, *J. Phys. Chem. Lett.* **2011**, *2*, 2200–2204.
- [119] A. Bergmann, E. Martinez-Moreno, D. Teschner, P. Chernev, M. Gliech, J. F. De Araújo, T. Reier, H. Dau, P. Strasser, *Nat. Commun.* **2015**, *6*, 8625.
- [120] M. García-Mota, M. Bajdich, V. Viswanathan, A. Vojvodic, A. T. Bell, J. K. Nørskov, *J. Phys. Chem. C* **2012**, *116*, 21077–21082.
- [121] S. Zhao, B. Rasimick, W. Mustain, H. Xu, *Appl. Catal. B Environ.* **2017**, *203*, 138–145.
- [122] B. S. Yeo, A. T. Bell, *J. Am. Chem. Soc.* **2011**, *133*, 5587–5593.
- [123] D. Ruchira Liyanage, D. Li, Q. B. Cheek, H. Baydoun, S. L. Brock, *J. Mater. Chem. A* **2017**, *5*, 17609–17618.
- [124] P. W. Menezes, A. Indra, O. Levy, K. Kailasam, V. Gutkin, J. Pfrommer, M. Driess, *Chem. Commun.* **2015**, *51*, 5005–5008.
- [125] E. Arciga-Duran, Y. Meas, J. J. Pérez-Bueno, J. C. Ballesteros, G. Trejo, *Electrochim. Acta* **2018**, *268*, 49–58.
- [126] H. Bode, K. Dehmelt, J. Witte, *Electrochim. Acta* **1966**, *11*, 1079–1087.
- [127] C. Bocca, A. Barbucci, M. Delucchi, G. Cerisola, *Int. J. Hydrogen Energy* **1999**, *24*, 21–26.
- [128] N. Li, D. K. Bediako, R. G. Hadt, D. Hayes, T. J. Kempa, F. Von Cube, D. C. Bell, L. X. Chen, D. G. Nocera, *Proc. Natl. Acad. Sci. U. S. A.* **2017**, *114*, 1486–1491.
- [129] C. Feng, M. B. Faheem, J. Fu, Y. Xiao, C. Li, Y. Li, *ACS Catal.* **2020**, *10*, 4019–4047.
- [130] S. Zou, M. S. Burke, M. G. Kast, J. Fan, N. Danilovic, S. W. Boettcher, *Chem. Mater.* **2015**, *27*, 8011–8020.
- [131] M. S. Burke, S. Zou, L. J. Enman, J. E. Kellon, C. A. Gabor, E. Pledger, S. W. Boettcher, *J. Phys. Chem. Lett.* **2015**, *6*, 3737–3742.
- [132] L. Trotochaud, S. L. Young, J. K. Ranney, S. W. Boettcher, *J. Am. Chem. Soc.* **2014**, *136*, 6744–6753.
- [133] Y. Li, C. Zhao, *Chem. Mater.* **2016**, *28*, 5659–5666.
- [134] A. Indra, P. W. Menezes, M. Driess, *ChemSusChem* **2015**, *8*, 776–785.
- [135] D. J. Vinyard, G. M. Ananyev, G. Charles Dismukes, *Annu. Rev. Biochem.* **2013**, *82*, 577–606.
- [136] Y. Matsumoto, S. Yamada, T. Nishida, E. Sato, *J. Electrochem. Soc.* **1980**, *127*, 2360–2634.
- [137] J. Suntivich, K. J. May, H. A. Gasteiger, J. B. Goodenough, Y. Shao-Horn, *Science* **2011**, *334*, 2010–2012.
- [138] N. Zhang, X. Feng, D. Rao, X. Deng, L. Cai, B. Qiu, R. Long, Y. Xiong, Y. Lu, Y. Chai, *Nat. Commun.* **2020**, *11*, 1–11.
- [139] A. Grimaud, C. E. Carlton, M. Risch, W. T. Hong, K. J. May, Y. Shao-Horn, *J. Phys. Chem. C* **2013**, *117*, 25926–25932.
- [140] U. Maitra, A. Govindaraj, C. N. R. Rao, *Proc. Natl. Acad. Sci. U. S. A.* **2013**, *110*, 11704–11707.
- [141] Y. Wang, M. Qiao, Y. Li, S. Wang, *Small* **2018**, *14*, 1–6.
- [142] D. K. Bediako, Y. Surendranath, D. G. Nocera, *J. Am. Chem. Soc.* **2013**, *135*, 3662–3674.
- [143] K. Juodkazis, J. Juodkazytė, R. Vilkauskaitė, V. Jasulaitienė, *J. Solid State Electrochem.* **2008**, *12*, 1469–1479.
- [144] Y. He, X. Liu, G. Chen, J. Pan, A. Yan, A. Li, X. Lu, D. Tang, N. Zhang, T. Qiu, R. Ma, T. Sasaki, *Chem. Mater.* **2020**, *32*, 4232–4240.
- [145] Y. Pan, Y. Lin, Y. Chen, Y. Liu, C. Liu, *J. Mater. Chem. A* **2016**, *4*, 4745–4754.
- [146] J. A. Vigil, T. N. Lambert, B. T. Christensen, *J. Mater. Chem. A* **2016**, *4*, 7549–7554.
- [147] Y. Pan, Y. Liu, J. Zhao, K. Yang, J. Liang, D. Liu, W. Hu, D. Liu, Y. Liu, C. Liu, *J. Mater. Chem. A* **2015**, *3*, 1656–1665.
- [148] J. Yu, Y. Zhong, X. Wu, J. Sunarso, M. Ni, W. Zhou, Z. Shao, *Adv. Sci.* **2018**, *5*, 1800514–1800522.
- [149] E. J. Popczun, C. G. Read, C. W. Roske, N. S. Lewis, R. E. Schaak, *Angew. Chemie Int. Ed.* **2014**, *53*, 5427–5430.
- [150] E. J. Popczun, J. R. McKone, C. G. Read, A. J. Biacchi, A. M. Wiltrout, N. S. Lewis, R. E. Schaak, *J. Am. Chem. Soc.* **2013**, *135*, 9267–9270.
- [151] M. Ledendecker, S. Krick Calderón, C. Papp, H.-P. Steinrück, M. Antonietti, M. Shalom, *Angew. Chemie Int. Ed.* **2015**, *54*, 12361–12365.
- [152] Z. Huang, Z. Chen, Z. Chen, C. Lv, M. G. Humphrey, C. Zhang, *Nano Energy* **2014**, *9*, 373–382.
- [153] X. Zhong, Y. Jiang, X. Chen, L. Wang, G. Zhuang, X. Li, J. Wang, *J. Mater. Chem. A* **2016**, *4*, 10575–10584.
- [154] J. Kupka, A. Budniok, *J. Appl. Electrochem.* **1990**, *20*, 1015–1020.
- [155] J. Ryu, N. Jung, J. H. Jang, H. J. Kim, S. J. Yoo, *ACS Catal.* **2015**, *5*, 4066–4074.

- [156] Y. Yang, H. Fei, G. Ruan, J. M. Tour, *Adv. Mater.* **2015**, *27*, 3175–3180.
- [157] D. Xiong, X. Wang, W. Li, L. Liu, *Chem. Commun.* **2016**, *52*, 8711–8714.
- [158] N. Ashokan, Iron Phosphide Nanostructures as an Efficient Bifunctional Catalysts for Water Splitting, Missouri University of Science and Technology, **2016**.
- [159] A. Dutta, S. Mutyala, A. K. Samantara, S. Bera, B. K. Jena, N. Pradhan, *ACS Energy Lett.* **2018**, *3*, 141–148.
- [160] L. Ai, Z. Niu, J. Jiang, *Electrochim. Acta* **2017**, *242*, 355–363.
- [161] L.-A. Stern, L. Feng, F. Song, X. Hu, *Energy Environ. Sci.* **2015**, *8*, 2347–2351.
- [162] J. Chang, Y. Xiao, M. Xiao, J. Ge, C. Liu, W. Xing, *ACS Catal.* **2015**, *5*, 6874–6878.
- [163] W. Li, D. Xiong, X. Gao, L. Liu, *Chem. Commun.* **2019**, *55*, 8744–8763.
- [164] Y. Wang, B. Kong, D. Zhao, H. Wang, C. Selomulya, *Nano Today* **2017**, *15*, 26–55.
- [165] A. R. J. Kucernak, V. N. Naranammalpuram Sundaram, *J. Mater. Chem. A* **2014**, *2*, 17435–17445.
- [166] K. Tang, X. Wang, M. Wang, Y. Xie, J. Zhou, C. Yan, *ChemElectroChem* **2017**, *4*, 2150–2157.
- [167] L. Tian, X. Yan, X. Chen, *ACS Catal.* **2016**, *6*, 5441–5448.
- [168] A. Dutta, N. Pradhan, *J. Phys. Chem. Lett.* **2017**, *8*, 144–152.
- [169] N. Jiang, B. You, M. Sheng, Y. Sun, *ChemCatChem* **2016**, *8*, 106–112.
- [170] F. D’Accriscio, E. Schrader, C. Sassoie, M. Selmane, R. F. André, S. Lamaison, D. Wakerley, M. Fontecave, V. Mougél, G. Le Corre, H. Grützmacher, C. Sanchez, S. Carencó, *ChemNanoMat* **2020**, *6*, 1208–1219.
- [171] R. Wu, D. P. Wang, K. Zhou, N. Srikanth, J. Wei, Z. Chen, *J. Mater. Chem. A* **2016**, *4*, 13742–13745.
- [172] X. Zhou, H. Gao, Y. Wang, Z. Liu, J. Lin, Y. Ding, *J. Mater. Chem. A* **2018**, *6*, 14939–14948.
- [173] F. Li, Y. Bu, Z. Lv, J. Mahmood, G. F. Han, I. Ahmad, G. Kim, Q. Zhong, J. B. Baek, *Small* **2017**, *13*, 1–6.
- [174] B. You, N. Jiang, M. Sheng, M. W. Bhushan, Y. Sun, *ACS Catal.* **2016**, *6*, 714–721.
- [175] X. Wang, W. Li, D. Xiong, L. Liu, *J. Mater. Chem. A* **2016**, *4*, 5639–5646.
- [176] J. Yu, Q. Li, Y. Li, C. Y. Xu, L. Zhen, V. P. Dravid, J. Wu, *Adv. Funct. Mater.* **2016**, *26*, 7644–7651.
- [177] D. Li, H. Baydoun, C. N. Verani, S. L. Brock, *J. Am. Chem. Soc.* **2016**, *138*, 4006–4009.
- [178] R. Dangol, Z. Dai, A. Chaturvedi, Y. Zheng, Y. Zhang, K. N. Dinh, B. Li, Y. Zong, Q. Yan, *Nanoscale* **2018**, *10*, 4890–4896.
- [179] A. Mendoza-Garcia, H. Zhu, Y. Yu, Q. Li, L. Zhou, D. Su, M. J. Kramer, S. Sun, *Angew. Chemie Int. Ed.* **2015**, *54*, 9642–9645.
- [180] Z. Pu, Y. Xue, W. Li, I. S. Amiinu, S. Mu, *New J. Chem.* **2017**, *41*, 2154–2159.
- [181] P. Wang, Z. Pu, Y. Li, L. Wu, Z. Tu, M. Jiang, Z. Kou, I. S. Amiinu, S. Mu, *ACS Appl. Mater. Interfaces* **2017**, *9*, 26001–26007.
- [182] J. Kibsgaard, C. Tsai, K. Chan, J. D. Benck, J. K. Nørskov, F. Abild-Pedersen, T. F. Jaramillo, *Energy Environ. Sci.* **2015**, *8*, 3022–3029.
- [183] L. Zeng, K. Sun, X. Wang, Y. Liu, Y. Pan, Z. Liu, D. Cao, Y. Song, S. Liu, C. Liu, *Nano Energy* **2018**, *51*, 26–36.
- [184] S. Prof, M. Driess, M. A. R. Anjum, M. S. Okyay, M. Kim, M. H. Lee, N. Park, J. S. Lee, *Nano Energy* **2018**, *53*, 286–295.
- [185] K. Liang, S. Pakhira, Z. Yang, A. Nijamudheen, L. Ju, M. Wang, C. I. Aguirre-Velez, G. E. Sterbinsky, Y. Du, Z. Feng, J. L. Mendoza-Cortes, Y. Yang, *ACS Catal.* **2019**, *9*, 651–659.
- [186] C. Li, X. Mei, F. L.-Y. Lam, X. Hu, *Catal. Today* **2020**, *358*, 215–220.
- [187] S. Han, Y. Feng, F. Zhang, C. Yang, Z. Yao, W. Zhao, F. Qiu, L. Yang, Y. Yao, X. Zhuang, X. Feng, *Adv. Funct. Mater.* **2015**, *25*, 3899–3906.
- [188] Z. Zhang, J. Hao, W. Yang, J. Tang, *ChemCatChem* **2015**, *7*, 1920–1925.
- [189] J. Masud, S. Umapathi, N. Ashokaan, M. Nath, *J. Mater. Chem. A* **2016**, *4*, 9750–9754.
- [190] Q. Liu, J. Tian, W. Cui, P. Jiang, N. Cheng, A. M. Asiri, X. Sun, *Angew. Chemie Int. Ed.* **2014**, *53*, 6710–6714.
- [191] C.-C. C. Hou, S. Cao, W.-F. F. Fu, Y. Chen, *ACS Appl. Mater. Interfaces* **2015**, *7*, 28412–28419.
- [192] J. Wang, W. Yang, J. Liu, *J. Mater. Chem. A* **2016**, *4*, 4686–4690.
- [193] T. Sun, S. Zhang, L. Xu, D. Wang, Y. Li, *Chem. Commun.* **2018**, *54*, 12101–12104.
- [194] Y. Kamihara, T. Watanabe, M. Hirano, H. Hosono, *J. Am. Chem. Soc.* **2008**, *130*, 3296–3297.
- [195] X. C. Wang, Q. Q. Liu, Y. X. Lv, W. B. Gao, L. X. Yang, R. C. Yu, F. Y. Li, C. Q. Jin, *Solid State Commun.* **2008**, *148*, 538–540.
- [196] Z.-A. Ren, J. Yang, W. Lu, W. Yi, X.-L. Shen, Z.-C. Li, G.-C. Che, X.-L. Dong, L.-L. Sun, F. Zhou, Z.-X. Zhao, *EPL-Europhysics Lett.* **2008**, *82*, 57002.

- [197] D. R. Parker, M. J. Pitcher, P. J. Baker, I. Franke, T. Lancaster, S. J. Blundell, S. J. Clarke, *Chem. Commun.* **2009**, 16, 2189–2191.
- [198] T. Stürzer, C. Stürzer, D. Johrendt, *Phys. status solidi* **2017**, 254, 1600417.
- [199] J. Gopalakrishnan, S. Pandey, K. K. Rangan, *Chem. Mater.* **1997**, 9, 2113–2116.
- [200] N. P. Dasgupta, J. Sun, C. Liu, S. Brittman, S. C. Andrews, J. Lim, H. Gao, R. Yan, P. Yang, *Adv. Mater.* **2014**, 26, 2137–2184.
- [201] P. Desai, N. Ashokan, M. Nath, *J. Nanomater.* **2015**, 2015, 1–11.
- [202] J. Masa, W. Schuhmann, *ChemCatChem* **2019**, 11, 5842–5854.
- [203] J. Masa, S. Piontek, P. Wilde, H. Antoni, T. Eckhard, Y. Chen, M. Muhler, U. Apfel, W. Schuhmann, *Adv. Energy Mater.* **2019**, 1900796.
- [204] J. Weidner, S. Barwe, K. Sliozberg, S. Piontek, J. Masa, U. P. Apfel, W. Schuhmann, *Beilstein J. Org. Chem.* **2018**, 14, 1436–1445.
- [205] A. Vahidnia, G. B. Van Der Voet, F. A. De Wolff, *Hum. Exp. Toxicol.* **2007**, 26, 823–832.
- [206] J. A. Gauthier, L. A. King, F. T. Stults, R. A. Flores, J. Kibsgaard, Y. N. Regmi, K. Chan, T. F. Jaramillo, *J. Phys. Chem. C* **2019**, 123, 24007–24012.
- [207] C. Panda, P. W. Menezes, M. Driess, *Angew. Chemie Int. Ed.* **2018**, 57, 11130–11139.
- [208] C. Walter, P. W. Menezes, S. Orthmann, J. Schuch, P. Connor, B. Kaiser, M. Lerch, M. Driess, *Angew. Chemie Int. Ed.* **2018**, 57, 698–702.
- [209] C. L. Daniels, D. L. Mendivelso-Perez, B. A. Rosales, D. You, S. Sahu, J. S. Jones, E. A. Smith, F. P. Gabbai, J. Vela, *ACS Omega* **2019**, 4, 5197–5203.
- [210] L. McElwee-White, *J. Chem. Soc. Dalton Trans.* **2006**, 5327–5333.
- [211] H. M. Manasevit, *J. Cryst. Growth* **1972**, 13–14, 306–314.
- [212] H. M. Manasevit, *Appl. Phys. Lett.* **1968**, 12, 156–159.
- [213] A. H. Cowley, R. A. Jones, *Polyhedron* **1994**, 13, 1149–1157.
- [214] H. Lu, D. S. Wright, S. D. Pike, *Chem. Commun.* **2020**, 56, 854–871.
- [215] W. E. Buhro, *Adv. Mater. Opt. Electron.* **1996**, 6, 175–184.
- [216] O. J. Bchir, S. W. Johnston, A. C. Cuadra, T. J. Anderson, C. G. Ortiz, B. C. Brooks, D. H. Powell, L. McElwee-White, *J. Cryst. Growth* **2003**, 249, 262–274.
- [217] M. Akhtar, M. A. Malik, J. Raftery, P. O'Brien, *J. Mater. Chem. A* **2014**, 2, 20612–20620.
- [218] Y. F. Lin, H. W. Chang, S. Y. Lu, C. W. Liu, *J. Phys. Chem. C* **2007**, 111, 18538–18544.
- [219] I. Y. Ahmet, M. S. Hill, A. L. Johnson, L. M. Peter, *Chem. Mater.* **2015**, 27, 7680–7688.
- [220] M. A. Ehsan, R. Naeem, V. McKee, A. S. Hakeem, M. Mazhar, *Sol. Energy Mater. Sol. Cells* **2017**, 161, 328–337.
- [221] J. Alemán, A. V. Chadwick, J. He, M. Hess, K. Horie, R. G. Jones, P. Kratochvíl, I. Meisel, I. Mita, G. Moad, S. Penczek, R. F. T. Stepto, *Pure Appl. Chem.* **2007**, 79, 1801–1829.
- [222] S. Polarz, A. V. Orlov, M. W. E. Van Den Berg, M. Driess, *Angew. Chemie - Int. Ed.* **2005**, 44, 7892–7896.
- [223] J. Wang, A. C. Johnston-Peck, J. B. Tracy, *Chem. Mater.* **2009**, 21, 4462–4467.
- [224] P. Buchwalter, J. Rosé, B. Lebeau, P. Rabu, P. Braunstein, J. L. Paillaud, *Inorganica Chim. Acta* **2014**, 409, 330–341.
- [225] J. Wang, G. Wang, S. Miao, X. Jiang, J. Li, X. Bao, *Carbon* **2014**, 75, 381–389.
- [226] W. Maneeprakorn, M. a. Malik, P. O'Brien, *J. Mater. Chem.* **2010**, 20, 2329–2335.
- [227] S. Wei, J. Lu, W. Yu, H. Zhang, Y. Qian, *Cryst. Growth Des.* **2006**, 6, 849–853.
- [228] H. Cao, Y. Xie, H. Wang, F. Xiao, A. Wu, L. Li, Z. Xu, N. Xiong, K. Pan, *Electrochim. Acta* **2018**, 259, 830–840.
- [229] L. C. C. Ferraz, W. M. Carvalho, D. Criado, F. L. Souza, *ACS Appl. Mater. Interfaces* **2012**, 4, 5515–5523.
- [230] X.-H. Li, C.-L. Xu, X.-H. Han, L. Qiao, T. Wang, F.-S. Li, *Nanoscale Res. Lett.* **2010**, 5, 1039–1044.
- [231] S. A. Khalate, S. A. Kadam, Y. R. Ma, S. S. Pujari, S. J. Marje, P. K. Katkar, A. C. Lokhande, U. M. Patil, *Electrochim. Acta* **2019**, 319, 118–128.
- [232] C. Ouyang, X. Wang, C. Wang, X. Zhang, J. Wu, Z. Ma, S. Dou, S. Wang, *Electrochim. Acta* **2015**, 174, 297–301.
- [233] R. Gao, H. Zhang, D. Yan, *Nano Energy* **2017**, 31, 90–95.
- [234] C. B. Murray, D. J. Norris, M. G. Bawendi, *J. Am. Chem. Soc.* **1993**, 115, 8706–8715.
- [235] P. W. Menezes, A. Indra, P. Littlewood, C. Göbel, R. Schomäcker, M. Driess, *ChemPlusChem* **2016**, 81, 370–377.
- [236] M. Tsaroucha, Y. Aksu, E. Irran, M. Driess, *Chem. Mater.* **2011**, 23, 2428–2438.

- [237] J. Pfrommer, M. Lublow, A. Azarpira, C. Göbel, M. Lücke, A. Steigert, M. Pogrzeba, P. W. Menezes, A. Fischer, T. Schedel-Niedrig, M. Driess, *Angew. Chemie Int. Ed.* **2014**, *53*, 5183–5187.
- [238] J. A. Vigil, T. N. Lambert, *RSC Adv.* **2015**, *5*, 105814–105819.
- [239] S. Anantharaj, P. N. Reddy, S. Kundu, *Inorg. Chem.* **2017**, *56*, 1742–1756.
- [240] N. Jiang, B. You, M. Sheng, Y. Sun, *Angew. Chemie Int. Ed.* **2015**, *54*, 6251–6254.
- [241] S. Kim, K. Lee, S. Kim, O. P. Kwon, J. H. Heo, S. H. Im, S. Jeong, D. C. Lee, S. W. Kim, *RSC Adv.* **2015**, *5*, 2466–2469.
- [242] K. Y. Yoon, Y. Jang, J. Park, Y. Hwang, B. Koo, J. G. Park, T. Hyeon, *J. Solid State Chem.* **2008**, *181*, 1609–1613.
- [243] B. Chakraborty, S. Kalra, R. Beltrán-Suito, C. Das, T. Hellmann, P. W. Menezes, M. Driess, *Chem. – An Asian J.* **2020**, *15*, 852–859.
- [244] B. D. Dhanapala, H. N. Munasinghe, L. Suescun, F. A. Rabuffetti, *Inorg. Chem.* **2017**, *56*, 13311–13320.
- [245] J. Song, C. Zhu, B. Z. Xu, S. Fu, M. H. Engelhard, R. Ye, D. Du, S. P. Beckman, Y. Lin, *Adv. Energy Mater.* **2017**, *7*, 1–9.
- [246] K. Xu, P. Chen, X. Li, Y. Tong, H. Ding, X. Wu, W. Chu, Z. Peng, C. Wu, Y. Xie, *J. Am. Chem. Soc.* **2015**, *137*, 4119–4125.
- [247] S. Anantharaj, S. Noda, *Small* **2020**, *16*, 1–24.
- [248] J. Liu, J. Nai, T. You, P. An, J. Zhang, G. Ma, X. Niu, C. Liang, S. Yang, L. Guo, *Small* **2018**, *14*, 1–8.
- [249] E. Tsuji, A. Imanishi, K. I. Fukui, Y. Nakato, *Electrochim. Acta* **2011**, *56*, 2009–2016.
- [250] R. Beltrán-Suito, P. W. Menezes, M. Driess, *J. Mater. Chem. A* **2019**, *7*, 15749–15756.
- [251] H. Alemu, K. Jüttner, *Electrochim. Acta* **1988**, *33*, 1101–1109.
- [252] E. B. Castro, M. J. De Giz, E. R. Gonzalez, J. R. Vilche, *Electrochim. Acta* **1997**, *42*, 951–959.
- [253] J. Wang, Z. Liu, Y. Zheng, L. Cui, W. Yang, J. Liu, *J. Mater. Chem. A* **2017**, *5*, 22913–22932.
- [254] L. Ai, Z. Niu, J. Jiang, L. Yang, H. Qi, C. Zhang, X. Sun, *Nanotechnology* **2016**, *27*, 23LT01.
- [255] J. Tian, Q. Liu, A. M. Asiri, X. Sun, *J. Am. Chem. Soc.* **2014**, *136*, 7587–7590.
- [256] Q. Li, Z. Xing, A. M. Asiri, P. Jiang, X. Sun, *Int. J. Hydrogen Energy* **2014**, *39*, 16806–16811.
- [257] A. Budniok, J. Kupka, *Electrochim. Acta* **1989**, *34*, 871–873.
- [258] J. Villalobos, D. González-Flores, K. Klingan, P. Chernev, P. Kubella, R. Urcuyo, C. Pasquini, M. R. Mohammadi, R. D. L. L. Smith, M. L. Montero, H. Dau, *Phys. Chem. Chem. Phys.* **2019**, *21*, 12485–12493.
- [259] M. Liu, J. Li, *ACS Appl. Mater. Interfaces* **2016**, *8*, 2158–2165.
- [260] C.-Z. Z. Yuan, S.-L. L. Zhong, Y.-F. F. Jiang, Z. K. Yang, Z.-W. W. Zhao, S.-J. J. Zhao, N. Jiang, A.-W. W. Xu, *J. Mater. Chem. A* **2017**, *5*, 10561–10566.
- [261] M. S. Burke, M. G. Kast, L. Trotochaud, A. M. Smith, S. W. Boettcher, *J. Am. Chem. Soc.* **2015**, *137*, 3638–3648.
- [262] M. Zhu, Y. Zhou, Y. Sun, C. Zhu, L. Hu, J. Gao, H. Huang, Y. Liu, Z. Kang, *Dalt. Trans.* **2018**, *47*, 5459–5464.
- [263] J. Masa, S. Barwe, C. Andronescu, I. Sinev, A. Ruff, K. Jayaramulu, K. Elumeeva, B. Konkena, B. Roldan Cuenya, W. Schuhmann, *ACS Energy Lett.* **2016**, *1*, 1192–1198.
- [264] Y.-P. Zhu, Y.-P. Liu, T.-Z. Ren, Z.-Y. Yuan, *Adv. Funct. Mater.* **2015**, *25*, 7337–7347.
- [265] P. Wang, F. Song, R. Amal, Y. H. Ng, X. Hu, *ChemSusChem* **2016**, *9*, 472–477.
- [266] Y. R. Liu, W. H. Hu, G. Q. Han, B. Dong, X. Li, X. Shang, Y. M. Chai, Y. Q. Liu, C. G. Liu, *Electrochim. Acta* **2016**, *220*, 98–106.
- [267] L. Ji, J. Wang, X. Teng, T. J. Meyer, Z. Chen, *ACS Catal.* **2020**, *10*, 412–419.
- [268] M. A. Granger, *Bull. Soc. Chim. Fr.* **1896**, *15*, 1086–1089.
- [269] K. Ishida, T. Nishizawa, *Bull. Alloy Phase Diagrams* **1990**, *11*, 555–560.
- [270] S. Fujii, S. Ishida, S. Asano, *J. Phys. F Met. Phys.* **1988**, *18*, 971–980.
- [271] N. Zhang, A. Shan, R. Wang, C. Chen, *CrystEngComm* **2012**, *14*, 1197–1200.
- [272] P. C. Donohue, *Mater. Res. Bull.* **1972**, *7*, 943–948.
- [273] J. Wang, Q. Yang, Z. Zhang, S. Sun, *Chem. - A Eur. J.* **2010**, *16*, 7916–7924.
- [274] S. Rundqvist, L. G. Sillén, D. Timm, K. Motzfeldt, O. Theander, H. Flood, *Acta Chem. Scand.* **1962**, *16*, 287–292.
- [275] J. Ackermann, A. Wold, *J. Phys. Chem. Solids* **1977**, *38*, 1013–1016.
- [276] M. Llunell, P. Alemany, S. Alvarez, V. P. Zhukov, A. Vernes, *Phys. Rev. B - Condens. Matter Mater. Phys.* **1996**, *53*, 10605–10609.
- [277] H. Jia, R. Jiang, W. Lu, Q. Ruan, J. Wang, J. C. Yu, *J. Mater. Chem. A* **2018**, *6*, 4783–4792.
- [278] B. You, N. Jiang, M. Sheng, S. Gul, J. Yano, Y. Sun, *Chem. Mater.* **2015**, *27*, 7636–7642.

- [279] C. M. Lukehart, S. B. Milne, S. R. Stock, *Chem. Mater.* **1998**, *10*, 903–908.
- [280] Y. Xie, H. L. Su, X. F. Qian, X. M. Liu, Y. T. Qian, *J. Solid State Chem.* **2000**, *149*, 88–91.
- [281] S. Yao, N. Lindenmaier, Y. Xiong, S. Inoue, T. Szilvási, M. Adelhardt, J. Sutter, K. Meyer, M. Driess, *Angew. Chemie Int. Ed.* **2015**, *54*, 1250–1254.
- [282] Y. Liu, D. G. Nocera, *J. Phys. Chem. C* **2014**, *118*, 17060–17066.
- [283] P. He, X.-Y. Y. Yu, X. W. D. Lou, *Angew. Chemie Int. Ed.* **2017**, *56*, 3897–3900.
- [284] Q. Wang, Z. Liu, H. Zhao, H. Huang, H. Jiao, Y. Du, *J. Mater. Chem. A* **2018**, *6*, 18720–18727.
- [285] L. Yan, L. Cao, P. Dai, X. Gu, D. Liu, L. Li, Y. Wang, X. Zhao, *Adv. Funct. Mater.* **2017**, *27*, 1–10.
- [286] S. S. He, S. S. He, X. Bo, Q. Q. Wang, F. Zhan, Q. Q. Wang, C. Zhao, *Mater. Lett.* **2018**, *231*, 94–97.
- [287] T. J. Chuang, C. R. Brundle, D. W. Rice, *Surf. Sci.* **1976**, *59*, 413–429.
- [288] A. P. Grosvenor, S. D. Wik, R. G. Cavell, A. Mar, *Inorg. Chem.* **2005**, *44*, 8988–8998.
- [289] D. Liu, L. Jing, P. Luan, J. Tang, H. Fu, *ACS Appl. Mater. Interfaces* **2013**, *5*, 4046–4052.
- [290] Z. Jin, P. Li, D. Xiao, *Green Chem.* **2016**, *18*, 1459–1464.
- [291] Q. Wang, L. Zhong, J. Sun, J. Shen, *Chem. Mater.* **2005**, *17*, 3563–3569.
- [292] F. Zhou, A. Izgorodin, R. K. Hocking, L. Spiccia, D. R. MacFarlane, *Adv. Energy Mater.* **2012**, *2*, 1013–1021.
- [293] Y.-C. Liu, J. A. Koza, J. A. Switzer, *Electrochim. Acta* **2014**, *140*, 359–365.
- [294] Q. He, H. Xie, Z. ur Rehman, C. Wang, P. Wan, H. Jiang, W. Chu, L. Song, *ACS Energy Lett.* **2018**, *3*, 861–868.
- [295] M. Zhang, S. Ci, H. Li, P. Cai, H. Xu, Z. Wen, *Int. J. Hydrogen Energy* **2017**, *42*, 29080–29090.
- [296] N. K. Chaudhari, H. Jin, B. Kim, K. Lee, *Nanoscale* **2017**, *9*, 12231–12247.
- [297] J. N. Hausmann, E. M. Heppke, R. Beltrán-Suito, J. Schmidt, M. Mühlbauer, M. Lerch, P. W. Menezes, M. Driess, *ChemCatChem* **2020**, *12*, 1–9.
- [298] C. Du, M. Shang, J. Mao, W. Song, *J. Mater. Chem. A* **2017**, *5*, 15940–15949.
- [299] J. S. Lee, G. S. Park, H. Il Lee, S. T. Kim, R. Cao, M. Liu, J. Cho, *Nano Lett.* **2011**, *11*, 5362–5366.
- [300] C. Zhang, S. Trudel, C. P. Berlinguette, *Eur. J. Inorg. Chem.* **2014**, *2014*, 660–664.
- [301] R. D. L. Smith, M. S. Prevot, R. D. Fagan, Z. Zhang, P. A. Sedach, M. K. J. Siu, S. Trudel, C. P. Berlinguette, *Science* **2013**, *340*, 60–63.
- [302] Y. Zhang, L. L. Gao, E. J. M. E. J. M. M. Hensen, J. P. J. P. Hofmann, *ACS Energy Lett.* **2018**, *3*, 1360–1365.
- [303] Z. Wu, Q. Gan, X. Li, Y. Zhong, H. Wang, *J. Phys. Chem. C* **2018**, *122*, 2848–2853.
- [304] B. R. Wygant, K. Kawashima, C. B. Mullins, *ACS Energy Lett.* **2018**, *3*, 2956–2966.
- [305] R. Gresch, W. Müller-Warmuth, H. Dutz, *J. Non. Cryst. Solids* **1979**, *34*, 127–136.
- [306] J. Yang, H. Liu, W. N. Martens, R. L. Frost, *J. Phys. Chem. C* **2010**, *114*, 111–119.
- [307] J.-K. Chang, C.-M. Wu, I.-W. Sun, *J. Mater. Chem.* **2010**, *20*, 3729–3735.
- [308] M. Risch, V. Khare, I. Zaharleva, L. Gerencser, P. Chernev, H. Dau, *J. Am. Chem. Soc.* **2009**, *131*, 6936–6937.
- [309] A. Bergmann, T. E. Jones, E. Martinez Moreno, D. Teschner, P. Chernev, M. Gliech, T. Reier, H. Dau, P. Strasser, *Nat. Catal.* **2018**, *1*, 711–719.
- [310] D. Friebel, M. W. Louie, M. Bajdich, K. E. Sanwald, Y. Cai, A. M. Wise, M. J. Cheng, D. Sokaras, T. C. Weng, R. Alonso-Mori, R. C. Davis, J. R. Bargar, J. K. Nørskov, A. Nilsson, A. T. Bell, *J. Am. Chem. Soc.* **2015**, *137*, 1305–1313.
- [311] M. Risch, K. Klingan, J. Heidkamp, D. Ehrenberg, P. Chernev, I. Zaharieva, H. Dau, *Chem. Commun.* **2011**, *47*, 11912–11914.
- [312] M. Risch, F. Ringleb, M. Kohlhoff, P. Bogdanoff, P. Chernev, I. Zaharieva, H. Dau, *Energy Environ. Sci.* **2015**, *8*, 661–674.
- [313] M. Bajdich, M. García-Mota, A. Vojvodic, J. K. Nørskov, A. T. Bell, *J. Am. Chem. Soc.* **2013**, *135*, 13521–13530.
- [314] Y. Tong, Y. Guo, P. Chen, H. Liu, M. Zhang, L. Zhang, W. Yan, W. Chu, C. Wu, Y. Xie, *Chem* **2017**, *3*, 812–821.
- [315] J. Wang, J. Liu, B. Zhang, F. Cheng, Y. Ruan, X. Ji, K. Xu, C. Chen, L. Miao, J. Jiang, *Nano Energy* **2018**, *53*, 144–151.
- [316] P. Xiao, M. A. Sk. L. Thia, X. Ge, R. J. Lim, J.-Y. Wang, K. H. Lim, X. Wang, *Energy Environ. Sci.* **2014**, *7*, 2624–2629.
- [317] J. Li, J. Li, X. Zhou, Z. Xia, W. Gao, Y. Ma, Y. Qu, *ACS Appl. Mater. Interfaces* **2016**, *8*, 10826–10834.

- [318] R. Li, Q. Guan, R. Wei, S. Yang, Z. Shu, Y. Dong, J. Chen, W. Li, *J. Phys. Chem. C* **2015**, *119*, 2557–2565.
- [319] P. Liu, J. A. Rodriguez, *J. Am. Chem. Soc.* **2005**, *127*, 14871–14878.
- [320] H. Li, Q. Li, P. Wen, T. B. Williams, S. Adhikari, C. Dun, C. Lu, D. Itanze, L. Jiang, D. L. Carroll, G. L. Donati, P. M. Lundin, Y. Qiu, S. M. Geyer, *Adv. Mater.* **2018**, *30*, 1–8.
- [321] L. Chen, Y. Zhang, H. Wang, Y. Wang, D. Li, C. Duan, *Nanoscale* **2018**, *10*, 21019–21024.
- [322] Y. Kamihara, H. Hiramatsu, M. Hirano, R. Kawamura, H. Yanagi, T. Kamiya, H. Hosono, *J. Am. Chem. Soc.* **2006**, *128*, 10012–10013.
- [323] Q. Si, *Nat. Phys.* **2009**, *5*, 629–630.
- [324] P. Desai, K. Song, J. Koza, A. Pariti, M. Nath, *Chem. Mater.* **2013**, *25*, 1510–1518.
- [325] M. Yuzuri, R. Tahara, Y. Nakamura, *J. Phys. Soc. Japan* **1980**, *48*, 1937–1941.
- [326] B. Saparov, J. E. Mitchell, A. S. Sefat, *Supercond. Sci. Technol.* **2012**, *25*, 084016.
- [327] J. Lu, Y. Xie, X. Jiang, W. He, G. Du, *J. Mater. Chem.* **2001**, *11*, 3281–3284.
- [328] Y. A. Bioud, A. Boucherif, A. Belarouci, E. Paradis, D. Drouin, R. Arès, *Nanoscale Res. Lett.* **2016**, *11*, 446.
- [329] P. Reiss, M. Carrière, C. Lincheneau, L. Vaure, S. Tamang, *Chem. Rev.* **2016**, *116*, 10731–10819.
- [330] P. Desai, N. Ashokaan, J. Masud, A. Pariti, M. Nath, *Mater. Res. Express* **2015**, *2*, 036102.
- [331] C. Autieri, C. Noce, *Philos. Mag.* **2017**, *97*, 3276–3295.
- [332] E. E. Rodriguez, C. Stock, K. L. Krycka, C. F. Majkrzak, P. Zajdel, K. Kirshenbaum, N. P. Butch, S. R. Saha, J. Paglione, M. A. Green, *Phys. Rev. B* **2011**, *83*, 134438.
- [333] A. Weisbach, *Jahrb. f. Mineral.* **1873**, 64.
- [334] F. Sandberger, *Jahrb. f. Mineral.* **1874**, 82.
- [335] F. W. Starke, H. L. Shock, F. Edgar, Smith, *J. Am. Chem. Soc.* **1897**, *19*, 948–952.
- [336] S. Hilpert, T. Dieckmann, *Berichte der Dtsch. Chem. Gesellschaft* **1911**, *44*, 2378–2385.
- [337] A. Brukl, *Zeitschrift für Anorg. und Allg. Chemie* **1923**, *131*, 236–246.
- [338] E. Vigoroux, *Chim. Ind.* **1925**, 283.
- [339] H. Okamoto, *J. Phase Equilibria* **1991**, *12*, 457–461.
- [340] H. Holseth, A. Kjekshus, A. F. Andresen, W. B. Pearson, *Acta Chem. Scand.* **1968**, *22*, 3284–3292.
- [341] A. Kjekshus, T. Rakke, A. F. Andresen, J. T. Southern, *Acta Chem. Scand.* **1974**, *28a*, 996–1000.
- [342] A. K. L. Fan, G. H. Rosenthal, H. L. McKinzie, A. Wold, *J. Solid State Chem.* **1972**, *5*, 136–143.
- [343] G. Dai, C. Zhang, S. Zhang, X. He, C. Ren, J. Zhao, X. Li, X. Wang, C. Jin, *Crystals* **2020**, *10*, 1–7.
- [344] S. Maaref, R. Madar, P. Chaudouet, R. Fruchart, J. P. Sénateur, M. T. Averbuch-Pouchot, M. Bacmann, A. Durif, P. Wolfers, *Mater. Res. Bull.* **1983**, *18*, 473–480.
- [345] J. Chen, H. Zhao, N. Chen, X. Wang, J. Wang, R. Zhang, C. Jin, *J. Power Sources* **2011**, *200*, 98–101.
- [346] J. H. Chen, K. H. Whitmire, *Coord. Chem. Rev.* **2018**, *355*, 271–327.
- [347] J. Wang, P. Yox, K. Kovnir, *Front. Chem.* **2020**, *8*, 186.
- [348] F. R. Klingen, A. Miehr, R. A. Fischer, W. A. Herrmann, *Appl. Phys. Lett.* **1995**, *67*, 822.
- [349] S. Wei, J. Lu, W. Yu, H. Zhang, Y. Qian, *Inorg. Chem.* **2005**, *44*, 3844–3849.
- [350] J. C. Fitzmaurice, I. P. Parkin, A. T. Rowley, *J. Mater. Chem.* **1994**, *4*, 285–289.
- [351] C. J. Carmalt, D. E. Morrison, I. P. Parkin, *Polyhedron* **2000**, *19*, 829–833.
- [352] X. M. Zhang, C. Wang, X. F. Qian, Y. Xie, Y. T. Qian, *J. Solid State Chem.* **1999**, *144*, 237–239.
- [353] A. Hinz, J. M. Goicoechea, *Angew. Chemie Int. Ed.* **2016**, *55*, 8536–8541.
- [354] S. Yao, Y. Grossheim, A. Kostenko, E. Ballester-Martínez, S. Schutte, M. Bispinghoff, H. Grützmacher, M. Driess, *Angew. Chemie Int. Ed.* **2017**, *56*, 7465–7469.
- [355] E. Ballester-Martínez, T. J. Hadlington, T. Szilvási, S. Yao, M. Driess, *Chem. Commun.* **2018**, *54*, 6124–6127.
- [356] G. Hierlmeier, A. Hinz, R. Wolf, J. M. Goicoechea, *Angew. Chemie Int. Ed.* **2018**, *57*, 431–436.
- [357] O. J. Scherer, *Acc. Chem. Res.* **1999**, *32*, 751–762.
- [358] K. Selte, A. Kjekshus, A. F. Andresen, M. J. Tricker, S. Svensson, *Acta Chem. Scand.* **1972**, *26*, 3101–3113.
- [359] K. Selte, A. Kjekshus, J. Sletten, L. Torbjörnsson, P.-E. Werner, U. Junggren, B. Lamm, B. Samuelsson, *Acta Chem. Scand.* **1969**, *23*, 2047–2054.
- [360] K. Selte, A. Kjekshus, C. Hyatt, G. D. Stucky, B. Lüning, C.-G. Swahn, *Acta Chem. Scand.* **1973**, *27*, 1448–1449.
- [361] A. P. Litvinchuk, V. G. Hadjiev, M. N. Iliev, B. Lv, A. M. Guloy, C. W. Chu, *Phys. Rev. B - Condens. Matter Mater. Phys.* **2008**, *78*, 4–7.

- [362] S. C. Zhao, D. Hou, Y. Wu, T. L. Xia, A. M. Zhang, G. F. Chen, J. L. Luo, N. L. Wang, J. H. Wei, Z. Y. Lu, *Supercond. Sci. Technol.* **2009**, *22*, 015017.
- [363] H. Li, Q. Zhang, C. C. R. Yap, B. K. Tay, T. H. T. Edwin, A. Olivier, D. Baillargeat, *Adv. Funct. Mater.* **2012**, *22*, 1385–1390.
- [364] A. P. Grosvenor, B. A. Kobe, M. C. Biesinger, N. S. McIntyre, *Surf. Interface Anal.* **2004**, *36*, 1564–1574.
- [365] B. J. Tan, K. J. Klabunde, P. M. A. Sherwood, *Chem. Mater.* **1990**, *2*, 186–191.
- [366] N. S. McIntyre, D. G. Zetaruk, *Anal. Chem.* **1977**, *49*, 1521–1529.
- [367] J. M. Epp, J. G. Dillard, *Chem. Mater.* **1989**, *1*, 325–330.
- [368] D. E. King, J. E. Fernandez, W. E. Swartz, *Appl. Surf. Sci.* **1990**, *45*, 325–339.
- [369] G. L. Elizarova, G. M. Zhidomirov, V. N. Parmon, *Catal. Today* **2000**, *58*, 71–88.
- [370] C. Huang, Y. Zou, Y. Q. Ye, T. Ouyang, K. Xiao, Z. Q. Liu, *Chem. Commun.* **2019**, *55*, 7687–7690.
- [371] H. Jiang, Q. He, X. Li, X. Su, Y. Zhang, S. Chen, S. Zhang, G. Zhang, J. Jiang, Y. Luo, P. M. Ajayan, L. Song, *Adv. Mater.* **2019**, *31*, 1–8.
- [372] R. L. Doyle, M. E. G. Lyons, *Phys. Chem. Chem. Phys.* **2013**, *15*, 5224–5237.
- [373] S. Anantharaj, S. Noda, *ChemElectroChem* **2020**, *7*, 2297–2308.
- [374] Q. Kang, L. Vernisse, R. C. Remsing, A. C. Thenuwara, S. L. Shumlas, I. G. McKendry, M. L. Klein, E. Borguet, M. J. Zdilla, D. R. Strongin, *J. Am. Chem. Soc.* **2017**, *139*, 1863–1870.
- [375] S. Anantharaj, S. Kundu, S. Noda, *J. Mater. Chem. A* **2020**, *8*, 4174–4192.
- [376] M. B. Stevens, L. J. Enman, A. S. Batchellor, M. R. Cosby, A. E. Vise, C. D. M. Trang, S. W. Boettcher, *Chem. Mater.* **2017**, *29*, 120–140.
- [377] M. Görlin, P. Chernev, J. F. De Araújo, T. Reier, S. Dresp, B. Paul, R. Krähnert, H. Dau, P. Strasser, *J. Am. Chem. Soc.* **2016**, *138*, 5603–5614.
- [378] M. Gorlin, J. F. De Araujo, H. Schmies, D. Bernsmeier, S. Dresp, M. Gliech, Z. Jusys, P. Chernev, R. Kraehnert, H. Dau, P. Strasser, *J. Am. Chem. Soc.* **2017**, *139*, 2070–2082.
- [379] H. Sun, Z. Ma, Y. Qiu, H. Liu, G. Gao, *Small* **2018**, *14*, 1800294.
- [380] M. S. Wu, C. Y. Jao, F. Y. Chuang, F. Y. Chen, *Electrochim. Acta* **2017**, *227*, 210–216.
- [381] P. W. Menezes, S. Yao, R. Beltrán-Suito, J. N. Hausmann, P. V. Menezes, M. Driess, *Angew. Chemie Int. Ed.* **2021**, *60*, 4640–4647.
- [382] W. H. Baur, *Acta Crystallogr.* **1956**, *9*, 515–520.
- [383] A. J. Esswein, Y. Surendranath, S. Y. Reece, D. G. Nocera, *Energy Environ. Sci.* **2011**, *4*, 499–504.
- [384] P. H. Masscheleyn, R. D. Delaune, W. H. Patrick, *Environ. Sci. Technol.* **1991**, *25*, 1414–1419.
- [385] J. C. Ng, J. Wang, A. Shraim, *Chemosphere* **2003**, *52*, 1353–1359.
- [386] L. J. Gao, B. E. Conway, *J. Electroanal. Chem.* **1995**, *395*, 261–271.
- [387] W. Chen, H. Wang, Y. Li, Y. Liu, J. Sun, S. Lee, J. S. Lee, Y. Cui, *ACS Cent. Sci.* **2015**, *1*, 244–251.
- [388] H. Cao, H. Shan, H. Ruan, G. Zheng, *Electrochem. commun.* **2012**, *23*, 44–47.
- [389] L. E. Verduzco, J. Oliva, A. I. Oliva, E. Macias, C. R. Garcia, M. Herrera-Trejo, N. Pariona, A. I. Mtz-Enriquez, *Mater. Chem. Phys.* **2019**, *229*, 197–209.
- [390] R. Santoyo-Cisneros, J. R. Rangel-Mendez, J. L. Nava, E. R. Larios-Durán, L. F. Chazaro-Ruiz, *J. Hazard. Mater.* **2020**, *392*, 122349.
- [391] E. Morallón, J. Arias-Pardilla, J. M. Calo, D. Cazorla-Amorós, *Electrochim. Acta* **2009**, *54*, 3996–4004.
- [392] D. E. Janney, J. M. Cowley, P. R. Buseck, *Clays Clay Miner.* **2000**, *48*, 111–119.
- [393] F. M. Michel, L. Ehm, S. M. Antao, P. L. Lee, P. J. Chupas, G. Liu, D. R. Strongin, M. A. A. Schoonen, B. L. Phillips, J. B. Parise, *Science* **2007**, *316*, 1726–1729.
- [394] J. L. Jambor, J. E. Dutrizac, *Chem. Rev.* **1998**, *98*, 2549–2586.
- [395] H. Bandal, K. K. Reddy, A. Chaugule, H. Kim, *J. Power Sources* **2018**, *395*, 106–127.
- [396] S. Das, M. Jim Hendry, J. Essilfie-Dughan, *Appl. Geochemistry* **2013**, *28*, 185–193.
- [397] K. Rout, M. Mohapatra, S. Anand, *Dalt. Trans.* **2012**, *41*, 3302–3312.
- [398] Z. Li, T. Zhang, K. Li, *Dalt. Trans.* **2011**, *40*, 2062–2066.
- [399] M. . Seehra, P. Roy, A. Raman, A. Manivannan, *Solid State Commun.* **2004**, *130*, 597–601.
- [400] L. Mei, L. Liao, Z. Wang, C. Xu, *Adv. Mater. Sci. Eng.* **2015**, *2015*, 1–10.
- [401] L. Mazzetti, P. J. Thistlethwaite, *J. Raman Spectrosc.* **2002**, *33*, 104–111.
- [402] H. Tüysüz, E. L. Salabaş, C. Weidenthaler, F. Schüth, *J. Am. Chem. Soc.* **2008**, *130*, 280–287.
- [403] M. Hanesch, *Geophys. J. Int.* **2009**, *177*, 941–948.
- [404] D. L. A. de Faria, S. Venâncio Silva, M. T. de Oliveira, *J. Raman Spectrosc.* **1997**, *28*, 873–878.
- [405] W. E. Morgan, J. R. Van Wazer, *J. Phys. Chem.* **1973**, *77*, 964–969.

- [406] I. Banerjee, Y. B. Kholam, C. Balasubramanian, R. Pasricha, P. P. Bakare, K. R. Patil, A. K. Das, S. V. Bhoraskar, *Ser. Mater.* **2006**, *54*, 1235–1240.
- [407] S. M. Bak, K. W. Nam, C. W. Lee, K. H. Kim, H. C. Jung, X. Q. Yang, K. B. Kim, *J. Mater. Chem.* **2011**, *21*, 17309–17315.
- [408] R. K. Kukkadapu, J. M. Zachara, J. K. Fredrickson, S. C. Smith, A. C. Dohnalkova, C. K. Russell, *Am. Mineral.* **2003**, *88*, 1903–1914.
- [409] X. Wang, M. Zhu, L. K. Koopal, W. Li, W. Xu, F. Liu, J. Zhang, Q. Liu, X. Feng, D. L. Sparks, *Environ. Sci. Nano* **2016**, *3*, 190–202.
- [410] A. Manceau, V. A. Drits, *Clay Miner.* **1993**, *28*, 165–184.
- [411] F. Maillot, G. Morin, Y. Wang, D. Bonnin, P. Ildefonse, C. Chaneac, G. Calas, *Geochim. Cosmochim. Acta* **2011**, *75*, 2708–2720.
- [412] L. Yang, C. I. Steefel, M. A. Marcus, J. R. Bargar, *Environ. Sci. Technol.* **2010**, *44*, 5469–5475.
- [413] S. Lan, X. Wang, Q. Xiang, H. Yin, W. Tan, G. Qiu, F. Liu, J. Zhang, X. Feng, *Geochim. Cosmochim. Acta* **2017**, *211*, 79–96.
- [414] S. Kato, K. Hashimoto, K. Watanabe, *Environ. Microbiol.* **2012**, *14*, 1646–1654.
- [415] L. Lei, D. Huang, C. Zhou, S. Chen, X. Yan, Z. Li, W. Wang, *Coord. Chem. Rev.* **2020**, *408*, 213177.
- [416] L. Zhuang, L. Ge, Y. Yang, M. Li, Y. Jia, X. Yao, Z. Zhu, *Adv. Mater.* **2017**, *29*, 1606793.
- [417] Z. Xiao, Y. Wang, Y. C. Huang, Z. Wei, C. L. Dong, J. Ma, S. Shen, Y. Li, S. Wang, *Energy Environ. Sci.* **2017**, *10*, 2563–2569.
- [418] B. Zhang, L. Wang, Y. Zhang, Y. Ding, Y. Bi, *Angew. Chemie Int. Ed.* **2018**, *57*, 2248–2252.
- [419] J. Hu, S. Li, J. Chu, S. Niu, J. Wang, Y. Du, Z. Li, X. Han, P. Xu, *ACS Catal.* **2019**, 10705–10711.
- [420] M. Lee, H. S. Oh, M. K. Cho, J. P. Ahn, Y. J. Hwang, B. K. Min, *Appl. Catal. B Environ.* **2018**, *233*, 130–135.
- [421] Y. Yang, H. Fei, G. Ruan, C. Xiang, J. M. Tour, *ACS Nano* **2014**, *8*, 9518–9523.
- [422] J. N. Hausmann, S. Mebs, K. Laun, I. Zebger, H. Dau, P. W. Menezes, M. Driess, *Energy Environ. Sci.* **2020**, *13*, 3607–3619.
- [423] D. Khalafallah, M. Zhi, Z. Hong, *Top. Curr. Chem.* **2019**, *377*, 29.
- [424] A. Han, H. Chen, Z. Sun, J. Xu, P. Du, *Chem. Commun.* **2015**, *51*, 11626–11629.
- [425] L. Wei, K. Goh, Ö. Birer, H. E. Karahan, J. Chang, S. Zhai, X. Chen, Y. Chen, *Nanoscale* **2017**, *9*, 4401–4408.
- [426] Y. Xu, S. Duan, H. Li, M. Yang, S. Wang, X. Wang, R. Wang, *Nano Res.* **2017**, *10*, 3103–3112.
- [427] P. Wilde, S. Dieckhöfer, T. Quast, W. Xiang, A. Bhatt, Y.-T. Chen, S. Seisel, S. Barwe, C. Andronescu, T. Li, W. Schuhmann, J. Masa, *ACS Appl. Energy Mater.* **2020**, *3*, 2304–2309.
- [428] P. Li, R. Chen, S. Tian, Y. Xiong, *ACS Sustain. Chem. Eng.* **2019**, *7*, 9566–9573.
- [429] Y. Bai, H. Zhang, L. Fang, L. Liu, H. Qiu, Y. Wang, *J. Mater. Chem. A* **2015**, *3*, 5434–5441.
- [430] Z. Zhang, S. Liu, J. Xiao, S. Wang, *J. Mater. Chem. A* **2016**, *4*, 9691–9699.
- [431] R. K. Shervedani, *J. Electrochem. Soc.* **1997**, *144*, 511.
- [432] F. Hu, S. Zhu, S. Chen, Y. Li, L. Ma, T. Wu, Y. Zhang, C. Wang, C. Liu, X. Yang, L. Song, X. Yang, Y. Xiong, *Adv. Mater.* **2017**, *29*, 1606570.
- [433] R. Beltrán-Suito, V. Forstner, J. N. Hausmann, S. Mebs, J. Schmidt, I. Zaharieva, K. Laun, I. Zebger, H. Dau, P. W. Menezes, M. Driess, *Chem. Sci.* **2020**, *11*, 11834–11842.
- [434] O. A. Derby, *Am. J. Sci.* **1895**, *s3-49*, 101–110.
- [435] J. Maronnean, *C. R. Hebd. Seances Acad. Sci.* **1900**, *130*, 657.
- [436] P. Jolibois, *C. R. Hebd. Seances Acad. Sci.* **1910**, *150*, 106–108.
- [437] H. Okamoto, *J. Phase Equilibria Diffus.* **2010**, *31*, 200–201.
- [438] E. Fleet, *Am. Mineral.* **1973**, *58*, 203–210.
- [439] E. Vigoroux, *Compt. rend.* **1909**, *147*, 426.
- [440] M. Singleton, P. Nash, *J. Phase Equilibria* **1987**, *8*, 419–422.
- [441] J. C. Fitzmaurice, A. Hector, I. P. Parkin, *J. Mater. Sci. Lett.* **1994**, *13*, 1–2.
- [442] Z. Wang, S. Wang, L. Ma, Y. Guo, J. Sun, N. Zhang, R. Jiang, *Small* **2021**, *2006770*, 1–9.
- [443] D. Wang, L. Bin Kong, M. C. Liu, W. Bin Zhang, Y. C. Luo, L. Kang, *J. Power Sources* **2015**, *274*, 1107–1113.
- [444] C. Tang, A. M. Asiri, Y. Luo, X. Sun, *ChemNanoMat* **2015**, *1*, 558–561.
- [445] R. Prins, M. E. Bussell, *Catal. Letters* **2012**, *142*, 1413–1436.
- [446] J. Gopalakrishnan, R. Mani, *J. Chem. Sci.* **2009**, *121*, 235–256.
- [447] M. M. Johnson, G. P. Nowack, D. C. Tabler, *J. Catal.* **1972**, *27*, 397–404.
- [448] G. A. Shaw, I. P. Parkin, *Inorg. Chem.* **2001**, *40*, 6940–6947.
- [449] I. P. Parkin, *Chem. Soc. Rev.* **1996**, *25*, 199–207.

- [450] K. Mandel, F. Dillon, A. A. Koos, Z. Aslam, K. Jurkschat, F. Cullen, A. Crossley, H. Bishop, K. Moh, C. Cavalius, E. Arzt, N. Grobert, *Chem. Commun.* **2011**, 47, 4108–4110.
- [451] Z. Yao, G. Wang, Y. Shi, Y. Zhao, J. Jiang, Y. Zhang, H. Wang, *Dalt. Trans.* **2015**, 44, 14122–14129.
- [452] L. Liu, D. A. Ruiz, F. Dahcheh, G. Bertrand, R. Suter, A. M. Tondreau, H. Grützmacher, *Chem. Sci.* **2016**, 7, 2335.
- [453] F. F. Puschmann, D. Stein, D. Heift, C. Hendriksen, Z. A. Gal, H.-F. Grützmacher, H. Grützmacher, *Angew. Chemie Int. Ed.* **2011**, 50, 8420–8423.
- [454] X. Liu, L. Xu, B. Zhang, *J. Solid State Chem.* **2014**, 212, 13–22.
- [455] B. Ma, X. Duan, W. Han, X. Fan, Y. Li, F. Zhang, G. Zhang, W. Peng, *J. Colloid Interface Sci.* **2020**, 567, 393–401.
- [456] L. Yan, H. Jiang, Y. Xing, Y. Wang, D. Liu, X. Gu, P. Dai, L. Li, X. Zhao, *J. Mater. Chem. A* **2018**, 6, 1682–1691.
- [457] A. Roguska, M. Pisarek, M. Andrzejczuk, M. Dolata, M. Lewandowska, M. Janik-Czachor, *Mater. Sci. Eng. C* **2011**, 31, 906–914.
- [458] V. Tallapally, D. Damma, S. R. Darmakkolla, *Chem. Commun.* **2019**, 55, 1560–1563.
- [459] V. Manorama, P. M. Dighe, S. V. Bhoraskar, V. J. Rao, P. Singh, A. A. Belhekar, *J. Appl. Phys.* **1990**, 68, 581–585.
- [460] K. Konya, K. Nakamoto, *Spectrochim. Acta Part A Mol. Spectrosc.* **1973**, 29, 1965–1973.
- [461] P. J. D. Park, P. J. Hendra, *Spectrochim. Acta Part A Mol. Spectrosc.* **1969**, 25, 909–916.
- [462] G. E. Coates, C. Parkin, *J. Chem. Soc.* **1963**, 421–429.
- [463] H.-W. Man, C.-S. Tsang, M. M.-J. Li, J. Mo, B. Huang, L. Y. S. Lee, Y. Leung, K.-Y. Wong, S. C. E. Tsang, *Chem. Commun.* **2018**, 54, 8630–8633.
- [464] Z. Huang, Z. Chen, Z. Chen, C. Lv, H. Meng, C. Zhang, *ACS Nano* **2014**, 8, 8121–8129.
- [465] C. H. Wang, G. Doornbos, G. Astromskas, G. Vellianitis, R. Oxland, M. C. Holland, M. L. Huang, C. H. Lin, C. H. Hsieh, Y. S. Chang, T. L. Lee, Y. Y. Chen, P. Ramvall, E. Lind, W. C. Hsu, L.-E. Wernersson, R. Droopad, M. Passlack, C. H. Diaz, *AIP Adv.* **2014**, 4, 047108.
- [466] A. Sivanantham, P. Ganesan, S. Shanmugam, *Adv. Funct. Mater.* **2016**, 26, 4661–4672.
- [467] S. Jung, C. C. L. L. McCrory, I. M. Ferrer, J. C. Peters, T. F. Jaramillo, *J. Mater. Chem. A* **2016**, 4, 3068–3076.
- [468] M. Wang, X. Wang, S. Feng, D. He, P. Jiang, *Nanotechnology* **2020**, 31, 455503.
- [469] A. A. Lobinsky, V. P. Tolstoy, I. A. Kodinzev, *Nanosyst. Physics, Chem. Math.* **2018**, 9, 669–675.
- [470] R. L. Doyle, I. J. Godwin, M. P. Brandon, M. E. G. Lyons, *Phys. Chem. Chem. Phys.* **2013**, 15, 13737–13783.
- [471] B. Mavis, M. Akinc, *Chem. Mater.* **2006**, 18, 5317–5325.
- [472] J. L. Bantignies, S. Deabate, A. Righi, S. Rols, P. Hermet, J. L. Sauvajol, F. Henn, *J. Phys. Chem. C* **2008**, 112, 2193–2201.
- [473] A. C. Garcia, T. Touzalin, C. Nieuwland, N. Perini, M. T. M. Koper, *Angew. Chemie Int. Ed.* **2019**, 58, 12999–13003.
- [474] O. Diaz-Morales, D. Ferrus-Suspedra, M. T. M. Koper, *Chem. Sci.* **2016**, 7, 2639–2645.
- [475] K. M. Cole, D. W. Kirk, S. J. Thorpe, *J. Electrochem. Soc.* **2018**, 165, J3122–J3129.
- [476] S. Lee, L. Bai, X. Hu, *Angew. Chemie Int. Ed.* **2020**, 59, 8072–8077.
- [477] J. Heinze, *Angew. Chemie Int. Ed. English* **1984**, 23, 831–847.
- [478] P. W. Menezes, A. Indra, V. Gutkin, M. Driess, *Chem. Commun.* **2017**, 53, 8018–8021.
- [479] E. L. Ratcliff, J. Meyer, K. X. Steirer, A. Garcia, J. J. Berry, D. S. Ginley, D. C. Olson, A. Kahn, N. R. Armstrong, *Chem. Mater.* **2011**, 23, 4988–5000.
- [480] Y. M. Shul'ga, A. V. Bulatov, R. A. T. Gould, W. V. Konze, L. H. Pignolet, *Inorg. Chem.* **1992**, 31, 4704–4706.
- [481] R. Zhang, Y. C. Zhang, L. Pan, G. Q. Shen, N. Mahmood, Y. H. Ma, Y. Shi, W. Jia, L. Wang, X. Zhang, W. Xu, J. Zou, *ACS Catal.* **2018**, 8, 3803–3811.
- [482] P. V. Kamath, G. N. Subbanna, *J. Appl. Electrochem.* **1992**, 22, 478–482.
- [483] M. Rajamathi, P. V. Kamath, R. Seshadri, *J. Mater. Chem.* **2000**, 10, 503–506.
- [484] S. Jahangiri, N. J. Mosey, *Phys. Chem. Chem. Phys.* **2018**, 20, 11444–11453.
- [485] D. K. Bediako, B. Lassalle-Kaiser, Y. Surendranath, J. Yano, V. K. Yachandra, D. G. Nocera, *J. Am. Chem. Soc.* **2012**, 134, 6801–6809.
- [486] H. Bartl, H. Bode, G. Sterr, J. Witte, *Electrochim. Acta* **1971**, 16, 615–621.
- [487] X. Yang, K. Takada, M. Itose, Y. Ebina, R. Ma, K. Fukuda, T. Sasaki, *Chem. Mater.* **2008**, 20, 479–485.

- [488] D. S. Hall, D. J. Lockwood, C. Bock, B. R. MacDougall, *Proc. R. Soc. A Math. Phys. Eng. Sci.* **2015**, *471*, 20140792.
- [489] Z. Yan, H. Sun, X. Chen, H. Liu, Y. Zhao, H. Li, W. Xie, F. Cheng, J. Chen, *Nat. Commun.* **2018**, *9*, 1–9.
- [490] C. W. Hu, Y. Yamada, K. Yoshimura, *J. Mater. Chem. C* **2016**, *4*, 5390–5397.
- [491] B. M. Hunter, W. Hieringer, J. R. Winkler, H. B. Gray, A. M. Müller, *Energy Environ. Sci.* **2016**, *9*, 1734–1743.
- [492] J. M. P. Martinez, E. A. Carter, *J. Am. Chem. Soc.* **2019**, *141*, 693–705.
- [493] T. Takashima, K. Hashimoto, R. Nakamura, *J. Am. Chem. Soc.* **2012**, *134*, 1519–1527.
- [494] Y. Surendranath, M. W. Kanan, D. G. Nocera, *J. Am. Chem. Soc.* **2010**, *132*, 16501–16509.
- [495] J. Masa, C. Andronescu, H. Antoni, I. Sinev, S. Seisel, K. Elumeeva, S. Barwe, S. Marti-Sanchez, J. Arbiol, B. Roldan Cuenya, M. Muhler, W. Schuhmann, *ChemElectroChem* **2019**, *6*, 235–240.
- [496] Y. Zhan, M. Lu, S. Yang, Z. Liu, J. Y. Lee, *ChemElectroChem* **2016**, *3*, 615–621.
- [497] D. B. G. Williams, M. Lawton, *J. Org. Chem.* **2010**, *75*, 8351–8354.
- [498] R. J. Kern, *J. Inorg. Nucl. Chem.* **1962**, *24*, 1105–1109.
- [499] J. M. Smith, R. J. Lachicotte, P. L. Holland, *Organometallics* **2002**, *21*, 4808–4814.
- [500] J. M. Smith, R. J. Lachicotte, P. L. Holland, *Chem. Commun.* **2001**, *1998*, 1542–1543.
- [501] P. H. M. Budzelaar, A. B. van Oort, A. G. Orpen, *Eur. J. Inorg. Chem.* **1998**, *1998*, 1485–1494.
- [502] C. Schwarzmaier, S. Heinl, G. Balázs, M. Scheer, *Angew. Chemie Int. Ed.* **2015**, *54*, 13116–13121.
- [503] C. von Hänisch, D. Fenske, *Zeitschrift für Anorg. und Allg. Chemie* **1998**, *624*, 367–369.
- [504] L. T. J. Delbaere, L. J. Kruczynski, D. W. McBride, *J. Chem. Soc., Dalton Trans.* **1973**, 307–310.
- [505] O. J. Scherer, M. Ehses, G. Wolmershäuser, *Angew. Chemie Int. Ed.* **1998**, *37*, 507–510.
- [506] A. S. Foust, M. S. Foster, L. F. Dahl, *J. Am. Chem. Soc.* **1969**, *91*, 5633–5635.
- [507] W. A. Herrmann, B. Koumbouris, T. Zahn, M. L. Ziegler, *Angew. Chemie Int. Ed.* **1984**, *23*, 812–814.
- [508] O. J. Scherer, *Angew. Chemie Int. Ed.* **1990**, *29*, 1104–1122.
- [509] A. J. Dimaino, A. L. Rheingold, *Chem. Rev.* **1990**, *90*, 169–190.
- [510] J. M. Smith, R. J. Lachicotte, P. L. Holland, *J. Am. Chem. Soc.* **2003**, *125*, 15752–15753.
- [511] H. Andres, E. L. Bominaar, J. M. Smith, N. A. Eckert, P. L. Holland, E. Münck, *J. Am. Chem. Soc.* **2002**, *124*, 3012–3025.
- [512] J. Vela, J. M. Smith, Y. Yu, N. A. Ketterer, C. J. Flaschenriem, R. J. Lachicotte, P. L. Holland, *J. Am. Chem. Soc.* **2005**, *127*, 7857–7870.
- [513] F. Gilbert, P. Refait, F. Lévêque, C. Remazeilles, E. Conforto, *J. Phys. Chem. Solids* **2008**, *69*, 2124–2130.
- [514] N. Koura, T. Tsukamoto, Hiromasa Shoji, T. Hotta, *Jpn. J. Appl. Phys.* **1995**, *34*, 1643–1647.
- [515] L. Besra, M. Liu, *Prog. Mater. Sci.* **2007**, *52*, 1–61.
- [516] D. Skoog, *Principles of Instrumental Analysis*, Cengage Learning, Inc, **2017**.
- [517] P. R. Griffiths, J. a. de Haseth, *Fourier Transform Infrared Spectrometry. Second Edition*, **2007**.
- [518] N. Kuhn, T. Kratz, *Synthesis* **1993**, *1993*, 561–562.
- [519] A. M. Venezia, *Catal. Today* **2003**, *77*, 359–370.
- [520] E. E. Alp, S. M. Mini, M. Ramanathan, *X-Ray Absorption Spectroscopy: EXAFS and XANES-A Versatile Tool to Study the Atomic and Electronic Structure of Materials*, **1990**.
- [521] H. Dau, P. Liebisch, M. Haumann, *Anal. Bioanal. Chem.* **2003**, *376*, 562–583.
- [522] A. L. Ankudinov, B. Ravel, J. J. Rehr, S. D. Conradson, *Phys. Rev. B* **1998**, *58*, 7565–7576.
- [523] S. Brunauer, P. H. Emmett, E. Teller, *J. Am. Chem. Soc.* **1938**, *60*, 309–319.
- [524] R. D. Condon, *Microchem. J.* **1966**, *10*, 408–426.
- [525] M. Eichelbaum, R. Stößer, A. Karpov, C. K. Dobner, F. Rosowski, A. Trunschke, R. Schlögl, *Phys. Chem. Chem. Phys.* **2012**, *14*, 1302–1312.
- [526] E. Hering, G. Schönfelder, Eds., *Sensoren in Wissenschaft Und Technik*, Springer, Weisbaden, **2012**.
- [527] P. Atkins, *The Elements of Physical Chemistry*, Oxford University Press, Bath, **2001**.
- [528] J. V. Wiertz, M. Mateo, B. Escobar, *Hydrometallurgy* **2006**, *83*, 35–39.
- [529] J. Heinze, *Angew. Chemie* **1984**, *96*, 823–840.
- [530] D. H. Evans, K. M. O’Connell, R. A. Petersen, M. J. Kelly, *J. Chem. Educ.* **1983**, *60*, 290–293.
- [531] E. Antolini, *ACS Catal.* **2014**, *4*, 1426–1440.
- [532] D. Pletcher, R. Greff, R. Peat, L. M. Peter, J. Robinson, in *Instrum. Methods Electrochem.*, Elsevier, **2010**, pp. 251–282.
- [533] B.-Y. Chang, S.-M. Park, *Annu. Rev. Anal. Chem.* **2010**, *3*, 207–229.

- [534] L. Negahdar, F. Zeng, S. Palkovits, C. Broicher, R. Palkovits, *ChemElectroChem* **2019**, *6*, 5588–5595.
- [535] A. R. C. Bredar, A. L. Chown, A. R. Burton, B. H. Farnum, *ACS Appl. Energy Mater.* **2020**, *3*, 66–98.
- [536] G. Li, L. Anderson, Y. Chen, M. Pan, P. Y. Abel Chuang, *Sustain. Energy Fuels* **2018**, *2*, 237–251.
- [537] M. V. Abrashev, P. Chernev, P. Kubella, M. R. Mohammadi, C. Pasquini, H. Dau, I. Zaharieva, *J. Mater. Chem. A* **2019**, *7*, 17022–17036.
- [538] H. Liang, A. N. Gandi, D. H. Anjum, X. Wang, U. Schwingenschlögl, H. N. Alshareef, *Nano Lett.* **2016**, *16*, 7718–7725.
- [539] Y. Yan, B. Y. Xia, B. Zhao, X. Wang, *J. Mater. Chem. A* **2016**, *4*, 17587–17603.
- [540] A. Voegelín, S. J. Hug, *Environ. Sci. Technol.* **2003**, *37*, 972–978.
- [541] M. Pena, X. Meng, G. P. Korfiatis, C. Jing, *Environ. Sci. Technol.* **2006**, *40*, 1257–1262.
- [542] Z. Yu, J. Huang, L. Hu, W. Zhang, I. M. C. Lo, *Environ. Sci. Water Res. Technol.* **2019**, *5*, 28–38.
- [543] A. S. Sukhochev, E. V. Tomina, I. Y. Mittova, *Glas. Phys. Chem.* **2008**, *34*, 724–741.
- [544] S. C. B. Myneni, S. J. Traina, G. A. Waychunas, T. J. Logan, *Geochim. Cosmochim. Acta* **1998**, *62*, 3285–3300.
- [545] J. Xu, J. Li, D. Xiong, B. Zhang, Y. Liu, K.-H. H. Wu, I. Amorim, W. Li, L. Liu, *Chem. Sci.* **2018**, *9*, 3470–3476.
- [546] B. Qiu, A. Han, D. Jiang, T. Wang, P. Du, *ACS Sustain. Chem. Eng.* **2019**, *7*, 2360–2369.
- [547] S. V. Mohite, R. Xing, B. Li, S. S. Latthe, Y. Zhao, X. Li, L. Mao, S. Liu, *Inorg. Chem.* **2020**, *59*, 1996–2004.
- [548] Y. Xie, M. Chen, M. Cai, J. Teng, H. Huang, Y. Fan, M. Barboiu, D. Wang, C. Y. Su, *Inorg. Chem.* **2019**, *58*, 14652–14659.
- [549] K. Wu, Z. Chen, W. C. Cheong, S. Liu, W. Zhu, X. Cao, K. Sun, Y. Lin, L. Zheng, W. Yan, Y. Pan, D. Wang, Q. Peng, C. Chen, Y. Li, *ACS Appl. Mater. Interfaces* **2018**, *10*, 44201–44208.
- [550] J. Sen Li, L. X. Kong, Z. Wu, S. Zhang, X. Y. Yang, J. Q. Sha, G. D. Liu, *Carbon* **2019**, *145*, 694–700.
- [551] F. Yu, H. Zhou, Y. Huang, J. Sun, F. Qin, J. Bao, W. A. Goddard, S. Chen, Z. Ren, *Nat. Commun.* **2018**, *9*, 1–9.
- [552] Y. Pan, K. Sun, S. Liu, X. Cao, K. Wu, W. C. Cheong, Z. Chen, Y. Wang, Y. Y. Y. Li, Y. Liu, D. Wang, Q. Peng, C. Chen, Y. Li, *J. Am. Chem. Soc.* **2018**, *140*, 2610–2618.
- [553] Y. Lu, W. Hou, D. Yang, Y. Chen, *Electrochim. Acta* **2019**, *307*, 543–552.
- [554] L. Jiao, Y. X. Zhou, H. L. Jiang, *Chem. Sci.* **2016**, *7*, 1690–1695.
- [555] M. Zhai, F. Wang, H. Du, *ACS Appl. Mater. Interfaces* **2017**, *9*, 40171–40179.
- [556] H. Hu, B. Guan, B. Xia, X. W. (David) Lou, *J. Am. Chem. Soc.* **2015**, *137*, 5590–5595.
- [557] F. Song, X. Hu, *Nat. Commun.* **2014**, *5*, 4477.
- [558] M. W. Louie, A. T. Bell, *J. Am. Chem. Soc.* **2013**, *135*, 12329–12337.
- [559] B. Zhang, X. Zheng, O. Voznyy, R. Comin, M. Bajdich, M. Garcia-Melchor, L. Han, J. Xu, M. Liu, L. Zheng, F. Pelayo García de Arquer, C. Thang Dinh, F. Fan, M. Yuan, E. Yassitepe, N. Chen, T. Regier, P. Liu, Y. Li, P. De Luna, A. Janmohamed, H. L. Xin, H. Yang, A. Vojvodic, E. H. Sargent, *Science* **2016**, *352*, 333–337.
- [560] J. A. Koza, Z. He, A. S. Miller, J. A. Switzer, *Chem. Mater.* **2012**, *24*, 3567–3573.
- [561] M. Al-Mamun, X. Su, H. Zhang, H. Yin, P. Liu, H. Yang, D. Wang, Z. Tang, Y. Wang, H. Zhao, *Small* **2016**, *12*, 2866–2871.
- [562] X. Long, J. Li, S. Xiao, K. Yan, Z. Wang, H. Chen, S. Yang, *Angew. Chemie Int. Ed.* **2014**, *53*, 7584–7588.
- [563] T. Liu, Y. Liang, Q. Liu, X. Sun, Y. He, A. M. Asiri, *Electrochem. commun.* **2015**, *60*, 92–96.
- [564] C. Xia, Q. Jiang, C. Zhao, M. N. Hedhili, H. N. Alshareef, *Adv. Mater.* **2016**, *28*, 77–85.
- [565] H. Liang, F. Meng, M. Cabán-Acevedo, L. Li, A. Forticaux, L. Xiu, Z. Wang, S. Jin, *Nano Lett.* **2015**, *15*, 1421–1427.
- [566] H.-W. Liang, S. Brüller, R. Dong, J. Zhang, X. Feng, K. Müllen, *Nat. Commun.* **2015**, *6*, 7992.
- [567] R. Zhang, X. X. Wang, S. Yu, T. Wen, X. Zhu, F. Yang, X. Sun, X. X. Wang, W. Hu, *Adv. Mater.* **2017**, *29*, 1605502.
- [568] B. Liu, Y.-F. Zhao, H.-Q. Peng, Z.-Y. Zhang, C.-K. Sit, M.-F. Yuen, T.-R. Zhang, C.-S. Lee, W.-J. Zhang, *Adv. Mater.* **2017**, *29*, 1606521–1606528.
- [569] C. Y. Son, I. H. Kwak, Y. R. Lim, J. Park, *Chem. Commun.* **2016**, *52*, 2819–2822.
- [570] A. B. Laursen, K. R. Patraju, M. J. Whitaker, M. Retuerto, T. Sarkar, N. Yao, K. V. Ramanujachary, M. Greenblatt, G. C. Dismukes, *Energy Environ. Sci.* **2015**, *8*, 1027–1034.

- [571] J. Zhang, T. Wang, P. Liu, Z. Liao, S. Liu, X. Zhuang, M. Chen, E. Zschech, X. Feng, *Nat. Commun.* **2017**, *8*, 1–8.
- [572] C. G. Read, J. F. Callejas, C. F. Holder, R. E. Schaak, *ACS Appl. Mater. Interfaces* **2016**, *8*, 12798–12803.
- [573] D. Zhou, L. He, W. Zhu, X. Hou, K. Wang, G. Du, C. Zheng, X. Sun, A. M. Asiri, *J. Mater. Chem. A* **2016**, *4*, 10114–10117.
- [574] X. Lv, J. Ren, Y. Wang, Y. Liu, Z. Y. Yuan, *ACS Sustain. Chem. Eng.* **2019**, *7*, 8993–9001.
- [575] R. Zhang, P. A. Russo, M. Feist, P. Amsalem, N. Koch, N. Pinna, *ACS Appl. Mater. Interfaces* **2017**, *9*, 14013–14022.
- [576] Y. Cheng, F. Liao, W. Shen, L. Liu, B. Jiang, Y. Li, M. Shao, *Nanoscale* **2017**, *9*, 18977–18982.
- [577] E. Loni, M. H. Siadati, A. Shokuhfar, *Mater. Today Energy* **2020**, *16*, 100398.
- [578] D. Li, H. Baydoun, B. Kulikowski, S. L. Brock, *Chem. Mater.* **2017**, *29*, 3048–3054.
- [579] Y. Yan, B. Y. Xia, X. Ge, Z. Liu, A. Fisher, X. Wang, *Chem. - A Eur. J.* **2015**, *21*, 18062–18067.
- [580] Y. Zhu, W. Zhou, Y. Chen, J. Yu, X. Xu, C. Su, M. O. Tadé, Z. Shao, *Chem. Mater.* **2015**, *27*, 3048–3054.
- [581] J. Zou, G. Peleckis, C. Y. Lee, G. G. Wallace, *Chem. Commun.* **2019**, *55*, 8808–8811.
- [582] X. Zou, Y. Wu, Y. Liu, D. Liu, W. Li, L. Gu, H. Liu, P. Wang, L. Sun, Y. Zhang, *Chem* **2018**, *4*, 1139–1152.
- [583] H. Li, P. Wen, Q. Li, C. Dun, J. Xing, C. Lu, S. Adhikari, L. Jiang, D. L. Carroll, S. M. Geyer, *Adv. Energy Mater.* **2017**, *7*, 1–12.
- [584] X. Zhang, L. An, J. Yin, P. Xi, Z. Zheng, Y. Du, *Sci. Rep.* **2017**, *7*, 1–10.
- [585] P. T. Babar, B. S. Pawar, A. C. Lokhande, M. G. Gang, J. S. Jang, M. P. Suryawanshi, S. M. Pawar, J. H. Kim, *J. Energy Chem.* **2017**, *26*, 757–761.
- [586] J. Lee, H. Lee, B. Lim, *J. Ind. Eng. Chem.* **2018**, *58*, 100–104.
- [587] X. Zhang, B. Zhang, S. Liu, H. Kang, W. Kong, S. Zhang, Y. Shen, B. Yang, *Appl. Surf. Sci.* **2018**, *436*, 974–980.
- [588] H. A. Bandal, A. R. Jadhav, A. A. Chaugule, W. J. Chung, H. Kim, *Electrochim. Acta* **2016**, *222*, 1316–1325.
- [589] M. Tavakkoli, T. Kallio, O. Reynaud, A. G. Nasibulin, J. Sainio, H. Jiang, E. I. Kauppinen, K. Laasonen, *J. Mater. Chem. A* **2016**, *4*, 5216–5222.
- [590] Y. Zhang, G. Jia, H. Wang, B. Ouyang, R. S. Rawat, H. J. Fan, *Mater. Chem. Front.* **2017**, *1*, 709–715.
- [591] G. Ren, L. Gao, C. Teng, Y. Li, H. Yang, J. Shui, X. Lu, Y. Zhu, L. Dai, *ACS Appl. Mater. Interfaces* **2018**, *10*, 10778–10785.
- [592] Y. Yan, B. Zhao, S. C. Yi, X. Wang, *J. Mater. Chem. A* **2016**, *4*, 13005–13010.
- [593] F. Yu, H. Zhou, Z. Zhu, J. Sun, R. He, J. Bao, S. Chen, Z. Ren, *ACS Catal.* **2017**, *7*, 2052–2057.
- [594] S. Chen, Z. Kang, X. Zhang, J. Xie, H. Wang, W. Shao, X. Zheng, W. Yan, B. Pan, Y. Xie, *ACS Cent. Sci.* **2017**, *3*, 1221–1227.
- [595] D. Zhong, L. Liu, D. Li, C. Wei, Q. Wang, G. Hao, Q. Zhao, J. Li, *J. Mater. Chem. A* **2017**, *5*, 18627–18633.
- [596] L. Yang, Z. Guo, J. Huang, Y. Xi, R. Gao, G. Su, W. Wang, L. Cao, B. Dong, *Adv. Mater.* **2017**, *29*, 1–9.
- [597] V. Mani, S. Anantharaj, S. Mishra, N. Kalaiselvi, S. Kundu, *Catal. Sci. Technol.* **2017**, *7*, 5092–5104.
- [598] L.-A. Stern, L. Feng, F. Song, X. Hu, *Energy Environ. Sci.* **2015**, *8*, 2347–2351.
- [599] S. Wei, K. Qi, Z. Jin, J. Cao, W. Zheng, H. Chen, X. Cui, *ACS Omega* **2016**, *1*, 1367–1373.
- [600] A. Han, H. Zhang, R. Yuan, H. Ji, P. Du, *ACS Appl. Mater. Interfaces* **2017**, *9*, 2240–2248.
- [601] B. K. Kim, S.-K. Kim, S. K. Cho, J. J. Kim, *Appl. Catal. B Environ.* **2018**, *237*, 409–415.

Acknowledgment for image rights

Some images contained in this thesis were previously published and are now included in this thesis with the kind permission of:

Figure 1.1 Taken from Figure “CO₂ in the atmosphere and annual emissions (1750-2019)” in Ref. [6] with permission from NOAA Climate.gov (without License number).

Figure 1.2 Taken from Figure 1 in Ref. [29] with permission from IOP Publishing (License number 1119473-1).

Figure 1.3 Taken from Figure 1 in Ref. [33] with permission from Elsevier (Open Access, CC BY-NC-ND 4.0).

Figure 1.6 Taken from Figure 6 in Ref [76] with permission from The Royal Society of Chemistry (License number 1119468-2).

Figure 1.7 Taken from Figure 2 in Ref [88] with permission from The Royal Society of Chemistry (License number 1119468-1).

Figure 1.11 Adapted from Figure 15 in Ref. [59] with permission from The Royal Society of Chemistry (Open Access, CC BY 3.0).

Figure 1.13 Adapted from Figure 3 in Ref. [161] with permission from The Royal Society of Chemistry (License number 1119475-1).

Figure 7.14 Adapted from Figure 6 in Ref. [163] with permission from The Royal Society of Chemistry (License number 1119507-1) and from Figure 1 in [528] with permission from Elsevier (License number 1119510-1).

Figure 7.15 adapted from Figures 1 and 2 in Ref. [533] with permission from Annual Reviews, Inc. (License number 1119503-1)

Statutory declaration

I, Rodrigo Beltrán Suito, hereby declare in lieu of oath that I wrote this dissertation myself. This thesis has not been submitted in whole or in part to another position as part of an examination procedure. Furthermore, I declare that the work was carried out in compliance with the rules of good scientific practice of the German Research Foundation. All sources and resources used are listed and passages taken are individually identified as such.

Rodrigo Beltrán Suito

